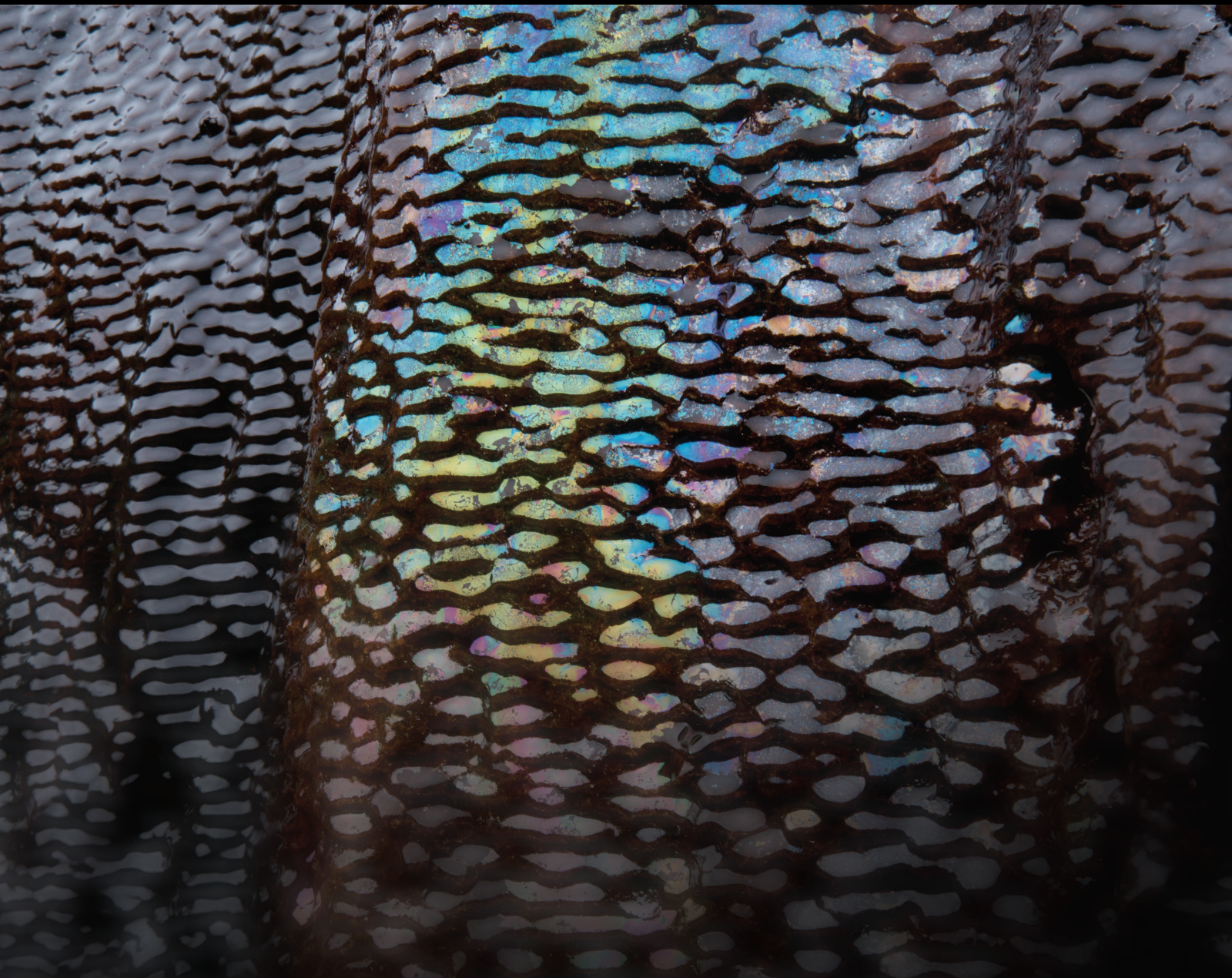


# Characterization of the Unconventional Continental Shale Oil Reservoirs

Lead Guest Editor: Kouqi Liu

Guest Editors: Mehdi Ostadhassan, Yujie Yuan, and Hui Pu



---



# **Characterization of the Unconventional Continental Shale Oil Reservoirs**

## **Characterization of the Unconventional Continental Shale Oil Reservoirs**

Lead Guest Editor: Kouqi Liu

Guest Editors: Mehdi Ostadhassan, Yujie Yuan, and  
Hui Pu



---

Copyright © 2022 Hindawi Limited. All rights reserved.

This is a special issue published in "Geofluids." All articles are open access articles distributed under the Creative Commons Attribution License, which permits unrestricted use, distribution, and reproduction in any medium, provided the original work is properly cited.

# Chief Editor

Umberta Tinivella, Italy

## Associate Editors

Paolo Fulignati , Italy  
Huazhou Li , Canada  
Stefano Lo Russo , Italy  
Julie K. Pearce , Australia

## Academic Editors

Basim Abu-Jdayil , United Arab Emirates  
Hasan Alsaedi , USA  
Carmine Apollaro , Italy  
Baojun Bai, USA  
Marino Domenico Barberio , Italy  
Andrea Brogi , Italy  
Shengnan Nancy Chen , Canada  
Tao Chen , Germany  
Jianwei Cheng , China  
Paola Cianfarra , Italy  
Daniele Cinti , Italy  
Timothy S. Collett , USA  
Nicoló Colombani , Italy  
Mercè Corbella , Spain  
David Cruset, Spain  
Jun Dong , China  
Henrik Drake , Sweden  
Farhad Ehya , Iran  
Lionel Esteban , Australia  
Zhiqiang Fan , China  
Francesco Frondini, Italy  
Ilaria Fuoco, Italy  
Paola Gattinoni , Italy  
Amin Gholami , Iran  
Michela Giustiniani, Italy  
Naser Golsanami, China  
Fausto Grassa , Italy  
Jianyong Han , China  
Chris Harris , South Africa  
Liang He , China  
Sampath Hewage , Sri Lanka  
Jian Hou, China  
Guozhong Hu , China  
Lanxiao Hu , China  
Francesco Italiano , Italy  
Azizollah Khormali , Iran  
Hailing Kong, China

Karsten Kroeger, New Zealand  
Cornelius Langenbruch, USA  
Peter Leary , USA  
Guangquan Li , China  
Qingchao Li , China  
Qibin Lin , China  
Marcello Liotta , Italy  
Shuyang Liu , China  
Yong Liu, China  
Yueliang Liu , China  
Constantinos Loupasakis , Greece  
Shouqing Lu, China  
Tian-Shou Ma, China  
Judit Mádl-Szonyi, Hungary  
Paolo Madonia , Italy  
Fabien Magri , Germany  
Micòl Mastroicco , Italy  
Agnes Mazot , New Zealand  
Yuan Mei , Australia  
Evgeniy M. Myshakin , USA  
Muhammad Tayyab Naseer, Pakistan  
Michele Paternoster , Italy  
Mandadige S. A. Perera, Australia  
Marco Petitta , Italy  
Chao-Zhong Qin, China  
Qingdong Qu, Australia  
Reza Rezaee , Australia  
Eliahu Rosenthal , Israel  
Gernot Rother, USA  
Edgar Santoyo , Mexico  
Mohammad Sarmadivaleh, Australia  
Venkatramanan Senapathi , India  
Amin Shokrollahi, Australia  
Rosa Sinisi , Italy  
Zhao-Jie Song , China  
Ondra Sracek , Czech Republic  
Andri Stefansson , Iceland  
Bailu Teng , China  
Tivadar M. Tóth , Hungary  
Orlando Vaselli , Italy  
Benfeng Wang , China  
Hetang Wang , China  
Wensong Wang , China  
Zhiyuan Wang , China  
Ruud Weijermars , Saudi Arabia

Bisheng Wu , China  
Da-yang Xuan , China  
Yi Xue , China  
HE YONGLIANG, China  
Fan Yang , China  
Zhenyuan Yin , China  
Sohrab Zendehboudi, Canada  
Zhixiong Zeng , Hong Kong  
Yuanyuan Zha , China  
Keni Zhang, China  
Mingjie Zhang , China  
Rongqing Zhang, China  
Xianwei Zhang , China  
Ye Zhang , USA  
Zetian Zhang , China  
Ling-Li Zhou , Ireland  
Yingfang Zhou , United Kingdom  
Daoyi Zhu , China  
Quanle Zou, China  
Martina Zucchi, Italy

## Contents

### **X-Ray Fluorescence for Laminated Silty Shale Reservoirs in Ordos Basin, China: Implications for Lithology Identification**

Wei Cheng , Hao Cheng , Hongyan Yu , Shaohua Zhang , Zhenliang Wang , Xiaolong Li , and Lukman Johnson 

Research Article (12 pages), Article ID 3207575, Volume 2022 (2022)

### **The Identification and Reservoir Architecture Characterization of Wandering Braided River in Nanpu 1-29 Area, Bohai Bay Basin**

Xueqian Pang , Cheng Xue, Yangping Liu, Li Yin, Yufeng Gao, and Yanshu Yin 

Research Article (17 pages), Article ID 4822714, Volume 2022 (2022)

### **Evaluation of the Oil-Bearing Properties of Shale and Shale Oil Mobility in the Fengcheng Formation in the Mahu Sag, Junggar Basin, Northwest China: A Case Study of Well Maye-1**

Wenjun He, Zhongliang Sun , Menhui Qian , Zhifeng Yang, Zhiming Li, Junying Leng, and Min Wan

Research Article (16 pages), Article ID 6206645, Volume 2022 (2022)

### **The Impact of Lamina Characteristics and Types on Organic Matter Enrichment of Chang 7<sub>3</sub> Submember in Ordos Basin, NW China**

Congsheng Bian , Wenzhi Zhao, Tao Yang, Wei Liu, Chaocheng Dai, Xu Zeng, Kun Wang, Yongxin Li, and Di Xiao

Research Article (19 pages), Article ID 6558883, Volume 2022 (2022)

### **A Method for the Inversion of Reservoir Effective Permeability Based on Time-Lapse Resistivity Logging Data and Its Application**

Hairong Zhang , Bin Zhao , Shiqi Dong , Xixin Wang , and Pengfei Jing 

Research Article (13 pages), Article ID 8704344, Volume 2022 (2022)

### **Estimation of Water Saturation in Shale Formation Using In Situ Multifrequency Dielectric Permittivity**

Yongchae Cho , Sean S. Dolan, Nishank Saxena, and Vishal Das

Research Article (16 pages), Article ID 9491979, Volume 2022 (2022)

### **Conformance Control for Tight Oil Cyclic Gas Injection Using Foam**

Falin Wei, Song Zhang, Yilin Xi, Zhouyuan Zhu , Chunming Xiong, Chuanzhen Zang, and Junjian Li 

Research Article (13 pages), Article ID 6571525, Volume 2022 (2022)

### **Study on Sedimentary Facies and Reservoir Characteristics of Paleogene Sandstone in Yingmaili Block, Tarim Basin**

Hanlie Cheng , Jianfei Wei, and Zhaoyuan Cheng

Research Article (14 pages), Article ID 1445395, Volume 2022 (2022)

### **Determination of the Fractal Dimension of CO<sub>2</sub> Adsorption Isotherms on Shale Samples**

Hongyan Qi , Zhenlin Wang , Jianglong Yu , Peirong Yu , and Guoqing Zheng 

Research Article (6 pages), Article ID 2206989, Volume 2022 (2022)

**Isothermal Desorption Hysteretic Model for Deep Coalbed Methane Development**

Songlei Tang , Hongbo Zhai , Hong Tang , and Feng Yang 

Research Article (9 pages), Article ID 5259115, Volume 2022 (2022)

**Shale Heterogeneity in Western Hunan and Hubei: A Case Study from the Lower Silurian Longmaxi Formation in Well Laidi 1 in the Laifeng-Xianfeng Block, Hubei Province**

Peng Zhang , Junwei Yang , Yuqi Huang , Jinchuan Zhang , Xuan Tang , and Chengwei Liu 

Research Article (15 pages), Article ID 8125317, Volume 2022 (2022)

**Stress Distribution and Mechanical Behaviour of Rock Mass Containing Two Openings Underground: Analytical and Numerical Studies**

Lihai Tan , Gaofeng Wang , Ting Ren, Linming Dou , Xiaohan Yang, and Shikang Song

Research Article (16 pages), Article ID 1917443, Volume 2021 (2021)

## Research Article

# X-Ray Fluorescence for Laminated Silty Shale Reservoirs in Ordos Basin, China: Implications for Lithology Identification

Wei Cheng <sup>1</sup>, Hao Cheng <sup>1</sup>, Hongyan Yu <sup>1</sup>, Shaohua Zhang <sup>2</sup>, Zhenliang Wang <sup>1</sup>, Xiaolong Li <sup>1</sup> and Lukman Johnson <sup>3</sup>

<sup>1</sup>State Key Laboratory of Continental Dynamics, Department of Geology, Northwest University, Xi'an, China

<sup>2</sup>Research Institute of Exploration & Development, Changqing Oilfield, PetroChina, Xi'an, China

<sup>3</sup>Department of Applied Geology, West Australian School of Mines, Curtin University, Perth, Australia

Correspondence should be addressed to Hongyan Yu; amelia-yu@hotmail.com

Received 23 December 2021; Accepted 16 July 2022; Published 31 July 2022

Academic Editor: Mohammed Fattah

Copyright © 2022 Wei Cheng et al. This is an open access article distributed under the Creative Commons Attribution License, which permits unrestricted use, distribution, and reproduction in any medium, provided the original work is properly cited.

Shale lithofacies were an important key for the exploration and development of unconventional oil and gas reservoirs. Previous studies usually use logging data, X-ray diffraction analysis (XRD), and scanning electron microscopy (SEM) to identify shale lithofacies, but these methods cannot accurately and quickly identify geochemical characteristics. Portable X-ray fluorescence (XRF) analysis can identify geochemical characteristics. However, few publications reported the feasibility of XRF identifying lithology. We tested the major elements of this formation systematically by X-ray fluorescence and compared the characteristics of these elements in the silty laminated shales against the calcareous laminated shale and the argillaceous shales. We analyzed the geochemical characteristics of shale using portable XRF and proposed a method to identify argillaceous shale, silty laminated shale, and calcareous laminated shale in the Chang 7 of Well Y1 (in Xiasiwan area). Furthermore, we established a lithoface identification standard. We also found that Ca/Mg of calcareous laminated shale was the highest which indicated a dry depositional environment; in contrast, lowest Ca/Mg of silty laminated shale indicated a humid depositional environment. Argillaceous shale was deposited in a strongly reducing environment because Fe content of argillaceous shale was the highest. Finally, this criterion is tested against the data from the Well Y2, and the results are in good agreement with the thin section analysis and core data.

## 1. Introduction

Shale is considered a fine-grained, brittle rock that acts as an important source of petroleum [1, 2]. There are various lithofacies in shale because of changes in the depositional environment, such as silty laminated shale, calcareous layered shale, and siliceous shale. Shale was proved to be an important source rock for conventional oil, also, as source and reservoir for unconventional oil [3]. Shale is mainly composed of fine-grained quartz, clay minerals, and other minerals that include feldspar, carbonate minerals, sulfide minerals, and oxide minerals [4]. Previous published articles proposed that there were many differences in the mineral composition and elemental concentrations of different shales [5–7]. Unfortunately, no

criteria for the classification of favorable shale lithofacies have been established.

Unconventional shale reservoirs contribute to an increased reservoir capacity as well as brittleness of shale units, which makes the shale reservoir conducive to formation of fractures during hydraulic fracturing as discussed [8–10]. There are many multiscale images techniques that can accurately identify shale microstructure at different scales in the past decade or so, such as 3D X-ray computed tomography ( $\mu$ -CT and nano-CT) and focus ion beam/scanning electron microscopy (FIB/SEM) [11, 12]. These techniques can be combined to describe shale pore space and microfracture networks at multiple length scales due to the highly anisotropic nature of shale; however, they provide no quantitative information about fine-grained

components. Silt shale and calcareous shale were more easily fractured than argillaceous shale because of the texture. Therefore, the identification of potential silty and calcareous shale is crucial for shale oil and gas development.

The lacustrine shale of Chang 7 in the Xiasiwang area developed a large number of silty laminated, which leads to its strong heterogeneity. This lacustrine shale is composed of fine-grained quartz, clay, and other minerals such as feldspar, carbonate minerals, sulfide minerals, and oxide minerals, which proposed by previous published studies [13–17]. However, these silty laminated shales and calcareous laminated shales are usually difficult to identify by conventional tools; result in the quantification and distribution of these shales cannot be obtained through direct measurement on the core or logging data. In this study, we proposed to directly measure the elemental composition on fresh cores by XRF to study the mineralogy and geochemical characteristics. We measured the major elements of Chang 7 of Well Y1 through X-ray fluorescence (XRF) and analyzed the characteristics of the major elements in silty laminated shales, argillaceous shales, and the calcareous laminated shales. There are only four XRD samples in Well Y1, and it is not representative to discuss the relationship between a little of XRD samples and XRF based on the only experimental data. Therefore, in this study, we only described the characteristics of different lithologies and minerals. Finally, a new identification model was developed to establish a criterion for lithology identification within shale laminated, based on the elemental differences in the different shales.

## 2. Geological Setting

The Ordos Basin is the second largest sedimentary basin in China with an area of  $25 \times 10^4 \text{ km}^2$ . It is located in the central part of the China and divided into six structural units, namely, the Yimeng Uplift, the Weibei Uplift, the Western Edge Thrusting Belt, the Jinxi Flexural Fold Belt, the Tianhuan Depression, and the Shanbei Slope (Figure 1).

The study area is located in the southeastern section of the Shanbei Slope, with a present dip less than  $1^\circ$  and no major faults or anticlines developed. The Yanchang Formation is one of the main oil-bearing series in this basin, and it is subdivided into 10 members, namely, Chang 10–Chang 1 from bottom to top [18]. The lacustrine Chang 7 Formation developed in the Late Triassic, with the shale members forming at specific phases of the basin development, showing the Chang 10 member was formed in the initial phase when the basin opened up, while Chang 9 to Chang 7 members was deposited during the basin expansion phase. Lastly, the Chang 6 to Chang 1 was deposited during the shrinkage phase of lacustrine basin [19, 20]. The peak of the expansion period is recorded in the Chang 7 member. During this stage, dark fine-grained shale and mudstone were deposited in semideep and deep lake settings, forming high-quality source rocks and reservoirs [21]. The study area is close to the depositional center of the lacustrine basin at this stage [22–24] and covered by the semideep and deep lake surfaces. The thickness of shale formation in this area ranges from 100 m to 135 m (Figure 2).

## 3. Materials and Methods

**3.1. X-Ray Diffraction Analysis.** The mineral composition of whole-rock has been identified by using X-ray diffraction analysis (XRD). Samples of the Chang 7 Formation from the Xiasiwang area of Ordos Basin were analyzed for whole-rock mineral composition using the D/MAX2500 X-ray diffractometer. Each sample was crushed and sieved to 200 mesh and fully dried. The angle range was  $3\text{--}85^\circ$  at the rate of  $2\theta$  for the whole-rock mineral analysis.

**3.2. X-Ray Fluorescence Analysis.** The X-ray fluorescence technique has been used to generate quantitative geochemical results for many years [25–29]. The implementation of the handheld XRF for elemental research can provide unique insights into the lithological analysis by measuring major elements with error less than 5% [30], such as silica (Si), aluminum (Al), iron (Fe), potassium (P), calcium (Ca), and magnesium (Mg). Samples from depths 1358 m to 1394 m in the Yanchang Formation in Well Y1 were measured at intervals of 0.1 m, and the lithology of the measuring points is shown in Figure 3. In order to ensure the accuracy of the measurement results, each sample was tested for up to 120 seconds, and each sample point is measured three times. The average value of each measurement was taken to analyze changes and distribution of the major elements from the shale in this shale layer.

## 4. Results

Based on core observations (Figure 4), the shale Yanchang Formation in the Well Y1 was measured from 1358 m to 1394 m. Lacustrine shale was controlled by climate and seasonal changes, which directly affected the density and thickness of laminated [31]. Moreover, the texture of lacustrine shale was sensitive to sediment environment, in turn leading to complicated laminated development. Hence, the density of laminated reflected vertical changes of lithofacies [32]. Then, we divided Well Y1 into ①~⑨ units on the basis of core observation (Table 1). Elemental measurement of these shale intervals reveals a total of 360 groups of major elements, and these were further characterized into distinct silty laminated shale and the argillaceous shale. Argillaceous shale was dark black with oily fresh surface. XRF results showed that argillaceous shale was mainly composed of Si, Al, and Fe, which consists of high clay content obtained from the XRD test. Silty laminated shale was interbed of dark shale and silt. The Si content of silty laminated shale was the highest among three types of shale, which also proved by high quartz and feldspar content. Calcareous laminated shale was black or gray black, consisting highest Ca content and lowest Al and K. XRD results indicated that calcite, dolomite, and pyrite were the highest in these three lithofacies.

**4.1. Lithologic Characteristics of Chang 7.** Through core observation, Chang 7 shale is mainly composed of argillaceous shale, silty laminated shale, and calcareous laminated shale (Figure 4). Argillaceous shale is characterized by high carbon content, thin flake, and well-developed foliation. Silty laminated shale is mainly light gray. The sandy lamina is straight, continuous, and vertically overlapping. Calcareous laminated shale is characterized by bright white calcareous lamina, clear

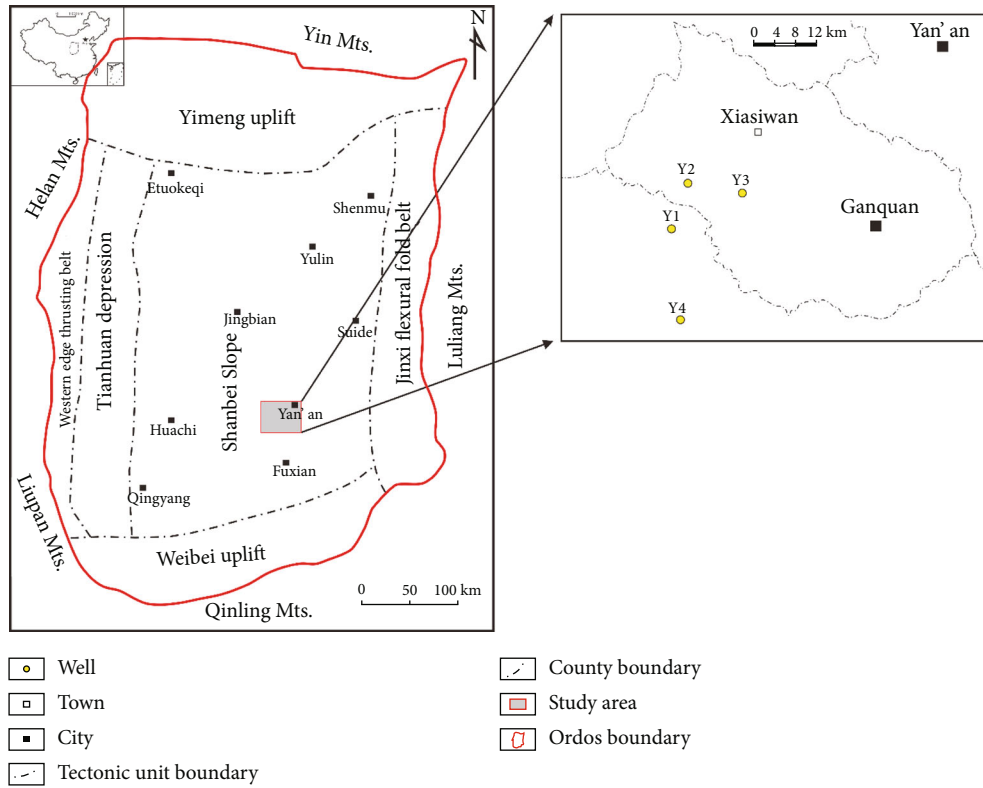


FIGURE 1: The location of Xiasiwan area in the tectonic units of Ordos Basin.

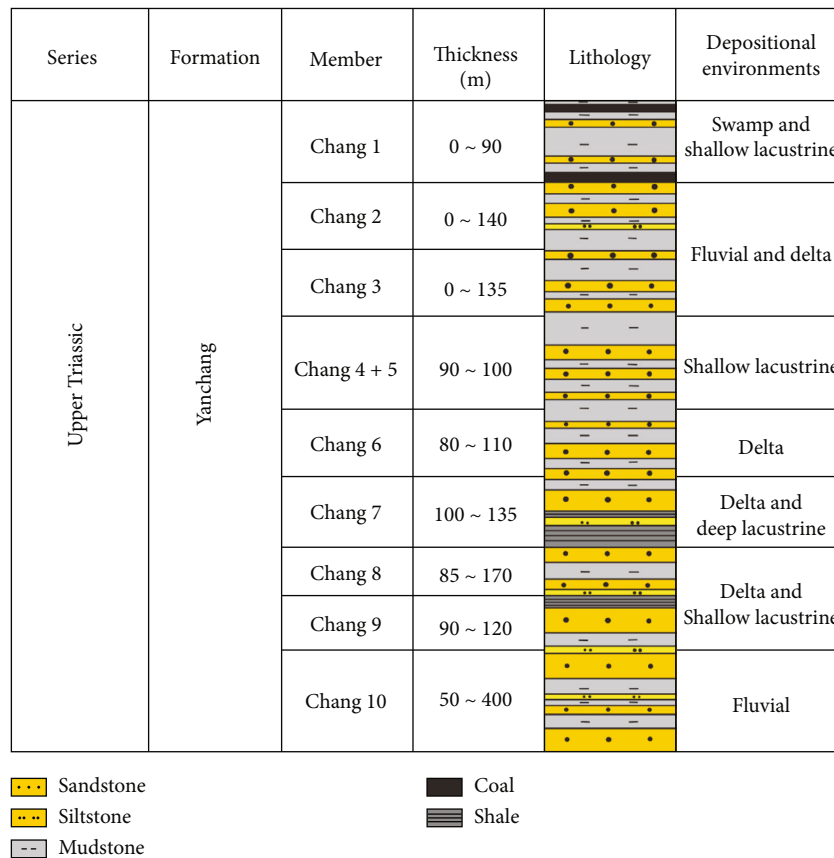


FIGURE 2: Stratigraphy and lithology of Upper Triassic Yanchang Formation (modified after [3]).

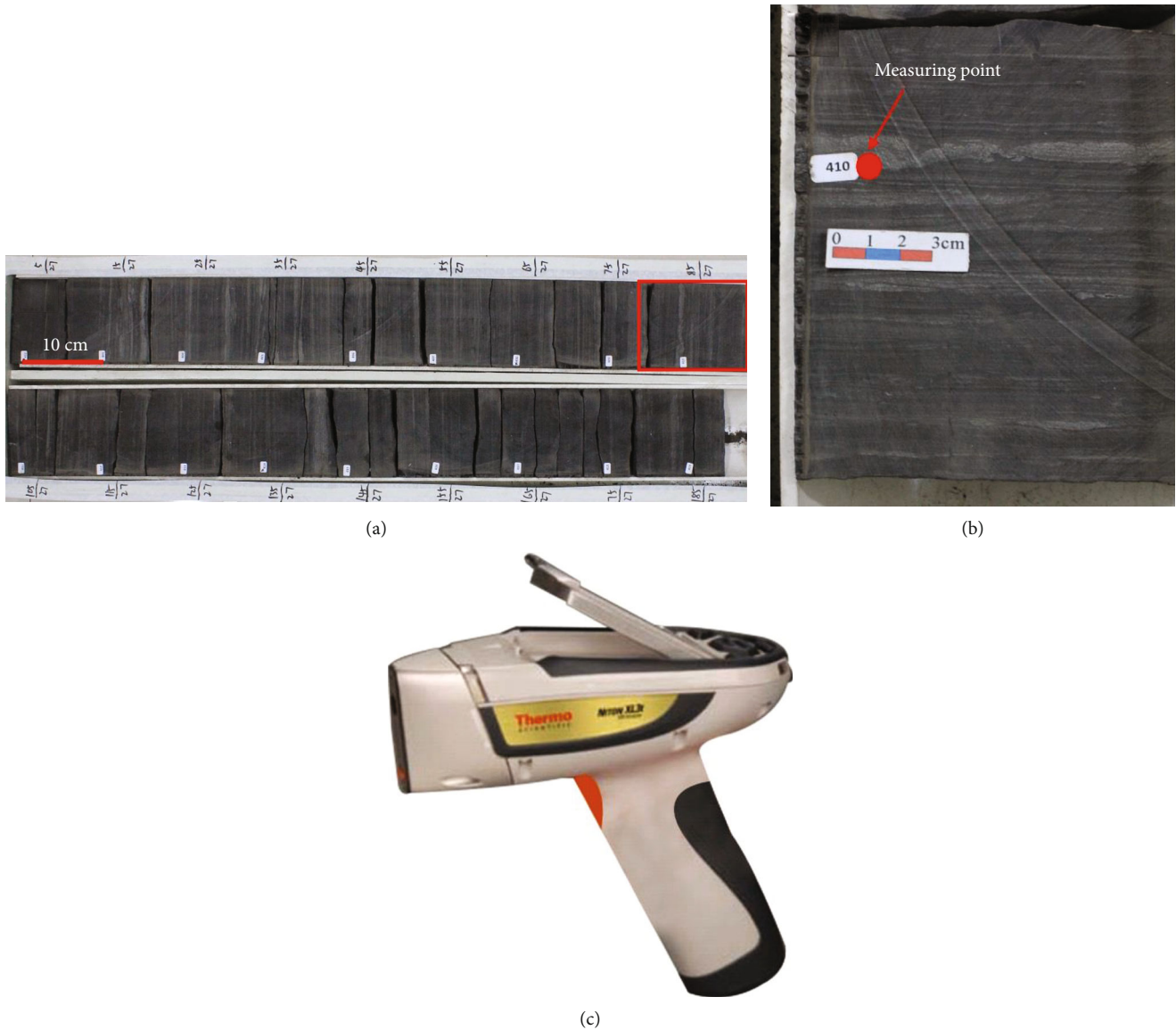


FIGURE 3: Major element test method.

boundary with shale, high brittleness, and easy to separate from shale.

**4.2. Mineralogic Characteristics of Chang 7.** X-ray diffraction analysis results from core samples show that the Chang 7 shale is composed of clay, quartz, feldspar, calcite, ankerite, siderite, and pyrite (Figure 5). Clay, quartz, and feldspar are main mineral composition. The mineral composition shows that argillaceous shale possesses higher content of clay mineral, with average values of 57.38%. The average contents of quartz and feldspar is 36.49% in argillaceous shale. Calcite, ankerite, siderite, and pyrite are merely lower than 5%. In silty laminated shales, quartz and feldspar are relatively high, with 57.38% in average, while the clay is significantly lower with proportion of 34.08%. The percentage of calcite and ankerite in calcareous laminated shale considerably larger than that of argillaceous

shale and silty laminated shale, with the proportion of 25.33% and 10.7%, respectively, and calcareous laminated shale has a relatively lower content in terms of quartz and feldspar.

**4.3. Element Composition Characteristics.** The results show that the major elements the Chang 7 shale in this well are Si, Al, Fe, K, Ca, Mg, P, S, Ti, and Mn (Table 2), with Si, Al, and Fe with concentrations greater than 5%. The concentration of Si element was the highest, with a mathematical average of 26.36%. The concentration of Al on the other hand has an average 7.91%. While, the Fe in this shale has an average concentration of 5.04%. In addition to the above three main elements, there are also a minimal amount of K (1.9% average concentration), Ca (2.9% average concentration), Mg (1.02% average concentration), and S (0.91% average concentration). The average content of P, Ti, and Mn are less than

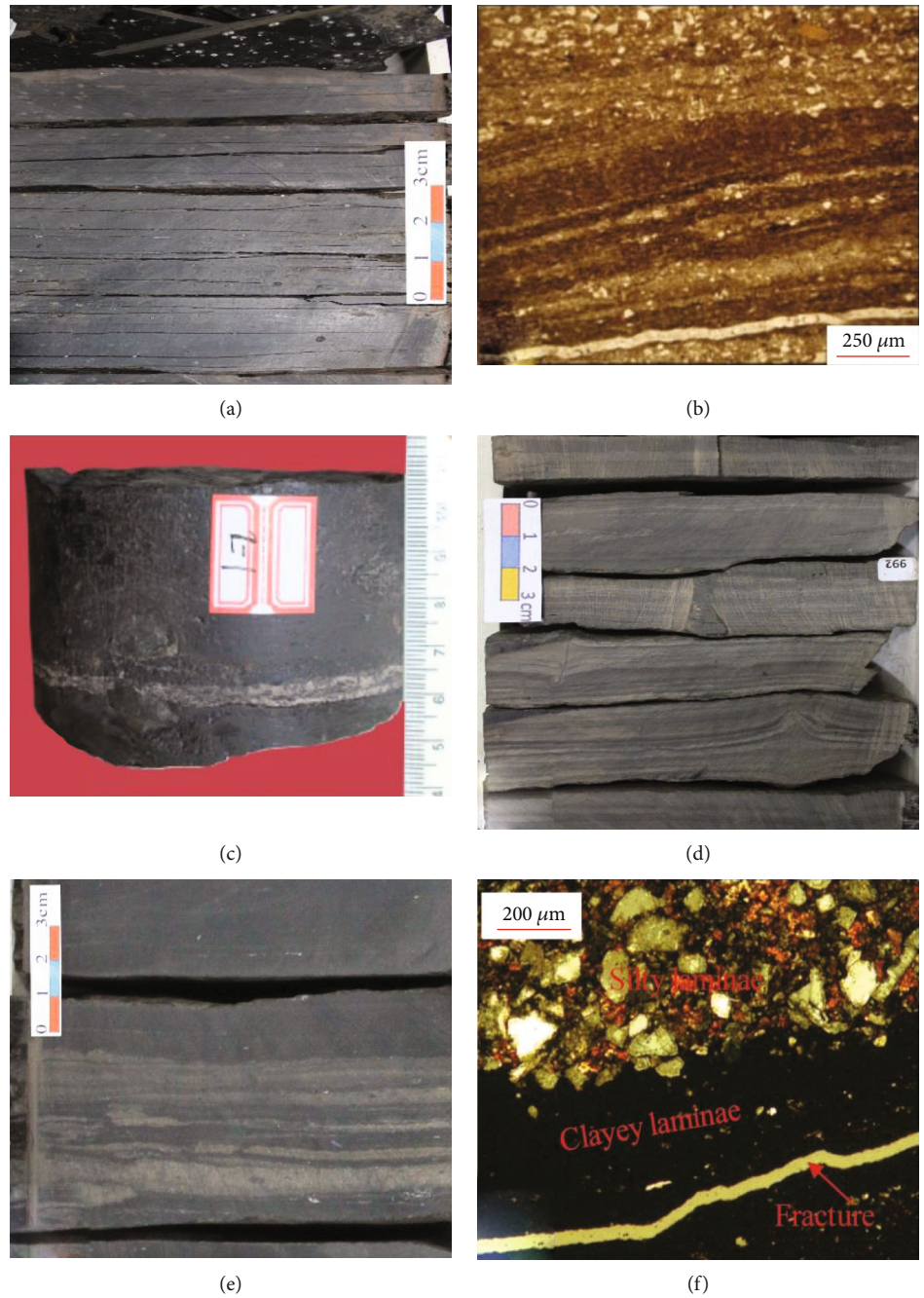


FIGURE 4: Lithologic characteristics of shale layers in Chang 7, Xiasiwan area. (a) 1369.11 m black shale in Well Y1. (b) Silty laminated in Well Y1 1371.35 m, single polarized light. (c) 1362.00 m calcareous laminated in Well Y1. (d) 1370.8 m silty laminated in Well Y1. (e) 1393.87 m silty laminated in Well Y1. (f) 1393.87 m silty laminated in Well Y1, single polarized light.

TABLE 1: Laminated density classified standard of Y1 units.

Unit	①	②	③	④	⑤	⑥	⑦	⑧	⑨
Laminated density (no./m)	31~43	5~33	20~42	6	20~56	2	16~48	5~20	42~55

0.5%. Compared with the North American shales [26], the geochemical observations of Chang 7 shale are similar to that of North American shales as shown in Table 1. See Table 1 for min and max elemental concentration of the elements discussed.

We found that the element content closely related to mineral content from XRF and XRD results plots, e.g., Ca vs. calcite, K vs. feldspar, Si vs. quartz, and (Al+Si) vs. clay (Figure 6).

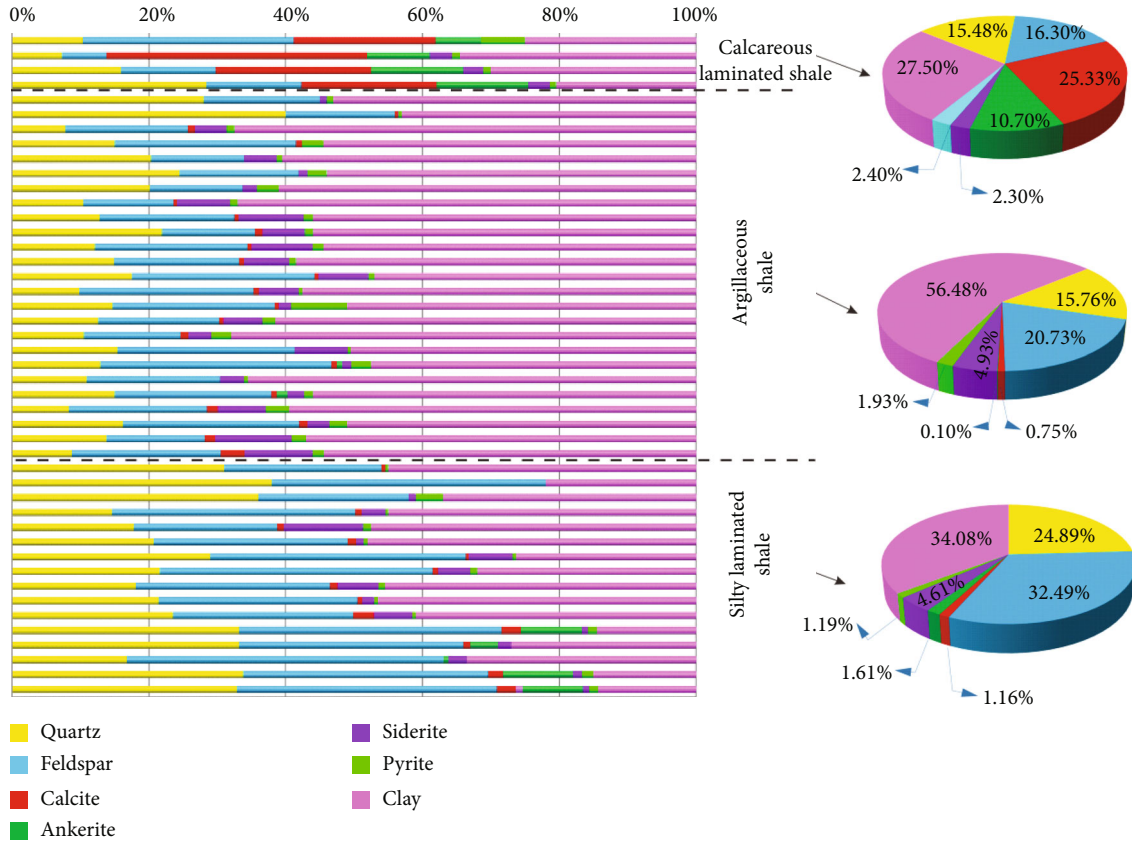


FIGURE 5: Mineral content of the studied area in Chang 7.

TABLE 2: North America Shale and Chang 7 Shale elemental concentrations.

Elements	North America shale						Chang 7 Shale				
	Woodford Fm		Barnett Fm		Ohio Shale		Eagle Ford Fm		Min	Max	Average
	Min	Max	Min	Max	Min	Max	Min	Max			
Si (%)	5.89	<b>38.2</b>	6.22	32.7	26.8	28.8	3.75	22.6	7.508	38.91	26.36
Al (%)	0.64	7.62	1.2	8.47	6.87	<b>10.77</b>	1.07	5.98	2.851	11.31	7.91
Fe (%)	0.61	<b>4.92</b>	0.64	3.54	3.09	4.6	0.43	3.57	1.72	13.81	5.04
K (%)	0.17	<b>3.51</b>	0.27	1.83	2.92	4.32	<b>0.14</b>	1.61	0.7	2.71	1.9
Ca (%)	0.07	18.1	2.77	<b>31.2</b>	0.19	0.71	9.36	34.7	0.32	24.07	2.02
Mg (%)	0.27	<b>10.25</b>	0.52	2.64	0.66	1.08	0.24	0.66	0.33	4.49	1.02
S (%)	0.46	<b>5.32</b>	0.25	2.24	0.72	2.25	0.33	3.81	0.026	5.024	0.91
P (%)	0.01	0.48	0.07	<b>0.98</b>	0.02	0.17	0.02	0.15	0.047	0.94	0.217
Ti (%)	0.04	0.33	0.07	0.46	0.4	<b>0.53</b>	0.04	0.39	0.083	0.575	0.42
Mn (%)	0.008	<b>0.325</b>	0.008	0.031	0.008	0.031	0.008	0.023	0.011	0.355	0.09

\*Bold and italic are the maximum and minimum values of this element, respectively.

## 5. Discussion

5.1. *Elemental Distribution across Chang 7 Unit.* Based on the observed lithologic changes and the distribution characteristics of silty laminated in cores in the Chang 7 (units ① ~ ⑨ Figure 7) of Well Y1, the elemental differences in each stratigraphic unit was recorded and described in sections. The frequency of occurrence of silty laminated is relatively large in

units ①, ③, ⑤, ⑦, and ⑨ units (in the upper, middle, and lower shale layers) in this Well (see Figure 7). These shales contain mainly between 16 counts and 56 counts per meter. The frequency of occurrence of silty laminated in upper ②, middle ④ and ⑥, and lower ⑧ shale units is relatively low, mainly between 5 counts per meter and 18 counts per meter.

The elemental composition in each unit was counted, respectively (Table 3), and the results show that units ①, ③,

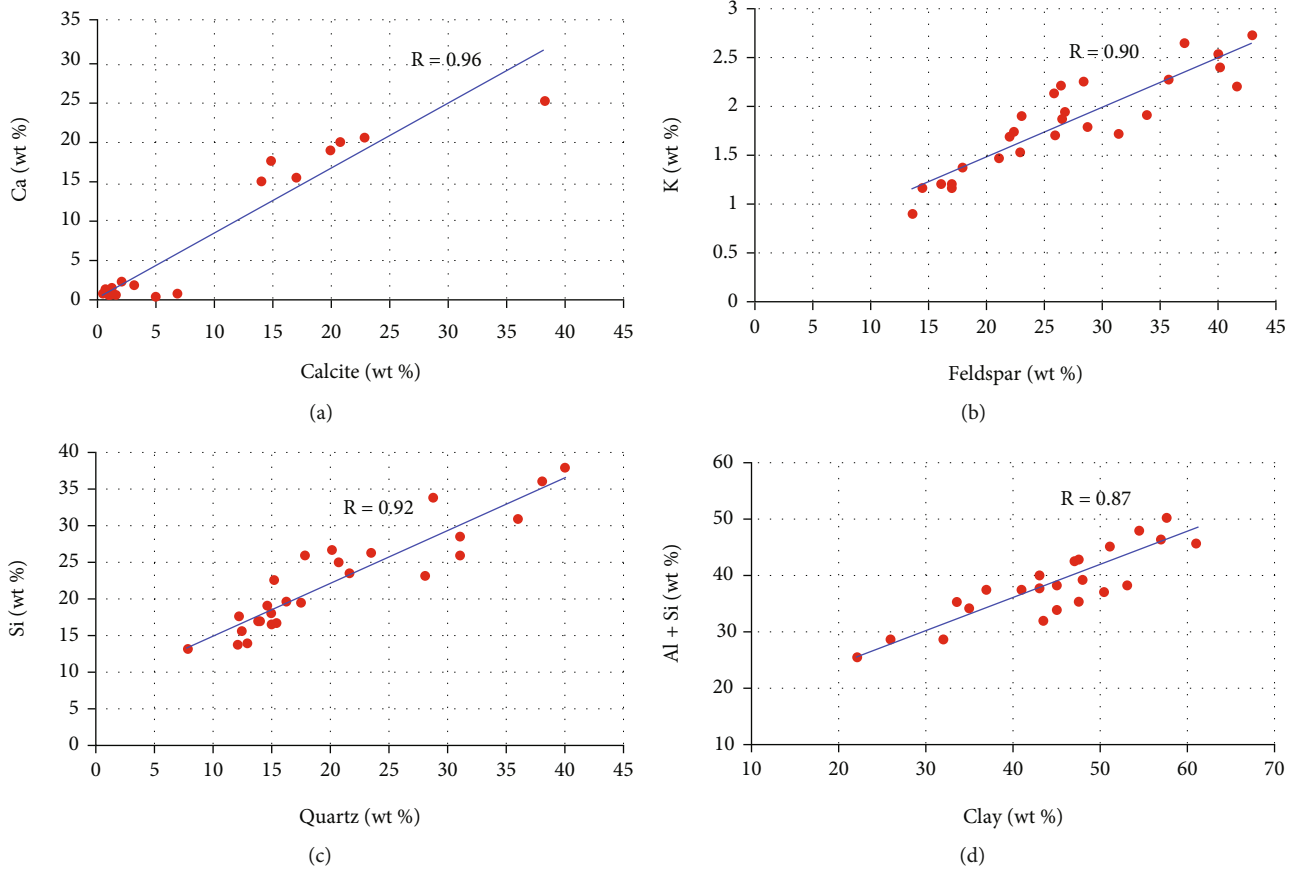


FIGURE 6: The plots of element content and mineral content.

⑤ (Figures 4(b) and 4(d)), ⑦, and ⑨ (Figures 4(e) and 4(f)), where the silty lamination is relatively dense has higher silica content, with Si values between 2.93% and approximately 38.91%. In these units, the concentration of aluminum (Al), iron (Fe), and potassium (K) is relatively low with respective values between 0.53% and approximately 10.73% for Al, 1.72%~10.10% for Fe, and 0.70%~2.51% for K. However, in units ②, ④ (Figure 4(a)), ⑥, and ⑧ with relatively lower silty lamina densities, the content of Si is relatively low, with values ranging from 11.87% to approximately 30.20%, while the content of Al, Fe, and K is relatively higher, with values 4.13%~10.63%, 3.76%~13.81%, and 0.92%~2.71%, respectively. The contents of Ca and Mg are relatively low, except for the extremely high values in ② (Figure 4(c)), ③, ⑤, ⑦, and ⑧ units.

Sedimentary rocks are the materials formed response to sedimentary environments, which is thus composed of different minerals and elements. Therefore, stratigraphic change in elemental composition implies that the sedimentary environment has slight changes during the deposition of Chang 7 shale. The unit with higher silica may be due to the relatively shallow water depth during the deposition or the inflow of a relatively large volume of water which carried siliceous debris to a deeper part s of the basin. The unit with higher concentration of Ca and Mg is due to the evolution of organic matter to form acids, and with further evolution, acid decarboxyl group to form hydrocarbons and carbonate ions. These carbonate

ions combine with Ca and Mg in water to form calcite and dolomite [9, 33–35]. Ca/Mg values can reflect climates humidity due to the varied solubility [36–38]. Calcareous laminated shale with high Ca/Mg value demonstrated dryer climate compared to other two lithofacies. Argillaceous shale showed lower Si/Al value, which can character grain size to deduce water depth [39, 40]. We thus concluded that argillaceous shale developed in deep lake. Silty laminated shale with lowest Fe content indicated that it was deposited in oxidizing environment.

The abundance of Si, Al, Fe, K, Ca, Mg, and other elements were calculated according to three lithologies, identified from drilled core and thin section analysis. These are argillaceous shales, silty laminated shales, and calcareous laminated shales. The elemental composition in the Y1 shale unit (Table 4) shows that the presence of Silica is highest in this shale, with values ranging from 14.25% to 34.17%. The contents of Al, Fe, K, and Ca were 4.12% to 11.31%, 2.48% to 13.81%, 1.14% to 2.71%, and 0.32% to 7.80%, respectively. The concentration of Mg element was the lowest in the unit, with the range between 0.33% and 1.75%.

In the silty laminated shales, Si content is the highest, which ranges from 18.30% to 38.91%. The abundance of Al, Fe, K, and Ca are 3.71% to 10.25%, 1.72% to 7.32%, 0.59% to 2.46%, and 0.51% to 7.57%, respectively. The distribution of Mg was the lowest, with 0.47% to 1.90%. On the other hand, the calcareous laminated shales have higher relative abundance of Ca, with values from 8.95% to 24.07%,

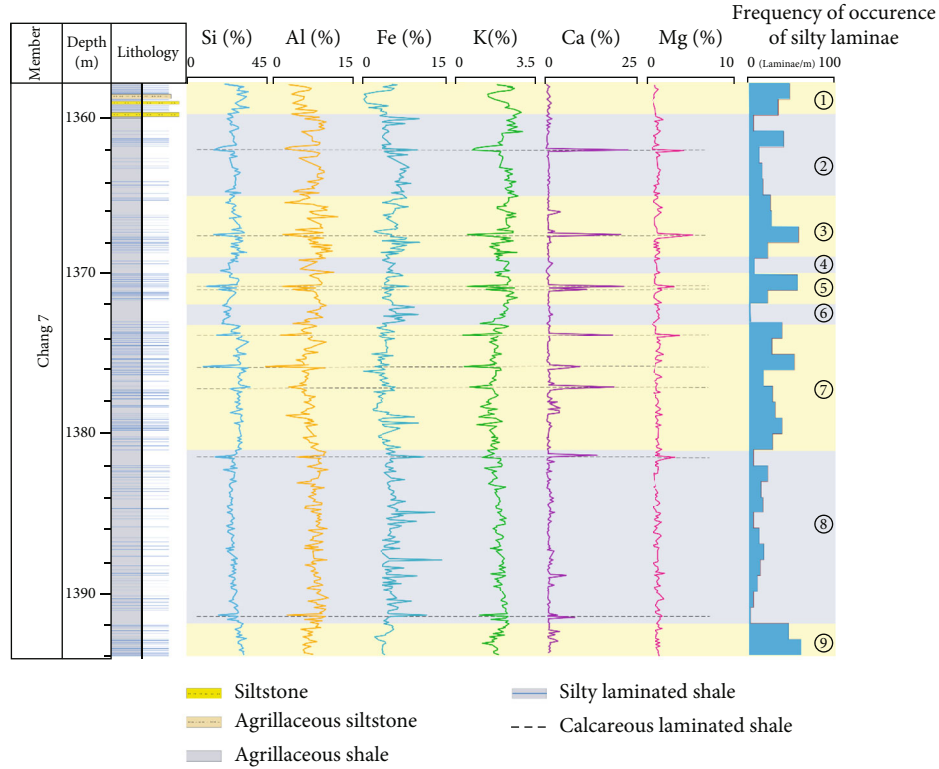


FIGURE 7: Lithology and element content of shale strata in Well Y1.

TABLE 3: Element contents of shale layers ① ~ ⑨ in Well Y1.

	Si (%)	Al (%)	Fe (%)	K (%)	Ca (%)	Mg (%)
①	26.84~38.91	5.18~9.02	1.72~5.67	1.47~2.38	0.54~1.36	0.71~1.05
②	11.87~30.20	4.13~10.16	3.76~9.98	0.92~2.71	0.32~24.07	0.33~3.57
③	7.58~30.55	2.93~10.73	2.87~10.03	0.74~2.51	0.70~22.18	0.61~4.49
④	17.16~21.24	5.57~11.31	4.32~6.30	1.78~2.51	0.44~1.27	0.67~1.23
⑤	9.96~30.03	2.58~8.68	2.87~7.23	0.73~2.42	0.63~21.87	0.62~2.62
⑥	17.16~22.56	4.47~9.57	4.55~9.81	1.69~2.55	0.59~1.43	0.36~1.19
⑦	2.93~32.41	0.53~9.61	2.76~10.10	0.70~1.95	0.66~17.75	0.47~3.15
⑧	14.5~29.76	4.55~10.63	3.77~13.81	1.14~2.22	0.51~7.80	0.52~2.71
⑨	25.37~31.72	6.06~9.19	3.14~4.85	0.91~1.81	0.62~3.65	0.67~1.22

TABLE 4: Element concentration of three types of lithology.

	Si (%)	Al (%)	Fe (%)	K (%)	Ca (%)	Mg (%)
Argillaceous shale	14.25~34.17	4.12~11.31	2.48~13.81	1.14~2.71	0.32~7.80	0.33~1.75
Silty laminated shale	18.30~38.91	3.71~10.25	1.72~7.32	0.59~2.46	0.51~7.57	0.47~1.90
Calcareous laminated shale	2.93~18.54	0.53~5.40	3.26~9.65	0.70~1.94	8.95~24.07	1.35~4.49

followed by Si, Al, Fe, and Mg, which range from 2.93% to 18.54%, 0.53% to 5.40%, 3.26% to 9.65%, and 1.35% to 4.49%, respectively. Also, the abundance of potassium is the lower with values between 0.70% and 1.94%. It can be observed that there are differences in the concentration of various elements in distinct lithologies in these shale layers. In consequence, the visual discrimination of the encountered shales in the Well Y1 can be attributed to the differences in these elemental compositions.

**5.2. Standard for Fine Scale Lithology Identification.** Based on the above analysis, we propose a criterion for lithology identification in shale layers with Si, Al, and Ca, which is sensitive to calcareous laminated shale. According to the ternary diagram of relative percentages of Si, Al, and Ca (Figure 8(a)), the content of Ca in calcareous laminated shale is obviously higher than that in argillaceous shale and silty laminated shale. Silty laminated shales contain relatively more Si element, while

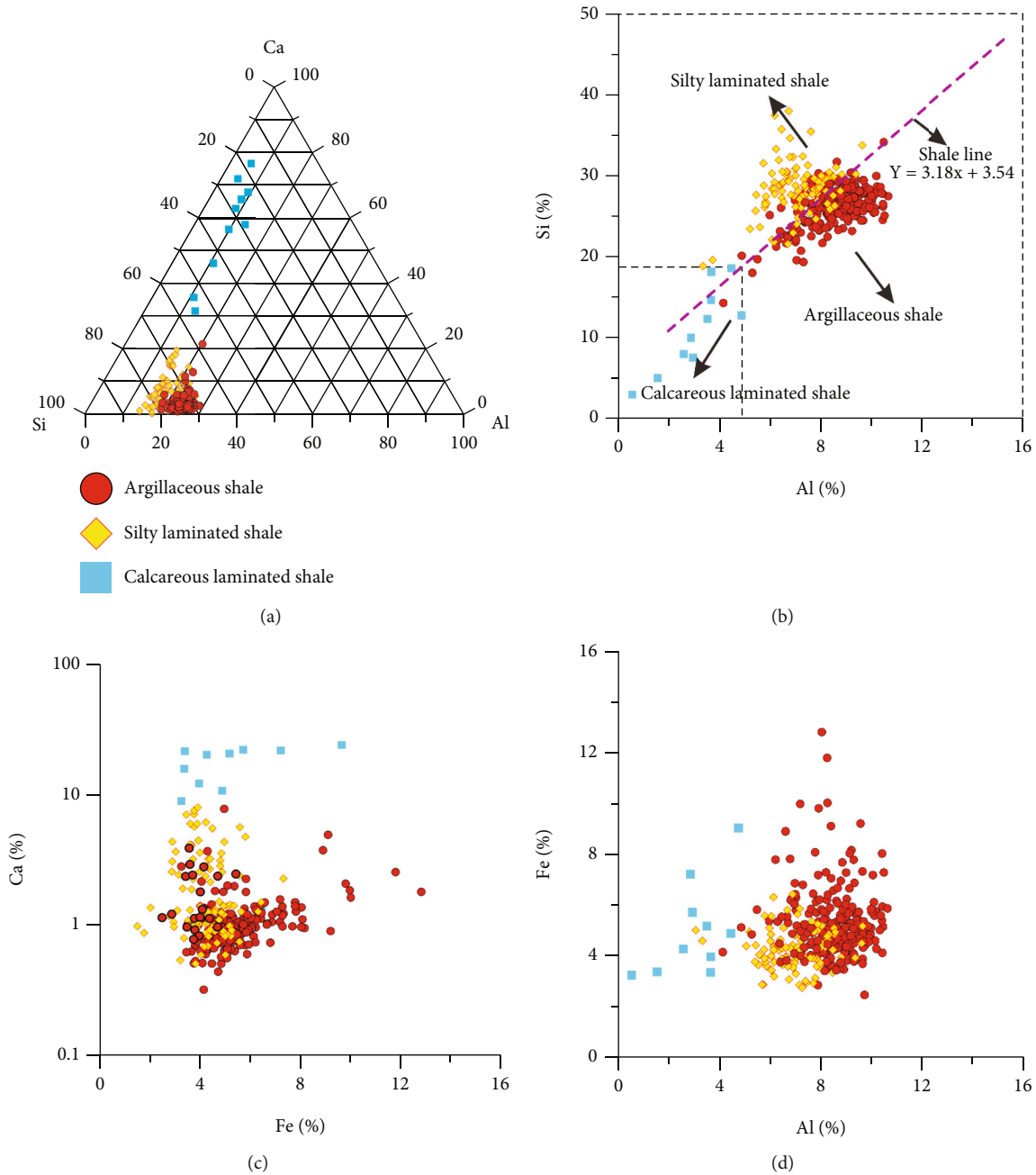


FIGURE 8: Element content relationship of different lithologies in Well Y1.

argillaceous shales contain a relatively higher Al element. However, the boundary between Ca and Al is not obvious in the ternary diagram. Cross-plot of Si and Al content (Figure 8(b)) shows that the content of Si and Al in argillaceous shale presents a linear relationship (shale line). Silty laminated shale plots above the shale line, and its Si content is relatively high. Using the shale line as the boundary, while argillaceous shale plots mainly below this line. The third type, the calcareous laminated shales, which are characterized by lower Si and Al content, thus plots in the lower quadrant of this plot.

In calcareous laminated shales, the concentration of Ca and Mg is relatively high, while the values of Si and Al is relatively low. Due to the influence of high concentration of Ca,

Si, and Al is diluted to a large extent. Calcareous laminated shale has relatively high Ca content (>8.95%) (Figure 8(c)), and Al content is less than 4.49% (Figure 8(d)). However, there is no significant difference between identifying argillaceous shale from silty laminated shale. Therefore, we used the shale line as a boundary (Figure 8(b)). Lithology interpretation for points which lie above shale line is identified as silty laminated shale; while the points below the shale line with Ca element content greater than 8.95% identified as calcareous shales. Also, in this case, the rest of data represent argillaceous shales. Based on this, a criterion for lithologic identification from elemental logging in shale layers is proposed.

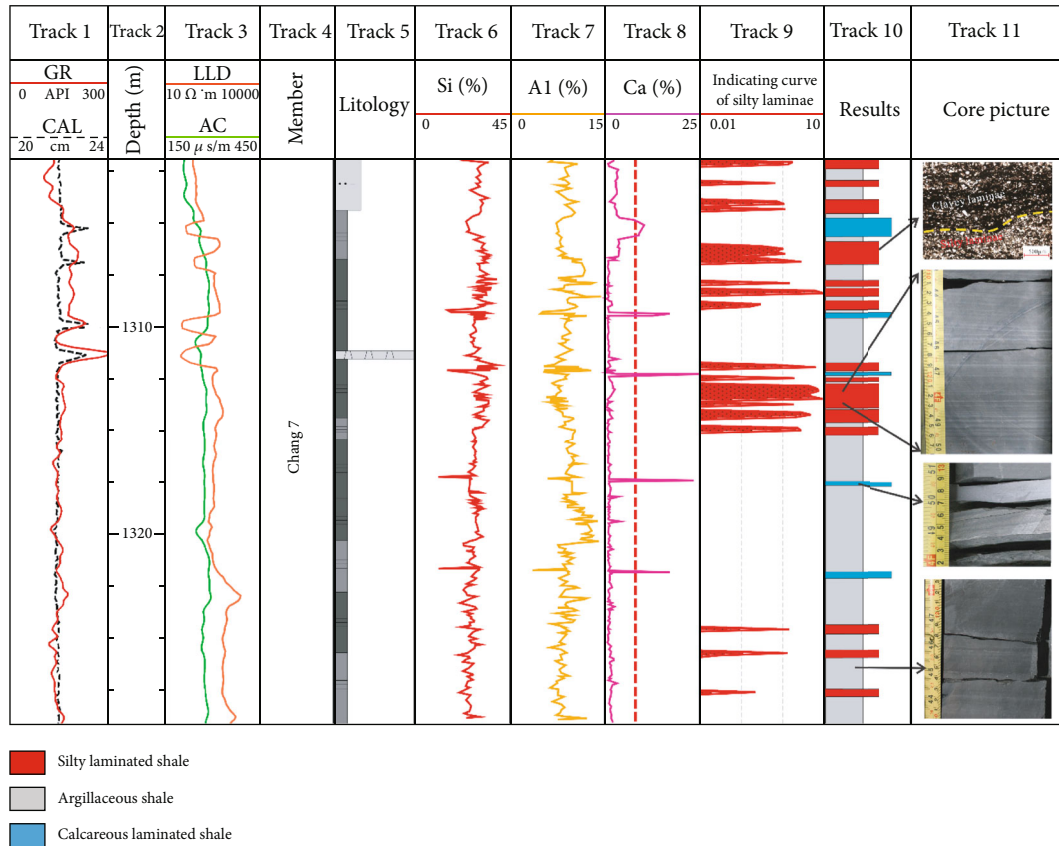


FIGURE 9: Identification results of silty laminated shale in Well Y2.

**5.3. Validation of Lithology Identification.** Based on the identification criteria described in this paper, the lithology of Chang 7 shale unit in Well Y2 was identified (Figure 9). The thickness of silty laminated shale in the well is between 0.33 m and 4.8 m (track 10 on the Figure 9). Calcareous laminated shale (track 10 on the Figure 9) is scattered throughout the shale series and are usually in thin laminated; the uncharacterized shale here is referred to as argillaceous shale.

The silty laminated shale is interbedded with gray or white silty laminated and black-gray shale. Under single polarized light, the light and dark layers are interbedded with the dark parts comprising of fine particle size, while the light layer comprises the coarser particle size. The results were validated with the thin section and drill cores and showed good agreement with the predicted lithology, while the core observation suggested silty laminated shales in depth (1312.9 ~ 1313.13 m), which is also consistent with the predicted results, thus indicating that the identification criteria established by XRF can be used to identify different suites of shales within a formation.

## 6. Conclusion

- (1) The elemental make up of shale layers varies greatly, and there are differences among different lithologies; the content of Fe, Al, and other elements in shale is relatively high, with Fe ranging from 2.48% to 13.81% and Al from 4.12% to 11.31% in the study well. Silty laminated shale is characterized by high abundance

of Si, ranging from 18.30% to 38.91%. Calcareous laminated shale on the other hand has relatively high concentration of Ca and Mg, ranging from 8.95% to 24.07% and Mg ranging from 1.35% to 4.49%, respectively

- (2) Based on the abundance of elements Si, Al, Fe, and Ca in shale layers, the lithology identification standard of shales was established. Taking the shale line as the boundary, lithologies with Si content above the shale line is interpreted as silty laminated shale, while the lithologies with Ca abundance greater than 8.95% and plots below the shale line is interpreted as calcareous laminated shale, the rest of data represent argillaceous shales
- (3) A test from Well Y2 shows that silty laminated shale, calcareous laminated shale, and argillaceous shale can be predicted by the lithologic identification criteria described, and the identification results are in good agreement with thin section analysis and visual identification from drilled core

## Data Availability

Data are available upon request to the corresponding author's email address: amelia-yu@hotmail.com.

## Conflicts of Interest

The authors declare that they have no competing interests.

## Acknowledgments

This work was jointly funded by the National Natural Science Foundation of China (41902145), Natural Science Basic Research Plan in Shaanxi Province of China (2020JQ-594), Young researcher of science and technology and foreign expert service plan in Shaanxi Province (2021KJXX-28, 2021JZY-016), and Changqing Oilfield, PetroChina (ZDZX2021-05).

## References

- [1] A. Aplin and J. Macquaker, "Mudstone diversity: origin and implications for source, seal, and reservoir properties in petroleum systems," *AAPG Bulletin*, vol. 95, no. 12, pp. 2031–2059, 2011.
- [2] K. Liu, L. Wang, M. Ostadhassan, J. Zou, B. Bubach, and R. Rezaee, "Nanopore structure comparison between shale oil and shale gas: examples from the Bakken and Longmaxi formations," *Petroleum Science*, vol. 16, no. 1, article 277, pp. 77–93, 2019.
- [3] Y. Yuan, R. Rezaee, E. Al-Khdheawi et al., "Impact of composition on pore structure properties in shale: implications for micro-/mesopore volume and surface area prediction," *Energy & Fuels*, vol. 33, no. 10, pp. 9619–9628, 2019.
- [4] J. Chermak and M. Schreiber, "Mineralogy and trace element geochemistry of gas shales in the United States: environmental implications," *International Journal of Coal Geology*, vol. 126, article S0166516213002723, pp. 32–44, 2014.
- [5] J. Rimstidt, J. Chermak, and M. Schreiber, "Processes that control mineral and element abundances in shales," *Earth-Science Reviews*, vol. 171, article S0012825216302860, pp. 383–399, 2017.
- [6] Y. Yuan, R. Rezaee, H. Yu, J. Zou, K. Liu, and Y. Zhang, "Compositional controls on nanopore structure in different shale lithofacies: a comparison with pure clays and isolated kerogens," *Fuel*, vol. 303, article S0016236121009583, p. 121079, 2021.
- [7] J. Du, L. Hu, J. Meegoda, and G. Zhang, "Shale softening: observations, phenomenological behavior, and mechanisms," *Applied Clay Science*, vol. 161, article S0169131718301935, pp. 290–300, 2018.
- [8] D. Ross and R. Bustin, "The importance of shale composition and pore structure upon gas storage potential of shale gas reservoirs," *Marine and Petroleum Geology*, vol. 26, no. 6, article S0264817208001153, pp. 916–927, 2009.
- [9] J. Yin, C. Gao, M. Zhu et al., "Oil accumulation model and its main controlling factors in Lower Yanchang Formation, Wuqi-Dingbian area, Ordos Basin, China," *Geofluids*, vol. 2021, Article ID 5511563, 10 pages, 2021.
- [10] M. Raji, D. Gröcke, H. Greenwell, J. Gluyas, and C. Cornford, "The effect of interbedding on shale reservoir properties," *Marine and Petroleum Geology*, vol. 67, article S0264817215001439, pp. 154–169, 2015.
- [11] M. Arif, M. Mahmoud, Y. Zhang, and S. Iglauer, "X-ray tomography imaging of shale microstructures: a review in the context of multiscale correlative imaging," *International Journal of Coal Geology*, vol. 233, article S0166516220306376, p. 103641, 2021.
- [12] H. Dong, Y. Zhang, M. Lebedev, M. Arif, Y. Yuan, and S. Iglauer, "Simulating coal permeability change as a function of effective stress using a microscale digital rock model," *Energy & Fuels*, vol. 35, no. 10, pp. 8756–8762, 2021.
- [13] H. Yu, Z. Wang, R. Rezaee et al., "Applications of nuclear magnetic resonance (NMR) logs in shale gas reservoirs for pore size distribution evaluation," in *SPE/AAPG/SEG Unconventional Resources Technology Conference*, One Petro, 2017.
- [14] H. Yu, Y. Zhang, M. Lebedev et al., "X-ray micro-computed tomography and ultrasonic velocity analysis of fractured shale as a function of effective stress," *Marine and Petroleum Geology*, vol. 110, article S0264817219303253, pp. 472–482, 2019.
- [15] B. Liu, H. Wang, X. Fu et al., "Lithofacies and depositional setting of a highly prospective lacustrine shale oil succession from the Upper Cretaceous Qingshankou Formation in the Gulong sag, northern Songliao Basin, northeast China," *AAPG Bulletin*, vol. 103, no. 2, pp. 405–432, 2019.
- [16] M. Arif, Y. Zhang, and S. Iglauer, "Shale wettability: data sets, challenges, and outlook," *Energy & Fuels*, vol. 35, no. 4, pp. 2965–2980, 2021.
- [17] B. Liu, Y. Lu, Y. Meng, X. Li, X. Gao, and Q. Ma, "Petrologic characteristics and genetic model of lacustrine lamellar fine-grained rock and its significance for shale oil exploration: a case study of Permian Lucaogou Formation in Malang sag, Santanghu Basin, NW China," *Petroleum Exploration and Development*, vol. 42, no. 5, article S1876380415300604, pp. 656–666, 2015.
- [18] J. Zhao, N. Mountney, C. Liu, H. Qu, and J. Lin, "Outcrop architecture of a fluvio-lacustrine succession: upper Triassic Yanchang Formation, Ordos Basin, China," *Marine and Petroleum Geology*, vol. 68, article S0264817215300891, pp. 394–413, 2015.
- [19] L. Xiao, Z. Li, Y. Hou, L. Xu, L. Wang, and Y. Yang, "Characteristics of organic macerals and their influence on hydrocarbon generation and storage: a case study of continental shale of the Yanchang Formation from the Ordos Basin, China," *Geofluids*, vol. 2021, Article ID 5537154, 17 pages, 2021.
- [20] H. Guo, W. Jia, P. Peng et al., "The composition and its impact on the methane sorption of lacustrine shales from the Upper Triassic Yanchang Formation, Ordos Basin, China," *Marine and Petroleum Geology*, vol. 57, article S026481721400186X, pp. 509–520, 2014.
- [21] J. Fu, S. Li, L. Xu, and X. Niu, "Paleo-sedimentary environmental restoration and its significance of Chang 7 member of triassic Yanchang formation in Ordos Basin, NW China," *Petroleum Exploration and Development*, vol. 45, no. 6, article S1876380418301046, pp. 998–1008, 2018.
- [22] Y. Yang, W. Li, and L. Ma, "Tectonic and stratigraphic controls of hydrocarbon systems in the Ordos basin: a multicycle cratonic basin in Central China," *AAPG Bulletin*, vol. 89, no. 2, pp. 255–269, 2005.
- [23] L. Zeng and X. Li, "Fractures in sandstone reservoirs with ultra-low permeability: a case study of the Upper Triassic Yanchang Formation in the Ordos Basin, China," *AAPG Bulletin*, vol. 93, no. 4, pp. 461–477, 2009.
- [24] X. Yuan, S. Lin, Q. Liu et al., "Lacustrine fine-grained sedimentary features and organic-rich shale distribution pattern: a case study of Chang 7 Member of Triassic Yanchang Formation in Ordos Basin, NW China," *Petroleum Exploration and Development*, vol. 42, no. 1, article S1876380415600040, pp. 37–47, 2015.

- [25] H. Rowe, N. Hughes, and K. Robinson, "The quantification and application of handheld energy-dispersive x-ray fluorescence (ED-XRF) in mudrock chemostratigraphy and geochemistry," *Chemical Geology*, vol. 324-325, pp. 122-131, 2012.
- [26] S. Lim, T. Murphy, K. Wilson, and K. Irvine, "Leaded paint in Cambodia—pilot-scale assessment," *Journal of Health and Pollution*, vol. 5, no. 9, pp. 18-24, 2015.
- [27] G. Hall, G. Bonham-Carter, and A. Buchar, "Evaluation of portable X-ray fluorescence (pXRF) in exploration and mining: phase 1, control reference materials," *Geochemistry: Exploration, Environment, Analysis*, vol. 14, no. 2, pp. 99-123, 2014.
- [28] D. Li, R. Li, Z. Zhu et al., "Rare earth elements geochemistry characteristics and their geological implications of lacustrine oil shale from Chang 7 oil layer in southern Ordos Basin, China," *Geological Journal*, vol. 52, pp. 119-131, 2017.
- [29] B. Liu, Y. Song, K. Zhu, P. Su, X. Ye, and W. Zhao, "Mineralogy and element geochemistry of salinized lacustrine organic-rich shale in the Middle Permian Santanghu Basin: implications for paleoenvironment, provenance, tectonic setting and shale oil potential," *Marine and Petroleum Geology*, vol. 120, article S0264817220303524, p. 104569, 2020.
- [30] H. Cao, H. Wang, and R. Zhao, "The application of the handheld energy-dispersive X-ray fluorescence (ED-XRF) in the cyclostratigraphy research—a case study from the Xiaogou formation of the lower cretaceous in the Qingxi Sag, Jiuquan Basin," *Earth Science*, vol. 42, no. 12, pp. 2299-2311, 2017.
- [31] O. Lazar, K. Bohacs, J. Macquaker, J. Schieber, and T. Demko, "Capturing key attributes of fine-grained sedimentary rocks in outcrops, cores, and thin sections: nomenclature and description guidelines," *Journal of Sedimentary Research*, vol. 85, no. 3, pp. 230-246, 2015.
- [32] T. Zhang, S. Hu, Q. Bu et al., "Effects of lacustrine depositional sequences on organic matter enrichment in the Chang 7 Shale, Ordos Basin, China," *Marine and Petroleum Geology*, vol. 124, article S0264817220305614, p. 104778, 2021.
- [33] R. Zhu, J. Cui, Z. Luo, Z. Mao, K. Xi, and L. Su, "A discussion on the genesis of carbonate concretions in the Chang 7 Member of the Middle-Upper Triassic Yanchang Formation of Ordos basin," *Acta Geologica Sinica*, vol. 95, no. 11, pp. 3442-3454, 2020.
- [34] W. Li and S. Li, "Review on the high-resolution varved lake sediments as a proxy of paleoenvironment," *Advances in Earth Science*, vol. 14, no. 2, p. 172, 1999.
- [35] G. Wang, "Laminae combination and genetic classification of Eocene shale in Jiyang Depression," *Journal of Jilin University (Earth Science Edition)*, vol. 42, no. 3, pp. 666-680, 2012.
- [36] P. Wignall and R. Twitchett, "Oceanic anoxia and the end Permian mass extinction," *Science*, vol. 272, no. 5265, pp. 1155-1158, 1996.
- [37] M. Adabi, M. Salehi, and A. Ghabeishavi, "Depositional environment, sequence stratigraphy and geochemistry of Lower Cretaceous carbonates (Fahliyan Formation), south-west Iran," *Journal of Asian Earth Sciences*, vol. 39, no. 3, article S1367912010000891, pp. 148-160, 2010.
- [38] J. Hu, W. Yang, S. Li et al., "Trace element and isotope (C, S, Sr, Nd, Fe) geochemistry constraints on the sedimentary environment of the early Neoproterozoic Shilu BIF and associated dolostones, South China," *Precambrian Research*, vol. 372, article S0301926822000547, p. 106610, 2022.
- [39] M. Caetano, R. Prego, C. Vale, H. Pablo, and J. Marmolejo-Rodríguez, "Record of diagenesis of rare earth elements and other metals in a transitional sedimentary environment," *Marine Chemistry*, vol. 116, no. 1-4, article S0304420309001273, pp. 36-46, 2009.
- [40] M. Yalcin, D. Nyamsari, O. Ozer Atakoglu, and F. Yalcin, "Chemical and statistical characterization of beach sand sediments: implication for natural and anthropogenic origin and paleo-environment," *International journal of Environmental Science and Technology*, vol. 19, no. 3, article 3280, pp. 1335-1356, 2022.

## Research Article

# The Identification and Reservoir Architecture Characterization of Wandering Braided River in Nanpu 1-29 Area, Bohai Bay Basin

Xueqian Pang <sup>1,2</sup>, Cheng Xue,<sup>3</sup> Yangping Liu,<sup>3</sup> Li Yin,<sup>1,2</sup> Yufeng Gao,<sup>1,2</sup>  
and Yanshu Yin <sup>1,2</sup>

<sup>1</sup>School of Geosciences, Yangtze University, Hubei, Wuhan 430100, China

<sup>2</sup>Key Laboratory of Exploration Technologies for Oil and Gas Resources, Yangtze University, Ministry of Education, Wuhan 430100, China

<sup>3</sup>Exploration and Development Research Institute, Jidong Oilfield, PetroChina, Hebei, Tangshan 063200, China

Correspondence should be addressed to Yanshu Yin; [yys@yangtzeu.edu.cn](mailto:yys@yangtzeu.edu.cn)

Received 8 March 2022; Revised 3 May 2022; Accepted 29 June 2022; Published 21 July 2022

Academic Editor: Yujie Yuan

Copyright © 2022 Xueqian Pang et al. This is an open access article distributed under the Creative Commons Attribution License, which permits unrestricted use, distribution, and reproduction in any medium, provided the original work is properly cited.

Nanpu 1-29 Area of Jidong Oilfield in China is currently in the stage of high water cut and low recovery degree. The remaining oil development and adjustment are difficult because of the complex reservoir heterogeneity and the lack of analysis of the reservoir architecture due to the unclear river type. This study first used sedimentary background, granularity, core, and sand body distribution to determine the river type and believed it belongs to the wandering braided river. Combined with core and logging data, four types of sedimentary architectural elements were found in the study area, namely, channel bar, braided channel, floodplain, and basalt. Based on the scale measurement of many similar modern wandering braided rivers, core data, and empirical formulas, the scales of the braided rivers were determined. The quantitative relationships among the scale of the braided river, the channel bar, and the braided channel were established. With this constraint, the reservoir architecture was anatomized. The results showed two filling types of the braided channels, including sandy filling and muddy filling. The combination patterns of the channel bars and the braided channels could be divided into three types, namely, superimposed, standalone, and contact, and the contact type was the primary type. On the whole, it showed the geometric morphological characteristics of the flat top convex at the bottom of the channel bar and the flat bottom convex at the top of the braided river channel. A careful measure of the architectural element was executed. The length of the single braided flow belts was 365.16-1349.72 m, and the width was 270.57-1160.54 m. The channel bar's length was distributed 158.89-318.32 m, and the width was distributed 75.97-116.41 m. The braided river's width was distributed 16.81-180.05 m. The length and width ratio of the channel bar was concentrated between 2 and 4, which manifested wide bar and narrow river channel mode. Finally, the static distribution model and dynamic response curve were compared to verify the correctness of the reservoir architecture characteristics to guide the subsequent development of the oilfield.

## 1. Introduction

Reservoir architecture originated from the study of outcrops in ancient rivers. In 1977, Allen, the American scholar, first introduced the architectural term “Architecture” into the study of river reservoir sedimentation, which was used to describe the geometric form of the braided channel, overflow sedimentation, and their internal structure characteristics [1]. Under the influence of Allen's thought, Miall first pro-

posed a complete analysis method of reservoir architecture elements of river facies [2], which defined the reservoir architecture as the geometry, size, direction, and interrelationship of reservoirs and their internal constituent units. Accordingly, the traditional meandering rivers and the braided rivers were subdivided. The braided rivers were divided into the sandy braided rivers and the gravel braided rivers. The sandy braided rivers included deeper and year-round sandy braided rivers, shallower and year-round sandy braided rivers, high-energy

sandy braided rivers, flood-end braided rivers, and other types [3]. Bridge and Tye used the ground penetrating radar technology to measure the scale of modern braided river sediments, and found that the shapes of the channel bar and the braided channel developed by braided river were very clear, and their thicknesses were similar [4]. Skelly et al. measured the sedimentary scale of the Niobrara River using ground penetrating radar, then found that the channel bars obviously could not be cut to the bottom by the braided channels, and their interfaces were poorly sharp and differed significantly [5]. Longxin and Guoliang and Dali et al. subdivided the sandy braided rivers into two categories based on the interpretation of the outcrop of the Datong braided river [6, 7], including branching type and wandering type. In her opinion, the branching type was a deeper water type with perennial flowing water, and the boundary between the channel bar and the river channel was clear. The wandering type was often unable to completely cut the channel bar due to the swing of the river, and the boundary between them was not noticeable. Controlled by the differences in their hydrodynamic environment and sedimentary environment, the developments of the muddy interlayers in the two different braided rivers were also various, resulting in apparent differences in sedimentary architecture and their control of oil-water distribution. In addition, the geometrical morphology of the channel developed in the deep water environment and the braided river is similar, but the sedimentary genesis of the two is quite different. The braided channel is traction flow deposition, while the deep water channel is gravity flow deposition. And during the development of deep water channel, sandbody complexes with different sizes and shapes are formed due to different degrees of vertical accretion and lateral migration [8, 9].

The primary layer of the study area is currently in the high water content stage, and the degree of production is low. However, geological studies have shown that the local remaining oil extraction has excellent potential. Therefore, it is urgent to carry out an architecture analysis to reveal the main controlling factors of the remaining oil distribution to provide a basis for oilfield development adjustment. In this paper, taking the Guantao Formation of Nanpu 1-29 Area as an example, the river type was determined based on sedimentary background, granularity, core, and sand body. On this basis, guided by the analytic hierarchy process, according to Miall's idea, the architecture research of the study area was carried out. Finally, the static distribution model and dynamic response curve of the study area were compared and analyzed to verify the correctness of the above reservoir architecture research and provide guidance for the subsequent development of the oilfield.

## 2. Overview of the Study Area

The Nanpu Depression is located in the northeast of North China and the southern edge of the Yanshan Terrace Fold Belt. It is a Meso-Cenozoic basin north of Huanghua Depression, Bohai Bay Basin. Drilling revealed the development of the strata from top to bottom in the area, including the Quaternary Plain Formation, the Upper Tertiary Minghuazhen Formation, the Guantao Formation, the Lower Tertiary Dongying Formation, the Shahejie Formation, the Mesozoic Cretaceous, Jurassic,

and the Paleozoic Ordovician strata. The Guantao Formation is in integrated contact with the overlying Minghuazhen Formation, and the lower tertiary Dongying Formation is in nonintegrated touch. Nanpu 1-29 Area in this study belongs to the No. 1 tectonic belt of the Nanpu Depression. The main target area is the Neogene Guantao Formation, which is mainly developed braided river deposits with reservoir thickness of 300-900 m.

The drilling of the NP 1 well opened the prelude to exploring the Nanpu Oilfield on May 23, 2004. The primary layer is currently in the high water cut stage, and the degree of production is low. However, geological studies have shown that the local remaining oil still has excellent potential. Therefore, it is urgent to carry out an architecture analysis to reveal the main controlling factors of the remaining oil distribution and provide a basis for oilfield development adjustment.

## 3. Identification of River Type

Longxin and Guoliang established the distribution pattern of the reservoir architecture of the branching braided rivers and the wandering braided rivers [6], believing that the branching braided rivers had large curvature on the horizontal, and the main river was relatively stable. In the same period, the braided channel was significantly divided by the channel bar, the braided channel and the channel bar were superimposed laterally, and the thickness was very similar. In the end, the geometric form of the flat top convex at the bottom of the channel bar and the flat bottom convex at the top of the braided channel was presented. Some silting layers and chutes developed in the interior of the channel bars. There were many channels in wandering braided rivers, the curvature was slight, and the locations of the channel bars and the braided channels changed rapidly [10-13]. Due to the rapid change of the river, the sand body would produce the phenomenon of undercutting and overlapping during the movement. The positions of the braided channel and the channel bars were not fixed, and it was challenging to preserve the silting layer under the erosion of the strong water power of the river. In addition, based on the sedimentary background, it was found that there were still significant differences between the branching braided rivers and the wandering braided rivers in terms of production conditions due to the difference between the number of the braided channel, curvature, and width-to-depth ratio. In general, the wandering rivers were affected by floods, and the short-term outbreak of flooding caused siltation. Because the rivers were often diverted, the number of channels increased. While the water supply of the branching river was relatively stable, the growth of the channel bars and the braided channels was steady. So the diversion effect was weak, and the number of waterways was relatively stable. Based on four indicators, including sedimentary background, granularity characteristics, core characteristics, and sand body distribution, the river type was comprehensively judged to be a wandering braided river in the study area.

*3.1. Sedimentary Background.* Previous studies have shown that due to the abundant source of materials, large slopes, and rapid water flow, the Guantao Formation mainly developed alluvial

fan and braided river in the initial stage of sedimentation [14]. However, with the rise of the base level, the sedimentary slope decreased, and the river velocity slowed down gradually, leading to a gradual decrease in the scour effect, so the granularity of the sediments in the provenance became smaller, and the depression gradually disappeared. Intense tectonic activity played a favorable role in forming the alluvial fans and the braided rivers.

Based on the previous studies on paleoclimatic conditions of Nanpu Depression [15], it is found that the Guantao Formation has a variety of plant types, mainly including angiosperms such as ulmpollenites, momipites, and juglanspollenites; ferns such as ceratopteris thalictroides and filicinaes; and gymnosperms such as abietinaepollenites and pinuspollenites. All this indicated that the paleoclimate conditions during the sedimentation process of the Guantao Formation were scorching and arid. This scorching and dry paleoclimate condition provided the clastic materials needed for the formation of alluvial fans and braided rivers and facilitated the development of the wandering braided rivers.

**3.2. Granularity Characteristics.** The granularity curve showed that the study area was mainly characterized by steep two-segment curves (Figure 1). The rolling was not very well developed, primarily jumping and suspension. The  $\phi$  values were concentrated primarily between 1 and 4, reflecting prominent fluvial facies granularity characteristics. According to the investigation of the modern Yongding River by Liao et al. [16], it was shown that there was a significant difference in the granularity curve of the braided river with a high slope and a low slope. In his opinion, the high slope braided rivers were mainly composed of three sections, and the proportions of rolling, jumping, and suspension were close to each other. The low-sloping braided rivers were dominated by two sections, and jumping occupied the main body. They also believed that it was possible to distinguish between low-slope and high-slope braided rivers according to the distribution of the granularity curve. Obviously, from the granularity curve characteristics, the braided river of the study area was closer to the low-slope type.

**3.3. Core Characteristics.** Different characteristics of granularity and bedding represent the variation of sedimentary hydrodynamic conditions, which plays a vital role in analyzing sedimentary genetic types and reservoir architecture [17]. According to the observation of the core wells, the lithology was mainly medium-coarse sandstone, with few fine-grained sedimentations and relatively few muddy interlayers in the sandstone (Figures 2 and 3). Thick muddy barriers were locally developed. Mudstone color was mainly brownish red, mixed with gray-green mudstone. Conglomerate could be seen locally. The gravel diameter was generally 2 cm. The directional column could be seen, and the roundness was general, reflecting the braided rivers' characteristics with near-source sedimentation.

There were abundant bedding structures and structural types, including scouring surface, massive bedding, large trough cross-bedding, parallel bedding, small cross-bedding, wave bedding, veined bedding, sand bedding, high/low angle cross-bedding, and deformation bedding (Figure 4). Massive bedding and trough cross-bedding were the main types. In contrast, the developments of high/low angle cross-bedding

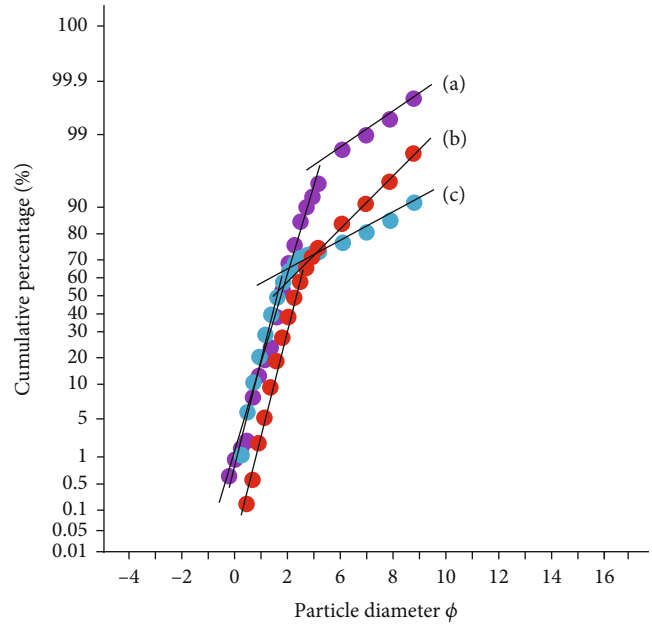


FIGURE 1: Granularity analysis of Nanpu 1-29 Area: (a) well NP12-86, 2773.07 m; (b) well NP12-43, 3014.13 m; (c) well NP12-X77, 2773.07 m.

and tabular cross-bedding were limited in the study area, reflecting that the stable channel bar was not developed. However, mudstone interlayer was rarely observed in the core, indicating that the channel migration was rapid and the preservation degree of muddy sediment was low, consistent with the sedimentary characteristics of the wandering braided rivers.

**3.4. Distribution Characteristics of Sand Body.** There are significant distinctions in lithology, logging characteristics of different sand bodies, and the geometrical shape of sand bodies in horizontal and vertical [18–20]. According to the sand body thickness map (Figure 5), it is found that the sand body was generally distributed in concentrated and contiguous pieces, and mud sedimentation was less. In addition, the boundary of the sand body was relatively straight, with more minor bending characteristics and mat distribution characteristics. Because of the accretion and lateral accretion brought by paroxysmal floods, the distribution of the channel bar was connected and filled in the channel, which led to the braided channel deposition was not noticeable. The channel bars were gradually formed by the influence of the inertial centrifugal force of the river and the continuous accumulation of sediment in the flood period. Therefore, the formation of the channel bars was closely related to the braided channels. On the whole, the trough cross-bedding formed by the migration of the channel bar was the primary structural type.

In this paper, the sedimentary scale of the modern braided rivers, sand body thickness, and logging characteristics was combined to determine whether the channel bars and the braided channels were developed, and the sedimentary facies profiles were drawn in detail (Figure 6). The scales of the channel bars and the braided channels shown on the profile were in good agreement with the sedimentary scale of the modern

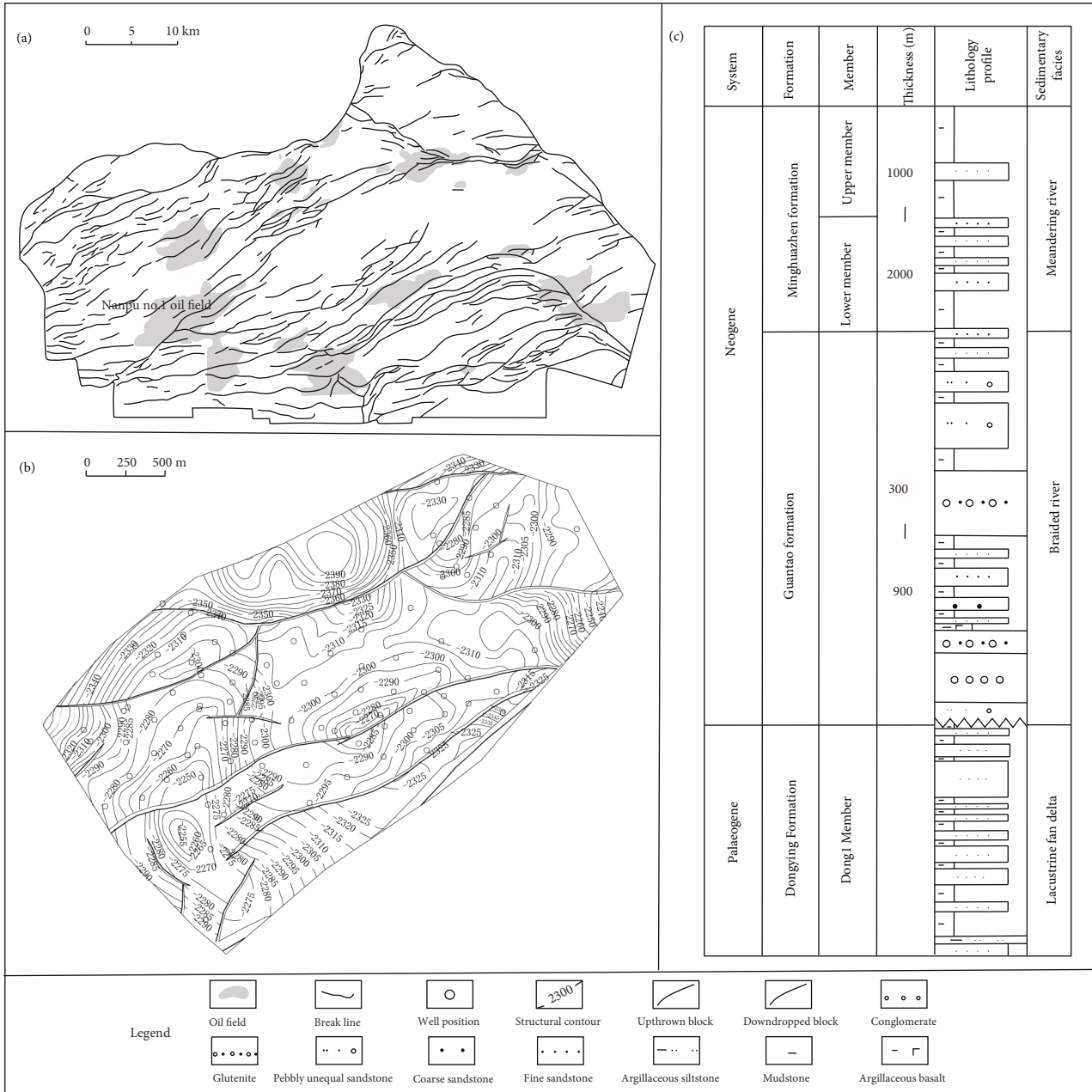


FIGURE 2: Structural location and comprehensive histogram of the study area: (a) structural location map of Nanpu Depression; (b) structural map of Nanpu 1-29 Area, located in Nanpu No. 1 oil field; (c) comprehensive histogram of Neogene in Nanpu Depression, the sedimentary sequences of a braided river and a meandering river were described.

braided rivers, which indicated that the sedimentary facies profiles were correct. In addition, the channel bars were relatively developed on the profile, interspersed with braided channels, and the proportion of latter development was relatively small. The thickness of the channel bar was slightly thicker than that of the braided channel, and the channel would not completely cut the channel bar. A small number of muddy interlayers were developed in the sand body, but very little was developed in the channel bar, and only the scour surface was retained, indicating that the river had strong hydrodynamic force and high sedi-

mentary energy, so it was difficult to form the muddy interlayer. On the whole, it showed the geometric morphological characteristics of the flat top convex at the bottom of the channel bar and the flat bottom convex at the top of the braided channel, which was manifested in the style of wide bar and narrow braided channel.

3.5. *Identification of River Type.* Based on four indicators that are sedimentary background, granularity characteristics, core characteristics, and sand body distribution, the river

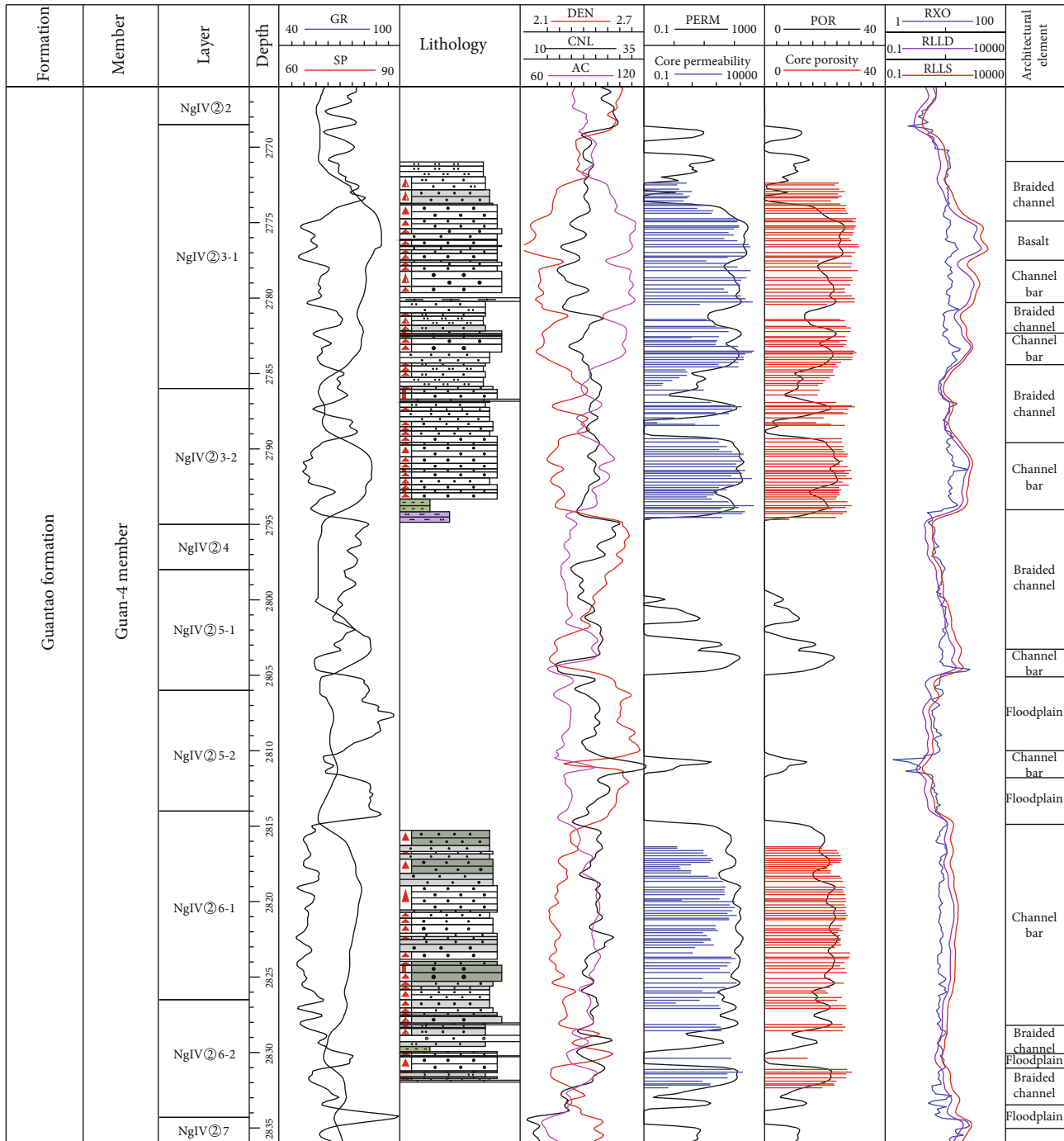


FIGURE 3: Comprehensive histogram of well NP12-X77 in Nanpu 1-29 Area.

type is comprehensively judged to be the wandering braided river in the study area. The specific reasons are as follows.

Firstly, the Guantao Formation of Nanpu 1-29 Area is in the late stage of structural depression, and the slope is relatively small on the whole.

Second, the braided rivers in the study area are close to the provenance area, and the hot and dry paleoclimate conditions will intensify the weathering. In this case, the seasonal flood events will lead to the scouring and silting of the river channel, and the river will be wandering on the horizontal.

Thirdly, according to the characteristics of bedding structure, it is found that trough bedding and massive bedding are primarily developed. In contrast, tabular cross-bedding with high/low angle is less developed, which indicates that the channel flow direction is easy to change, the deposition location of the channel bar is not fixed, and braided channel and channel bar cut and eroded each other.

Fourthly, combined with the contour map of sand body thickness, it is found that most of the sand bodies in Nanpu 1-29 Area present mat distribution with a low bending degree,

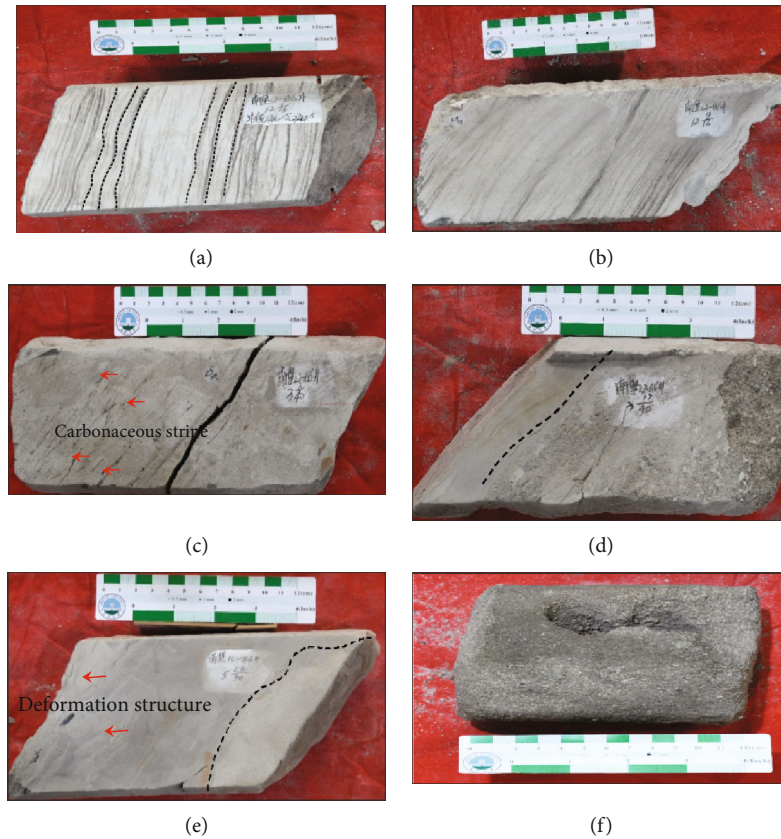


FIGURE 4: Sedimentary tectonic features of Nanpu 1-29 Area. (a) Wavy bedding, the bedding units that are symmetrical or asymmetrical wavy. (b) Ripple lamination fine sandstones, whose composition, color, and grain size change along the direction of sediment accumulation. (c) Veined carbonaceous fine sandstone, the sandstone is relatively sufficient, and there are abundant carbonaceous strips. (d) Massive bedding fine conglomerate, developed at the bottom of a river with a scour surface visible. (e) Sandy mass, which belongs to abnormal predrainage deposition, with deformation structure visible. (f) Massive bedded coarse sandstone, formed by rapid fluvial deposition.

less development of muddy interlayer on the profile, and width to depth ratio of more than 100.

In conclusion, the braided river type is determined to be the wandering braided river.

#### 4. Characteristics of Sedimentary Architectural Elements

According to the core and logging curve data in the study area, it was found that the braided rivers in Nanpu 1-29 Area mainly developed four types of sedimentary architectural elements, namely, channel bar, braided channel, floodplain, and basalt (Figure 3). The logging characteristics of different sedimentary architectural elements were quite different [21].

**4.1. Channel Bar.** Channel bar is the main sedimentary architectural element of the braided rivers, with large sand thickness and a wide distribution range. The downstream accumulation of sediments forms the channel bar. The lithology is dominated by medium-fine sandstone as cemented fine sand, with uniform granularity and large sand body thickness. The logging curve presents a medium-high amplitude microdentate box shape, bell-shaped, and box-shaped form. These characteristics can be used as the basis to determine the channel bar. The erosion surface could be visible at

the bottom, and pebbled sandstones are locally developed. The sedimentary structure is dominated by the trough cross-bedding and the low-angle cross-bedding.

**4.2. Braided Channel.** Like the channel bar, the braided channel is also the main sedimentary architectural element of the braided river, which is widely distributed in the study area. The braided channel is characterized by medium and low microtoothed bell shape, abrupt change at the bottom and gradual change at the top. The lithology is dominated by medium-fine sandstone. All these can be used as the basis for judging the braided channels. Compared with the channel bar of the same period, the sand body thickness is slightly smaller, reflecting cross-bedding and parallel bedding under strong hydrodynamic conditions.

According to the difference between filling lithofacies and filling thickness, it is found that there were two types of filling for the braided channel's development in the study area, namely, sandstone filling and mudstone filling. The braided channel of sandstone filling referred to the braided channel where sandstone filling sediment was the main part [22]. Due to the low flow rate and the low load capacity of the river, the sediment carried by the river was deposited, thus forming the sandstone filling channel, which presented a lenticular shape with a top flat and a convex bottom on the

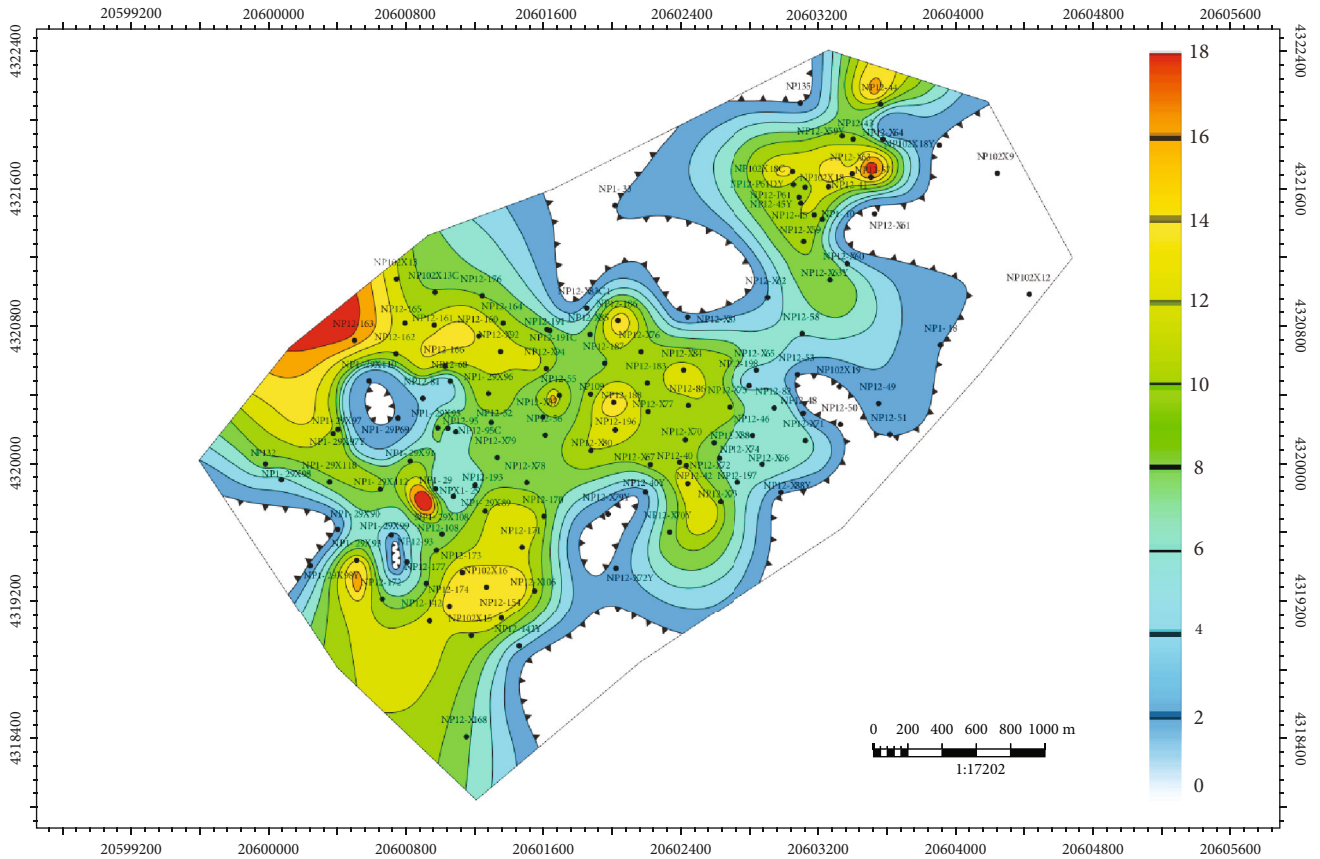


FIGURE 5: Contour map of NgIV@6-1 sand thickness in Nanpu 1-29 Area.

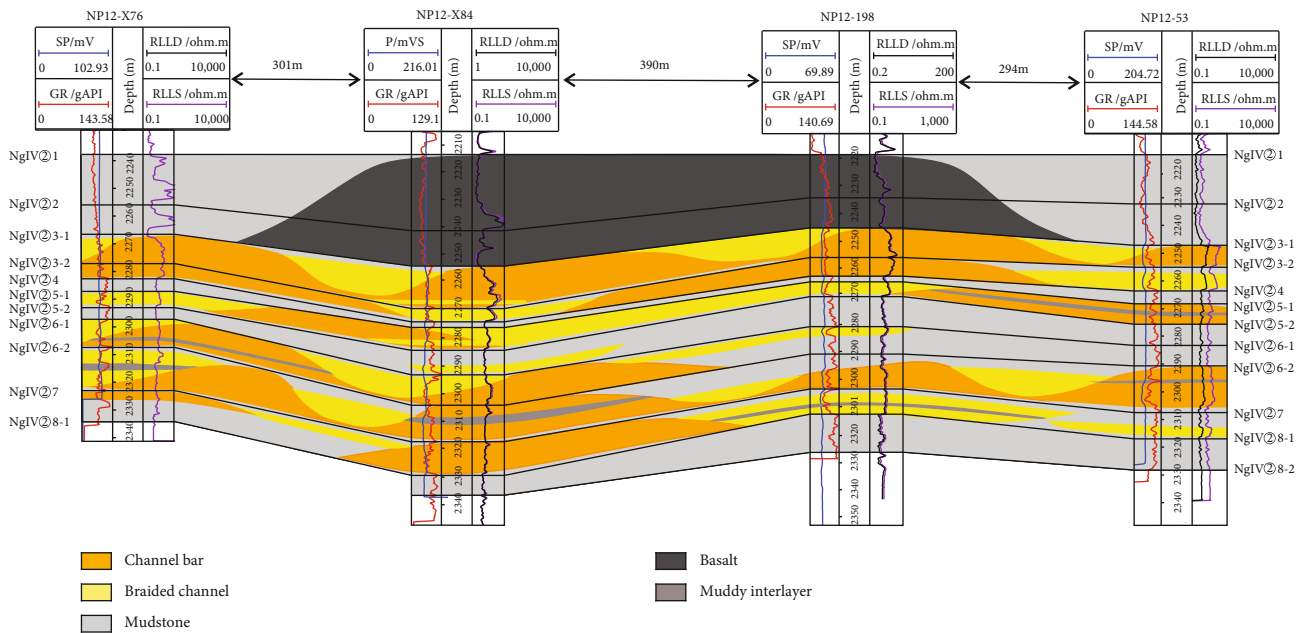


FIGURE 6: The vertical profile of sedimentary facies in Nanpu 1-29 Area. The study area and the scale of modern typical wandering braided river deposits and the scales of sedimentary architectural elements were determined.

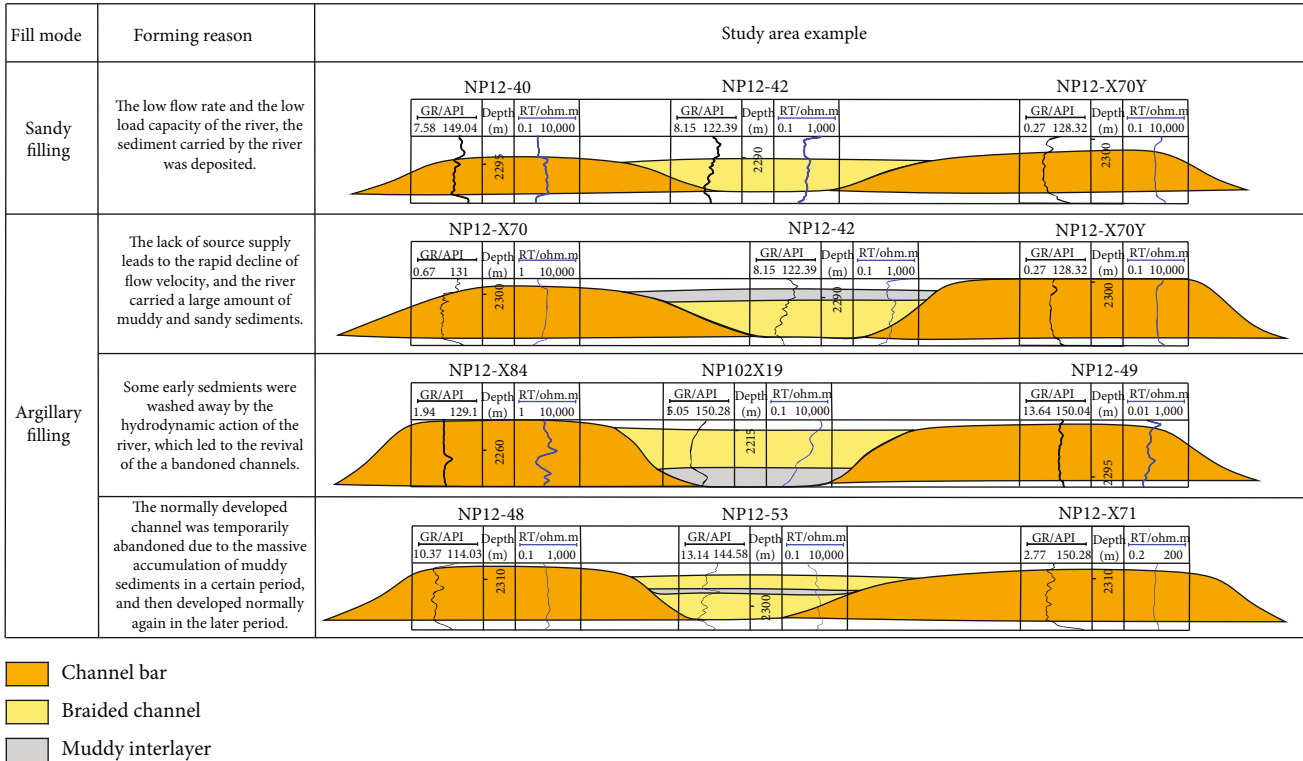


FIGURE 7: Filling pattern of the braided river in the study area.

profile. The braided channel mudstone filling was manifested in three [23] (Figure 7). The first was a form referring to the sandstone sediments filling in the bottom of the river channel and the mudstone sediments filling in the upper of the river channel. The reason for this phenomenon was that the lack of source supply led to the rapid decline of flow velocity, and the river carried a large amount of muddy and sandy sediments, which eventually led to the braided channel presenting a state of mudstone in the upper part and sandstone in the lower part. The second was the muddy sediments filling in the bottom of the river channel and the sandstone sediments filling in the upper of the river channel. This phenomenon occurred because some early sediments were washed away by the hydrodynamic action of the river, which led to the revival of the abandoned channels, thus forming the state of mudstone in the bottom part of the channel and sandstone in the upper part. The third was that the muddy sediments filling in the middle of the sandy river channel; that was, the normally developed channel was temporarily abandoned due to the massive accumulation of muddy sediments in a certain period and then developed normally again in the later period.

**4.3. Floodplain.** The floodplain is mainly developed on both sides of the braid flow belt, the lithology is dominated by massive mudstone and muddy siltstone, and the color is predominantly brown and dark brown, with no apparent bedding. The effective sand body thickness is thin, and the logging curve shows the linear characteristics with low amplitude microtoothed.

**4.4. Basalt.** There is also a special lithology affected by the volcanic eruption, namely, basalt, a kind of dense rock formed after the condensation of volcanic eruption magma. The lithology is dominated by basaltic mudstone, and the GR curve and SP curve on the logging curve are displayed as low values, showing a box-shaped form.

## 5. Classification and Quantitative Characterization of Reservoir Architectures

**5.1. Classification of Reservoir Architecture.** According to Miall's reservoir architecture classification scheme, the reservoir architecture interface of the study area was divided into 5-3 levels by using the hierarchical analysis method. The fifth level interface was a single braided flow belt, which belonged to the river channel filling unit. The fourth level interface was the sedimentary architectural element, where the single braided flow belt was mainly refined into the channel bars and the braided channels. The third level interface was the inner muddy interlayer level of the channel bar, with a thickness of about 1 to 2 cm.

Due to the thin thickness and difficulty preserving muddy interlayer, it was more difficult to track between wells accurately. In contrast, the braided flow belt was more accessible to identify than the muddy interlayer. Therefore, this study focused on the single braided flow belt, channel bars, and braided channels within the single flow belt. We first investigated the scale information of the modern braided rivers to

TABLE 1: Scale measurement results of typical wandering braided. All data are based on measurements taken on Google Earth.

River name	Channel bar width/m	Channel bar length/m	Braided channel width/m	Distance from the source area	Plains/mountains
Thjorsa River	29.80	128.97	16.25	Distant source	Plain
Torrente Ferro River	30.38	139.14	10.84	Near source	Plain
Huseyjarkvisl River	61.77	152.97	17.67	Distant source	Plain
Rakaia River	157.68	534.82	25.56	Near source	Plain
Waimakari River	128.38	365.95	41.53	Near source	Plain
The front section of the Markham River	92.43	383.06	18.80	Near source	Plain
Buha River	56.45	220.80	14.05	Distant source	Plain
New Zealand River	61.69	155.81	22.04	Distant source	Plain
Godley River	66.90	253.96	11.42	Distant source	Mountain area
Rakaia River	265.52	747.40	89.22	Distant source	Mountain area
Lhasa River	124.48	356.52	28.08	Near source	Mountain area

get the quantitative relations of the reservoir architectural elements, to guide the anatomization of the subsurface reservoir.

**5.2. Scale Investigation of Braided River Sedimentation.** It is necessary to estimate the scale of the braided river for boundary identification to guide oilfield reservoir anatomy. Previous studies have determined the relationship among the cross strata, paleowater depth, and paleochannel based on many modern sediment and ancient outcrop analyses. The scale of the braided rivers in Nanpu 1-29 Area is predicted based on the scale of interbedded strata based on core statistics. The core statistics show that the average thickness of the cross strata in the study area was 0.3 cm.

The formula for estimating the thickness of a dune based on Leclair and Bridge [24] is

$$H = (2.9 \pm 0.7)h, \quad (1)$$

where  $H$  represents the dune's height and  $h$  represents the average thickness of the staggered stratigraphy.

According to the formula provided by Allen (1970), the relationship between the height of dunes and the paleowater depth is determined as follows:

$$d = 11.6 \times H^{0.84}, \quad (2)$$

where  $d$  is the water depth of the paleochannel.

The relationship between the water depth of the average paleochannel and paleochannel is as follows:

$$d_m = \frac{d}{2}, \quad (3)$$

where  $d_m$  is the average paleochannel water depth; the depth distribution range of paleochannel is strongly compared with previous studies [25].

The formula for predicting the braided channel's width according to Bridge and Tye [4], after the paleochannel

depth is obtained, the width of the braided flow belt could be predicted:

$$Ch_w = 59.9d_m^{1.8}, \quad (4)$$

where  $Ch_w$  represents the braided channel's width.

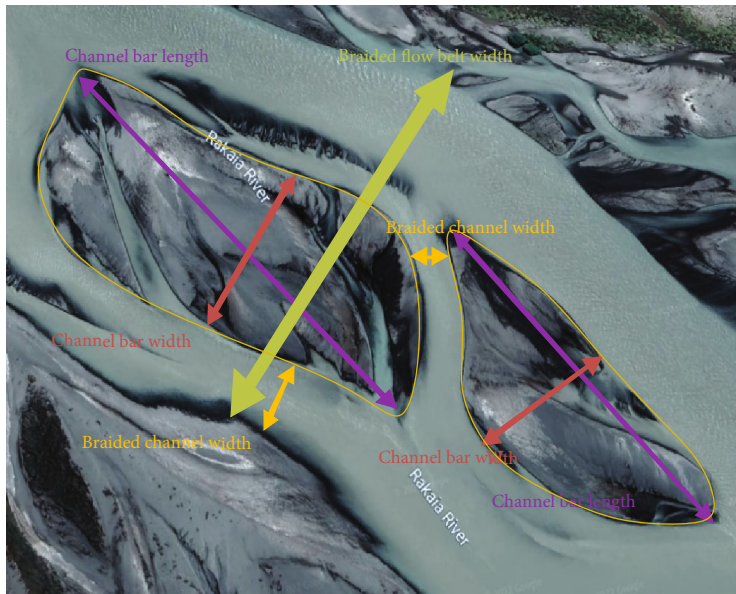
According to the above formulas, the predicted water depth of the study area was 4.43-6.7 m, the thickness of the statistical channel bar was 1.8-5.92 m, and the width of the braided river was 872-1838 m.

On this basis, the sedimentary scale of 11 wandering braided rivers similar to the braided river in the study area was measured based on Google Earth [26] (Table 1), and the quantitative relationships between the channel bar's length and the channel bar's width, as well as between the width of channel bars and the width of the braided channels, were determined (Figure 8). These quantitative relationships could be used to delineate the boundary between braided flow belts, braided channels, and channel bars.

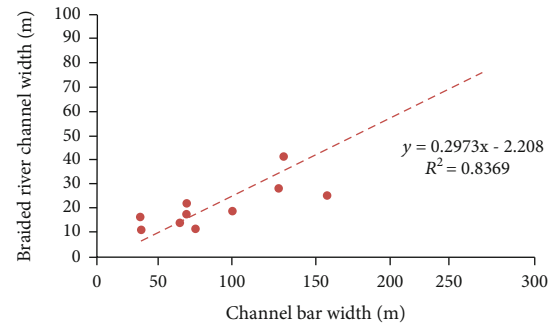
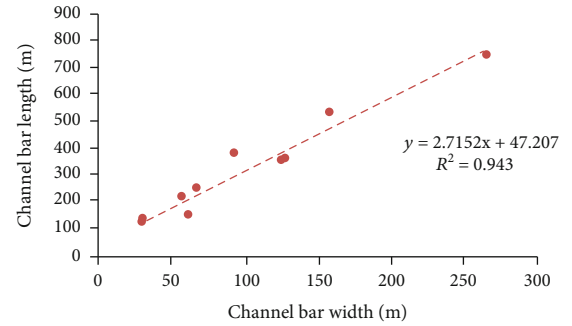
### 5.3. Characteristics of Reservoir Architecture

**5.3.1. Characteristics of Level 5 Reservoir Architecture.** Reservoir architecture of level 5 in the study area refers to the single braided flow belt, and the identification of the single braided flow belt can provide a rich geological basis for determining the injection of oil and water and the direction of water flow, the connectivity between sand body, and the direction of channel extension. The identification methods of the single braided flow belt are as follows.

First is the method of sand body thickness analysis. The overall sedimentation of the braided river is characterized by the thicker inner center and the slightly thinner wings of the braided river belt; the channel top surface of the same river is isochronously deposited, and the braided flow belts of different periods within the same single layer will cause local sedimentation due to rapid migration and change. Therefore, the interfluvial sand body with the discontinuous distribution



(a)



(b)

FIGURE 8: Sedimentary scale of the modern typical wandering braided rivers. (a) The demonstration measurements of the channel bars, the braided channels, and a single braided flow belt based on Google Earth, taking the Rakaia River for example. (b) The relationships between the channel bar's length and the channel bar's width and between the channel bar's width and the braided channel's width based on the result data.

can be used as one of the markers for demarcating the boundary of the braided flow belt. Second is the floodplains between the braided flow belts. During the flood period, the sediments carried by the river are easy to deposit and form the floodplains, which can be used to judge the boundary of the braided flow belt. Finally, it can be judged by the top elevation difference of the sand body. During the flood period, the river level is higher than that of the channel bar, and the channel bar is exposed to the water surface during the dry period. The rapid change of the braided channels leads to the river sand gradually undercut and overlapping in continuous erosion. Due to the significant difference in the sedimentary environment required by the development of the sand body at different periods [27], the elevation difference of the top surface of the braided channel sand body might be quite different, which could be used as an identification mark of the sand body boundary.

This study fully referred to the scale of modern braided river deposition, combined with the empirical formula and the braided flow belt identification mark, to complete the horizontal map of sedimentary facies. The study found that the length and width of the single braided flow belt in the study area were 365.16-1349.72 m and 270.57-1160.54 m, which was consistent with previous studies and modern braided river deposition, indicating the correctness of the sedimentary facies map in the study area.

**5.3.2. Characteristics of Level 4 Reservoir Architecture.** Reservoir architecture of level 4 refers to the spread study of the channel bar and the braided channel inside the single braided

flow belt, which is the premise of studying the muddy inter-layer inside the sand body.

The change of thickness and width in the sand body is obviously due to the frequent swing of the channel. Sand body superposition relationship is a comprehensive reflection of hydrodynamic conditions, sediment supply efficiency, channel changes, and vertical evolution of sedimentary facies [28]. Many previous studies have been carried out on the superimposed shape and contact relationship of sand bodies. Although there are significant differences, the formation mechanism is relatively similar. Based on previous research results, Guo et al. made a comprehensive analysis of core data, logging data, sand body morphology, and sand body thickness and finally divided the superimposition types of sand bodies in southeastern Sulige into four types, including massive sand bodies, multilayered sand bodies, sectional interbedded sand bodies, and thin interbedded sand bodies [29].

Based on the characteristics study of single well facies and sedimentary architectural elements, it is found that the combination modes of the channel bars and the braided channels could be divided into three types, namely, superposed, standalone, and contact (Figure 9), and the contact type is the main type. The superposed mode refers to the fact that the single sand body developed in different periods has certain contact or no contact vertically, and the single sand body formed in the late period has no strong erosion and scouring effect on the single sand body formed in the early period [30]. The independent type refers to the pattern in which the single sand bodies developed at different times

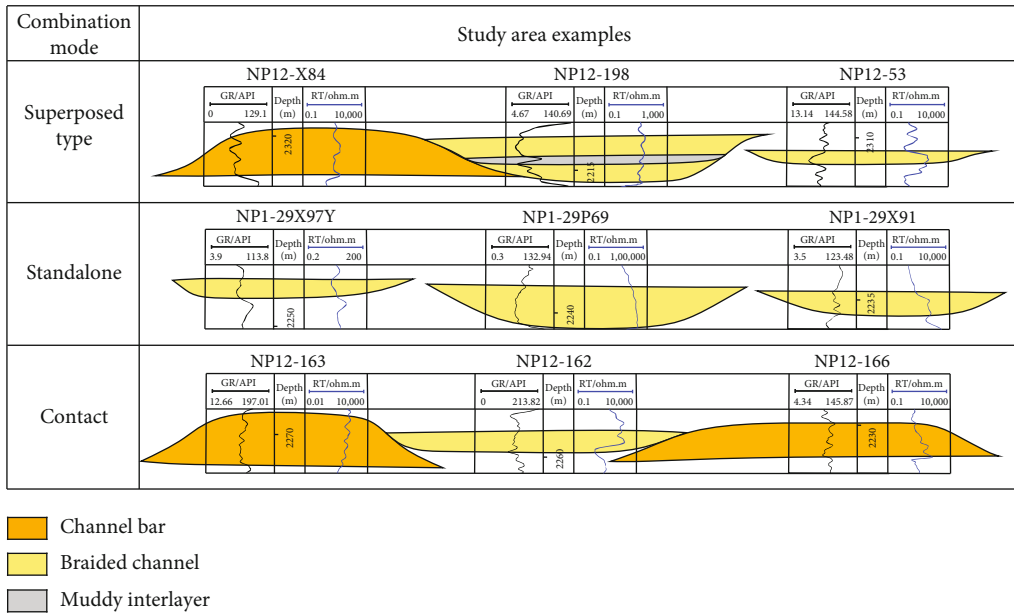


FIGURE 9: Combination pattern of the sand body in Nanpu 1-29 Area. The determination of the channel bar and the braided channel is mainly based on logging curve morphology and sand body thickness. The scale of channel bar and braided channel was obtained by referring to the scale of modern typical wandering braided river deposits, empirical formula, cores, and logging data in the study area.

are separated by some muddy sediments and do not contact each other [31]. The contact type refers to the vertical contact between the two periods of a single sand body, and the single sand body formed in the later period has some certain erosion and scouring effect on the single sand body formed in the earlier period. According to the above observations, the combination modes between the braided channels and the channel bars were more familiar.

Different overlapping styles of the sand body have different effects on development. The core data shows that each single sand body has different reservoir property characteristics, which indicates that each single sand body has a strong heterogeneity. Injected water will preferentially enter the areas with good physical properties and high permeability, and the areas with poor physical properties and low permeability will have less impact. Therefore, given this situation, the development of the remaining oil should focus on the physical properties and permeability parameters of the study area.

It is observed that there were more stable small layers in the study area, most of which were independent lenticular single sand bodies with great differences in thickness and shape. At this time, the effect could only be one-way. By contrast, the oil layer, closing to the injection well, had a faster flooding speed. This resulted in the good side of enrichment of remaining oil being more relative to the other side of the situation. In this case, the remaining oil development needed to pay more attention to the degree of water flooding by wells.

Combined with the characteristics of core, logging curve, sand body thickness, top surface elevation difference, and sedimentary facies transition, it is found that the combination mode between the channel bars and the braided channels was more contact type. The composite arc rhythms between the contacting composite sand bodies were obvious, and the heterogeneity was very strong, which led to the inconsistency

of water displacement degree in each part and the formation of remaining oil. Therefore, it is necessary to pay attention to the uneven degree of water flooding for each oil layer in the process of remaining oil development.

In this study, the scale of modern typical wandering braided river deposition was measured based on Google Earth; thus, a quantitative reference was obtained for the actual drawing of sedimentary facies horizontal map and vertical profile. At the same time, combined with the characteristics of the logging curve and sand body thickness, the sedimentary scales of the channel bars and the braided channels could be identified and determined. The results were in good agreement with the scale of modern braided river deposition, indicating that the mapping results were accurate. Taking NgIV@6-1 as an example (Figure 10), it is observed that the maximum length of the channel bar was 318.32 m, the minimum was 158.89 m, and the average was 208.72 m. The maximum width of the channel bar was 116.41 m, the minimum was 75.97 m, and the average was 91.27 m. The maximum width of the braided channel was 180.05 m, the minimum was 16.81 m, and the average was 35.67 m. The anatomy reproduced well the distribution and scale characteristics of the channel bar and the river channel.

Dissecting each small layer of the study area and calculating its size (Table 2 and Figure 11), it showed that the length of a single channel bar was about 158.89-318.32 m, with an average of 209 m, and the width of a single channel bar was 75.97-116.41 m, with an average of 91 m. The width of the braided channel was about 16.81 m-180.05 m, with an average of 36 m. Meanwhile, the ratio of length and width for the channel bar was concentrated between 2 and 4.

In the horizontal map, the determination of which wells were distributed in the same channel bar was mainly based on the logging curve morphology and sand body thickness. If the logging curve morphology of several wells was all shown

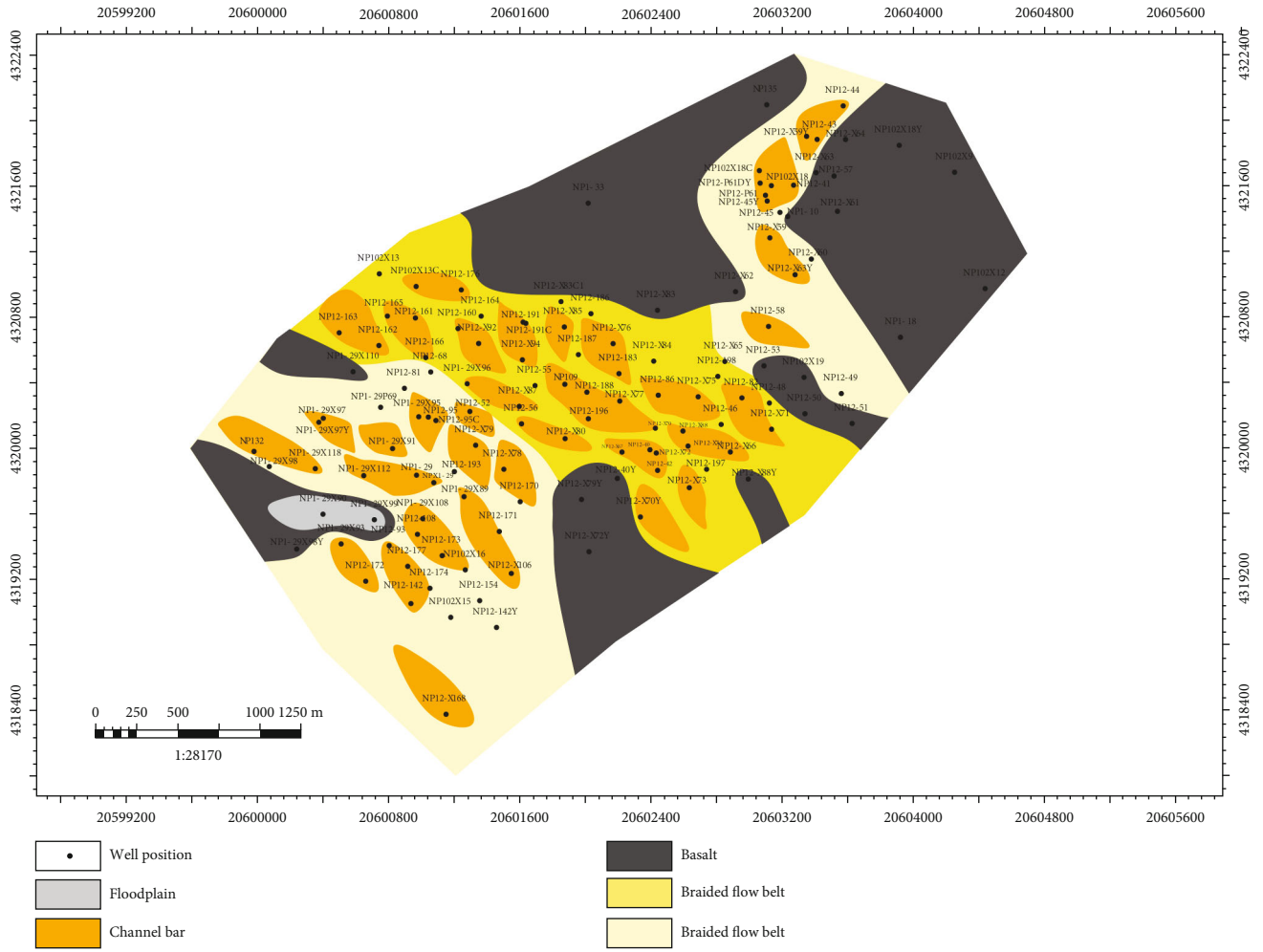


FIGURE 10: Sedimentary facies horizontal map of NgIV@6-1 in Nanpu 1-29 Area. The scale of the sedimentary architectural elements was obtained by referring to the scale of modern typical wandering braided river deposits, core data, and logging data in the study area. Different colors were used here to help distinguish the braided flow belt.

TABLE 2: Table of scale quantitative statistics between the channel bars and the braided channels in Nanpu 1-29 Area.

The layer number	Channel bar length/m			Channel bar width			Braided channel width		
	Maximum	Minimum	Average	Maximum	Minimum	Average	Maximum	Minimum	Average
3-1	188.69	177.00	183.00	86.59	75.97	81.00	23.51	18.62	21.00
3-2	242.35	232.10	237.00	99.23	84.65	92.00	30.33	21.12	26.00
5-1	200.60	158.89	185.00	87.22	81.25	85.00	61.93	18.34	40.00
5-2	204.43	158.91	181.00	93.71	78.07	83.00	180.05	20.12	75.00
6-1	207.23	175.84	193.00	95.53	84.23	91.00	48.78	18.42	30.00
6-2	247.97	213.46	231.00	114.00	98.90	106.00	23.60	19.93	22.00
7	211.85	206.37	208.00	101.85	96.25	98.00	31.18	21.60	25.00
8-1	219.93	205.23	213.00	89.86	87.08	88.00	29.69	16.81	23.00
8-2	318.32	289.52	304.00	116.41	90.25	103.00	35.68	34.10	35.00

as channel bar and the sand body thickness was relatively similar, these wells were judged to be in the same channel bar. If only one well was distributed or the other wells were distributed far away and the log showed medium-high amplitude microtooth box, bell-box, and thick sand, the channel bar was controlled by only one well.

5.3.3. *Characteristics of Level 3 Reservoir Architecture.* The result of core observation showed that there was a small number of muddy interlayer sediments in the channel bars [32] (Figure 12), which represented the migration of the bottom type caused by small floods. Affected by channel oscillation, these muddy interlayers were often difficult to preserve due

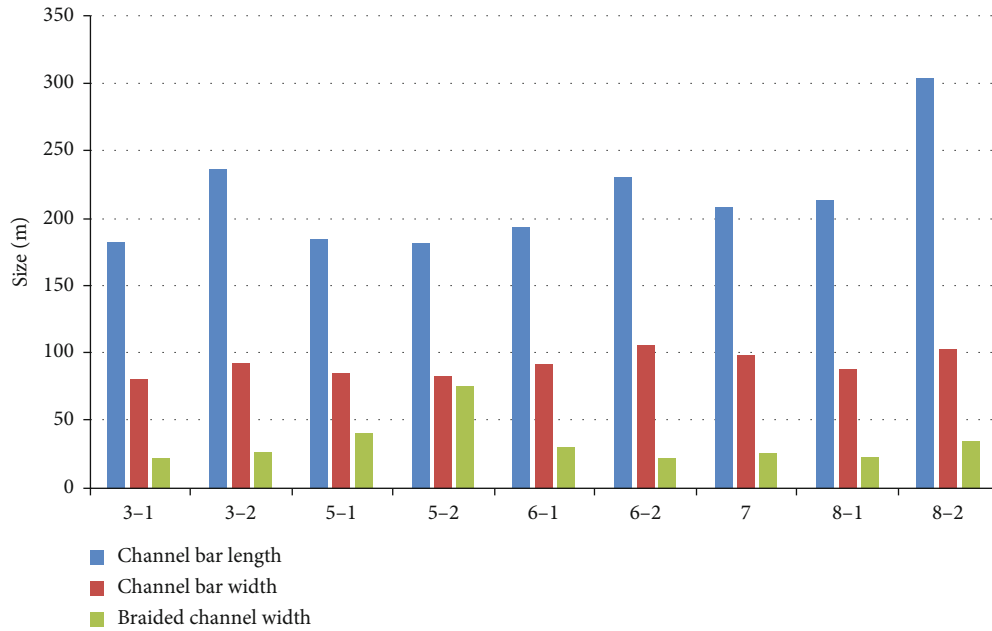


FIGURE 11: Quantitative statistical histogram of Nanpu 1-29 Area.

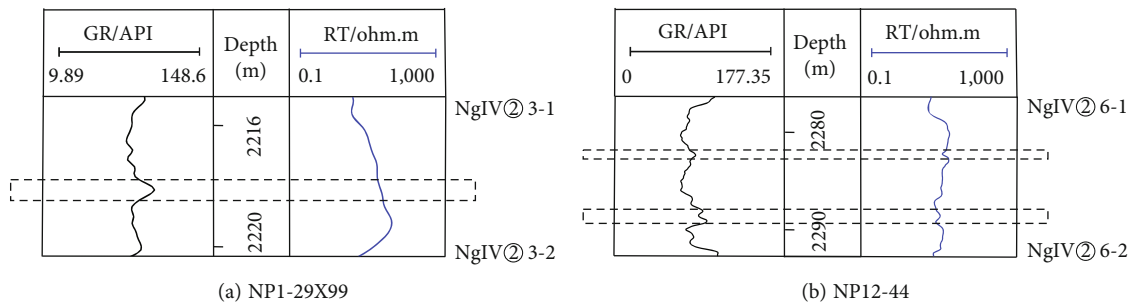


FIGURE 12: Identification mark of muddy interlayer in Nanpu 1-29 Area.

to extreme erosion, primarily manifested as fine-grained muddy interlayers inside the channel bars, mainly identified by the local return of the core and logging curve. Combined with the development process of the channel bars, considering the influence of water erosion and river accretion, the development scope and characteristics of the muddy interlayers inside the channel bars were studied, and the thickness of these muddy interlayers was about 1 to 2 cm.

### 6. Dynamic Data Verification

The dynamic development data of the oil field can be used as a verification of the reservoir architecture work [33], including the oil production, liquid production, and comprehensive water cut of the production wells and injection volume of the injection wells. For example, after water is injected into the reservoir from the injection wells, the crude oil will flow to the production wells in the direction of better connectivity and then be produced from the production wells. The fluctuation of the fluid production in the production wells is closely related

to the connectivity of the injection wells. Generally, the better the connectivity, the more pronounced the correlation between the injection volume of the injection wells and the fluctuation amplitude of the liquid production volume in the production wells. Conversely, the poorer the connectivity, the smaller the correlation. Therefore, the static distribution model and dynamic response curve of the study area were compared and analyzed based on the dynamic development data to verify the correctness of the reservoir architecture research.

Four production wells named well NP12-172, well NP12-173, well NP12-142, and well NP12-174 and one injection well named well NP12-177 were selected, and the injection well was taken as the center of the well group. A static distribution model (Figures 13 and 14) was established based on the reservoir architecture interface of the 5-3 stage to analyze the dynamic connectivity between the two wells. By observing the static distribution model of the NP12-177 well group, it is found that the connectivity was good because the sand bodies between the well NP12-177 and well NP12-173 were mostly developed, while the development degree of muddy interlayer

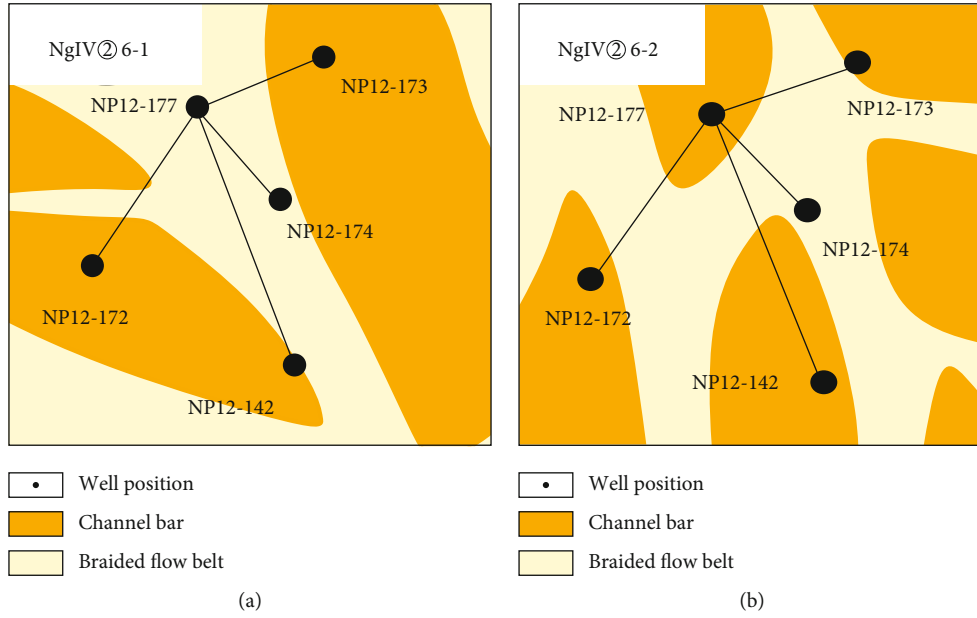


FIGURE 13: Perforating interval map of well group NP12-177.

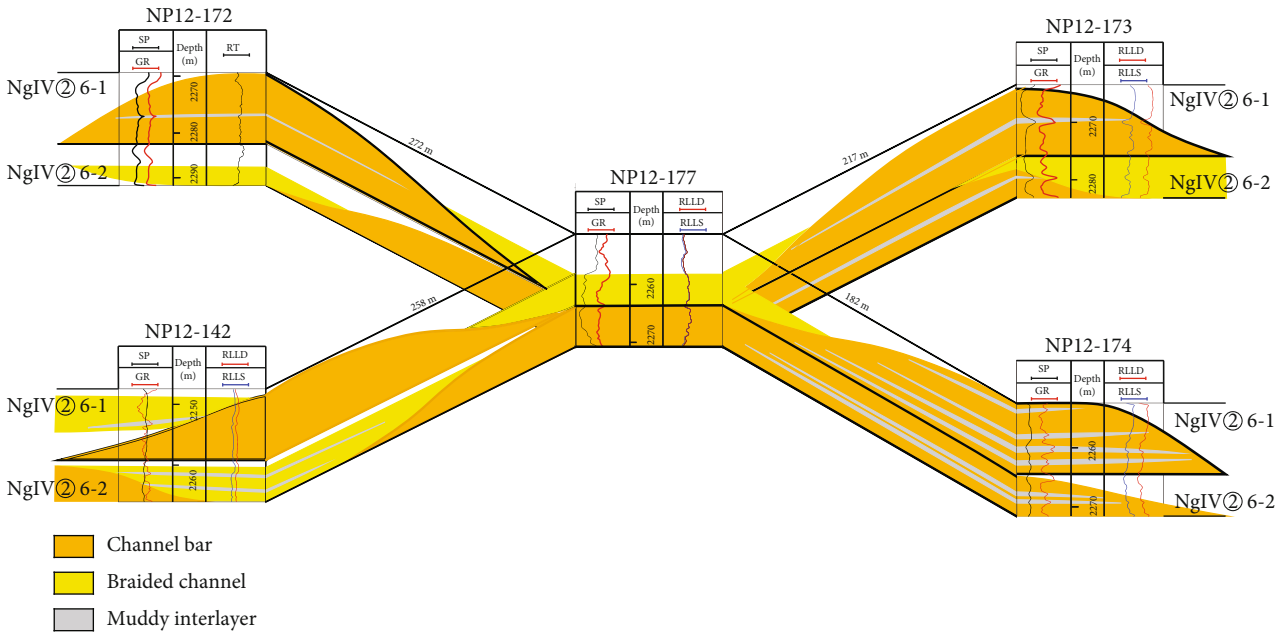


FIGURE 14: Static distribution model of NP12-177 well group in Nanpu 1-29 Area. Injection well NP12-177, the water injection method is general water injection and the water injection depth of 2258.11-2268.19 m.

was low. However, the area between well NP12-177 and well NP12-174 had many muddy interlayers, which hindered sand connectivity between the two wells.

In addition, based on the dynamic development data including oil production, liquid production, comprehensive water cut of the production wells, and injection volume of injection wells, the dynamic response curve was established (Figure 15). The accuracy of the research on reservoir architecture is verified by comparing the dynamic response curve with the static distribution model [34, 35]. The dynamic response

curve selected March 2016 to September 2020 as the evaluation period of dynamic data.

Combined with the dynamic response curve of the NP12-177 well group, it was found that from the beginning of water injection in July 2016 to August 2018, the water injection of well NP12-177 showed a steady upward trend, and the liquid production capacity of the corresponding well NP12-173 maintained a steady increase, and the liquid production capacity of well NP12-174 of the producing well showed a slow downward trend from July 2016 to March 2018. From September 2018 to

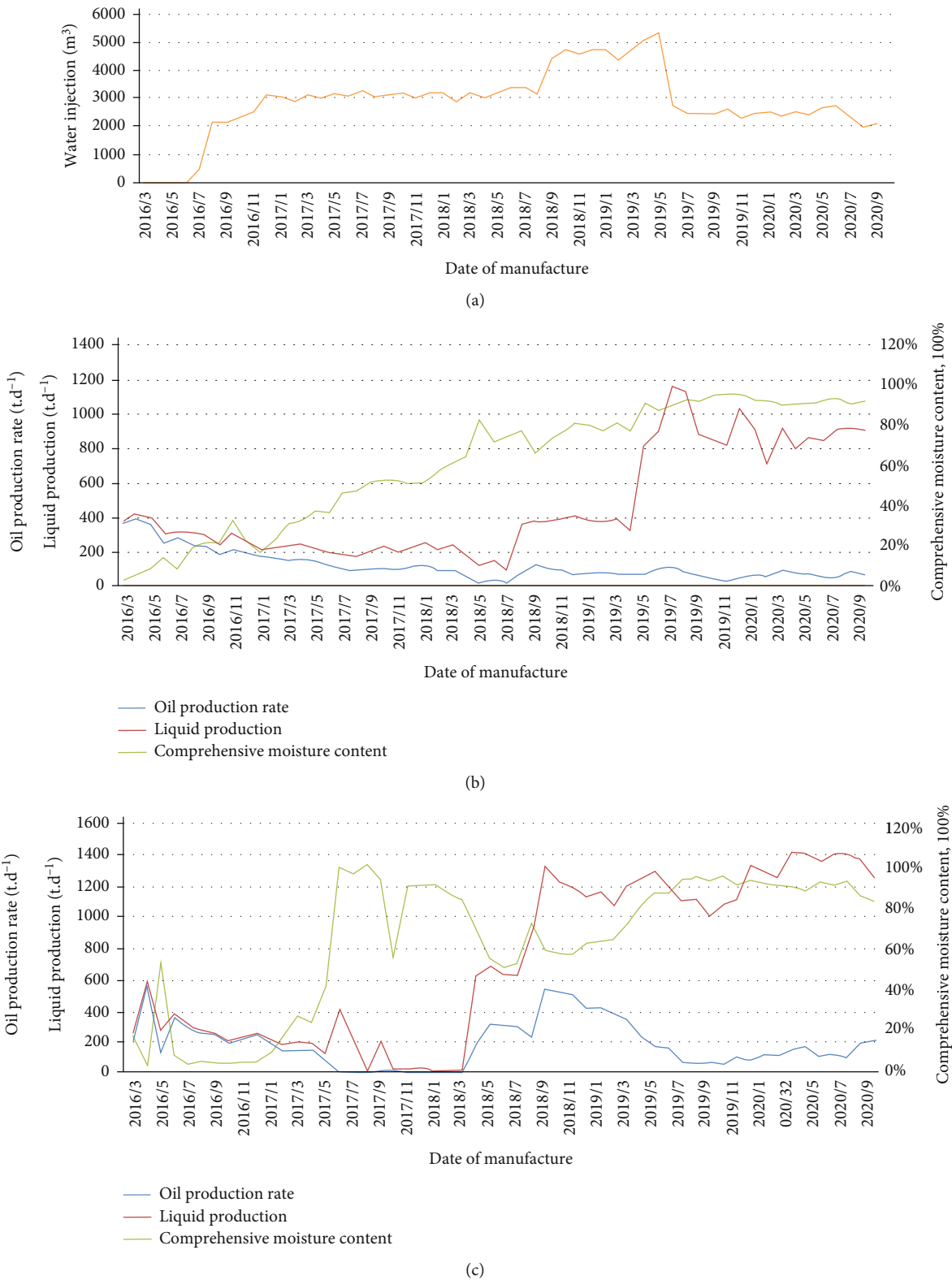


FIGURE 15: Dynamic response curve of NP12-177 well group in Nanpu 1-29 Area: (a) NP12-177, injection well; (b) NP12-173, production well; (c) NP12-174, production well.

May 2019, the water injection of well NP12-177 in the injection well showed a significant upward trend, and the production capacity of well NP12-173 also realized a substantial increase

during this period, while the production capacity of the well NP12-174 showed a steady decline. From June 2019 to September 2020, the water injection capacity of well NP12-177 slowly

declined, but it continued to inject water. At the same time, the fluid production of well NP12-173 also showed a gentle downward trend, while the fluid production of well NP12-174 kept a basic upward trend. Therefore, the study found that the injection volume of well NP12-177 was significantly correlated with the fluctuation range of production capacity of well NP12-173, which was consistent with the good connectivity between well NP12-177 and well NP12-173 in the static distribution model. However, the dynamic response curves of well NP12-177 and well NP12-174 were negatively correlated or irrelevant, which was consistent with the analysis result that the connectivity between well NP12-177 and well NP12-174 was poor due to the development of numerous shale inter-layers. Therefore, based on the dynamic development data, the static distribution model and dynamic response curve were compared and analyzed, and it was found that they had good consistency, which confirmed that the above research on reservoir architecture was very correct and reasonable.

## 7. Conclusions

- (1) According to the sedimentary background, granularity characteristics, core characteristics, and sand body distribution characteristics, the braided river type in the study area was determined as wandering braided river
- (2) The classification and quantitative architecture characterization in the study area were realized. The architecture classification of the study area was divided into 5-3 levels, including a single braided flow belt, channel bar and braided channel, and interlayer architecture of channel bar
- (3) The length of the single braided flow belts was 365.16-1349.72 m, and the width was 270.57-1160.54 m. The channel bar length was distributed 158.89-318.32 m, and the width was 75.97-116.41 m. The braided river width was distributed 16.81-180.05 m. The length and width ratio of the channel bar was concentrated between 2 and 4
- (4) Dynamic analysis showed that the research on reservoir architecture was reasonable and accurate. The sand body in the study area was mostly in contact type, so the unevenness of water flooding degree should be paid attention to in the remaining oil development process, to guide the later oilfield development and adjustment

## Data Availability

The data used to support the findings of this study are available from the corresponding authors.

## Conflicts of Interest

The authors declare that they have no conflicts of interest.

## Acknowledgments

This study was financially supported by the National Natural Science Foundation of China (Grant Nos. 42130813 and 41872138).

## References

- [1] J. R. L. Allen, "Studies in fluvial sedimentation: bars, bar-complexes and sandstone sheets (low-sinuosity braided streams) in the brownstones (L. devonian), welsh borders," *Sedimentary Geology*, vol. 33, no. 4, pp. 237–293, 1983.
- [2] A. D. Miall, "Architectural-element analysis: a new method of facies analysis applied to fluvial deposits," *Earth-Science Reviews*, vol. 22, no. 4, pp. 261–308, 1985.
- [3] A. D. Miall, *The Geology of Fluvial Deposits: Sedimentary Facies, Basin Analysis, and Petroleum Geology*, Springer, Berlin, 2013.
- [4] J. S. Bridge and R. S. Tye, "Interpreting the dimensions of ancient fluvial channel bars, channels, and channel belts from wireline-logs and cores," *AAPG Bulletin*, vol. 84, no. 8, pp. 1205–1228, 2000.
- [5] R. L. Skelly, C. S. Bristow, F. G. Ethridge et al., "Architecture of channel-belt deposits in an aggrading shallow sandbed braided river: the lower Niobrara River, northeast Nebraska," *Sedimentary Geology*, vol. 158, no. 3-4, pp. 249–270, 2003.
- [6] M. U. Longxin and Z. H. A. O. Guoliang, "Architecture analysis of reservoirs in branching- and wandering-based braided rivers: taking FN field, Sudan as an example," *Earth Science Frontiers*, vol. 24, no. 2, pp. 246–256, 2017.
- [7] D. Yue, W. Li, J. Li et al., "Variable architecture models of fluvial reservoir controlled by base-level cycle - a case study of Jurassic outcrop in Datong Basin," *Earth Science*, vol. 42, no. - article 20220418, 2022.
- [8] W. Wu, Q. Li, J. Yu, C. Lin, D. Li, and T. Yang, "The Central Canyon depositional patterns and filling process in east of Lingshui Depression, Qiongdongnan Basin, northern South China Sea," *Geological Journal*, vol. 53, no. 6, pp. 3064–3081, 2018.
- [9] Q. Li, W. Wu, J. Liang et al., "Deep-water channels in the lower Congo basin: evolution of the geomorphology and depositional environment during the Miocene," *Marine and Petroleum Geology*, vol. 115, article 104260, 2020.
- [10] Y. Dali, *The Study on Architecture Analysis and Remaining Oil Distribution Patterns of Meandering River Reservoir: A case study of Guantao Formation, Gudao Oilfield*, China University of Petroleum(Beijing), 2006.
- [11] X. Wang, Y. Liu, J. Hou et al., "The relationship between syn-sedimentary fault activity and reservoir quality—a case study of the Ek1 formation in the Wang Guantun area, China," *Interpretation*, vol. 8, no. 3, p. SM15, 2020.
- [12] X. Wang, X. Zhou, S. Li, N. Zhang, L. Ji, and H. Lu, "Mechanism study of hydrocarbon differential distribution controlled by the activity of growing faults in faulted basins: case study of Paleogene in the Wang Guantun area," *Lithosphere*, vol. 2021, p. 7115985, 2022.
- [13] H. Zhang, M. Li, Y. Kang, Z. Wu, and G. Wang, "Reservoir architecture and fine characterization of remaining oil of Chang 3 reservoir in Zhenbei oilfield, Ordos Basin," *Lithologic Reservoirs*, vol. 33, no. 6, pp. 1–12, 2021.

- [14] Z. Lin, H. Wang, H. Jiang et al., "Volcanic events at the stage of Guantao Formation in Nanpu San and its petroleum geological significance," *Marine Geology & Quaternary Geology*, vol. 31, no. 3, pp. 79–85, 2011.
- [15] C. G. Liang, "Sedimentary microfacies of the Q4 member of cretaceous in Fuyu Oilfield, Songliao basin," *Journal of Southwest Petroleum University (Science & Technology Edition)*, vol. 30, no. 2, pp. 69–73, 2008.
- [16] L. Baofang, Z. Weimin, L. Lie et al., "Study on modern deposit of a braided stream and facies model: taking the Yongding River as an example," *Acta Sedimentologica Sinica*, vol. 16, no. 1, p. 34, 1998.
- [17] H. Liu, C. Y. Lin, and X. G. Zhang, "Reservoir architecture and remaining oil distribution in braided river of Guantao Formation, Kongdian oilfield," *Journal of Jilian University (Earth Science Edition)*, vol. 48, no. 3, pp. 665–677, 2018.
- [18] J. Yuanpeng, Z. Lan, Z. Guangyi et al., "Lobate shallow-water delta reservoir architecture characterization in the southern Bohai Sea," *Special Oil & Gas Reservoirs*, vol. 27, no. 6, pp. 88–95, 2020.
- [19] X. Wang, S. Yu, S. Li, and N. Zhang, "Two parameter optimization methods of multi-point geostatistics," *Journal of Petroleum Science & Engineering*, vol. 208, p. 109724, 2022.
- [20] X. Wang, J. Hou, S. Li et al., "Insight into the nanoscale pore structure of organic-rich shales in the Bakken Formation, USA," *Journal of Petroleum Science & Engineering*, vol. 191, p. 107182, 2020.
- [21] G. Qin, S. Wu, and X. Song, "Sedimentary characteristics of distal fine-grain delta and architecture analysis of single sand body," *Journal of China University of Petroleum (Edition of Nature Science)*, vol. 41, no. 6, pp. 9–19, 2017.
- [22] X. J. Wu, H. B. Su, S. J. Zhang, L. J. Feng, J. Wang, and S. L. Jie, "Architecture anatomy and hierarchical modeling of sand-gravel braided river reservoirs: a case study of Zhong32 wells area, Qigu Formation reservoir, Fengceng oilfield," *Acta Sedimentologica Sinica*, vol. 38, no. 5, pp. 933–945, 2020.
- [23] J. Li, C. Huo, X. Ye, P. Wang, J. Xu, and J. Yang, "Internal architecture characteristics of sandy braided-river reservoirs in L Oilfield, Bohai Bay Basin," *Petroleum Geology and Recovery Efficiency*, vol. 24, no. 6, pp. 48–53, 2017.
- [24] S. F. Leclair and J. S. Bridge, "Quantitative interpretation of sedimentary structures formed by river dunes," *Journal of Sedimentary Research*, vol. 71, no. 5, pp. 713–716, 2001.
- [25] L. Shunming, S. Xinmin, J. Youwei, L. Lang, C. Nengxue, and S. Jingmin, "Architecture and remaining oil distribution of the sandy braided river reservoir in the Gaoshangpu Oilfield," *Petroleum Exploration and Development*, vol. 38, no. 4, pp. 474–482, 2011.
- [26] D. Q. Xu, Z. X. Sun, Y. F. Ren, and C. Yang, "Geological modeling of braided river tight reservoir based on geological knowledge database," *Fault-Block Oil & Gas Field*, vol. 25, no. 1, pp. 57–61, 2018.
- [27] L. Huang, W. He, P. Tao, J. Li, X. Wang, and X. Wang, "Reservoir architecture and remaining oil enrichment pattern of braided river—a case study from Huanjiang oilfield in Ordos Basin," *Petroleum Geology and Engineering*, vol. 31, no. 1, pp. 96–103, 2017.
- [28] H. Zhao, X. W. Yang, W. C. Yue et al., "Sedimentary facies characteristics and sandbody superimposition relation of Yan'an Formation in Jing'an area," *Journal of Xi'an University of Science and Technology*, vol. 40, no. 4, pp. 646–657, 2020.
- [29] Y. Guo, Z. Cai, F. Yu, X. Zhang, and B. Li, "Sandbody superimposition relation of 8th member of Shihezi Formation in southeastern Sulige and its influence on gas-water distribution," *Journal of Xi'an Shiyou University (Natural Science Edition)*, vol. 33, no. 4, pp. 1–7, 2018.
- [30] C. J. Feng, Z. D. Bao, C. M. Dai, and Z. Q. Zhang, "Superimposition patterns of underwater distributary channel sands in deltaic front and its control in remaining oil distribution: a case study from  $K_1q^4$  in J19 block, Fuyu oilfield," *Oil & Gas Geology*, vol. 36, no. 1, pp. 128–135, 2015.
- [31] X. Wang, F. Zhang, S. Li et al., "The architectural surfaces characteristics of sandy braided river reservoirs, case study in Gudong Oil Field, China," *Geofluids*, Article ID 8821711, 2021.
- [32] Y. Gao, Y. Yin, P. Pan, S. Yu, and Y. Gu, "The effects of incline heterolithic strata on SAGD development," *Oil Drilling & Production Technology*, vol. 42, no. 6, pp. 767–771, 2020.
- [33] L. Xuyan, *Study on the Method of the Spatial Locating of Macroscopic Throats and the Potential Technology in HYJZ9-3 Oilfield*, China University of Petroleum, 2019.
- [34] L. Xu, S. Li, X. Yu, T. Zhang, X. Luo, and G. Jiang, "Analysis of reservoir architecture in the braided river delta front: a case study of the Sangonghe Formation in Block Cai9 of Cainan oilfield," *Petroleum Geology and Recovery Efficiency*, vol. 23, no. 5, pp. 50–57, 2016.
- [35] C. Lyu, X. Wang, X. Lu et al., "Evaluation of hydrocarbon generation using structural and thermal modeling in the thrust belt of Kuqa Foreland Basin, NW China," *Geofluids*, vol. 2020, Article ID 8894030, 18 pages, 2020.

## Research Article

# Evaluation of the Oil-Bearing Properties of Shale and Shale Oil Mobility in the Fengcheng Formation in the Mahu Sag, Junggar Basin, Northwest China: A Case Study of Well Maye-1

Wenjun He,<sup>1</sup> Zhongliang Sun ,<sup>2,3</sup> Menhui Qian ,<sup>2,3</sup> Zhifeng Yang,<sup>1</sup> Zhiming Li,<sup>2,3</sup> Junying Leng,<sup>2,3</sup> and Min Wan<sup>1</sup>

<sup>1</sup>Research Institute of Exploration and Development, Xinjiang Oilfield Company, PetroChina, Karamay 834000, China

<sup>2</sup>Wuxi Research Institute of Petroleum Geology, Petroleum Exploration & Production Research Institute, Sinopec, Wuxi 214126, China

<sup>3</sup>State Key Laboratory of Shale Oil and Gas Enrichment Mechanisms and Effective Development, Wuxi, Jiangsu 214126, China

Correspondence should be addressed to Zhongliang Sun; 995974375@qq.com

Received 4 January 2022; Accepted 13 May 2022; Published 7 July 2022

Academic Editor: Kouqi Liu

Copyright © 2022 Wenjun He et al. This is an open access article distributed under the Creative Commons Attribution License, which permits unrestricted use, distribution, and reproduction in any medium, provided the original work is properly cited.

Due to an increasing energy demand and the depletion of conventional oil, there is ever increasing demand for unconventional shale oil and gas resources. As the most hydrocarbon-rich sag in the Junggar Basin, the development prospects for shale oil in the Mahu Sag have become a focus of research. However, so far, there have been few studies of the oil-bearing properties of shale and shale oil mobility in the sag. This paper redresses this using a range of methods, such as pyrolysis and multi-temperature step pyrolysis. The results show that the Fengcheng Formation shales are generally good quality source rocks. The main body of the shale is low mature-mature, and the type of organic matter is mostly Type II kerogen. In the depth intervals at 4616.45~4640.30 m, 4661.25~4695.20 m, 4728.30~4759.80 m, 4787.60~4812.30 m, and 4876.70~4940.25 m, the oil-bearing properties of the shale and shale oil mobility are good, with an average  $S_1$  of more than 1.5 mg/g, OSI of more than 100 mg/g.TOC<sup>-1</sup>, a ratio of free/adsorbed oil ( $(S_{1-1} + S_{1-2})/S_{2-1}$ ) of more than 3, and a ratio of free/total oil ( $(S_{1-1} + S_{1-2})/(S_{1-1} + S_{1-2} + S_{2-1})$ ) of more than 80%. The second member ( $P_1f_2$ ) and the lower part of the first member ( $P_1f_1$ ) of the formation offer the most promising commercial prospects. Shale oil mobility in the formation is greatly affected by the abundance of organic matter. The higher the TOC value, the greater the hydrocarbon generation capacity, and the better its adsorption capability in the shale. The Fengcheng Formation shale is mature, and shale oil mobility is good. Impacted by the main reservoir space, the felsic shale in the formation has optimal shale oil mobility, with the shale oil being characterized by self-generation and self-storage, and accumulation in adjacent layers.

## 1. Introduction

Evaluation of the oil bearing properties of shale systems is a fundamental requirement in shale oil exploration. It has a great impact on research into the mobility of residual hydrocarbons in shale strata [1]. However, there are no unified criteria for determining good oil-bearing properties. Shale series of strata contain both residual hydrocarbons and kerogen, with residual hydrocarbons including both light hydrocarbons (oil with carbon numbers less than 15, which can be effectively produced) and heavy hydrocarbons (carbon num-

bers greater than 15). According to the nature of the interaction between light hydrocarbon and media, the occurrence state of light hydrocarbons is divided into free state, dissolved state, physical adsorption state, chemical adsorption state, and a hydrated state. Free movable hydrocarbons are the principal contributors to shale oil productivity [2, 3]. However, there is no mature resource evaluation method for retained hydrocarbons. Common research methods use the pyrolysis parameter  $S_1$  (free hydrocarbon) and the content of original chloroform bitumen "A" to calculate retained hydrocarbons, but there are obvious disadvantages in the amounts calculated by both

methods. The amount of retained hydrocarbons calculated using  $S_1$  is basically the content of free hydrocarbon released under rapid artificial heating to a constant temperature of 300°C, and the carbon numbers of the hydrocarbon compounds are mainly between  $C_{14}$  and  $C_{18}$  [4]. Compared with crude oil in the field, there is light hydrocarbon loss and absent of heavy hydrocarbon, so the retained hydrocarbon content given will generally be lower than the actual content. The content of chloroform bitumen "A" represents free hydrocarbons, asphaltene, non-hydrocarbons, and adsorbed hydrocarbons which are soluble in organic solvents, with carbon numbers distributed between  $C_6$  and  $C_{38}$ . The composition of chloroform bitumen "A" is similar to that of crude oil, but the content of macromolecular compounds is higher [4–7]. Analysis of  $S_1$  and TOC data from the major pay zones in North America led Jarvie to believe that there is a characteristic threshold value for the flow of crude oil in shale strata [8, 9]. Excess hydrocarbons are only expelled once the hydrocarbons generated in shales exceed the adsorption and reservoir saturation. The oil saturation index (OSI) ( $S_1/TOC$ ) is therefore included in the scope of oil-bearing property evaluation for shale. An OSI value of 100 mg/g.TOC is regarded as the threshold for movable hydrocarbons in shale oil. Chinese practice suggests that the movable hydrocarbon threshold for shale oil determined by Jarvie may not be applicable to lacustrine shale strata, which are prevalent in China's sedimentary basins, due to the differences in geological conditions. For example, the OSI values of intra-salt shale oil accumulations in the Qianjiang Sag can reach hundreds or even higher, but some formations with low  $S_1$  contents have not achieved expected hydrocarbon production during exploration [10], so the theory needs to be combined with the actual situation to be applicable in practice. To accurately characterize shale oil-bearing property and mobility, new experimental methods, such as two-dimensional NMR and multi-temperature step pyrolysis, have also been applied to more accurately evaluate shale oil. Multi-temperature step pyrolysis has been widely used to evaluate shale oil-bearing properties and hydrocarbon mobility because of the comparative accuracy of the results and the low cost of application [4, 11]. The thermally released hydrocarbon peaks obtained under constant-rate heating can be used to define the occurrence characteristics of shale oil and evaluate their contents under various occurrence states. The thermally released hydrocarbon peak at a temperature of 200°C indicates light hydrocarbons ( $S_{1-1}$ ) and represents the actual amount of movable oil in the shale. When the temperature reaches 350°C, the  $S_{1-2}$  peak represents the medium-heavy component of thermally released free oil. The medium-heavy component is not completely movable. The sum of  $S_{1-1}$  and  $S_{1-2}$  represents the total amount of free oil in the shale (also known as the maximum movable oil).  $S_{2-1}$  represents oil in an adsorbed-intermiscible or adsorbed state. The sum of these three parameters is the total generated oil and gas [4, 11].

The Mahu Sag is the richest of the petroliferous sags in the Junggar Basin. The lacustrine source rocks of the Lower Permian Fengcheng Formation in the Mahu Sag provide the material basis for the formation of two major oil provinces of enormous length in the northwest margin of the basin:

the Karamay-Wuerhe and Mahu oil areas. [12–15]). Geological background analysis suggests that the high-quality middle-high mature alkaline lacustrine source rocks of the Fengcheng Formation in the northwest margin of the Mahu Sag [16, 17]) are the most likely to form in-source and outside-source oil and gas enrichment and whole petroleum system. Based on this understanding, the Xinjiang Oilfield deployed well Maye-1, the first shale oil risk exploration well in the basin. This well adopted the vertical well + multistage separate-layer fracturing process for the first time and obtained high and stable hydrocarbon flow. The reserves scale is preliminarily estimated at 600 million tons. Despite this success, there has still been little research on the oil-bearing properties and oil mobility characteristics of the shale in the Mahu Sag. This paper uses methods such as X-ray diffraction, pyrolysis, and multi-temperature step pyrolysis to study the cored interval of the Fengcheng Formation in well Maye-1. The mineral compositions, lithofacies classification, oil-bearing properties, and movable oil characteristics of various members of the Lower Permian Fengcheng Formation shale are described, and the characteristics of the source rocks in the formation analyzed. The main controlling factors affecting shale oil mobility are discussed, identifying the favorable lithofacies for the occurrence of movable shale oil and their reservoir-forming modes. This will provide data support for future shale oil development in the Fengcheng Formation.

## 2. Geological Settings

The Mahu Sag is located in the northwest of the Junggar Basin, between the Kebai-Wuxia fault zone and the western segment of the Luliang Uplift (Figure 1).

It is a Carboniferous-Quaternary sag with a sedimentary thickness of tens of thousands of meters developed on pre-Carboniferous basement. It is a hydrocarbon generating sag, with the highest degree of oil and gas enrichment in the Junggar Basin. There are four sets of effective source rocks: the Jiamuhe Formation, the Fengcheng Formation, the lower Wuerhe Formation, and the Carboniferous. The Fengcheng Formation source rocks are the most important [18, 19]). The Fengcheng Formation source rocks are considered to be the oldest high-quality alkaline lacustrine source rocks in the world. They were formed under semiarid conditions, with a humid, seasonal environment alternating with arid conditions [20]. From bottom to top, the sedimentary strata in the Mahu Sag consist of the Lower Permian Jiamuhe and Fengcheng Formations, the Middle Permian Xiazijie and Lower Wuerhe Formations, the Lower Triassic Baikouquan Formation, the Middle Triassic Karamay Formation, the Upper Triassic Baijiantan Formation, the Lower Jurassic Badaowan and Sangonghe Formations, the Middle Jurassic Xishanyao and Toutunhe Formations, the Upper Jurassic Qigu Formation, and the overlying Cretaceous strata (Figure 2).

The Fengcheng area is at the junction of the northwest of the Mahu Sag and the south of the Wuerhe-Xiazijie fault zone (the Wuxia fault zone) (Figure 1). It is an enrichment area for shale oil, with the lower Permian Fengcheng

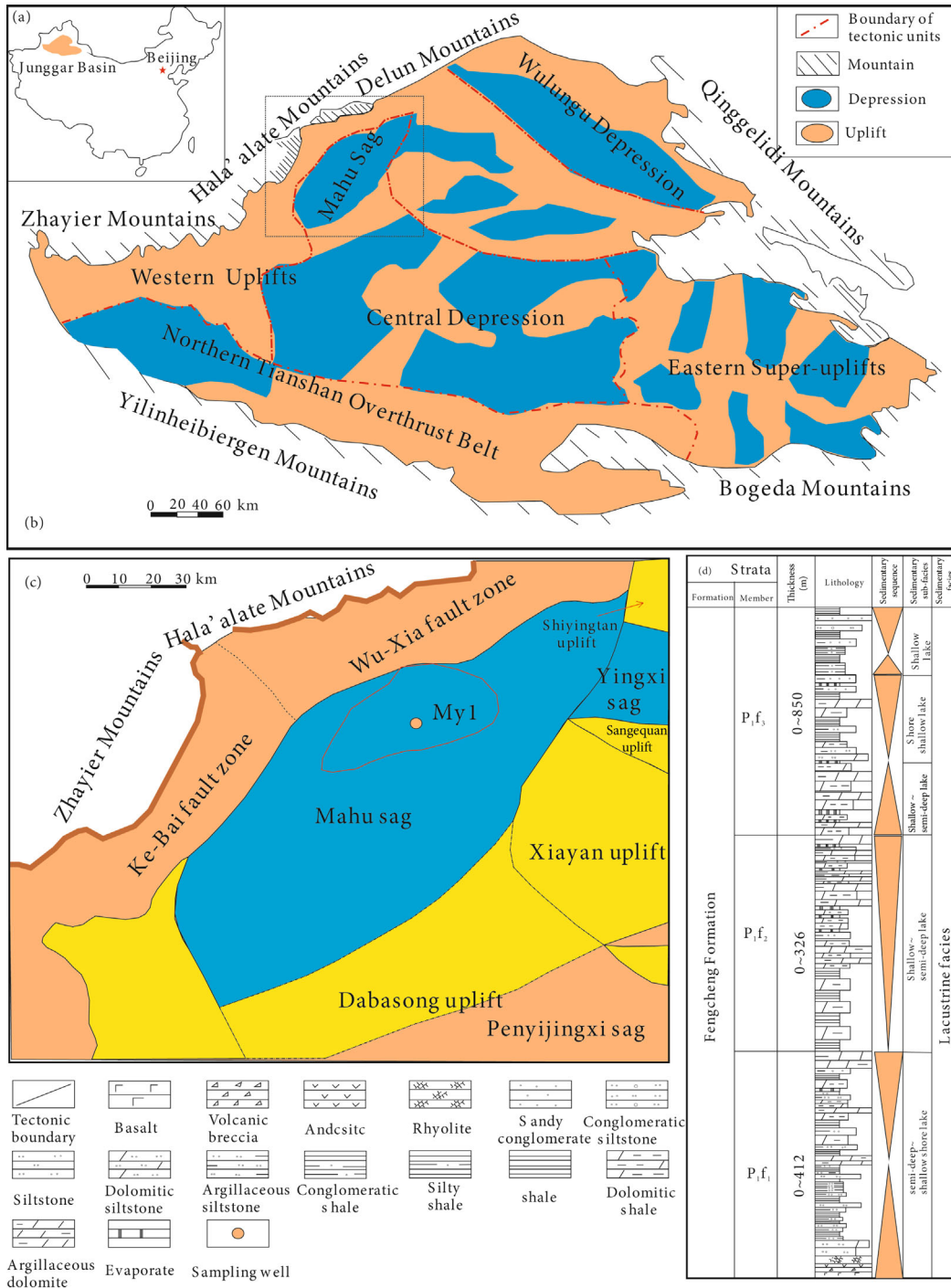


FIGURE 1: (a) Map of the Junggar Basin in China. (b) The division of tectonic units in the Junggar Basin and the location of the Mahu scheme. (c) The division of subtectonic units and thickness contour of Fengcheng Formation in Mahu Sag. (d) Lithology and sedimentary facies profile of the Fengcheng Formation in the Mahu Sag [22].

Formation providing good source rocks and reservoirs. The Fengcheng Formation is divided into three members: the first member (P<sub>1</sub>f<sub>1</sub>), the second member (P<sub>1</sub>f<sub>2</sub>), and the third member (P<sub>1</sub>f<sub>3</sub>), from bottom to top. It is basically a multi-source mixed fine-grained sedimentary formation deposited in a semi deep-deep alkaline lacustrine environment [21]. Mixed deposition of endogenous chemical material generated in the arid and hot evaporation environment, volcanic

material provided by peripheral volcanic activity, and near-source terrigenous debris formed by denudation of the nappe in the western margin, as well as endogenous carbonate and other provenances, combined to create the complex mineral deposition characteristics and frequently interbedded structure of the formation, providing plentiful reservoir space for enrichment of oil and gas in the source rocks. In addition, due to its unique alkaline lacustrine deposition

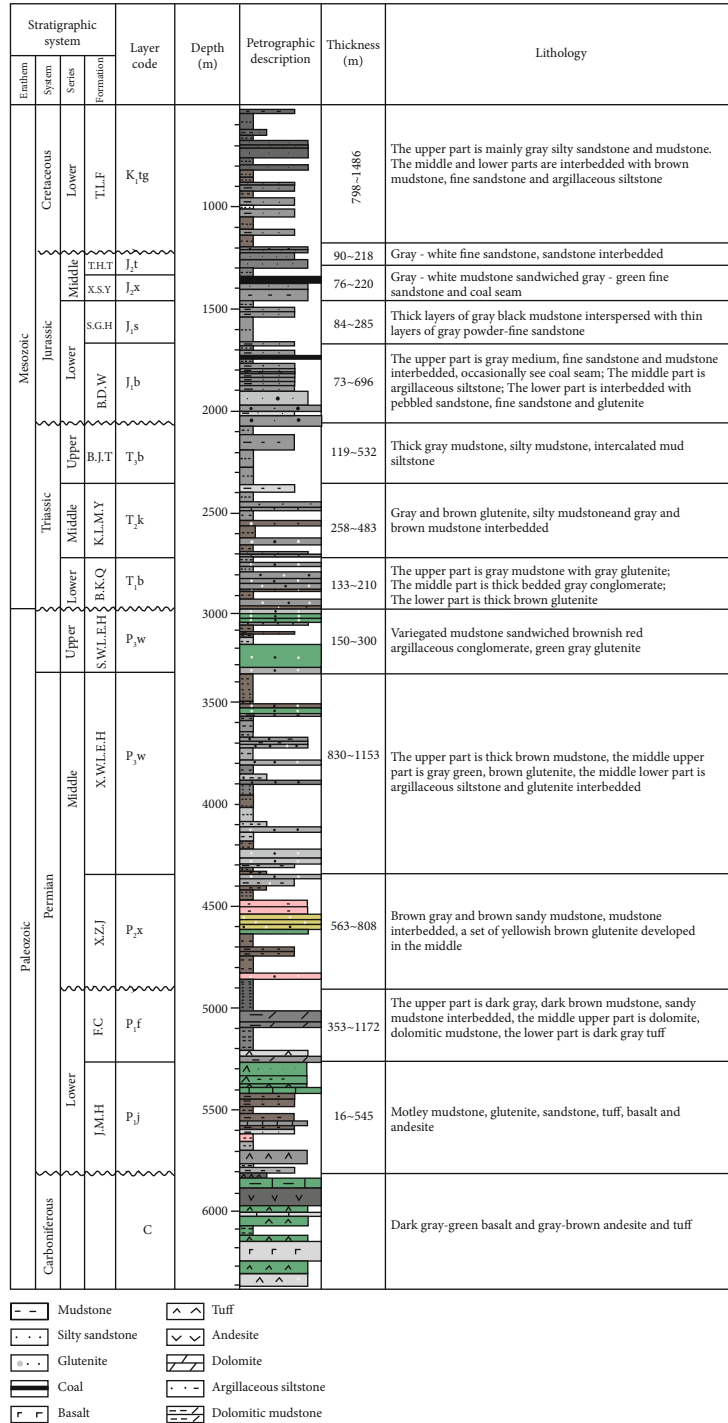


FIGURE 2: Comprehensive stratigraphic column of the Mahu Sag.

environment, the development process of the Mahu Sag was accompanied by episodes of alternate transgression and volcanism, which provided abundant nutrients for the propagation of microorganisms and algae on an enormous scale, providing luxuriant sapropelic parent material for hydrocarbons. This environment also meant that the source rocks of the Fengcheng Formation remained at the peak of oil generation in the high maturity ( $R_o > 1.5\%$ ), so the oil generation stage was much longer than that of other high-quality lacustrine

source rocks. The Fengcheng Formation source rocks are therefore characterized by more oil and less gas, high conversion rates, continuous hydrocarbon generation, multistage peaks, long oil generation windows, and light oil quality [18].

### 3. Samples and Methods

3.1. *Sample Collection.* Well Maye-1 lies in the Northern Slope of the Mahu Sag, with no discordogenic faults

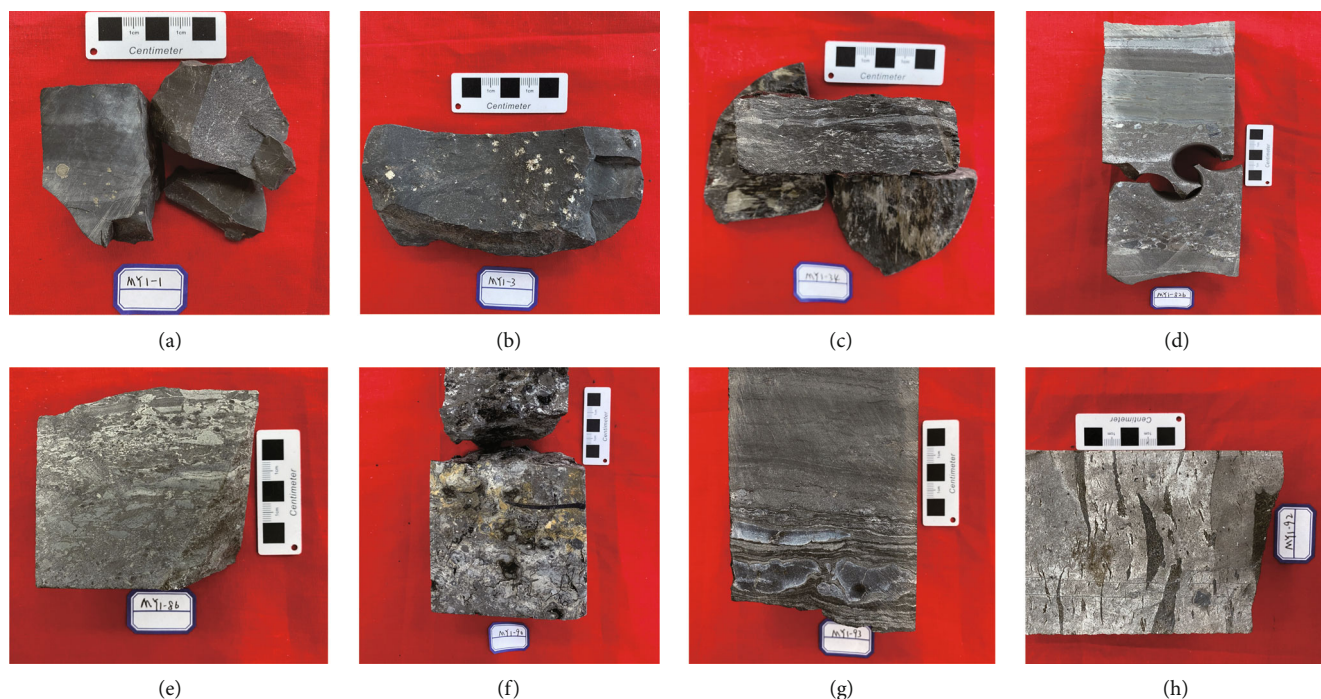


FIGURE 3: Cores of the Fengcheng Formation in the Mahu Sag. (a) Silty mudstone,  $P_{1f_3}$ , depth 4587.55 m; (b) argillaceous siltstone containing pyrite,  $P_{1f_3}$ , depth 4591.08 m; (c) mudstone intercalated with lime belts,  $P_{1f_2}$ , depth 4693.15 m; (d) alternate development of limerock, clastic rocks, siltstone, and argillaceous siltstone,  $P_{1f_1}$ , depth 4879.96 m; (e) hybrid sedimentary rock, chaotic mélange of terrigenous clast,  $P_{1f_1}$ , depth 4876.36 m; (f) ignimbrite,  $P_{1f_1}$ , depth 4912.92 m; (g) siltstone intercalated with lime lenticles,  $P_{1f_1}$ , depth 4917.6 m; (h) tuff,  $P_{1f_1}$ , depth 4916.43 m.

developed in the periphery, and the strata are relatively completely developed from the Paleozoic Carboniferous to the Cenozoic Quaternary. From base to top, the Permian is divided into the Lower Permian Jiamuhe Formation and Fengcheng Formation, the Middle Permian Xiazijie Formation, and Lower Wuerhe Formation, and the Upper Permian Upper Wuerhe Formation is absent. The evolution of the study area from the early Carboniferous to the Permian formed distinct alkaline lake deposition of Fengcheng Formation. Well Maye-1 is located at the edge of the alkali lake and mainly develops shore-shallow lacustrine sediment. The focus of this study is the Fengcheng Formation at sampling depths ranging from 4585 to 4940 m. The coring depths in  $P_{1f_3}$ ,  $P_{1f_2}$ , and  $P_{1f_1}$  are 4585~4595 m, 4607~4787 m, and 4790~4940 m, respectively. Core observation shows that the lithology of the cores of the formation includes silty mudstone, argillaceous dolomite, siltstone, tuff, terrigenous clastic rock, and pyroclastic rocks (Figure 3). There are apparent differences in lithologic assemblages between various members.  $P_{1f_1}$  is mainly composed of dark gray-gray mudstone, tuffaceous mudstone intercalated with dolomitic sandstone, dolomite, tuffaceous dolomite, argillaceous dolomite, and tuff. Volcanic activity has been relatively intense, with pyroclastic rocks occurring, and the member is rich in salt rocks, shortite, and other distinctive alkaline minerals.  $P_{1f_2}$  consists of dolomitic sandstone and gray mudstone intercalated with argillaceous dolomite, with a large number of alkaline minerals, primarily characterized by rhythmic,

diverse thicknesses of layered alkaline minerals, and dark dolomitic mudstone.  $P_{1f_3}$  comprises gray mudstone, argillaceous dolomite, and dolomitic mudstone, with relatively small contents of alkaline minerals.

**3.2. Experimental Method.** For X-ray diffraction analysis, a D8 AD-VANCE X-ray diffractometer from the Bruker Company, Germany, was used, with the sample broken down to about 0.1 mm particles. The test was carried out with reference to the standard SY/T 5163-2010 at a temperature of 25 °C and relative humidity of 50%. Test conditions were as follows: Cu target, X-ray tube voltage 40 kV, electric current 100 mA, scanning speed 4° ( $2\theta$ )/min, and scanning step width 0.02° ( $2\theta$ ).

A Rock-Eval 6 pyrolysis machine was used for the pyrolysis and multi-temperature step pyrolysis tests, with different temperature programs for each. For the rock pyrolysis experiment, the temperature was first raised to 300 °C, then held for 3 min to measure the  $S_1$  peak, and then increased at 25 °C/min to 650 °C, where it was maintained for 1 min to obtain the  $S_2$  and  $T_{max}$  values.

For the multi-temperature step pyrolysis experiment, the temperature was first kept at 200 °C for 1 min to measure  $S_{1-1}$ , then raised to 350 °C at 25 °C/min, where it was maintained for 1 minute to measure  $S_{1-2}$ , then raised again to 450 °C at 25 °C/min, where it was maintained for 1 min to measure  $S_{2-1}$ , and then finally raised to 650 °C at 25 °C/min to measure  $S_{2-2}$ . Both rock pyrolysis and multi-temperature pyrolysis required sample particles smaller than 0.1 mm.

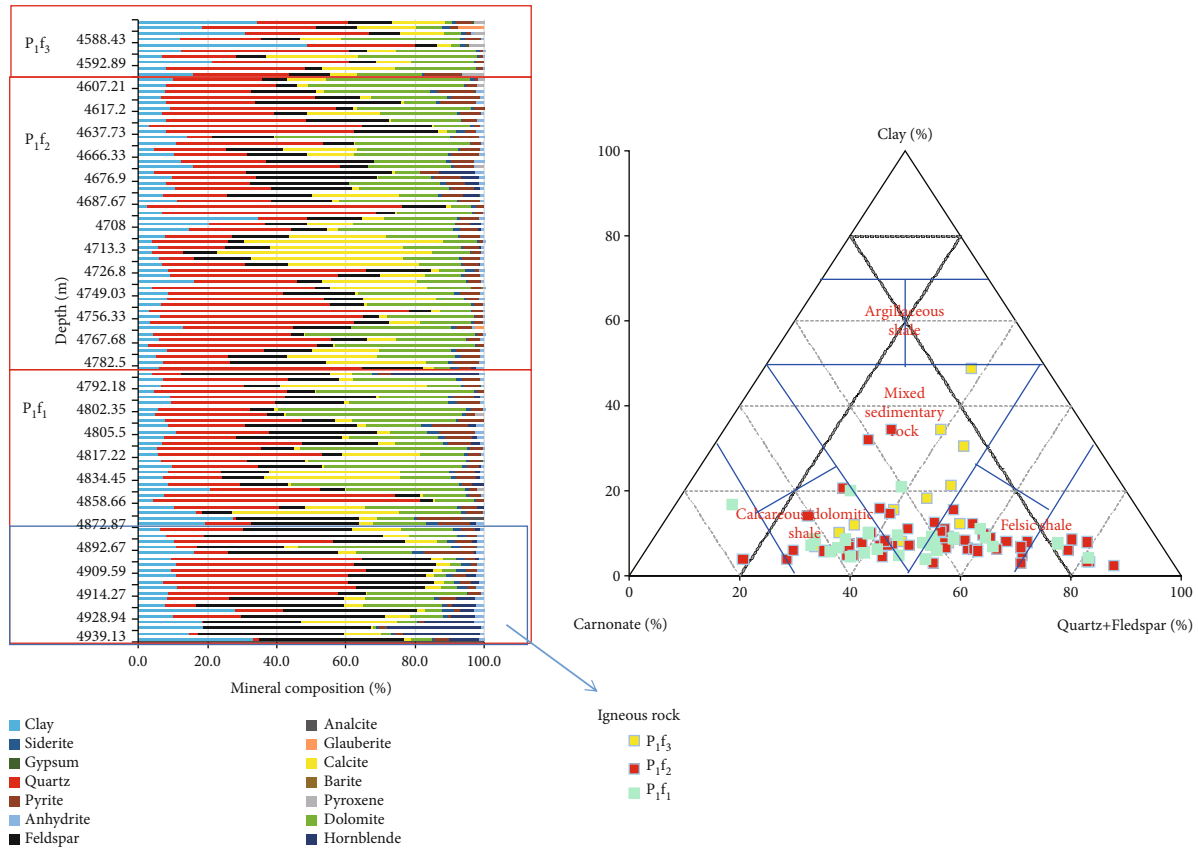


FIGURE 4: Mineral composition and lithofacies division of Fengcheng Formation shale.

X-ray diffraction analysis, pyrolysis, and multi-temperature step pyrolysis experiments were carried out in the Wuxi Research Institute of Petroleum Geology, Sinopec Petroleum Exploration, and Development Research Institute.

## 4. Results

**4.1. Mineral Composition and Lithofacies Division.** Figure 4 shows the basic mineral compositions of the cores from well Maye-1. It shows that the mineral composition of the Fengcheng Formation shale principally consists of three types of minerals: clay minerals, felsic minerals (quartz and feldspar), and carbonate minerals (dolomite and calcite). There are also smaller quantities of siderite, pyrite, and other sulfate minerals, as well as alkaline minerals such as gypsum, anhydrite, and glauberite. There are significant differences in the main mineral compositions of the three members of the formation. The content of clay minerals in the 48 cores from  $P_{1f_1}$ , 48 cores from  $P_{1f_2}$ , and 11 cores from  $P_{1f_3}$  ranges from 4.0% to 37.5% (average 12.3%), 3.0% to 34.5% (average 9.0%) and 7.1% to 48.9% (average 20.9%). Correspondingly, the content of quartz ranges from 0.2% to 58.6% (average 26.8%), 7.0% to 73.7% (average 34.5%), and 21% to 48.7% (average 32.7%), respectively. Correspondingly, the content of feldspar ranges from 3.6% to 51.7% (average 22.8%), 4.0% to 42.3% (average 15.3%), and 5.1% to 12.8% (average 9.0%), respectively; the content of calcite ranges from 0.2%

to 42.6% (average 8.1%), 0.1% to 62.2% (average 11.8%), and 4.3% to 26.3% (average 13.6%), respectively; the content of dolomite ranges from 0.8% to 54.4% (average 18.5%), 2.7% to 49.5% (average 22.1%), and 2.0% to 34.5% (average 16.9%), respectively. The cores from the lower part of  $P_{1f_1}$  (4870~4940 m) are characterized by high feldspar and low quartz, which is quite different from the overall mineral characteristics of the formation, suggesting that the lower part of the Fengcheng Formation is composed of pyroclastic rocks.

The cores were divided on the basis of lithofacies, revealing a predominance of felsic shale facies, mixed sedimentary facies, and lime/dolomitic shale facies. There are discrepancies in the distributions of lithofacies in the various members. The  $P_{1f_1}$  lithofacies is primarily lime/dolomitic shale facies and felsic shale facies. All three lithofacies are extensively distributed in  $P_{1f_2}$ . The  $P_{1f_3}$  cores are basically hybrid sedimentary rock facies.

**4.2. Characteristics of Quality of Source Rocks.** Source rocks are the basis for oil generation. The quality of source rocks is a crucial factor affecting hydrocarbon accumulation quality. From an organic geochemical perspective, the hydrocarbon potential of source rocks depends on the abundance, type, and maturity of organic matter. These three factors complement each other. Source rocks with high abundance of organic matter and moderately mature Type I or Type II organic matter have great hydrocarbon potential. This

TABLE 1: Evaluation index of organic matter abundance of continental source rocks [26].

Evaluation indicator	Lake salinity	Non-source	Poor	Fair	Good	Excellent
TOC (%)	Fresh-brackish	<0.4	0.4~0.6	0.6~1.0	1.0~2.0	>2.0
PG (mg/g)		/	<2	2~6	6~20	>20

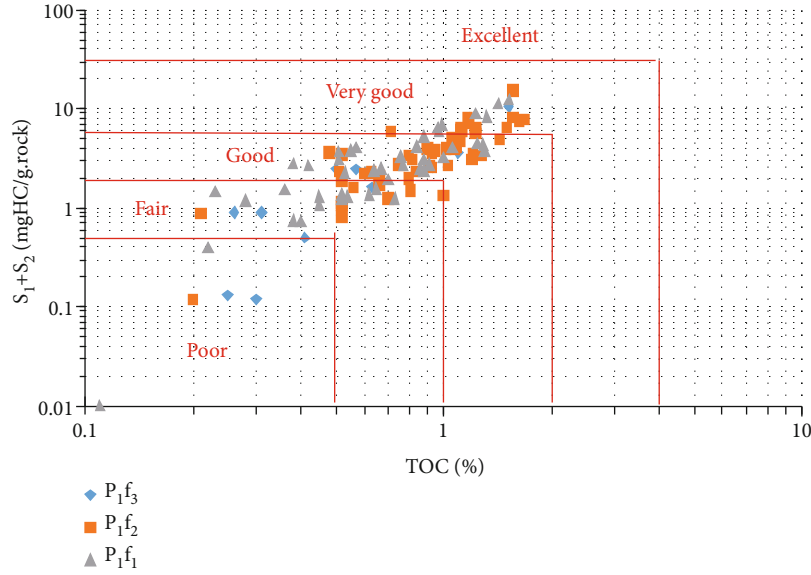


FIGURE 5: Quality classification of source rocks of the Fengcheng Formation shale in the Mahu Sag.

paper primarily evaluates three aspects of the Fengcheng Formation shale source rock: quality of the source rock, organic matter maturity, and organic matter type.

This paper uses hydrocarbon generation potential PG ( $S_1 + S_2$ ) and TOC to classify the quality of continental source rocks [23, 24]. The current prevailing evaluation method for continental source rocks is mainly applicable to freshwater or brackish lakes [25, 26] (Table 1). The most appropriate evaluation criteria for alkaline lacustrine source rocks are still debated. Previous studies have shown that, compared with fresh water or brackish lacustrine source rocks, alkaline lacustrine source rocks have high hydrocarbon-generating transformation ratios and longer continuous hydrocarbon generation periods [18]. Hence, even if the TOC value is low, the hydrocarbon potential of a source rock may be high, so the application of traditional evaluation criteria may underestimate its resource potential. This is arguably true of the Fengcheng Formation. Tang et al. [27] combined the actual situation of the Mahu Sag with a large number of experimental results and classified the quality of the source rocks into five categories: nonhydrocarbon, fair, good, very good, and excellent, with (respectively) TOC < 0.3%, 0.3~0.5%, 0.5~0.7%, 0.7~1.4%, and > 1.4% and hydrocarbon potential PG ( $S_1 + S_2$ ) < 0.5 mg/g, 0.5~1.5 mg/g, 1.5~3.0 mg/g, 3.0~7.0 mg/g, and >7.0 mg/g. In this paper, the quality of source rocks in the study interval is determined according to this classification standard, and Figure 5 shows that the Fengcheng Formation shale is generally of good-excellent

quality. The  $P_{1f_2}$  source rock has the best quality but the main body of the formation also contains generally good-very good-excellent source rocks. The quality of some of the  $P_{1f_1}$  source rocks is only fair, a few are poor, but the main body of the formation contains generally good-very good-excellent source rocks. The quality of source rocks in  $P_{1f_3}$  is comparatively poor, and the rocks are of mixed quality, with some in every category.

The degree of thermal evolution is a vital factor for determining the resource potential of shale oil accumulations [28], and  $T_{max}$  is one of the most commonly used parameters for evaluating the degree of thermal evolution [29]. Analysis of pyrolysis data  $T_{max}$  (Figure 6) for the shale samples in the study area shows that the  $T_{max}$  values are generally distributed in the range 410 to 460 °C. However, the distributions of  $T_{max}$  values in the various members are quite different. The deeper  $P_{1f_1}$  cores generally have low  $T_{max}$  values, mostly in the interval 415~445 °C. The  $T_{max}$  values of the  $P_{1f_2}$  cores in the middle are relatively high, largely in the interval 430~445 °C. The cores in the shallowest member,  $P_{1f_3}$ , have the highest thermal maturity, with  $T_{max}$  values chiefly between 430 and 450 °C. This apparent anomaly may indicate that  $P_{1f_1}$  contains a proportion of oil that migrated from elsewhere. Figure 7 shows that the  $S_1$  value in the lower part of  $P_{1f_1}$  (4915~4940 m) is generally high, but the  $S_2$  and HI values are low, showing typical reservoir characteristics. This strongly suggests that most of the oil and gas in  $P_{1f_1}$  migrated into the member. The  $T_{max}$  values decrease with increasing oil saturation, and the PI

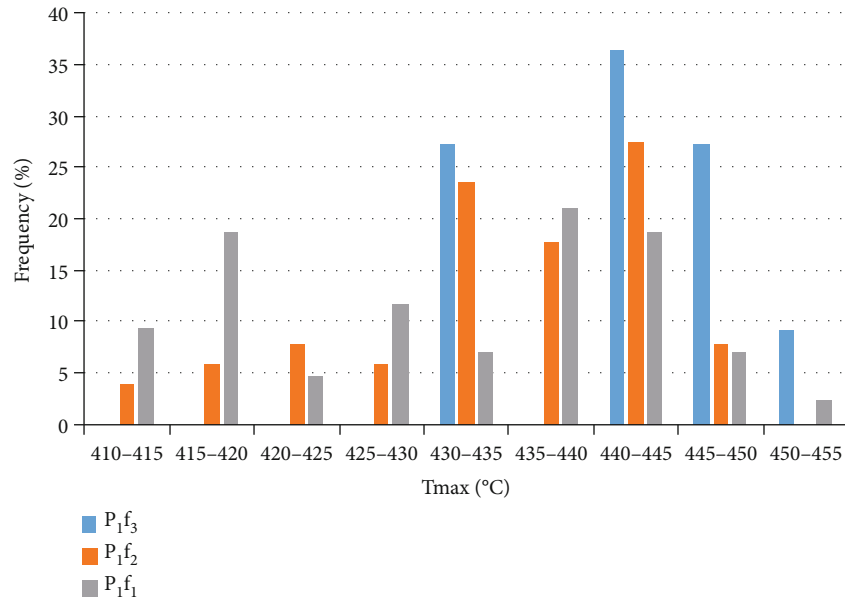


FIGURE 6: Maturity of shale in the Fengcheng Formation.

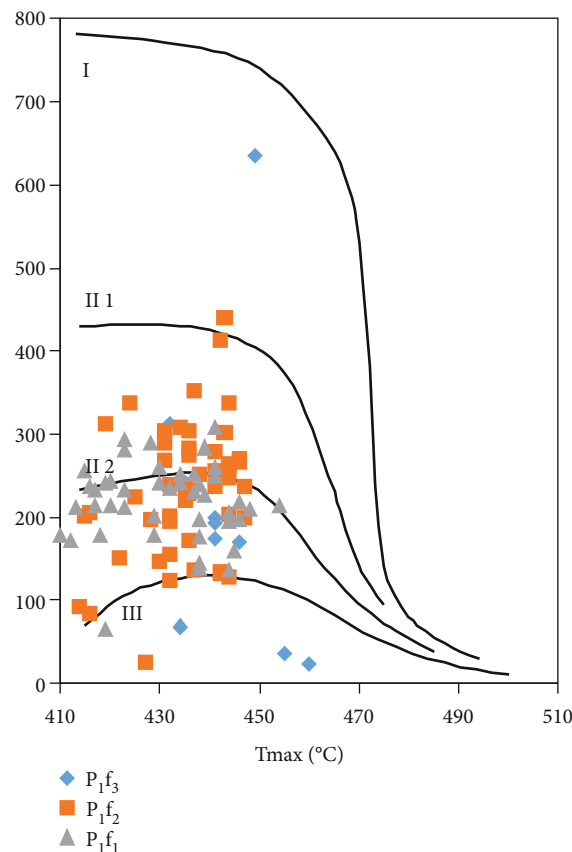


FIGURE 7: Classification of organic matter types in the Fengcheng Formation.

values increase significantly (Figure 8), which, again, signifies the presence of migrated oil in the area. This set of alkaline lacustrine dolomitic hybrid sedimentary rocks contains abundant residual hydrocarbons, resulting in a false low  $T_{\max}$  reading. The actual thermal evolution degree of

the source rocks in the Fengcheng Formation is very likely to be higher [9]. The variation of  $T_{\max}$  values with depth shows that the  $T_{\max}$  values of the Fengcheng Formation shale are mostly between 440 °C and 450 °C, representing a mature stage. The change of vitrinite reflectance with depth

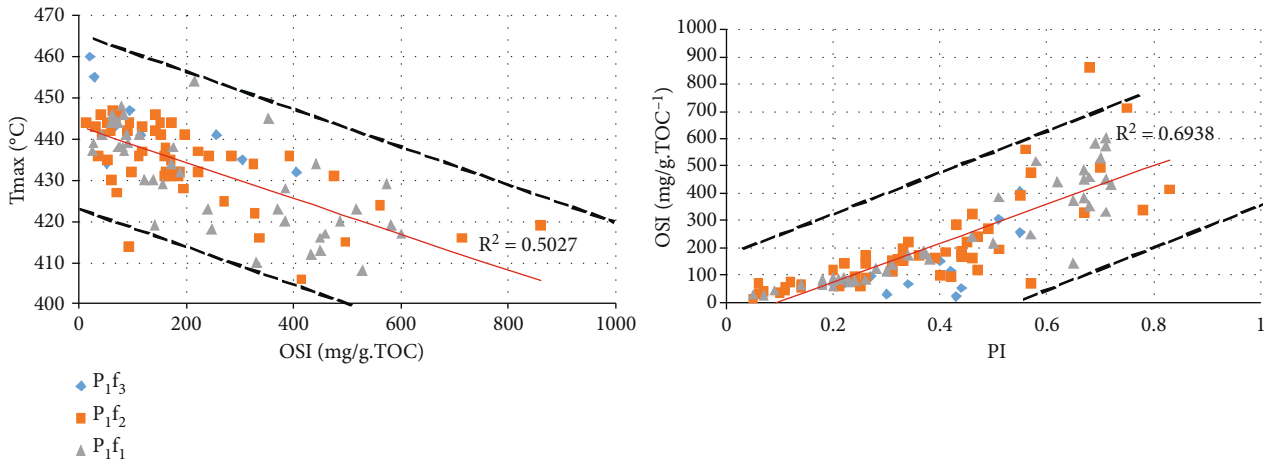


FIGURE 8: Variation of maturity with oil-bearing properties of the Fengcheng Formation shale and correlation between productivity and oil saturation indices (OSI).

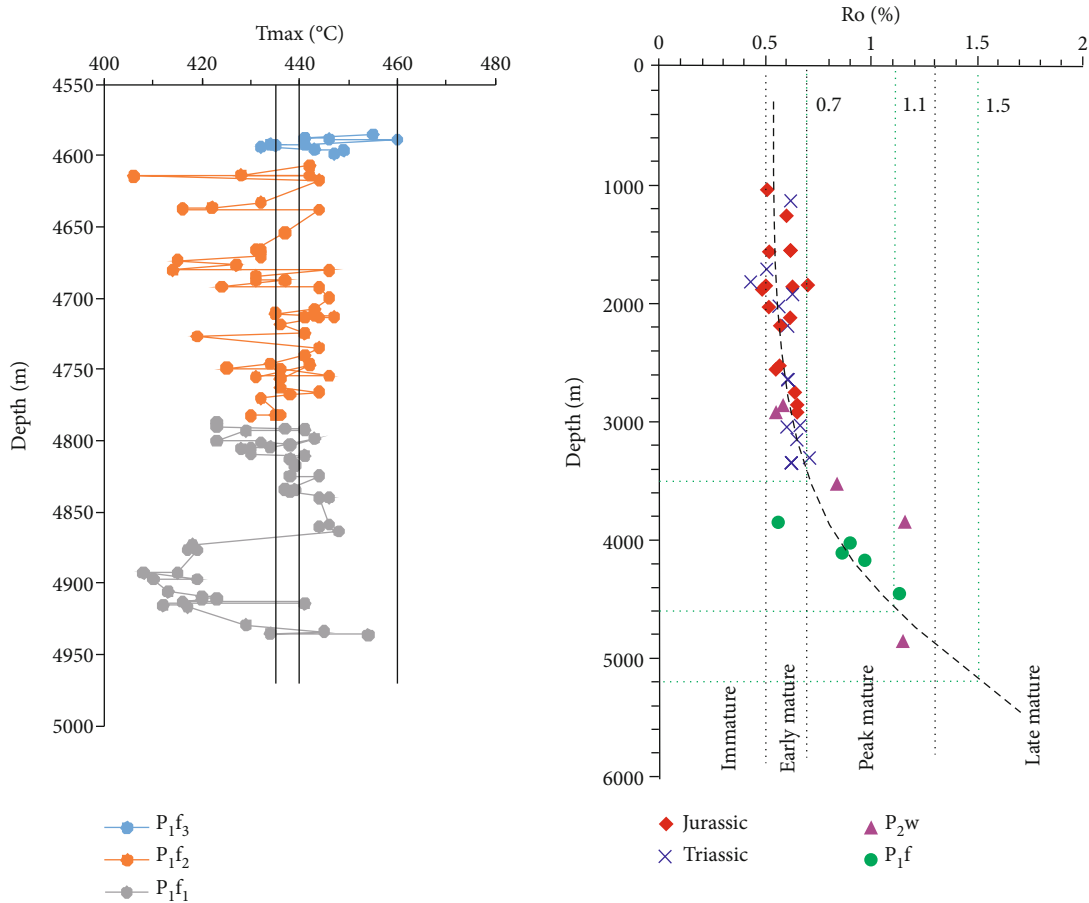


FIGURE 9: Change of  $T_{max}$  value and vitrinite reflectance  $R_o$  of the Fengcheng Formation shale with depth.

in the Mahu area indicates that the vitrinite reflectance of the Fengcheng Formation is mostly about 1.1%, which, again, represents a mature stage (Figure 9).

The hydrogen index ( $HI = S_2/TOC$ ) and  $T_{max}$  can be used together to determine the type of organic matter [30]. The results for the study area show that the HI range is 21.62-304.41 mg HC/g.TOC (average 164.96 mg HC/g.TOC).

According to the resulting Van Krevelen diagram, the Fengcheng Formation shale is dominated by Type II<sub>1</sub> and Type II<sub>2</sub> kerogen, with little difference in the type of organic matter between the different members (Figure 9). Previous studies have identified the organic matter in the Fengcheng Formation shale in the Mahu Sag as mainly sapropelic organic matter derived from algae [9]. This is different from the results

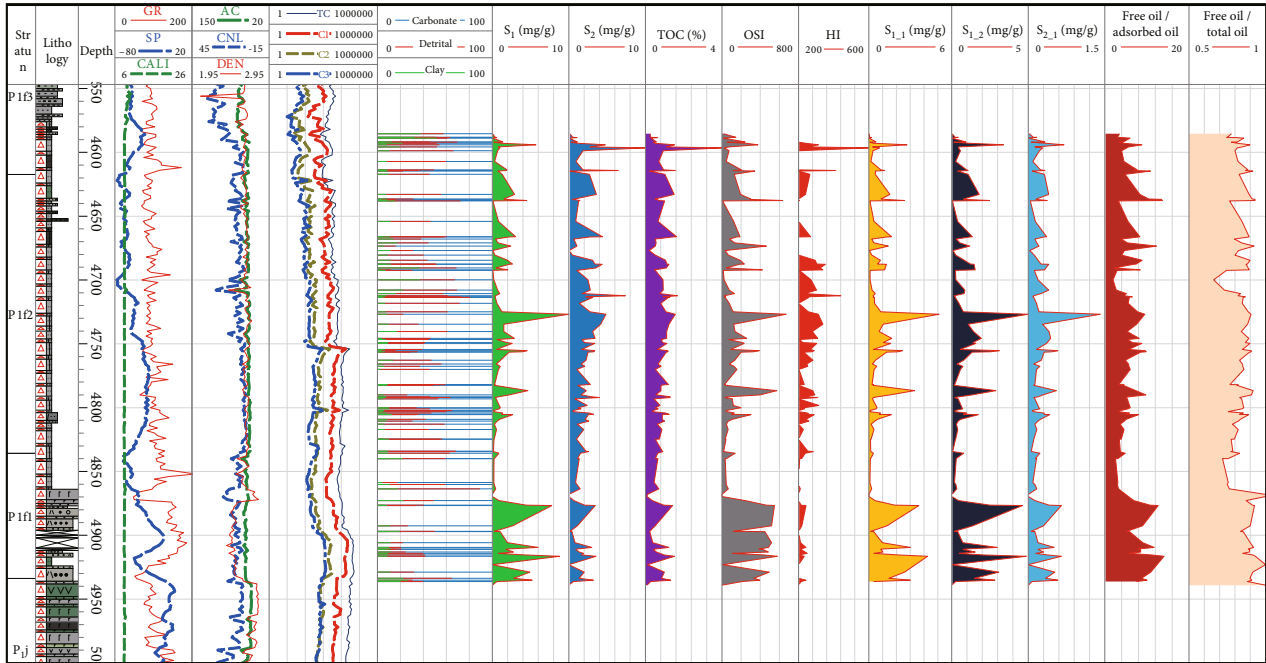


FIGURE 10: Oil-bearing property of the Fengcheng Formation shale and shale oil mobility characteristics in the Mahu Sag.

obtained in this paper. However, previous research results have assumed that the organic matter in the area has reached the mature stage, which may have led to low values for  $S_2$  at the calculated  $T_{max}$ . The Van Krevelen diagram may therefore be inaccurate. Residual hydrocarbons in the samples may also have caused the low test value for  $T_{max}$ .

## 5. Discussion

**5.1. Evaluation of Oil-Bearing Properties.** Oil-bearing properties are crucial for determining whether a research interval has commercial potential. The parameters used in pyrolysis experiments include free hydrocarbon ( $S_1$ ), pyrolyzed hydrocarbon (PHC) which reflects genetic potential ( $S_2$ ), and residual organic carbon (TOC). These parameters are applied to determine the oil-bearing properties of the Fengcheng Formation in well Maye-1. Figure 10 shows that the distribution range of  $S_1$ ,  $S_2$ , and the TOC content of the shale in the Fengcheng Formation are 0.04~10.46 mg/g, 0.07~26.49 mg/g, and 0.28~4.17%, respectively. In the  $P_{1f_1}$  shale,  $S_1$  is 0.04~5.71 mg/g (average 1.03 mg/g),  $S_2$  is 0.07~26.49 mg/g (average 3.40 mg/g), and TOC content is 0.25~4.17% (average 0.91%). In the  $P_{1f_2}$  shale,  $S_1$  content is 0.07~10.46 mg/g (average 1.54 mg/g),  $S_2$  is 0.05~7.37 mg/g (average 2.38 mg/g), and TOC content is 0.21~1.67% (average 0.93%). In the  $P_{1f_3}$  shale,  $S_1$  content is 0.15~9.26 mg/g (average 2.97 mg/g),  $S_2$  content is 0.14~4.64 mg/g (average 1.79 mg/g), and TOC content is 0.28~1.81% (average 0.77%). Correlation between depth and oil-bearing properties indicates that the optimum oil-bearing properties of the Fengcheng Formation shale in well Maye-1 occur in the intervals at 4580.00~4600.00 m, 4616.45~4640.30 m, 4661.25~4695.20 m, 4728.30~4759.80 m,

4787.60~4812.30 m, and 4876.70~4940.25 m. The average values of  $S_1$  at these depths are 1.03 mg/g, 2.01 mg/g, 1.55 mg/g, 2.97 mg/g, 1.25 mg/g, and 3.92 mg/g, respectively. The average values of  $S_2$  are 3.40 mg/g, 1.71 mg/g, 2.19 mg/g, 3.05 mg/g, 2.07 mg/g, 1.92 mg/g, and 1.5 mg/g, respectively. The average TOC is 0.91%, 0.9%, 0.86%, 1.09%, 0.81%, and 0.86%. These six intervals are identified as “sweet spot” intervals with good oil-bearing properties.

In addition, OSI evaluation of the shale (Figure 11) shows that most core samples from  $P_{1f_2}$  have high oil saturation, with OSI greater than  $100 \text{ mg/g.TOC}^{-1}$ , which indicates good commercial development potential. The OSI of the lower section of  $P_{1f_1}$  is particularly high (Figures 10 and 11), with the OSI of some samples exceeding  $400 \text{ mg/g.TOC}^{-1}$ . This interval generally has good oil-bearing properties, with the OSI of some cores from  $P_{1f_3}$  also surpassing  $100 \text{ mg/g.TOC}^{-1}$ . However, in this case, strata with good oil-bearing properties are frequently interbedded with poorer layers. Nevertheless, this represents a suitable target interval for future commercial development.

**5.2. Evaluation of Mobility.** Free movable hydrocarbons are the main contributors to shale oil productivity, so evaluation of shale oil mobility is recognized as a vital factor in evaluating the accumulation qualities of shales. Multi-temperature step pyrolysis has the advantage of accurately determining the amounts of oil in a variety of occurrence states in shales. The free hydrocarbon parameters include light hydrocarbons ( $S_{1-1}$ ), heavy hydrocarbon ( $S_{1-2}$ ), and adsorbed-miscible or adsorbed hydrocarbons ( $S_{2-1}$ ). These parameters can be used to evaluate shale oil mobility. Figure 10 shows that the overall distribution ranges of  $S_{1-1}$ ,  $S_{1-2}$ , and  $S_{2-1}$  in the Fengcheng

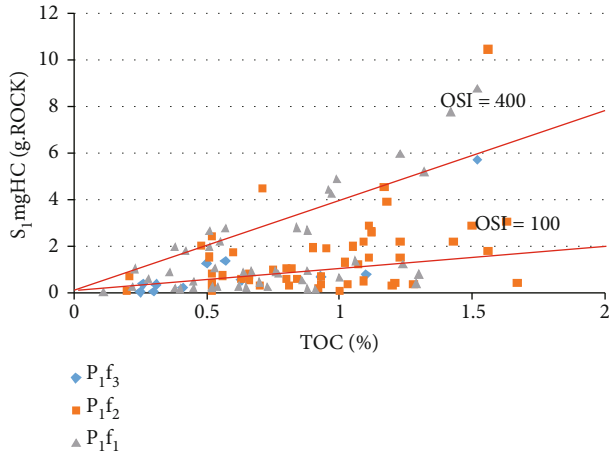


FIGURE 11: Oil saturation characteristics of the Fengcheng Formation shale in the Mahu Sag.

Formation shale of the Mahu sag are 0.1~5.09 mg/g, 0.18~8.33 mg/g, and 0.06~1.41 mg/g, respectively.

For the shale of the  $P_{1f_1}$  member,  $S_{1-1}$  content is 0.03~2.77 mg/g (average 0.47 mg/g),  $S_{1-2}$  content is 0.04~3.39 mg/g (average 0.68 mg/g), and  $S_{2-1}$  content is 0.01~0.70 mg/g (average 0.20 mg/g). For the  $P_{1f_2}$  shale,  $S_{1-1}$  content is 0.08~3.32 mg/g (average 0.88 mg/g),  $S_{1-2}$  content is 0.05~3.11 mg/g (average 1.04 mg/g), and  $S_{2-1}$  content is 0.03~1.41 mg/g (average 0.26 mg/g). For the  $P_{1f_3}$  shale,  $S_{1-1}$  content is 0.09~5.03 mg/g (average 0.99 mg/g),  $S_{1-2}$  content is 0.08~5.53 mg/g (average 1.12 mg/g), and  $S_{2-1}$  content is 0.06~0.89 mg/g (average 0.25 mg/g). In terms of identifying sweet spot layers, the Fengcheng Formation shale in well Maye-1 has high  $S_{1-1}$  and  $S_{1-2}$  contents at depths of 4580.00~4600.00 m, 4616.45~4640.30 m, 4661.25~4695.20 m, 4728.30~4759.80 m, 4787.60~4812.30 m and 4876.70~4940.25 m. In these intervals, the average values of  $S_{1-1}$  are 0.47 mg/g, 1.33 mg/g, 0.83 mg/g, 1.6 mg/g, 0.8 mg/g and 1.85 mg/g, respectively, and the average values of  $S_{1-2}$  are 0.68 mg/g, 1.39 mg/g, 0.91 mg/g, 2.16 mg/g, 0.83 mg/g and 2.03 mg/g, respectively. The oils in all of these intervals display good mobility, which is conducive to commercial shale oil development.

The free oil/adsorbed oil ratio  $(S_{1-1} + S_{1-2})/S_{2-1}$  and the free oil/total oil ratio  $(S_{1-1} + S_{1-2})/(S_{1-1} + S_{1-2} + S_{2-1})$  are considered to be important indicators for evaluating shale oil mobility. The values of  $(S_{1-1} + S_{1-2})/S_{2-1}$  for the Fengcheng Formation shale in the Mahu Sag are almost all greater than 3 (the average is 6.63), and most of the values of  $(S_{1-1} + S_{1-2})/(S_{1-1} + S_{1-2} + S_{2-1})$  exceed 80% (average 85%). The proportion of movable oil is therefore high. For shale oil exploration and development in North America, OSI ( $S_1/TOC * 100$ ) greater than 100 is regarded as a significant indicator of exploitability [8, 9]. However, as noted in that study, pyrolyzed  $S_1$  is not all free oil. According to the more comprehensive free oil-bearing saturation index,  $(S_{1-1} + S_{1-2})/TOC$  (Figure 12), most of the intervals in  $P_{1f_2}$  have index values exceeding 100 mg/g.TOC<sup>-1</sup> and are therefore within the optimal range for movable oil.

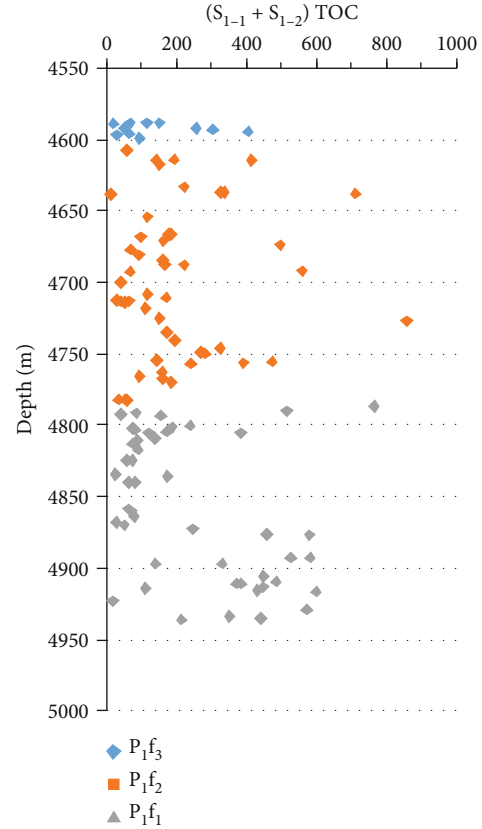


FIGURE 12: Variation of oil saturation with depth in the Fengcheng Formation shale.

### 5.3. Analysis of Factors Influencing Mobility

**5.3.1. Relationship between Free Oil, Adsorbed Oil, and Organic Matter.** Shale oil retained in shale systems is mostly in either free or adsorbed states. However, due to differences in mineral/kerogen surface wettability and molecular polarity, there are great variations in the conditions in which movable shale oils can be brought into production. Figure 13 reflects the relationship between adsorbed oil and free oil and TOC in the shale in the Mahu Sag. There is a very good positive correlation between adsorbed oil and TOC, indicating that the adsorbed oil is mainly related to kerogen. Physical simulation experiments have shown that the adsorption capacity of organic matter is nearly 10 times greater than that of minerals [31]. However, the correlation between free oil and TOC in the study area is poor. This is because, although increased amounts of kerogen result in increased hydrocarbon generation, the shale oil accumulations in this area are primarily sandwiched reservoirs, so the hydrocarbons generated in the source rocks are mostly stored in adjacent reservoirs, resulting in greatly reduced amounts of free hydrocarbons in the shales themselves [32].

**5.3.2. Relationship between Free Oil, Adsorbed Oil, and Maturity.** The content of adsorbed oil is related to the abundance of organic matter and also changes with variations in its thermal maturity. With increasing thermal maturity,

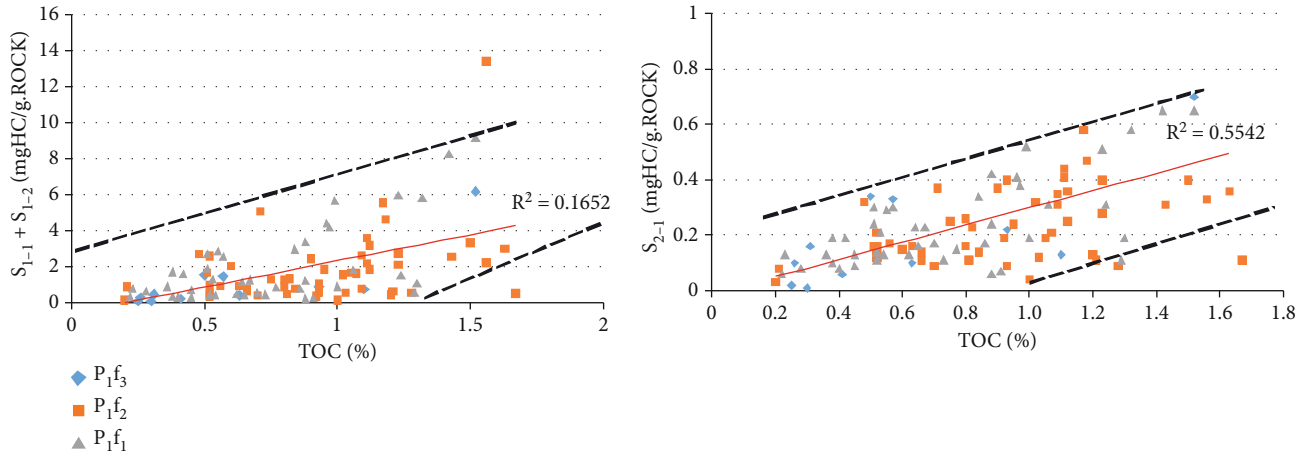


FIGURE 13: Relationship between free oil, adsorbed oil, and organic matter in the Fengcheng Formation shale.

disproportionation leads to removal of heteroatoms from solid organic matter, gradual aromatization of organic macromolecular structures, more stable chemical properties, and relatively reduced polarity. The generated hydrocarbons gradually become lighter and the relative content of polar molecules decreases, resulting in relative reduction of the adsorption capability and miscibility of the oil and kerogen in shales. Effective source rocks both generate and expel hydrocarbon. If the source rocks produce hydrocarbons but cannot expel them, they are not effective source rocks. Theoretically, generated oil and gas must first satisfy the source rock's own capacity for adsorption and pore filling, and only then can superfluous oil and gas be expelled. For  $S_{2-1}/\text{TOC}$ , the oil adsorption capacity of organic matter is far below that of kerogen in the early stage of kerogen evolution, so adsorption in the kerogen increases. Once the amount of generated oil and gas exceeds the adsorption capacity of the kerogen, hydrocarbon expulsion begins, reducing the amounts of movable hydrocarbons remaining in the source rocks [33, 34]. Because the depth range in the study formation is small and  $T_{\max}$  values are generally distributed at about  $440^\circ\text{C}$ , it is difficult to precisely determine the variations in free oil and adsorbed oil with maturity in the area. However, the previously established variation characteristics of  $S_1/\text{TOC}$  and chloroform asphalt "A"/TOC with burial depth (Figures 14(a) and 14(b)) showed a main peak of hydrocarbon generation at about 4600 m. With increasing depth, the ratios of  $S_1/\text{TOC}$  and chloroform asphalt "A"/TOC gradually decrease, the amount of gas generated increases, the gas-oil ratio increases, and mobility also increases (Figure 14(c)). In the main depth section studied in this paper (below 4600 m), the values of  $(S_{1-1} + S_{1-2})/S_{2-1}$  are almost greater than 3, and the values of  $(S_{1-1} + S_{1-2})/(S_{1-1} + S_{1-2} + S_{2-1})$  mostly exceed 70% (Figure 10), indicating good mobility.

**5.3.3. Relationship between Free and Adsorbed Oil and Mineral Composition, Lithology, and Lithofacies.** The mineral composition in the study area includes clay minerals,

carbonate minerals, and detrital minerals. This paper establishes the ratios of free hydrocarbons to adsorbed hydrocarbons and to the various types of minerals and determines the available pore space for free hydrocarbons accordingly. Figure 15 shows that the ratio of free hydrocarbon to adsorbed hydrocarbon in the study area is positively correlated with detrital minerals. This indicates that the occurrence space for free hydrocarbons is mostly pores in detrital minerals. This accords with the known development of intergranular pores in feldspar and quartz in the area [32]. The ratio of free hydrocarbons to adsorbed hydrocarbons is negatively correlated with carbonate minerals. This is primarily because the carbonate minerals are lacustrine authigenic minerals with poorly developed pores, which cannot provide effective space for the occurrence of free hydrocarbons [32]. The ratio of free hydrocarbons to adsorbed hydrocarbons is also negatively correlated with clay minerals. This is largely because, due to their surface characteristics, clay minerals have good ability to adsorb hydrocarbons so that, when clay minerals increase, the content of adsorbed hydrocarbons increases. In addition, a handful of interlayer pores in clay provide the reservoir space for free oil [32], and hence the increase of clay minerals may also result in an increase in the amount of free hydrocarbons.

Figure 4 shows that the lithofacies in the Fengcheng Formation are generally of three types: hybrid sedimentary rock facies, lime/dolomitic shale facies, and felsic shale facies. Shale oil mobility and its geneses in the various lithofacies are explored within this context. Figure 16 shows the changes in the free oil ( $S_{1-1} + S_{1-2}$ ), and free oil/adsorbed oil ( $(S_{1-1} + S_{1-2})/S_{2-1}$ ) ratios and TOC with depth in various depth sections in the formation (excluding the igneous facies in the lower section of  $P_{1f_1}$ ). The lithofacies of  $P_{1f_1}$  cores changes frequently, and the three lithofacies types are interbedded. Felsic shale facies show optimal shale oil mobility, followed by hybrid sedimentary rock facies. Shale oil mobility varies synchronously with TOC, indicating that the upper section of  $P_{1f_1}$  is a self-generation and self-storage oil accumulation. The lithofacies in  $P_{1f_2}$  is significantly different

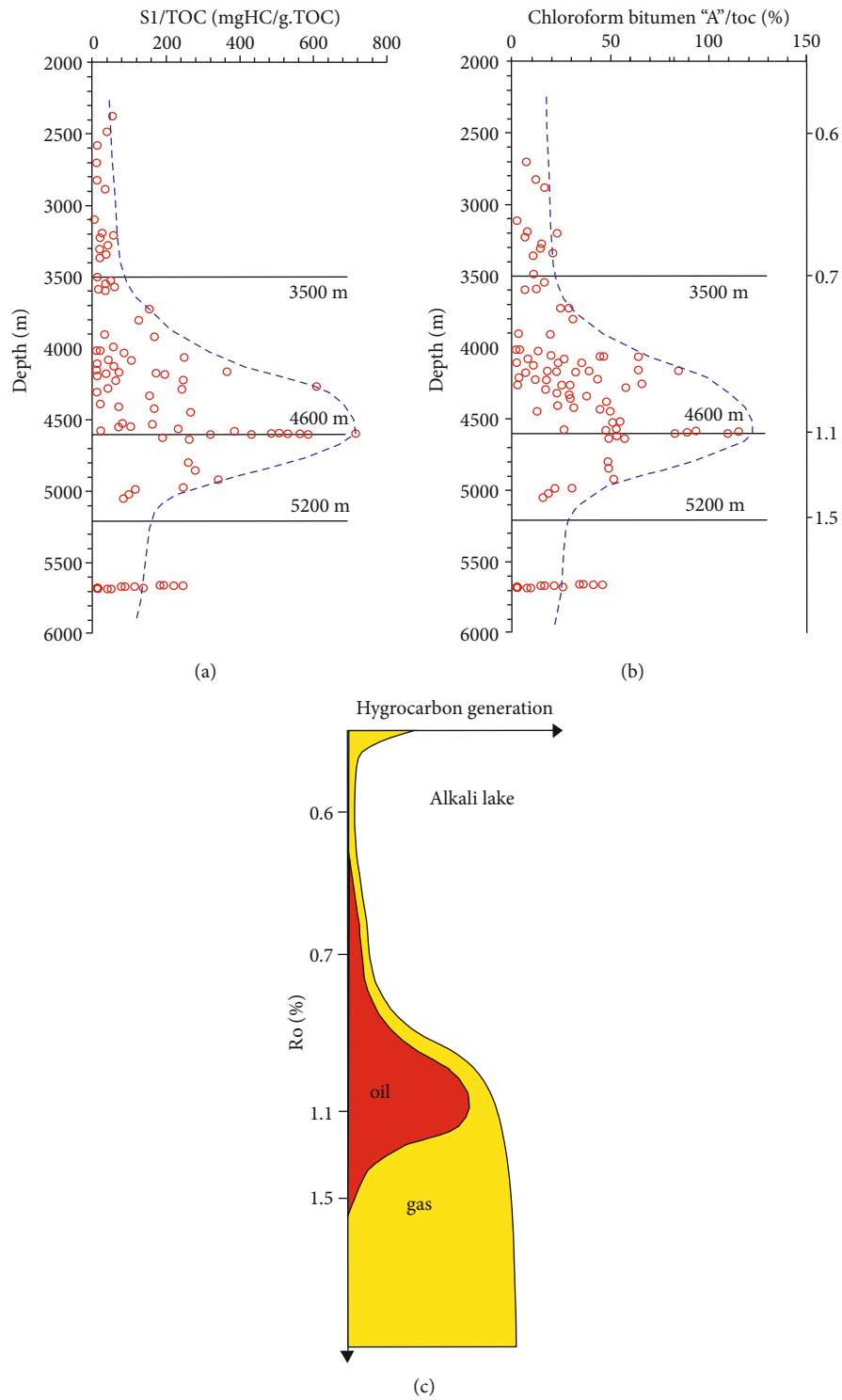


FIGURE 14: Relationships between hydrocarbon generation and burial depth in the Fengcheng Formation source rocks. (a) Main oil generation stage according to changes in S<sub>1</sub>/TOC with depth and R<sub>O</sub>. (b) Main stage of oil generation according to variations in chloroform asphalt "A"/TOC with depth and R<sub>O</sub>. (c) Hydrocarbon generation model for source rocks [27].

from P<sub>1</sub>f<sub>1</sub>. In P<sub>1</sub>f<sub>2</sub> the lithofacies is generally of a single type, with thin layers of other lithofacies occasionally intercalated in the predominant lithofacies. The lithofacies with optimal shale oil mobility in P<sub>1</sub>f<sub>2</sub> cores is felsic shale facies, followed by lime/dolomitic shale facies. However, there are two types

of oil and gas accumulation in P<sub>1</sub>f<sub>2</sub>, accumulation in adjacent intervals and self-generation/self-reservoir, and there is an obvious regularity. When hybrid sedimentary rock facies, lime/dolomitic shale facies, and felsic shale facies are contiguously developed, the TOC values of the hybrid

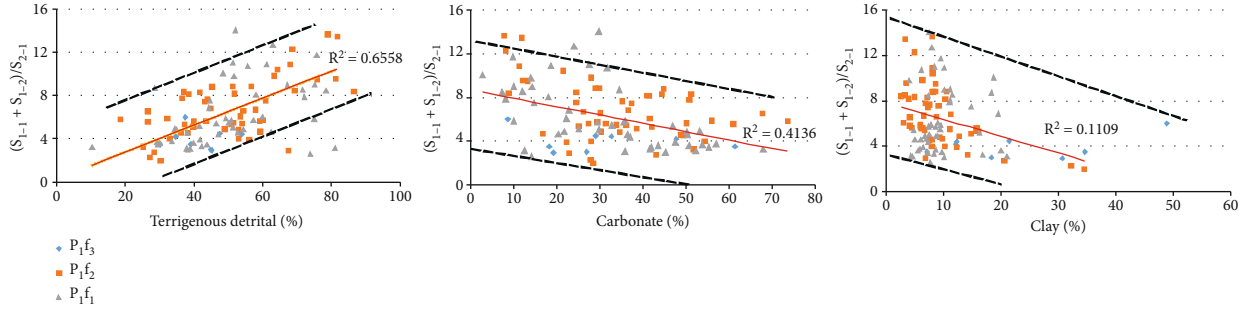


FIGURE 15: Relationship between free oil, adsorbed oil, and mineral composition in the Fengcheng Formation shale.

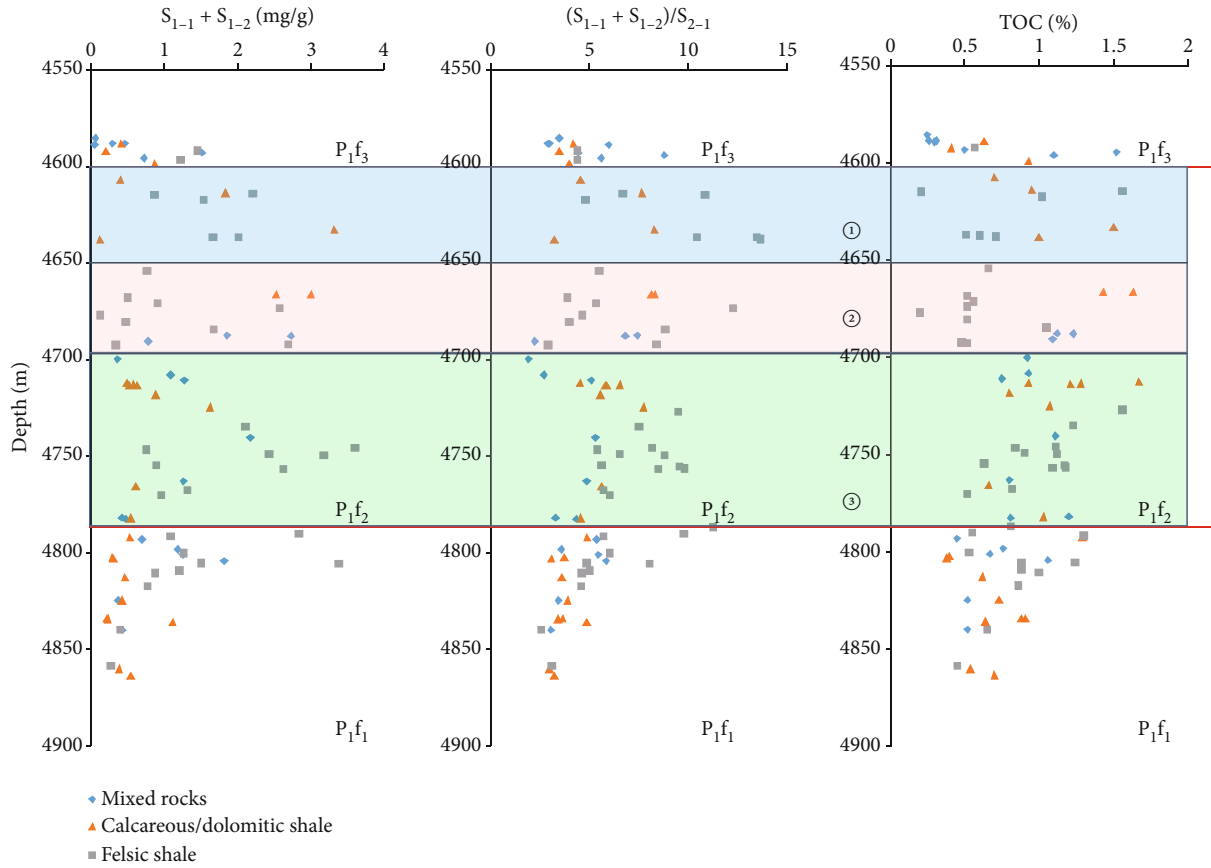


FIGURE 16: Shale oil mobility in different lithofacies in the Fengcheng Formation. (1) Interbedded development of lime/dolomitic shale facies and felsic shale facies; (2) continuous development of felsic shale facies intercalated with thin layers of lime/dolomitic shale facies; (3) continuous development of hybrid sedimentary rock facies, lime/dolomitic shale facies, and felsic shale facies.

sedimentary rock facies and lime/dolomitic shale facies are high, but the values of  $(S_{1-1} + S_{1-2})$  and  $(S_{1-1} + S_{1-2})/S_{2-1}$  are apparently low. The TOC content of the adjacent felsic shale facies is low, but the values of  $(S_{1-1} + S_{1-2})$  and  $(S_{1-1} + S_{1-2})/S_{2-1}$  are significantly higher, indicating that the oil and gas generated in the hybrid sedimentary rock facies and lime/dolomitic shale facies have migrated to the felsic shale facies. The same law applies to the interbedded development of lime/dolomitic shale facies and felsic shale. When continuously developed felsic shale facies is intercalated with a thin layer of lime/dolomitic shale facies, the lime/dolomitic shale becomes a self-generation/self-storage oil accumulation, and the values for TOC,  $(S_{1-1} + S_{1-2})$ ,

and  $(S_{1-1} + S_{1-2})/S_{2-1}$  are correspondingly high. Similar to  $P_{1f_1}$  cores, the three lithofacies are frequently interbedded in most  $P_{1f_3}$  cores, but in  $P_{1f_3}$ , the lithofacies with optimal shale oil mobility are hybrid sedimentary rock facies and felsic shale facies.

## 6. Conclusions

- (1) The mineral composition of the Fengcheng Formation shale in the Mahu Sag includes clay minerals, carbonate minerals (calcite, dolomite), and felsic minerals (quartz, feldspar), with some alkaline minerals. There are three basic lithofacies:

lime/dolomitic shale facies, felsic shale facies, and hybrid sedimentary rock facies. In  $P_{1f_1}$ , the main lithofacies are lime/dolomitic shale facies and felsic shale facies. In  $P_{1f_2}$  and  $P_{1f_3}$ , the three lithofacies are all widely distributed, but the primary type is hybrid sedimentary rock facies. The quality of the source rocks in the Fengcheng Formation shale is mostly very good-excellent, low-mature, or mature, and the organic matter is mostly Type II kerogen

- (2) The oil-bearing properties and shale oil mobility of the Fengcheng Formation shale are good. The depth ranges with the best oil-bearing properties are at 4616.45~4640.30 m, 4661.25~4695.20 m, 4728.30~4759.80 m, 4787.60~4812.30 m, and 4876.70~4940.25 m.  $S_1$  is generally greater than 1.5 mg/g, OSI is greater than 100 mg/g.TOC<sup>-1</sup>, and the free oil/adsorbed oil ratio  $(S_{1-1} + S_{1-2})/S_{2-1}$  is greater than 3. The free oil/total oil ratio  $(S_{1-1} + S_{1-2})/(S_{1-1} + S_{1-2} + S_{2-1})$  exceeds 80%.  $P_{1f_2}$  and the lower section of  $P_{1f_1}$  are the preferred intervals for commercial development
- (3) Shale oil mobility in the Fengcheng Formation is related to the adsorption of organic matter, the level of maturity, and the available pore space in inorganic minerals. The higher the TOC, the better the adsorption capacity for shale oil, and consequently the worse the mobility. With increasing maturity, shale oil mobility begins to increase once the ability of the kerogen to adsorb shale oil has reached saturation. Shale oil mobility in pore spaces formed by terrigenous debris is particularly good
- (4) Shale oil occurrence in the Fengcheng Formation is characterized by self-generation and self-reservoir and by accumulation in adjacent intervals. The upper section of  $P_{1f_1}$  is primarily self-generation and self-storage oil accumulation, and the felsic shale facies have optimal shale oil mobility.  $P_{1f_2}$  is characterized by self-generation and self-reservoir and by accumulation in adjacent intervals. Shale oil mobility is high in both the predominant felsic shale facies and in the intercalated lime/dolomitic shale facies.  $P_{1f_3}$  is also essentially a self-generation/self-storage oil accumulation, with the hybrid sedimentary rock facies and felsic shale facies offering the optimum shale oil mobility

## Data Availability

The figures and tables used to support the findings of this study are included in the article.

## Conflicts of Interest

The authors declare that there is no conflict of interest regarding the publication of this paper.

## Authors' Contributions

The evaluation of oil content was completed by Wenjun He, the division of sweet spots was completed by Menhui Qian and Zhifeng Yang, the data analysis was completed by Zhongliang Sun, the text modification was completed by Zhiming Li, and the evaluation of hydrocarbon generation was completed by Junying Leng.

## Acknowledgments

This research was funded by the Natural Science Foundation of China Grant No. 42090022 "Shale oil generation, dynamic evolution, and occurrence mechanisms in organic-rich lacustrine strata."

## References

- [1] J. J. Li, Y. L. Shi, X. W. Zhang et al., "Control factors of enrichment and producibility of shale oil: a case study of Biyang Depression," *Earth Science*, vol. 39, no. 7, pp. 848–857, 2014.
- [2] J. Yuqiang, D. Dazhong, Q. Lin, S. Yanfei, J. Chan, and H. Puwei, "Basic features and evaluation of shale gas reservoirs," *Natural Gas Industry*, vol. 30, no. 10, pp. 7–12, 2010.
- [3] S. Brunauer, P. H. Emmett, and E. Teller, "Adsorption of gases in multimolecular layers," *American Chemical Society*, vol. 60, no. 2, pp. 309–319, 1938.
- [4] Q. Jiang, M. Li, M. Qian et al., "Quantitative characterization of shale oil in different occurrence states and its application," *Petroleum Geology & Experiment*, vol. 38, no. 6, pp. 842–849, 2016.
- [5] K. G. Zink, G. Scheeder, H. L. Stueck, S. Biermann, and M. Blumenberg, "Total shale oil inventory from an extended Rock-Eval approach on non-extracted and extracted source rocks from Germany," *International Journal of Coal Geology*, vol. 163, pp. 186–194, 2016.
- [6] H. T. Xue, S. S. Tian, W. M. Wang, W. H. Zhang, and M. G. D. Du TT, "Correction of oil content-one key parameter in shale oil resource assessment," *Oil & Gas Geology*, vol. 37, no. 1, pp. 15–22, 2016.
- [7] M. L. Bordenave, *Geochemical methods and tools in petroleum exploration*, Applied Petroleum Geochemistry, Technip, Paris, 1993.
- [8] D. M. Jarvie, "Shale resource systems for oil and gas: part 2: shale-oil resource systems," *AAPG Memoir*, vol. 97, pp. 89–119, 2012.
- [9] D. M. Jarvie, "Components and processes affecting producibility and commerciality of shale resource systems," *Geologica Acta*, vol. 12, no. 4, pp. 307–325, 2014.
- [10] L. Jijun, W. Weiming, C. Qun, S. Yinglin, Y. Xintong, and T. Shansi, "Impact of hydrocarbon expulsion efficiency of continental shale upon shale oil accumulations in eastern China," *Marine and Petroleum Geology*, vol. 59, pp. 467–479, 2015.
- [11] J. Li, C. Jiang, M. Wang et al., "Adsorbed and free hydrocarbons in unconventional shale reservoir: a new insight from NMR  $T_1$ - $T_2$  maps," *Marine and Petroleum Geology*, vol. 116, article 104311, 2020.
- [12] L. Kuang, T. A. Yong, L. E. Dewen et al., "Formation conditions and exploration potential of tight oil in the Permian saline lacustrine dolomitic rock, Junggar Basin, NW China,"

- Petroleum Exploration and Development*, vol. 39, no. 6, pp. 657–667, 2012.
- [13] Z. Shanwen, “Identification and its petroleum geologic significance of the Fengcheng Formation source rocks in Hala’alt area, the northern margin of Junggar Basin,” *Oil & Gas Geology*, vol. 34, no. 2, pp. 145–152, 2013.
- [14] T. A. Yong, X. U. Yang, Q. U. Jianhua, M. E. Xiangchao, and Z. Zhiwen, “Fandelta group characteristics and its distribution of the Triassic Baikouquan reservoirs in Mahu sag of Junggar basin,” *Xinjiang Petroleum Geology*, vol. 35, no. 6, pp. 628–635, 2014.
- [15] L. E. Dewen, Q. U. Jianhua, A. N. Zhiyuan, Y. O. Xincui, and W. U. Tao, “Hydrocarbon accumulation conditions and enrichment regularity of low-permeability glutenite reservoirs of Baikouquan Formation in Mahu Sag, Junggar Basin,” *Xinjiang Petroleum Geology*, vol. 36, no. 6, pp. 642–647, 2015.
- [16] C. A. Jian, L. E. Dewen, L. I. Yuwen, T. Yong, and C. Qiusheng, “Ancient high-quality alkaline lacustrine source rocks discovered in the lower Permian Fengcheng Formation, Junggar Basin,” *Acta Petrolei Sinica*, vol. 36, no. 7, pp. 781–790, 2015.
- [17] J. Cao, L. W. Xia, T. T. Wang, D. Zhi, Y. Tang, and W. Li, “An alkaline lake in the Late Paleozoic Ice Age (LPIA): a review and new insights into paleoenvironment and petroleum geology,” *Earth Science Reviews*, vol. 202, article 103091, 2020.
- [18] D. M. Zhi, J. Cao, and B. L. Xiang, “Fengcheng alkaline lacustrine source rocks of Lower Permian in Mahu Sag in Junggar Basin: hydrocarbon generation mechanism and petroleum resources reestimation,” *Xinjiang Petroleum Geology*, vol. 37, no. 5, pp. 499–506, 2016.
- [19] J. Chen, X. Wang, C. Deng et al., “Oil and gas source, occurrence and petroleum system in the Junggar Basin,” *Northwest China. Acta Geologica Sinica*, vol. 90, no. 3, pp. 421–450, 2016.
- [20] Q. I. Zhijun, C. H. Lihua, L. I. Yuwen, W. Tingting, and C. Jian, “Paleosedimentary setting of the Lower Permian Fengcheng alkali lake in Mahu sag, Junggar basin,” *Xinjiang Petroleum Geology*, vol. 37, no. 1, pp. 1–6, 2016.
- [21] Z. H. Dongming, S. O. Yong, H. E. Wenjun, J. I. Xiyu, Z. O. Yang, and H. U. Liliang, “Geological characteristics, resource potential and exploration direction of shale oil in Middle-Lower Permian, Junggar Basin,” *Xinjiang Petroleum Geology*, vol. 40, no. 4, pp. 389–401, 2019.
- [22] Z. H. I. Dongming, T. A. N. G. Yong, H. E. Wenjun, G. U. O. Xuguang, M. Zheng, and L. Huang, “Orderly coexistence and accumulation models of conventional and unconventional hydrocarbons in Lower Permian Fengcheng Formation, Mahu sag, Junggar Basin,” *Petroleum Exploration and Development*, vol. 48, no. 1, pp. 43–59, 2021.
- [23] K. E. Peters, M. R. Cassa, L. B. Magoon, and W. G. Dow, “The petroleum system—from source to trap,” *AAPG Mem*, vol. 60, pp. 93–120, 1994.
- [24] D. F. Huang and J. C. Huang, *Quantitative Evaluation of Source Rocks. Continental Hydrocarbon Generation in China*, Petroleum Industry Press, Beijing, 1982.
- [25] J. Y. Hu and D. F. Hang, *The Bases of Non marine Petroleum Geology in China*, Petroleum Industry Press, Beijing, China, 1991.
- [26] F. Huang and M. A. Xin, *Geochemical Evaluation Method of Nonmarine Source Rocks*, China National Petroleum Corporation, Beijing, China, 1995.
- [27] Y. Tang, W. He, Y. Bai et al., “Source rock evaluation and hydrocarbon generation model of a Permian alkaline lakes—a case study of the Fengcheng Formation in the Mahu Sag, Junggar Basin,” *Minerals*, vol. 11, no. 6, p. 644, 2021.
- [28] E. Z. Wang, C. R. Li, Y. Feng et al., “Novel method for determining the oil moveable threshold and an innovative model for evaluating the oil content in shales,” *Energy*, vol. 239, p. 121848, 2022.
- [29] J. Espitalié, “Use of Tmax as a maturation index for different types of organic matter: Comparison with vitrinite reflectance,” *Collection colloques et séminaires-Institut français du pétrole*, vol. 44, pp. 475–496, 1986.
- [30] B. P. Tissot and D. H. Welte, *Petroleum Formation and Occurrence*, vol. 699, Springer Verlag, Berlin Heidelberg New York, Tokyo, 2nd edition, 1984.
- [31] D. Zhang, Y. Yi, and X. Zheng, “Soil adsorption to petroleum and release in meadow soils,” *Journal of Shenyang Agricultural University*, vol. 36, no. 1, pp. 53–56, 2005.
- [32] Z. F. Yang, Y. Tang, X. G. Guo, L. L. Huang, Z. Q. Wang, and X. M. Zhao, “Occurrence states and potential influencing factors of shale oil in the Permian Fengcheng Formation of Mahu Sag, Junggar Basin,” *Petroleum Geology & Experiment*, vol. 43, no. 5, pp. 784–796, 2021.
- [33] X. Q. Pang, M. W. Li, and M. Su, “Geochemistry of petroleum systems in the Niuzhuang south slope of Bohai Bay Basin: part 3. Estimating petroleum expulsion from the Shahejie formation,” *Organic Geochemistry*, vol. 36, no. 4, pp. 497–510, 2005.
- [34] E. Wang, G. Liu, X. Pang et al., “An improved hydrocarbon generation potential method for quantifying hydrocarbon generation and expulsion characteristics with application example of Paleogene Shahejie Formation, Nanpu Sag, Bohai Bay Basin,” *Marine and Petroleum Geology*, vol. 112, article 104106, 2020.

## Research Article

# The Impact of Lamina Characteristics and Types on Organic Matter Enrichment of Chang 7<sub>3</sub> Submember in Ordos Basin, NW China

Congsheng Bian <sup>1</sup>, Wenzhi Zhao,<sup>1</sup> Tao Yang,<sup>1</sup> Wei Liu,<sup>1</sup> Chaocheng Dai,<sup>2</sup> Xu Zeng,<sup>1</sup> Kun Wang,<sup>1</sup> Yongxin Li,<sup>1</sup> and Di Xiao<sup>2</sup>

<sup>1</sup>PetroChina Research Institute of Petroleum Exploration and Development, Beijing 100083, China

<sup>2</sup>East China University of Technology, College of Earth Sciences, Nanchang 330013, China

Correspondence should be addressed to Congsheng Bian; [biancongsheng@126.com](mailto:biancongsheng@126.com)

Received 4 February 2022; Accepted 17 May 2022; Published 18 June 2022

Academic Editor: Kouqi Liu

Copyright © 2022 Congsheng Bian et al. This is an open access article distributed under the Creative Commons Attribution License, which permits unrestricted use, distribution, and reproduction in any medium, provided the original work is properly cited.

The Chang 7 member in Ordos Basin is an important shale oil exploration layer, with new shale-oil discoveries in recent years. The Chang 7<sub>3</sub> submember is rich in organic shale, which is the main source rock of shale oil in the Yanchang Formation. In order to clarify the lamina structure, composition, types, and distribution characteristics in Chang 7<sub>3</sub> submember and its influence on organic matter enrichment, a full coring well in Chang 7<sub>3</sub> submember located in deep-lacustrine facies is selected to obtain intensive systematic core samples. Core observation, thin section identification, X-ray fluorescence element analysis, X-diffraction analysis, scanning electron microscope, electron probe, rock pyrolysis, and other techniques are performed to systematically analyze the morphology, structure, thickness, mineral compositions, and organic matter content of the shale lamina in the Chang 7<sub>3</sub> submember. Five types of lamina are identified: silty felsic lamina (SF), tuffaceous lamina (TF), organic-rich clay lamina (ORC), organic-bearing clay lamina (OBC), and homogeneous clay lamina (HC), which are further subdivided into eight subtypes. The lamina types change greatly vertically in the Chang 7<sub>3</sub> submember, in which the lower part is mainly silty felsic lamina, organic-rich clay, and tuffaceous lamina, the middle part is mainly organic rich and organic clay lamina and organic-bearing clay lamina, and the upper part is mainly homogeneous clay lamina and a small amount of silty felsic organic-bearing clay lamina and organic-bearing clay lamina. Different laminae show various organic matter types, organic matter content (TOC), and organic matter occurrence states which can be divided into four occurrence types. The TOC in organic-rich clay lamina and part of homogeneous clay lamina is high, while that of silty felsic lamina is lower. The relationship between shale lamina and organic matter enrichment is established according to the correlation analysis of laminar characteristics, mineral content, and organic matter content. Among them, the organic-rich lamina is richest of TOC and is a favorable “sweet point” for shale oil exploration.

## 1. Introduction

Research on organic-rich shale has increasingly become a hotspot with the development of shale oil exploration in many basins. The lamina characteristics of fine-grained shale not only reflect the microstructure and quality of shale reservoir but also directly affect the fracture expansion law and fracturing effect of horizontal well volume fracturing [1–5]. Lamina study is an important content in fine-grained sedimentation, which con-

tains lamina morphology, continuity, mineral composition, granularity change, and interface contact relationship [5–9], especially the formation mechanism of lamina [5, 10–15].

The classification of laminae is usually based on the organic matter as well as the composition and content of minerals. For example, Shi et al. [8] found that the Silurian Longmaxi Formation in Sichuan Basin developed four types of laminae, containing organic-rich, organic-bearing, clay, and silty; Xi et al. [9] thought that the shale of Chang 7<sub>3</sub>

submember of Yanchang Formation in Ordos Basin includes four types of lamina: tuffaceous, organic, silty, and clay rich. As the most important and widely developed sedimentary feature in shale rock, lamina structure not only controls the reservoir physical properties of shale [16–21] but also leads to strong heterogeneity of shale reservoir, thus affecting the quality of shale reservoir. In particular, the lamina characteristics and types of continental shale are more complex than those of marine shale. Therefore, the study of laminar types and structures has become an indispensable content in the study of sedimentology in unconventional oil and gas, which has attracted the attention of geologists and explorers recently [22–24]. For example, Hua et al. [16] believe that the reservoir properties of coarse laminar shale of Longmaxi Formation in Sichuan Basin are better than thin laminar shale, and thin laminar shale is better than massive mudstone.

The types and characteristics of laminae are closely related to the lithology and lithofacies of shale. Exploration and research show that the lithology types of shale mainly include clay rich, siltstone and carbonate, or their combination [25–27]. Compared with lithology, the lithofacies types of shale are more complex [28]. In early studies, the lithofacies types of shale are usually divided according to mineral composition and organic matter content (TOC). The mineral composition usually includes felsic, clay, and carbonate, and TOC can be high or lower. For example, Wang and Carr divided the Marcellus Shale into seven types including organic siliceous shale, organic mixed shale, and gray mudstone [29]. Later, the sedimentary structure was considered in the lithofacies classification, which can generally be divided into laminated, bedded, and massive. For example, Song et al. carefully made the lithofacies classification of Shahejie Formation shale in the Raoyang Sag according to the difference of rock type, sedimentary structure, and TOC [30]. Liu et al. divided the Qingshankou shale in the northern Songliao Basin into 7 lithofacies types according to the TOC, fabric, and mineral composition [31].

It is found that the shale of the Chang 7<sub>3</sub> submember in Ordos Basin has complex lithology, containing felsic, clay, sandstone, and siltstone, as well as the tuffaceous and carbonate, which results in diversified lamina structure and types, complex combination modes, and great differences in the distribution of mineral composition and organic matter in lamina [9, 22, 32]. The type, structure, and mineral composition of different laminae often control the type, enrichment, and occurrence characteristics of organic matter, thus affecting the hydrocarbon generation potential of organic matter and the quality of source rock [33]. In addition, the lamina influences the pore type and pore space distribution of shale, which in turn have an important impact on the content and occurrence of retained hydrocarbons [7, 34, 35].

Research also found that the organic-rich lamina shale in Chang 7<sub>3</sub> member of Ordos Basin is poor in porosity, but the situation in felsic rich shale is opposite, and the pore relatively developed [36, 37]. In addition, the TOC and porosity in tuffaceous and carbonate rich lamina are of great difference, which makes it more difficult to study formation

mechanism of lamina, as well as the favorable area evaluation of shale oil exploration. Therefore, the fine research on the type, structure, and influence on organic matter enrichment of shale lamina in Chang 7<sub>3</sub> member is of great significance; however, the previous research in these aspects is relatively weak. Taking a fully cored well in Chang 7<sub>3</sub> member shale in the deep lacustrine faces as the research object, by systematic and intensive sampling, using thin section, X-ray diffraction analysis, scanning electron microscope, electron probe, and other analysis methods, combined with the principle of fine-grained sedimentology analysis, this paper describes the lamina types, structure, and mineral composition. Furthermore, the effects of laminar types on the occurrence forms and enrichment characteristics of organic matter are discussed in order to provide a reference for the enrichment characteristics and evaluation of shale oil in Chang 7<sub>3</sub> submember, Ordos Basin.

## 2. Geologic Background

Ordos Basin is a large superimposed basin in Central China, which is composed of six structural units, containing Western thrust belt, Tianhuan depression, Weibei uplift, Yimeng uplift, Yishan slope, and Jinxi fault-fold belt [38] (Figure 1(c)). During the sedimentary period of Yanchang Formation in the Late Triassic, the basin developed a large inland depression lake, deposited a set of clastic rock including lake and fluvial facies, which can be divided into 10 members from top to bottom (Figures 1(a)). The Chang 7 member in Yanchang Formation developed a greatest lake, and only the area of deep lacustrine faces can reach  $6.5 \times 10^4 \text{ km}^2$ , with abundant aquatic organisms and plankton, enrichment of organic matter, and black mudstone and shale [39]. The average thickness of Chang 7 member is about 80–100 m, of which Chang 7<sub>3</sub> submember is a section with concentrated distribution of organic-rich shale, with a cumulative thickness of 30–50 m (Figure 1(b)), rich in raspberry pyrite and Collophanite [40–42].

Ordos Basin is an important shale oil exploration field in China. The discovery of Qingcheng shale oil field in 2019 with 1 billion ton geological reserves has achieved a historic breakthrough in shale oil exploration progress in Chang 7 member. Moreover, Cy 1 and Cy 2 wells have obtained more than 100-ton oil flow per day in Chang 7<sub>3</sub> submember, with thick organic-rich shale and thin siltstone. In 2020, the shale oil output of Changqing Oilfield reached  $143 \times 10^4 \text{ t}$ , realizing the scale benefit development of shale oil in Ordos Basin [39].

The core samples in this study are from the well that located in Wuqi area in the middle of Ordos Basin. The Chang 7<sub>3</sub> submember is a deep lacustrine faces deposit with a thickness of 46 m. The lithology is mainly shale mixed with siltstone and tuff. It can be divided into three positive cycles from top to bottom, by which Chang 7<sub>3</sub> submember is divided into three sublayers. A total of 152 samples are taken in the whole Chang 7<sub>3</sub> cores, with an average of 3 samples per meter (Figure 2), which makes a good foundation for the fine description of shale lamina types and structural characteristics.

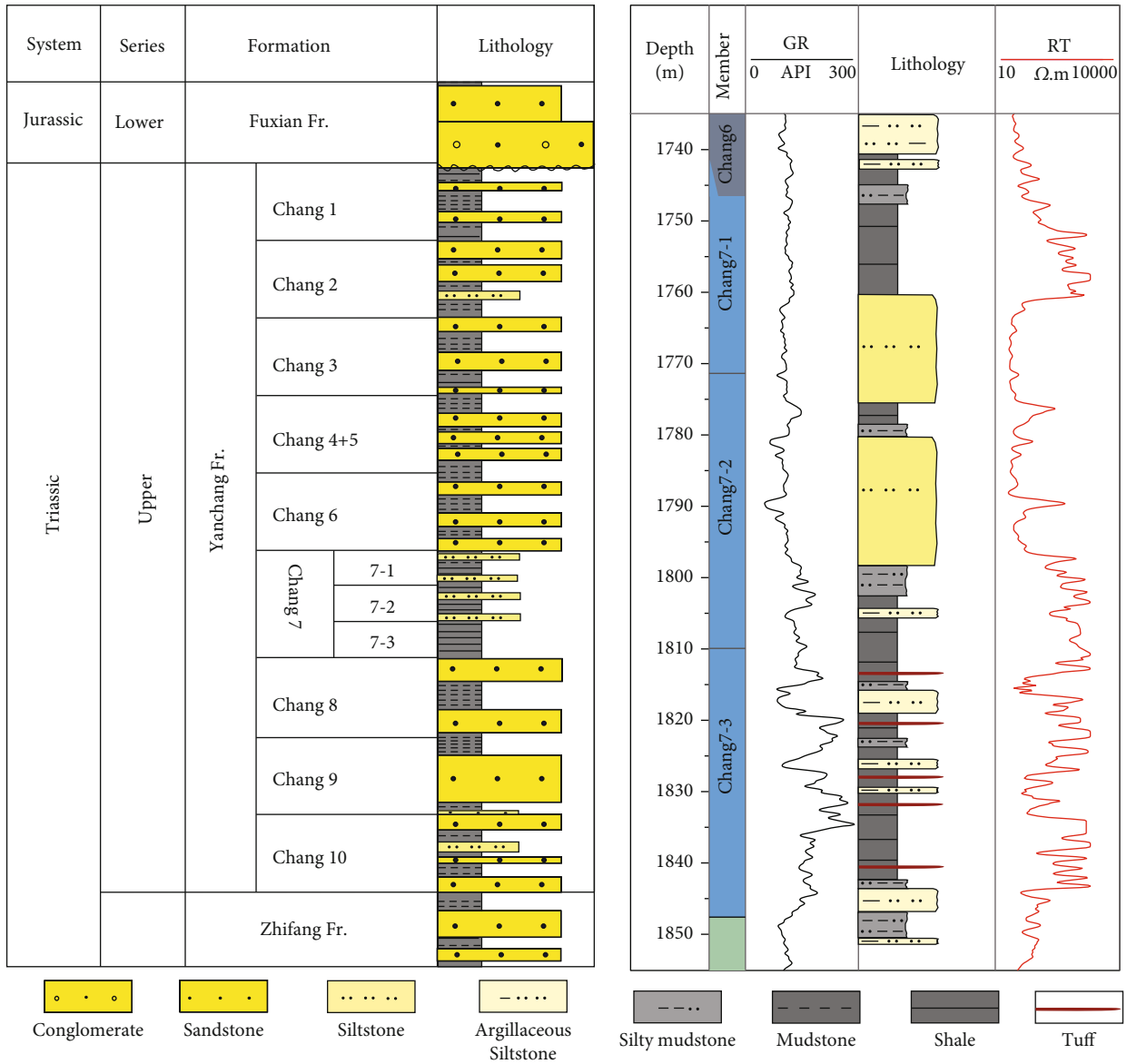


FIGURE 1: Continued.

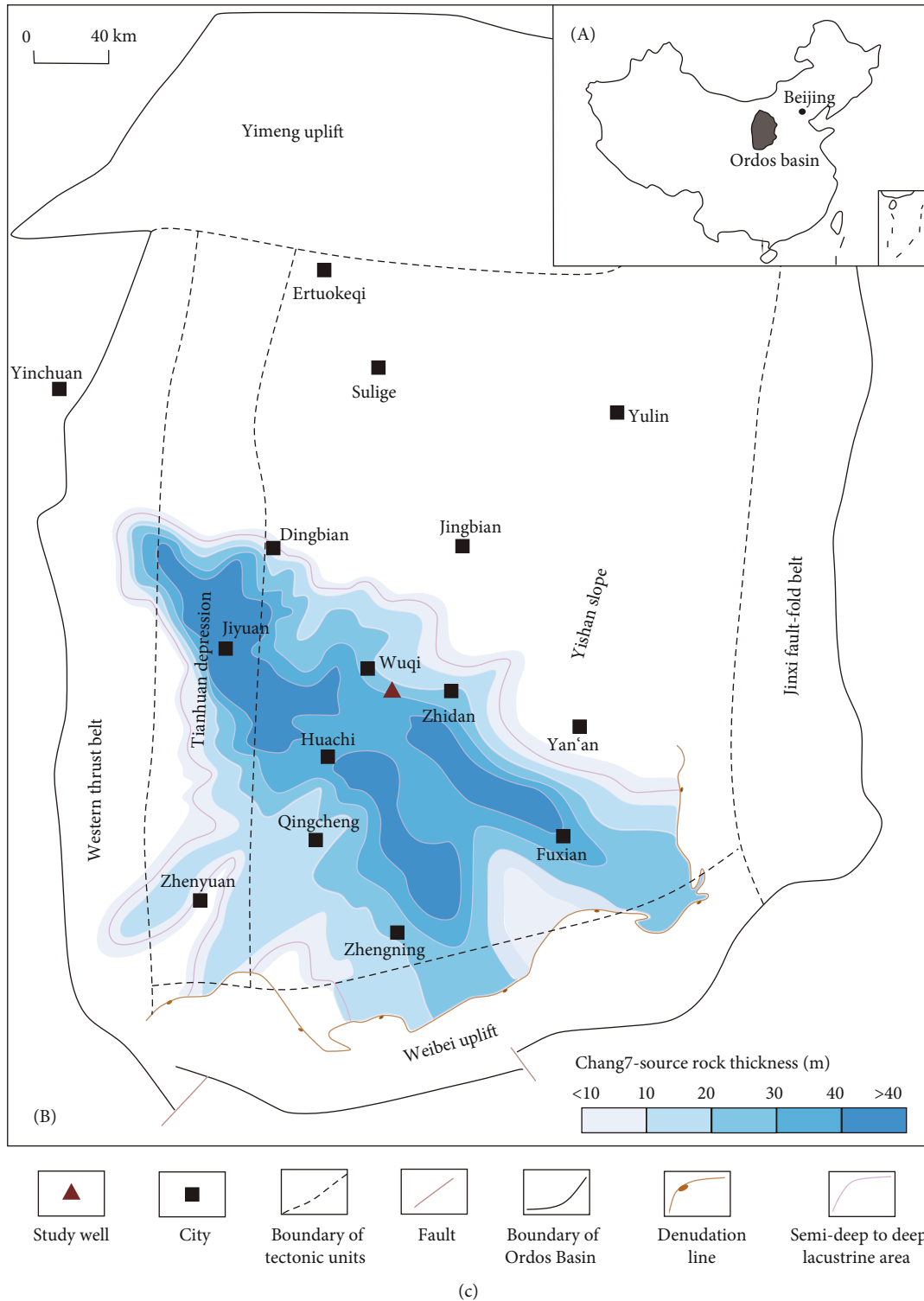


FIGURE 1: Comprehensive geological figure of Chang 7<sub>3</sub> member in Ordos Basin. (a) Stratigraphic histogram of Yanchang Formation (modified from [43]). (b) Well logging and stratigraphic histogram of Chang 7 member. (c) Sedimentary facies diagram of Chang 73 member (from [37]).

### 3. Data and Methods

Samples are from the cores of Chang 7<sub>3</sub> submember of Yanchang Formation in G well, with the depth of 1803.35~1853.5 m, and total 152 samples are analyzed with

a sampling interval of 0.3-0.4 m. The lithology is mainly black shale, grayish black mudstone, dark gray silty shale, and brown tuff (Figure 2).

Shale lamina structures are analyzed by core description and thin section observation. The rock mineral composition

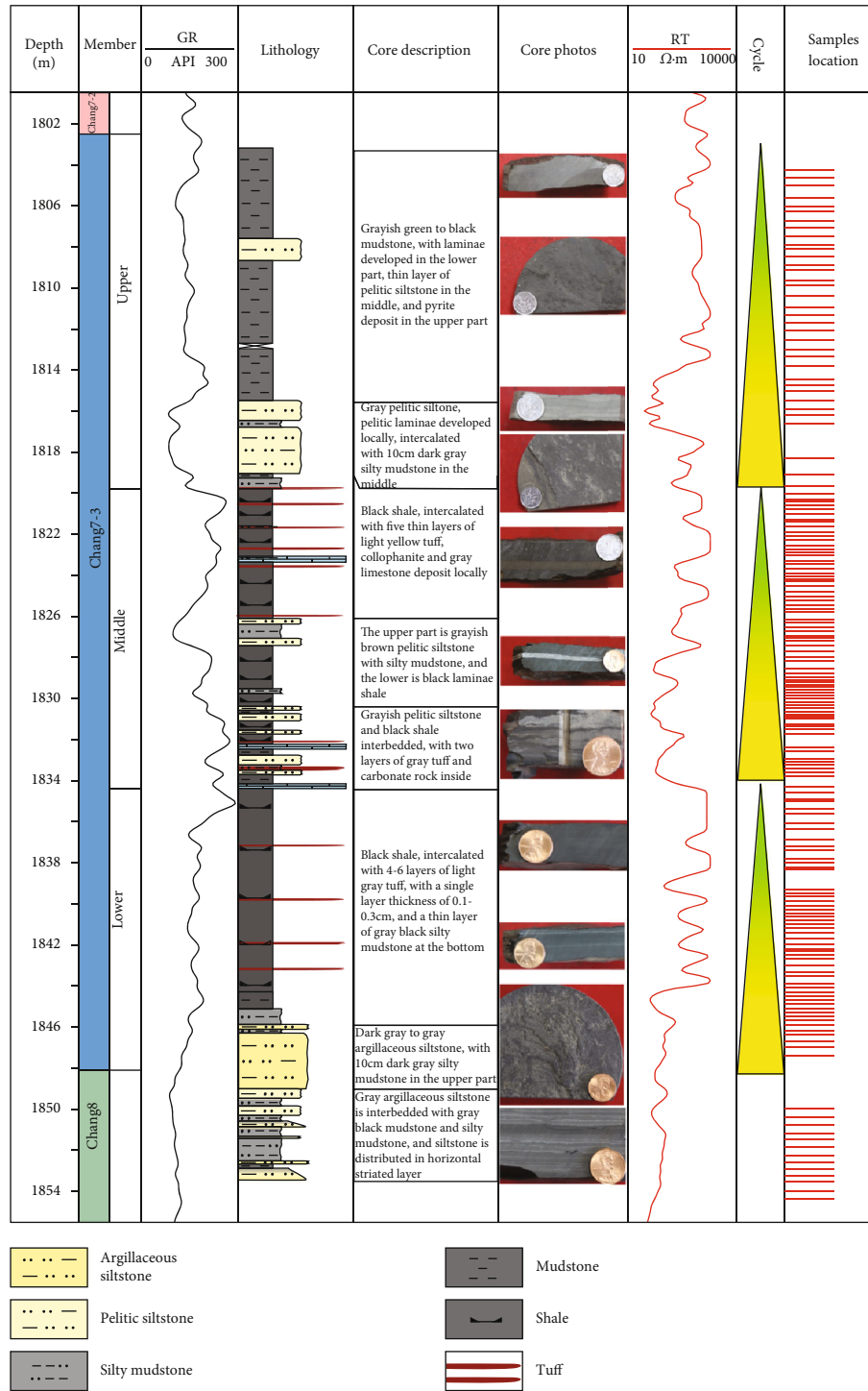


FIGURE 2: Core description and stratigraphic histogram of Chang 7<sub>3</sub> submember in Ordos Basin.

is determined by X-ray diffraction, scanning electron microscopy, and electron microprobe. Organic matter type and TOC value was obtained by CS-I carbon sulfur analyzer.

Optical microscope is the German Zeiss polarizing microscope, the eyepiece is 10 times, the objective lens is 5-20 times, single polarized light, and orthogonal transmission light. X-ray diffraction is done by d8advance X-ray dif-

fractometer, which has Cu target, voltage 35kV, and current 15 mA, and the analysis samples are 200 mesh powder. The scanning electron microscope is FEI Nova NanoSEM 450 thermal field emission scanning electron and Oxford Inca energy X-MAX 20 Oxford energy spectrometer. The test conditions are voltage 10kV, current 86 Ma, and beam spot 3.5  $\mu$ m, WD 5.0mm. The electron probe adopts jeoljxa-

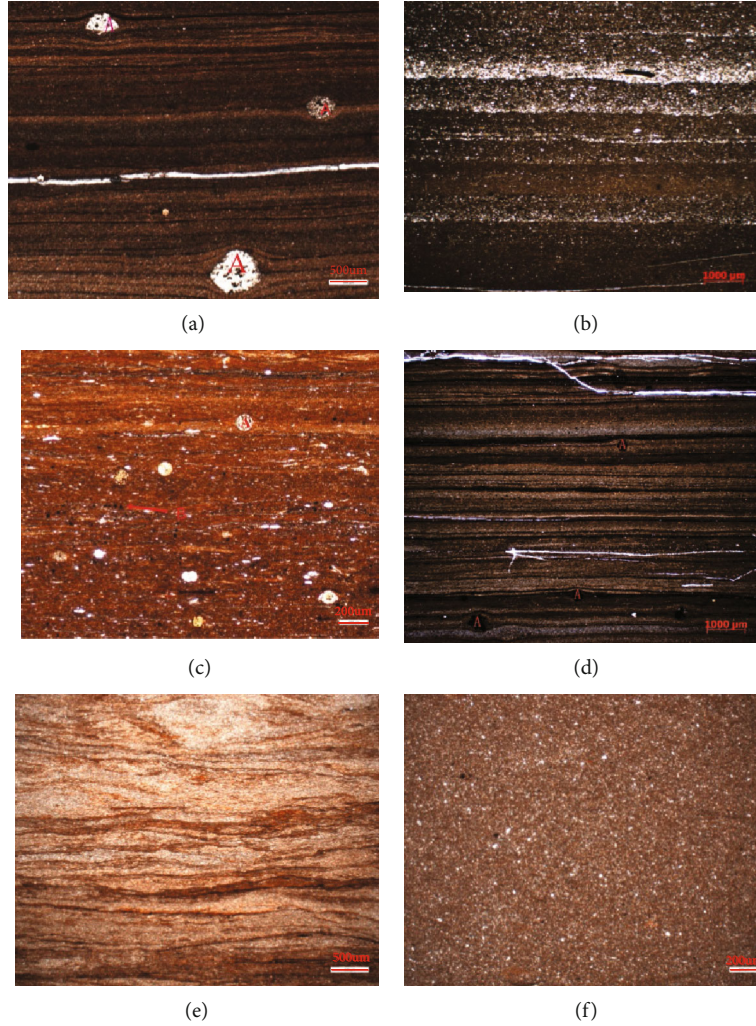


FIGURE 3: Micrograph of shale lamina of the Chang 7<sub>3</sub> member in Ordos Basin. (a) Extremely thin parallel plate-like lamina, algae (a) has strong anticompaction effect, 1830.00 m. (b) Thin parallel plate-like lamina, the content of quartz and feldspar in the lamina bottom is high, 1845.5 m. (c) Thin parallel plate laminae, high content of algae (a) and strawberry pyrite (b), 1832.9 m. (d) Extremely thin parallel plate-like laminae, black spots are strawberry pyrite (a), 1830.1 m. (e) Extremely thin parallel wavy lamina, 1827.1 m. (f) Homogeneous (block) bed, 1827.66 m.

TABLE 1: Average mineralogical composition for each section in Chang 7<sub>3</sub> member (unit: %).

Chang7 <sub>3</sub> member	Quartz	Feldspar	Clay	Calcite	Dolomite	Pyrite	Others
Upper	21.3	15.3	57	1.9	0.3	3.1	1.1
Middle	17.9	21.3	42	2.5	7.5	6.4	2.4
Lower	21.1	23.2	47.7	1.9	2.6	1.6	1.9
Overall average	20.1	19.9	48.9	2.1	3.4	3.7	1.9

8800 m electron probe instrument. The working conditions are acceleration voltage 15 kV, probe current 10 mA, and beam spot diameter  $< 1 \mu\text{m}$ . The above three instruments accept the rock slices with Argon ion polishing and gold/carbon plating pretreatment. The CS-I carbon sulfur analyzer processes samples with 200 mesh powder and normal temperature and pressure.

## 4. Results

**4.1. Lamina Structure.** As for the lamina structure, different scholars have put forward different classification schemes according to the lamina thickness and shape [8, 44, 45]. Ingram called the lamina with thickness less than 3 mm as extremely thin lamina, the lamina with thickness of

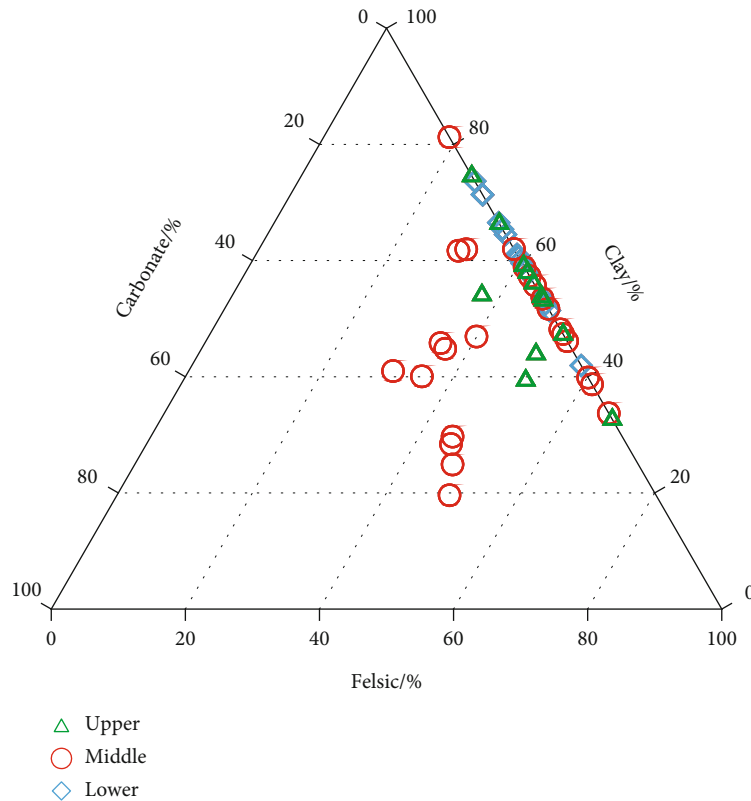


FIGURE 4: Ternary diagram of the bulk mineralogical composition of shale in Chang 7<sub>3</sub> member.

3 mm~1 cm as thin lamina, the lamina with thickness of 1 cm~3 cm as medium lamina, and the lamina with thickness of 3 cm~10 cm as thick lamina. From the perspective of lamina morphology, Campbell first divided lamina into three types: uniform lamina, wavy lamina, and curved lamina. For each type, it can be further divided into continuous parallel, intermittent parallel, continuous unparallelled, and intermittent unparallelled lamina [41]; Liu et al. put forward the concept of bright lamina and dark lamina shale of the Yanchang Formation in Ordos Basin, pointing out that the bright lamina is mainly made up of quartz and plagioclase, while the dark lamina mainly contains quartz and illite [42]. In the process of shale classification of Chang 7<sub>3</sub> member, predecessors mainly considered the lamina thickness and mineral composition and paid less attention to the lamina morphology. In this paper, based on the development form, thickness, and mineral composition of lamina, the lamina is divided into plate-like, wavy, and block types. Thereafter, according to the change of lamina thickness, the lamina with thickness less than 0.5 mm is called extremely thin lamina; the lamina with thickness of 0.5 mm~1 mm is thin lamina; the lamina with thickness of 1 mm~5 mm is medium lamina; the lamina with thickness of 5 mm~10 mm is thick lamina; this thicker than 10 mm is called bed.

The shale lamina in Chang 7<sub>3</sub> member of G well is mainly made up of extremely thin-thin plate-like laminae (Figures 3(a)–3(d)), and wavy as well as massive laminae is locally developed (Figures 3(e) and 3(f)). The plate-like laminae occur in continuous horizontal layers (Figures 3(a)–

3(d)), in which the bright lamina and the dark one appear alternately. The bright lamina mostly contains quartz and feldspar, and the quartz particles are relatively bigger than other. The content of illite, mica, and other clay minerals as well as organic matter is higher in the dark lamina. The thickness of single lamina is mainly 0.05~1.0 mm (Figure 3(b)). The wavy laminae present near parallel wavy shape, and the bright lamina and dark one appear alternately too. Compared with the plate-like lamina, the clastic particles of the wavy lamina are finer, the single lamina is thinner, and the thickness is mainly distributed in 0.01~0.5 mm. The mineral composition in the bright and dark layer is similar to that in the plate-like lamina (Figure 3(e)). The massive lamina is dark brown to gray, with good homogeneity (Figure 3(f)), which is mainly composed of clay minerals and small amount of very fine silt. The clastic particles such as quartz and feldspar are rounded often, and clay minerals are mainly illite, with a maximum content of 80%, followed by quartz and feldspar, as well as a small amount of pyrite and muscovite, and the content of organic matter changes greatly.

**4.2. Lamina Mineral Composition.** The shale minerals in Chang 7<sub>3</sub> member of Ordos Basin are mainly clay minerals, feldspar, quartz, calcite, and dolomite [43]. The X-ray diffraction test results of 152 samples from G well show that the mineral composition of Chang 7<sub>3</sub> shale is mainly clay and felsic (Table 1), and the clay mineral is mainly illite, containing a small amount of montmorillonite and kaolinite (Figures 4 and 5). The clastic minerals are mainly feldspar

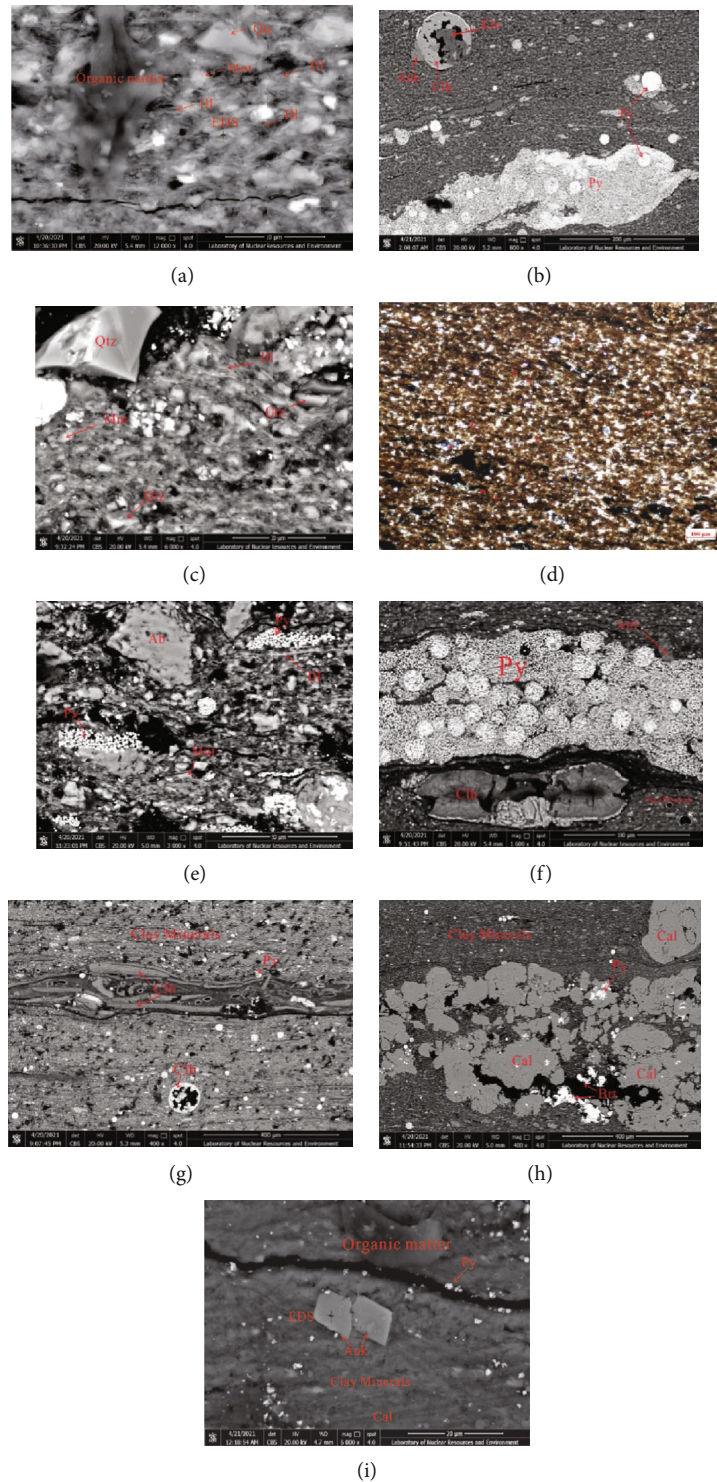


FIGURE 5: Micrograph of shale minerals of shale in Chang 7<sub>3</sub> member. (a) Illite (Ill) in clay minerals is in the shape of cotton wadding, hair, or long thin plate, 1830.00 m. (b) Authigenic kaolinite (Kn) shows the shape of authigenic sheet, which distributes in the inner cavity of algal fossils, 1845.5 m. (c) The surface of quartz particles (Qtz) is relatively smooth and produced in granular, lenticular, or strip shape, 1823.9 m. (d) Siliceous spots and veins, 1845.3 m. (e) Pyrite (Py) aggregates are produced in plate and strawberry shapes, 1825.25 m. (f) Pyrite (Py) aggregates of strawberry shapes, 1832.9 m. (g) Layered collophanite (Clh), 1832.9 m. (h) Spotted calcite (Cal), 1825.25 m. (i) Ankerite (Ank) single crystal is produced in self-shaped rhombic shape, 1821.85 m.

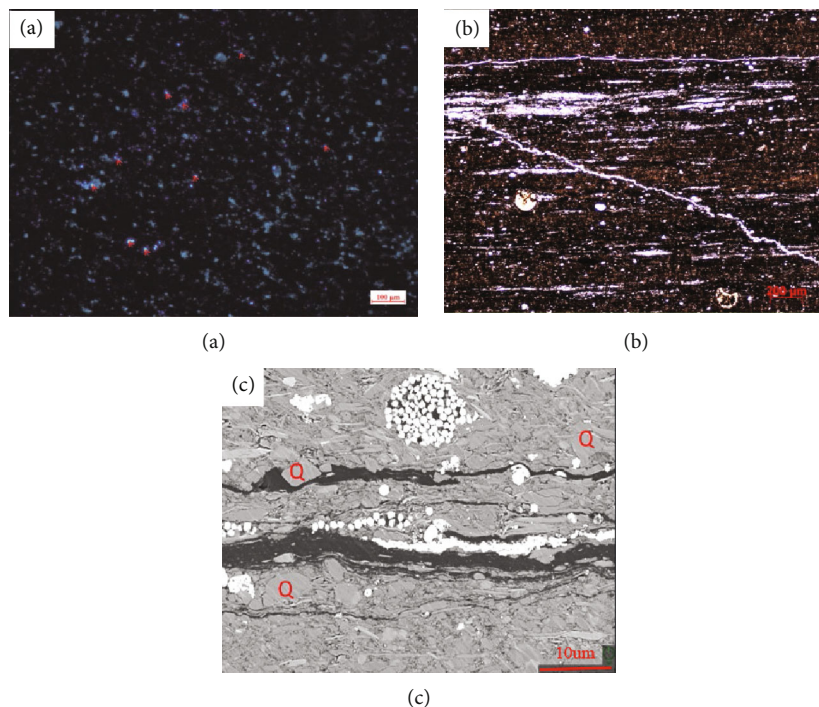
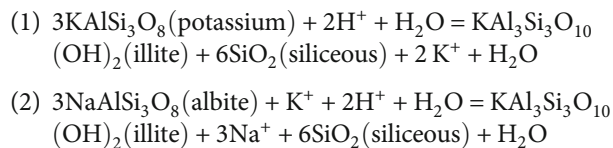


FIGURE 6: Micrograph of authigenic siliceous minerals in Chang 7<sub>3</sub> member. (a) Siliceous spots (red arrow) under fluorescent, 1845.3 m. Single polarized photo is shown in Figure 5(a); (b) siliceous veins, 1841.8 m; (c) SEM photos of siliceous spots, Q in the figure is authigenic quartz, 1841.8 m.

and quartz, with an average content of 40%. Only in the middle part of the Chang 7<sub>3</sub> submembers, there are 20-30% proportion of calcite and dolomite (Figure 4). The content of clay minerals varies greatly, mainly 42-57%, with an average content of 48.9%. According to the observation of scanning electron microscope, illite in clay minerals is in the shape of cotton wadding, hair, or long thin plate (Figure 5(a)), symbiotic with fine quartz and montmorillonite. Montmorillonite is spherical or lenticular, weakly oriented under the influence of compaction (Figure 5(b)). Authigenic kaolinite shows the shape of authigenic sheet, which distributes in the inner cavity of algal fossils (Figure 5(b)), indicating the existence of late low-temperature hydrothermal process. The mineral compositions of algae are iron dolomite→pyrite (PY)→collophanite (CLH)→iron dolomite (ANK)→organic matter (O-M)→authigenic kaolinite (KLN) from outside to inside.

In the clastic minerals of Chang 7<sub>3</sub> shale, the content of quartz is about 15-40%, with an average of 20.1%. The surface of quartz particles is relatively smooth and produced in granular, lenticular, or strip shape (Figure 5(c)). Plagioclase content is about 5-32%, with an average of about 14.5%. Albite is produced in thin plate, granular and angular shape. Dissolution holes are developed in the particles and filled with organic matter. More special, siliceous spots and veins are relatively developed (Figures 5(d)), which commonly show fluorescence (Figure 6). In order to understand its genesis, the siliceous area was analyzed in detail by electron microprobe (Table 2). The data shows that the content of SiO<sub>2</sub> is basically more than 50%, and the content of aluminum, potassium, and sodium minerals is also high, indicat-

ing a good associated relationship with feldspar. It is considered that the spotted and vein quartz comes from the dissolution and precipitation of SiO<sub>2</sub> from feldspar. The formula is as follows [46]:



Oval authigenic quartz is symbiotic with rectangular irregular feldspar and clay, indicating that there is a genetic relationship between them, and there is no obvious crystal form of quartz (Figure 6(c)). This phenomenon is mainly found in the shale of middle and lower part of Chang 7<sub>3</sub> member.

Pyrite is mainly sulfide of Chang 7<sub>3</sub> member shale, with a diameter of 1.1-25 μm, self-shaped crystal of quadrilateral, hexagonal, or colloidal. The aggregates of pyrite are like strawberry, radial, lenticular, and other forms (Figures 5(e) and 5(f)). Pyrites in different aggregates have complex contact relationships and multistage growth characteristics. Collophanite is common in Chang 7<sub>3</sub> member shale, with a diameter of 10 μm-2.5 mm, in shape of plate, crescent, or ring. The aggregate of collophanite shows banded, lenticular, or irregular (Figure 5(g)). Collophanite is partially transformed into apatite and calcite during diagenesis.

The content of carbonate in Chang 7<sub>3</sub> member is relatively small, which is mainly composed of calcite, ankerite. Calcite often developed dissolution holes and later filled with

TABLE 2: EPMA data in siliceous area of Chang 7<sub>3</sub> member shale (unit: %).

Number	Depth	Na <sub>2</sub> O	K <sub>2</sub> O	SiO <sub>2</sub>	FeO	CaO	Al <sub>2</sub> O <sub>3</sub>	P <sub>2</sub> O <sub>5</sub>	MgO	Total
1	1828.8	0.928	1.543	97.221	0.944	1.33	9.153	0.448	0.434	99.001
2	1849.9	0	0.003	96.886	0.193	0.011	0.019	0.036	0	97.148
3	1849.9	0	0.007	95.985	0.09	0.005	0	0.032	0.002	96.121
4	1849.9	0	0.016	94.323	0.201	0.002	0	0	0.02	94.562
5	1846.5	0.023	0.013	93.162	0	0.032	0.023	0	0.024	93.277
6	1846.5	0	0	91.867	0.073	0.025	0.021	0.032	0	92.018
7	1826.55	0	0.033	87.185	0.129	0.052	0.978	0	0	88.377
8	1805.15	0	0	81.133	0.039	0.035	0.007	0.036	0	81.25
9	1820.5	2.886	1.774	77.479	1.183	0.227	10.578	0.035	0.405	94.567
10	1808.25	7.076	0.452	76.272	0.189	7.204	1.305	0	3.972	96.47
11	1818.75	11.013	0.441	72.763	0.171	0.15	18.064	0.004	0.119	99.725
12	1818.75	7.167	2.081	69.812	0.409	0.775	16.259	0.106	0.331	96.94
13	1820.1	1.797	2.17	68.732	0.34	0.261	9.116	0.024	0.158	82.598
14	1808.25	6.533	0.448	66.423	0.342	6.682	1.432	0.039	3.385	85.284
15	1818.75	1.031	13.851	66.292	0.114	0.027	16.934	0.03	0	98.279
16	1850.6	2.967	5.735	65.565	0.521	0.383	16.868	0.004	0.175	92.218
17	1828.7	3.644	4.087	64.32	0.55	1.041	16.682	0.047	0.139	90.51
18	1805.15	1.502	14.146	64.312	0.111	0.057	17.243	0	0	97.371
19	1827.3	3.104	11.17	63.37	0.253	0.163	16.933	0.008	0	95.001
20	1828.7	4.531	2.164	62.531	0.714	1.01	14.229	0.047	0.214	85.44
21	1827.66	1.03	13.279	61.776	0.148	0.827	17.499	0.261	0	94.82
22	1850.6	1.071	16.88	61.373	0.218	0.041	15.126	0.013	0	94.722
23	1821.85	0.249	1.276	58.615	1.49	0.553	24.981	0.023	3.069	90.256
24	1828.7	1.918	2.675	57.923	2.091	2.149	11.823	0.719	0.648	79.946
25	1830	0.885	4.025	56.185	5.376	0.685	21.317	0.119	2.302	90.894
26	1843	7.663	0.148	55.233	0.05	10.764	24.159	0.004	0	98.021
27	1827.3	6.927	1.167	54.993	0.118	10.338	13.716	4.664	0.117	92.04
28	1819.15	1.807	3.408	54.641	1.878	0.679	18.715	0.108	1.407	82.643
29	1850.6	1.687	15.058	53.981	0.026	0.055	13.762	0.013	0	84.582
30	1833.7	1.063	3.441	53.776	3.096	1.645	12.782	1.109	1.242	78.154

pyrite and organic matter (Figure 5(h)). The ankerite crystal occurs with rhombic and bicrystals (Figure 5(i)).

4.3. *Laminar Types*. Based on the analysis of morphology, thickness, mineral composition, and TOC value, the lamina of Chang 7<sub>3</sub> member constitutes five types: silty felsic lamina (SF), tuffaceous lamina (TF), organic-rich clay lamina (ORC), organic-bearing clay lamina (OBC), and homogeneous clay layer (HC) (Table 3 and Figure 7), which are further subdivided into eight subcategories.

(1) *Silty Felsic Lamina (SF)*. The grain in the lamina is mainly feldspar and quartz, with a content of up to 60-70%, but the content of organic matter is low, only 1-5%. This lamina shows light color, developing silt grade positive grain sequence, and particle size decreases upward as well as clay content increases, with the main particle size of 10-50  $\mu\text{m}$ . The minerals are sorted medium to good, and the thickness of a single lamina is about 0.4 mm-10 mm (Figure 7(a)).

(2) *Tuffaceous Lamina (TF)*. The lamina is mainly light gray volcanic tuff material, occurring nearly horizontal, including angular volcanic glass and crystal chips, interbedded with intermittent organic matter bands. Authigenic pyrite is widely developed where tuffaceous matter often contacts banded or dispersed organic matter. The content of organic matter is about 3-5%, and the thickness of a single lamina is about 0.2-1 mm.

(3) *Organic-Rich Clay Lamina (ORC)*. The lamina can be further subdivided into two subtypes. ① Organic-rich plate-like clay lamina: this lamina has a dark color and presents a horizontal mud grade structure, in which a small amount of bright color striated lamina occurs, showing high content of felsic. The thickness of a single lamina is about 0.1-1 mm. A great amount of dispersed organic matter fragments, algal fossils, and collophanite can be seen, and the content of organic matter is about 8-12% (Figures 7(c) and 7(d)). ② Organic-rich wavy clay

TABLE 3: Shale lamina type division scheme of shale in Chang 7<sub>3</sub> member.

Code	Types	Subtypes	Key attributes
SF	Silty felsic lamina	/	Composition: silty quartz (30%~40%), feldspar (30%~40%), and clay minerals (20%~40%) Structure: coarse grain; structure: the single lamina is lenticular or linear, locally wavy, continuous, or intermittent, and the lamina is superimposed in parallel or nonparallel
TF	Tuffaceous lamina	/	Composition: clay minerals (5%~10%), other clastic minerals (70%~90%), and organic matter (3%~5%) Structure: fine grain; structure: the single lamina is continuous or intermittent plate-like in parallel
ORC	Organic-rich clay lamina	Organic-rich plate-like clay lamina Organic-rich wavy clay lamina	Composition: clay minerals (50%~75%), other clastic minerals (10%~20%), and organic matter (6%~15%) Structure: fine grain; structure: the single lamina is continuous plate-like or wavy in parallel
OBC	Organic-bearing clay lamina	Organic-bearing tabular clay lamina Organic-bearing wavy clay lamina	Composition: clay minerals (50%~75%), other clastic minerals (15%~25%), and organic matter (3%~6%) Structure: fine grain; structure: the single lamina is continuous plate-like or wavy in parallel
HC	Homogeneous clay layer	/	Composition: clay minerals (50%~75%), other clastic minerals (8%~20%), and organic matter (2%~10%) Structure: fine grain; structure: massive, with no obvious bedding

lamina: this lamina is yellow to brownish red and also presents mud grade structure. Clay minerals and organic matter form wavy lamina in lenticular and gentle waves. The thickness of a single lamina is about 0.05-0.5 mm. The organic matter content is about 6-12% (Figure 7(e)).

- (4) *Organic-Bearing Clay Lamina (OBC)*. This lamina has a similar structure and mineral composition to organic-rich clay lamina. It is also further subdivided into two subtypes according to the lamina shapes: ① organic-bearing plate-like clay lamina, which is brownish yellow and a low content of organic matter about 3-6% and ② organic-bearing wavy clay lamina. Clay minerals and organic matter form wavy lamina in lenticular or gentle wavy shape. The thickness of a single lamina is about 0.05-0.5 mm. The organic matter content is about 4-5% (Figures 7(f) and 7(g)).
- (5) *Homogeneous Clay Bed (HC)*. This lamina is further subdivided into two subclasses according to the content of organic matter. ① Homogeneous organic-rich clay bed: this lamina is black or gray black as to plenty of clay minerals and organic matter, showing a mud clastic structure, and light colored felsic particles dot it. The thickness of the single layer is greater than 10 mm, and the content of clay and organic matter is about 50-80% and 6-10%, respectively (Figure 7(h)). ② Homogeneous organic-bearing clay bed. The lamina has lighter color compared with the former, because of lower content of organic matter, only 2-6% (Figure 7(i)).

4.4. *Longitudinal Distribution of Lamina*. Through the statistical analysis of the core samples, extremely thin and thin

plate-like lamina are mainly types in Chang 7<sub>3</sub> submember of well G, and wavy lamina or massive bed develop locally. Moreover, the organic-rich clay lamina most developed, mainly in the middle and lower part of Chang 7<sub>3</sub> member (Figure 8), and the TOC is basically more than 8%. The organic-bearing clay lamina is distributed almost whole Chang 7<sub>3</sub> member, which is complementary to the distribution of organic-rich lamina and homogeneous clay bed, and homogeneous clay bed developed mainly in the up part of Chang 7<sub>3</sub> member. The silty lamina mainly distributes at the top and bottom part where the siltstone deposits, and the tuffaceous lamina occurs mainly at the lower and the middle part. The proportion of these two laminas is relatively low, less than 20%. What conditions may affect this combination? What is the impact on organic matter enrichment?

Several combinations of laminar types often occur in the same depth section from Figure 8, which is related to the complex sedimentary environment [8] and the influence of external material events during the deposition of Chang 7<sub>3</sub> member in Ordos Basin. In the middle and lower part of Chang 7<sub>3</sub> member, the shale of semideep to deep lacustrine facies [47] is mainly deposited, which usually develops ORC and OBS lamina combination. However, at the same time, volcanic events [32] and gravity flow [48] occurs often, and the SF and TF laminae are developed. In the upper part, the shale and mudstone mainly deposit under the semideep lacustrine environment. Meantime, affected by gravity flow and terrigenous input, a small amount of SF and OBC lamina combination developed.

4.5. *Characteristics and Types of Organic Matter in Lamina*. The type of organic matter has a great influence on its hydrocarbon generation capacity and the types of generation products [49, 50]. The results of slices analysis show that the shale of Chang 7<sub>3</sub> submember is mainly sapropelic and

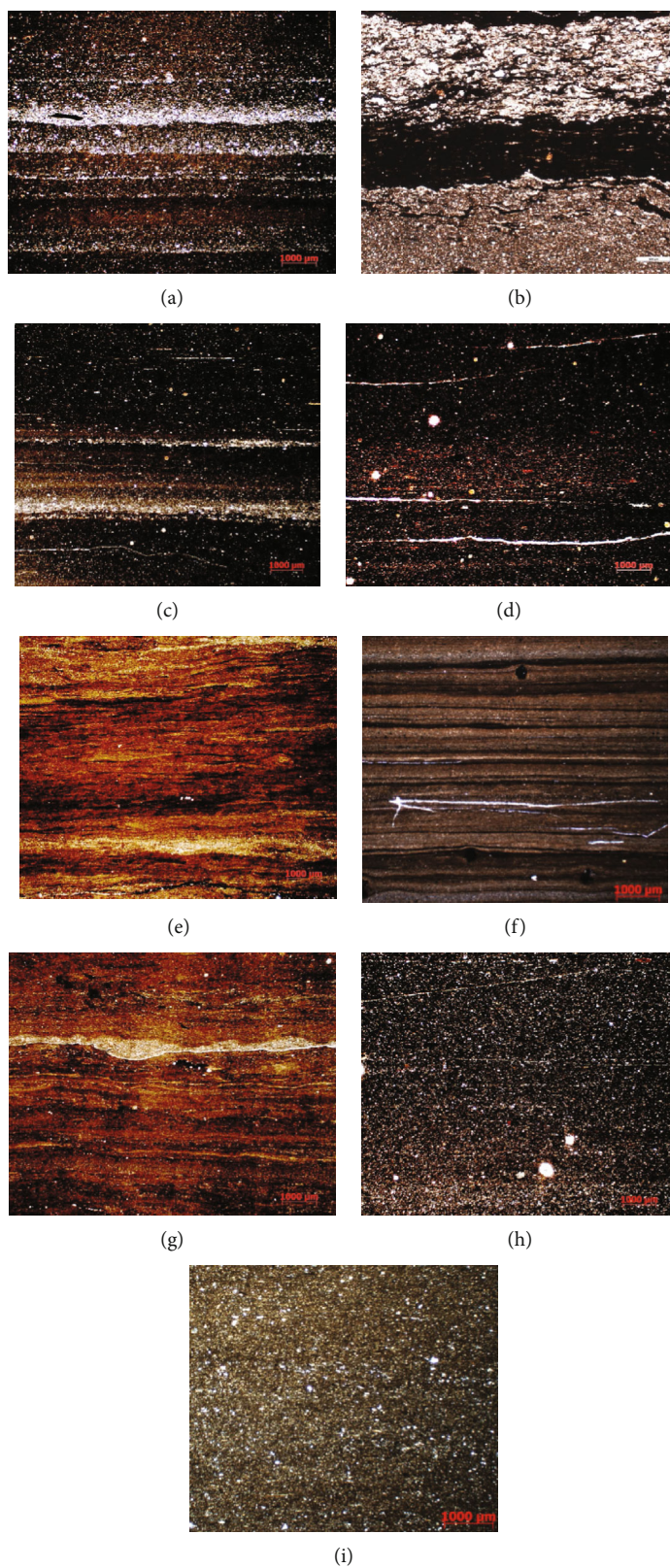


FIGURE 7: Micrograph of shale lamina types of the Chang 7<sub>3</sub> member in Ordos Basin. (a) Silty felsic lamina, 1845.5 m. (b) Tuffaceous lamina, 1833.4 m. (c) Organic-rich plate-like clay lamina, 1833.7 m. (d) Organic-rich plate-like clay lamina, 1824.5 m. (e) Organic-rich wavy clay lamina, 1826.8 m. (f) Organic-bearing plate-like clay lamina, 1825.5 m. (g) Organic-rich plate-like clay lamina, 1824.5 m. (h) Organic-bearing wavy clay lamina, 1825.4 m. (i) Homogeneous clay layer, 1844.8 m.

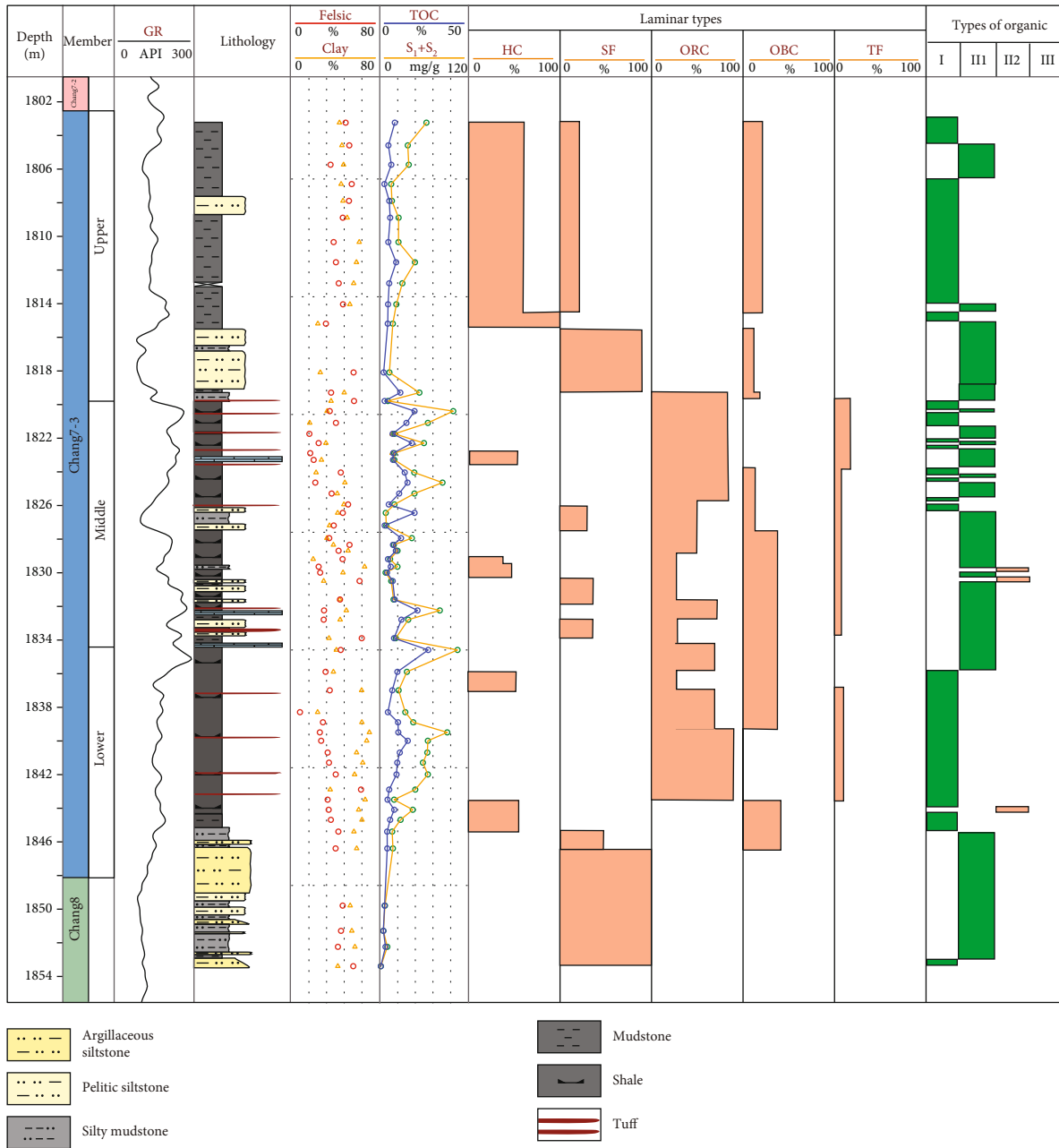


FIGURE 8: Shale lamina types and distribution of the Chang 7<sub>3</sub> member in Ordos Basin.

vitritine, accounting for 68.8% and 22.7%, respectively, followed by crustite, inertinite, and secondary organic units. Sapropelic is mainly composed of structural algae, layered algae, and asphaltene, which all accounts for about 0.9% of the whole rock. Vitritine is mainly composed of hydrogen rich vitritine, normal vitritine, and recycled vitritine, accounting for about 1.2% of whole rock. It is flaky and structureless under microscope. Exinite is mainly composed of sporopollen, cutinite, corkite, resinite, and shell debris, only accounting for 0.2% of whole rock and 4.2% of the relative maceral content. Inertinite is mainly composed of filaments, coarse stereoliths, fungi, and inertinites, only accounting for about 0.1% of whole rock and 2.6% of the relative macerals. The secondary organic units are mainly com-

posed of hydrogen-rich and hydrogen-poor secondary components, only accounting for 0.1% of whole rock and 1.7% of the relative macerals.

Shale in Chang 7<sub>3</sub> submember contains high sapropelic and vitritine group and has high hydrogen index (between 300-700 mg/g.TOC). It can be clear from the cross plot of hydrogen index (IH) and Tmax that kerogen types are mainly type I and type II<sub>1</sub>, with great hydrocarbon generation potential and oil generation (Figure 9).

4.6. *Distribution Characteristics of Organic Matter in Lamina.* Through the observation of microscope and scanning electron microscope, the organic matter in Chang 7<sub>3</sub> member shows four occurrence forms: ① dense

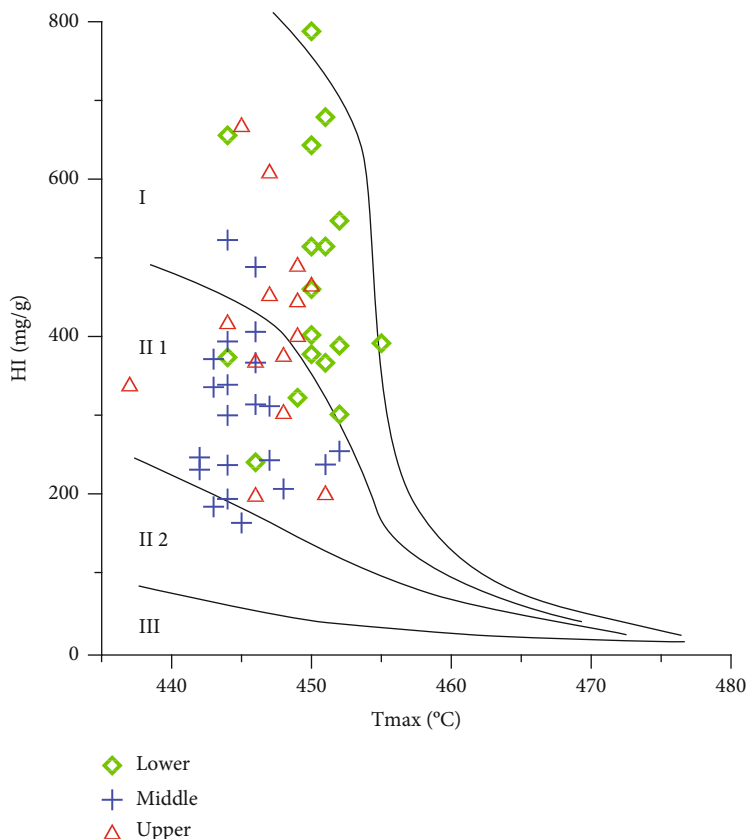


FIGURE 9: Classification of shale organic matter types of the Chang 7<sub>3</sub> member in Ordos Basin.

disseminated: the organic matter is densely disseminated and evenly distributed (Figures 10(a) and 10(b)), and the average TOC is about 10%. This type is mainly distributed in plate-like clay lamina and homogeneous clay bed, with low content of felsic, and the thickness of single lamina is usually large; ② sparsely dispersed: organic matter is dispersed in shale (Figures 10(c) and 10(d)), and the TOC is low, mostly less than 8%. This type mainly distributed in silty felsic lamina and clay layer. The content of felsic or clay is high, and the lamina is thin, usually 0.1-0.05 mm; ③ vein and lenticular like; organic matter is densely distributed in vein and lenticular shape (Figure 10(e)), which is often symbiotic with pyrite and collophanite. The TOC is usually high, mostly more than 8%. This type is mainly distributed in organic-rich clay lamina. According to the statistical data, the thinner the lamina, the higher the content of organic matter is. ④ Lamina-like; organic matter is distributed in relatively continuous lamina (Figure 10(f)), but the density of organic matter lamina is low, so the TOC is also low (3-8%), which is mainly distributed in thin parallel plate lamina.

## 5. Discussion

**5.1. Effect of Lamina on Organic Matter Types and TOC.** The analysis results of 152 shale samples show that the organic matter types of Chang 7<sub>3</sub> member shale are mainly type I and type II<sub>1</sub>, and the organic matter types of different types

of laminae are significantly different (Figures 8 and 9). The organic matter in organic-rich clay lamina, tuffaceous lamina, and homogeneous clay layer is mainly type I; however, the organic matter types of silty felsic lamina and organic-bearing clay lamina are mainly type II<sub>1</sub>. Qiu et al. also put forward that the organic-rich shale of Lucaogou Formation in the Jimusar Sag contained mainly type I-II<sub>1</sub> kerogen, while the silty shale often deposited type II<sub>1</sub>-II<sub>2</sub> kerogen [26]. This is related to the fact that different laminae represent different sedimentary environments and different hydrodynamic conditions. The deposit hydrodynamics of silty felsic lamina is relatively strong, the oxygen content of water body is high, and the organic matter is mainly from land input. The deposit hydrodynamic conditions of organic-rich clay lamina are between silty felsic lamina and homogeneous clay layer. Under relatively weak hydrodynamic conditions, aquatic algae dominated by plankton are easy to deposit, and the organic matter is dominated by lipid compounds (Figures 3(c) and 10(a)). Therefore, this kind of lamina has good organic matter type and high TOC. This is consistent with the understanding of the formation environment of lamina types of Longmaxi formation in Sichuan Basin discussed by Shi et al. [8].

However, there are two different kerogen types in the homogeneous clay layer, and the content of organic matter is quite different. Among them, the hydrodynamic conditions of the homogeneous clay layer rich in organic matter are the weakest, and the oxygen content at the bottom of

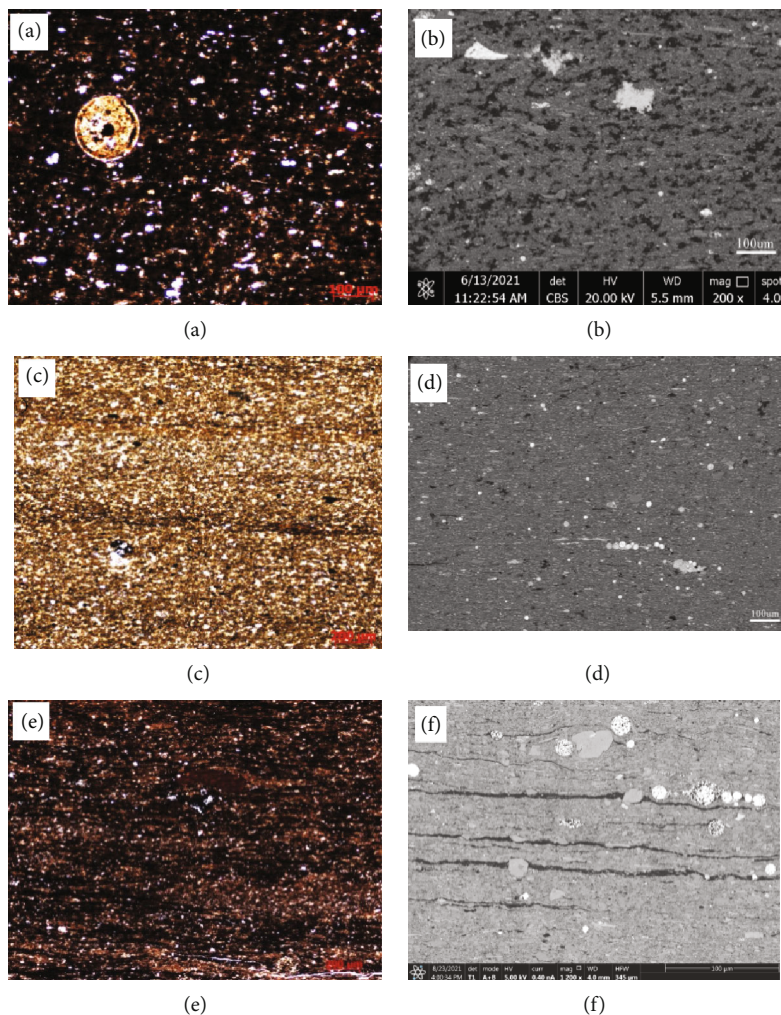


FIGURE 10: Microscopic characteristics of shale organic matter distribution of the Chang 7<sub>3</sub> member. (a) Dense disseminated organic matter, 1826.05 m. (b) Dense disseminated organic matter, 1828.7 m. (c) Sparsely dispersed organic matter, 1832.9 m. (d) Sparsely dispersed organic matter, 1821.85 m. (e) Vein and lenticular-like organic matter, 1830.6 m. (f) Lamina-like organic matter, 1814.15 m.

the water is lower, which is conducive to the preservation of organic matter. Therefore, the content of organic matter is mostly more than 6%, and the organic matter is densely disseminated. The content of felsic in the homogeneous clay layer containing organic matter is high, indicating that there are certain hydrodynamic conditions and relatively poor preservation conditions. The main organic matter is type II<sub>1</sub>, and the abundance of organic matter is also low. The tuffaceous lamina itself does not contain organic matter, but volcanic ash can bring a lot of nutrients. Algae and collophanite are developed on both sides of the tuffaceous lamina (Figure 7(b)). Therefore, although the content of organic matter in tuffaceous lamina is relatively low, it can promote the growth of organic matter in other lamina. Zhang et al. [33] and Liu et al. [51] also proposed that volcanic eruptions form a large amount of nutrients, which has a “fertilization” effect on aquatic organisms in the lake.

### 5.2. Effect of Lamina Mineral on Organic Matter Enrichment.

Through the statistical analysis of the relationship between

mineral composition and organic matter enrichment of different types of laminae, the TOC of shale in Chang7<sub>3</sub> member is generally negatively correlated with quartz and feldspar and positively correlated with pyrite, but no obvious relationship with clay minerals (Figure 11). Previous studies [52] have shown that the higher the content of felsic, the increase of terrigenous substances, good water fluidity, and high oxygen content. It is not easy to preserve after biological death, which is not conducive to the enrichment of organic matter. The deposition of pyrite requires still water and strong reduction environment. Therefore, the increase of pyrite content indicates that the water body has strong reduction, which is conducive to the preservation of organic matter. For different types of laminae, the mineral content of silty felsic laminae changes the most with the TOC. For example, when the TOC increases from 0% to 5%, the content of feldspar and quartz decreases from 40% to 15-20% (Figure 11), while the content of clay increases from 30% to 60%, which indicates that the change of terrestrial input and water energy has the greatest impact on the change of TOC in this kind of lamina. Related to other types of

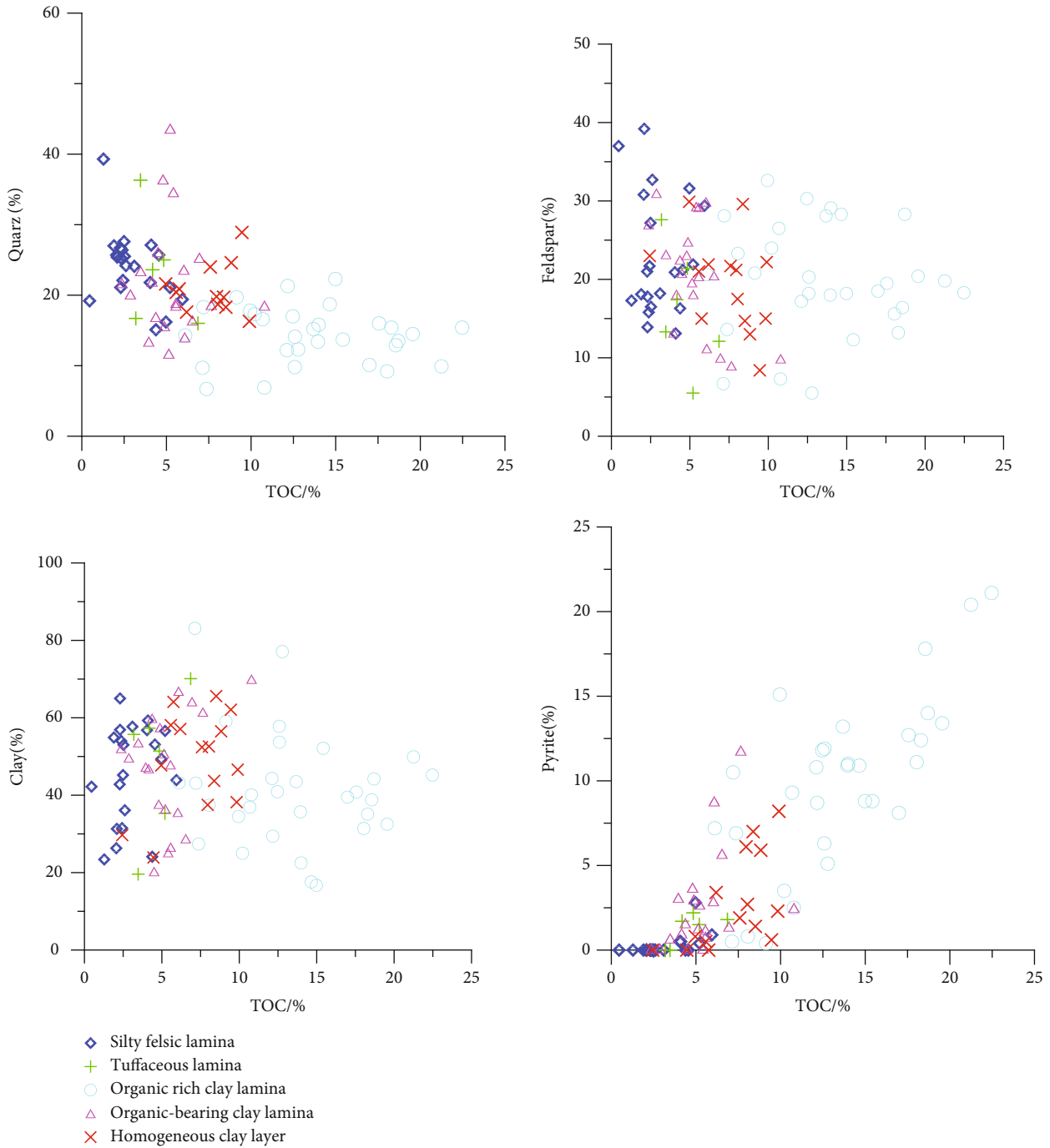


FIGURE 11: Relationship between TOC and mineral composition of different types of lamina shale of the Chang 7<sub>3</sub> member.

laminae, the TOC of silty felsic laminae is the lowest, so it basically contains no pyrite. The relationship between minerals and organic matter in organic-bearing clay lamina is basically similar to that of silty felsic lamina, except that the content of pyrite increases in the range of 0-10%, which is related to the increase of TOC in this kind of lamina and the enhancement of reducibility of water body. The shale of Qingshankou Formation in the Gulong sag, northern Songliao, also show this law [31], that is, the shale with high TOC (>2-5%) often contains high clay (30-45%) and lower felsic (50-70%) minerals; however, the shale with low TOC

(<2) often contains high felsic (65-90%) and lower clay (5-30%) minerals.

The relationship between minerals and organic matter enrichment in organic-rich clay lamina has the largest variation range, which is due to the large variation of TOC in this kind of lamina, which is 6%~24%. However, the TOC of this kind lamina has a significant relationship with quartz and pyrite. When TOC is more than 10%, the content of quartz is obviously less than 20%, while the content of pyrite is more than 10%, which basically represents the strong reduction environment of still water in deep lake area.

However, the content of clay minerals tends to decrease from 50% to 40%, which may be caused by the dilution of organic matter enrichment. The change relationship between minerals and organic matter in homogeneous clay layer is complex, in which the content of feldspar decreases with the increase of TOC, while that of pyrite is the opposite. However, the relationship between the content of quartz and clay minerals and the TOC is not obvious, indicating that the enrichment mechanism of organic matter in this kind of lamina is more complex and there are more influencing factors. For tuffaceous lamina, due to its low organic matter content and small number of laminae, the correlation is not very clear, too.

The development of multiple laminar assemblages at the same depth also has a certain impact on the enrichment of organic matter. Firstly, the tuffaceous lamina developed by volcanic activity dilutes the TOC of the formation due to its low organic matter content or no organic matter. However, tuffaceous matter contains rich nutrients which promote the growth of algae and leads to the rapid enrichment of organic matter in the shale deposited later. Secondly, the activity of silty gravity flow also dilutes the TOC of the formation, damages the anoxic sedimentary and preservation environment, and reduces the TOC of shale deposited nearly the same time.

## 6. Conclusions

In this study, the laminae of the Chang 7<sub>3</sub> member in well G occur in the form of extreme thin to thin parallel plate-like, and parallel wavy and massive are locally developed. The thickness of a single lamina is between 0.05 and 1.0 mm. According to the shape, thickness, mineral composition, and organic matter content of shale lamina, the lamina types of section Chang 7<sub>3</sub> are divided into 5 types and 7 subtypes.

Shale minerals are mainly composed of clay, feldspar, quartz, and Pyrite, with a small amount of collophanite and carbonate. Clay mainly includes illite and illite/smectite mixed layer. Felsic minerals are mainly quartz, and some of them are developed in the form of siliceous spots and siliceous veins. SEM and probe analysis show that they come from the dissolution and precipitation of SiO<sub>2</sub> in feldspar. Some spherical alga fossils are filled with hydrothermal minerals of different stages, indicating that there was hydrothermal activity in diagenetic stage.

The vertical distribution of shale laminae types in Chang 7<sub>3</sub> member varies greatly. The middle and lower part is mainly rich in ORC and OBC, bearing a small amount of TF, and the upper part is mainly HC and SF. The organic matter in ORC and HC is mainly algae and type I, distributed in dense disseminated or lenticular shape, and the TOC is high, usually greater than 8%. The organic matter in SF and OBC is dominated by type II<sub>1</sub>, containing many terrigenous structures, which are sparse dispersed or laminar distribution, and the TOC is usually less than 8%.

Different laminar types deposit different minerals, representing different sedimentary and water environment. The lamina rich in clay, tuffaceous, and pyrite represents large

water depth, lack of oxygen at the bottom, less terrigenous input, and good preservation conditions of organic matter, resulting in high TOC and rich shale oil resources. On the contrary, the lamina rich in silt and felsic represents more terrigenous input, turbulent water body, oxidizing environment, and poor preservation conditions of organic matter, leading to low TOC.

## Data Availability

Data is not available for confidential reasons.

## Conflicts of Interest

The authors declare that they have no conflicts of interest.

## Authors' Contributions

Congsheng Bian designed the framework and ideas of the article and wrote the manuscript and polished the language. Wenzhi Zhao put forward research methods, technology, and viewpoint promotion.

## Acknowledgments

This study was funded by the National Natural Science Foundation of China (42090020 and 42090025). The Petro-China Changqing Oilfield Company provided the core data. We sincerely appreciate their help.

## References

- [1] T. X. Jiang, X. B. Bian, H. T. Wang et al., "Volume fracturing of deep shale gas horizontal wells," *Natural Gas Industry*, vol. 37, no. 1, pp. 90–96, 2017.
- [2] S. Heng, C. H. Yang, Y. T. Guo, C. Y. Wang, and L. Wang, "Influence of bedding planes on hydraulic fracture propagation in shale formations," *Chinese Journal of Rock Mechanics and Engineering*, vol. 34, no. 2, pp. 4228–4237, 2015.
- [3] D. Xu, R. L. Hu, W. Gao, and J. Xia, "Effects of laminated structure on hydraulic fracture propagation in shale," *Petroleum Exploration and Development*, vol. 42, no. 4, pp. 573–579, 2015.
- [4] O. R. Lazar, K. M. Bohacs, J. H. S. Macquaker, J. Schieber, and T. M. Demko, "Capturing key attributes of fine-grained sedimentary rocks in outcrops, cores, and thin sections: nomenclature and description guidelines," *Journal of Sedimentary Research*, vol. 85, no. 3, pp. 230–246, 2015.
- [5] N. R. O'Brien, "Shale lamination and sedimentary processes," *Geology Society*, vol. 116, no. 1, pp. 23–36, 1996.
- [6] D. Genty and Y. Quinif, "Annually laminated sequences in the internal structure of some Belgian stalagmites; importance for paleoclimatology," *Journal of Sedimentary Research*, vol. 66, no. 1, pp. 275–288, 1996.
- [7] C. Liang, Y. Cao, K. Liu, Z. Jiang, J. Wu, and F. Hao, "Diagenetic variation at the lamina scale in lacustrine organic-rich shales: implications for hydrocarbon migration and accumulation," *Geochimica et Cosmochimica Acta*, vol. 229, pp. 112–128, 2018.
- [8] Z. Shi, Z. Qiu, D. Dong, B. Lu, P. Liang, and M. Zhang, "Laminae characteristics of gas-bearing shale fine-grained sediment

- of the Silurian Longmaxi Formation of Well Wuxi 2 in Sichuan Basin, SW China,” *Petroleum Exploration and Development*, vol. 45, no. 2, pp. 358–368, 2018.
- [9] K. Xi, K. Li, Y. Cao et al., “Laminae combination and shale oil enrichment patterns of Chang 7 organic-rich shales in the Triassic Yanchang Formation, Ordos Basin, NW China,” *Petroleum Exploration and Development*, vol. 47, no. 6, pp. 1342–1353, 2020.
- [10] A. Negri, “Possible origin of laminated sediments of the anoxic Bannock Basin (eastern Mediterranean),” *Geo-Marine Letter*, vol. 16, no. 2, pp. 101–107, 1996.
- [11] S. F. Leclair and R. W. C. Arnott, “Parallel lamination formed by high-density turbidity currents,” *Journal of Sedimentary Research*, vol. 75, no. 1, pp. 1–5, 2005.
- [12] D. Walker and J. A. K. Owen, “The characteristics and source of laminated mud at Lake Barrine, Northeast Australia,” *Quaternary Science Review*, vol. 18, no. 14, pp. 1597–1624, 1999.
- [13] G. M. Barbara and J. Mitchell, “Formation of 30- to 40-micrometer-thick laminations by high-speed marine bacteria in microbial mats,” *Applied and Environmental Microbiology*, vol. 62, no. 11, pp. 3985–3990, 1996.
- [14] X. Zhang and J. Sha, “Sedimentary laminations in the lacustrine Jianshangou bed of the Yixian formation at Sihetun, western Liaoning, China,” *Cretaceous Research*, vol. 36, pp. 96–105, 2012.
- [15] D. D. Liu, Z. Li, Z. X. Jiang et al., “Impact of laminae on pore structures of lacustrine shales in the southern Songliao Basin, NE China,” *Journal of Asian Earth Sciences*, vol. 182, p. 103935, 2019.
- [16] G. L. Hua, S. T. Wu, Z. Qiu, Z. H. Jin, J. L. Xu, and M. D. Guan, “Lamination texture and its effect on reservoir properties: a case study of Longmaxi Shale, Sichuan Basin,” *Acta Sedimentologica Sinica*, vol. 39, no. 2, pp. 281–296, 2021.
- [17] C. Wang, B. Q. Zhang, Z. G. Shu et al., “Shale lamination and its influence on shale reservoir quality of Wufeng Formation-Longmaxi Formation in Jiashiba area,” *Earth Science*, vol. 44, no. 3, pp. 972–982, 2019.
- [18] R. G. Loucks, R. M. Reed, S. C. Ruppel, and D. M. Jarvie, “Morphology, genesis, and distribution of nanometer-scale pores in siliceous mudstones of the Mississippian Barnett Shale,” *Journal of Sedimentary Research*, vol. 79, no. 12, pp. 848–861, 2009.
- [19] L. Chen, Z. Jiang, K. Liu et al., “Application of Langmuir and Dubinin-Radushkevich models to estimate methane sorption capacity on two shale samples from the Upper Triassic Chang 7 member in the southeastern Ordos Basin, China,” *Energy Exploration Exploitation*, vol. 35, no. 1, pp. 122–144, 2017.
- [20] R. Yang, F. Hao, S. He et al., “Experimental investigations on the geometry and connectivity of pore space in organic-rich Wufeng and Longmaxi shales,” *Marine and Petroleum Geology*, vol. 84, pp. 225–242, 2017.
- [21] W. Yang, R. S. Zuo, Z. X. Jiang et al., “Effect of lithofacies on pore structure and new insights into pore-preserving mechanisms of the over-mature Qiongzhusi marine shales in Lower Cambrian of the southern Sichuan Basin, China,” *Marine and Petroleum Geology*, vol. 98, pp. 746–762, 2018.
- [22] S. X. Li, X. B. Niu, G. D. Liu et al., “Formation and accumulation mechanism of shale oil in the 7th member of Yanchang Formation, Ordos Basin,” *Oil & Gas Geology*, vol. 41, no. 4, pp. 719–729, 2020.
- [23] D. M. Jarvie, “Shale resource systems for oil and gas: part 2—shale-oil resource systems,” *AAPG Memoir*, vol. 97, pp. 89–119, 2012.
- [24] D. M. Jarvie, “Components and processes affecting producibility and commerciality of shale resource systems,” *Geologica Acta*, vol. 12, pp. 307–325, 2014.
- [25] L. Sun, H. Liu, W. He et al., “An analysis of major scientific problems and research paths of Gulong shale oil in Daqing Oilfield, NE China,” *Petroleum Exploration and Development*, vol. 48, no. 3, pp. 527–540, 2021.
- [26] Z. Qiu, H. Tao, C. Zou, H. Wang, H. Ji, and S. Zhou, “Lithofacies and organic geochemistry of the Middle Permian Lucaogou Formation in the Jimusar Sag of the Junggar Basin, NW China,” *Journal of Petroleum Science and Engineering*, vol. 140, pp. 97–107, 2016.
- [27] S. Hu, B. Bai, S. Tao et al., “Heterogeneous geological conditions and differential enrichment of medium and high maturity continental shale oil in China,” *Petroleum Exploration and Development*, vol. 49, no. 2, pp. 257–271, 2022.
- [28] C. Teichert, “Concepts of facies,” *AAPG Bulletin*, vol. 42, no. 11, pp. 2718–2744, 1958.
- [29] G. C. Wang and T. R. Carr, “Organic-rich Marcellus Shale lithofacies modeling and distribution pattern analysis in the Appalachian Basin,” *AAPG Bulletin*, vol. 97, no. 12, pp. 2173–2205, 2013.
- [30] Z. Song, J. Li, X. Li et al., “Coupling relationship between lithofacies and brittleness of the shale oil reservoir: a case study of the Shahejie Formation in the Raoyang Sag,” *Geofluids*, vol. 2022, Article ID 2729597, 17 pages, 2022.
- [31] B. Liu, H. L. Wang, X. F. Fu et al., “Lithofacies and depositional setting of a highly prospective lacustrine shale oil succession from the Upper Cretaceous Qingshankou Formation in the Gulong sag, northern Songliao Basin, northeast China,” *AAPG Bulletin*, vol. 103, no. 2, pp. 405–432, 2019.
- [32] C. Y. Liu, J. Q. Wang, D. D. Zhang et al., “Genesis of rich hydrocarbon resources and their occurrence and accumulation characteristics in the Ordos Basin,” *Oil & Gas Geology*, vol. 42, no. 5, pp. 1011–1030, 2021.
- [33] B. Zhang, Z. Mao, Z. Zhang et al., “Black shale formation environment and its control on shale oil enrichment in Triassic Chang 7 Member, Ordos Basin, NW China,” *Petroleum Exploration and Development*, vol. 48, no. 6, pp. 1304–1314, 2021.
- [34] G. R. Chalmers, R. M. Bustin, and I. M. Power, “Characterization of gas shale pore systems by porosimetry, pycnometry, surface area, and field emission scanning electron microscopy/transmission electron microscopy image analyses: examples from the Barnett, Woodford, Haynesville, Marcellus, and Doig units,” *AAPG Bulletin*, vol. 96, no. 6, pp. 1099–1119, 2012.
- [35] E. J. Mathia, L. Bowen, K. M. Thomas, and A. C. Aplin, “Evolution of porosity and pore types in organic-rich, calcareous, Lower Toarcian Posidonia Shale,” *Marine and Petroleum Geology*, vol. 75, pp. 117–139, 2016.
- [36] M. Wang, R. Ma, J. Li et al., “Occurrence mechanism of lacustrine shale oil in the Paleogene Shahejie Formation of Jiyang Depression, Bohai Bay Basin, China,” *Petroleum Exploration and Development*, vol. 46, no. 4, pp. 833–846, 2019.

- [37] Y. Y. Chen, S. H. Lin, B. Bai et al., "Effects of petroleum retention and migration within the Triassic Chang 7 Member of the Ordos Basin, China," *International Journal of Coal Geology*, vol. 225, article 103502, 2020.
- [38] S. T. Fu, J. L. Yao, S. X. Li, X. P. Zhou, and M. R. Li, "Enrichment characteristics and resource potential of continental shale oil in Mesozoic Yanchang Formation, Ordos Basin," *Petroleum Geology & Experiment*, vol. 42, no. 5, pp. 698–711, 2020.
- [39] S. T. Fu, Z. J. Jin, J. H. Fu, S. X. Li, and W. W. Yang, "Transformation of understanding from tight oil to shale oil in the member 7 of Yanchang Formation in Ordos Basin and its significance of exploration and development," *Acta Petrolei Sinica*, vol. 42, no. 5, pp. 561–569, 2021.
- [40] S. H. Lin, X. J. Yuan, and Z. Yang, "Comparative study on lacustrine shale and mudstone and its significance: a case from the 7~(th) member of Yanchang Formation in the Ordos Basin," *Oil & Gas Geology*, vol. 38, no. 3, pp. 517–523, 2017.
- [41] F. Jinhua, N. Xiaobing, D. Weidong et al., "The geological characteristics and the progress on exploration and development of shale oil in Chang 7 member of Mesozoic Yanchang Formation, Ordos Basin," *China Petroleum Exploration*, vol. 24, no. 5, pp. 601–614, 2019.
- [42] G. Liu, Z. Huang, Z. Jiang, J. Chen, C. Chen, and X. Gao, "The characteristic and reservoir significance of lamina in shale from Yanchang Formation of Ordos Basin," *Natural Gas Geoscience*, vol. 26, no. 3, pp. 408–417, 2015.
- [43] C. N. Zou, S. Q. Pan, B. Horsfield et al., "Oil retention and intrasource migration in the organic-rich lacustrine Chang 7 shale of the Upper Triassic Yanchang Formation, Ordos Basin, Central China," *AAPG Bulletin*, vol. 10, no. 11, pp. 2627–2663, 2019.
- [44] R. L. Ingram, "Terminology for the thickness of stratification and parting units in sedimentary rocks," *GSA Bulletin*, vol. 65, no. 9, pp. 937–938, 1954.
- [45] C. V. Campbell, "Lamina, laminaset, bed and bedset," *Sedimentology*, vol. 8, no. 1, pp. 7–26, 1967.
- [46] K. K. Huang, S. J. Huang, H. P. Tong, and L. H. Liu, "Thermodynamic calculation of feldspar dissolution and its significance on research of clastic reservoir," *Geological Bulletin of China*, vol. 28, no. 4, pp. 474–482, 2009.
- [47] Q. Liu, X. J. Yuan, S. H. Lin, H. Guo, and D. W. Cheng, "Depositional environment and characteristic comparison between lacustrine mudstone and shale: a case study from the Chang 7 member of the Yanchang Formation, Ordos Basin," *Oil & Gas Geology*, vol. 39, no. 3, pp. 531–540, 2018.
- [48] F. Liu, X. Zhu, Y. Li et al., "Sedimentary characteristics and facies model of gravity flow deposits of Late Triassic Yanchang Formation in southwestern Ordos Basin, NW China," *Petroleum Exploration and Development*, vol. 42, no. 5, pp. 633–645, 2015.
- [49] B. P. Tissot and D. H. Welte, *Petroleum Formation and Occurrence: A New Approach to Oil and Gas Exploration*, Springer, Verlag Berlin Heidelberg, 1978.
- [50] M. D. Lewan, M. J. Kotarba, J. B. Curtis, D. Więclaw, and P. Kosakowski, "Oil-generation kinetics for organic facies with type-II and -IIS kerogen in the Menilite Shales of the Polish Carpathians," *Geochimica et Cosmochimica Acta*, vol. 70, no. 13, pp. 3351–3368, 2006.
- [51] Q. Y. Liu, P. Li, Z. J. Jin et al., "Organic-rich formation and hydrocarbon enrichment of lacustrine shale strata: a case study of Chang 7 member," *Science China Earth Sciences*, vol. 65, no. 1, pp. 118–138, 2022.
- [52] A. D. Aubry and P. B. Lauren, "Sediment dispersal and organic carbon preservation in a dynamic mudstone-dominated system, Juana Lopez Member, Mancos Shale," *Sedimentology*, vol. 66, no. 3, pp. 1002–1041, 2019.

## Research Article

# A Method for the Inversion of Reservoir Effective Permeability Based on Time-Lapse Resistivity Logging Data and Its Application

Hairong Zhang <sup>1</sup>, Bin Zhao <sup>1</sup>, Shiqi Dong <sup>2</sup>, Xixin Wang <sup>3</sup>, and Pengfei Jing <sup>2</sup>

<sup>1</sup>College of Geophysics and Oil Resources, Yangtze University, Wuhan Hubei, China

<sup>2</sup>Southern Marine Science and Engineering Guangdong Laboratory (Zhanjiang), Zhanjiang, China

<sup>3</sup>College of Geosciences, Yangtze University, Wuhan Hubei, China

Correspondence should be addressed to Bin Zhao; zhaobin@yangtzeu.edu.cn

Received 20 January 2022; Revised 8 March 2022; Accepted 31 March 2022; Published 22 April 2022

Academic Editor: Kouqi Liu

Copyright © 2022 Hairong Zhang et al. This is an open access article distributed under the Creative Commons Attribution License, which permits unrestricted use, distribution, and reproduction in any medium, provided the original work is properly cited.

Effective permeability is a key parameter for evaluating reservoirs and their productivity. With the wide application of resistivity logging tools in drilling, the advantages of resistivity logging in response to the dynamic invasion process of drilling fluids have become increasingly prominent. We analyzed the variation law of the measured resistivity data for different permeability formations at different times. In this study, we proposed an effective permeability modeling method based on the time-lapse resistivity logging data. First, based on the resistivity measurement data at different times, the dynamic resistivity profile of the reservoir was obtained through joint inversion; we then obtained the invasion depth and invasion zone resistivity of the drilling fluid at different times, along with the original formation resistivity. Subsequently, combined with parameters such as the soaking time, fluid viscosity, and saturation change of the drilling fluid, we obtained the phase permeability curve of the reservoir and dynamic effective permeability of the fluid near the wellbore. This study provides basic parameters for subsequent formation analyses and productivity prediction and substantially improves the reservoir evaluation technology from static to dynamic.

## 1. Introduction

The seepage characteristics of the reservoir are key parameters that control the decision-making for its completion, oil-field development, and reservoir management. The most important parameter for evaluating the seepage characteristics of a reservoir is the effective permeability and can be obtained through testing. However, the cost of testing is extremely high; therefore, the effective permeability is generally extrapolated by the absolute permeability of the laboratory, such as core analysis, log comparison, and well testing [1–6]. The existing methods for obtaining effective permeability have certain limitations in practical applications. For example, core analysis provides an average permeability equivalent to a few cubic inches of samples, and the sample size is too small to describe a reservoir in general terms.

However, the scale of formation testing is several thousand cubic feet and cannot provide a detailed description of the reservoir heterogeneity. In view of the aforementioned limitations, an increasing number of scholars at home and abroad have begun to characterize the microscopic pore structure and seepage characteristics of reservoirs through numerical simulation techniques through digital cores, especially in the field of unconventional reservoirs such as shale oil and shale gas [7–13]. With the development of logging and drilling technology, many scholars have begun to pay attention to the multi-angle correlation between the logging data and reservoir permeability. In the early stages, foreign scholars proposed a method of inversion to obtain the absolute permeability of the reservoir by combining the measured data from three types of tools, such as resistivity logging, neutron logging, and density logging, through the

history matching method [14–17]. To ensure the reliability of the formation permeability parameters obtained through resistivity logging and other data, scholars began to use nuclear magnetic resonance (NMR), formation testing, pump sampling, and other data to correct the inversion results and estimate the relative permeability curve and capillary pressure of the reservoir curve [18–21]. Through a comparative study, we observed that the main aim of previous research was to invert the permeability of the reservoir by comparing the measured and simulated curves; however, less attention has been paid to the dynamic resistivity profile of the reservoir after considering the drilling fluid invasion and reservoir rocks. The quantitative relationship between the physical parameters, especially the dynamic change in the resistivity profile of the reservoir, is caused by the difference in logging time and reservoir permeability.

The Dongfang Block in western South China Sea is a high-pressure gas field. The well sections of the target layers were all measured using the Schlumberger ARC675 electromagnetic wave resistivity logging tool (ARC675); the resistivity logging is commonly affected by the drilling fluid. Considering the phenomenon of low invasion effect, repeated logging was conducted in each well logging operation, and there was abundant time-lapse resistivity logging data. Considering the actual measurement of electromagnetic wave resistivity while drilling in this area, the author combined the vector finite element method and front-line solution method to solve the forward model of the logging-while-drilling (LWD) resistivity response. The dynamic resistivity profiles of the formation, including the drilling fluid invasion depth, invasion zone resistivity at different times, and the undisturbed formation resistivity, were combined with the changes in formation drilling time, fluid viscosity, and saturation to obtain discrete phase permeability curve characteristic points. The functional relationship between saturation and relative permeability was obtained by fitting the least squares algorithm. Finally, the dynamic effective permeability of the fluid near the wellbore was obtained according to the saturation curve at different times.

## 2. Method of Joint Inversion of Time-Shift Resistivity

The combined inversion results based on the resistivity logging data at different times can accurately reflect the changing process of the dynamic invasion of the reservoir drilling fluid. First, the vector finite element method was used according to the Maxwell equation of electromagnetic wave response. This method began from the formation model (including the layered structure of the wellbore) to simulate the measurement response of electromagnetic wave resistivity while drilling in the nonuniform formation and to establish and verify a forward modeling method. On this basis, three sets of formation models were constructed as the solution parameters, namely, the radius of the invasion zone ( $R_i$ ), the resistivity of the invasion zone ( $R_{xo}$ ), and the formation resistivity ( $R_t$ ). The drilling fluid invasion depth, resistivity of the invasion zone, and true resistivity of the formation were obtained at different times, and the dynamic

resistivity profile was obtained to provide basic data for the subsequent calculation of the effective permeability.

*2.1. Method of Joint Inversion of Time-Shift Resistivity.* Measurement theory of electromagnetic wave resistivity while drilling involves solving Maxwell's equations under the given boundary conditions [22]. The electromagnetic field in the logging problem satisfies the following Maxwell equation:

$$\nabla \times E = -i\omega\mu H \quad (1)$$

$$\nabla \times H = \sigma E + J \quad (2)$$

According to Equations (1) and (2), we deduced that the vector wave equation satisfied by the electric field is

$$\nabla \times \nabla \times E - \omega^2 \mu \epsilon_c E = -j\omega\mu J \quad (3)$$

where  $\epsilon_c = \epsilon - i\sigma/\omega$  is the complex dielectric constant and  $\epsilon$  is the dielectric constant of the formation.

In layered structured media, the numerical simulation of electrical logging tools is vital for obtaining the tool parameters in complex environments. Several numerical methods have been successfully applied to simulate complex media, including the finite difference time domain (FDTD), finite element method (FEM), and numerical mode matching (NMM). The author first established a physical model of the layered stratigraphic structure including the wellbore (as shown in Figure 1), discretized the stratigraphic model space according to the electromagnetic field distribution law, and then established a two-dimensional discrete grid space (as shown in Figure 2). The vector finite element method and the front-line solution method were combined to solve the aforementioned Maxwell equation to realize the forward modeling of the measurement response of the electromagnetic wave resistivity while drilling in the nonuniform formation. To verify the reliability of the forward modeling model and algorithm, the Schlumberger's ARC675 instrument was used as an example to conduct relevant forward modeling simulations, and the results were verified with the Schlumberger calibration plate for accuracy.

Figures 3(a), 3(b), 4(a), and 4(b) show the comparison results of the borehole calibration chart for the ARC675 tool. In the chart, the abscissa is the apparent resistivity ( $R_{ps}$  and  $R_{ad}$  are the apparent resistivities of the phase difference and amplitude ratio, respectively), and the ordinate is the true value of the formation and apparent resistivity. The ratio between resistivity represents the correction factor. Compared with the Schlumberger borehole calibration chart, the data error of each source distance chart was less than 3%, indicating that the forward modeling algorithm was reliable.

*2.2. Time-Shift Resistivity Joint Inversion.* Joint inversion refers to the inversion of geological model parameters using two or more types of logging data with different physical mechanisms [23]. The resistivity data collected at different

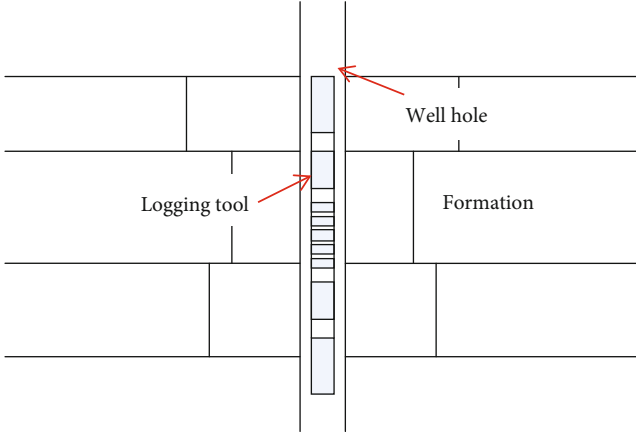


FIGURE 1: Physical model of the vertical well.

times have different invasion depths and resistivity values of the invasion zone due to the different soaking times of the drilling fluid. However, the resistivity of the undisturbed formation is unique, and the time-lapse resistivity joint inversion can more accurately reflect the geological model parameters because it increases the amount of effective information for the specific detection targets. Compared with the static resistivity profile of iterative inversion, the dynamic resistivity profile of the reservoir was obtained by inversion by considering the influence of logging time on the resistivity profile.

The time-lapse resistivity joint inversion is based on the damped least-squares method and organically unifies the resistivity logging response at different times and the dynamic profile of the formation resistivity for inversion. First, the least-squares objective function is constructed, assuming that  $y$  is the actual measured logging curve data and  $f(x)$  is the response function of the tool to the formation model, and the objective function is assumed to be in the form of the sum of squares:

$$\varphi(\vec{x}) = \sum_{k=1}^m [y_k - f_k(\vec{x})]^2 \quad (4)$$

where  $m$  is the number of logging curves and  $f$  is the multivariate nonlinear response function for the parameters. The response function is related to the working principle of the tool, structure of the tool, and formation model. This is the parameter to be inverted, including the resistivity measurement at time T1. A total of five sets of formation model parameters can be obtained through the foregoing resistivity forward model to solve for  $f(x)$ : namely, the intrusion zone radius  $Ril$ , intrusion zone resistivity  $Rxol$  at time T2, intrusion zone radius  $Rih$ , intrusion zone resistivity  $Rxoh$  when the resistivity is measured at T2, and the formation resistivity  $Rt$ .

Marquette's algorithm was used to solve the least-squares problem. Gauss proposed a linearization method

to expand  $f(\vec{x})$  into a Taylor series near  $\vec{x}^{(0)}$  and omit the quadratic term  $\vec{\delta}_i$  and the above quadratic terms. The formula used is as follows:

$$f_k(\vec{x}^{(0)} + \vec{\delta}) = f_k(\vec{x}^{(0)}) + \sum_{i=1}^n \frac{\partial f_k(\vec{x})}{\partial x_i} \Big|_{\vec{x}=\vec{x}^{(0)}} \vec{\delta}_i \quad (5)$$

It is abbreviated as

$$f(\vec{x}^{(0)} + \vec{\delta}) = f(\vec{x}^{(0)}) + p\vec{\delta} \quad (6)$$

where  $p$  is called the Jacobian matrix.

$$p_{m \times n} = \begin{pmatrix} \frac{\partial f_1}{\partial x_1} & \dots & \frac{\partial f_1}{\partial x_n} \\ \vdots & \ddots & \vdots \\ \frac{\partial f_m}{\partial x_1} & \dots & \frac{\partial f_m}{\partial x_n} \end{pmatrix} \quad (7)$$

The linear approximate expression of the function after substituting Equation (6) into Equation (4) is as follows:

$$\begin{aligned} \varphi(\vec{x}^{(0)} + \vec{\delta}) &= [\vec{y} - \vec{f}(\vec{x}^{(0)}) - p\vec{\delta}]^T [\vec{y} - \vec{f}(\vec{x}^{(0)}) - p\vec{\delta}] \\ &= [\vec{y} - \vec{f}(\vec{x}^{(0)})]^T [\vec{y} - \vec{f}(\vec{x}^{(0)})] \\ &\quad - 2[\vec{y} - \vec{f}(\vec{x}^{(0)})]^T p\vec{\delta} + \vec{\delta}^T p^T p\vec{\delta} \end{aligned} \quad (8)$$

The purpose of this equation is to solve the minima of the function  $\varphi$ ; thus,  $\vec{\delta}$  should satisfy the following conditions:

$$\frac{\partial \varphi}{\partial \vec{\delta}} = -2P^T [\vec{y} - \vec{f}(\vec{x}^{(0)})] + 2P^T P\vec{\delta} = 0 \quad (9)$$

wherein,

$$A\vec{\delta} = \vec{g} \quad (10)$$

in the formula:

$$A = P^T P \quad (11)$$

$$\vec{g} = P^T [\vec{y} - \vec{f}(\vec{x}^{(0)})] \quad (12)$$

Therefore,

$$\vec{\delta} = A^{-1}\vec{g} \quad (13)$$

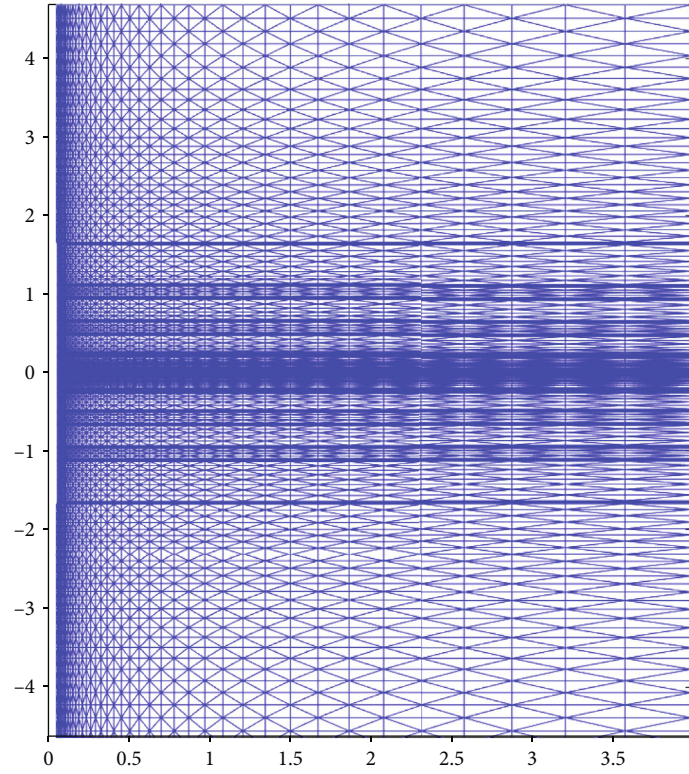


FIGURE 2: 2D grid of the stratigraphic model.

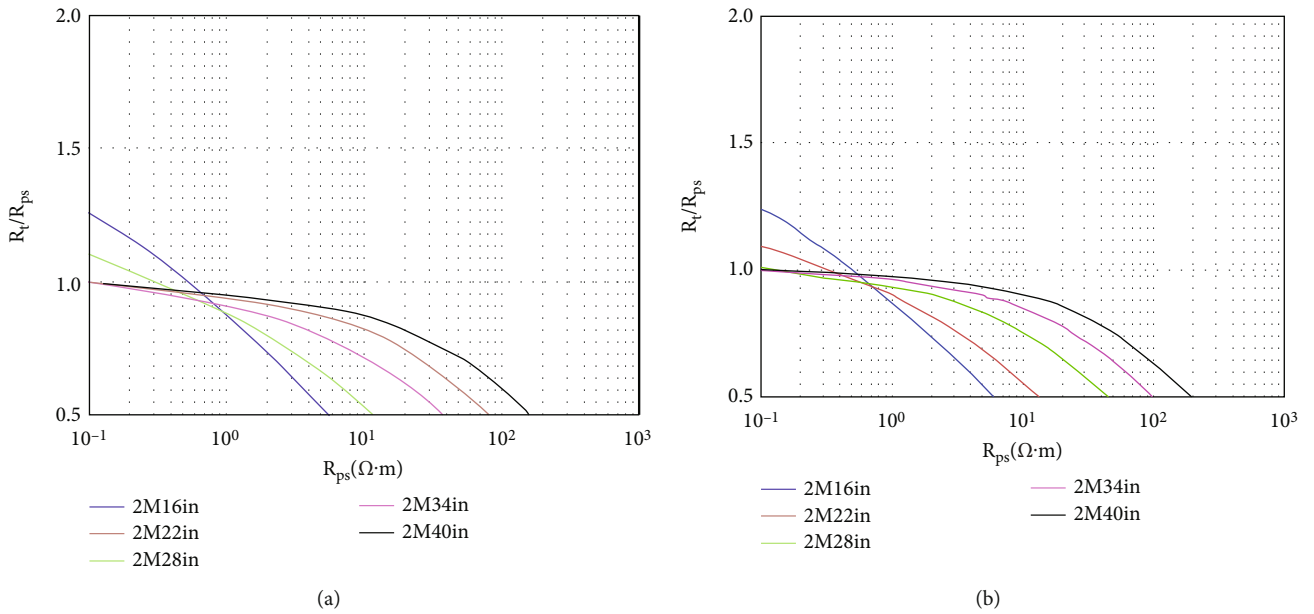


FIGURE 3: (a) Charts of ARC675 (2 MHz, dh = 14 in, Rm = 0.02 Ω · m) in the references. (b) Charts of ARC675 (2 MHz, dh = 14 in, Rm = 0.02 Ω · m) in this paper.

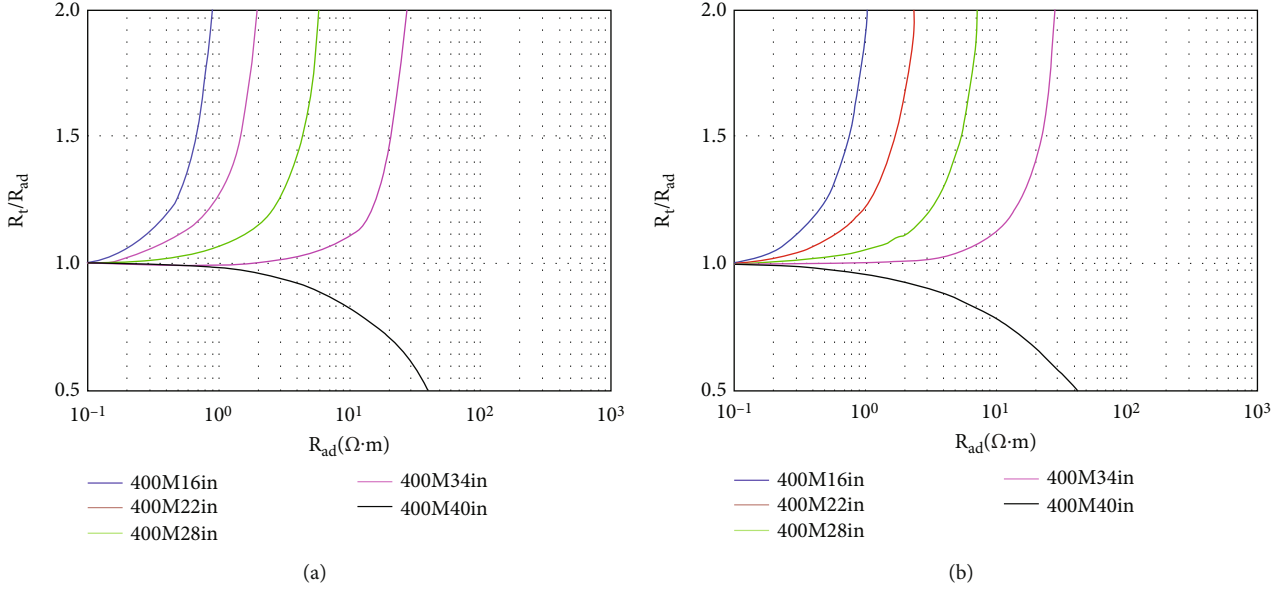


FIGURE 4: (a) Charts of ARC675 (400 kHz, dh = 14 in, Rm = 0.02 Ω · m) in the references. (b) Charts of ARC675 (400 kHz, dh = 14 in, Rm = 0.02 Ω · m) in this paper.

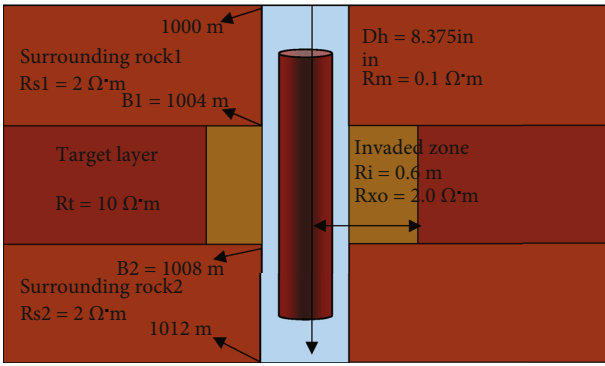


FIGURE 5: Schematic diagram of the time-lapse resistivity joint inversion formation model.

To prevent the appearance of the local optimal solution and improve the convergence of the solution, we introduced a damping factor  $\eta$ , and Equation (13) is transformed into

$$\vec{\delta} = (A + \eta I)^{-1} \vec{g} \quad (14)$$

where  $I$  is the identity matrix.

In practical problems, when the observed value is given, the appropriate model and initial values are selected;  $P$ ,  $A$ ,  $\vec{g}$ , and  $\vec{\delta}^{(0)}$  can be obtained.

$$\vec{x}^{(1)} = \vec{x}^{(0)} + \vec{\delta}^{(0)} \quad (15)$$

Subsequently,  $\vec{x}^{(1)}$  is considered the initial value, and the calculation is repeated to find  $\vec{\delta}^{(1)}$  until the absolute value

$\sum |\vec{\delta}^{(k)}|$  of component of  $\vec{\delta}^{(k)}$  is less than the error  $\epsilon$  given in advance.

**2.3. Joint Inversion Convergence and Confidence.** A three-layer stratigraphic model (Figure 5) was used to examine the convergence and confidence of the joint inversion. The stratigraphic model is rotationally symmetric about the well axis and is uniform. The model parameters are set as follows: The formation thickness is 4.0 m, the formation interface values are 1004.0 and 1008.0 m, the borehole diameter is  $Dh = 8.375$  in, the mud resistivity is  $Rm = 0.1 \Omega \cdot m$ , the upper and lower surrounding rock formation resistivity values are  $Rs1 = Rs2 = 2.0 \Omega \cdot m$ , the radius of the invasion zone while drilling in the target layer is  $Ri = 0.6$  m, the resistivity of the invasion zone while drilling is  $Rxo = 2.0 \Omega \cdot m$ , and the formation resistivity is  $Rt = 10.0 \Omega \cdot m$ . The sampling point range and sampling interval are 1000.0 to 1012.0 m and 0.2 m, respectively; a total of 61 points were used.

The resistivity joint inversion of the model was conducted according to the above model parameter settings, and the results are shown in Figure 6. The first trace in the figure is the invasion depth trace, and the blue dotted line is the inversion result of the model invasion radius. The third trace is the resistivity trace, and the red dotted line is the model formation true resistivity inversion result. The green dotted line in the  $RXOL$  curve is the model inversion of intrusive zone resistivity. The remaining curves show the phase difference and attenuation resistivity results obtained by inversion.

We analyzed the errors of the invasion radius, invasion zone resistivity, and true formation resistivity obtained by model inversion. As presented in Table 1, the relative errors of the three parameters were within 1.5%, and the inversion

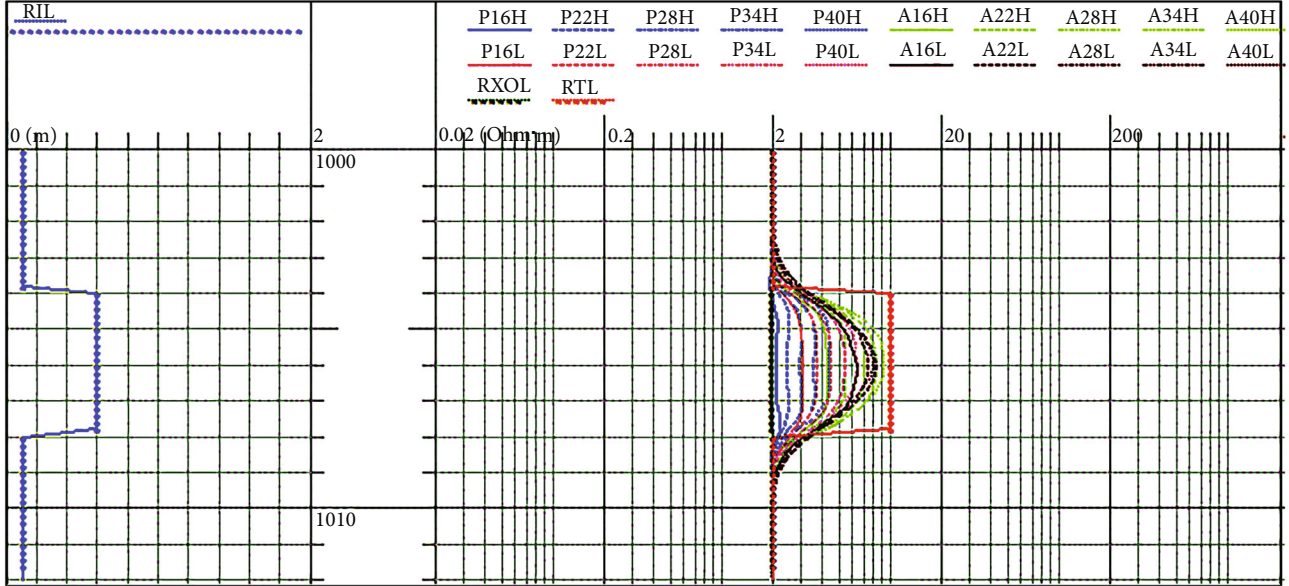


FIGURE 6: Inversion results.

TABLE 1: Evaluation of the inversion results.

Parameter	True value	Inversion initial value	Inversion results	Error
RT ( $\Omega \cdot m$ )	10	13	9.92	0.83%
Rxo ( $\Omega \cdot m$ )	2	2.5	1.97	1.31%
RiL (m)	0.6	0.48	0.59	0.85%

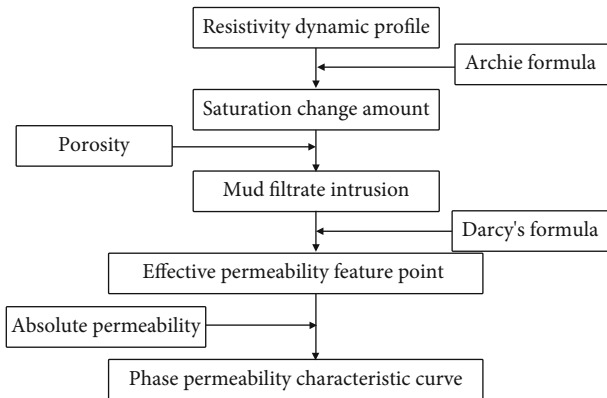


FIGURE 7: Flow chart of the construction of the phase permeability characteristic curve.

exhibited good convergence. This result converges to the true value.

### 3. Construction Method of the Characteristic Permeability Curve

The time-lapse resistivity joint inversion considers the logging time factor; therefore, the inversion obtains the

dynamic resistivity profile of the reservoir. The change in the dynamic profile of the reservoir was mainly caused by the invasion of mud filtrate into the formation to replace the movable oil and gas in it with the passage of logging time. The change in the formation resistivity reflects the change in the formation fluid saturation, and the change in saturation reflects the intrusion of the mud filtrate. The intrusion amount of mud filtrate per unit time is related to the permeability of each phase fluid; therefore, the effective permeability of the reservoir can be obtained by further analysis based on the dynamic resistivity profile of the joint inversion.

Figure 7 shows the basic flow chart of the effective permeability construction. First, based on the dynamic resistivity profile of the reservoir, the resistivity is converted into saturation parameters using Archie's formula, including the water saturation in the invasion zone and that in the original formation. The saturation change amount  $\Delta S_{wx}$  of the intrusion zone at the intrusion depth is as follows:

$$\Delta S_{wx} = \sqrt[n]{\frac{a * R_{mf}}{\phi^m * R_{xo}}} - \sqrt[n]{\frac{a * R_w}{\phi^m * R_t}}, \quad (16)$$

Assuming that the porosity of the reservoir remains unchanged during mud invasion, the change in volume of the fluid water in the rock can be obtained by combining the definitions of porosity and saturation (Equation (19)). Combined with the specific logging time (i.e., the drilling fluid soaking time), the flow formula (Equation (20)) can be calculated, namely, the invasion amount of the mud filtrate per unit time (q):

$$S_w = \frac{V_w}{V_p}, \quad (17)$$

$$\varnothing = \frac{V_p}{V_b}, \quad (18)$$

$$V_w = \Delta S_{wx} * \varnothing * V_b, \quad (19)$$

$$q = \frac{\Delta S_{wx} * \varnothing * \pi * R_i^2 * H}{\Delta T}, \quad (20)$$

where  $\varnothing$  is the formation porosity,  $V_b$  is the rock volume of the reservoir,  $\Delta T$  is the logging interval,  $\Delta S_{w_{x-x}}$  is the change in water saturation,  $R_i$  is the drilling fluid invasion depth at the  $\Delta T$  interval, and  $H$  is the reservoir thickness.

By combining the initial pressure of the formation and the pressure difference of the drilling string, the permeability of the water phase can be deduced by substituting Equation (20) into Darcy's formula (21). As we considered the real logging environment when calculating the saturation change, namely, the simultaneous existence of multiphase fluids (water, oil, or gas) in the rock, the calculated permeability at this time is the effective permeability of the water phase.

$$q = \frac{K * \Delta P * A_c}{\mu * \Delta L}, \quad (21)$$

$$K_{ew} = \frac{\Delta S_{wx} * \varnothing * \pi * R_i^2 * H * \mu_w * R_h}{2\pi * R_h * H * (P_m - P_w) * \Delta T} = \frac{\Delta S_{wx} * \varnothing * R_i^3 * \mu_w}{2 * R_h * (P_m - P_w) * \Delta T}, \quad (22)$$

where  $K_{ew}$  is the effective permeability of the water phase,  $R_h$  denotes the wellbore radius,  $\mu_w$  denotes the viscosity of water,  $P_m$  denotes the pressure of the drilling string, and  $P_w$  denotes the initial pressure of the undisturbed formation.

Assuming that there are only two-phase fluids in the reservoir, and that they are incompatible and incompressible, because the total reservoir fluid saturation remains unchanged, the amount of change in water saturation in the invasion zone and that in oil and gas saturation remains the same. In a complementary relationship, the intrusion of mud filtrate in the reservoir is equal to the displacement of oil and gas, and the effective permeability of oil and gas can be obtained similarly. The relative permeability of each fluid phase can be obtained by calculating the ratio of the effective permeability to the absolute permeability.

$$K_{rw} = \frac{K_{ew}}{K}, \quad (23)$$

$$K_{rnw} = \frac{K_{enw}}{K}, \quad (24)$$

The effective permeability calculated above was constructed based on the dynamic resistivity profile of the reservoir, and the dynamic resistivity profile of the reservoir was obtained based on the time-lapse resistivity curve using the joint inversion technique. Therefore, the constructed phase-permeability curve is a discrete characteristic phase permeability curve. It is necessary to obtain a continuous functional relationship between saturation and relative permeability using data fitting technology. The basic functional

relationship between saturation and relative permeability is modified by the Brooks-Corey model as follows:

$$K_{rw} = K_{rw0} * (S_{we})^{ew}, \quad (25)$$

$$K_{rnw} = K_{rnw0} * (1 - S_{we})^{enw}, \quad (26)$$

Among them,  $K_{rw0}$ ,  $K_{rnw0}$ ,  $ew$ , and  $enw$  represent the undetermined coefficients to be solved;  $K_{rw0}$  and  $K_{rnw0}$  represent the relative permeability endpoint values of the aqueous and non-aqueous phases;  $ew$  and  $enw$  represent the exponential coefficients; and  $S_{we}$  represents the effective saturation, which is defined as:

$$S_{we} = \frac{S_w - S_{wi}}{1 - S_{wi} - S_{gr}}, \quad (27)$$

where  $S_{wi}$  is the irreducible water saturation and  $S_{gr}$  is the residual oil and gas saturation.

#### 4. Oilfield Application Examples

Well xx adopted a drill bit diameter of 8.375 in; the drilling fluid type was PDF-THERM; the mud resistivity was 0.23 at 23.89 °C; the mud filtrate resistivity is 0.09 at 27.2 °C; and the reservoir lithology was gray mudstone and siltstone. Schlumberger's EcoScope was the electromagnetic wave resistivity instrument used while drilling, including two time-lapse resistivity measurement datasets of real-time measurement during the drilling and upward remeasurement. The reservoir porosity was 14-19%, and the permeability was 5-62 mD. The resistivity curves of different probing depths measured in real time during drilling were separated to some extent, indicating that a certain amount of drilling fluid invaded the formation. Compared with those measured in real time, the resistivity curves of different probing depths remeasured, while drilling exhibited a greater decrease in resistivity. This shows that the drilling fluid invaded deeper and the change in resistivity corresponded well with the permeability of the reservoir, as shown in Figure 8.

*4.1. Reservoir Dynamic Resistivity Profile Inversion.* Figure 9 shows the combined inversion results of the main and remeasured resistivity logging in a well, including the invasion depth and invasion zone resistivity measured in real time during drilling, invasion depth and invasion zone resistivity of remeasurement while drilling, and true resistivity of the formation. The first trace in the figure represents the invasion depth trace, including the gamma curve and the inversion depth of the mud invasion at different times. *LXO\_T1\_INV* represents the mud invasion depth of joint inversion measured in real time, and *LXO\_T2\_INV* represents the remeasured mud invasion depth of the joint inversion. The third and fourth traces show a comparison of the phase difference and amplitude-specific resistivity curves measured in real time, along with the joint inversion results of the resistivity of the invasion zone and true resistivity of the formation, respectively. Traces 5 and 6 show the

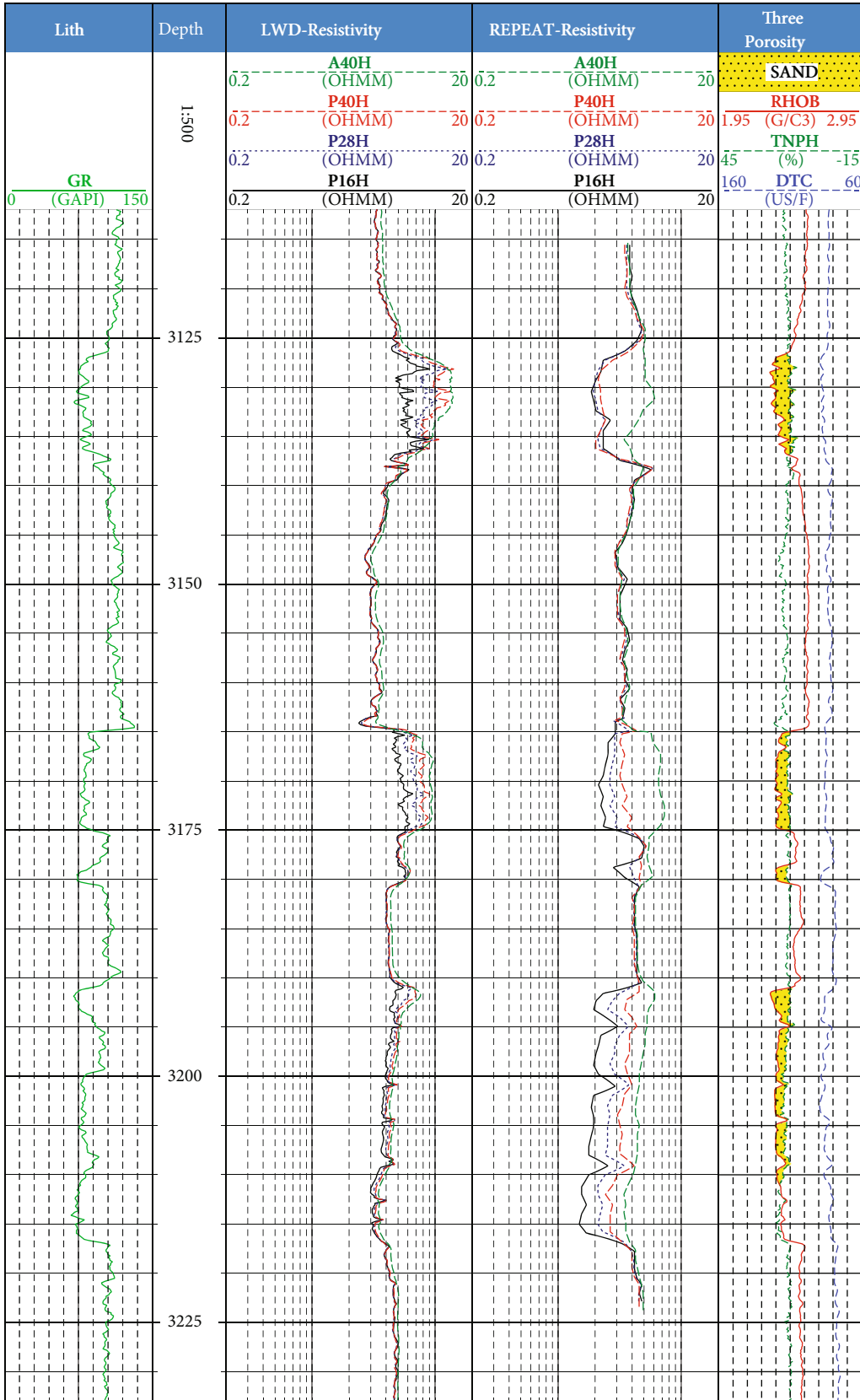


FIGURE 8: Electromagnetic wave resistivity measurement curve of well xx during the drilling and re-measurement.

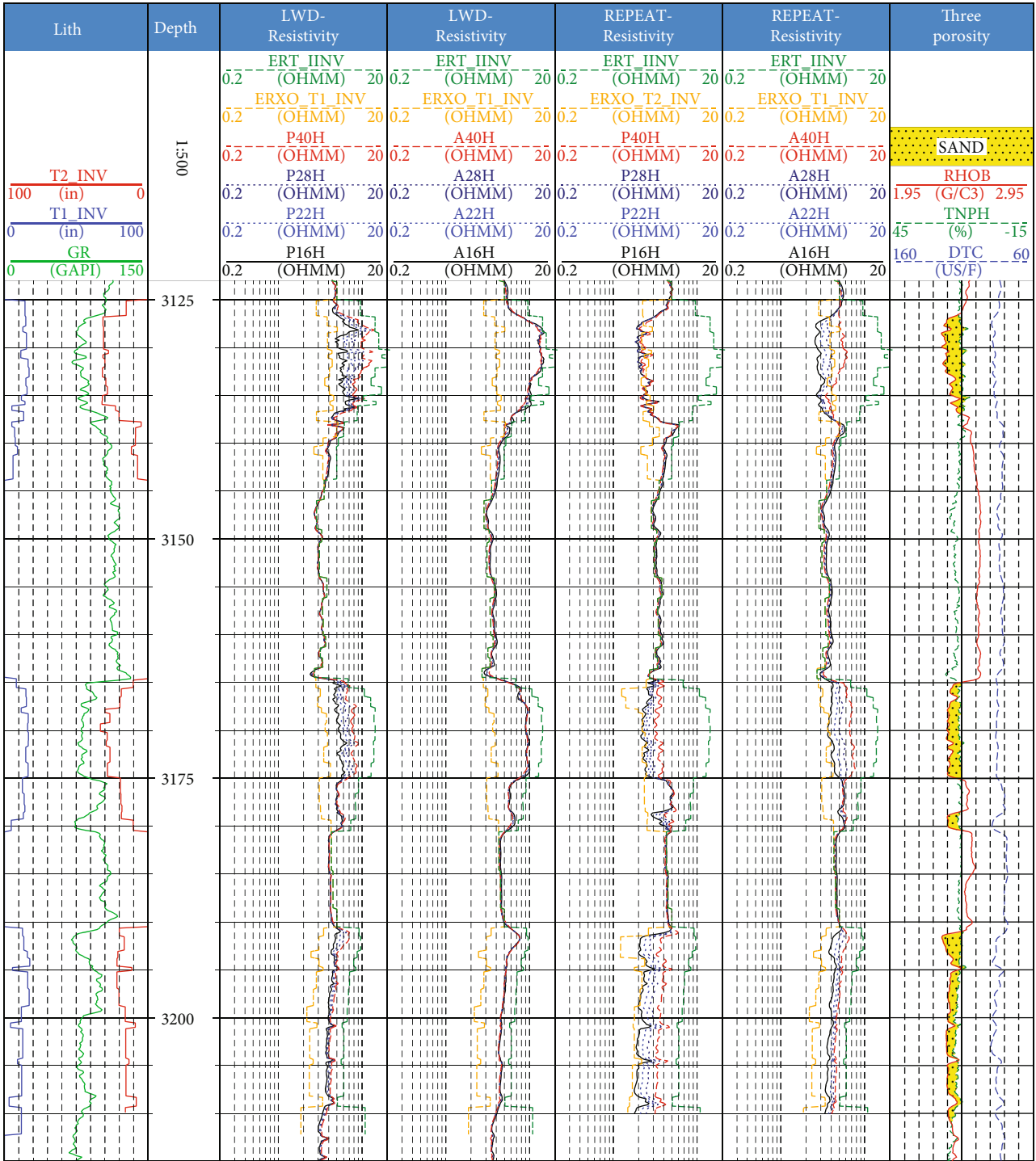


FIGURE 9: Results of joint inversion of electromagnetic wave resistivity while drilling in well xx at different times.

comparison of the phase difference and amplitude-specific resistivity curves obtained by the remeasurement using the combined inversion results of the resistivity of the invasion zone and true resistivity of the formation, respectively. *ERXO\_T1\_INV* represents the intrusion zone resistivity of joint inversion measured in real time, *ERXO\_T2\_INV* represents the remeasured intrusion zone resistivity of the joint inversion, and *ERT\_IINV* represents the true resistivity of

joint inversion. The seventh trace represents the neutron density porosity curve. The above joint inversion results showed that the inversion depth curve has a good corresponding relationship with the *GR* lithology curve, as well as with the neutron density curve. The remeasured mud filtrate of the combined inversion of the reservoir with large porosity and good permeability has a greater invasion depth, which demonstrates the rationality of the inversion results.

TABLE 2: Physical parameters and joint inversion results of the target interval.

Layer number	Top depth m	Bottom depth m	Porosity %	Permeability mD	LXO_T1 In	LXO_T2 In	Rxo_T1 $\Omega.m$	Rxo_T2 $\Omega.m$	Rt $\Omega.m$
1	3126.8	3133.0	16.79	19.02	14.87	30.79	4.1	2.4	17.10
2	3133.0	3137.0	14.62	4.99	13.04	28.13	4.0	2.5	12.76
4	3165.1	3166.4	15.44	8.25	12.43	15.48	3.0	1.7	9.28
5	3166.7	3175.2	16.33	14.63	15.56	26.98	3.6	2.2	13.45
6	3178.6	3180.6	16.28	20.39	7.45	12.49	3.9	2.7	7.55
7	3191.0	3192.6	17.23	37.11	13.23	17.61	3.2	1.6	9.48
8	3192.6	3194.5	16.69	20.00	16.03	20.21	2.8	1.7	8.63
10	3195.1	3200.6	16.76	20.39	14.87	19.04	2.6	2.0	6.84
12	3201.2	3204.0	18.74	61.73	12.76	15.51	2.4	1.8	6.06
14	3204.8	3208.1	18.10	41.60	11.88	15.25	2.4	1.7	6.03

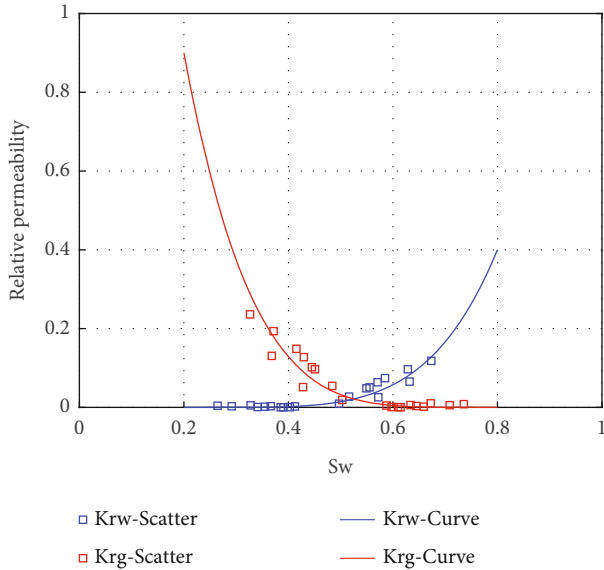


FIGURE 10: Characteristic scattered permeability curve diagram.

**4.2. Determination of Permeability Characteristic Scattering Points and Construction of Permeability Curve.** The dynamic resistivity profile of the reservoir is based on the “layer-to-layer” joint inversion, which expresses the variation law of the electrical profile of the reservoir after drilling-fluid invasion at different times. Therefore, the obtained permeability is the characteristic point of the effective permeability in the near-wellbore zone after drilling fluid invasion at a certain time. Assuming that the porosity of the reservoir remains unchanged during the process of mud filtrate invasion, the pressure difference between the pressure of the drilling fluid column and that of the original formation is experienced on both sides of the formation invasion zone, and the resistivity and saturation are converted using Archie’s equation. The cementation index and porosity index adopt regional empirical values such as  $m = 1.6$  and  $n = 1.8$ ; the coefficient  $a = 0.23$ ; the formation water resistivity ( $R_w$ ), mud filtrate resistivity ( $R_{mf}$ ), and viscosity of formation water are  $0.21 \Omega.m$ ,  $0.09 \Omega.m$ , and  $1.01 \times 10^{-6} \text{ m}^2/s$ , respectively; and the gas

viscosity under formation conditions is  $2.75 \times 10^{-6} \text{ m}^2/s$ . Table 2 lists the average values of the resistivity, invasion depth, porosity, permeability, and other curves of each target feature layer.

Combined with the above reservoir physical parameters and joint inversion results, Equations (16), (22), (23), and (24) can be used to obtain the characteristic phase dispersion point of the target interval; and a characteristic scatter point phase permeability curve relationship diagram is obtained (Figure 10). Based on the data shown in Figure 10, the functional relationship between the water saturation and the relative permeability of each fluid phase can be obtained by fitting Equations (28) and (29).

The fitting function relationship between the formation water saturation and relative permeability of water is

$$K_{rw} = 0.4 * (S_{we})^{4.8}. \quad (28)$$

The fitting function relationship between the formation water saturation and relative permeability of gas is

$$K_{rg} = 0.9 * (1 - S_{we})^{4.8}, \quad (29)$$

where  $S_{we}$  represents the effective saturation, which is defined as

$$S_{we} = \frac{S_w - S_{wi}}{1 - S_{wi} - S_{gr}}, \quad (30)$$

where  $S_{wi}$  represents the irreducible water saturation and  $S_{gr}$  represents the residual gas saturation. During actual data processing, the  $S_{wi}$  and  $S_{gr}$  values need to be selected in combination with the core analysis results. We conducted a comprehensive analysis of the core NMR and high-temperature and high-pressure gas-water permeability experimental results of the actual application case wells to obtain the irreducible water saturation of the treated well section;  $S_{gr}$  and  $S_{wi}$  are both 0.2.

**4.3. Effective Penetration Rate and Its Damage Analysis.** Based on the aforementioned relationship curve of

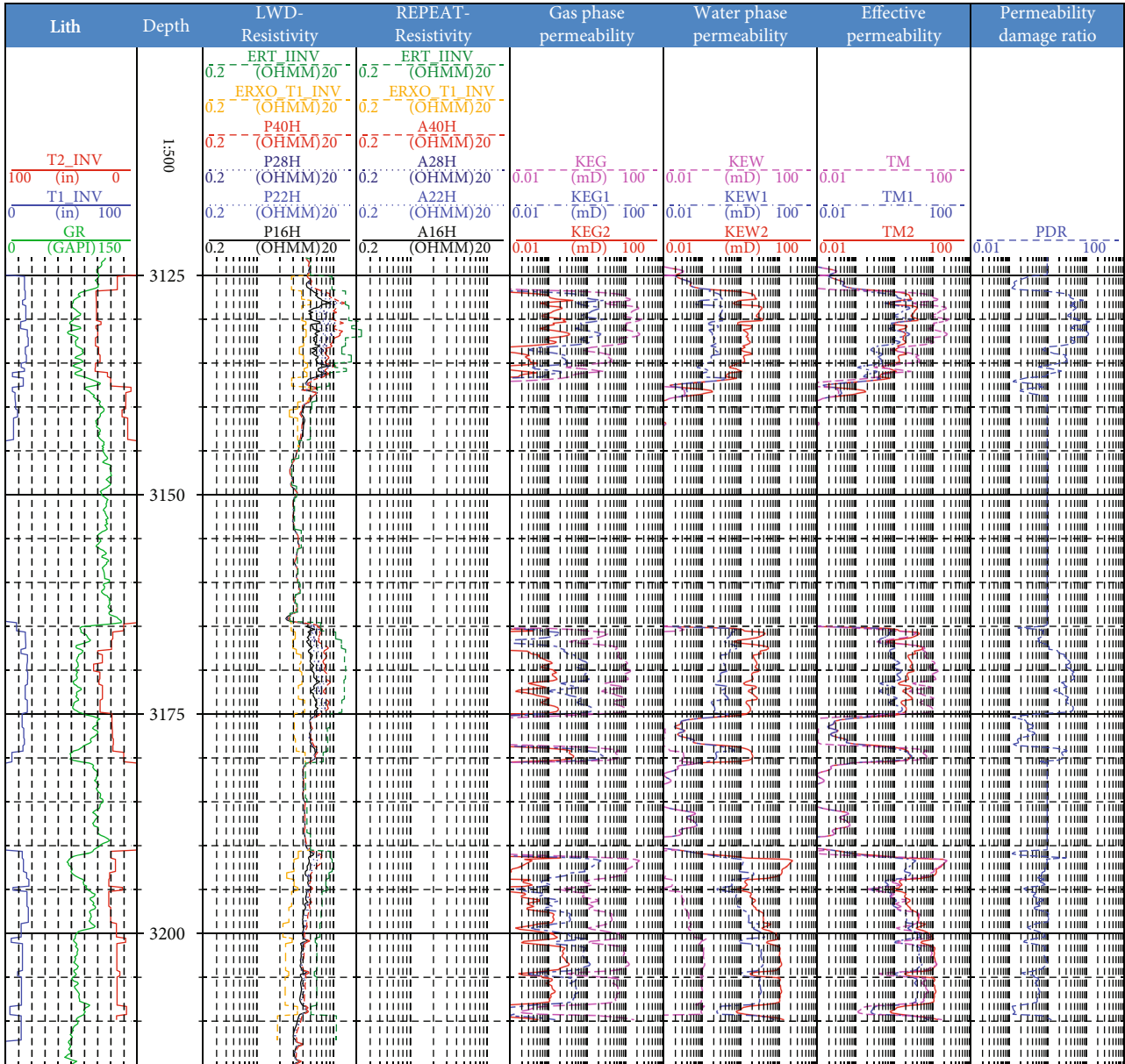


FIGURE 11: Effective permeability and permeability damage results of well xx.

saturation and relative permeability, combined with the dynamic resistivity profile of the reservoir inversion and the logging permeability, a continuous effective permeability curve can be obtained; this includes the original formation (before drilling fluid invasion) and the effective permeability of the gas and water phases at time 1 of real-time logging (drilling fluid immersion for 1 h) and time 2 of re-logging (drilling fluid immersion for 3 h). KEG and KEW in Figure 11 represent the effective permeability curves of the gas and water phases of the undisturbed formation, respectively; KEG1 and KEW1 represent the effective permeability curves of the gas and water phases at time 1 of real-time logging; KEG2 and KEW2 represent the effective permeability curves of the gas and water phases at time 2 of re-logging; TM, TM1, and TM2 represent the comprehensive fluid effective permeability curve of the original formation, real-time

logging time 1, and re-logging time 2, respectively, namely, the fluid flow capacity. PDR represents the permeability damage ratio of the reservoir, which is defined both in the original formation and during the re-logging measurement; comprehensive permeability ratio and PDR values less than 1 in a well at time 2 indicate that the reservoir has been benignly improved; a PDR value equal to 1 indicates that the reservoir is free of pollution; and PDR values greater than 1 and larger indicate a strong pollution degree of the reservoir. The third trace is the electromagnetic wave resistivity curve during drilling and the joint inversion result at time 1 of real-time logging; the fourth trace is the electromagnetic wave resistivity curve during drilling and the joint inversion result at time 2 of re-logging; the fifth trace shows the effective permeability of the gas phase at different times in the near-wellbore zone; the sixth trace represents the

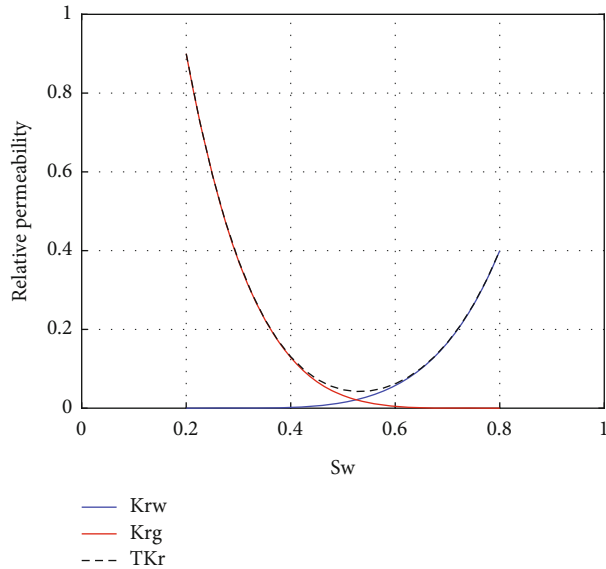


FIGURE 12: Permeability curve of each phase fluid and comprehensive phase permeability curve.

water phase effective permeability in the near-wellbore zone at different times; the seventh trace represents the comprehensive fluid mobility capacity of the near-wellbore zone at different times; and the eighth trace represents the coefficient of the reservoir PDR.

From the above calculation results, we observed that the gas layer sections (3126-3137 m and 3165-3175 m) are affected by the drilling fluid invasion; only the effective permeability of the gas phase of the well zone gradually decreases and that of the water phase gradually increases. The effective permeability of the water phase near the wellbore was almost zero before drilling fluid invasion, indicating that the saturated water in the formation was irreducible. In the gas-water interval (3200-3208 m) affected by the drilling fluid invasion, the variable law of the effective permeability of the gas and water phases in the near-wellbore zone is consistent with that of the pure gas interval; however, the variation amplitude is smaller than that of the pure gas interval. The effective permeability of the gas and water phases in the near-wellbore zone before the drilling fluid invasion in the same interval of gas and water is not zero, indicating that it contains both movable water and gas. The permeability and PDR curve shows that the 3126-3137 m interval of the gas reservoir is seriously polluted, the 3165-3175 m interval is slightly polluted, and the 3200-3208 m interval of the gas-water reservoir is slightly improved. From the comprehensive permeability curve of the reservoir fluid, the effective permeability of the reservoir before and after drilling fluid invasion in the pure gas interval decreases, while that of the reservoir in the same gas and water interval increases. In particular, as the water saturation of the reservoir increases, the variation law of the integrated fluid in the reservoir shows that the permeability decreases first and increases subsequently (TKr curve in Figure 12).

## 5. Conclusions

- (1) The time-lapse resistivity logging data and reservoir dynamic and static permeability have multi-angle correlations. The characteristic phase permeability curve calculation model can be derived using Darcy's formula, the resistivity dynamic invasion profile, and the water saturation model. By combining the regional interpretation model, we realized an effective permeability evaluation of reservoirs based on time-lapse resistivity logging. The calculation results are more representative than the effective permeability parameters obtained by conventional core analysis and more accurately reflect the seepage characteristics of the reservoir
- (2) By comprehensively analyzing the dynamic resistivity profile of the reservoir, and combined with the calculated effective permeability parameters of the reservoir before and after drilling fluid invasion, we obtained the permeability damage ratio of the reservoir. This ratio can provide guidance for evaluating reservoir pollution and testing the formation
- (3) This study did not consider the differences in the relative permeability curves of different reservoirs when calculating the effective permeability. To improve the accuracy of the effective permeability calculation results, it is necessary to analyze the variation law of the characteristic relative permeability curves of the reservoirs in the study area and select the appropriate relative permeability according to the reservoir-type and curve parameters

## Data Availability

The well data used to support the findings of this study are available from the corresponding author upon request.

## Conflicts of Interest

The authors declare that they have no conflicts of interest.

## References

- [1] D. Yang, H. R. Zhang, Y. X. Wu, H. R. Zhang, and W. Tan, "Application of cable formation test data in productivity prediction of low permeability gas reservoirs," *China Offshore Oil and Gas*, vol. 30, no. 6, pp. 109-114, 2019.
- [2] P. C. Dong, Z. W. Ma, and C. S. Zhao, "Evaluating method of relative permeabilities of a reservoir," *Petroleum Geology & oil-field Development in Daqing*, vol. 27, no. 6, pp. 55-58, 2008.
- [3] L. Jaedong and M. John, "Enhance wireline formation tests in low-permeability formations quality control through formation rate analysis," *Rocky Mountain Regional/Low-Permeability Reservoirs Symposium and Exhibition*, 2000.
- [4] H. Liu, W. H. Wang, M. G. Chen, Q. G. Liu, and X. H. Hu, "Seepage experiment and mathematical model of multi-scale shale reservoir," *Journal of Xi'an Shiyou University (Natural Science Edition)*, vol. 33, no. 4, pp. 66-71, 2018.

- [5] S. S. Gao, W. Xiong, and X. G. Liu, "Experimental research status and several novel understandings on gas percolation mechanism in low permeability sandstone gas reservoirs," *Natural Gas Industry*, vol. 30, no. 1, pp. 52–55, 2010.
- [6] H. Lei, Y. H. Zheng, J. H. He, and Z. G. Hu, "A new method for physical simulation of flow characteristics of fluids in shale oil reservoirs," *Acta Petrolei Sinica*, vol. 42, no. 10, pp. 1346–1356, 2021.
- [7] F. R. Wang, S. He, and Y. H. Zheng, "Mineral composition and brittleness characteristics of the inter-salt shale oil reservoirs in the Qianjiang Formation," *Petroleum Geology & Experiment*, vol. 38, no. 2, pp. 211–218, 2016.
- [8] C. N. Zou, Z. Yang, and J. W. Cui, "Formation mechanism geological characteristics and development strategy of non-marine shale oil in China," *Petroleum Exploration and Development*, vol. 40, no. 1, pp. 15–27, 2013.
- [9] Y. L. Su, H. Wang, S. Y. Zhan, W. D. Wang, and J. L. Xu, "Research progress on characterization and simulation of shale oil flow in microscale," *Journal of Shenzhen University (Science and Engineering)*, vol. 38, no. 6, pp. 579–589, 2021.
- [10] L. C. Kuang, L. H. Hou, and Z. Yang, "Key parameters and methods of lacustrine shale oil reservoir characterization," *Acta Petrolia Sinica*, vol. 41, no. 1, 2021.
- [11] F. Javadpour, H. Singh, A. Rabbani, M. Babaei, and S. Enayati, "Gas flow models of shale: a review," *Energy & Fuels*, vol. 35, no. 4, pp. 2999–3010, 2021.
- [12] T. Zhang, X. F. Li, Y. Yin et al., "The transport behaviors of oil in nanopores and nanoporous media of shale," *Fuel*, vol. 242, no. 12, pp. 305–315, 2019.
- [13] A. Oblger, J. Ulmf, and R. Pellenq, "Impact of nano-porosity on hydrocarbon transporting shales' organic matter," *Nano Letters*, vol. 18, no. 2, pp. 832–837, 2018.
- [14] D. P. Tobola and S. A. Holditch, "Determination of reservoir permeability from repeated induction logging," *SPE Formation Evaluation*, vol. 6, no. 1, pp. 20–26, 1991.
- [15] C. Y. Yao and S. A. Holditch, "Reservoir permeability estimation from time-lapse log data," *SPE25513*, 1993.
- [16] M. Jesús, "Estimation of permeability from borehole array induction measurements: application to the petrophysical appraisal of tight gas sands," *PETROPHYSICS*, vol. 47, no. 6, pp. 527–544, 2006.
- [17] M. Jesús, "Automatic estimation of permeability from array induction measurements: applications to field data," in *SPWLA 46th Annual Logging Symposium*, New Orleans, Louisiana, USA, 2005.
- [18] S. J. Li and L. C. Shen, "Dynamic invasion profiles and time-lapse electrical logs," in *SPWLA 44th Annual Logging Symposium*, Galveston, Texas, USA, 2003.
- [19] L. Lin and S. H. Wang, "Estimating in-situ relative permeability and capillary pressure from multiphysics wireline measurements," in *SPWLA 59th Annual Logging Symposium*, Old Billingsgate, London, UK, 2018.
- [20] N. David and S. J. Li, "Invasion effects on time-lapsed array induction logs," in *SPWLA 48th Annual Logging Symposium*, Austin, Texas, USA, 2007.
- [21] J. S. Chen and A. Dicman, "Physics-based permeability modeling," in *SPWLA 52th Annual Logging Symposium*, Colorado Springs, Colorado, 2011.
- [22] D. G. Wu, J. Chen, and C. R. Liu, "An efficient FDTD method for axially symmetric LWD environments," *IEEE*, vol. 46, no. 6, pp. 1652–1656, 2008.
- [23] S. Alireza, T. Michael, and A. Lori, "Carbonate formation evaluation using joint inversion of resistivity and dielectric logs," in *SPWLA 58th Annual Logging Symposium*, Oklahoma City, Oklahoma, USA, 2017.

## Research Article

# Estimation of Water Saturation in Shale Formation Using In Situ Multifrequency Dielectric Permittivity

Yongchae Cho <sup>1</sup>, Sean S. Dolan,<sup>2,3</sup> Nishank Saxena,<sup>1</sup> and Vishal Das<sup>4</sup>

<sup>1</sup>Shell International Exploration and Production Inc., 150 N Dairy Ashford Road, Houston, TX 77079, USA

<sup>2</sup>Shell International Exploration and Production Inc., 3333 S Texas 6, Houston, TX 77082, USA

<sup>3</sup>Sakhalin Energy Investment Company, Russia

<sup>4</sup>Amazon Web Services Inc., 825 Town and Country Lane, Houston, TX 77024, USA

Correspondence should be addressed to Yongchae Cho; [yongchae.cho@shell.com](mailto:yongchae.cho@shell.com)

Received 6 December 2021; Revised 17 February 2022; Accepted 21 February 2022; Published 11 March 2022

Academic Editor: Mehdi Ostadhassan

Copyright © 2022 Yongchae Cho et al. This is an open access article distributed under the Creative Commons Attribution License, which permits unrestricted use, distribution, and reproduction in any medium, provided the original work is properly cited.

Estimating water saturation via conventional logging tool such as resistivity cannot provide an accurate solution in a formation with low conductivity water and tight porosity. As an alternative, we employed a dielectric permittivity, which makes it easy to differentiate the water from the other fluids in pore structures. A multichannel frequency dielectric logging tool is used for measuring in situ permittivity. To simulate a dielectric permittivity, we used two analytic models: Lichtenecker-Rother (LR) and Stroud-Milton-De (SMD) models. The key goal of this research is to propose a workflow to evaluate an equivalent Archie's parameter which can generate the same dielectric logging tool responses with core measurement results using a given analytic models. According to the results of the LR model curve-fitting, the estimated Archie's parameter shows inversely proportional relationship with clay volumes. The estimated Archie's parameter from the SMD model is sensitive to the lower frequency channels of the multifrequency dielectric logging tool. Nevertheless, utilizing the response of the dielectric logging tool in the frequency range, where interfacial polarization effect does not exist, can provide an alternative to estimate water saturation in shale formations with relatively less conductive waters.

## 1. Introduction

Accurate calculation of water saturation in a target formation is crucial for estimating the potential volume of hydrocarbon. Also, estimating the volume of water is a key factor in building a concrete plan for hydrocarbon exploration. A standard approach of estimating water saturation is using Archie's equation with deep resistivity logging tools. When we apply the Archie's equation for calculating water saturation, the cementation factor and tortuosity factor are measured in core samples that require numerous representative core samples of the formation. In addition, this measurement is not rigorous when dealing with tight formations that have a small pore volume. Also, when the matrix mineral components and pore structures are complex, the conventional Archie's law based method cannot provide reliable fluid estimation results [1] since it assumes pure sandstone. Especially, Archie's equation cannot handle the core samples

with tight pore structures such as shale. Hence, many scientists have studied variety types of analytic models to explain the gaps between well logs and core data to estimate accurate total organic contents (TOC) and water saturation [2, 3].

For a common reservoir, geoscientists can convert the resistivity and conductivity information acquired by well logging to fluid saturation based on the given saturation model. Another limitation of the conventional method for calculating water saturation is that the resistivity logging tool cannot differentiate water from hydrocarbon when the water is less conductive (or lower salinity). This issue becomes more problematic when we work on unconventional reservoir due to clay bound water (Cho et al. [4, 5], Kadkhodaie and Rezaee [6], Sotelo et al. [7], and Tathed et al. [8]). As an alternative, for last decade, the measurement of dielectric permittivity has been gaining attention in the oil and gas industry. Most current logging techniques are not sensitive to the permittivity of formations, except for logging-while-

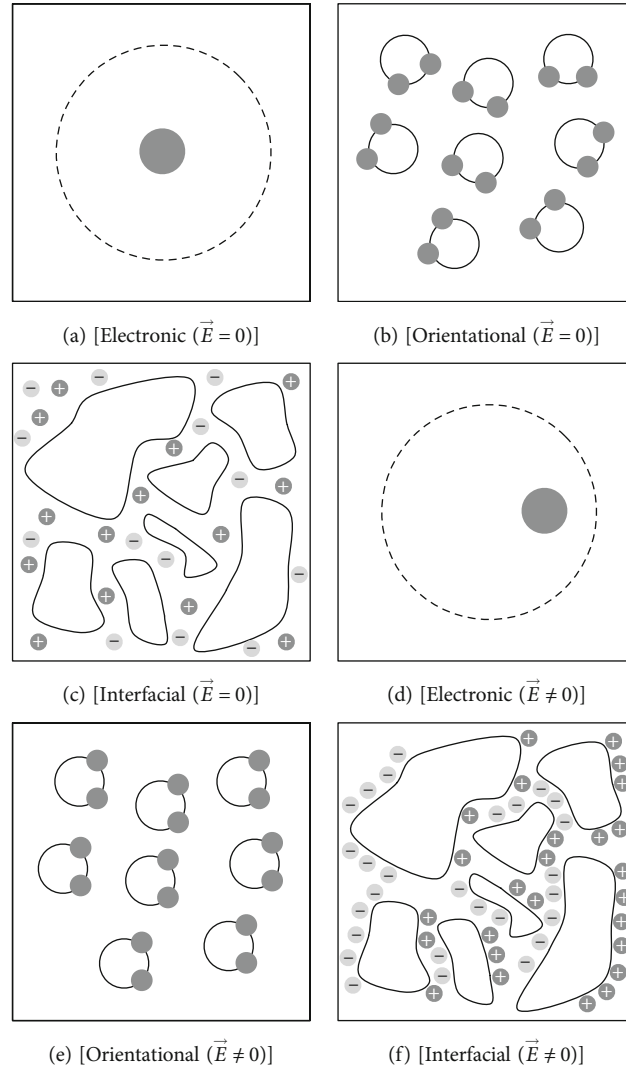


FIGURE 1: Comparison of different polarization types: (1) ionic contributions (a  $\rightarrow$  d), (2) dipolar polarization (b  $\rightarrow$  e), and (3) interfacial polarization (c  $\rightarrow$  f). The interfacial polarization (f) is the most common type in the rock consisting of matrix and fluids.

drilling (LWD) resistivity tools in specific conditions. The understanding of permittivity enables inferring the physical reasons for its main characteristics as a complex, frequency-dependent quantity. The relative permittivity of a formation is a real number when there is no dissipation of the energy carried by the electric field in the medium. However, when the formation dissipates energy, which is true in most of cases, the relative permittivity of the formation becomes a complex number which decreases from the low-frequency to the high frequency through several transitions, so-called frequency dispersion (Donadille et al. [9], Myers [10]).

Numerous lab measurements have been done to define the permittivity of rock samples. For example, Zinszner and Pellerin [11] made electrical measurements in sandstone and limestone. Also, there are several validated approaches for performing measurements of clay-bearing rocks (Fam and Dusseault [12], Myers [10, 13], Reil et al. [14], Seleznev et al. [15]), especially Josh and Clennell [16] demonstrated the lab measurement of the permittivity on clay and shale

using a parallel plate measurement tool. However, evaluating in situ permittivity is still challenging. Donadille et al. [9] have developed a multifrequency dielectric logging tool to measure the dielectric permittivity at four different frequency components in in situ conditions. The responses from the lower frequency channels are still under the influence of interfacial polarization effect; however, we can get more stabilized signal as the frequency becomes higher. Baker and Kenyon [17] introduced an application of the data measured by multifrequency dielectric permittivity scanners to invert the cementation and the tortuosity factor by assuming that both terms are identical. In addition, Baker and Kenyon [17] estimated the salinity of the shallow zones using dielectric logging tools.

In this paper, we introduce the background theory of dielectric permittivity and demonstrate the theory by applying them to a set of core samples acquired in shale reservoir. One of the key tasks is that we calibrate a dielectric permittivity log for water saturation that is generally higher than the core measurement. We then apply analytic models to

TABLE 1: Dielectric constant ranges of common rocks, minerals, and fluids.

Rocks, minerals, and fluids	Dielectric constants
Anhydrite	6.3
Dolomite	6.8
Barite	7 ~ 12.2
Sulphur	3.6 ~ 4.7
Biotite	4.7 ~ 9.3
Gneiss	8.5
Limestone	7.5 ~ 9.2
Fluorite	6.2 ~ 6.8
Calcite	7.8 ~ 8.5
Apatite	7.4 ~ 11.7
Plagioclase feldspar	5.4 ~ 7.1
Gypsum	5 ~ 11.5
Quartz	4.2 ~ 5
Pyrite	10.9
Sandstone (dry to moist)	4.7 ~ 12
Clay (dry to moist)	7 ~ 43
Petroleum	2.07 ~ 2.14
Water (20°C)	80.36

estimate the dielectric permittivity under the given condition, such as mineral composition and different water salinity. One of the simplest approaches to defining the dielectric permittivity of the solids may be to add volumetrically to the fluids' dielectric permittivity (Hipel [18]); however, this approach is not applicable to a porous media since the interacting solid and fluid surfaces results in additional mobile charge carriers that can be polarized. Therefore, we employed two different analytic models: complex refractive index model (CRIM) (Birchak et al. [19], Seleznev et al. [15]) based approach for a mono frequency analysis and Stroud-Milton-De (SMD) (Stroud et al. [20]) model for frequency dispersion analysis using multichannel frequency measurement data. Then, we used the estimated permittivity value to define an optimum value of Archie's parameter by applying nonlinear least square method. In each model case, we validated the analytic model via tests on core samples and then estimated Archie's parameter in a field dataset.

## 2. Theory and Method

**2.1. Physics of Dielectric Permittivity.** When an electric field is applied to a material, redistribution of bound charges occurs locally to new equilibrium positions. This phenomenon of charge redistribution is called polarization. The reason for this phenomenon can be described in three cases as presented in Figure 1. An electronic contribution arises from the distortion of the electron shell relative to the atomic nucleus. Ionic contributions are attributed to the relative displacement and deformation of charged ions with respect to each other. Dipolar polarization arises when molecules pos-

sessing a permanent electric moment are oriented along an applied field. In addition, there can be a space-charge (interfacial or Maxwell-Wagner) polarization due to local migration of charged particles. This type of polarization is a common phenomenon in heterogeneous materials such as porous rocks saturated with different types of fluids (Sen [21]). The measured permittivity of common rocks (Manning and Athavale [22], Parasnis [23]) is displayed in Table 1. In addition to the matrix (solid) permittivity, the bound water molecules in the pore structure also contribute to the dielectric response (Goncalves and Tremosa [24]).

There is a similarity among all polarization phenomena in that they are effective at a low-enough frequency but vanish past a certain frequency which is called relaxation frequency (Lima and Sharma [25]). This term can be determined by the inertial moment of the particles in frictions and electrostatic forces. If the electric field rotates too fast, the particles cannot follow it; thus, it is difficult to induce polarization and permittivity is reduced. Therefore, relative permittivity decreases with increasing frequency [26, 27] demonstrates the existence of this phenomena by comparing the varying rates of decay of interfacial polarization due to clay and that due to conductive minerals as a function of frequency.

In dielectric logging, the logging tool generates an external electric field. The relative permittivity of a formation is a real number when there is no dissipation of the energy carried by the electric field in the medium. However, when the formation dissipates energy, then the relative permittivity of the formation becomes a complex number as follows:

$$\epsilon = \epsilon' + i\epsilon'', \quad (1)$$

where  $i$  is the imaginary unit defined by  $i^2 = -1$ . The real part  $\epsilon'$  is related to the energy trapped within the formation by the electric field, while the imaginary part  $\epsilon''$  represents the amount of energy dissipation within the formation into other forms of energy. The complex dielectric permittivity consists of immobile part ( $\epsilon_m$ ) and mobile part ( $\epsilon_w$  and  $\epsilon_{oil}$ ). Generally, the immobile part represented by the rock permittivity which can be found from Table 1 [28, 29] demonstrated the importance of the complex permittivity formulation and the interpretation of the dissipative components.

Fuller and Ward [30] demonstrated mathematically that the existence of imaginary conduction (Chelidze et al. [31], Garrouch and Sharma [32], Revil et al. [14]) with corresponding physical models. Both the real and imaginary terms of the complex permittivity are frequency-dependent since most formations are dispersive. The complex relative permittivity  $\epsilon(\omega)$  of the formation with respect to angular frequency accounts for two types of current sources as follows:

$$\epsilon(\omega) = \epsilon'(\omega) + i \frac{\sigma(\omega)}{\omega\epsilon_0}, \quad (2)$$

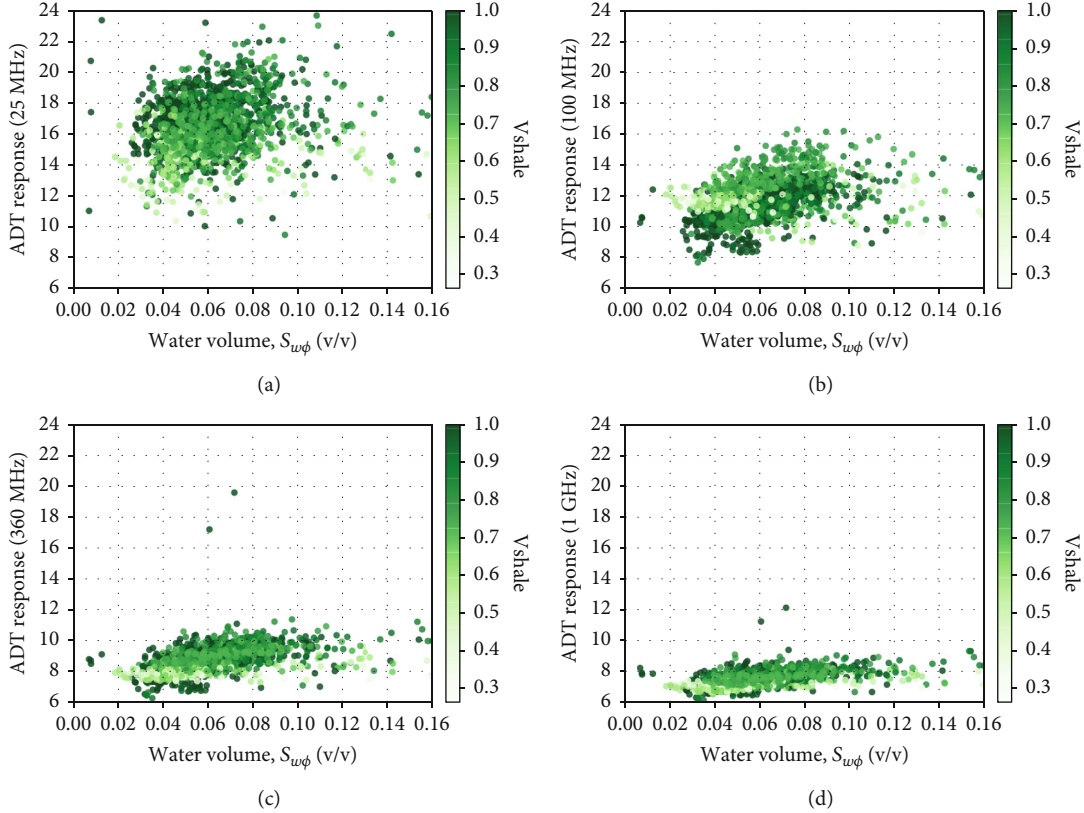


FIGURE 2: Response of multifrequency dielectric permittivity scanner in a borehole: (a) channel 1, (b) channel 2, (c) channel 3, and (d) channel 4, vs. water volume fraction color coded with shale volume. The frequency increases from channel 1 to channel 4.

combining the real-values permittivity and the frequency-dependent conductivity  $\sigma(\omega)$  yields

$$\sigma(\omega) = \sigma_{DC} + i\omega\varepsilon_0\varepsilon'', \quad (3)$$

where  $\varepsilon_0$  means the permittivity of a vacuum. The DC conductivity  $\sigma_{DC}$  comes in phase with  $\varepsilon''$  in the imaginary part of the complex permittivity. In addition, DC conduction currents also dissipate in the form of heat energy. The conductivity and permittivity are both frequency-dependent due to the dispersive nature of the medium.

**2.2. Measurement of Dielectric Permittivity.** We employed multifrequency dielectric permittivity scanner (Ligneul et al. [33]) to measure the dielectric constant in situ conditions. The tool makes measurements at high frequencies, in the megahertz (MHz) to gigahertz (GHz) range. Normally, low-frequency measurements are dominated by the conductivity of the formation, but as the frequency increases, dielectric effects begin to appear and then dominate. Measurements at high frequency (over  $10^8$  Hz) enable us to evaluate formation permittivity and conductivity simultaneously, which are used to define water saturation and salinity in invaded zones. Therefore, a multifrequency dielectric logging tool (Ligneul et al. [33], Seleznev et al. [34]) is designed to measure the permittivity and conductivity at four different frequency components ( $f_{max} = 1$  GHz). The responses from the lower frequency channels are still

under the influence of interfacial polarization effect. However, we can obtain more stable permittivity logs as the frequency becomes higher than 1 GHz (Figure 1). Thus, we can observe more obvious relationship between the water volume in formation and the response of permittivity scanners with multifrequency channels as presented in Figure 2.

**2.3. Analytic Models of Dielectric Permittivity.** We employed two different analytic models; complex refractive index model (CRIM) based approach for a mono frequency analysis and Stroud-Milton-De (SMD) for frequency dispersion analysis using multichannel frequency measurement data, to simulate the bulk dielectric permittivity. The CRIM and SMD model are common in that they can incorporate the volume fraction of fluids and minerals. However, they have a different applicable frequency range. The CRIM is applied for a formation in the frequency range where textural effects have disappeared, which is at the highest-frequency (1 GHz) of the dielectric logging tool. In contrast, the SMD model can simulate a dispersion relation under the frequency range which can cover the frequency of multichannel dielectric permittivity scanner. For both models, the water permittivity  $\varepsilon_w^*$  is calculated based on analytic solutions (Stogryn [35]). Also, inspired by Baker and Kenyon [17], we assume that the cementation factor ( $m$ ) and tortuosity factor ( $n$ ) are identical in Archie's equation (Archie [36]). For conciseness, we will refer to those terms; tortuosity and cementation factor, as Archie's parameter for the rest of the paper.

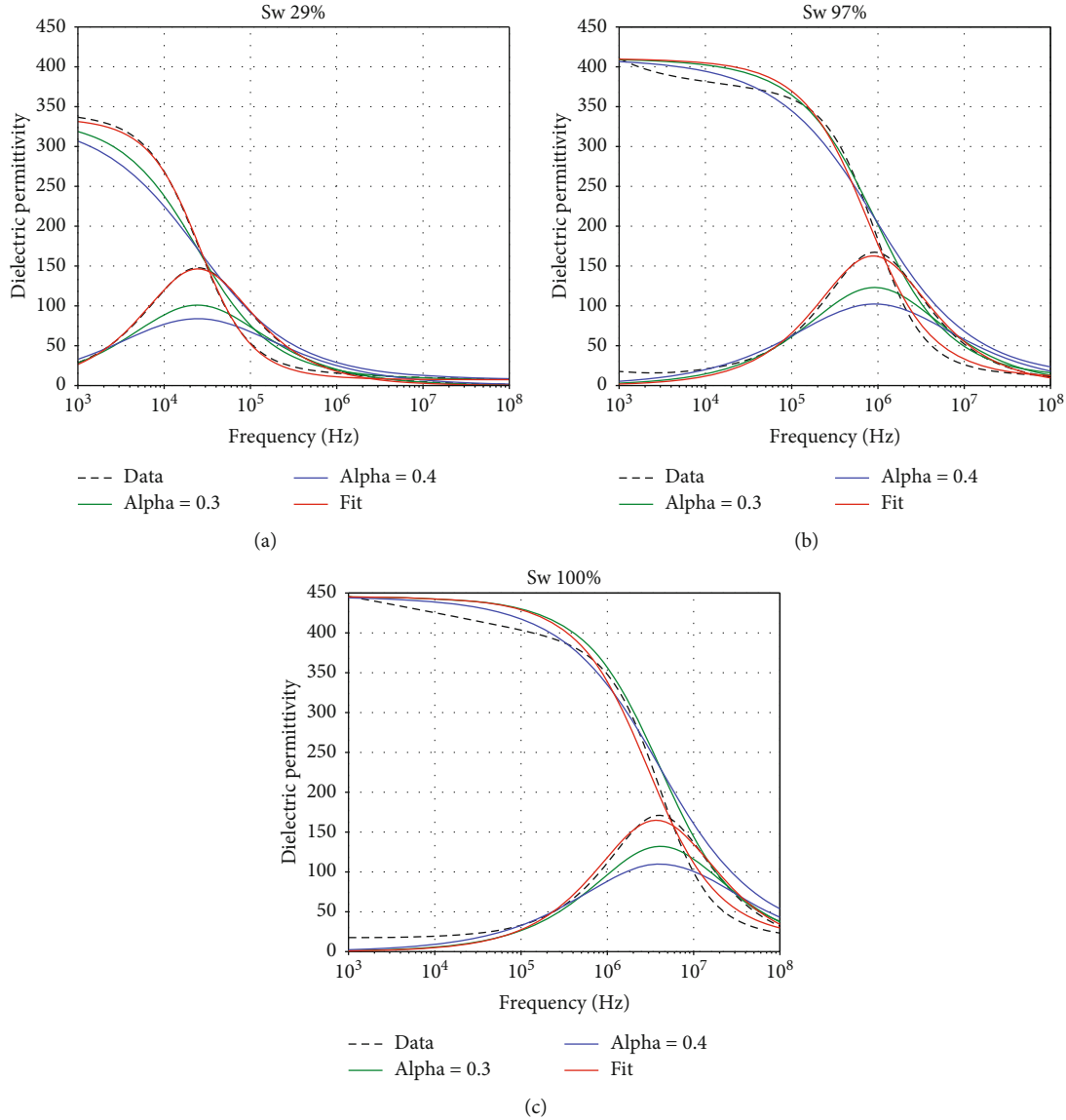


FIGURE 3: Core measurements of dielectric permittivity showing different frequency dispersion trend according to the water saturation changes: (a) 29%, (b) 97%, and (c) 100%. The green ( $\alpha=0.3$ ) and blue ( $\alpha=0.4$ ) curves are calculated permittivity by applying the constant Archie's parameter), and black dashed line means the measured permittivity from a core sample.

2.3.1. *Complex Refractive Index Model (CRIM)*. The most popular model to define a bulk permittivity in porous rock is the complex refractive index model (CRIM) (Birchak et al. [19], Greaves et al. [37], Seleznev et al. [15]). There have been several trials to incorporate additional term into the CRIM to demonstrate the surficial polarization (Knight and Abad [38], Knight and Endres [39]). In this paper, however, we start from a standard CRIM to generalize the model.

The CRIM does not allow variation of the texture because the texture affects the interfacial polarization (or Maxwell-Wagner effect). For example, in porous rocks filled with saline water, the relative permittivity becomes dispersive under the frequency range of the dielectric logging tool device. The reason for the occurrence of dispersion is that they are subjected to interfacial polarization, which has a relaxation frequency within the frequency of interest in the dielectric logging tool. All the frequencies of the dielectric

logging tool are close to the interfacial polarization relaxation frequency, so they are in a transition zone where permittivity decreases and conductivity increases as frequency increases. Therefore, the CRIM is applied for a formation in the frequency range where textural effects have disappeared, which is at the highest frequency (1 GHz) of the dielectric logging tool. The equation of standard CRIM can be written as follows:

$$\sqrt{\epsilon^*} = (1 - \phi)\sqrt{\epsilon_m} + \phi \left[ S_w \sqrt{\epsilon_w^*} + (1 - S_w)\sqrt{\epsilon_{oil}} \right], \quad (4)$$

where  $S_w$  denotes water saturation.  $\epsilon^*$  is the effective complex dielectric permittivity of the rock, and corresponding subscript index denotes the materials;  $m$  and  $w$  denote matrix and water, respectively.  $\epsilon^*$  and  $\epsilon$  mean the complex and real number of permittivity, respectively.  $\phi$  means total

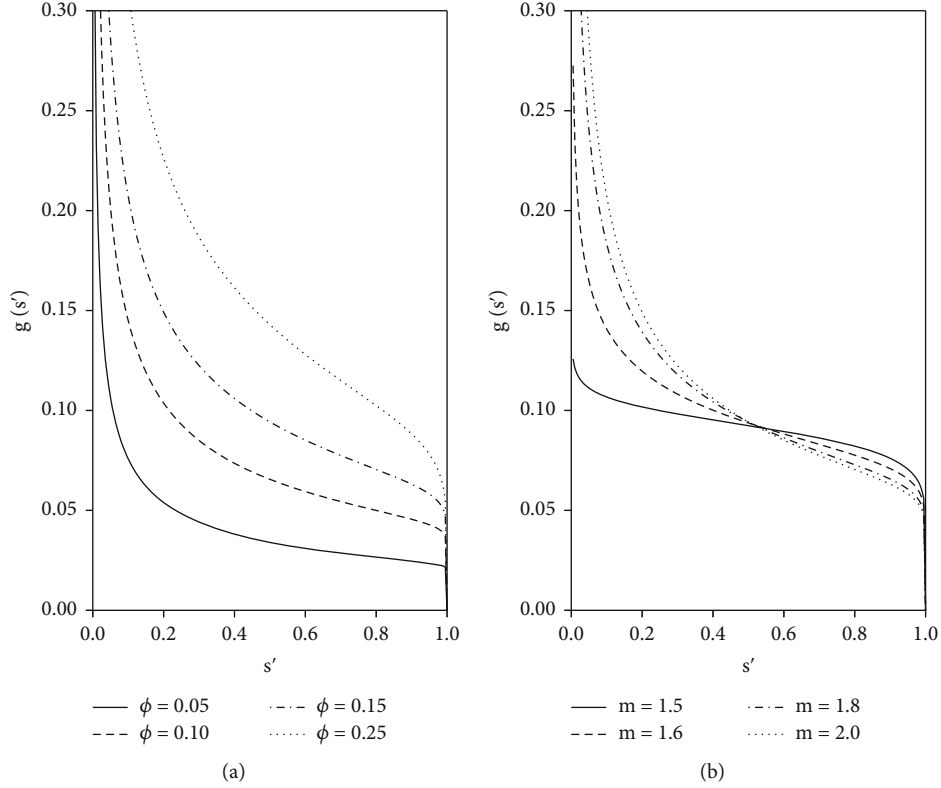


FIGURE 4: Dependence of the spectral density function on (a) water volume fractions and (b) Archie's parameters.

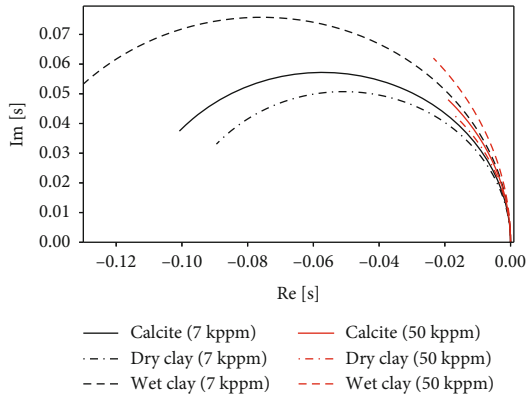


FIGURE 5: Trajectory of the variable,  $s = (1 - \epsilon_w/\epsilon_m)^{-1}$ , for a sandstone and shale core samples.

porosity. According to equation (4), CRIM shows that the refractive index of the bulk formation is the volumetric average of its constituents' refractive indices. Total organic carbon (TOC) needs to be included in immobile part,  $\epsilon_m$ , which contains the volume of TOC ( $v/v$ ) and permittivity of bitumen (2.07 ~ 2.14).

We applied CRIM to core samples which are fully saturated with brine under 1000 psi. Mineral fraction of the cores samples is measured using an X-ray diffraction (XRD) device. However, we need to note that there might exist uncertainty in the water saturation since injecting water under high pressure, over long periods of time, does not always guarantee 100% saturation of water in core samples.

For instance, it is hard to make a core sample fully saturated when the rock contains large portions of secondary porosity.

**2.3.2. Lichtenecker-Rother (LR) Model.** According to the results, the CRIM with the exponent 0.5 could not reproduce the measured permittivity. In this regard, we combined the Archie's equation and CRIM to replicate the response of dielectric logging tool. By plugging in the Archie's equation, we proposed the generalized CRIM, which can be derived as follows:

$$\epsilon^{*\alpha} = (1 - \phi)\epsilon_m^\alpha + \phi[S_w\epsilon_w^{*\alpha} + (1 - S_w)\epsilon_{oil}^\alpha], \quad (5)$$

where  $\alpha$  is inverse of Archie's parameter ( $\alpha = 1/m$ ). We set the water salinity 20 kppm for the calculation of water permittivity. This generalized CRIM model is termed as Lichtenecker-Rother (LR) model [40]. Nevertheless, even in the LR model, a core sample with extremely small pore volume (<1%) could not reproduce the measured permittivity. Theoretically, the calculated dielectric permittivity can be separated in real part and imaginary part as displayed in equation (1). For clear illustration of the frequency dispersion in dielectric permittivity, we presented the core measurement example in Figure 3. The green ( $\alpha = 0.3$ ) and blue ( $\alpha = 0.4$ ) curves are calculated permittivity by applying the constant Archie's parameter, and black dashed line means the measured permittivity from a core sample. The red curve exhibits the dielectric permittivity acquired by the curve fitting. By calculating the optimum Archie's parameter which minimizes the error between the calculated and observed dielectric permittivity, we can apply the correction to inaccurate water saturation which is estimated

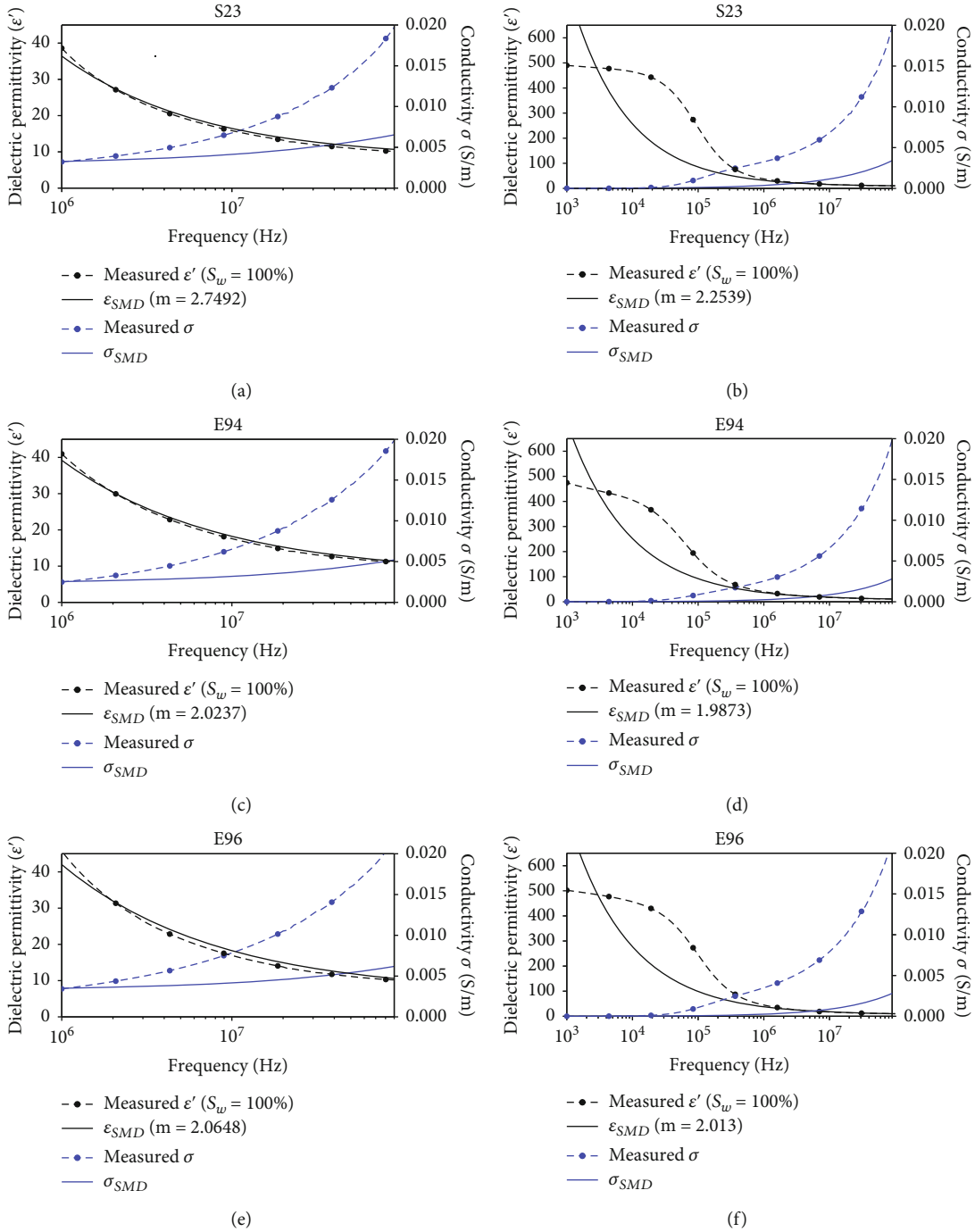


FIGURE 6: SMD model-fitting for the core data that are fully saturated with water. Note that the implementation of curve-fitting only focuses on real part of the permittivity  $\epsilon'$ .  $\sigma_{SMD}$  is calculated DC conductivity from the estimated permittivity. Each panel (a, c, e) shows the expanded part of the high frequencies ( $>10^6$  Hz) as highlighted with red rectangles in each panel (b, d, f), respectively.

mainly by using resistivity logs. In Figure 3, the shape of dispersion curve varies according to the water saturation (29%, 97%, and 100%). The diminishing curve from low-frequency end and concave curve with peak frequency denote imaginary and real part of the permittivity, respectively.

**2.3.3. Stroud-Milton-De (SMD) Model.** Stroud et al. [20] proposed a textural model which is generally referred to as the SMD model. In this model, the spectral density

function of the composites plays a key role in simulating the dispersive response of dielectric constant with respect to frequencies. The spectral density function can be determined by the distribution and composition of the interfaces among different phase, incorporating the depolarization factor of the phases. We used a two-phase model (Mavko et al. [41]), which consists of water and a mix of rock and oil. We can start developing SMD model by considering the complex relative fraction of water and

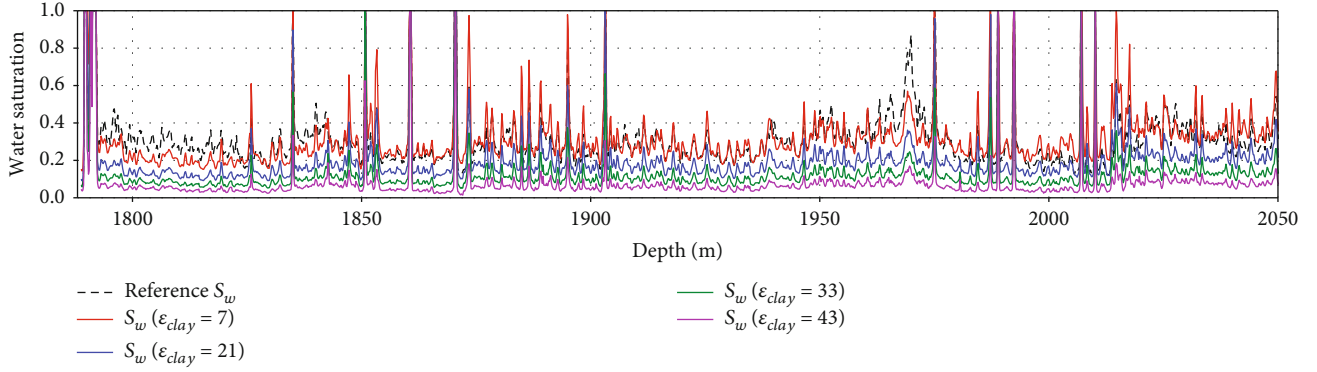
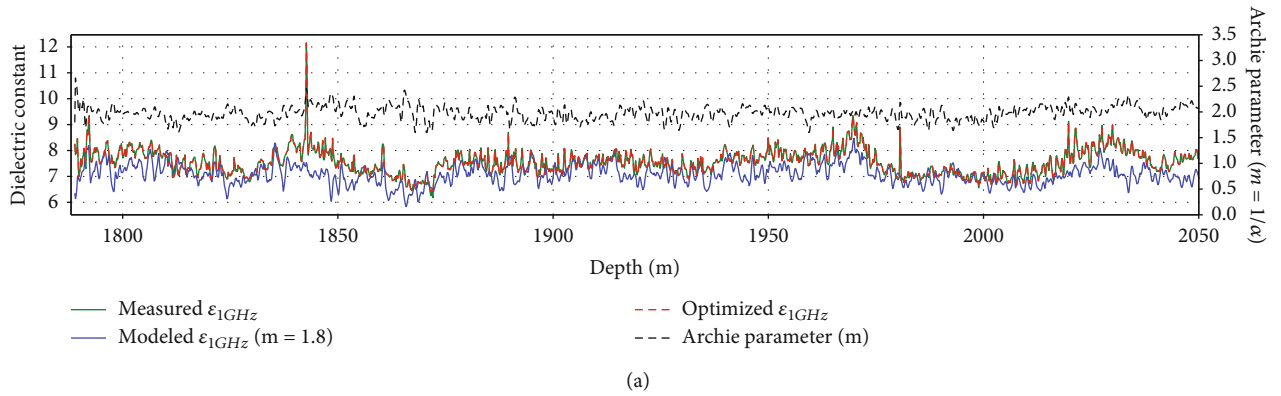
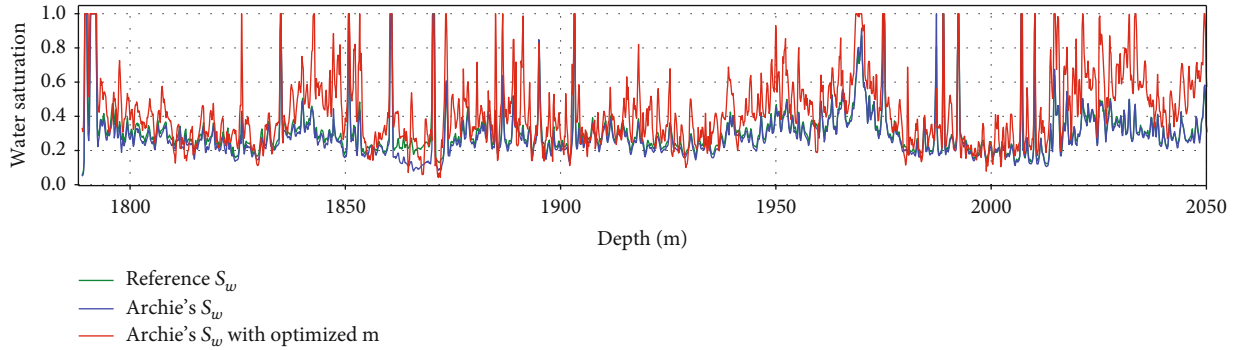


FIGURE 7: Bulk dielectric permittivity with different value of clay permittivity: 7, 21, 33, and 43.



(a)



(b)

FIGURE 8: (a) Model-fitting results where black dash line is the optimized Archie's parameter which can replicate the dielectric permittivity log (red dash line). (b) Water saturation calculated by using the optimized Archie's parameter in red solid line. The optimization of Archie's parameter provides the correction level of water saturation.

matrix permittivity  $(1 - \epsilon_w/\epsilon_m)$ . However, working with the inverse of this relative fraction makes tasks easier

$$s = \left(1 - \frac{\epsilon_w}{\epsilon_m}\right)^{-1}. \quad (6)$$

By applying the above relation and integral representation, the analytic function  $f(s)$  (Stroud et al. [20]) can be set as

$$f(s) = \frac{A}{s} + \int_0^1 \frac{g(s')}{s-s'} ds', \quad (7)$$

where the constant  $A$  consists of the actual volume fraction of water and Archie's parameter. Therefore,  $A$  can be rewritten as  $(S_w\phi)^m$ , where  $\phi$  denotes the volume fraction occupied by pore structures. Since Stroud et al. [20] only introduced the test results with 100% brine saturated case, they assumed that the  $A$  term only depends on the porosity ( $S_w = 1$ ).

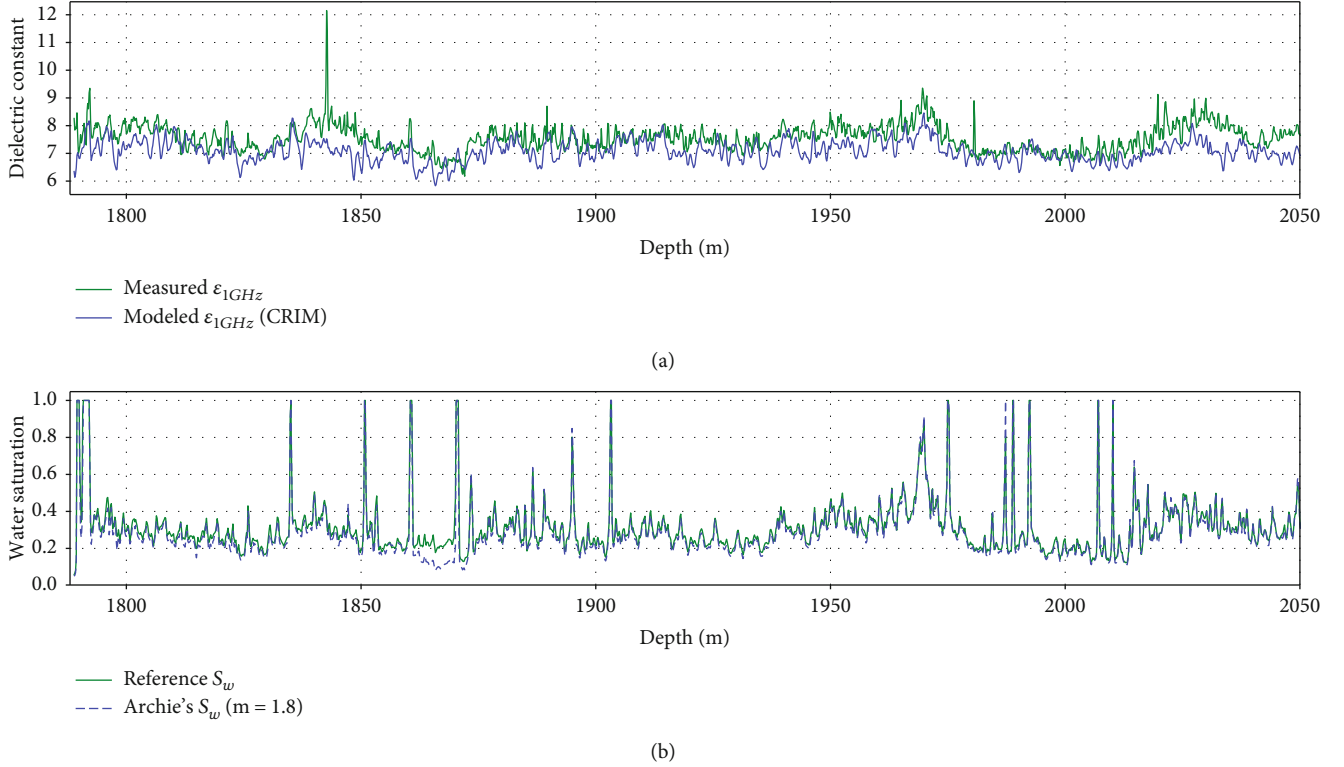


FIGURE 9: Comparison of dielectric permittivity and water saturation calculated by the standard CRIM. (a) Measured (green) and estimated (blue) dielectric response, and (b) reference (green) and calculated water (blue) saturation.

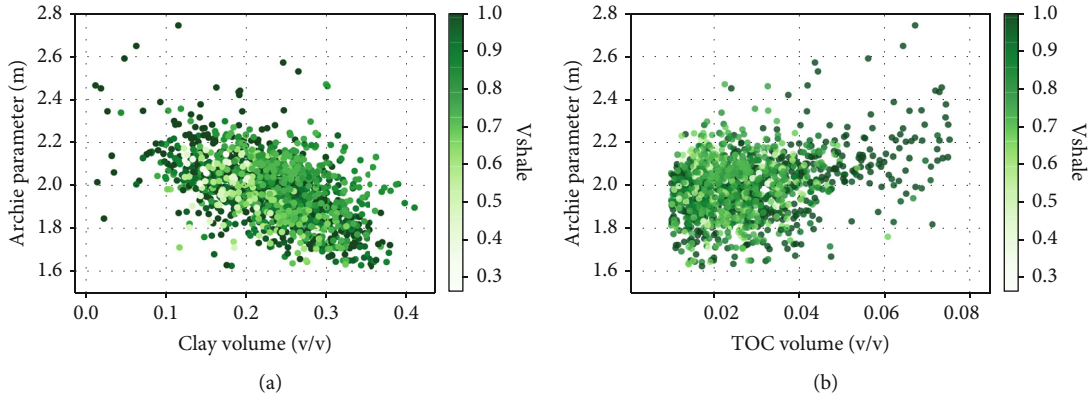


FIGURE 10: (a) Optimized Archie's parameter vs. clay volume, and (b) clay and TOC volume color-coded by shale volume. Note that the shale volume is calculated using gamma ray logs and the clay volume is measured by the core analysis.

The spectral density function  $g(s')$  takes positive real values, and the density function can be expressed as

$$g(s') = C(s')^{-0.5} (1-s')^{0.5}, \quad (8)$$

where the exponent 0.5 is motivated by the standard CRIM (Birchak et al. [19], Seleznev et al. [15]). Stroud et al. [20] proposed different forms of the density function as shown in the following equation

$$g(s') = C(s')^{-b} (1-s')^e, \quad (9)$$

where  $C$ ,  $b$ , and  $e$  are parameters which can be determined as follows:

$$C = \frac{\Gamma(2-b+e)}{\Gamma(1-b)\Gamma(1-e)} (\phi_w - A), \quad (10)$$

where

$$b = 1 - \frac{\phi_w(1-\phi_w)}{2\phi_w - A(3-\phi_w)}, e = \frac{\phi_w(\phi_w - A)}{2\phi_w - A(3-\phi_w)}. \quad (11)$$

Note that both the exponents  $b$  and  $e$  are positive values over the entire range of water volume fraction, when

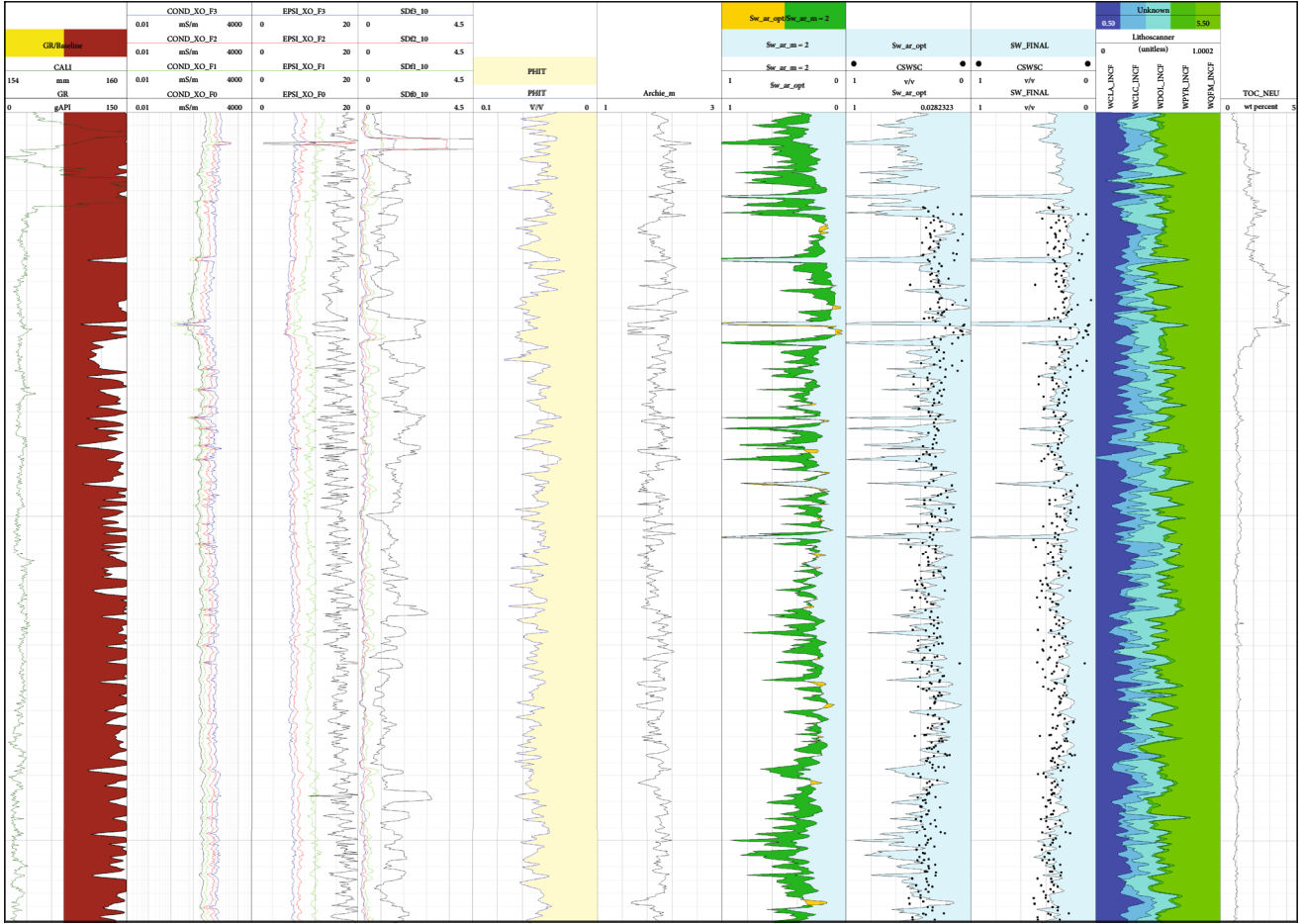


FIGURE 11: Log view of the well dataset. Comparison of different water saturation logs that are obtained by applying Archie's equation, CRIM, and reference which is combination of Archie and Luffel's equation. Each track shows (1) gamma ray and caliper, (2) conductivity, (3) dielectric permittivity, (4) degree of noisiness (standard deviation), (5) porosity, (6) optimized Archie's parameter, (7) water saturation  $S_w$ :  $m=2$  vs. optimized  $m$ , (8)  $S_w$  from optimized  $m$  vs.  $S_w$  core measurement, (9) reference  $S_w m$  vs.  $S_w$  core measurement, (10) lithology scanner, and (11) total organic carbon. The noisiness logs of dielectric logging tool's response are obtained by calculating the standard deviation of dielectric permittivity logs that are inside of the given interval window; 1.3 m (10 sampling points) in this example.

Archie's parameter is two ( $m=2$ ). Figure 4 exhibits the behavior of the density function  $g(s')$  according to the change of water volume fraction and Archie's parameter. Observing Figure 3, we can find that the value of  $g(s')$  becomes unstable at large  $s'$  as the water volume fraction  $\phi_w$  decreases; however, as far as  $\phi_w$  is greater than 7%, we could utilize SMD model for the estimation of dielectric permittivity. When we varied Archie's parameter to demonstrate the behavior of the density function, the results rarely change as Archie's parameter becomes greater than 1.8 as shown in Figure 3. The low-frequency components ( $\omega \ll \sigma_w / \epsilon_0 \epsilon$ ) correspond to small absolute values of  $s$  as shown in Figure 5, where the values of  $s$  are plotted for core samples saturated with two types of brine: one conductive (higher salinity) and the other moderately conductive (lower salinity). Stroud et al. [20] demonstrated the example of sandstone (black and red solid line) in Figure 5. We additionally displayed the

example of clay samples by varying the amount of clay bound water and displayed the results with dashed line in Figure 5. According to the result, as the clay contains more water, the radius of the circular curve becomes greater. Also, when the core samples become more conductive, all the responses are concentrated to the smaller range of  $s$ , which means that the core samples saturated with higher salinity brine show smaller variations of  $s$  with respect to the frequencies.

To investigate the dispersion relationship between the dielectric permittivity and frequency, we can examine the asymptotic behavior of the complex dielectric permittivity. The asymptotic behavior of  $\epsilon'$  and  $\sigma$  can be expressed as

$$\epsilon' = \epsilon^{1-b} \left( \frac{\sigma_w}{\omega \epsilon_0} \right)^b \frac{C\pi}{2 \sin(b\pi/2)}, \quad (12)$$

$$\sigma = A\sigma_w + \epsilon^{1-b} \sigma_w^b (\epsilon_0 \omega)^{1-b}.$$

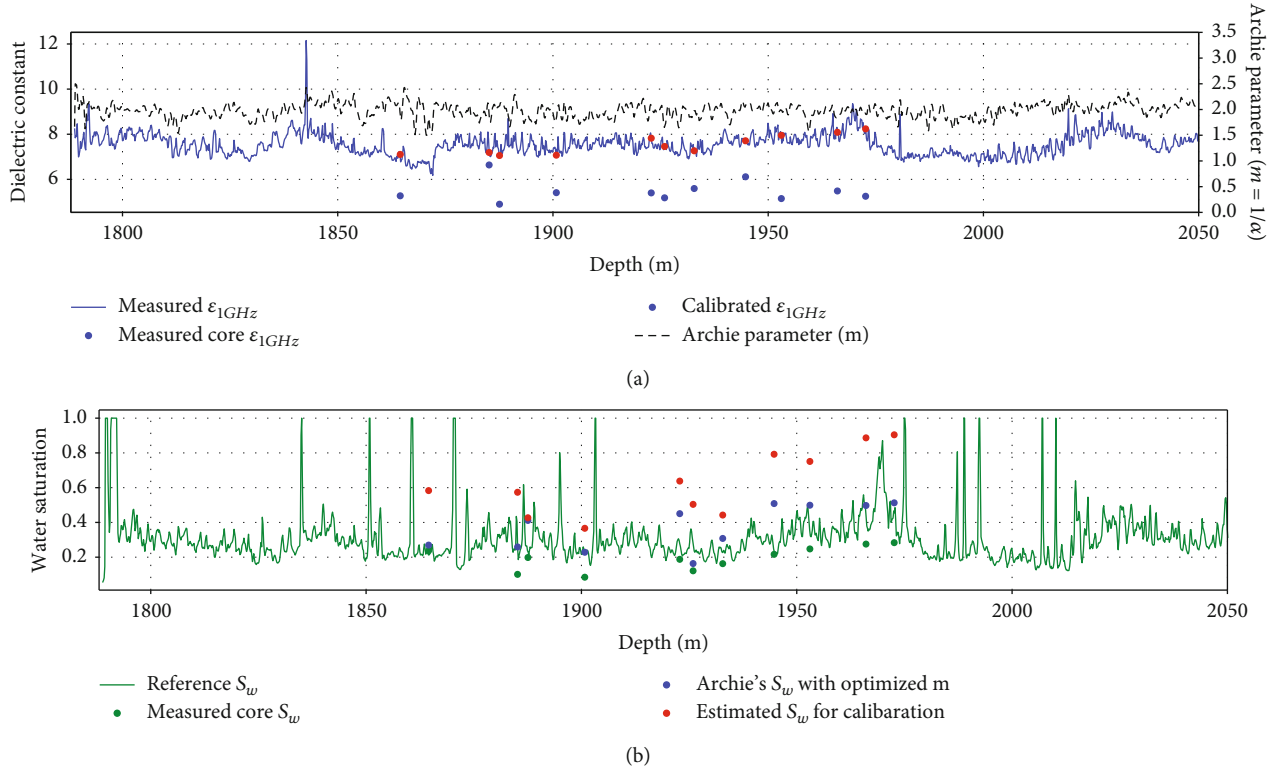


FIGURE 12: Calibration of dielectric core measurement and corresponding water saturation that are required for cores samples to replicate dielectric response of the scanner. (a) Black dashed line is the Archie's parameter optimized to core measurements. (b) Red points are the results after calibration, and they show the amount of water being required to generate the same dielectric response under the condition of core samples.

We use the above asymptotic behavior to simulate the frequency dependent dispersive dielectric permittivity and conductivity in the core samples. In this research, we applied the SMD model to the core data to validate the behavior of the SMD model in shale formation. In addition, we calculated the optimum value of Archie's parameter through the curve-fitting using nonlinear least square inversion. We calculated the Archie's parameter by fitting the permittivity values and applied the estimated Archie's parameter to obtain conductivity. In other words, conductivity is not considered to optimize the Archie's parameter, but only used to validate the optimum value of Archie's parameter that is obtained from the model fitting of dielectric permittivity by comparing the calculated conductivity with the measured conductivity.

For utilizing the SMD model in observation of the dispersion relation as a function of frequency, note that the frequency range is a crucial factor to consider. Stroud et al. [20] introduced sandstone examples at high-frequency range ( $10^7$  Hz  $\sim$  1 GHz). In such a high-frequency range, we cannot define the key parameters of energy dissipation and frequency dispersion. Accordingly, we extended the frequency range to cover the low-frequency part ( $10^3$  Hz  $\sim$   $10^7$  Hz) by applying the asymptotic approach of the SMD model as presented in equation (12) since there is little change on the slope of dispersion curve.

The result of the SMD model fitting with optimum Archie's parameters is presented in Figure 6. Each figure shows the case of 100% water saturation. According to

the measured data, as the amount of water saturation increases, the low-end permittivity  $\epsilon_0$  and the relaxation time  $\tau$  also increase. Nonetheless, the SMD model could not simulate the ideal curve of frequency dispersion for the dielectric permittivity to define a knee point of the energy dissipation. Therefore, we put more weight on the higher frequency band ( $10^7$  Hz  $\sim$  1 GHz) for estimation of the Archie's parameter as Stroud et al. [20] exhibited. As the frequency becomes lower ( $<10^6$  Hz), the SMD model experiences a bias toward higher frequencies due to a higher density of data available at the high-frequency band. Therefore, the inversion algorithm used for curve-fitting puts more weight on higher frequency, which might result in inaccurate permittivity estimation on the low-frequency end.

### 3. Field Data Examples and Discussion

**3.1. Lichtenecker-Rother (LR) Model.** Since the LR model (generalized CRIM) yields more reliable results than the standard CRIM, we directly employed the LR method without demonstrating the CRIM. For the application of the LR model to the field data, we assume that the matrix consists of 5 lithologies: clay, calcite, quartz, dolomite, and pyrite. For the calculation of dielectric constant of water  $\epsilon_w^*$  using [35]'s approach, temperature gradient is fixed to  $0.03^\circ\text{C}/\text{m}$  with  $0^\circ\text{C}$  at surface. Water salinity is set to 50 kppm. One of key factors that might have an influence on water

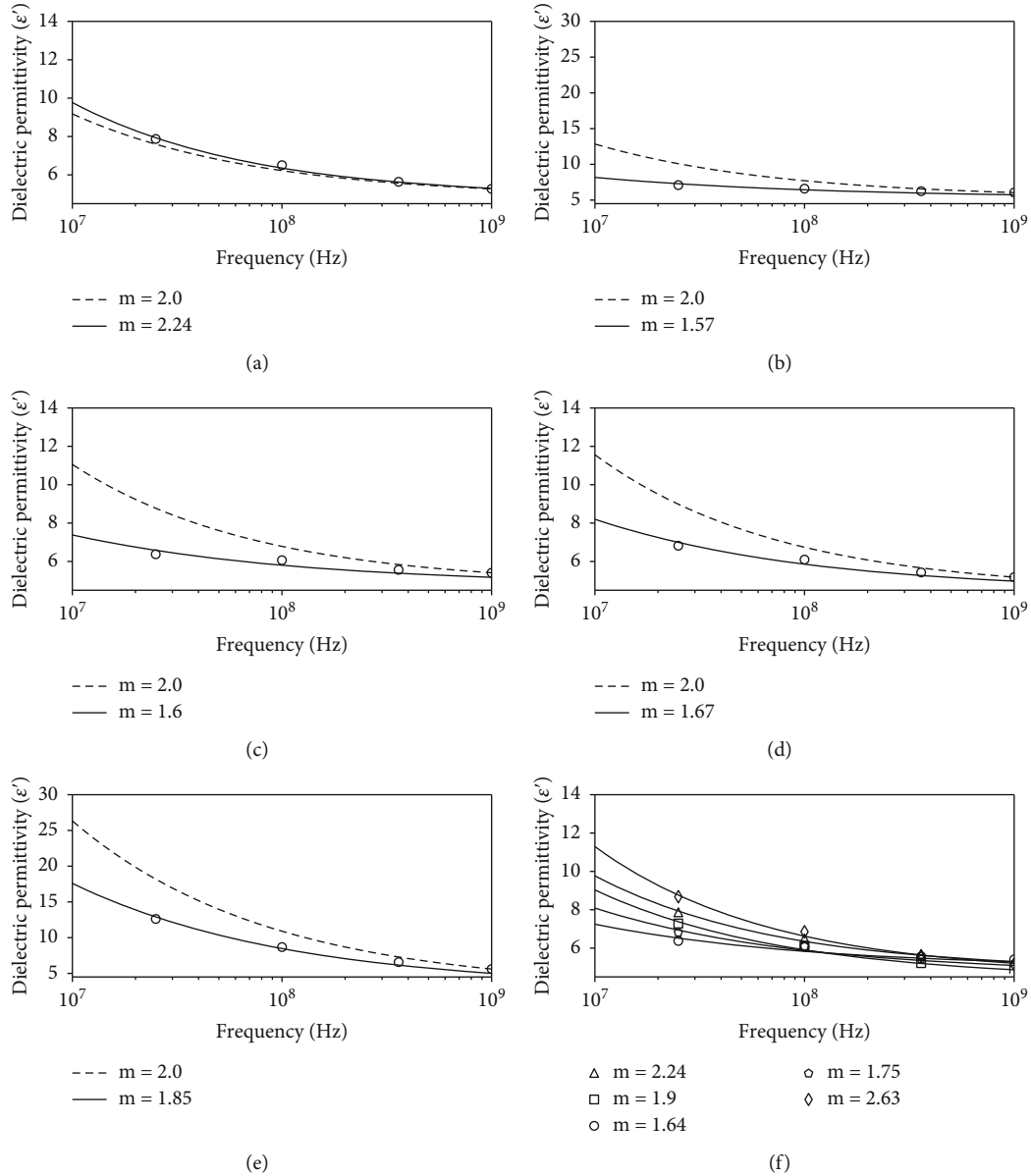


FIGURE 13: SMD model-fitting for the side core samples of the well.

saturation is permittivity of clay. As the permittivity of clay varies depends on the amount of clay bound water, we set different conditions for the clay permittivity. The major difference between those assumptions is to use different dielectric constant: from dry clay ( $\epsilon_{\text{clay}}=7$ ) to wet clay ( $\epsilon_{\text{clay}}=43$ ), as shown in Figure 7. As the formation does not contain a large portion of clay bound water in the study area, the assumption with dry clay produces better fit with the reference water saturation, while wet clay assumptions yield somewhat smaller amount of water saturation than reference values. This phenomenon is attributed to the fact that clay bound water is considered as immobile part and included in  $\epsilon_m$  term, which contributes to the decrease in the amount of water saturation under the given permittivity.

The reference water saturation is calculated by combining the Luffel et al.'s (Luffel et al. [42]) and Archie's (Archie

[36]) equation. When applying Archie's equation, we used the constant cementation and tortuosity factor ( $m = n = 1.8$ ). The Luffel's equation is employed only for the depth interval with high TOC ( $>2\%$  in weight percent).

Given the water saturation estimated using dielectric permittivity log (Figure 7), the calculated water saturation using the constant cementation factor ( $m = 1.8$ ) shows good agreement since it is computed using similar regime of the reference one. However, the corresponding response of calculated dielectric logging tool which is displayed in Figure 7 has a somewhat different range of amplitude compared to the measured permittivity response, though it shows similar shape of curve throughout the survey range. Hence, we are to estimate the amount of correction in water saturation by reproducing the measured dielectric permittivity.

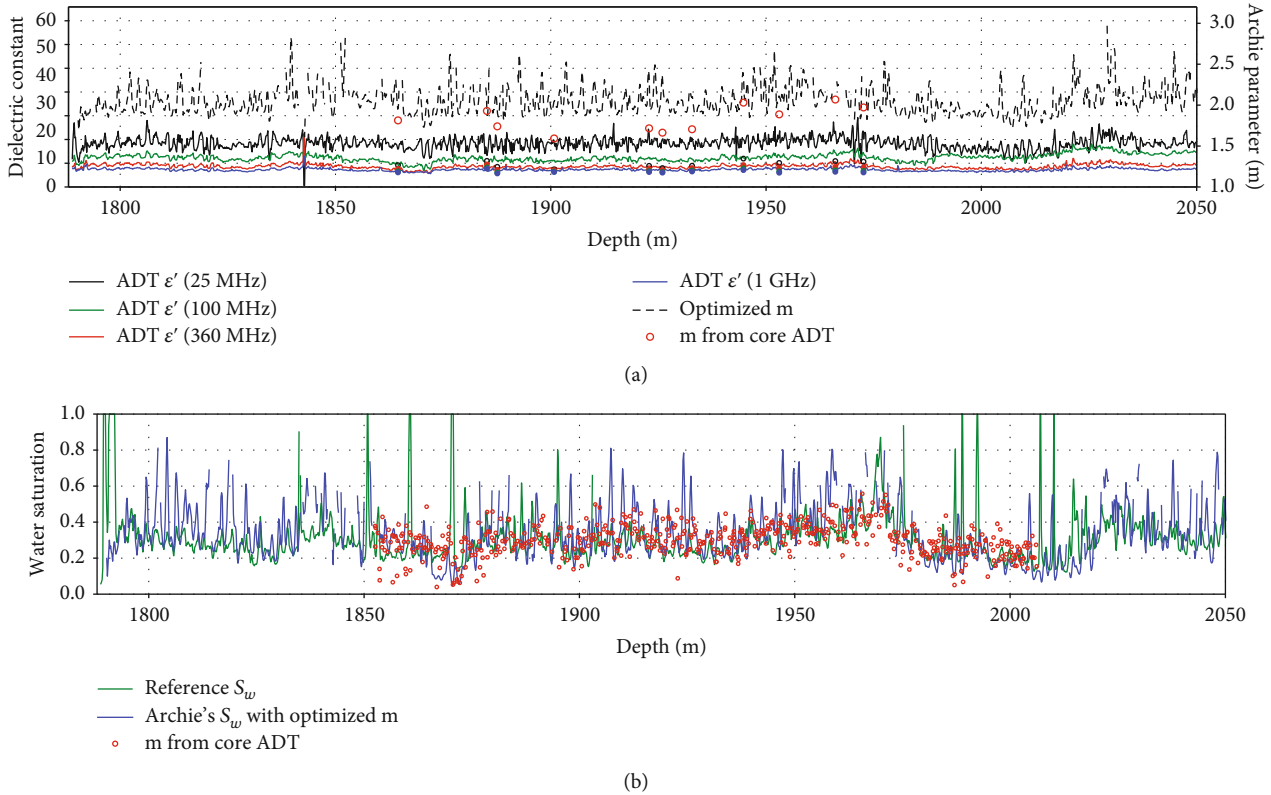


FIGURE 14: (a) Optimized Archie’s parameter obtained by the SMD model fitting, and (b) the water saturation from the optimized Archie’s parameter.

By applying equation (5), we can compute the dielectric logging tool response as shown in Figure 8. The nonlinear least square method is used to find an optimized Archie’s parameter,  $m$ . The black dashed line in Figure 8 means the Archie’s parameter ( $m = 1/\alpha$ ) which can minimize the error ( $\epsilon_{\text{measured},1\text{GHz}} - \epsilon_{\text{modeled},1\text{GHz}}$ ) at each measured depth point. The optimized Archie’s parameter can generate the dielectric responses which show good agreement with the measured data as displayed in Figure 8 with red dashed lines. The corresponding water saturation from optimized  $m$  is presented in Figure 9. According to the calculated well logs, the optimized Archie’s parameter has higher value at the point where larger volume of organic carbon exists. This phenomenon is attributed to the low conductivity of organic carbon that is located among the pore volumes. One possible interpretation is that those organic carbon make current difficult to flow, so it results in the elevation of tortuosity level. Similarly, the optimized Archie’s parameter shows inversely proportional trend with clay volume. This is because the larger volume of clay may decrease the tortuosity level due to its relatively high conductivity. Given that TOC contributes considerably small portion to the bulk permittivity, it is intriguing that the optimized Archie’s parameter shows similar trend with TOC volume. We displayed a crossplot (Figure 10) to demonstrate the relation between the estimated Archie’s parameter and clay volume.

The log view displayed in Figure 11 shows difference between estimated and measured water saturation with relevant well logs. All the water saturation curves in Figure 11

are displayed in volume fraction. First, the reference water saturation curve is corrected at high TOC region, and Luffel’s equation is used for making this correction. The 8th track shows water saturation curve calculated by using the LR model with optimized Archie’s parameter which has better agreement with the core measurement compared to the reference one in 9th track. The amount of over- or underestimation is highlighted with green and orange colors in 7th track, respectively.

In general, dielectric constants that are measured in the lab tend to have smaller values than those that are measured using a dielectric logging tool. One of key goal of this research is to develop a method for calibrating the dielectric measurement of the core samples. Given that smaller values of dielectric permittivity in core samples are attributed to the loss of water volume, it is important to estimate the amount of water that is required for core samples to generate the same dielectric response with well logs. Below is a summary of the workflow we developed for calibrating core dielectric measurements:

- (i) Defining clay permittivity by performing a modeling of water saturation (well log) using different type of clay assumption: dry clay or wet clay
- (ii) Estimation of optimized Archie’s parameter (well log) using the LR model and non-linear least-square method
- (iii) Calculate water saturation (well log) using CRIM with optimized Archie’s parameter

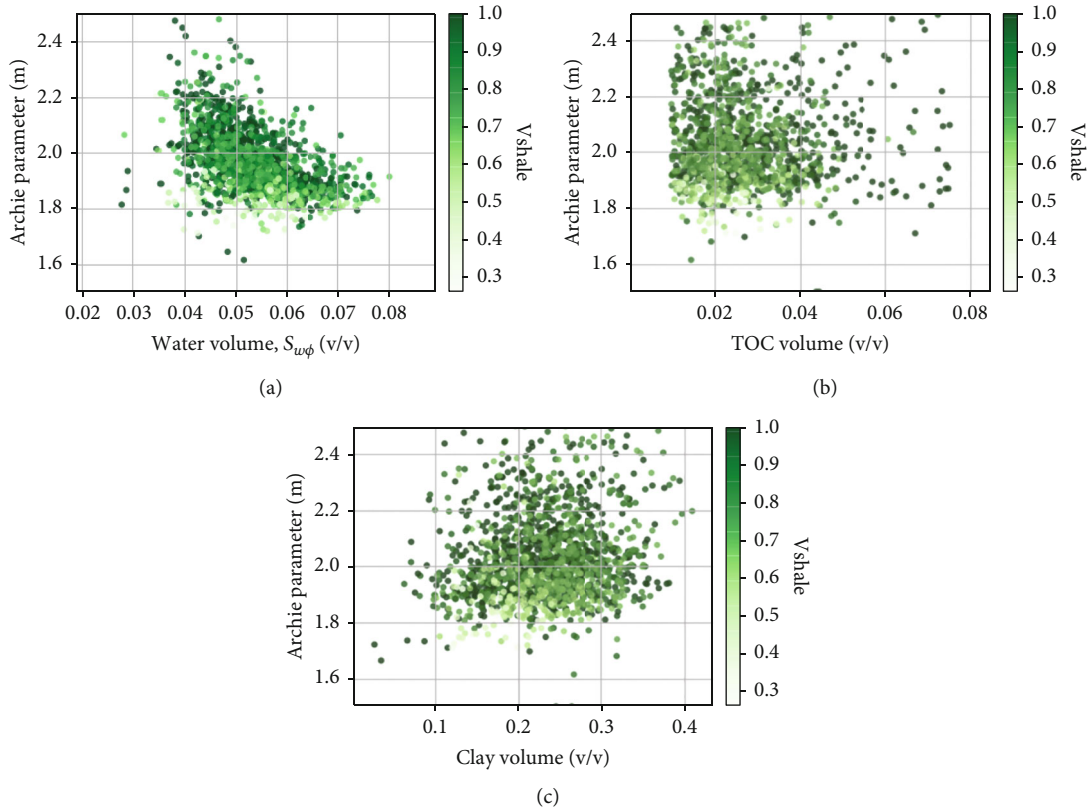


FIGURE 15: Crossplot showing the correlation between the optimized Archie's parameter and formation properties: (a) water volume, (b) TOC, and (c) clay volume.

- (iv) Applying the optimized Archie's parameter to core data
- (v) Estimation of water saturation that is required to replicate the dielectric logging tool responses under the given condition of core sample such as mineral composition and water saturation by using nonlinear least-square method. Note that we used log-based optimum Archie's parameter to estimate the required amount of water saturation for the calibration of core measurement

As shown in the core sample case, similarly, XRD measurement is performed to investigate mineral fractions for calculating the matrix permittivity. The optimized Archie's parameter shown in 6th track of Figure 11 is obtained based on the trend of dielectric logs measured using multifrequency dielectric logging tool. As we described in well log examples, similarly, the optimized Archie's parameter in core samples tends to diminish as depth becomes greater. The red dots presented in Figure 12 demonstrate that the optimized Archie's parameter with dashed black line can replicate the complex permittivity which is obtained via lab experiments.

**3.2. SMD Model.** In addition to the study on the core samples using the LR model as shown in the previous section, we also applied the SMD model fitting to the field dataset.

We displayed several SMD model fitting of core samples from the borehole in Figure 13. In each subfigure, the dashed line shows the modeled permittivity using SMD model ( $m = 2$ ). The solid line is the result of curve-fitting with optimized Archie's parameter. We performed model-fitting only in the high-frequency band since the behavior of the SMD model does not match well with the lab-measured data.

The black-dashed line in Figure 14(a) shows the optimized Archie's parameter to replicate the dielectric permittivity in the SMD model. We also applied this cementation factor (or tortuosity factor) to calculate the water saturation by using Archie's equation as shown in Figure 14(b). We also displayed the water saturation measured in core samples (red dots). We can find that there are several depth intervals which do not have optimum Archie's parameter and water saturation. This is attributed to the noisy permittivity especially in lower frequency channel of the multifrequency dielectric logging tool. As the SMD model measures the dispersive response of dielectric constant, it is sensitive to the permittivity at low-frequency channels in the scanner. There occurs interfacial polarization of fluids in a porous rock, and this phenomenon becomes more dominant as the frequency decreases. Thus, it is still challenging to make a stable measurement of permittivity at low frequency under the borehole condition.

To further the validation of the calculated Archie's parameter, we created crossplots showing correlation between the estimated Archie's parameter and water volume

(Figure 15). We could find exponentially decreasing relation from the crossplot with Archie's parameter and water volume. However, although we expected the negative correlation between the estimated Archie's parameter and clay volume as we demonstrated in the LR model examples, there is no tangible relation in the other crossplots of Figure 15 due to the inherited errors from the low-frequency channel measurement.

#### 4. Conclusion

We applied two different analytic models to demonstrate (1) which model is the most appropriate to calculate the dielectric permittivity in shale formations, and (2) which model provides more reliable Archie's parameter combined with dielectric permittivity logs. First, the LR model can be applied to the frequency range without the effect of interfacial polarization (over 1 GHz). As we tested with the standard CRIM with exponent 0.5, the model could not replicate the actual permittivity measured in a lab. Therefore, we used a combined model (LR model and Archie) to calculate the dielectric permittivity and water saturation using 1 GHz frequency component; where the exponent of the LR model is identical to the cementation (or tortuosity) factor of the Archie's equation. Throughout an application of the LR model, we compared the dielectric permittivity from the core plugs and the well logs. We then demonstrated that core plugs has smaller value of dielectric permittivity than the in situ permittivity. Given that the measurement on core plugs is made one year after the core being acquired, there might be loss of water volume in core samples. Fitting the response of the dielectric logging tool, we could estimate the water volume being required to replicate the same dielectric permittivity response. While fitting the CRIM, we estimated the optimum Archie's parameter. The estimated Archie's parameter shows inversely proportional relationship with clay volumes. We also employed the SMD model to estimate Archie's parameter and corresponding water saturation. We found a limitation of the model in that the SMD model, which could not generate the actual behavior of the permittivity dispersion (a sigmoidal dispersion curve) with varied frequencies, especially at the low-frequency channel. The SMD model is designed based on the spectral density model which is sensitive to the water volume. As the water volume becomes smaller (less than 7%), the behavior of the spectral density function also becomes unstable and it bears a greater level of uncertainty as we lower the target frequencies. Therefore, the SMD model is not applicable to the rock saturated with considerably small volume of water. In addition, estimated Archie's parameter from the SMD model is extremely sensitive in the lower frequency channels of the multifrequency dielectric logging tool, and it is not trivial task suppressing the low-frequency noises that are associated with the borehole conditions in the subsurface. Nevertheless, utilizing the response of the dielectric logging tool in the frequency range where interfacial polarization effect does not exist can provide an alternative to estimate water saturation in shale formations with relatively less conductive waters.

#### Data Availability

The raw and processed data presented in this paper and the materials required to reproduce these findings cannot be shared since authors do not have the legal right to release the data.

#### Conflicts of Interest

The authors declare that they have no conflicts of interest.

#### Acknowledgments

We thank Shell International Exploration & Production Inc. for permission to publish this work.

#### References

- [1] X. Nie, J. Lu, R. R. Djaroun, P. Wang, J. Li, and C. Zhang, "Oil content prediction of lacustrine organic-rich shale from wireline logs: a case study of intersalt reservoirs in the Qianjiang Sag, Jiangnan Basin, China," *Interpretation*, vol. 8, no. 3, pp. -SL79-SL88, 2020.
- [2] X. Nie, J. Lu, J. Chi, P. Wang, and C. Zhang, "Oil content prediction method based on the toc and porosity of organic-rich shales from wireline logs: a case study of lacustrine intersalt shale plays in Qianjiang Sag, Jiangnan Basin, China," *Geofluids*, vol. 2021, 8 pages, 2021.
- [3] L. Zhu, C. Zhang, Z. Zhang, and X. Zhou, "High-precision calculation of gas saturation in organic shale pores using an intelligent fusion algorithm and a multi-mineral model," *Advances in Geo-Energy Research*, vol. 4, no. 2, pp. 135-151, 2020.
- [4] Y. Cho, R. L. G. Jr, J. Lee, and C. Shin, "Linear-slip discrete fracture network model and multiscale seismic wave simulation," *Journal of Applied Geophysics*, vol. 164, pp. 140-152, 2019.
- [5] Y. Cho, R. L. Gibson Jr., M. Vasilyeva, and Y. Efendiev, "Generalized multiscale finite elements for simulation of elastic-wave propagation in fractured media," *Geophysics*, vol. 83, no. 1, pp. WA9-WA20, 2018.
- [6] A. Kadkhodaie and R. Rezaee, "A new correlation for water saturation calculation in gas shale reservoirs based on compensation of kerogen-clay conductivity," *Journal of Petroleum Science and Engineering*, vol. 146, pp. 932-939, 2016.
- [7] E. Sotelo, Y. Cho, and R. L. Gibson Jr., "Compliance estimation and multiscale seismic simulation of hydraulic fractures," *Interpretation*, vol. 6, no. 4, pp. T951-T965, 2018.
- [8] P. Tathed, Y. Han, and S. Misra, "Hydrocarbon saturation in upper wolfcamp shale formation," *Fuel*, vol. 219, pp. 375-388, 2018.
- [9] J. M. Donadille, O. Faivre, and R. Leech, *Fundamental of Dielectric Dispersion Logging*, Schlumberger, 2016.
- [10] M. T. Myers, "A pore geometry dependent dispersion model for the dielectric constant," in *SCA International Conference*, p. 9626, Washington DC, USA, 1996.
- [11] B. Zinszner and F. M. Pellerin, *Geoscientist Guide to Petrophysics*, IFP Publications, 2007.
- [12] M. A. Fam and M. B. Dusseault, "High-frequency complex permittivity of shales (0.02-1.30 GHz)," *Canadian Geotechnical Journal*, vol. 35, no. 3, pp. 524-531, 1998.

- [13] M. T. Myers, "A saturation interpretation model for the dielectric constant of shaly sands," in *SCA International Conference*, vol. 9118, San Antonio, TX, USA, 1991.
- [14] A. Revil, W. F. Woodruff, C. Torres-Verdin, and M. Prasad, "Complex conductivity tensor of anisotropic hydrocarbon-bearing shales and mudrocks," *Geophysics*, vol. 78, no. 6, pp. D403–D418, 2013.
- [15] N. V. Seleznev, R. L. Kleinberg, M. M. Herron et al., "Applications of dielectric dispersion logging to oil-shale reservoirs," in *SPWLA 52nd Annual Logging Symposium*, Colorado Springs, Colorado, 2011.
- [16] M. Josh and B. Clennell, "Broadband electrical properties of clays and shales: comparative investigations of remolded and preserved samples," *Geophysics*, vol. 80, no. 2, pp. D129–D143, 2015.
- [17] P. L. Baker and W. E. Kenyon, "Ept interpretation using textural model," in *SPWLA 26th Annual Logging Symposium*, Dallas, Texas, 1985.
- [18] A. R. V. Hipel, *Dielectric Materials and Their Applications*, Technology Press of M.I.T, 1954.
- [19] J. R. Birchak, C. G. Gardner, J. E. Hipp, and J. M. Victor, "High dielectric constant microwave probes for sensing soil moisture," *Proceedings of the IEEE*, vol. 62, no. 1, pp. 93–98, 1974.
- [20] D. Stroud, G. W. Milton, and B. R. De, "Analytical model for the dielectric response of brine-saturated rocks," *Physical Review B*, vol. 34, no. 8, pp. 5145–5153, 1986.
- [21] P. N. Sen, "Grain shape effects on dielectric and electrical properties of rocks," *Geophysics*, vol. 49, no. 5, pp. 586–587, 1984.
- [22] M. J. Manning and K. A. Athavale, "Dielectric properties of pyrite samples at 1100 MHz," *Geophysics*, vol. 51, no. 1, pp. 172–182, 1986.
- [23] D. S. Parasnis, "The electrical resistivity of some sulphide and oxide minerals and their ores," *Geophysical Prospecting*, vol. 4, no. 3, pp. 249–278, 1956.
- [24] J. Goncalves and J. Tremosa, "Estimating thermo-osmotic coefficients in clay-rocks: I. Theoretical insights," *Journal of Colloid and Interface Science*, vol. 342, no. 1, pp. 166–174, 2010.
- [25] O. A. L. D. Lima and M. M. Sharma, "A generalized Maxwell-Wagner theory for membrane polarization in shaly sands," *Geophysics*, vol. 57, no. 3, pp. 431–440, 1992.
- [26] Y. Jin, S. Misra, and D. Homan, "Estimation of in-situ wettability using multi-frequency electromagnetic measurements," in *Unconventional Resources Technology Conference (URTeC)*, pp. 4181–4199, 2020a.
- [27] Y. Jin, S. Misra, D. Homan, and J. Rasmus, "Effects of wettability of conductive particles on the multifrequency conductivity and permittivity of fluid-filled porous material," *Fuel*, vol. 268, article 117411, 2020.
- [28] Y. Han and S. Misra, "Bakken petroleum system characterization using dielectric-dispersion logs," *Petrophysics*, vol. 59, no. 2, pp. 201–217, 2018.
- [29] S. Misra, C. Torres-Verdin, D. Homan, and J. Rasmus, "Dispersive and directional electrical conductivity and dielectric permittivity of conductive-mineral-bearing samples derived from multifrequency tensor electromagnetic induction measurements," *Geophysics*, vol. 82, no. 4, pp. D211–D223, 2017.
- [30] B. D. Fuller and S. H. Ward, "Linear system description of the electrical parameters of rocks," *IEEE Transactions on Geoscience Electronics*, vol. 8, no. 1, pp. 7–18, 1970.
- [31] T. L. Chelidze, Y. Gueguen, and C. Ruffet, "Electrical spectroscopy of porous rocks: a review ? Ii. Experimental results and interpretation," *Geophysical Journal International*, vol. 137, no. 1, pp. 16–34, 1999.
- [32] A. A. Garrouch and M. M. Sharma, "Dielectric properties of partially saturated rocks," *Energy and Fuels*, vol. 9, no. 3, pp. 413–419, 1995.
- [33] P. Ligneul, F. Pairoys, P. Primiero, T. Zhang, and S. M. Al-Ofi, "Device for dielectric permittivity and resistivity high temperature measurement of rock samples," 2013, US Patent App. 13/173, 753.
- [34] N. Seleznev, T. Habashy, A. Boyd, and M. Hizem, "Technique for determining properties of earth formations using dielectric permittivity measurements," 2008, US Patent 7, 363, 160.
- [35] A. Stogryn, "Equations for calculating the dielectric constant of saline water (correspondence)," *IEEE Transactions on Microwave Theory and Techniques*, vol. 19, no. 8, pp. 733–736, 1971.
- [36] G. E. Archie, "Electrical resistivity log as an aid in determining some reservoir characteristics," *Transactions AIME*, vol. 146, no. 1, pp. 54–62, 1942.
- [37] R. J. Greaves, D. P. Lesmes, J. M. Lee, and M. N. Toksoz, "Velocity variations and water content estimated from multi-offset, ground-penetrating radar," *Geophysics*, vol. 61, no. 3, pp. 683–695, 1996.
- [38] R. Knight and A. Abad, "Rock/water interaction in dielectric properties: experiments with hydrophobic sandstones," *Geophysics*, vol. 60, no. 2, pp. 431–436, 1995.
- [39] R. Knight and A. Endres, "A new concept in modeling the dielectric response of sandstones: defining a wetted rock and bulk water system," *Geophysics*, vol. 55, no. 5, pp. 586–594, 1990.
- [40] K. Lichtenecker and K. Rother, "Derivation of the logarithmic mixing law for the general case of stationary flow," *Physikalische Zeitschrift*, vol. 32, pp. 255–260, 1931.
- [41] G. Mavko, T. Mukerji, and J. Dvorkin, *The Rock Physics Handbook*, Cambridge University Press, 1998.
- [42] D. L. Luffel, F. K. Guidry, and J. B. Curtis, "Evaluation of Devonian shale with new core and log analysis methods," *Journal of Petroleum Technology*, vol. 44, no. 11, pp. 1192–1197, 1992.

## Research Article

# Conformance Control for Tight Oil Cyclic Gas Injection Using Foam

Falin Wei,<sup>1</sup> Song Zhang,<sup>1</sup> Yilin Xi,<sup>2</sup> Zhouyuan Zhu ,<sup>2</sup> Chunming Xiong,<sup>1</sup> Chuanzhen Zang,<sup>3</sup> and Junjian Li <sup>2</sup>

<sup>1</sup>Research Institute of Petroleum Exploration & Development of PetroChina, Beijing, China

<sup>2</sup>China University of Petroleum (Beijing), China

<sup>3</sup>Xinjiang Oilfield Company of PetroChina, Karamay, China

Correspondence should be addressed to Zhouyuan Zhu; zhuzy02@cup.edu.cn

Received 29 September 2021; Revised 19 January 2022; Accepted 21 February 2022; Published 11 March 2022

Academic Editor: Kouqi Liu

Copyright © 2022 Falin Wei et al. This is an open access article distributed under the Creative Commons Attribution License, which permits unrestricted use, distribution, and reproduction in any medium, provided the original work is properly cited.

Cyclic gas injection has been proven to be an effective enhanced oil recovery (EOR) technique for tight oil reservoirs. During such processes, we expect recovery mechanisms such as oil swelling, oil viscosity reduction, vaporization, and pressure support, which highly relies on the successful conformance control of the injected gas. In this work, we present the numerical simulation study of using foam for improving the conformance control of cyclic gas injection in tight oil reservoir. We focus on improving two categories of conformance control problems using foam, making the injection profile for single well more evenly distributed and mitigating the gas breakthrough to adjacent wells through the connected hydraulic fractures in a multiwell setting. The simulation results show that foam has shown major impact in improving the gas conformance control in both cases. Typical recovery factor improvements are estimated to be up to 1% for lean gas injection in this tight oil reservoir. In conclusion, we have demonstrated the great potential of using foam to improve the conformance in tight oil cyclic gas injection process.

## 1. Introduction

Tight oil reservoirs are typically developed using horizontal wells completed with multistage hydraulic fracturing, which are produced using primary recovery as the most dominant recovery method. In this case, the recovery factors for tight oil reservoirs are typically relatively low. For example, the recovery factors of the Mahu tight oil reservoirs in Xinjiang Oilfield, PetroChina, are typically 15%-20%. This leaves large amount of unrecovered oil resources in the reservoir, considering the total volume of tight oil resources globally. Thus, there is an urgent need to explore possible EOR techniques for tight oil reservoirs.

Cyclic gas injection or gas huff and puff has been proposed to enhance the oil recovery in tight oil reservoirs [1-4]. It is implemented through injecting certain type of gas into the multistage hydraulically fractured horizontal well, soaked for some time, and produced back from the

same well. The injected gas could be hydrocarbon gas (lean or rich), carbon dioxide, or even nitrogen. And the process can be miscible or immiscible, depending on the reservoir pressure and the composition of the injected gas and the oil. The primary recovery mechanisms for such process are oil swelling, oil viscosity reduction, vaporization, and pressure support [5]. It is documented that several hundred wells have been converted to cyclic gas injection up to date in the Eagle Ford Shale play in the United States with pleasant performance reported. In recent years, due to the increasing level of greenhouse gas emission and global warming, CO<sub>2</sub> geologic sequestration has been proposed by various researchers. CO<sub>2</sub> wettability of seal and reservoir rocks and the implications for CO<sub>2</sub> sequestration have been studied [6]. The effect of wettability heterogeneity and reservoir temperature on CO<sub>2</sub> storage efficiency in deep saline aquifers has also been studied [7]. Researchers also studied the impact of injected water salinity and reservoir wettability

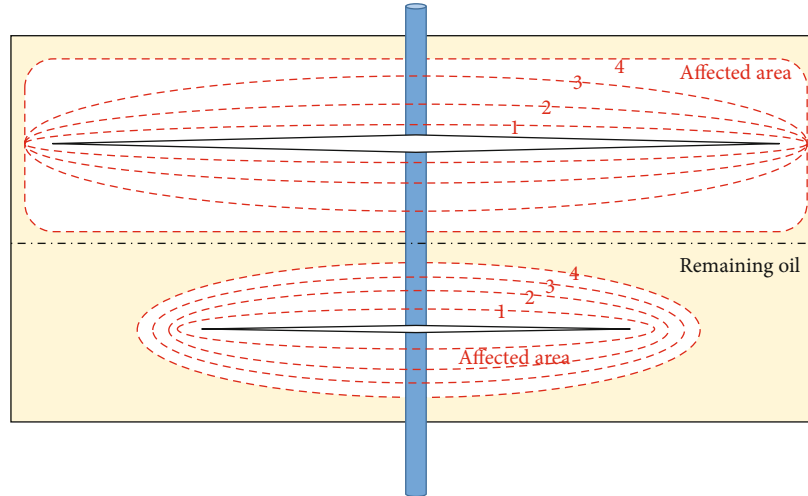


FIGURE 1: Preferential depletion for the more conductive long fracture, with much remaining oil unrecovered around the short and less conductive fracture, in a single well setting. Numbers 1-4 demonstrate the different numbers of cycles in cyclic gas injection process.

and heterogeneity on  $\text{CO}_2$  storage efficiency in saline aquifers [8, 9]. The influence of injection well configuration and rock wettability on  $\text{CO}_2$  sequestration has also been studied [10].

During any gas injection process, conformance of the injected gas is always an important issue for the success of such process. This is because gas is highly mobile as compared to the water and oil in the reservoir so that the adverse mobility ratio can lead to poor sweep and insufficient contact of the injected gas with the oil. On one hand, the injection/production profile for a single multistage fractured horizontal well is always unevenly distributed. This is due to the fact that each hydraulic fracture never grows to the same geometric size, shape, and conductivity, whether in a “plug and perf” or “open hole” setting. Such phenomenon has been well documented in reservoir studies implementing Production Logging Tool (PLT) surveys. This causes the reservoir volume around certain fractures to be preferentially drained in primary production and stimulated in cyclic gas injection process and vice versa. On the other hand, premature gas breakthrough to adjacent wells through the connected hydraulic fractures may happen in a multiwell setting. In the Bakken formation in the United States, it is reported that gas injected in a well under cyclic gas injection has broken through to the adjacent wells through the extended and connected hydraulic fractures between wells, i.e., “fracture hits.” In recent cyclic nitrogen injection field trials in the Mahu tight oil reservoirs in China, similar premature breakthrough to adjacent wells has been clearly observed. This causes the loss of the injected gas, insufficient contact of the injected gas with the oil, and the reservoir pressure to be inadequately raised in the injection period of the process. For both cases, the conformance issue could jeopardize the success of the tight oil cyclic gas injection process.

Foam has been demonstrated as an effective mobility control or conformance improvement agent for gas injection process in conventional oil reservoirs [11–13]. In a recent continuous gas injection field trial in a low permeability oil

reservoir in Texas, foam has been proven to be effective in diverting the injected gas to sweep the previously poorly swept region of the reservoir [14]. Based on this, we propose the use of foam to improve the conformance control in cyclic gas injection processes in tight oil reservoirs.

In this work, we present the numerical simulation study of using foam for improving the conformance control of cyclic gas injection in tight oil reservoir. We set up two categories of simulation problems: single well and multiwell cyclic gas injection processes. We test the effects of implementing gas injection with and without foam. We demonstrate that foam can help to make the injection profile for single well to be more evenly distributed and help to mitigate the amount of gas breakthrough to adjacent wells through the connected hydraulic fractures in a multiwell setting. The simulation results show that foam has shown major impact in improving the gas conformance control in both cases.

## 2. Methodology

*2.1. Foam Improvement Mechanisms.* We here demonstrate the foam improvement mechanisms for the two basic types of conformance control problems in tight oil cyclic gas injection process.

The first type is to make the injection profile for single well more evenly distributed for a single hydraulically fractured horizontal well. Figure 1 shows that preferential depletion occurs for the more conductive long fracture, with much remaining oil unrecovered around the short and less conductive fracture, in a single well setting. This remaining oil is an obvious target for enhanced oil recovery, if more gas can be directed into the short and less conductive fracture by using foam. We introduce the concept of oil exchange ratio for cyclic gas injection, which is defined as the incremental oil recovery divided by the amount of gas injected for each cycle. It measures the efficiency of a cyclic gas injection process, in which the injected gas causes certain amount of incremental oil to be recovered. Figure 2 shows

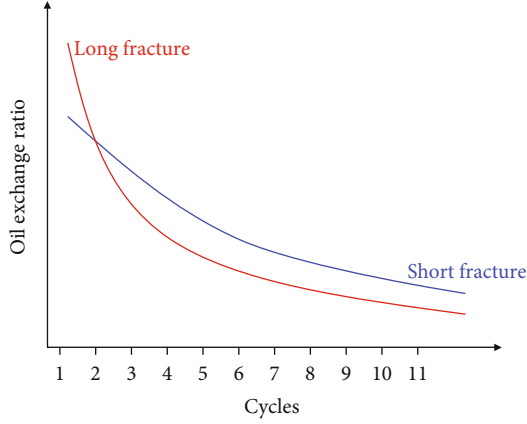


FIGURE 2: Oil exchange ratio for the long fracture and the short fracture for different cycles of the cyclic gas injection process in the tight oil reservoir.

the oil exchange ratio for the long fracture and the short fracture for different cycles of the cyclic gas injection process in tight oil reservoir. It can be seen that the oil exchange ratio for the long fracture decreases faster than that of the short fracture. This is due to the fact that the oil within the reservoir volume near the long fracture depletes faster as shown in Figure 1, because more gas has been injected into the long fracture. Using foam as profile control agent to divert the injected gas into the short fracture makes better use of the gas, since the short fracture has higher oil exchange ratio in the late cycles. In return, we would expect higher oil production rate and recovery.

The second type is to mitigate the gas breakthrough to adjacent wells through the connected hydraulic fractures in a multiwell setting. Figure 3 shows the potential gas breakthrough or channeling to adjacent producer due to connected hydraulic fractures in the cyclic gas injection process for hydraulically fractured horizontal wells in the tight oil reservoir. As gas breaks through to the adjacent well, the injected gas will be lost and has no effect on the recovery process. The reservoir pressure also cannot be raised due to such connected fracture. Using foam to block the gas flow in the connected fracture can efficiently reduce the amount of gas breaks through to the adjacent well. It also helps to raise the reservoir pressure to higher levels. In this way, more gas will be efficiently utilized for the cyclic gas injection process with more oil recovered.

**2.2. Simulation Model Setup.** The reservoir simulator we used in this study is CMG GEM [15]. We have developed a compositional fluid model for this simulation study, which is shown in Table 1. We use the standard Peng-Robinson equation of state for the flash calculation.

Over the years, the foam simulation model has two major categories: the mechanistic model and the empirical model. A mechanistic foam model allows direct simulation of foam creation, propagation, and coalescence, which can be observed in laboratory experiments [16, 17]. The empirical model, on the other hand, appears to be more appropriate for foam scoping studies and field pilot history matching

[15]. We have used the empirical model in CMG GEM to simulate the field scale tight oil foam-assisted cyclic gas injection problem. The basic assumption in this approach is that foam creation and coalescence occur rapidly relative to flow. Foam effects on gas mobility and sweep efficiency are handled via modified gas relative permeability curves, i.e., introducing a gas relative permeability or mobility reduction factor. Such factor and its corresponding terms are defined as follows [15]:

$$\begin{aligned}
 FM &= \frac{1}{1 + FM_{MOB} \times F_{Surf} \times F_{S_{oil}} \times F_{Cap} \times F_{GCP} \times F_{OMF} \times F_{Salt}} \\
 F_{Surf} &= \left( \frac{W_{Surf}}{FMSURF} \right)^{EPSURF} \\
 F_{S_{oil}} &= \left( \frac{FMOIL - S_{oil}}{FMOIL - FLOIL} \right)^{EPOIL} \\
 F_{Cap} &= \left( \frac{FMCAP}{N_C} \right)^{EPCAP} \\
 F_{GCP} &= \left( \frac{FMGCP - N_C}{FMGCP} \right)^{EPGCP} \\
 F_{OMF} &= \left( \frac{FMOMF - X_{oil}}{FMOMF} \right)^{EPOMF} \\
 F_{Salt} &= \left( \frac{W_{Salt} - FLSALT}{FMSALT - FLSALT} \right)^{EPSALT}
 \end{aligned} \tag{1}$$

where FM is the gas mobility reduction factor, FM<sub>MOB</sub> is the reference foam mobility reduction factor,  $W_{Surf}$  is the surfactant mole fraction in the water phase, FMSURF is critical mole fraction of surfactant component in the water phase, EPSURF is the exponent for surfactant contribution to FM calculation,  $S_{oil}$  is the oil saturation, FMOIL and FLOIL are the critical oil saturation and lower oil saturation values, EPOIL is the exponent for oil saturation contribution to FM calculation,  $N_C$  is the capillary number, FMCAP is the reference rheology capillary number, EPCAP is the exponent for capillary number contribution to FM calculation, FMGCP is the critical generation capillary number, EPGCP is the exponent for generation capillary number contribution to FM calculation,  $X_{oil}$  is the mole fraction of a certain component in the oil phase, FMOMF is the critical oil mole fraction for a certain component, EPOMF is the exponent for the contribution of the a certain oil phase component to FM calculation,  $W_{Salt}$  is the salt mole fraction in the water phase, FMSALT and FLSALT are critical salt mole fraction the and lower salt mole fraction, and EPSALT is the exponent for salt contribution to FM calculation. The corresponding values for these parameters in our simulation study are defined in Table 2.

Figure 4 further shows the relative permeability curves implemented in this study. Gas relative permeability  $k_{rg}$

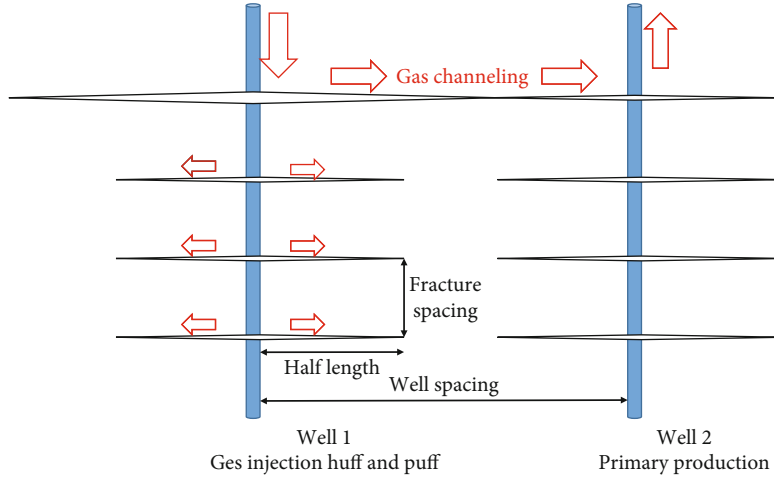


FIGURE 3: Gas breakthrough to adjacent producer due to connected hydraulic fractures in the cyclic gas injection process for hydraulically fractured horizontal wells in the tight oil reservoir.

TABLE 1: Compositional model for the simulation study.

Component name	Initial mole fraction	Critical temperature (K)	Critical pressure (bar)	Acentric factor	Molecular weight (g/mole)
C1	0.5	190.6	46.0421	0.0130	16.04
C2-4	0.03	369.8	42.4957	0.1524	44.10
C5-7	0.07	507.4	30.1239	0.3007	86.18
C8-12	0.2	617.7	20.9641	0.4885	142.29
C13-18	0.15	705.6	13.7903	0.6500	206.00
C19+	0.05	766.7	11.1660	0.8500	282.00

TABLE 2: Parameters for the empirical foam model for the simulation study.

Parameter name	Value	Parameter name	Value	Parameter name	Value
FMMOB	1000.0	FLOIL	0.2	EPGCP	0.5
FMSURF	0.00005	EPOIL	1.0	EPOMF	3
EPSURF	1.0	FMCAP	2.0e-4	FLSALT	1.0e-3
FMOIL	1.0	EPCAP	0.5	FMSALT	2.0e-3
$S_{oil}$	0.545	FMGCP	2.0e-4	EPSALT	-3.0

values are reduced by a factor of 0.1 in the case of strong foam as compared to the case of no foam.

The reservoir models are designed to be a generic thin box-shaped tight oil reservoir with Cartesian grid blocks. “Plug and perf” well completions are assumed in this study. We implement planar-shaped hydraulic fractures at the locations of each fracture cluster (perforation), perpendicular to the hydraulic well trajectory. Logarithmic local grid refinements are used to refine the grids around the planar hydraulic fractures. We assume single porosity reservoir in this simulation study, typically with homogeneous permeability of 0.1 mD and porosity of 0.12. For the hydraulic fractures, we assume they are equally spaced according to the corresponding fracture spacing. And we set the permeability of the inner most line of grid blocks to such high values that the product of this permeability and the width of the inner

most grid block equals the specified conductivity of the hydraulic fracture. The detailed reservoir parameters for each simulation case will be presented in the later section.

### 3. Results

**3.1. Single Well with Two Hydraulic Fractures.** We first present the case of single well with only two hydraulic fractures to demonstrate the capability of foam to create a more evenly distributed injection profile for a single hydraulically fractured horizontal well. The reservoir is 400 m wide, 80 m long, and 10.5 m thick. We discretize the reservoir using Cartesian grid ( $100 \times 20 \times 1$ ), with local grid refinements around the hydraulic fractures. We implement such fine grid blocks so that the typically observed numerical dispersion error in simulating gas injection process will be controlled

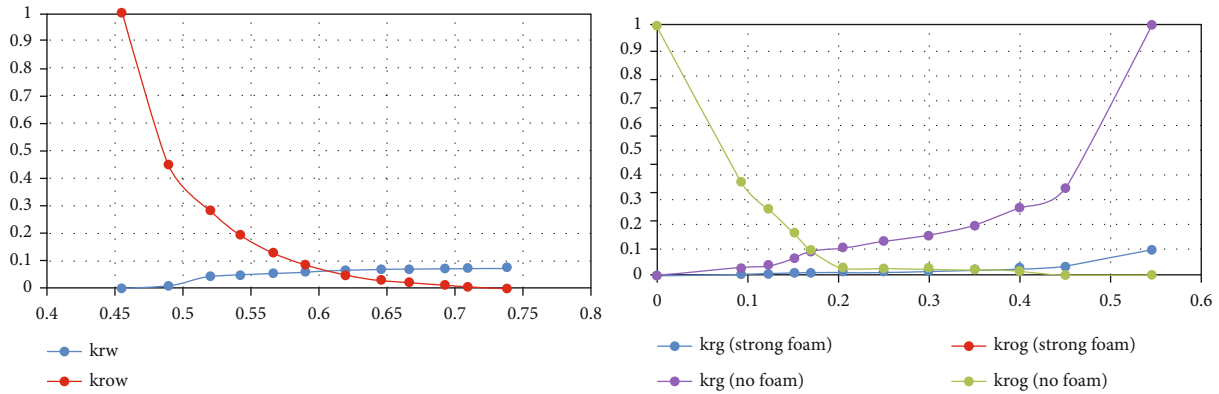


FIGURE 4: Relative permeability curves implemented in this simulation study, with gas relative permeability  $k_{r_g}$  values reduced by a factor of 0.1 in the case of strong foam as compared to the case of no foam.

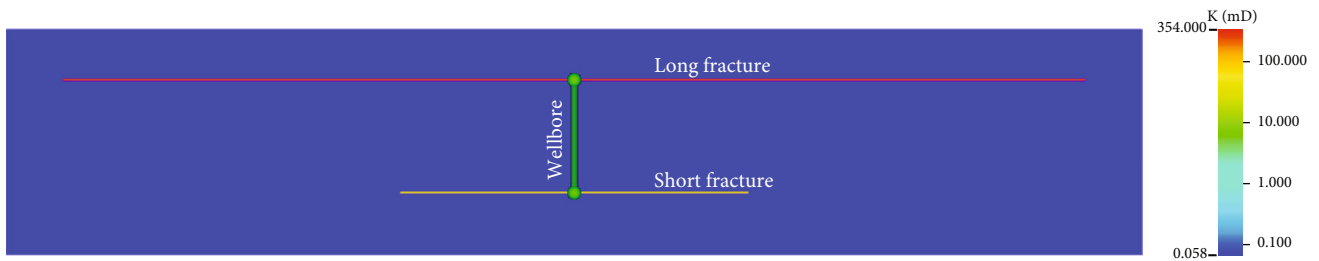


FIGURE 5: Permeability distribution for the simulation case of single well with two hydraulic fractures. The long fracture has half-length of 180 m and fracture conductivity of 240 mD-m. The short fracture has half-length of 60 m and fracture conductivity of 80 mD-m.

within a certain level. In this way, the simulation accuracy is guaranteed. Figure 5 shows the permeability distribution for the simulation case of single well with only two hydraulic fractures. The long fracture has half-length of 180 m and fracture conductivity of 240 mD-m. The short fracture has half-length of 60 m and fracture conductivity of 80 mD-m. The oil compositional model is described in Table 1. We inject a lean gas in the cyclic gas injection process with 100% C1. The initial reservoir temperature is 70°C, and the initial reservoir pressure is 25.5 MPa. The other simulation settings are the same as described in the previous section.

We start the process at the time of 2019-01-01 with 6 years of primary production, followed by 2 cycles of cyclic gas injection without foam. During primary production and the producing back period of cyclic gas injection, we set the single well maximum liquid rate to be 45 m<sup>3</sup>/day and minimum bottom hole pressure to be 10 MPa. In each cycle, we inject gas for 2 months at a rate of 20000 m<sup>3</sup>/day, directly followed by 10 months of producing back. Beginning at the 3<sup>rd</sup> cycle, we either continue with pure cyclic gas injection without foam or start the foam-assisted cyclic gas injection process by coinjecting the surfactant solution with the gas. In both cases, the amount of gas injected is the same, which is 20000 m<sup>3</sup>/day for 2 months. In the foam case, within each cycle, we inject an extra stream of surfactant solution with the rate of 5 m<sup>3</sup>/day and surfactant mole fraction of 0.3% for 1 month. We continue the process for a total of 9 cycles.

Figure 6 shows the results of total cumulative oil production for the entire well with and without foam, cumulative oil production from the long fracture with and without foam, and cumulative oil production from the short fracture with and without foam. It can be clearly seen that the cumulative oil production for the entire well has been increased for the foam case. And the major contribution for this increase comes from the short hydraulic fracture. For the long hydraulic fracture, the oil production actually decreases slightly. Figure 7 further shows the cumulative gas injection into the long fracture with and without foam and cumulative gas injection into the short fracture with and without foam. As envisioned previously in the mechanism sector, we observe increased gas injection into the short fracture with lower fracture conductivity and shorter fracture half-length, and vice versa. Figure 8 shows the average reservoir pressure for the cases with foam and without foam. The extra stream of injected surfactant solution in the case of foam injection does not cause the reservoir pressure to increase to a large extent. Figure 9 further shows the pressure at the end of gas injection during the 9<sup>th</sup> cycle, for the case with and without foam. It can be seen that more high pressure gradient exists around the short hydraulic fracture in the foam case as compared to the case without foam. This also indicates that more gas is injected into the short hydraulic fracture with the aid of foam. Thus, by injecting foam, we successfully improve the injection profile for this single well problem so that the gas injection amount is more

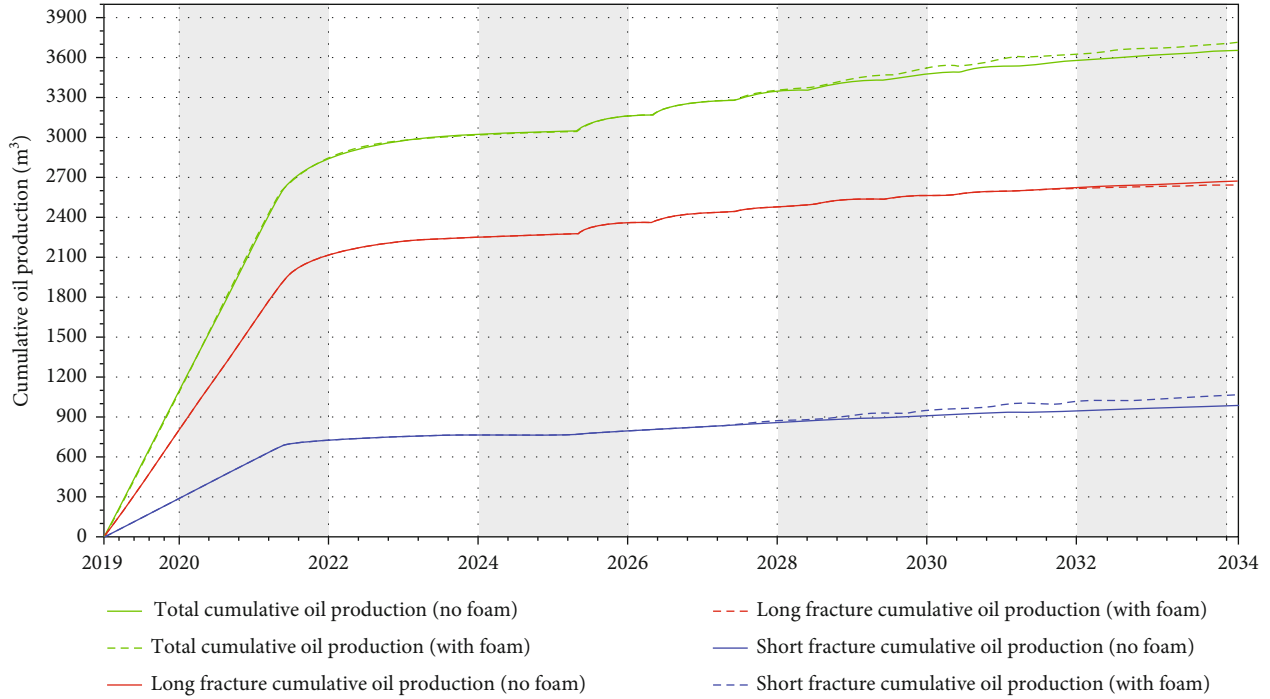


FIGURE 6: Total cumulative oil production for the entire well with and without foam, cumulative oil production from the long hydraulic fracture with and without foam, and cumulative oil production from the short hydraulic fracture with and without foam.

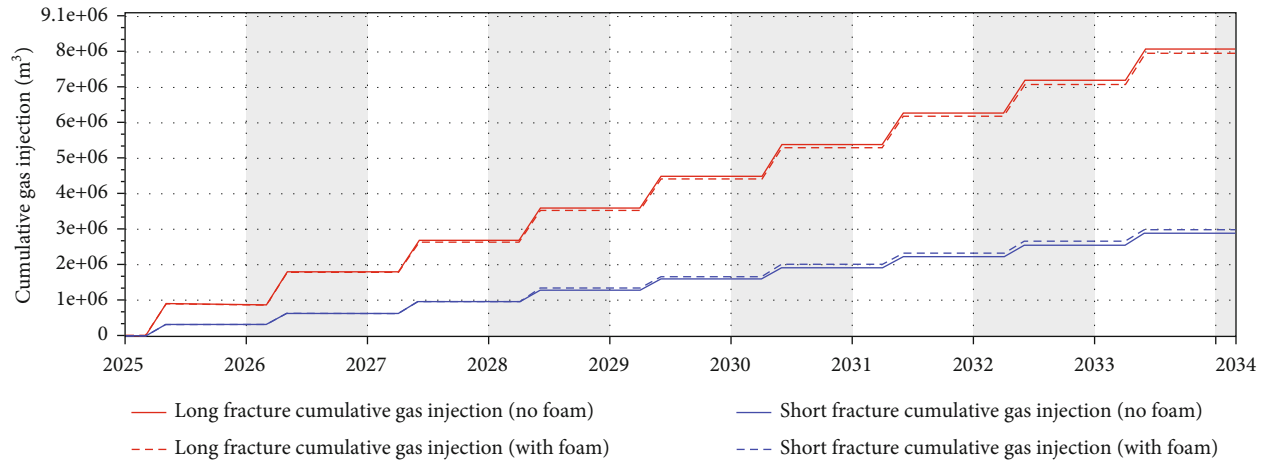


FIGURE 7: Cumulative gas injection into the long hydraulic fracture with and without foam and cumulative gas injection into the short hydraulic fracture with and without foam.

evenly distributed among different hydraulic fractures. In this case, the oil recovery factor for primary depletion stage is 17.2%. The ultimate recovery factor for the case with pure cyclic gas injection is 20.6%. And the ultimate recovery factor for the case with foam-assisted cyclic gas injection is 21.0%.

**3.2. Single Well with Multiple Fractures.** Second, we present the case for a single well with multiple hydraulic fractures. This case is also intended to demonstrate such more evenly distributed injection profile for a single horizontal well. The reservoir is 400 m wide, 960 m long, and 10.5 m thick.

We also discretize the reservoir using Cartesian grid ( $100 \times 240 \times 1$ ), with local grid refinements around the hydraulic fractures. The grid block sizes are small so that the numerical dispersion is not significant. Figure 10 shows the permeability distribution for the simulation case of single well with multiple hydraulic fractures. The long fractures have half-length of 180 m and conductivity of 240 mD-m. The short fractures have half-length of 60 m and conductivity of 80 mD-m. Again, we inject the lean gas which is 100% C1. The initial reservoir temperature is 70°C, and the initial reservoir pressure is 25.5 MPa. The other simulation settings are the same as described previously.

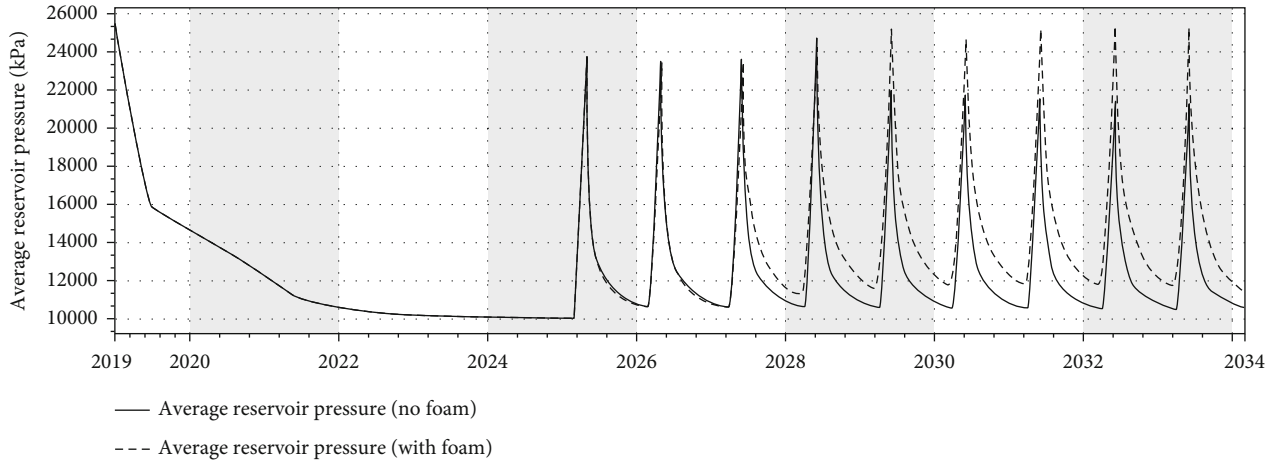
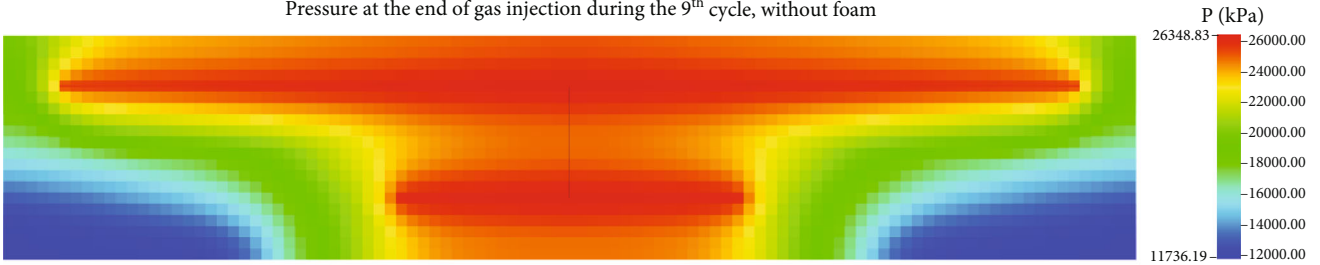


FIGURE 8: Average reservoir pressure for the cases with foam and without foam.

Pressure at the end of gas injection during the 9<sup>th</sup> cycle, without foam



Pressure at the end of gas injection during the 9<sup>th</sup> cycle, with foam

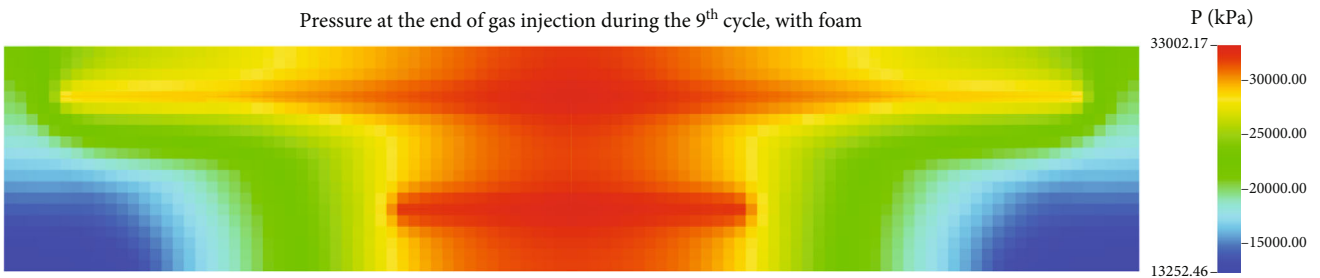


FIGURE 9: Pressure at the end of gas injection during the 9<sup>th</sup> cycle (2033-06-01), for the simulation case with and without foam.

We again start the process with 6 years of primary production, followed by 2 cycles of cyclic gas injection without foam. During primary production and the producing back period of cyclic gas injection, we set the single well maximum liquid rate to be 45 m<sup>3</sup>/day and minimum bottom hole pressure to be 10 MPa. In each cycle, we inject gas for 2 months at a rate of 240000 m<sup>3</sup>/day, directly followed by 10 months of producing back. Beginning at the 3<sup>rd</sup> cycle, we either continue with pure cyclic gas injection without foam or start the foam-assisted cyclic gas injection process by coinjecting the surfactant solutions. In both cases, the amount of gas injected is the same, which is 240000 m<sup>3</sup>/day for 2 months. In the foam case, within each cycle, we inject an extra stream of surfactant solution with the rate of 60 m<sup>3</sup>/day and surfactant mole fraction of 0.3% for 1 month. We continue the process for a total of 4 cycles. We

extend the production time period a few months longer for the case with foam, so that its average reservoir pressure drops to the similar level as the case without foam.

Figure 11 shows the cumulative oil production for the entire well with and without foam. Figure 12 shows the average reservoir pressure for the cases with foam and without foam. Figure 13 shows the cumulative oil production from the short hydraulic fractures with and without foam. Figure 14 shows the cumulative oil production from the long hydraulic fractures with and without foam. By extending the production time period, we let the average reservoir pressure for the foam case to drop to the similar level as the case without foam. It can be seen that the cumulative oil production for the entire well has been increased for the foam case. And the major contribution for this increase comes from the short hydraulic fracture. The oil production from the

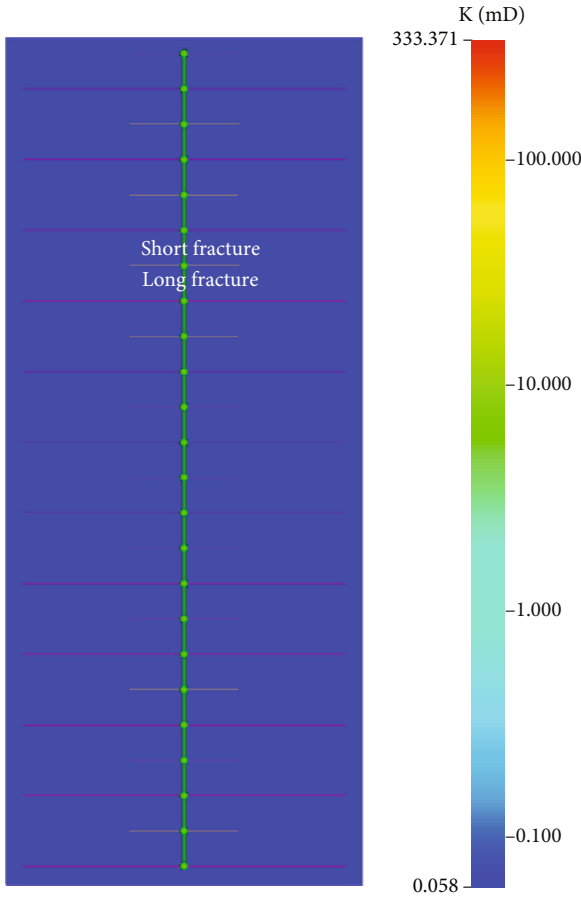


FIGURE 10: Permeability distribution for the simulation case of single well with multiple hydraulic fractures. The long fractures have half-length of 180 m and fracture conductivity of 240 mD·m. The short fractures have half-length of 60 m and fracture conductivity of 80 mD·m.

long hydraulic fractures actually decreases slightly. Figure 15 further shows the cumulative gas injection into the long and short hydraulic fractures with and without foam. We again observe increased gas injection into the short fractures with lower fracture conductivity and shorter fracture half-length, and vice versa. By injecting foam, we improve the injection profile for the multiple fracture single well problem so that the gas injection is more evenly distributed among different hydraulic fractures in cyclic gas injection process. In this case, the oil recovery factor for primary depletion stage is 17.3%. The ultimate recovery factor for the case with pure cyclic gas injection is 18.8%. And the ultimate recovery factor for the case with foam-assisted cyclic gas injection is 19.0%.

**3.3. Dual Well with Connected Fracture.** Third, we present the case for dual well with connected hydraulic fracture between the wells. This case is intended to show that foam can mitigate the gas breakthrough to adjacent wells through the connected hydraulic fractures in a multiwell setting. The reservoir is 800 m wide, 160 m long, and 10.5 m thick. We also discretize the reservoir using Cartesian grid

( $200 \times 40 \times 1$ ), with local grid refinements around the hydraulic fractures. The grid block sizes are small enough so that the numerical dispersion is controlled within a certain level. Figure 16 shows the permeability distribution for the simulation case of dual well with connected fracture. The single long fractures has a total length of 600 m and conductivity of 240 mD·m. The short fractures have half-length of 100 m and conductivity of 80 mD·m. Again, we inject the lean gas which is 100% C1. The initial reservoir temperature is 70°C, and the initial reservoir pressure is 25.5 MPa. The other simulation settings are the same as described previously.

In our simulation, we have Producer 1 produced with cyclic gas injection in the late period, while Producer 2 is under primary depletion for the entire simulation. The Producer 1 starts with 6 years of primary production, followed by 2 cycles of cyclic gas injection without foam. During primary production and the producing back period of cyclic gas injection, we set the single well maximum liquid rate to be 45 m<sup>3</sup>/day and minimum bottom hole pressure to be 10 MPa. In each cycle, we inject gas for 2 months at a rate of 40000 m<sup>3</sup>/day, directly followed by 10 months of producing back. Beginning at the 3<sup>rd</sup> cycle, we either continue with pure cyclic gas injection without foam or start the foam-assisted cyclic gas injection process by coinjecting the surfactant solutions. In both cases, the amount of gas injected is the same, which is 40000 m<sup>3</sup>/day for 2 months. In the foam case, within each cycle, we inject an extra stream of surfactant solution with the rate of 10 m<sup>3</sup>/day and surfactant mole fraction of 0.3% for 1 month. We continue the process for a total of 7 cycles.

Figure 17 shows the cumulative gas production for Producer 2 from the long fracture and the short fractures, with and without foam. It can be seen that due to the existence of the long fracture which connects the Producer 1 and Producer 2, large amount of gas injected into the Producer 1 gets produced back to surface from the Producer 2 by traveling through the long fracture. This gas recycling is ineffective for the cyclic gas injection EOR process. With the aid of foam, we are able to create flow resistance within the long fracture that hinders the flow of gas from Producer 1 to Producer 2 through the high conductivity long fracture. In this way, the gas production for Producer 2 from the perforation connecting to the long fracture is much reduced. Figure 18 further shows the bottom hole pressure for Producer 1 with and without foam. Through the use of foam, the injected gas is better contained within the reservoir volume around Producer 1. Thus, the bottom hole pressure can be raised to a higher value, which is of great importance to the success of cyclic gas injection process since high reservoir pressure is the key driving force for compaction drive and solution gas drive during the producing back period. Figure 19 shows the  $F_{\text{Surf}}$  distribution for the simulation case with foam. It shows the area where foam-induced flow resistance exists. It can be seen that the long fracture has been partially filled with surfactant, thus creating major flow resistance inside. Finally, Figure 20 shows the field cumulative oil production for the simulation cases with foam and without foam. In this case, the oil recovery factor for the primary depletion stage is 16.1%. The ultimate recovery factor for the case with pure

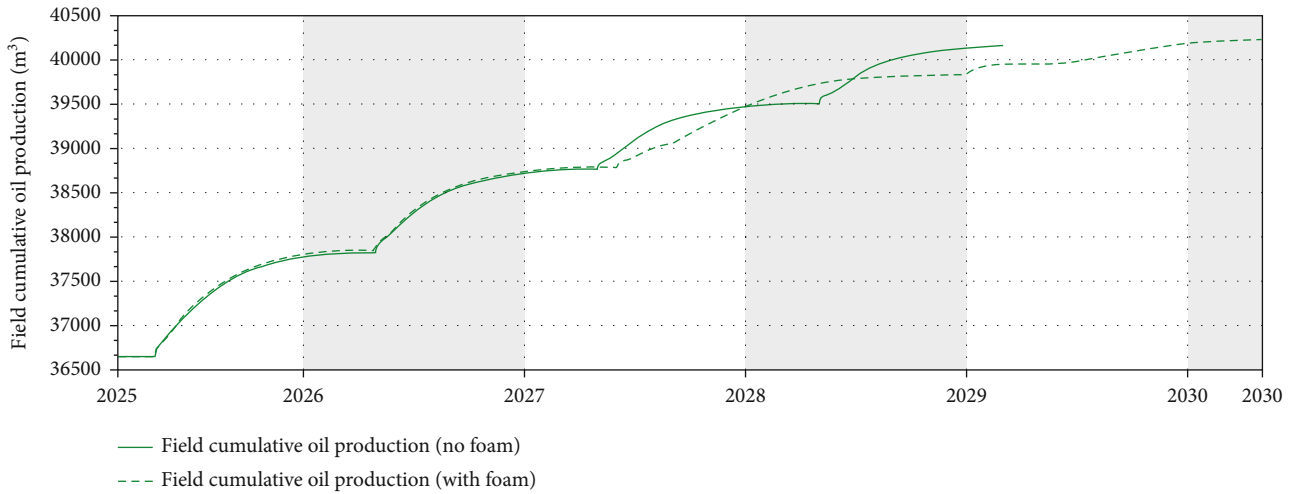


FIGURE 11: Cumulative oil production for the entire well with and without foam.

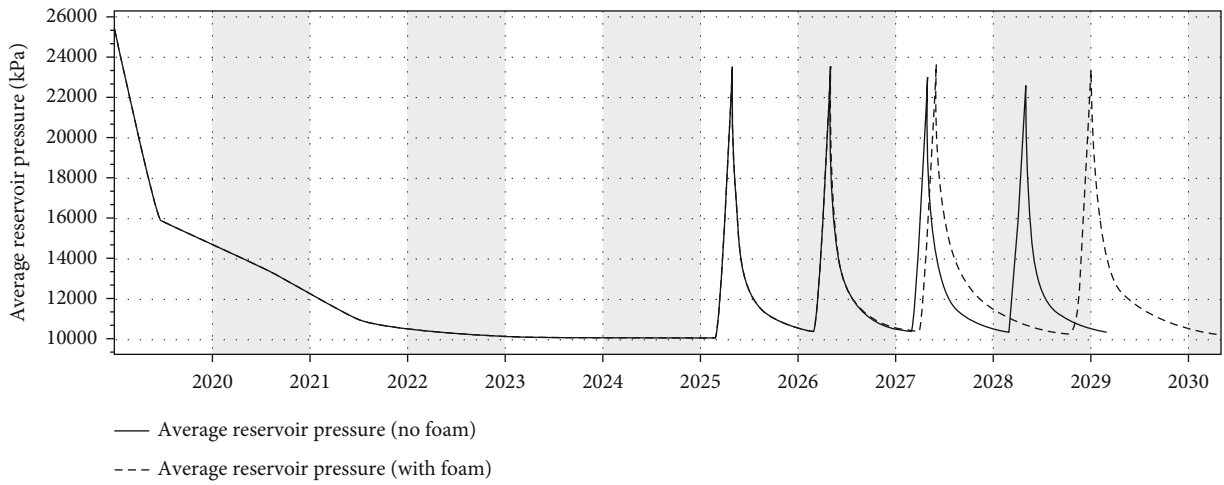


FIGURE 12: Average reservoir pressure for the cases with foam and without foam.

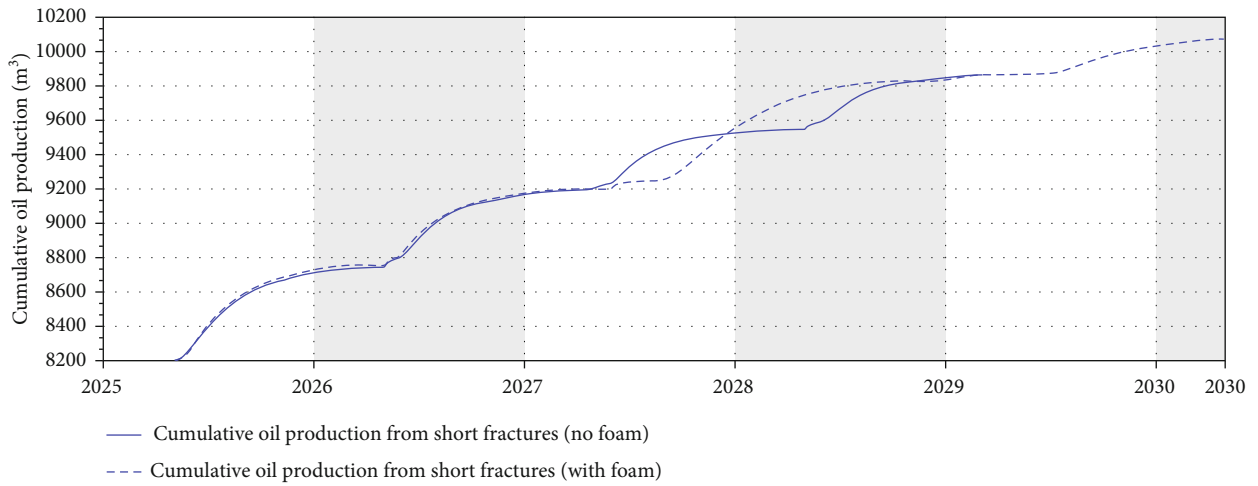


FIGURE 13: Cumulative oil production from the short hydraulic fractures with and without foam.

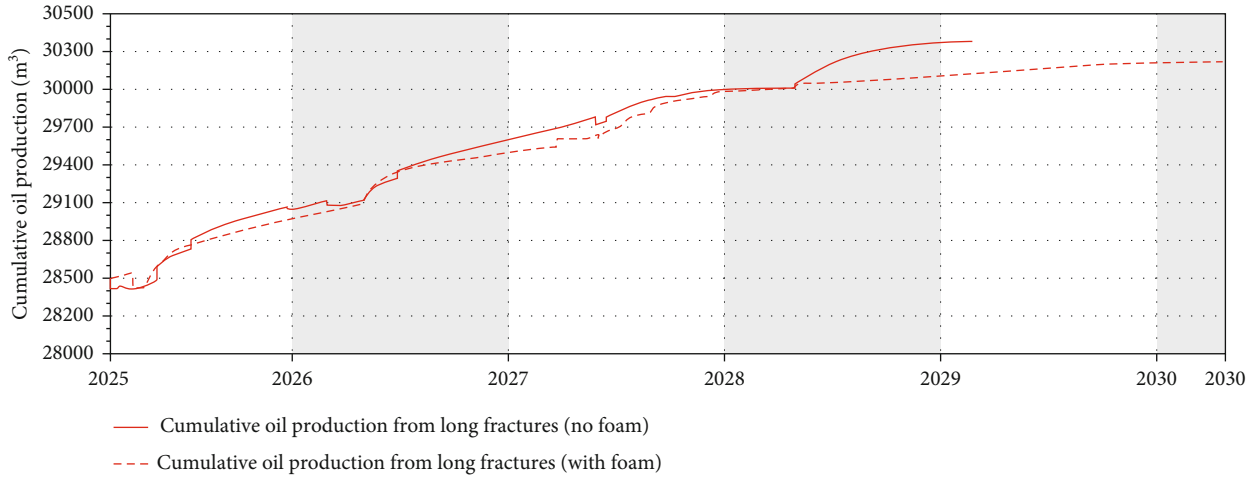


FIGURE 14: Cumulative oil production from the long hydraulic fractures with and without foam.

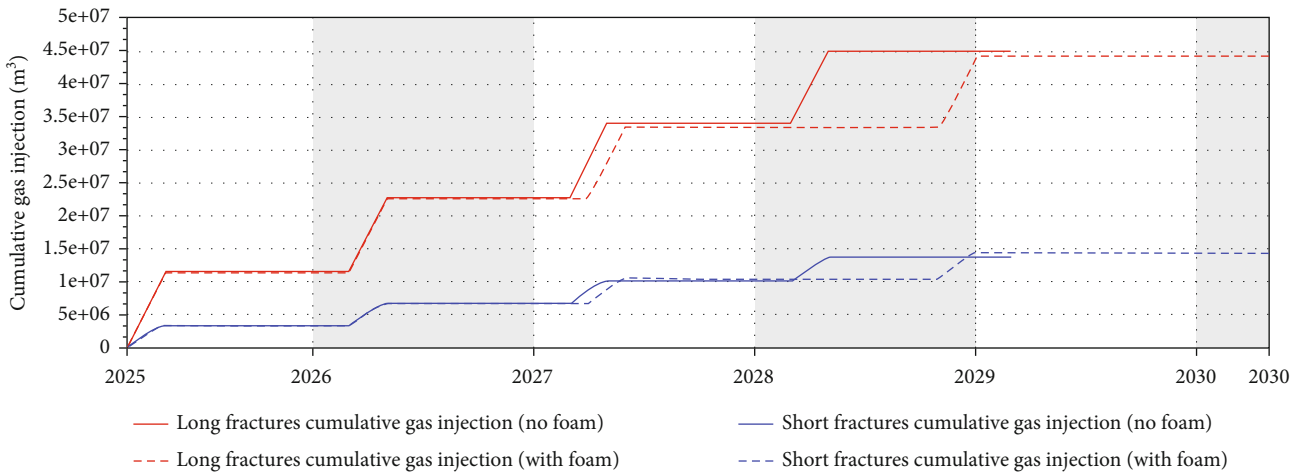


FIGURE 15: Cumulative gas injection into the hydraulic long fractures with and without foam and cumulative gas injection into the short hydraulic fractures with and without foam.

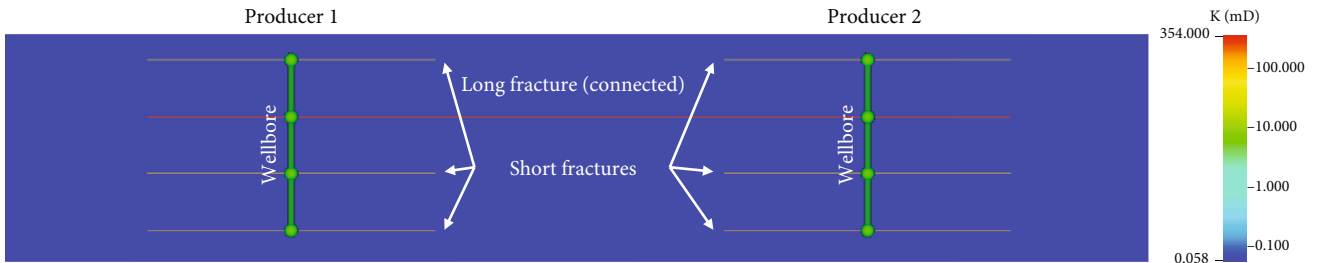


FIGURE 16: Permeability distribution for the simulation case of dual well with connected hydraulic fracture. The long fractures have total length of 600 m and fracture conductivity of 240 mD-m. The short fractures have half-length of 100 m and fracture conductivity of 80 mD-m.

cyclic gas injection is 19.3%. And the ultimate recovery factor for the case with foam-assisted cyclic gas injection is 19.6%. Foam-assisted cyclic gas injection process has achieved higher cumulative oil production than the case without foam.

#### 4. Discussion

We have demonstrated through our simulation studies that foam can improve the performance of cyclic gas injection process in tight oil reservoirs through the two mechanisms

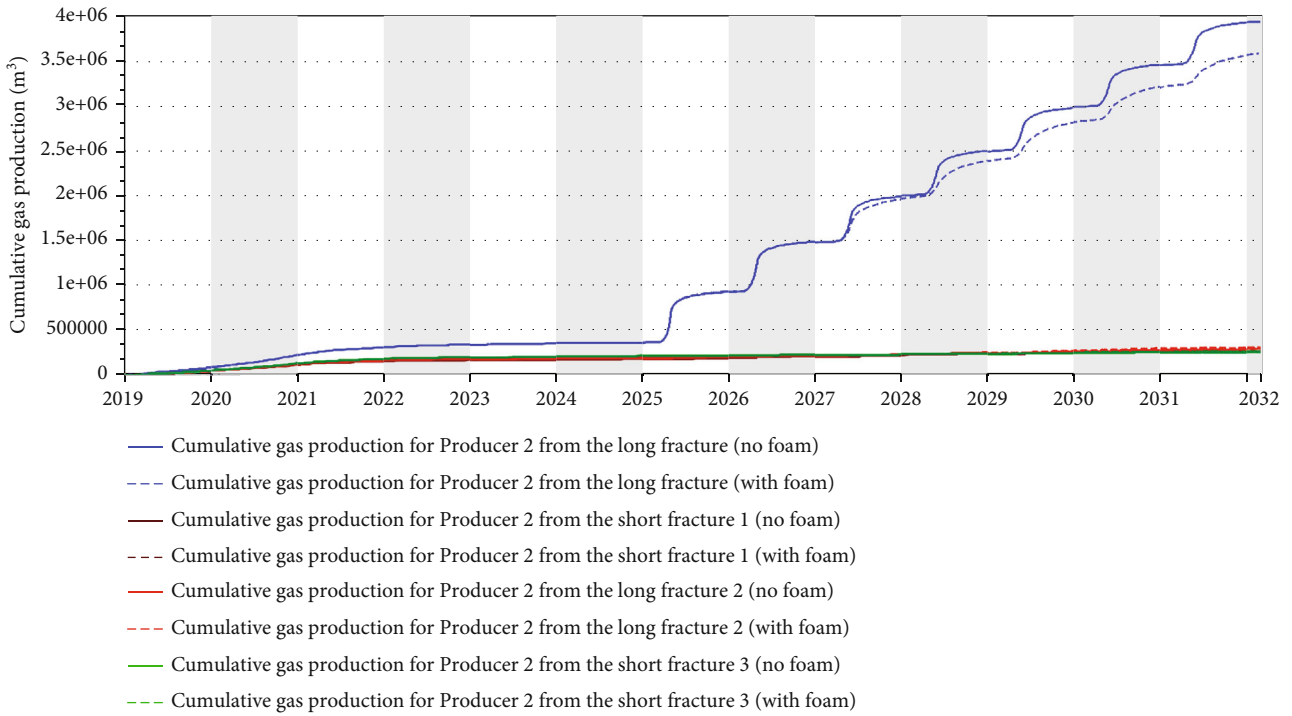


FIGURE 17: Cumulative gas production for Producer 2 from the long fracture and the short fractures, with and without foam.

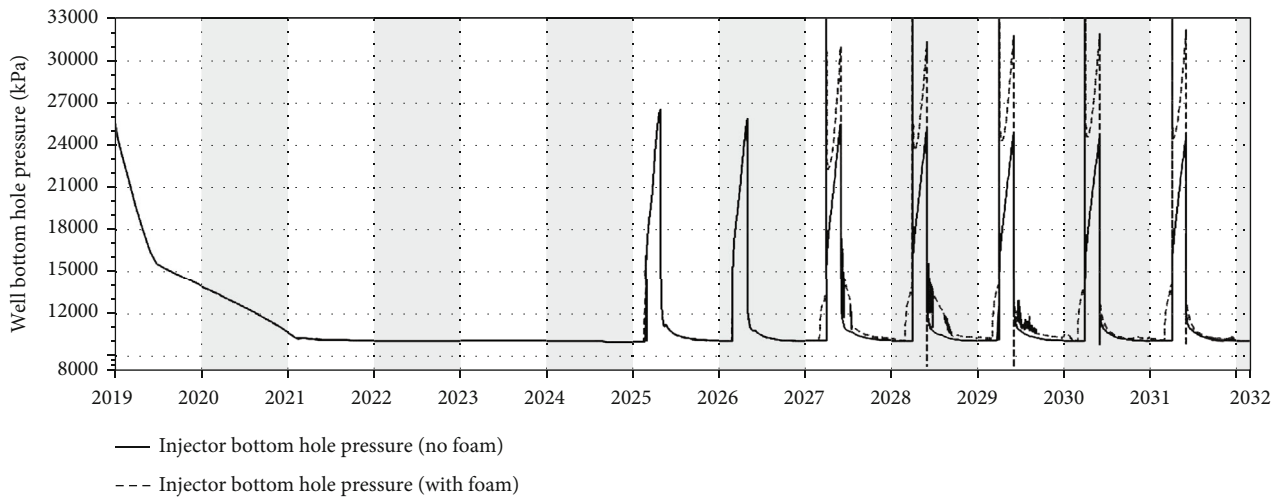


FIGURE 18: Bottom hole pressure for Producer 1 with and without foam.

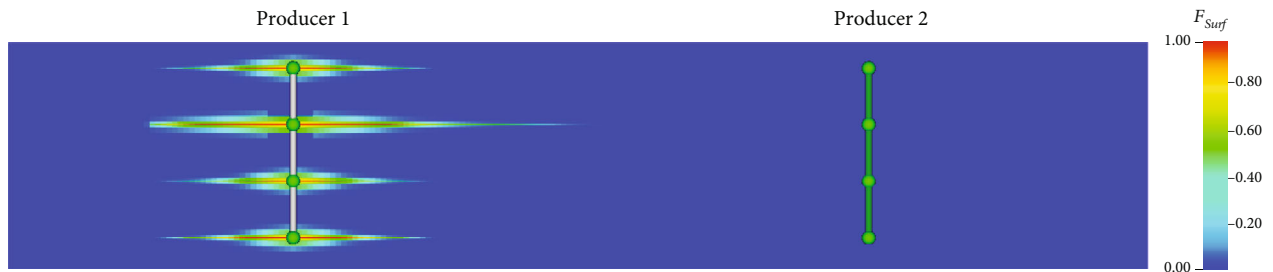


FIGURE 19:  $F_{Surf}$  distribution for the simulation case with foam showing the area where foam-induced flow resistance exists.

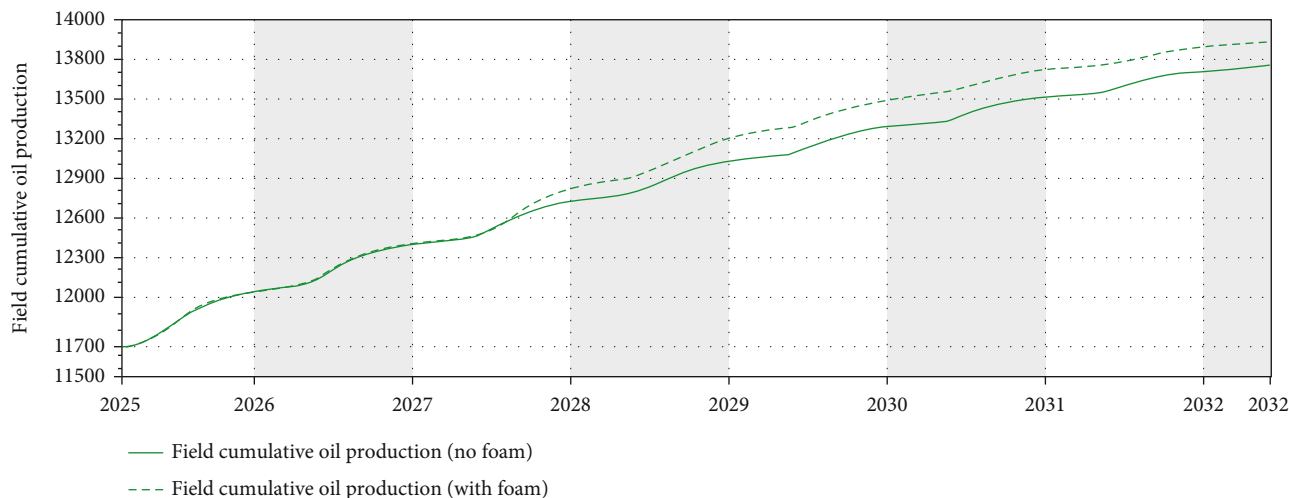


FIGURE 20: Field cumulative oil production for the simulation cases with foam and without foam.

discussed in this work. Further work includes and is not limited to laboratory experiments to screen the suitable surfactants for tight oil foaming purposes, large-scale 3D laboratory experiment to test the performance of the process, and single well or multiwell field pilots to demonstrate the actual performance of foam-assisted cyclic gas injection process.

## 5. Conclusion

In this work, we explore the use of foam for improving the conformance control and sweep of cyclic gas injection process. We conduct numerical simulation for the currently producing for a generic tight oil reservoir. We show the effect of foam in improving the conformance of cyclic gas injection for basic categories of conformance control problems, i.e., making the injection profile for single well more evenly distributed and mitigating the gas breakthrough to adjacent wells through the connected hydraulic fractures in a multiwell setting. The simulation results show that foam has demonstrated clear improvement in the gas conformance control in both cases. Incremental recovery factors are estimated to be up to 1% for lean gas injection in this tight oil reservoir. In conclusion, through the numerical simulation of the foam-assisted cyclic gas injection for the tight oil reservoir in this study, we have demonstrated the great potential of using foam to improve the conformance in tight oil cyclic gas injection process.

## Data Availability

The data used to support the findings of this study are available from the corresponding author upon request.

## Conflicts of Interest

The authors declare that they have no conflicts of interest.

## Acknowledgments

We appreciate PetroChina for permission to publish this work. This work was supported by “CNPC major technology project 2019E-2607” research and application of key technologies for the exploration and development of continental mid-high maturity shale oil. This work was also supported by “CNPC major technology project ks2020-01-09” research on key technology of enhanced oil recovery in low permeability-tight oil reservoirs.

## References

- [1] P. L. McGuire, R. Okuno, T. L. Gould, and L. W. Lake, “Ethane-based EOR: an innovative and profitable EOR opportunity for a low price environment,” in *SPE Improved Oil Recovery Conference*, Tulsa, Oklahoma, USA, 2016.
- [2] G. Grinestaff, C. Barden, J. Miller, W. Franklin, C. Barden, and E. Ding, “Evaluation of Eagle Ford cyclic gas injection EOR: field results and economics,” in *SPE Improved Oil Recovery Conference*, Virtual, 2020.
- [3] A. Fragoso, T. G. Harding, K. Selvan, and R. Aguilera, “Coupling of wellbore and surface-facilities models with reservoir simulation to optimize recovery of liquids from shale reservoirs,” *SPE Reservoir Evaluation & Engineering*, vol. 21, no. 4, pp. 1058–1082, 2018.
- [4] D. Orozco, A. Fragoso, K. Selvan, G. Noble, and R. Aguilera, “Eagle ford huff ‘n’ puff gas-injection pilot: comparison of reservoir-simulation, material balance, and real performance of the pilot well,” *SPE Reservoir Evaluation & Engineering*, vol. 23, no. 1, pp. 247–260, 2020.
- [5] B. T. Hoffman and D. Reichhardt, “Quantitative evaluation of recovery mechanisms for huff-n-puff gas injection in unconventional reservoirs,” in *SPE/AAPG/SEG Unconventional Resources Technology Conference*, Denver, Colorado, USA, 2019.
- [6] S. Iglauer, C. H. Pentland, and A. Busch, “CO<sub>2</sub> wettability of seal and reservoir rocks and the implications for carbon sequestration,” *Water Resources Research*, vol. 51, pp. 729–774, 2014.

- [7] E. A. Al-Khdheawi, S. Vialle, A. Barifcani, M. Sarmadivaleh, and S. Iglauer, "Effect of wettability heterogeneity and reservoir temperature on CO<sub>2</sub> storage efficiency in deep saline aquifers," *International Journal of Greenhouse Gas Control*, vol. 68, pp. 216–229, 2018.
- [8] E. A. Al-Khdheawi, S. Vialle, A. Barifcani, M. Sarmadivaleh, and S. Iglauer, "Impact of injected water salinity on CO<sub>2</sub> storage efficiency in homogenous reservoirs," *The APPEA Journal*, vol. 58, no. 1, p. 44, 2018.
- [9] E. A. Al-Khdheawi, S. Vialle, A. Barifcani, M. Sarmadivaleh, and S. Iglauer, "Impact of reservoir wettability and heterogeneity on CO<sub>2</sub>-plume migration and trapping capacity," *International Journal of Greenhouse Gas Control*, vol. 58, pp. 142–158, 2017.
- [10] E. A. Al-Khdheawi, S. Vialle, A. Barifcani, M. Sarmadivaleh, and S. Iglauer, "Influence of injection well configuration and rock wettability on CO<sub>2</sub> plume behaviour and CO<sub>2</sub> trapping capacity in heterogeneous reservoirs," *Journal of Natural Gas Science and Engineering*, vol. 43, pp. 190–206, 2017.
- [11] E. Delamaide, A. Cuenca, and C. Max, "State of the art review of the steam foam process," in *SPE Latin America and Caribbean Heavy and Extra Heavy Oil Conference*, Lima, Peru, 2016.
- [12] A. Katiyar, A. Hassanzadeh, P. Patil et al., "Successful field implementation of CO<sub>2</sub>-foam injection for conformance enhancement in the EVGSAU field in the Permian Basin," in *SPE Improved Oil Recovery Conference*, Virtual, 2020.
- [13] M. Mirzaei, D. Kumar, D. Turner et al., "CO<sub>2</sub> foam pilot in a west Texas field: design, operation and results," in *SPE Improved Oil Recovery Conference*, Virtual, 2020.
- [14] A. Katiyar, P. D. Patil, N. Rohilla et al., "Industry-first hydrocarbon-foam EOR pilot in an unconventional reservoir: design, implementation, and performance analysis," in *SPE/AAPG/SEG Unconventional Resources Technology Conference*, Denver, Colorado, USA, 2019.
- [15] Computer Modeling Group Ltd, *GEM Version 2019 User's Guide*, Computer Modeling Group Ltd., Calgary, Canada, 2019.
- [16] A. R. Kovscek, T. W. Patzek, and C. J. Radke, "Mechanistic foam flow simulation in heterogeneous and multidimensional porous media," *SPE Journal*, vol. 2, no. 4, pp. 511–526, 1997.
- [17] Q. Chen, *Assessing and Improving Steam-Assisted Gravity Drainage: Reservoir Heterogeneities, Hydraulic Fractures, and Mobility Control Foams*, no. article 3363948, 2009Stanford University, ProQuest Dissertations Publishing, 2009.

## Research Article

# Study on Sedimentary Facies and Reservoir Characteristics of Paleogene Sandstone in Yingmaili Block, Tarim Basin

Hanlie Cheng <sup>1</sup>, Jianfei Wei,<sup>1</sup> and Zhaoyuan Cheng<sup>2</sup>

<sup>1</sup>COSL-EXPRO Testing Services (Tianjin) Co., Ltd., Tianjin 300457, China

<sup>2</sup>College of Petroleum Engineering, Xi'an Shiyou University, Xi'an, Shaanxi 710065, China

Correspondence should be addressed to Hanlie Cheng; [chenghl@cosl-expro.com](mailto:chenghl@cosl-expro.com)

Received 9 January 2022; Accepted 16 February 2022; Published 7 March 2022

Academic Editor: Kouqi Liu

Copyright © 2022 Hanlie Cheng et al. This is an open access article distributed under the Creative Commons Attribution License, which permits unrestricted use, distribution, and reproduction in any medium, provided the original work is properly cited.

Block Yingmai 7 is structurally located in the western segment of the southern margin of the Kuqa Depression in the Tarim Basin. In the foreland basin, huge continental Mesozoic and Cenozoic strata have been deposited. In recent years, the Paleogene bottom sandstone section has been the main oil and gas exploration horizon. In order to further improve the oil and gas exploration effect of the Paleogene bottom sandstone in the study area and improve the accuracy of reservoir prediction, based on the related theory of sedimentology and petrology, this paper analyzes and studies the cores obtained by drilling in the Paleogene through laboratory core analysis experiments. The study shows that the Paleogene bottom sandstone is a braided river delta sedimentary system, and the sedimentary microfacies are mainly underwater distributary channels. The sandstone type is mainly light gray lithic feldspar fine sandstone, the sandstone debris particle sorting degree is medium-good, and the roundness is sub-edge-sub-circular. The microscopic characteristics of the reservoir are large pore throat radius, low displacement pressure, mainly intergranular pores, and good pore connectivity. It is a thin-layered mesoporous, medium-permeable, large-throat, and strongly heterogeneous reservoir. Finally, a classification evaluation table of reservoirs in block Yingmai 7 is established, and it is considered that the reservoirs of types I and II are enriched areas of oil and gas resources. The research results provide evidence for the prediction of oil and gas reservoirs.

## 1. Introduction

The Tarim Basin is the largest hydrocarbon-bearing basin in China. It is a superimposed composite basin which is located between the Tianshan Mountains, Kunlun Mountains, and Altun Mountains in Xinjiang Uygur Autonomous Region [1]. The basin area is  $56 \times 10^4 \text{ km}^2$ . The Proterozoic-Cenozoic was developed from bottom to top in the basin, with a maximum thickness of more than 10 000 m, containing rich oil and gas resources. In the past 30 years, large-scale exploration has been carried out around the Tabei uplift and the Tazhong uplift in the platform basin, the Kuqa Depression, and the southwest depression in the foreland area [2–4]. Important discoveries have been made in three areas of clastic rocks in the basin area. The clastic rock in the platform basin is the key area for oil and gas exploration in the Tarim Basin [5]. In recent years, the exploration has mainly focused on the Meso-Cenozoic continental clastic

rocks in the northern Tabei area and the Silurian-Carboniferous marine clastic rocks in the platform area [6–8]. The types of oil and gas reservoirs are complex, including anticlines, faulted anticlines, fault blocks, structural-stratigraphic, and structural-lithologic reservoirs [9]. The oil and gas source analysis results of the discovered oil and gas reservoirs show that the oil and gas from the Kuqa Depression are mainly distributed in the Neogene, Paleogene, Cretaceous, and Jurassic in the Luntai uplift and the Yingmaili low uplift in the western Tabei uplift and Silurian buried hill formations [10, 11].

The Paleogene condensate gas reservoir in the Yingmaili area is one of the earliest oil and gas reservoirs discovered in the Cenozoic in the Kuqa Depression [12–14]. Well YM9 is the first well in the area. It was completed and tested in the 4683–4690 m well section in April 1992. The 11.11 mm nozzle was used to obtain production, with a daily oil production of  $43.6 \text{ m}^3$  and a daily gas production of  $15.7 \times 10^4 \text{ m}^3$ ,

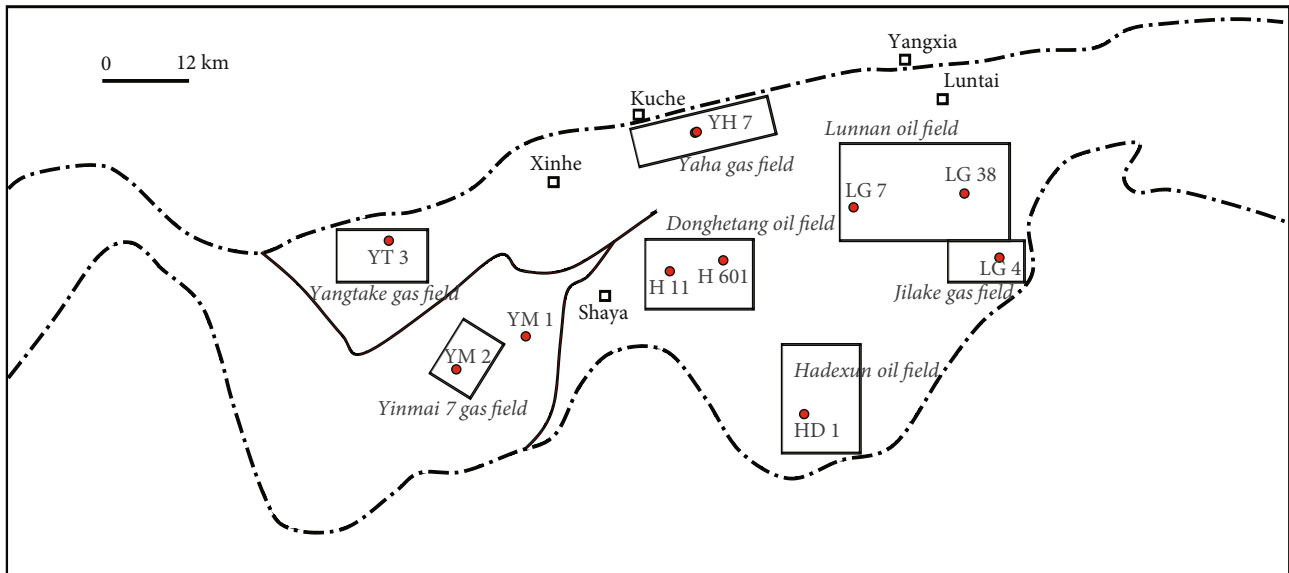


FIGURE 1: The structural location map of Yingmai 7 block area.

which proves that the Paleogene in the Yingmaili area has the conditions for forming oil and gas reservoirs [15, 16]. The Yingmai 7 fault structural belt is located in the western segment of the frontal uplift belt of the Kuqa Depression in the Tarim Basin, adjacent to the Yangtake anticline to the north, and the Karayergun structural belt to the west. The structural belt is NE-SW trending, about 70km long and 10km wide (Figure 1) [17]. The entire fault tectonic belt has experienced three development periods: the Hercynian-Indosinian period, which is dominated by strong reverse fault activities and developed a series of large thrust faults below the Cretaceous; Yanshan-Xishan early stage: after the deposition of the Genian system, fault activity was the mainstay, and a series of north-dipping normal faults developed, forming beaded anticlines and fault noses on the upper wall of the fault; Himalayan period: due to the change in the form and direction of fault activity, the Neogene strata developed thrust faults with different properties from those formed earlier, resulting in the uneven thickness of the Neogene strata on the upper and lower walls of the fault [18].

With the continuous deepening of the exploration of the Paleogene condensate gas reservoirs in the Yingmaili area, the problems of increasing difficulty in reservoir prediction and difficult reservoir identification have emerged, which have brought great challenges to the oil and gas exploration in this area. Sedimentary facies are stratigraphic units that reflect the characteristics of paleo-sedimentary environments and have certain lithology and paleobiological markers. From the lithology, structure, and paleontology of sediments (rocks), the environment and process of deposition can be judged. The concept of sedimentary facies was first put forward by Swiss A-Gressly in 1838. The analysis of sedimentary facies for oil and gas reservoirs is an important research process in oil and gas exploration. In the early stage of exploration, laboratory experiments were carried out on the Paleogene reservoir cores. However, due to the large

differences in reservoir characteristics between different strata and different regions in the Yingmaili block, it is still necessary to conduct detailed analysis and research on key exploration areas. In this paper, taking the Yingmai 7 fault structural zone in the Yingmaili block as the research area, the core samples obtained through a large number of drillings and the laboratory core test method are used to analyze the sedimentary facies and reservoir characteristics of the sandstone at the bottom of the Paleogene in detail. Oil and gas exploration provides a research basis.

## 2. Materials and Methods

**2.1. Stratigraphic Characteristics.** The strata drilled from top to bottom in block Yingmai 7 are as follows: Quaternary in Cenozoic, Kuqa Formation, Kangcun Formation, Jidike Formation in Neogene, Paleogene, Cretaceous and Jurassic in Mesozoic Department, and the Ordovician of the Lower Paleozoic (Table 1). The main hydrocarbon-bearing intervals are the Paleogene bottom sandstone and the Cretaceous Bashiji Formation top sandstone.

**2.2. Test Materials and Equipment.** The test material comes from a large number of core samples obtained from drilling in the sandstone section at the bottom of the Paleogene in block Yingmai 7. The core samples were prepared according to the experimental method to prepare the core slices to be tested. In the thin section production process, we first select representative rock samples, wash the samples with oil, keep the vacuum state during the production process, and cut and number the produced cast thin sections. After rough grinding, fine grinding, and fine grinding, the thickness is 0.03 mm, and it is ready for use after sticking the label.

The experimental instruments are as follows: X-ray diffractometer (D2 PHASER), grinding machine (ZHM-1B), pressing machine (ZHY-500), rock pore casting instrument (JS-5), scanning electron microscope (Thermo Quattro



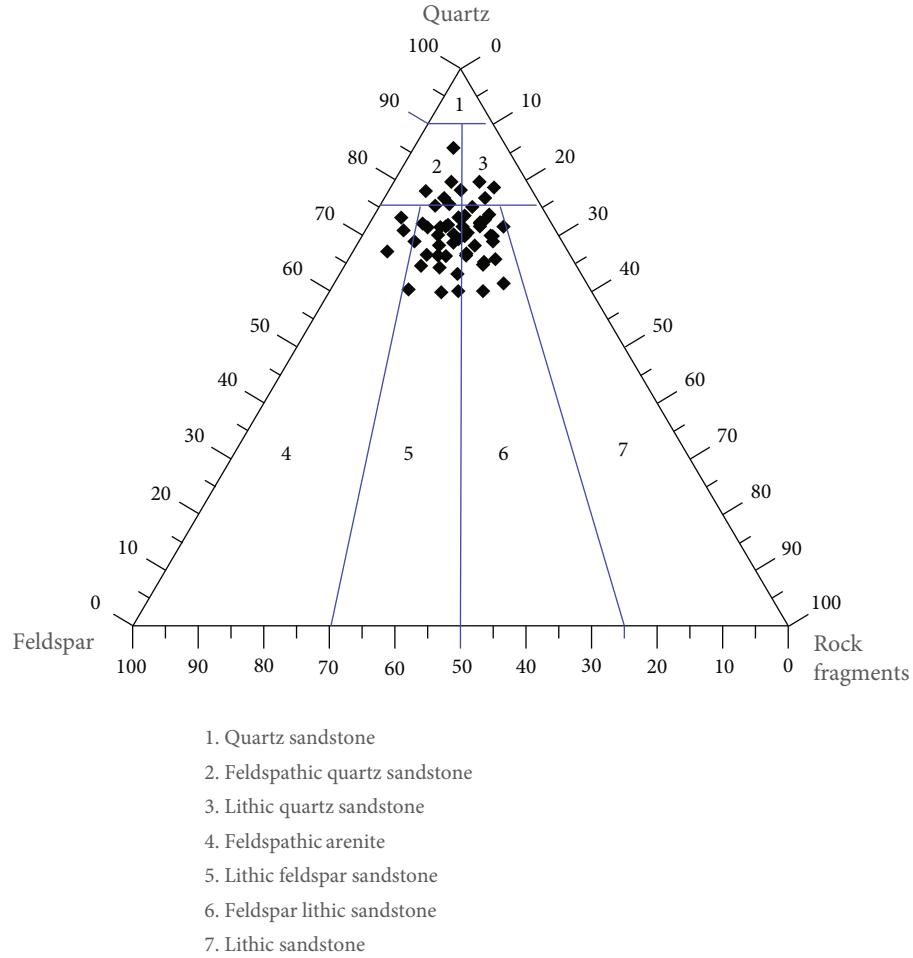


FIGURE 2: Triangle map of Paleogene sandstone composition in Yingmai 7 block.

ESEM), full diameter core permeability tester (DYX-2), core cathodoluminescence electron microscope (CL8200 MK5), rock cutting machine (DQ1-6), automatic specific surface area and pore size distribution tester (MiniX-1), Zeiss Primotech polarizing microscope, core holders, etc. Auxiliary materials include emery, epoxy resin, curing agent, coloring agent, fir glue, etc.

### 3. Result

#### 3.1. Characteristics of Sedimentary Facies

**3.1.1. Reservoir Petrological Characteristics.** The target layer of block Yingmai 7 is the sandstone section at the bottom of the Paleogene. The rock type is mainly lithic feldspar sandstone, accounting for 54.7% of the rock type, followed by feldspar lithic sandstone and quartz sandstone, accounting for 23.2% and 22.1% of the rock type, respectively (Figure 2).

The Paleogene sandstone reservoirs in Yingmai 7 block have high quartz content, concentrated at more than 70%, feldspar content at 15-20%, and debris content at 10-15%, reflecting that the Paleogene rock composition maturity is relatively high. The overall grain size of sandstone is mainly

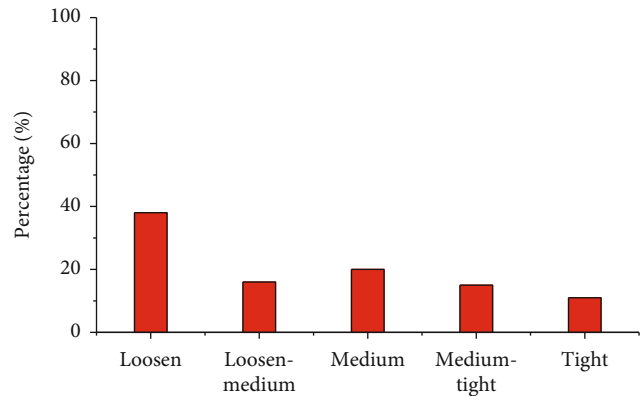


FIGURE 3: Histogram of frequency distribution of tightness degree of reservoir debris in block Yingmai 7.

fine sand, accounting for 69.03% of the rock particles, followed by silt, accounting for 19.12% of the rock particles. The sandstone reservoirs in the Paleogene target layer are mainly loose in density, with rounded edges and corners from subedge to subround, and the sorting grade is medium-good (Figure 3).

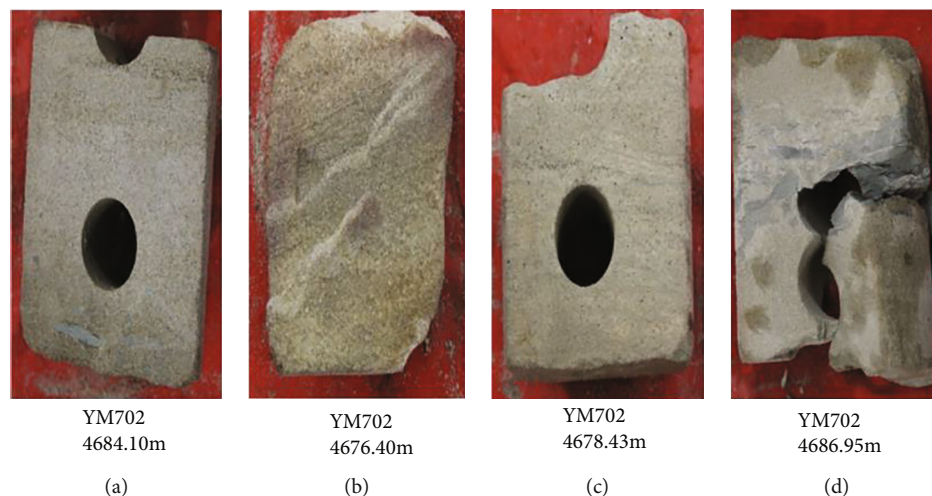


FIGURE 4: Core photos of Paleogene sedimentary structural types in Yingmai 7 block: (a) parallel bedding; (b) oblique bedding; (c) wavy bedding; (d) scour surface.

**3.1.2. Sedimentary Structure and Particle Size Analysis.** The Paleogene Kumugelimu Formation in Yingmai 7 block develops parallel bedding, oblique bedding, wavy bedding, and erosion surface, which are typical characteristics of braided river delta deposition, reflecting unstable sedimentary hydrodynamic conditions.

For parallel bedding, in the coarse silt sandstone and fine sandstone in the 4684.8 m section of Well YM702, the parallel bedding sometimes has clear laminations and sometimes blurred laminae, showing the depositional characteristics of high flow water flow, which is deposited under the condition of continuous and stable water flow. As a result, they are generally deposited under broad flow conditions, such as the channel flanks at the ends of distributary channels (Figure 4(a)).

For oblique bedding, oblique bedding is developed in the sandstone in the 4676.4 m section of Well YM702, and the interface between layers is relatively straight. The layer system is composed of many thin layers that are inclined in the same direction, and the thin layer and the layer system interface are oblique. If the adjacent layers are parallel to each other, the medium and fine layers in each layer are inclined in one direction, which is called monoclinic bedding. It is formed when water flows in a single direction, and the sloping direction of its thin layers indicates the downstream direction of water flow and is commonly found in river deposits and other sediments with flowing water (Figure 4(b)).

For wavy bedding, wavy bedding is formed when the hydrodynamic conditions alternate between strong and weak. It is more developed in delta fronts, rivers, tides, and other environments (Figure 4(c)).

For erosion surface, the undulating structural surface formed by the erosion and erosion of the underlying sediment due to the sudden increase of the flow velocity reflects the characteristics of strong hydrodynamics. The sediments on the scour surface are coarser than the underlying sediments and are more developed in the braided river delta environment (Figure 4(d)).

According to the particle size analysis data of Yingmai 7 block, the C-M map of the Paleogene was established. The samples of the C-M map of the Paleogene were concentrated in the QR section, and the reaction sediments were mainly transported by the gradient suspension of the tractive flow (Figure 5). The grain size probability curve of Paleogene braided river delta facies has two segments. The two-stage grain size probability curve is composed of jumping and suspending populations, and the jumping population is the main one, reflecting the transport and deposition mechanism of tractive flow, mainly developed in siltstone and fine sandstone (Figure 6).

**3.1.3. Sedimentary Microfacies Division.** Through the analysis of rock color, rock mineral composition, rock structure, grain size, and comprehensive analysis of a large number of sedimentary structures in coring wells, the target layer of the Paleogene in the study area is divided into a lake-braided river delta sedimentary system, and the subfacies is divided into a shallow lake and braided river delta fronts. The microfacies are divided into shallow lake mud, underwater distributary channels, and underwater interdistributary bays (Table 2).

**3.1.4. Distribution Characteristics of Sedimentary Microfacies.** During the Paleogene sedimentary period, the provenance came from the southeast, and a set of braided river delta frontal deposits developed, and the overall performance from bottom to top was a water-transgressive sedimentary sequence.

During the E2 depositional period, a braided river delta sedimentary system was developed in the Yingmai 7 block. The provenance came from the southeast. The sand bodies were thin, but the lateral continuity was good. As a whole, the sand bodies in the southeast were more developed than those in the northwest. The planar facies distribution is dominated by underwater distributary channels, with mouth bars developed at the front of the underwater distributary channels, subaqueous interdistributary bays developed

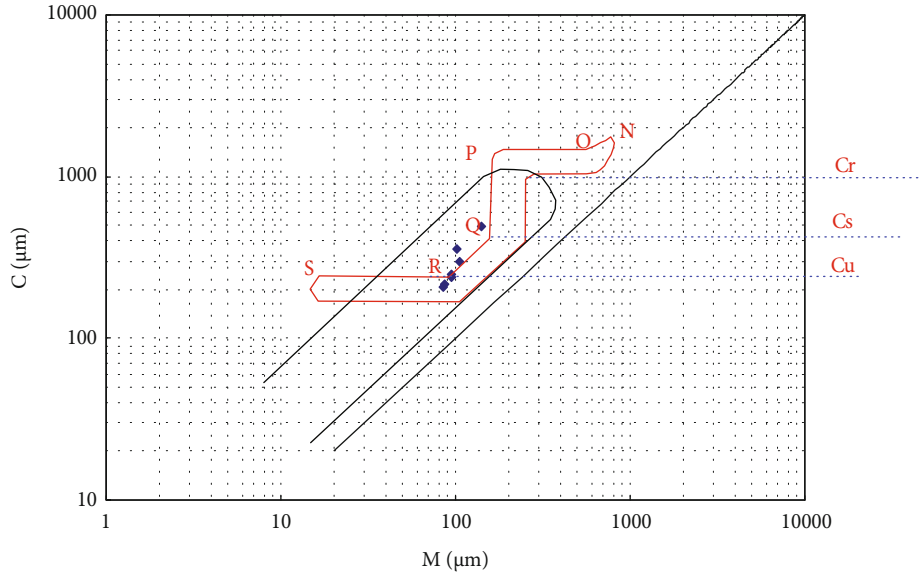


FIGURE 5: C-M map of Paleogene Kumugelimu Formation reservoir in Yingmai 7 block.

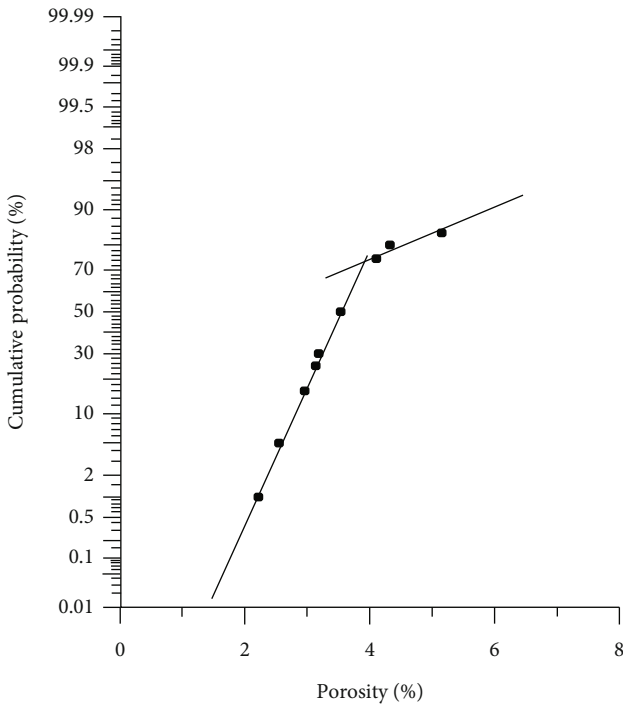


FIGURE 6: Reservoir particle size probability curve of Paleogene Kumugelimu Formation in block Yingmai 7.

locally, and front sheet sand deposits developed outside the mouth bars (Figure 7).

During the E1 depositional period, the provenance came from the southeast. Compared with the E2 period, the water inflow occurred. Affected by water flow in paleosedimentary environment, the main body of the work area was the lake facies coastal shallow lake subfacies, mainly developed shallow lake mud (Figure 8).

### 3.2. Reservoir Characteristics

**3.2.1. Microscopic Characteristics of Reservoir.** According to the analysis data of the core casting thin section, the pore types of the E2 layer are mainly intergranular pores, and the intergranular porosity ranges from 16.33 to 20.25% (Table 3).

Through the analysis of the mercury intrusion data of Yingmai 7 block, the capillary pressure curve can be roughly divided into four types: Type A is dominated by high porosity and high permeability, the curve is platform-shaped, the pore throat is well sorted, the displacement pressure low, and the median pore throat radius is greater than  $2\ \mu\text{m}$ . The porosity and permeability of type B are still high, the curve is platform-shaped, the displacement pressure is low, and the median pore throat radius is greater than  $1\ \mu\text{m}$ . The C-type curve is slope-shaped, the displacement pressure is 0.06-0.1 MPa, and the median pore throat radius is less than  $1\ \mu\text{m}$ . Type D is dominated by low porosity and low permeability, the curve is slope-shaped, the pore throat sorting is poor, the displacement pressure is 0.5-3 MPa, and the median pore throat radius is less than  $0.5\ \mu\text{m}$  (Figure 9, Table 4).

**3.2.2. Distribution Characteristics of Reservoir Physical Properties.** According to the statistics of the physical property analysis data of 64 Paleogene cores in Yingmai 7 block, the core analysis porosity is concentrated between 18 and 26%, with an average value of 15.44%. The permeability is concentrated in the range of  $80$  to  $8000 \times 10^{-3}\ \mu\text{m}^2$ ; the average value is  $192.37 \times 10^{-3}\ \mu\text{m}^2$ . The Paleogene target layers belong to mesoporous and medium permeability reservoirs (Figures 10 and 11; the reference standard is SY/T 6285-1997).

The Paleogene has obvious upward variation characteristics. The porosity distribution range of E2 layer is

TABLE 2: Sedimentary microfacies division of Yingmai 7 block.

Formation	Sedimentary facies		Micro
	Face	Sub	
E	Lake	Shallow lake	Shallow lake mud
	Braided river delta	Braided river delta front	Underwater distributary channel Underwater bay

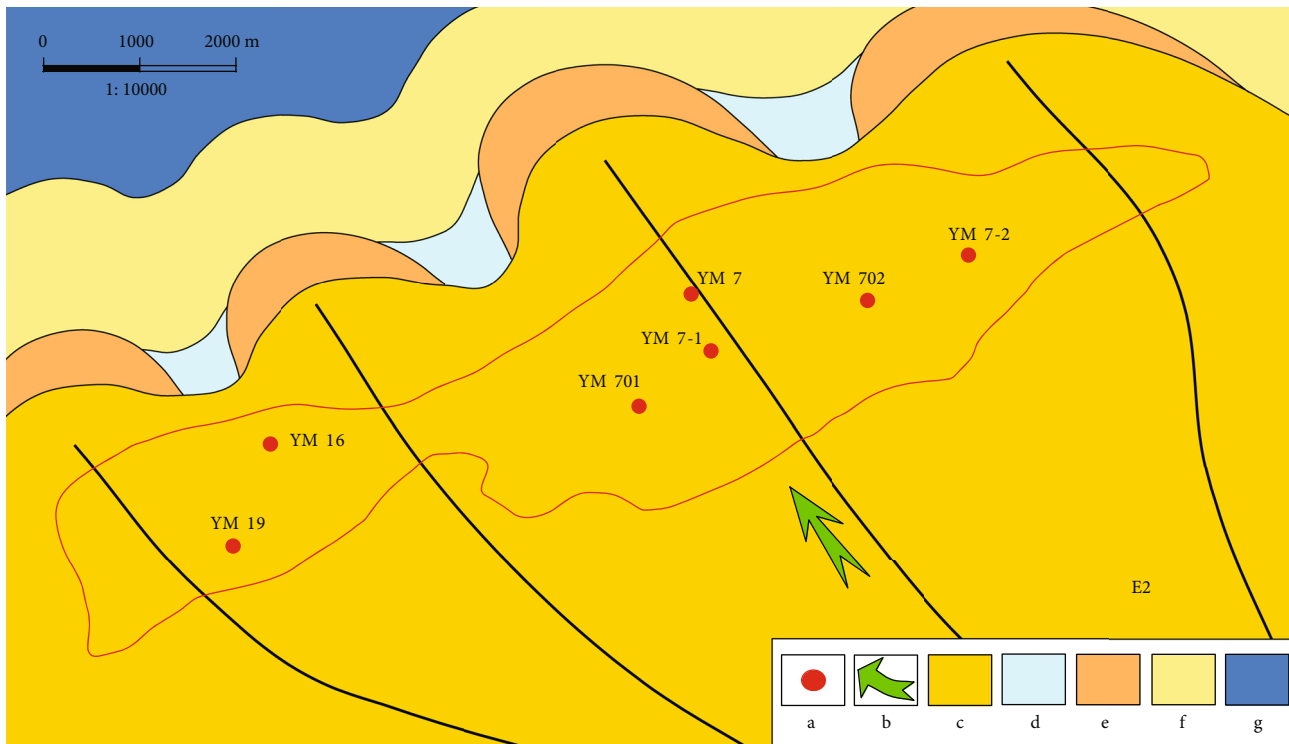


FIGURE 7: Plane distribution of sedimentary microfacies of layer E2 in Yingmai 7 block: (a) well location; (b) provenance direction; (c) underwater distributary channel; (d) underwater distributary bay; (e) mouth bar; (f) front edge sheet sand; (g) shallow lake mud.

13.06-25.00% with the average value of 21.80%, and the permeability distribution range is  $4.75-6829.40 \times 10^{-3} \mu\text{m}^2$  with the average value of  $381.54 \times 10^{-3} \mu\text{m}^2$ . The porosity distribution range of E1 layer is 8.03~10.13%, the average value is 9.08%, the permeability distribution range is  $2.54-4.27 \times 10^{-3} \mu\text{m}^2$ , and the average value is  $3.20 \times 10^{-3} \mu\text{m}^2$  (Table 5).

According to the statistics of porosity and permeability explained by logging in Yingmai 7 block, the variation range of Paleogene porosity is 14.50-24.60%, with an average value of 20.46%. The variation range of permeability is  $58.60-2482.50 \times 10^{-3} \mu\text{m}^2$ , and the average value is  $599.45 \times 10^{-3} \mu\text{m}^2$ , which indicates that the plane porosity and permeability of the Paleogene reservoirs are quite different, and the physical properties are highly nonuniform (Table 6).

The average porosity of the E1 layer is 19.46%, and the average permeability is  $432.71 \times 10^{-3} \mu\text{m}^2$ . The minimum values of porosity and permeability are 14.53% and  $58.63 \times 10^{-3} \mu\text{m}^2$  of Well YM701, respectively. The plane distribution of porosity and permeability contours is controlled by sedimentation and sand body distribution shape, and the plane contours are densely distributed, reflecting the large difference in plane physical properties of this layer (Figure 12).

The average porosity of the E2 layer is 21.46%, and the average permeability is  $766.19 \times 10^{-3} \mu\text{m}^2$ . The minimum values of porosity and permeability are 16.47% and  $155.73 \times 10^{-3} \mu\text{m}^2$  in Well YM16, respectively. The plane distribution of porosity and permeability contours is controlled by sedimentation and sand body distribution, and the plane contours are unevenly distributed, reflecting the large difference in

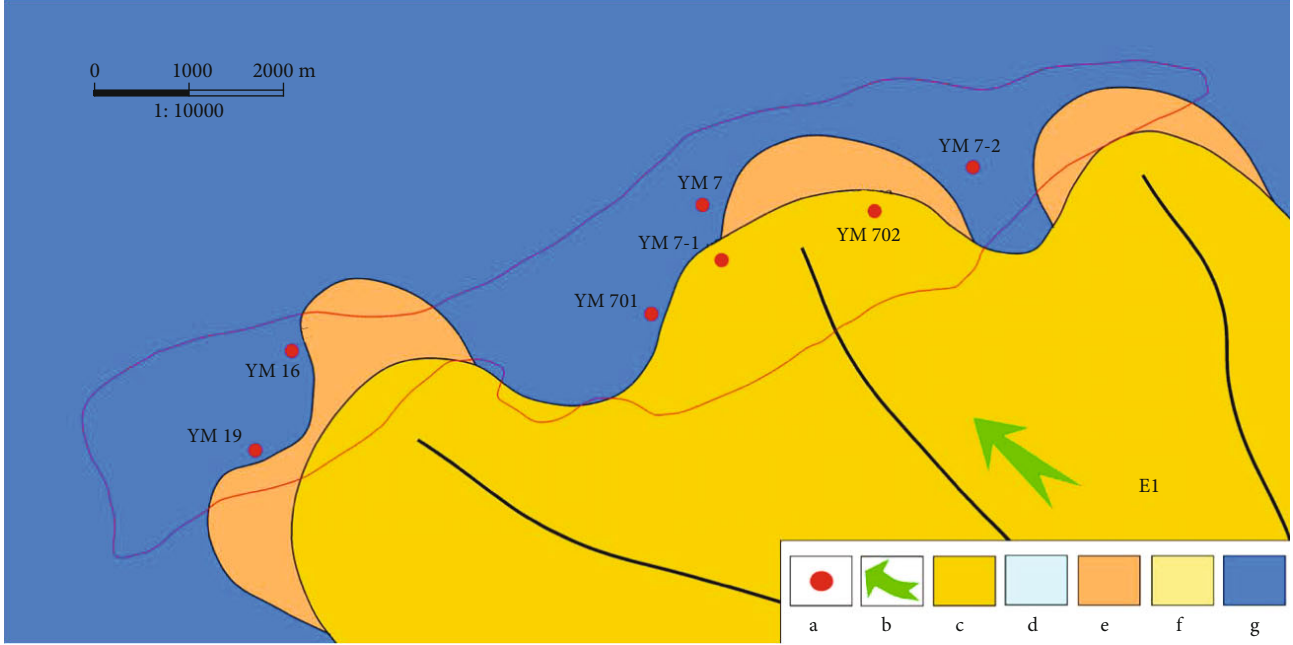


FIGURE 8: Plane distribution map of sedimentary microfacies of layer E1 in Yingmai 7 block: (a) well location; (b) provenance direction; (c) underwater distributary channel; (d) underwater distributary bay; (e) mouth bar; (f) front edge sheet sand; (g) shallow lake mud.

TABLE 3: Statistics of reservoir pore characteristics in block Yingmai 7.

Formation	Number of samples	Interparticle pores, %		Mold pores, %	Intraparticle pores, %	Fractures, %
		Primary	Secondary			
E2	10	5.44	10.89	1~2	1~2	0.5

plane physical properties of this layer, but the difference is smaller than that of E1 (Figure 13).

### 3.3. Reservoir Heterogeneity

**3.3.1. Reservoir Heterogeneity between Layers.** In this study, the following parameters are mainly used to evaluate the heterogeneity of reservoir physical properties.

Sand ratio refers to the ratio of the total thickness of sandstone on the vertical section to the total thickness of the formation, expressed as a percentage, equivalent to the ratio of sand to ground (%). According to the stratum thickness of Yingmai 7 block and the statistical results of sand body thickness interpreted by logging, the sand-to-ground ratio is calculated. The average total thickness of the two Paleogene layers in block Yingmai 7 is 63.09 m, the average total sandstone thickness is 33.55 m, and the average sand-to-ground ratio is 0.51 (Table 7).

For interlayer permeability heterogeneity, the physical property statistics show that the minimum permeability of each sublayer of Paleogene in Yingmai 7 block is  $58.60 \times 10^{-3} \mu\text{m}^2$ , the maximum value is  $2482.50 \times 10^{-3} \mu\text{m}^2$ , and the average value is  $645.50 \times 10^{-3} \mu\text{m}^2$ . The permeability difference between layers is larger, indicating that the degree of heterogeneity between layers is strong.

Formula (1) and formula (2) show the calculation of permeability coefficient of variation (VK):

$$V_K = \frac{\delta}{\bar{K}}, \quad (1)$$

$$\delta = \sqrt{\sum_{i=1}^{n-1} \frac{(k_i - \bar{k})^2}{n}}. \quad (2)$$

In the formula,  $K$  is the average permeability of the core,  $10^{-3} \mu\text{m}^2$ ;  $k_i$  is the permeability of each core sample,  $10^{-3} \mu\text{m}^2$ ;  $\delta$  is the permeability variance,  $10^{-3} \mu\text{m}^2$ ; and  $n$  is the number of core samples.

Generally, when  $V_K < 0.5$ , it means that the degree of heterogeneity is weak; when  $V_K$  is 0.5 to 0.7, it means that the degree of heterogeneity is moderate; when  $V_K > 0.7$ , it means that the degree of heterogeneity is strong.

The calculation of the rush factor (TK) is shown in formula (3):

$$T_K = \frac{K_{\max}}{\bar{K}}. \quad (3)$$

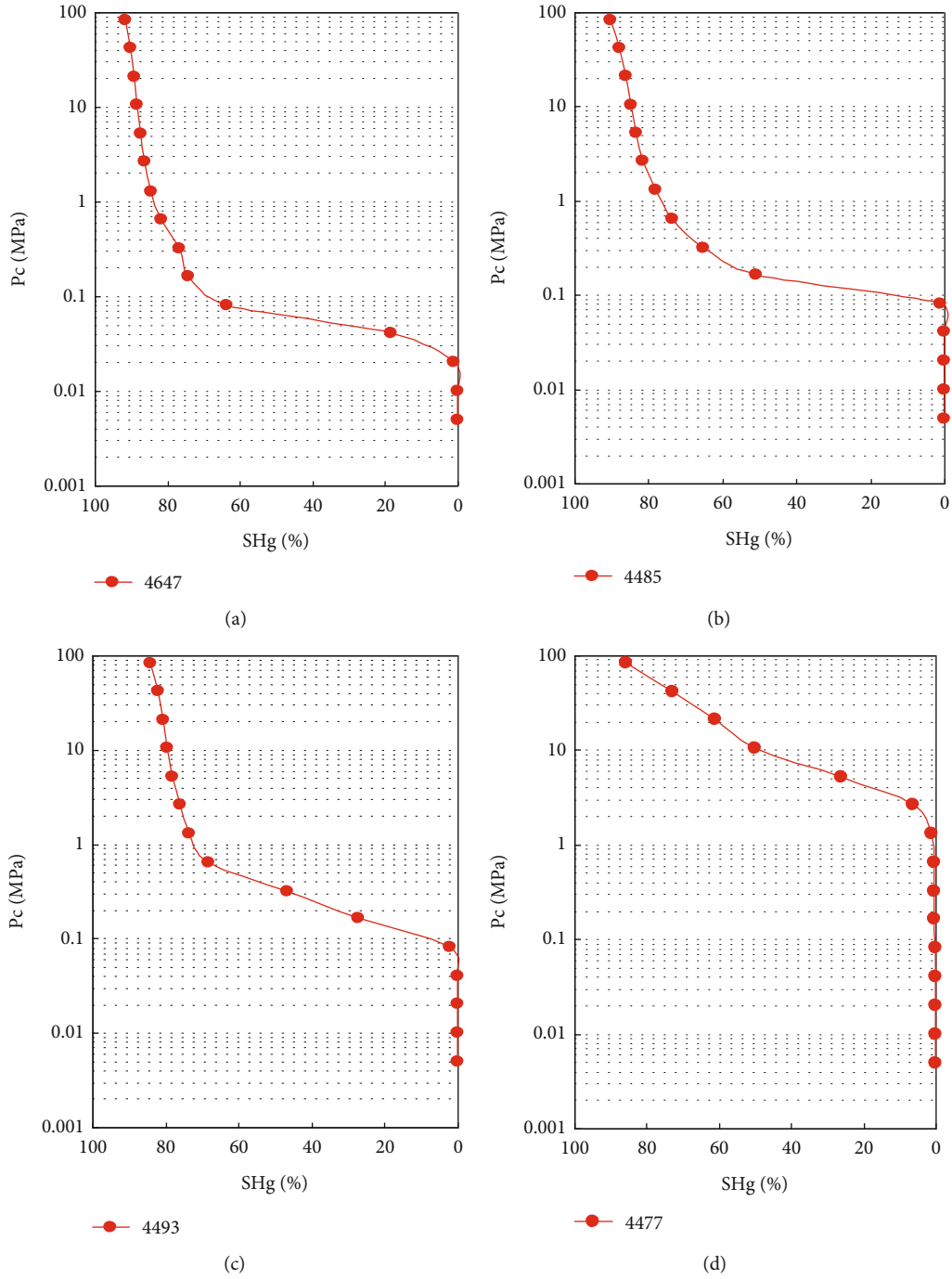


FIGURE 9: Typical mercury intrusion curve of Yingmai 7 block.

TABLE 4: Statistics of the average pore structure characteristic parameters of block Yingmai 7.

Type	Number of samples	Permeability, $10^{-3} \mu\text{m}^2$	Porosity, %	Displacement pressure, MPa	Median pressure, MPa	Sorting coefficient	Maximum throat size, $\mu\text{m}$	Median throat size, $\mu\text{m}$
A	39	509.60	20.37	0.03	0.47	2.26	34.18	3.78
B	11	145.07	18.70	0.07	0.43	1.91	15.84	1.80
C	5	67.70	14.88	0.07	0.49	2.43	10.85	0.83
D	2	1.49	7.25	1.96	23.05	1.68	0.42	0.02

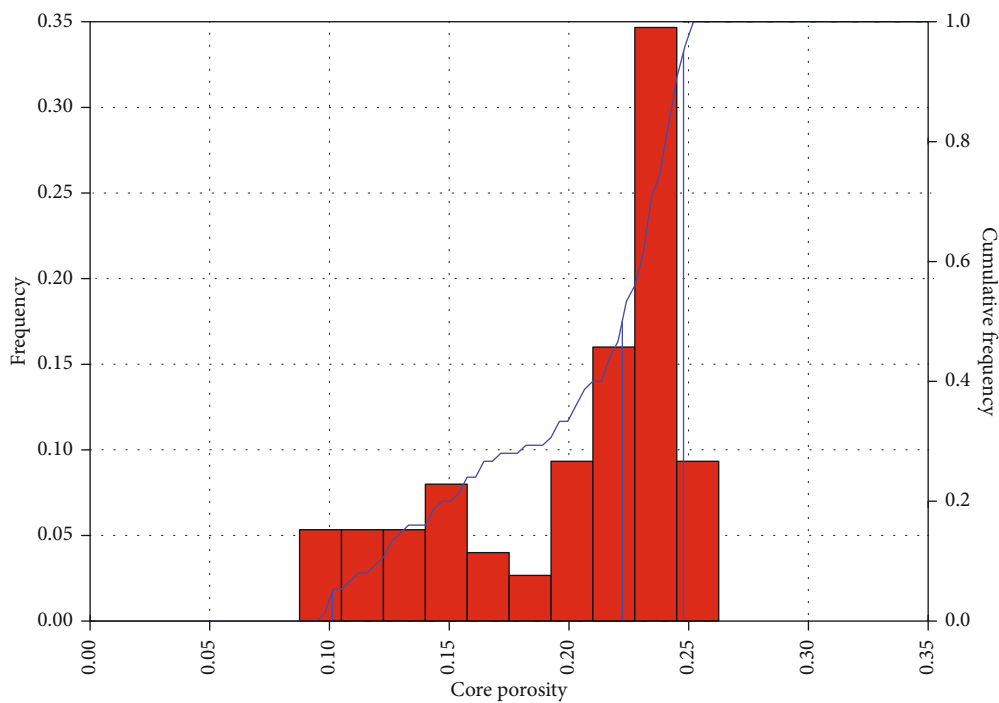


FIGURE 10: Histogram of frequency distribution of porosity in Paleogene core analysis of block Yingmai 7.

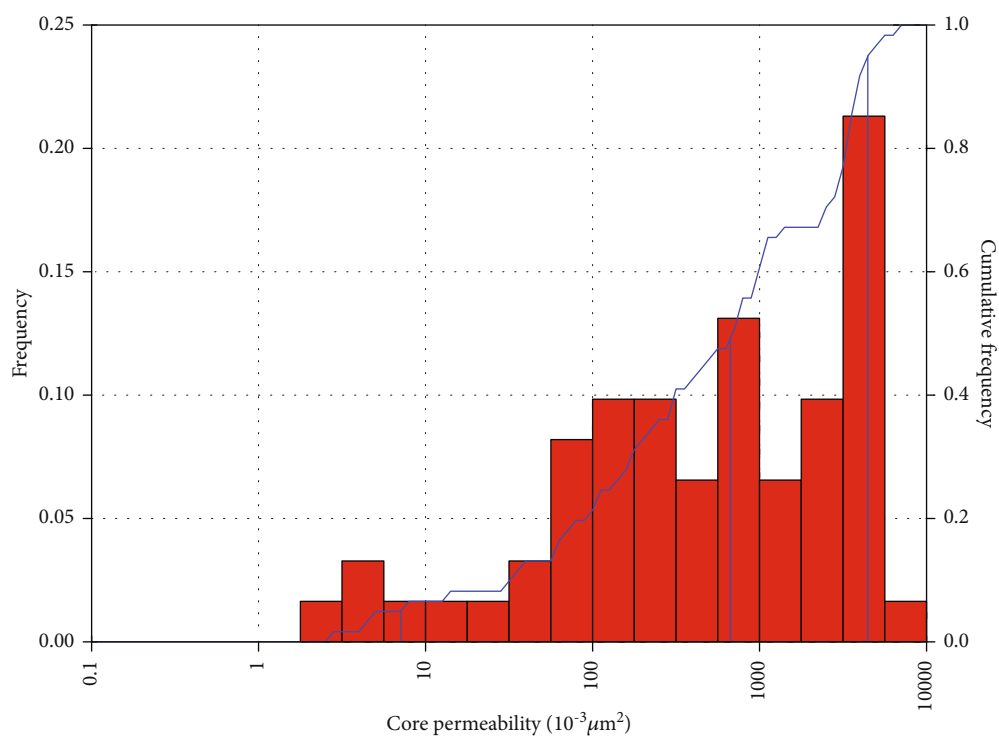


FIGURE 11: Histogram of permeability frequency distribution of Paleogene core analysis in Yingmai 7 block.

TABLE 5: Reservoir physical property statistics for core analysis of block Yingmai 7.

Formation	Sample number	Porosity, %			Permeability, $10^{-3} \mu\text{m}^2$		
		Maximum	Minimum	Mean	Maximum	Minimum	Mean
E1	2	8.03	10.13	9.08	2.54	4.27	3.20
E2	62	13.06	25.00	21.80	4.75	6829.40	381.54

TABLE 6: Reservoir physical property statistics for logging interpretation in block Yingmai 7.

Formation	Porosity, %			Permeability, $10^{-3} \mu\text{m}^2$		
	Maximum	Minimum	Mean	Maximum	Minimum	Mean
E1	14.50	22.00	19.46	58.60	2482.50	432.71
E2	16.50	24.60	21.46	155.70	2482.50	766.19
E	14.50	24.60	20.46	58.60	2482.50	599.45

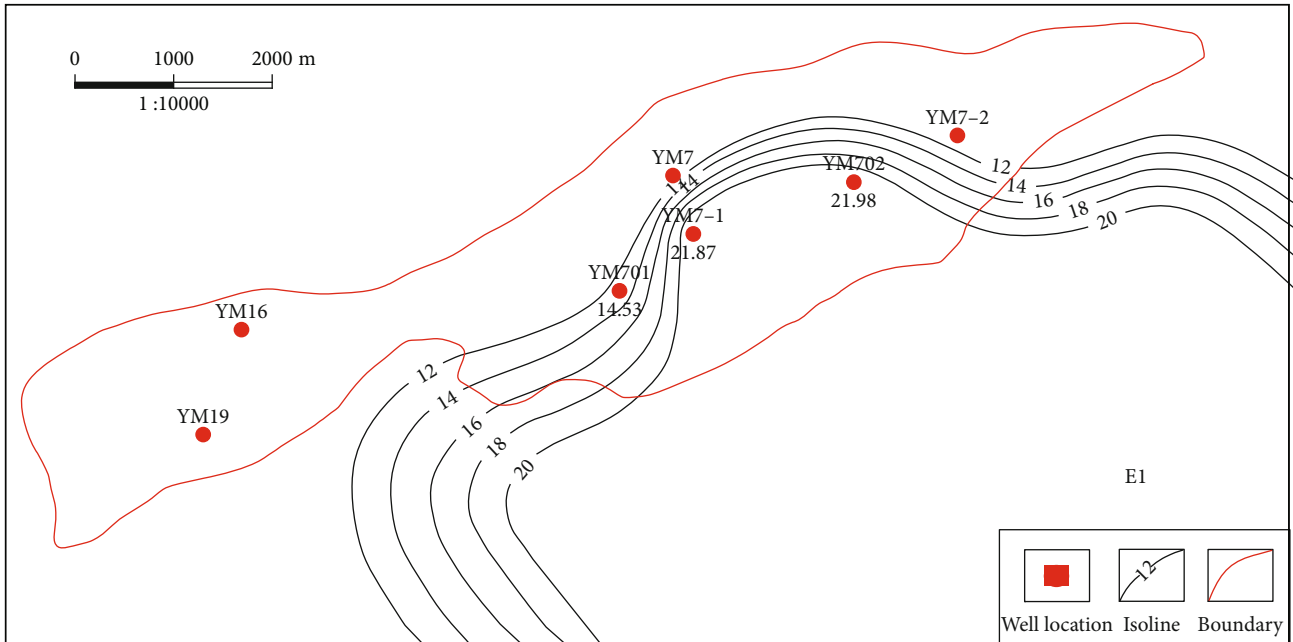


FIGURE 12: Contour map of porosity in the E1 layer of block Yingmai 7.

In the formula,  $K_{\text{max}}$  is the maximum permeability of the core sample,  $10^{-3} \mu\text{m}^2$ .

When  $T_K < 2$ , it means that the degree of heterogeneity is weak; when  $T_K$  is 2 to 3, it means that the degree of heterogeneity is moderate; when  $T_K > 3$ , it means that the degree of heterogeneity is strong.

The difference ( $J_K$ ) calculation is shown in formula (4):

$$J_K = \frac{K_{\text{max}}}{K_{\text{min}}} \quad (4)$$

In the formula,  $K_{\text{min}}$  is the minimum permeability of the core sample,  $10^{-3} \mu\text{m}^2$ .

When  $J_k < 20$ , it means that the degree of heterogeneity is weak; when  $J_k$  is 20-30, it means that the degree of heterogeneity is moderate; when  $J_k > 30$ , it means that the degree of heterogeneity is strong.

Through the calculation of the heterogeneity parameters of the interlayer permeability in the Yingmai 7 block, the coefficient of variation of the Paleogene permeability is 1.46, the inrush coefficient is 3.85, and the gradient is 42.36, reflecting the characteristics of strong interlayer heterogeneity (Table 8).

3.3.2. *Reservoir Heterogeneity.* According to the vertical variation of intralayer permeability, the intralayer heterogeneity in this area can be divided into four types, namely,

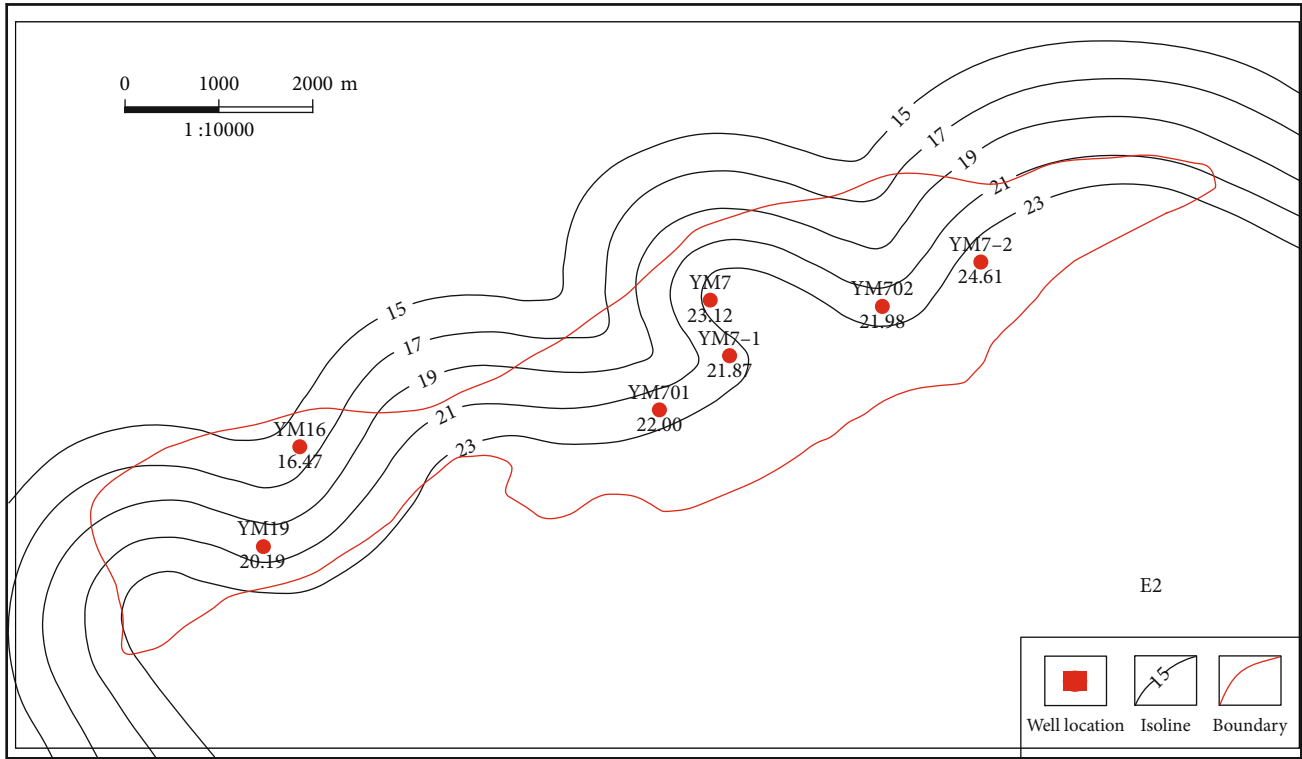


FIGURE 13: Porosity plane contour map of layer E2 in Yingmai 7 block.

positive rhythm type, inverse rhythm type, compound rhythm type, and homogeneous rhythm type. Generally, the permeability heterogeneity of the compound rhythm type is higher, followed by the positive rhythm type, the inverse rhythm type has relatively good homogeneity, and the homogeneous rhythm type has weak permeability heterogeneity.

For positive rhythm type, permeability increases vertically from bottom to top, and the highest permeability segment is distributed in the lower or middle-lower part. The natural gamma curve presents a box-bell shape. The acoustic transit time decreases slightly from bottom to top. The curve does not change much from bottom to top.

For inverse rhythm type, permeability increases from small to large vertically from bottom to top, the highest permeability segment is distributed in the upper or middle-upper part, the natural gamma curve presents a funnel-box shape, the acoustic time difference increases slightly from bottom to top, and the resistivity curve decreases slightly from bottom to top.

For compound rhythm type, compound rhythm mainly occurs in thick sand layers (thick single sand layer or thick superimposed sand layer); there are four types of compound rhythms: one is multiphase positive rhythm combination type, the second is multiphase antiarrhythmic combination type, the third is the combination type of inverse rhythm-positive rhythm, and the fourth is the combination type of positive rhythm-inverse rhythm. Multiphase positive rhythm combination is a common type of permeability

TABLE 7: Statistical table of sand-to-ground ratio parameters of Yingmai 7 block.

Formation	Total thickness, m	Total thickness of sandstone, m	Sand ratio
E1	58.82	7.10	0.12
E2	67.35	60.00	0.89
Mean	63.09	33.55	0.81

combination in thick sand bodies. It is composed of multiple positive permeability rhythms. Natural gamma logging often shows a box-bell combination type, and the resistivity curve slightly reduced from bottom to top, and the sonic curve also slightly reduced.

For homogeneous rhythm type, if the permeability changes vertically without rhythm, it is called homogeneous rhythm.

The Paleogene in Yingmai 7 block developed compound rhythm and inverse rhythm, among which compound rhythm was the main one, which indicated that it had the characteristics of strong intralayer heterogeneity. The intralayer permeability heterogeneity evaluation of the Paleogene reservoir shows that the intralayer permeability gradient is 75.76, the inrush coefficient is 4.09, and the variation coefficient is 2.25, showing a strong degree of heterogeneity (Table 9).

TABLE 8: Statistics of interlayer heterogeneity parameters of reservoirs in block Yingmai 7.

Formation	Permeability, $10^{-3} \mu\text{m}^2$			Gradation	Inrush coefficient	Coefficient of variation
	Maximum	Minimum	Mean			
E1	58.60	2482.50	432.71	42.36	3.85	1.46
E2	155.70	2482.50	766.19			

TABLE 9: Statistical table of heterogeneity parameters in the reservoir of Yingmai 7 block.

Formation	Permeability, $10^{-3} \mu\text{m}^2$			Gradation	Inrush coefficient	Coefficient of variation
	Maximum	Minimum	Mean			
E1	2.54	4.27	3.20	1.68	1.33	—
E2	4.75	711.70	103.87	149.83	6.85	2.25
E	2.54	711.70	53.53	75.76	4.09	2.25

TABLE 10: Reservoir classification evaluation table in Yingmai 7 block of Yingmaili gas field.

Compare items	Reservoir type				
	I	II	III	IV	
Thickness of single layer, m	$\geq 4$	4~2	2~1	<1	
Lithology	Fine sandstone, siltstone	Fine sandstone, siltstone	Fine sandstone, siltstone	Siltstone	
Microphase	Underwater distributary channel estuary dam	Underwater distributary channel estuary dam	Underwater distributary channel estuary dam	Underwater distributary channel	
Reservoir physical properties	Porosity, %	$\geq 18$	18~15	8~15	<8
	Permeability, $10^{-3} \mu\text{m}^2$	$\geq 200$	200~100	100~2.5	<2.5
	Displacement pressure, MPa	0.005~0.04	0.04~0.08	0.04~0.3	>0.3
Mercury intrusion parameter	Median pressure, MPa	0.07~0.86	0.19~2.40	0.43~2.56	>2.25
	Median pore throat radius, $\mu\text{m}$	1.27~10.53	0.58~5.33	0.29~1.71	<0.29
	Maximum pore throat radius, $\mu\text{m}$	18.06~72.06	2.13~18.15	9.04~2.23	<2.23

3.3.3. *Reservoir Type Division.* According to the sand body thickness, lithology, microfacies, physical properties, and mercury intrusion data, a classification evaluation table of reservoirs in block Yingmai 7 is designated, which is divided into four categories. Type II reservoirs account for 11.7% of the reservoir types (Table 10). Among them, type I and II reservoirs are high-quality reservoirs for key drilling.

#### 4. Conclusion

The Paleogene of Yingmai 7 block is a set of braided river delta sedimentary system, the microfacies is mainly underwater distributary channel, the reservoir rocks are mainly light gray lithic feldspar fine sandstone, and the rock density is loose-medium. The reservoir has average sand-to-ground ratio of 0.51%, strong interlayer and plane heterogeneity, well-developed interlayers, large thickness, and strong intra-layer heterogeneity. The average porosity of the reservoir is 15.44%, and the microscopic characteristics of the reservoir

are large pore throat radius, low displacement pressure, mainly intergranular pores, and good pore connectivity. The reservoir is a thin-layered mesoporous, medium permeability, large throat, and strongly heterogeneous reservoir.

#### Data Availability

The figures and tables used to support the findings of this study are included in the article.

#### Conflicts of Interest

The authors declare that they have no conflicts of interest.

#### Acknowledgments

The authors would like to show sincere thanks to those techniques who have contributed to this research.

## References

- [1] C. Z. Jia and G. Q. Wei, "Structural characteristics and petroliferous features of Tarim Basin," *Chinese Science Bulletin*, vol. 47, no. S1, pp. 1–11, 2002.
- [2] D. F. He, "Unconformities and oil and gas accumulation in Tarim Basin," *Acta Petrolei Sinica*, vol. 16, no. 3, pp. 14–21, 1995.
- [3] D. G. Liang, S. C. Zhang, J. P. Chen, F. Y. Wang, and P. R. Wang, "Organic geochemistry of oil and gas in the Kuqa depression, Tarim Basin, NW China," *Organic Geochemistry*, vol. 34, no. 7, pp. 873–888, 2003.
- [4] H. T. An, H. Y. Li, J. Z. Wang, and X. F. Du, "Tectonic evolution and its controlling on oil and gas accumulation in the northern Tarim Basin," *Geotectonica et Metallogenia*, vol. 33, no. 1, pp. 142–147, 2009.
- [5] T. Jun, "Petroleum exploration history and enlightenment in Tarim Basin," *Xinjiang Petroleum Geology*, vol. 42, no. 3, p. 272, 2021.
- [6] Y. H. Lu, Z. Y. Xiao, Q. Y. Gu, and Q. C. Zhang, "Geochemical characteristics and accumulation of marine oil and gas around Halahatang depression, Tarim Basin, China," *Science in China Series D: Earth Sciences*, vol. 51, no. S1, pp. 195–206, 2008.
- [7] G. Y. Zhu, X. W. Liu, Y. F. Zhu, J. Su, and K. Wang, "The characteristics and the accumulation mechanism of complex reservoirs in the Hanilcatam area, Tarim Basin," *Bulletin of Mineralogy, Petrology and Geochemistry*, vol. 32, no. 2, pp. 231–242, 2013.
- [8] C. C. Pan, Z. Y. Zhou, S. F. Fan, and Q. L. Xie, "Thermal history of Tarim Basin," *Bulletin of Mineralogy, Petrology and Geochemistry*, vol. 15, no. 3, pp. 150–152, 1996.
- [9] Z. J. Zhao, J. H. Luo, Y. B. Zhang, X. N. Wu, and W. Q. Pan, "Lithofacies paleogeography of Cambrian sequences in the Tarim Basin," *Acta Petrolei Sinica*, vol. 32, no. 6, pp. 937–948, 2011.
- [10] L. J. Tang, "Evolution and tectonic patterns of Tarim Basin," *Earth Science - Journal of China University of Geosciences*, vol. 19, no. 6, pp. 742–754, 1994.
- [11] Z. Q. Zhang, J. T. Dou, J. G. Fu, J. Pu, and Y. Z. Wu, "Drilling fluid research for Paleogene strata in Yingmaili area," *Petroleum Drilling Techniques*, vol. 41, no. 2, pp. 54–58, 2013.
- [12] S. L. Su, X. Q. Pang, B. S. Zhang, H. Sun, and A. Y. Sun, "Marine oil source of the Yingmaili Oilfield in the Tarim Basin," *Marine and Petroleum Geology*, vol. 68, pp. 18–39, 2015.
- [13] Y. Y. Zhang and X. Q. Luo, "K-Ar dating authigenic illites and the hydrocarbon accumulation history of the Silurian bituminous sandstone reservoirs in the Yingmaili area, Tarim Basin," *Petroleum Exploration and Development*, vol. 38, no. 2, pp. 203–210, 2011.
- [14] Z. M. Wang and A. D. He, "Hydrocarbon enrichment, and exploration domains in mid-western Tabei uplift, Tarim Basin," *Xinjiang Petroleum Geology*, vol. 30, pp. 153–156, 2009.
- [15] L. D. Sun, X. Y. Zhou, and G. L. Wang, "Contributions of petroleum geology and main directions of oil-gas exploration in the Tarim Basin," *Chinese Journal of Geology*, vol. 40, no. 2, pp. 167–178, 2005.
- [16] N. N. Zhang, D. F. He, F. Y. Sun, and B. L. Gui, "Formation mechanism and structural model of Yingmai 2 anticline in Tabei uplift, Tarim Basin," *Chinese Journal of Geology*, vol. 48, no. 1, pp. 133–148, 2013.
- [17] J. F. Chen, Y. C. Xu, and D. F. Huang, "Geochemical characteristics and origin of natural gas in Tarim Basin, China," *AAPG Bulletin*, vol. 84, no. 5, pp. 591–606, 2000.
- [18] F. P. Wang, Z. Y. Wang, X. Y. Liu, and D. S. Wu, "Characters of Triassic-Jurassic reservoirs in northern Tarim Uplift," *Oil & Gas Geology*, vol. 16, no. 3, pp. 277–284, 1995.

## Research Article

# Determination of the Fractal Dimension of CO<sub>2</sub> Adsorption Isotherms on Shale Samples

Hongyan Qi , Zhenlin Wang , Jianglong Yu , Peirong Yu , and Guoqing Zheng 

Petro China Xinjiang Oilfield Company, Karamay 834000, China

Correspondence should be addressed to Zhenlin Wang; wzhenl@petrochina.com.cn

Received 19 January 2022; Accepted 31 January 2022; Published 22 February 2022

Academic Editor: Kouqi Liu

Copyright © 2022 Hongyan Qi et al. This is an open access article distributed under the Creative Commons Attribution License, which permits unrestricted use, distribution, and reproduction in any medium, provided the original work is properly cited.

The fractal theory has been widely applied to the analysis of gas adsorption isotherms, which are used for the pore structure characterization in unconventional reservoirs. Fractal dimension is a key parameter that can indicate the complexity of the pore structures. So far, most fractal models for gas adsorption are for N<sub>2</sub> adsorption, while fractal models for CO<sub>2</sub> adsorption are rarely reported. In this paper, we built a fractal model for CO<sub>2</sub> adsorption by combining a thermodynamic model and the Dubinin–Astakhov model. We then applied the new model to three CO<sub>2</sub> adsorption isotherms measured on shale samples. The results show that the fractal dimension from the new model lies between 2 and 3, which agrees with the fractal geometry. The new model presented in this paper can be used for the CO<sub>2</sub> adsorption analysis, which allows characterizing micropore structures in shales.

## 1. Introduction

Knowing the pore structures of shale rocks is an essential part for the reservoir characterization which could assist in understanding the original oil/gas in place and the flow characteristics of the shale rocks [1–3]. The gas adsorption method is now a standard method for pore structure correction. The gas adsorption method involves bringing the gas/vapor into contact with the solid surface [4–6]. For shale rocks, N<sub>2</sub> and CO<sub>2</sub> are the two gases that are typically used for gas adsorption. N<sub>2</sub> adsorption (at 77 k) can be used to derive the specific surface area (using the Brunauer, Emmett, and Teller equation) and pore size distribution (using the Barrett–Joyner–Halenda model or density functional theory) [7, 8]. N<sub>2</sub> adsorption can mainly get the meso-macropore information (pore size >2 nm) and cannot provide the micropore information. Under low temperature, the N<sub>2</sub> molecule is kinetically restricted from accessing the micropores [9]. In order to overcome the limitations of N<sub>2</sub> adsorption, CO<sub>2</sub> adsorption is commonly performed. The critical dimensions of the CO<sub>2</sub> molecule and the N<sub>2</sub> molecule are very similar (0.28 nm for CO<sub>2</sub> and 0.30 nm for N<sub>2</sub>), but the higher working temperature for CO<sub>2</sub> adsorption (273 k for CO<sub>2</sub> adsorption) helps the CO<sub>2</sub> molecule to enter into the

micropores [9]. CO<sub>2</sub> adsorption (273 k) is usually complemented by the N<sub>2</sub> adsorption (77 K) to get a wider pore size information in shale reservoir characterization.

The pore structure of shale samples is very complicated, which has been shown by many researchers using the scanning electron microscope [10–15]. In order to understand the complexity of the pore structures, the fractal theory can be applied. Avnir et al. [16] found that at the molecular level, the surface of most materials has a fractal behavior with fractal dimension varying from 2 to 3, where 2 means a perfectly smooth surface and 3 denotes significantly rough and a disordered surface. Several fractal models have been developed for N<sub>2</sub> adsorption, such as the Frenkel–Halsey–Hill (FHH) theory [17] or the thermodynamic model by Neimark [18]. These models for N<sub>2</sub> adsorption are mainly focused on the meso-macro pore (>2 μm) capillary condensation by using Kelvin's equation. However, Kelvin's equation is not valid for the pores with sizes smaller than 7.5 nm [19], which indicates that these current fractal models cannot be used for CO<sub>2</sub> adsorption. Most researchers only analyzed the fractal dimension from the N<sub>2</sub> adsorption, even when they performed both N<sub>2</sub> adsorption and CO<sub>2</sub> adsorption experiments [3, 20, 21]. To the best of the authors' knowledge, the fractal model for the CO<sub>2</sub> adsorption in shale

studies has not been yet reported. In this paper, we present a fractal model for CO<sub>2</sub> adsorption built by combining the thermodynamic model and the Dubinin–Astakhov analysis model.

## 2. Model Description

From the thermodynamic viewpoint, the differential of the interface area  $ds$  can be calculated from the balance between the work of forming the interface and the work from the adsorption of CO<sub>2</sub> [18]:

$$\sigma ds = \Delta\mu dN, \quad (1)$$

where  $\sigma$  is the surface tension,  $\mu$  is the differential chemical potential of CO<sub>2</sub>, and  $N$  is the adsorption amount of CO<sub>2</sub>.

For CO<sub>2</sub>, the differential chemical potential under pressure  $p$  can be calculated using the following equation [22, 23]:

$$\Delta\mu = RT \ln \frac{p}{p_0}, \quad (2)$$

where  $R$  is the universal gas constant, 8.314 Jmol<sup>-1</sup>K<sup>-1</sup>;  $T$  is the temperature, 273 K;  $p$  is the working pressure; and  $p_0$  is the CO<sub>2</sub> saturation pressure under 273 K.

By combing equations (1) and (2), we can obtain the following equation:

$$S = \frac{1}{\sigma} \int_{N_{(p/p_0)}}^{N_{\max}} RT \ln \frac{p}{p_0} dN, \quad (3)$$

where  $N_{\max}$  is the maximum cumulative adsorption quantity and  $N_{(p/p_0)}$  is the cumulative adsorption quantity under the relative pressure ( $p/p_0$ ).

The correlation of the area for a fractal surface and the volume circumscribed by the surface obeys the following equation [24]:

$$S^{1/D} \sim V^{1/3}, \quad (4)$$

where  $D$  is the fractal dimension.

If the fractal surface is measured on a Euclidean area, equation (4) can be changed to the following equation by the dimensional analysis [25]:

$$S = k^D r^{2-D} V^{D/3}, \quad (5)$$

where  $k$  is a correlation factor between the surface and the volume,  $r$  is the radius, and  $V$  is the volume.

Assuming that the gas molecules cannot be compressed, the volume can be calculated using the following equation:

$$V = \left( N_{\max} - N_{N_{(p/p_0)}} \right) V_L, \quad (6)$$

where  $V_L$  is the molecular volume of CO<sub>2</sub>.

By combining equations (3) and (6), we obtain the following expression:

$$\frac{1}{\sigma} \int_{N_{(p/p_0)}}^{N_{\max}} RT \ln \frac{p}{p_0} dN = k^D r_{p/p_0}^{2-D} \left( N_{\max} - N_{p/p_0} \right)^{D/3} V_L^{D/3}, \quad (7)$$

which can be further rewritten as

$$\frac{\int_{N_{(p/p_0)}}^{N_{\max}} \ln (p/p_0) dN}{r_{p/p_0}^2} = \frac{\sigma}{RT} k^D V_L^{D/3} \left[ \frac{N_{\max} - N(p/p_0)}{r_{p/p_0}} \right]^D, \quad (8)$$

where  $r_{p/p_0}$  is the pore radius under the relative pressure  $p/p_0$ .

The form of equation (8) is similar to the equation which was provided by Wang and Li [25] for the N<sub>2</sub> adsorption analysis. However, in their model, they applied the Kelvin equation to obtain the pore radius for the mesopore capillary condensation stage, which is not suitable for the micropores. For the micropores,  $r_{p/p_0}$  can be derived from the Dubinin–Astakhov model [26]:

$$\frac{W}{W_0} = \exp \left[ - \left( \frac{-RT \ln (p/p_0)}{E} \right)^n \right], \quad (9)$$

where  $w_0$  is the limiting adsorption volume,  $w$  is the occupied adsorption volume,  $E$  is the characteristic energy of the system, and  $n$  is an empirical constant.

Then, the pore size of the sample can be calculated using the following equation:

$$\frac{d(W/W_0)}{dr_{p/p_0}} = 3n \left( \frac{D_0}{E} \right)^n r_{p/p_0}^{-(3n+1)} \exp \left[ - \left( \frac{D_0}{E} \right)^n r_{p/p_0}^{-3n} \right], \quad (10)$$

where  $D_0$  is the dispersion interaction energy.

If we combine equations (9) and (10), we can express the radius:

$$r_{p/p_0} = \left( \frac{-RT \ln (p/p_0)}{D_0} \right)^{-1/3}. \quad (11)$$

For equation (8), let  $A_{p/p_0} = \ln \left( \int_{N_{(p/p_0)}}^{N_{\max}} \ln (p/p_0) dN / r_{p/p_0}^2 \right)$  and  $B_{p/p_0} = \ln \left( (N_{\max} - N(p/p_0)) / r_{p/p_0} \right)$ ; then, equation (8) can be written in the following form:

$$A_{p/p_0} = C + DB_{p/p_0}. \quad (12)$$

Thus, if  $A$  and  $B$  values are calculated under different relative pressure for a CO<sub>2</sub> adsorption isotherm, then the fractal dimension  $D$  can be easily determined from the slope of the function in equation (12).  $C$  is a constant which can be derived from curve fitting.

## 3. Results and Discussion

**3.1. Model Verification.** In order to verify this model, we performed the CO<sub>2</sub> adsorption experiment on three shale samples and calculated their fractal dimension using equation (12). Figure 1 shows the adsorption isotherms of the three samples (the relative pressure is from 0.001 to 0.03).

**3.2. Impact of  $D_0$  on the Results.** We applied the new model to calculate the  $A$  and  $B$  values of each sample under different relative pressure values and then plot  $A$  as a function of  $B$  (Figure 2) (here, we assume that  $D_0$  is 1500 Jnm<sup>3</sup>mol<sup>-1</sup>, from Hiden Isochema). Very strong linear relations exist between  $A$  and  $B$  for all three samples, indicating that the CO<sub>2</sub> adsorption isotherm shows the fractal behavior. The fractal

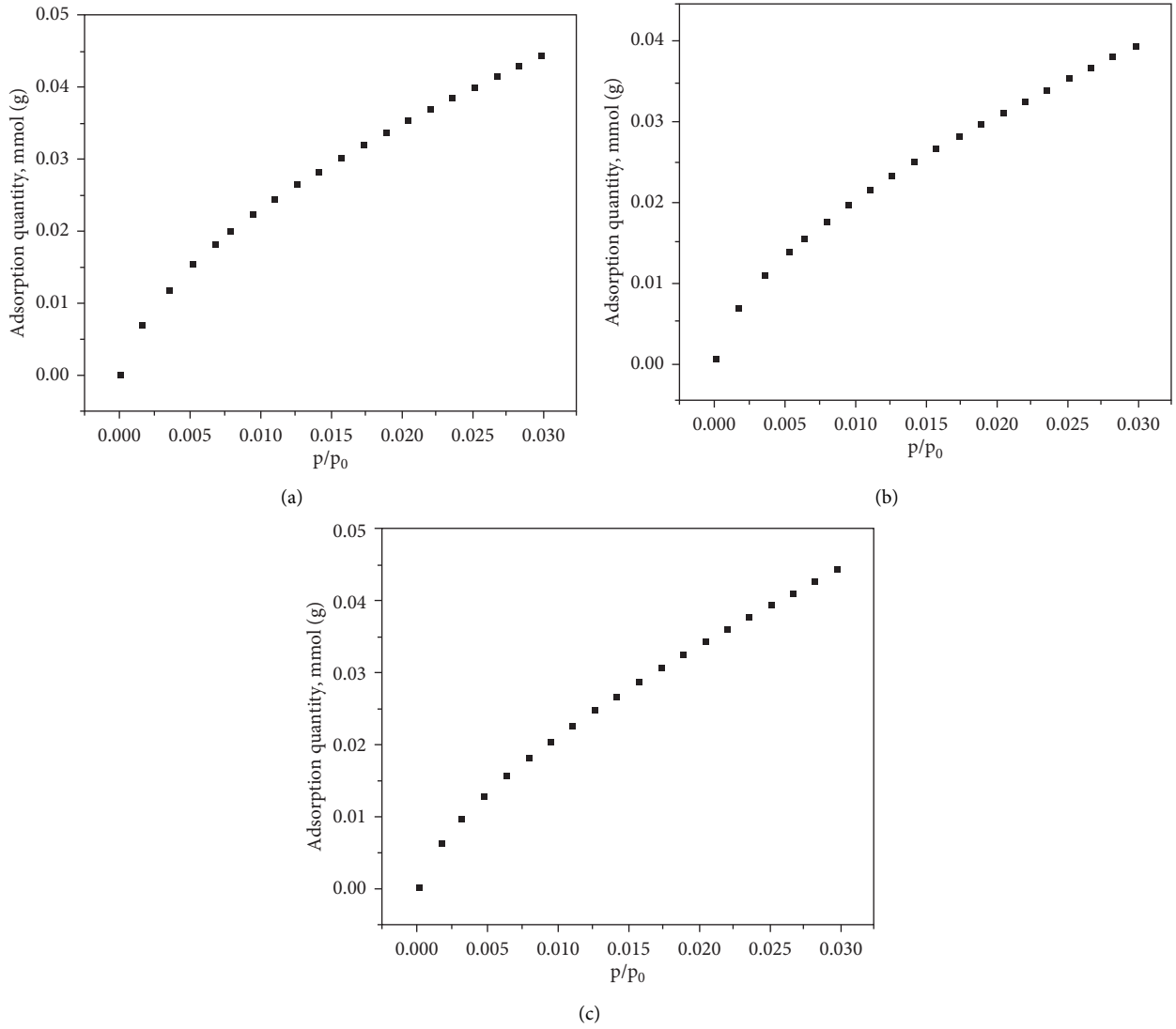


FIGURE 1: Measured CO<sub>2</sub> adsorption isotherms of three shale samples. (a) Sample 1. (b) Sample 2. (c) Sample 3.

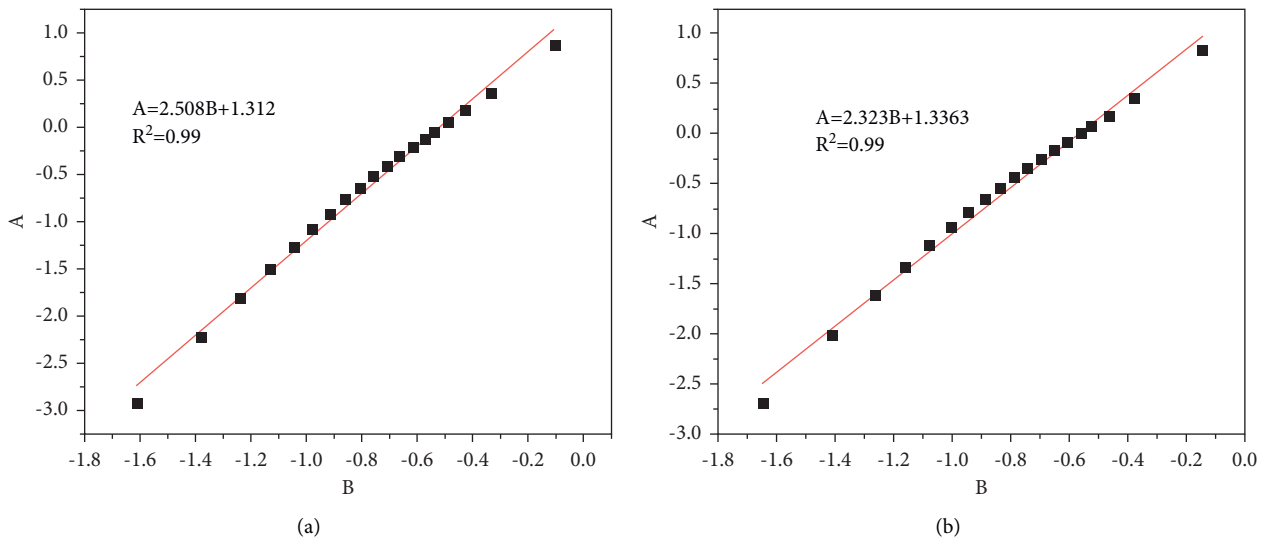
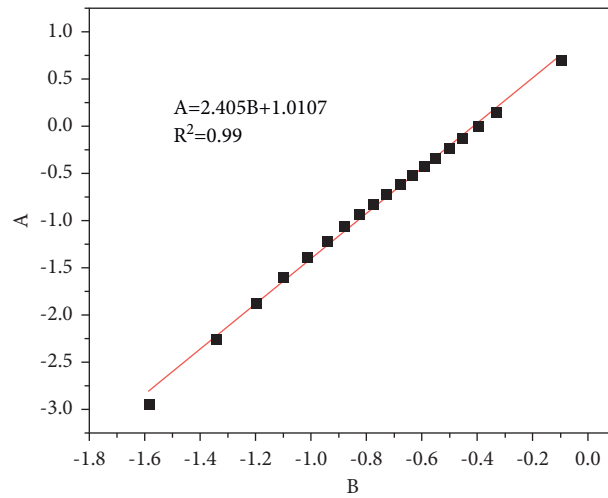
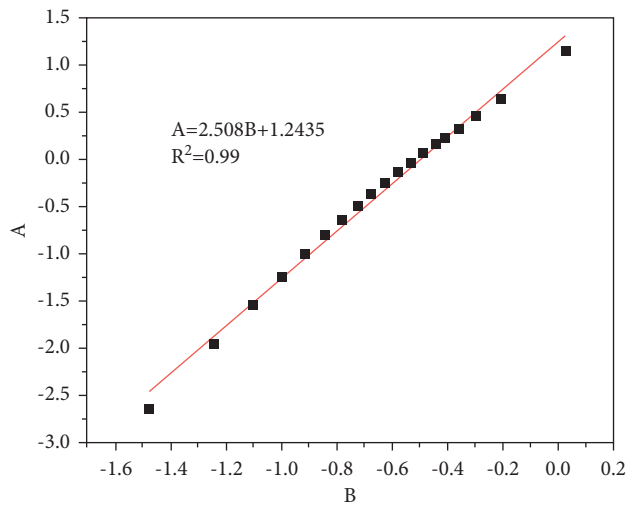


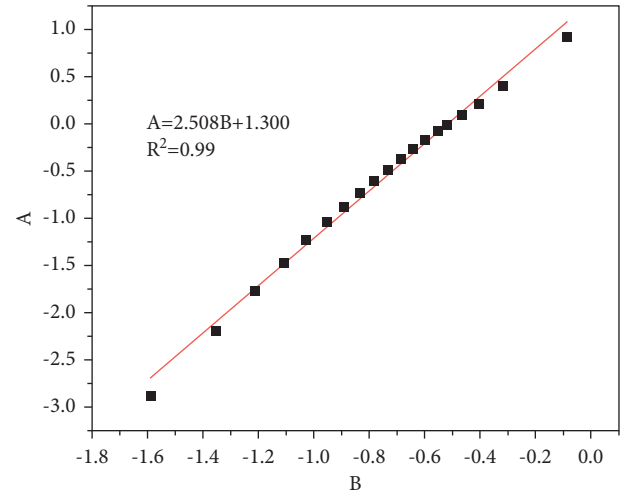
FIGURE 2: Continued.



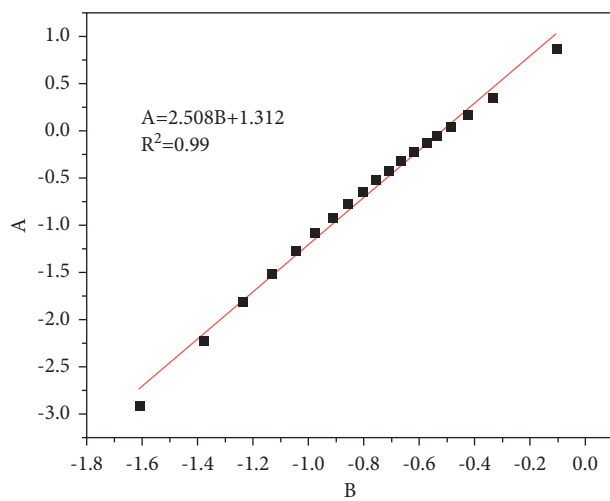
(c)

FIGURE 2: Fractal analysis of the CO<sub>2</sub> adsorption isotherms of the three shale samples. (a) Sample 1. (b) Sample 2. (c) Sample 3.

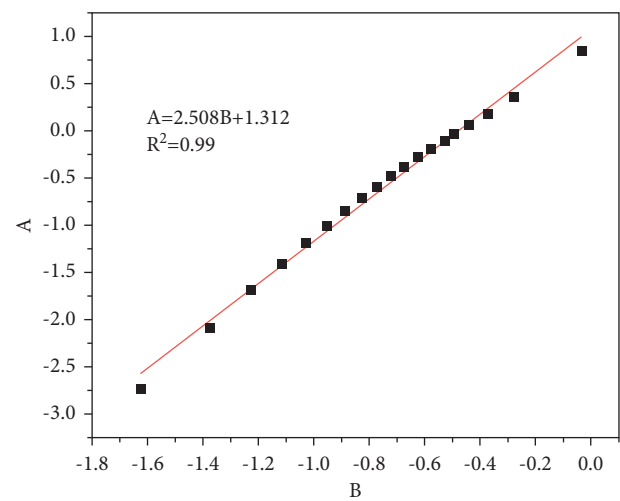
(a)



(b)



(c)



(d)

FIGURE 3: Continued.

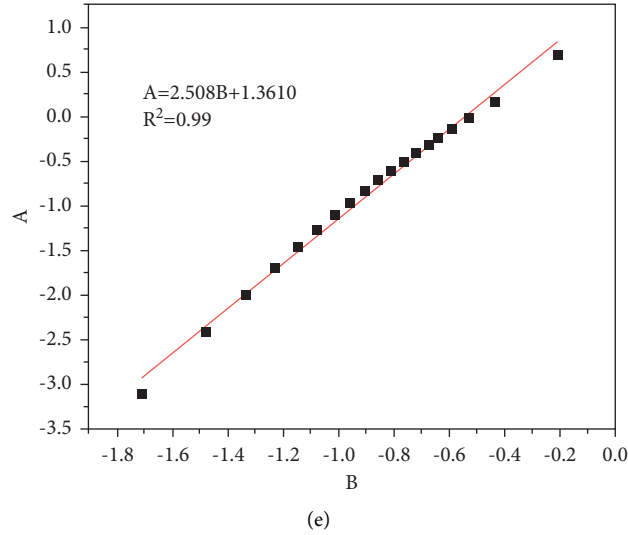


FIGURE 3: The impact of  $D_0$  on the fractal dimension (sample 1). (a)  $D_0 = 1000 \text{ Jnm}^3 \text{ mol}^{-1}$ . (b)  $D_0 = 1400 \text{ Jnm}^3 \text{ mol}^{-1}$ . (c)  $D_0 = 1500 \text{ Jnm}^3 \text{ mol}^{-1}$ . (d)  $D_0 = 1600 \text{ Jnm}^3 \text{ mol}^{-1}$ . (e)  $D_0 = 2000 \text{ Jnm}^3 \text{ mol}^{-1}$ .

dimensions of these three samples are 2.508, 2.323, and 2.405, respectively. The fractal dimension falls within the expected range of  $2 < D < 3$ , predicted by the fractal geometry [25, 27]. Thus, the model yields robust results and can be used to calculate the fractal dimension of  $\text{CO}_2$  adsorption on shale samples.

In the previous examples, we had to assume a value for  $D_0$  in order to calculate  $r_{p/p_0}$ .  $D_0$  is the dispersion interaction energy of  $\text{CO}_2$ , which is not well constrained but is usually set to around  $1500 \text{ Jnm}^3 \text{ mol}^{-1}$  [28]. In this part, we further studied the effect of  $D_0$  value on the fractal dimension. We set three  $D_0$  values (1000, 1400, 1500, 1600, and  $2000 \text{ Jnm}^3 \text{ mol}^{-1}$ ) and then calculated the fractal dimension of sample 1 for all three cases. Figure 3 shows that the absolute values of the  $A$  and  $B$  values do vary for different  $D_0$ , but the slope of the linear regression of  $A$  to  $B$  remains the same. Therefore, the choice of  $D_0$  value does not affect the fractal dimension calculation. The fractal dimension value of the  $\text{CO}_2$  adsorption isotherm from shale samples can be derived even when the exact  $D_0$  value is not well constrained.

**3.3. Future Research.** Clay bound water is an important factor that could affect the fractal dimensions of the gas adsorption which has been studied by many researchers [29–31]. Under different moisture content, the fractal dimension changes. However, in this study, we preheated the samples under  $105^\circ\text{C}$  for over 12 hours and we believe that the effect of the clay bound water effect can be neglected. In this study, our focus is to derive a model to describe the fractal model for the analyzing the fractal dimensions of the  $\text{CO}_2$  gas adsorption. Thus, the samples we choose are from a single basin and very simple. More samples from the different shale basins will be collected and analyzed to verify the applicability of this model. In addition, based on the studies by other researchers, the fractal dimension from  $\text{N}_2$  gas adsorption could be correlated with the pore structures [32]. Whether the fractal dimension from  $\text{CO}_2$

gas adsorption is correlated with the microstructures of the samples and how the microstructures affect the fractal dimension will be the target for the next step research.

## 4. Conclusions

- (1) Based on the Dubinin–Astakhov analysis model and the thermodynamic model, we built the fractal analysis model for  $\text{CO}_2$  adsorption on shale samples.
- (2) We applied the new model to calculate the fractal dimensions of the  $\text{CO}_2$  adsorption isotherms for three shale samples. We found that the  $\text{CO}_2$  adsorption isotherms had the fractal behavior, and the fractal dimension value was between 2 and 3. This agrees with the fractal geometry and indicates the robust performance of the new model.
- (3) We conducted a sensitivity analysis to investigate the effect of the dispersion interaction energy  $D_0$  on the fractal dimension calculation and demonstrated that the choice of the  $D_0$  value does not affect the model outcomes.

## Data Availability

The data used to support the findings of this study are available from the corresponding author upon request.

## Conflicts of Interest

The authors declare that they have no conflicts of interest.

## Acknowledgments

The authors appreciate PetroChina Xinjiang Oilfield Company and shale oil research team. This study was supported by the Forward-Looking Basic Projects of CNPC (grant no. 2021DJ1803).

## References

- [1] R. M. Bustin, A. M. Bustin, A. Cui, D. Ross, and V. M. Pathi, "Impact of shale properties on pore structure and storage characteristics," in *Proceedings of the SPE Shale Gas Production Conference*, November 2008.
- [2] C. R. Clarkson, N. Solano, R. M. Bustin, A. M. M. Bustin, and G. R. L. Chalmers, "Pore structure characterization of North American shale gas reservoirs using USANS/SANS, gas adsorption, and mercury intrusion," *Fuel*, vol. 103, pp. 606–616, 2013.
- [3] K. Liu, M. Ostadhassan, J. Zhou, T. Gentzis, and R. Rezaee, "Nanoscale pore structure characterization of the bakken shale in the USA," *Fuel*, vol. 209, pp. 567–578, 2017.
- [4] L. M. Anovitz and D. R. Cole, "Characterization and analysis of porosity and pore structures," *Reviews in Mineralogy and Geochemistry*, vol. 80, no. 1, pp. 61–164, 2015.
- [5] S. Scaife, P. Kluson, and N. Quirke, "Characterization of porous materials by gas adsorption: do different molecular probes give different pore structures?" *The Journal of Physical Chemistry B*, vol. 104, no. 2, pp. 313–318, 2000.
- [6] K. S. Sing, "Adsorption methods for the characterization of porous materials," *Advances in Colloid and Interface Science*, vol. 76, pp. 3–11, 1998.
- [7] M. Jaroniec, M. Kruk, and J. Choma, "The 50th anniversary of the barrett-joyner-halenda method for mesopore size analysis: critical appraisal and future perspectives," *Fundamentals of Adsorption*, vol. 7, pp. 570–577, 2001.
- [8] P. I. Ravikovitch, A. Vishnyakov, and A. V. Neimark, "Density functional theories and molecular simulations of adsorption and phase transitions in nanopores," *Physical Review E*, vol. 64, no. 1, Article ID 011602, 2001.
- [9] J. Garrido, A. Linares-Solano, J. M. Martin-Martinez, M. Molina-Sabio, F. Rodriguez-Reinoso, and R. Torregrosa, "Use of nitrogen vs. carbon dioxide in the characterization of activated carbons," *Langmuir*, vol. 3, no. 1, pp. 76–81, 1987.
- [10] R. G. Loucks, R. M. Reed, S. C. Ruppel, and D. M. Jarvie, "Morphology, genesis, and distribution of nanometer-scale pores in siliceous mudstones of the Mississippian Barnett Shale," *Journal of Sedimentary Research*, vol. 79, no. 12, pp. 848–861, 2009.
- [11] R. G. Loucks, R. M. Reed, S. C. Ruppel, and U. Hammes, "Spectrum of pore types and networks in mudrocks and a descriptive classification for matrix-related mudrock pores," *AAPG Bulletin*, vol. 96, no. 6, pp. 1071–1098, 2012.
- [12] M. E. Curtis, R. J. Ambrose, and C. H. Sondergeld, "Structural characterization of gas shales on the micro-and nano-scales," in *Proceedings of the Canadian unconventional resources and international petroleum conference*, Society of Petroleum Engineers, Calgary, Canada, October 2010.
- [13] S. Kelly, H. El-Sobky, C. Torres-Verdin, and M. T. Balhoff, "Assessing the utility of FIB-SEM images for shale digital rock physics," *Advances in Water Resources*, vol. 95, pp. 302–316, 2016.
- [14] A. Golparvar, Y. Zhou, K. Wu, J. Ma, and Z. Yu, "A comprehensive review of pore scale modeling methodologies for multiphase flow in porous media," *Advances in Geo-Energy Research*, vol. 2, no. 4, pp. 418–440, 2018.
- [15] Y. Yang, J. Liu, J. Yao, J. Kou, Z. Li, and T. Wu, "Adsorption behaviors of shale oil in kerogen slit by molecular simulation," *Chemical Engineering Journal*, vol. 387, Article ID 124054, 2020.
- [16] D. Avnir, D. Farin, and P. Pfeifer, "Molecular fractal surfaces," *Nature*, vol. 308, no. 5956, p. 261, 1984.
- [17] P. Pfeifer, "Fractal dimension as working tool for surface-roughness problems," *Applications of Surface Science*, vol. 18, no. 1-2, pp. 146–164, 1984.
- [18] A. Neimark, "A new approach to the determination of the surface fractal dimension of porous solids," *Physica A: Statistical Mechanics and its Applications*, vol. 191, no. 1-4, pp. 258–262, 1992.
- [19] R. T. Yang, *Adsorbents: Fundamentals and Applications*, John Wiley & Sons, Hoboken, NJ, USA, 2003.
- [20] R. Yang, S. He, J. Yi, and Q. Hu, "Nano-scale pore structure and fractal dimension of organic-rich Wufeng-Longmaxi shale from Jiaoshiba area, sichuan basin: investigations using FE-SEM, gas adsorption and helium pycnometry," *Marine and Petroleum Geology*, vol. 70, pp. 27–45, 2016.
- [21] X. Wang, Z. Jiang, S. Jiang et al., "Full-scale pore structure and fractal dimension of the Longmaxi shale from the Southern Sichuan Basin: investigations using FE-SEM, gas adsorption and mercury intrusion porosimetry," *Minerals*, vol. 9, no. 9, p. 543, 2019.
- [22] V. K. Dobruskin, "Micropore volume filling. A condensation approximation approach as a foundation to the Dubinin–Astakhov equation," *Langmuir*, vol. 14, no. 14, pp. 3840–3846, 1998.
- [23] T. T. Trinh, D. Bedeaux, J. M. Simon, and S. Kjelstrup, "Calculation of the chemical potential and the activity coefficient of two layers of CO<sub>2</sub> adsorbed on a graphite surface," *Physical Chemistry Chemical Physics*, vol. 17, no. 2, pp. 1226–1233, 2015.
- [24] B. B. Mandelbrot, *The Fractal Geometry of Nature*, p. 109, Freeman, Dallas, TX, USA, 1982.
- [25] F. Wang and S. Li, "Determination of the surface fractal dimension for porous media by capillary condensation," *Industrial & Engineering Chemistry Research*, vol. 36, no. 5, pp. 1598–1602, 1997.
- [26] M. M. Dubinin and V. A. Astakhov, "Molecular sieve. Zeolites II," *Journal of the American Chemical Society*, vol. 102, p. 69, 1971.
- [27] J. Lai, G. Wang, Z. Fan, Z. Zhou, J. Chen, and S. Wang, "Fractal analysis of tight shaly sandstones using nuclear magnetic resonance measurements," *AAPG Bulletin*, vol. 102, no. 2, pp. 175–193, 2018.
- [28] Hiden Isochema Laboratory, "The determination of the pore size distribution of an activated carbon using Dubinin-Astakhov analysis of CO<sub>2</sub> adsorption at 273 K," 2016, <https://hidenisochema.com/content/uploads/2016/04/Hiden-Isochema-Application-Note-126.pdf>.
- [29] Y. Yuan, R. Rezaee, M. Verrall, S. Y. Hu, J. Zou, and N. Testamanti, "Pore characterization and clay bound water assessment in shale with a combination of NMR and low-pressure nitrogen gas adsorption," *International Journal of Coal Geology*, vol. 194, pp. 11–21, 2018.
- [30] Y. Yuan and R. Rezaee, "Fractal analysis of the pore structure for clay bound water and potential gas storage in shales based on NMR and N<sub>2</sub> gas adsorption," *Journal of Petroleum Science and Engineering*, vol. 177, pp. 756–765, 2019.
- [31] K. Liu, Z. Jin, L. Zeng, Y. Yuan, and M. Ostadhassan, "Determination of clay bound water in shales from NMR signals: the fractal theory," *Energy & Fuels*, vol. 35, no. 22, pp. 18406–18413, 2021.
- [32] K. Liu, N. Zakharova, T. Gentzis, A. Adeyilola, H. Carvajal-Ortiz, and H. Fowler, "Microstructure characterization of a biogenic shale gas formation—insights from the antrim shale, Michigan basin," *Journal of Earth Science*, vol. 31, no. 6, pp. 1229–1240, 2020.

## Research Article

# Isothermal Desorption Hysteretic Model for Deep Coalbed Methane Development

Songlei Tang , Hongbo Zhai , Hong Tang , and Feng Yang 

*Xi'an Modern Chemistry Research Institute, 710065, Xi'an, China*

Correspondence should be addressed to Hongbo Zhai; [zhaihongbo@qq.com](mailto:zhaihongbo@qq.com)

Received 10 September 2021; Revised 25 December 2021; Accepted 29 December 2021; Published 25 January 2022

Academic Editor: Kouqi Liu

Copyright © 2022 Songlei Tang et al. This is an open access article distributed under the Creative Commons Attribution License, which permits unrestricted use, distribution, and reproduction in any medium, provided the original work is properly cited.

The adsorption/desorption mechanism of coalbed methane is significant for gas control and coalbed methane exploitation; scholars have done a lot of research on it and generally have confidence in that temperature, pressure, and moisture are central factors affecting the adsorption of coalbed methane. Considering the reduction of recovery efficiency caused by desorption hysteresis in deep coalbed methane drainage, the effects of high reservoir pressure, high gas content, and low permeability on the hysteresis index were analyzed. A desorption hysteresis model based on the combination of dual-porosity media and traditional Langmuir adsorption theory was proposed. By comparing with the four experimental data of Ma et al., the advantages of the new model in fitting desorption data were investigated. Based on the new desorption hysteresis model, the hysteresis index was calculated from the adsorption capacity and desorption capacity under the abandonment pressure. The hysteresis index under different coal sizes and adsorption pressure were calculated, and a good linear relationship was found between the adsorption pressure and the hysteresis index. Through a large number of field production data analysis, the following conclusions are drawn: as the adsorption pressure increases, the hysteresis index enhances; when the coal sample size increases, the hysteresis index also increases. Finally, by comparing experimental data from deep and shallow coal samples, the influence of desorption hysteresis on deep coalbed methane mining was explored. This paper draws the conclusion that although the gas content in deep coalbed methane is considerable, its hysteresis index is also enhanced, which makes coalbed methane development more difficult. The findings of this study can provide theoretical support for coal bed gas control and coal bed methane heat injection mining.

## 1. Introduction

Deep coalbed methane (CBM) resources have huge potential and are a new field for unconventional natural gas exploration and development. With the decline of shallow coalbed methane and coal resources, increasing demand for energy and intensity of mining, deep coalbed methane resources with depth of 1500~3000 m have gradually received attention. The development of coalbed methane has also entered a state of deep resources [1]. The increase in gas emissions from deep coal reservoirs has led to increasingly serious gas disasters, and deep coal rocks are susceptible to high geostress and pore pressure environments, and coal seam permeability is relatively low. The production of coalbed methane causes changes in pore pressure, which results in changes in coal seam skeleton

stress and significant pore deformation. Therefore, the deformation of the pore space changes the movement resistance of the fluid through the pore channel, which leads to considerable change in permeability [2].

The development of coalbed methane is a dynamic process. After the confined water in the fractures is discharged, the adsorbed gas in the coal matrix desorbs flows to the pore fractures, while the free gas in the pore fractures flows to the borehole, as shown in Figure 1.

The discharge and extraction of coalbed methane lead to the reduction of gas pressure and gas concentration in the fractures. Under the effect of concentration gradient, the free gas in the matrix pores diffuses into the fractures, which promotes desorption of the gas adsorbed in the pores. In the early recognition, the process of gas adsorption and desorption in coal is generally considered to be completely reversible [3]. The

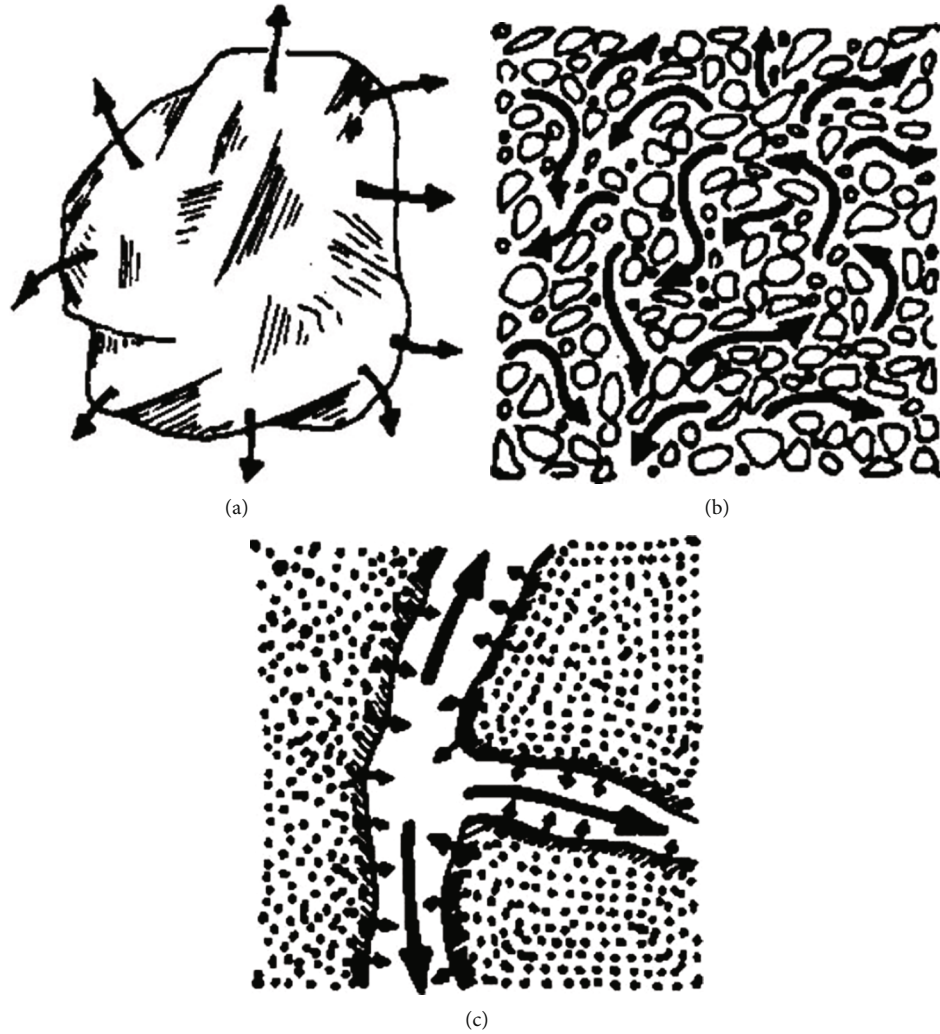


FIGURE 1: Schematic diagram of desorption-diffusion flow of coalbed methane [3]. (a) Desorbs from the inner surface of coal, (b) diffuses through matrix and micropores, and (c) flows in natural fracture networks.

Langmuir volume, Langmuir pressure, and recoverable reserves of coalbed methane are usually obtained by measuring the isotherm adsorption line. However, in recent years, many scholars have found that the adsorption and desorption of coalbed methane in coal are not completely reversible in most cases, and there is a hysteresis phenomenon in adsorption and desorption. As shown in Figure 2, during the adsorption and desorption cycle, the desorption gas content is always greater than the adsorption capacity under the same pressure. For deep coalbed methane, as the burial depth increases, the volatile content of coal decreases, the degree of metamorphism increases, and the gas content and gas pressure increase. As the gas pressure increases, the desorption hysteresis degree increases. In the process of deep-seated coalbed methane development, the desorption hysteresis will be more serious, which will produce larger deviations compared with the traditional reversible desorption model.

Changes in the state of the deep stress field will inevitably lead to the formation of deep coalbed methane reservoirs that vary from those of shallow formations. The gas content, gas adsorption characteristics, stress, and permeability of

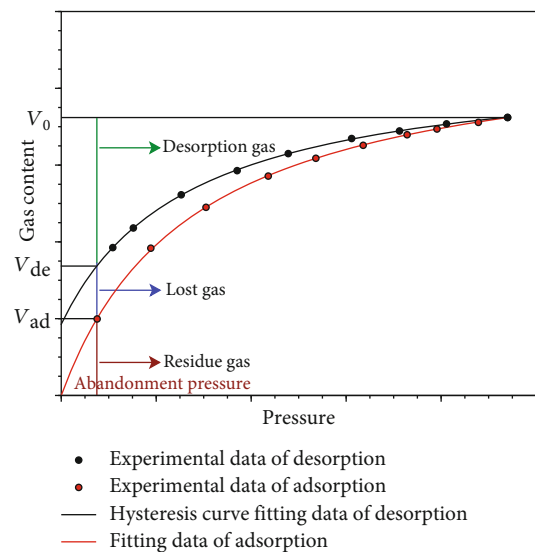


FIGURE 2: Illustration of adsorption/desorption hysteresis evaluation model.

deep coal seams are largely different from shallow coal reservoirs: (1) coal seam gas content generally rises first and then decreases as burial depth increases; (2) logarithm of permeability has a negative linear correlation with the burial depth, that is, the burial depth of the coal seam increases, and the permeability decreases exponentially; (3) although the geostress field varies from region to region as the tectonic geological environment changes, the ratio of average horizontal stress to vertical stress decreases with increasing burial depth; (4) the total porosity of deep coal seam change is not significant compared to shallow coal seam, but the distribution of pores in the shallow is more dispersed, while the deep is more concentrated, mostly microporous.

Jessen et al. [4] found that different desorption hysteresis exists for the same coal rock sample at different maximum adsorption pressures, but the degree of hysteresis is not the same. Harpalani et al. [5] indicated that lignite in the San Juan Basin and the Illinois Basin both have coal seam gas hysteresis, but the hysteresis index is less than that of carbon dioxide. Pan et al. [6] studied coal samples in Sydney Basin with different water contents, and there was hysteresis in all the experimental groups. Zhang et al. [7] carried out isothermal desorption experiments of component gases and multicomponent gases with different ratios and proposed the relative reversibility and desorption hysteresis characteristics of the coalbed methane adsorption and desorption process. Liu et al. [8] studied the pore distribution of coal and its adsorption-desorption characteristics, and the research showed that the difference in the  $\text{CO}_2/\text{CH}_4$  adsorption capacity is the primary cause of the phenomenon of desorption hysteresis. Song et al. [9] studied different types of deformed coal in Pingdingshan, and the experimental results showed that the adsorption and desorption of deformed coal are irreversible, and the degree of irreversible increases with the increase of coal destruction. Jian et al. [10] also found that the hysteresis of Pingdingshan pulverized coal is more obvious than that of primary structure coal. Ma et al. [11–13] studied the hysteresis phenomenon in various aspects from the perspective of CBM development, examined the effects of temperature, moisture, and other factors, and analyzed that the phenomenon does exist. It can be verified from CBM well test and drainage data that the main reason is that the micropores and pores have a strong binding capacity to gas molecules. Su et al. [14, 15] found that  $^{13}\text{CH}_4$  has the characteristics of preferential adsorption and delayed desorption compared with  $^{12}\text{CH}_4$  and explained it with the adsorption potential theory. Qiu et al. [16] found that the total heat of capillary condensation is identical to that of capillary evaporation for all systems examined, regardless of the presence of hysteresis. He et al. [17] found that original gas of three wells in the Fuling Shale in China calculated by the conventional method was lower than that calculated by the refined method, which explained the desorption hysteresis.

The above studies are only corresponding improvements based on the Langmuir model, mainly in terms of temperature, but rarely modify the adsorption analytical model in dual porous media. On this basis, four sets of coal samples from different regions are taken as the research objects. On

this basis, four sets of coal samples from different regions are taken as the research objects, and the coalbed methane adsorption model under the combined action of pressure and temperature is established and revised on the high-pressure coal rock matrix. However, the influence of water content on adsorptive and desorptive gas quantity is neglected in this paper, and the influence of water content needs further study.

On the basis of previous work, a quantitative evaluation index was proposed to understand the degree of hysteresis, and this index was used to evaluate the difference in the degree of adsorption and desorption hysteresis between shallow coal seams and deep coal seams. Then, on the basis of Ma's hysteresis model, a new adsorption and desorption hysteresis model was established, and the constant correction term was modified into a linear correction term to better understand the laws of adsorption and hysteresis. Finally, we attempt to explicate the mechanism of desorption hysteresis and discuss the negative effects of desorption hysteresis in deep coalbed methane mining, so as to provide guidance for engineering practice.

## 2. Modified Desorption Hysteresis Model for Dual Porous Media

Porous media with fractures and pores are called dual-porous media. Fractures are mainly used as fluid flow channels, while pores are mainly used as gas storage spaces. The permeability of fractures and matrixes varies widely. According to the concept of dual-porosity medium, coal seams have a large number of micropores and fractures connecting micropores, and the permeability of pores is generally much smaller than the permeability of fractures. Therefore, most coal seams can be regarded as dual-porous media.

For the desorption hysteresis in the dual-porosity medium model, Ma et al. [13] conducted an isothermal adsorption experiment. The experimental results show that the isothermal adsorption curve conforms to the Langmuir equation, with a high degree of data fitting and small errors. The Langmuir equation of the isothermal desorption curve has a low degree of fit, indicating that the coal seam gas desorption process does not obey the Langmuir equation. Then, they proposed a modified model that included residual adsorption capacity under waste pressure. Wang et al. [18] improved the dual isothermal desorption curve of the pore model and found that it is more suitable to describe the isothermal desorption hysteresis curve. Based on Wang's model and Ma's improved model, we propose a new isothermal desorption curve. The new model assumes that the coal seam adsorbed gas volume is

$$V = kP + C_r + V_0^d \frac{P}{P_L^d + P}, \quad (1)$$

where  $k$  is Henry gas dissolution constant,  $V_0^d$  and  $P_L^d$  are Langmuir constants in the dual-porosity model, and  $C_r$  is residual adsorption amounts.

TABLE 1: Comparison table of four groups of experimental data fitting parameters.

Sample	Adsorption fitting parameters		Desorption fitting parameters				Improve model desorption fitting parameters				
	$a$	$b$	$a$	$b$	$c$	$R^2$	$C_r$	$k$	$V_0^d$	$P_L^d$	$R^2$
Huangling 2 <sup>#</sup> RN	18.132	0.233	17.153	0.215	1.301	0.999	1.525	-0.289	23.621	6.615	0.9996
Zhaiyadi 9 <sup>#</sup> JM	19.252	0.643	16.561	0.824	2.154	0.999	2.389	-0.034	16.928	1.356	0.9994
Xiangshan 3 <sup>#</sup> SM	20.837	0.297	16.030	0.322	3.111	0.998	0.773	0.402	12.319	1.116	0.9996
Sihe 3 <sup>#</sup> WY	34.031	0.253	28.642	0.212	4.654	0.999	4.809	-0.608	42.363	7.040	0.9992

According to the pressure and temperature data of adsorption experiment collected by Ma, combined with the above-mentioned improved double-pore model, the fitting degree  $R^2$  is obtained, as shown in Table 1.

By comparing the fitting degree  $R^2$ , the improved model has a higher fitting degree of and smaller error, which verifies the accuracy of the modified model. Since the dual porous media model is introduced into the model for understanding hysteresis, the modified model fits better. The fractures of the coal matrix satisfy the Darcy flow equation, and the micropores and nanopores satisfy the Langmuir adsorption equation.

The fitting and comparison curves of the adsorption and desorption experiment results are shown in Figure 3. When analyzing the experimental data of four different coal samples obtained by Ma et al., it was found that there were abandonment pressure points during the desorption process. The abandonment pressure point is the minimum pressure point that can be reached during the decompression and desorption process of drainage. It is impossible for the drainage decompression process to reach a state of zero pressure during the production process. Therefore, the gas content at the abandonment pressure point is an important physical quantity with a reference value.

By fitting the experimental data, the desorption effect lags behind the adsorption effect in several groups of experimental coal samples. Based on the phenomenon of adsorption hysteresis, Liu and Kang [19] defined the coalbed gas adsorption hysteresis effect as under certain conditions, the gas adsorption capacity of coal is not a single value function of matrix potential; it depends on the historical process of coalbed methane adsorption or desorption. In the practice of CBM development, affected by the hysteresis effect of coalbed methane desorption, it is necessary to use desorption isotherms instead of adsorption isotherms to evaluate gas production, gas recovery rate, recoverable reserves, and recovery efficiency.

### 3. Quantitative Evaluation Index of Desorption Hysteresis

Many scholars have proposed several evaluation indexes for different desorption hysteresis. The following sections briefly introduce several evaluation indicators.

**3.1. Freundlich Index Method.** The Freundlich index method decomposes the adsorption and desorption into two curves.

The adsorption process was fitted with the function  $S_{ad} = K_{ad}Ce_{ad}^n$ , and the desorption process with  $S_{de} = K_{de}Ce_{de}^n$ , where  $S$  is the concentration of the adsorbent;  $Ce$  is the equilibrium concentration of the adsorbent;  $K$  is the Freundlich adsorption parameters;  $n$  is the Freundlich index; the subscripts ad and de denote the adsorption and desorption processes, respectively.

The expression of the degree of hysteresis HI in this irreversible segmentation process is

$$HI = \left( \frac{n_{ad}}{n_{de}} - 1 \right) \times 100\%. \quad (2)$$

The evaluation index based on the Freundlich formula was first used to indicate the concentration of adsorbed gas in the soil. It does not rely on Langmuir equations but on mathematical models in exponential form. However, the CBM content in the coal is more in line with the Langmuir curve.

**3.2. Solid Phase Equilibrium Concentration Method.** The solid phase equilibrium concentration method is an improvement of the Freundlich index method. The adsorption and desorption processes are still fitted with two-stage functions  $S_{ad} = K_{ad}Ce_{ad}^n$  and  $S_{de} = K_{de}Ce_{de}^n$ , and the final evaluation index of the hysteresis becomes

$$HI = \frac{\max \{S_{ad} - S_{de}\}}{S_{ad}} \times 100\%. \quad (3)$$

The evaluation model based on the slope and the adsorption equilibrium concentration of the solid phase describes the relative relationship between the saturated adsorption amount and the maximum desorption amount at the same temperature and pressure, but the error at this measurement point is large, and it has a great impact on the final evaluation result.

**3.3. Langmuir Adsorption and Desorption Curve Area Method.** The adsorption process is fitted with a Langmuir adsorption curve  $V = V_{ad}P/(P + P_L)$ , and the desorption process is fitted with a Langmuir desorption curve  $V = V_{de}P/(P + P_L)$ , where  $V$  represents the volume of the adsorbed gas;  $P$  represents the gas pressure;  $P_L$  represents the Langmuir pressure, which is the amount of adsorbed gas pressure at  $0.5 V_{ad}$  or  $0.5 V_{de}$ ; and  $V_{ad}$  and  $V_{de}$  represent maximum

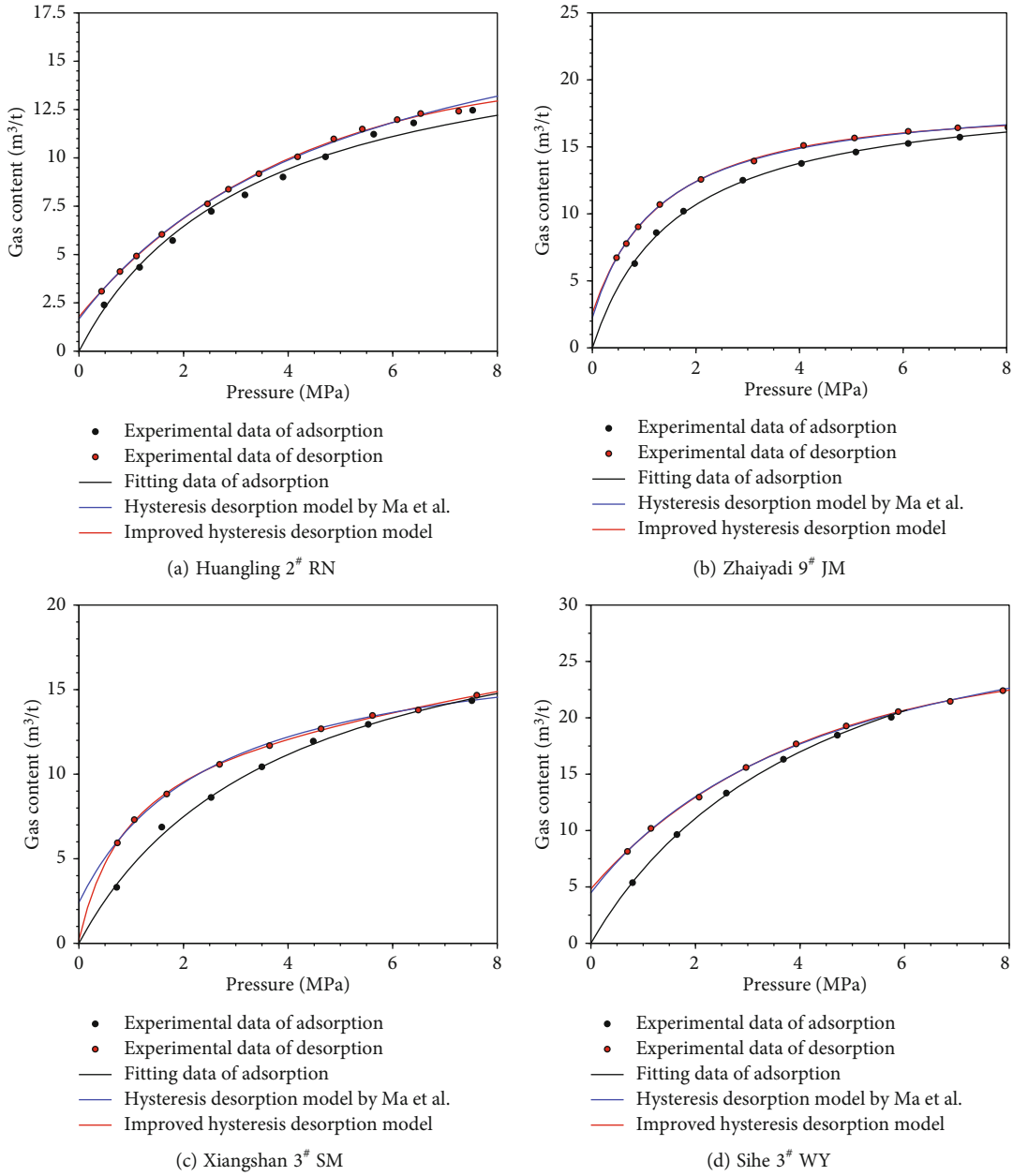


FIGURE 3: Experimental data and improved fitting curves of four different coal samples.

gas adsorption and maximum desorption, respectively. The evaluation indicators of the degree of hysteresis are

$$HI = \frac{A_{de} - A_{ad}}{A_{ad}} \times 100\%, \quad (4)$$

where  $A_{ad}$  and  $A_{de}$  are the areas under the adsorption and desorption curves. In this method, the area of the hysteresis area generated by the adsorption and desorption processes is used as the index of the degree of hysteresis.

Wang et al. [18] developed a new hysteresis evaluation model based on the area integral method. The pore-fractured dual-medium model Langmuir-like adsorption-desorption curve was used to fit the isothermal adsorption

test data, and then, the area of the hysteresis was used to calculate the degree of hysteresis. The new evaluation index of hysteresis is

$$IHI = \frac{A_{hy}}{A_{hf}} = \frac{A_{de} - A_{ad}}{A_{sf} - A_{ad}} \times 100\%, \quad (5)$$

where  $A_{hy}$  is the actual measured hysteresis area;  $A_{hf}$  is the area of ideal nonreversible hysteresis;  $A_{sf}$  is the area of ideal nonreversible adsorption area.

Based on the adsorption and desorption hysteresis evaluation model by Wang et al. [18], we have made further improvements. First, use an isothermal hysteresis curve as shown in Equation (1) to fit the desorption curve. As shown

TABLE 2: Industrial and petrographic analysis of coal sample in Sydney Basin (%).

Industrial analysis		Fixed carbon	Vitrinite reflectance	Vitrinite group	Lithofacies analysis	
Moisture	Volatile matter				Chitin group	Inertia group
1.3	21.7	71.4	1.28	41.6	0.1	55.3

in Figure 2, according to the abandonment pressure point determined in the experimental data, the corresponding adsorption and desorption amount at the abandonment pressure can be calculated. The difference between the adsorption amount and the analytical amount is divided by the saturated adsorption amount to determine the coefficient of hysteresis,

$$HI = \frac{V_{de} - V_{ad}}{V_0} \times 100\%. \quad (6)$$

The above-mentioned hysteresis degree coefficient reflects the desorption hysteresis coefficient under abandonment pressure. This hysteresis degree coefficient reflects the percentage of gas lost in the coal seam due to the desorption hysteresis when the downhole flow pressure reaches the abandonment pressure during the CBM drainage. The degree of hysteresis has guiding significance for the drainage and production of coalbed methane, because gas-bearing formations have a pressure limit for drainage and production, that is, the abandonment pressure. Under abandonment pressure, the degree of hysteresis directly affects the calculation of recovery factor. The only difficulty of this model is how to determine the abandonment pressure of the mine. The current mainstream abandonment pressure is 0.4~1.38 MPa, and the general compromise in the calculation process is 0.6 MPa.

Considering that the coal seam reservoir pressure at different depths is different, with the increase of the depth, the pressure of the coal seam gas reservoir will increase. Wang et al. [18] studied the methane adsorption and desorption hysteresis of coal samples in the Sydney Basin, and the industry and petrographic analysis results of coal samples in Sydney Basin are shown in Table 2. We used a modified dual-porosity medium adsorption-desorption hysteresis model to fit the data.

The experiment determined the adsorption and desorption laws of methane at three different maximum adsorption pressures (10, 20, and 30 MPa) and performed filtration experiments on three groups of coal samples with different particle sizes, and the results are shown in Figure 4. The experimental data is fitted according to Equation (1). The fitting results show the understanding of the absorption hysteresis law. It can be seen from Figure 3 that the lower the adsorption pressure, the closer the desorption curve is to the adsorption fitting curve, indicating that during the development of deep coalbed methane, the degree of coalbed methane desorption hysteresis rises. It is more difficult to reduce the pressure of drainage, and the efficiency is lower. The desorption hysteresis effect should be taken into account when predicting the recovery factor. In order to

facilitate the analysis of the desorption hysteresis from the perspective of particle size, the desorption hysteresis degree HI of coal samples with different particle sizes was calculated separately. In order to visualize the trend, a linear fit was made to the calculation results, as shown in Figure 5.

It can be clearly seen that as the particle size of coal samples increases, the degree of desorption hysteresis of the corresponding coal samples also increases. The reason is that the hysteresis of adsorption and desorption is caused by gas molecules being embedded in micropores with poor connectivity under high pressure and unable to be desorbed from the pores. Large-particle coal samples have good integrity and contain a large number of micropores and nanopores, and there are many gas molecules that cannot be desorbed, so the relative hysteresis is relatively large.

#### 4. Desorption Hysteresis in Deep Coalbed Methane Mining

In this paper, the experimental results of several groups of coal samples are fitted, and it can be found that each group of coal samples has a high desorption hysteresis in the deep environment, even up to 10%. The adsorption and desorption processes of deep coal samples are two completely different processes. In the process of coal diagenesis for millions of years, coalbed methane has continuously accumulated and adsorbed in the coal matrix. Therefore, the coalbed methane mining process is a very fast process; the desorption process can be completed in only about ten years, so the disturbance of the coal matrix during the desorption process is more severe. The coalbed methane adsorption takes place in a long process of coalification, which is a very complicated physicochemical process. In contrast, there is an essential difference between the passive desorption of coalbed methane and the adsorption process in the drainage and depressurization process. During the passive desorption process, the gas adsorbed in the pores quickly desorbs and escapes, causing irreversible damage to the coal sample. In the process of coalbed methane exploitation, greater irreversible damage will be caused due to greater formation pressure. Gas molecules are embedded in micropores with poor connectivity under high pressure and cause pore deformation. The adsorbed gas molecules are restricted by narrow pore channels and cannot be desorbed from the pores, resulting in desorption hysteresis.

The difference in porosity of deep and shallow reservoir coal seams is also an important reason for the hysteresis phenomenon of adsorption and desorption. As mentioned earlier, there is no significant difference in the total porosity of deep coal rocks and shallow coal rocks, but the distribution of pores in the shallow parts is more dispersed, while the deep parts are more concentrated, mostly micropores

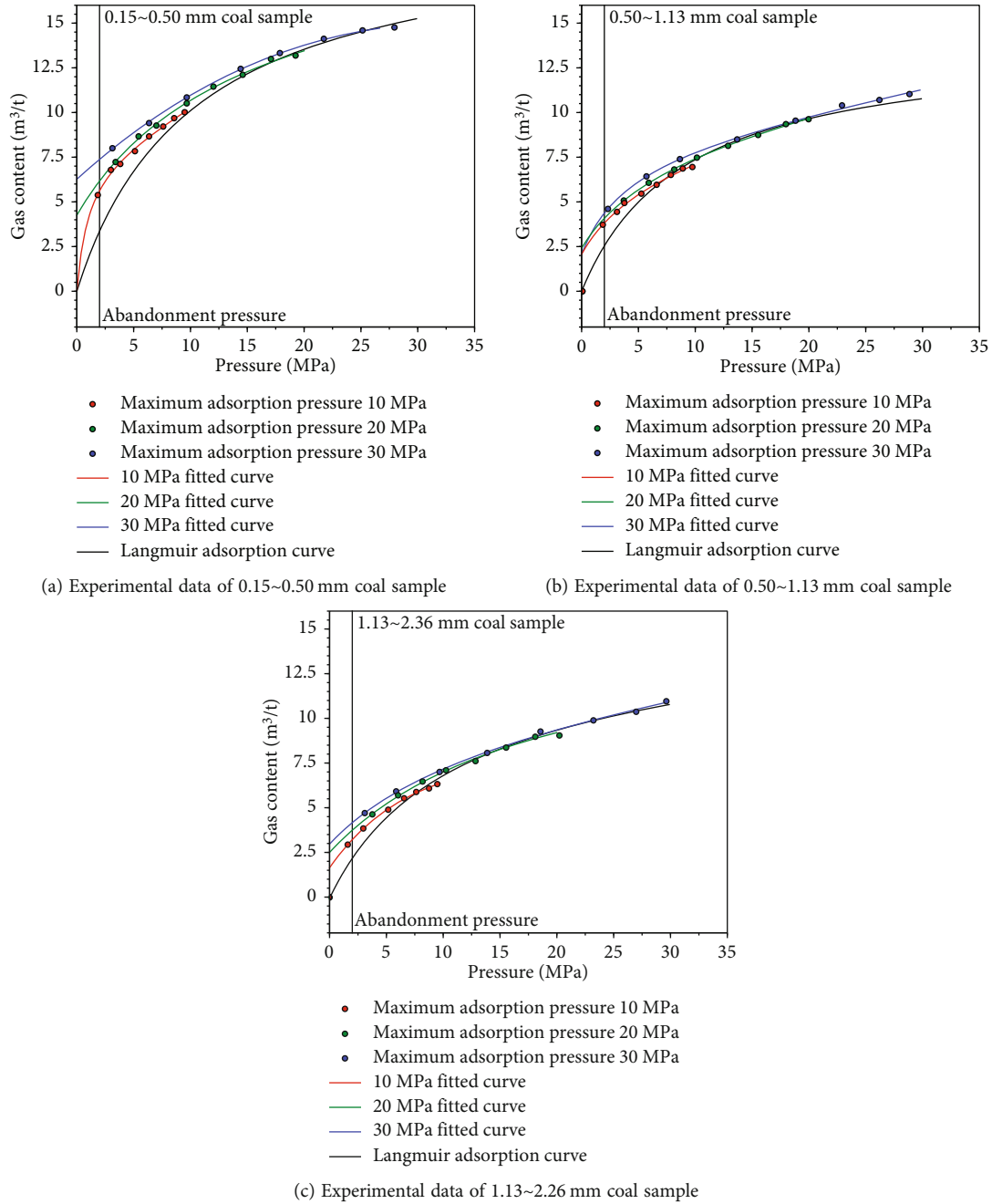


FIGURE 4: Comparison of isothermal desorption lines of methane at different highest adsorption pressures.

and nanopores. According to the definition of the International Association of Pure and Applied Chemistry (IUPAC), the diameter of a micropore is a pore structure smaller than 50 nm. Although the molecular diameter of methane gas molecules is smaller than the diameter of the micropores, the interaction between molecules makes it extremely tough to enter the micropores. When the storage pressure is relatively low, there are a small amount of methane molecules in the micropores, but as the storage pressure increases, the amount of methane gas stored in the micropores increases. Because the permeability of the pores is deteriorated during the adsorption process, the gas adsorbed during

the desorption process cannot escape, resulting in the hysteresis phenomenon of adsorption and desorption. Under the action of deep high pressure, the number of gas molecules that can be contained in the pores of coal rocks increases, and in addition, the gas molecules can be embedded in the ultramicropores in the coal that could not be accessed under the original low-pressure conditions, which in turn exacerbates the phenomenon of pore expansion and deformation, resulting in more pronounced adsorption hysteresis.

Compared with shallow coal seams, deeper coal seams have higher temperature, higher metamorphism, and higher

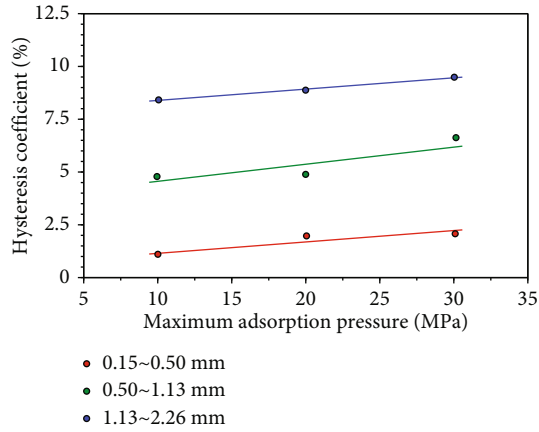


FIGURE 5: Degree of hysteresis and relationship between maximum adsorption pressure and coal particle size.

gas pressure, which is one of the reasons for the hysteresis of adsorption and desorption. As the gas pressure increases and the degree of coal rock metamorphism increases, the proportion of micropores in the coal body increases, the possibility of micro- and nanopore sizes further increases, and the degree of desorption hysteresis increases.

It can be inferred that the gas content of deep coalbed methane is higher than that of shallow coalbed methane, but affected by the phenomenon of desorption hysteresis, it is more difficult for the gas adsorbed in the pores to move from the pores to the fractures. The outflow rate may be a factor restricting the development of deep coalbed methane. Therefore, under the combined effect of other characteristics such as adsorption and desorption hysteresis and low permeability caused by high geostress, the difficulty of mining deep coalbed methane increases. Making the development of coalbed methane fail to reach the expected output caused huge economic losses.

## 5. Summary and Conclusions

- (1) A quantitative evaluation index of the degree of desorption hysteresis based on the theory of dual-porosity media was proposed in this paper, which can accurately reflect the irreversibility of desorption under abandonment pressure. The accuracy of the new model was verified by fitting and comparison with the experimental data of adsorption and desorption by Ma et al. The proposed improved evaluation index was used to calculate the coal rock test results in the Sydney Basin. The results show that the higher the adsorption pressure, the greater the hysteresis; the larger the coal particle size, the stronger the hysteresis
- (2) In the passive desorption process, the gas adsorbed in the pores quickly desorbs and escapes, causing irreversible damage to the coal sample and causing pore deformation, which is an important factor causing the hysteresis phenomenon of desorption

- (3) There is no significant difference in the total porosity of deep coal rocks and shallow coal rocks, but the proportion of micro- and nanopores in deep coal rocks is high. The existence of micro- and nanopore and methane molecular diameters in the coal body, and only high-pressure gas can enter into it, resulting in deformation of the coal body and expansion from the inside to the outside, which eventually increases the degree of desorption hysteresis
- (4) With the combined effects of high geostress and low permeability, the hysteresis phenomenon of desorption is more significant, and the difficulty of mining deep coalbed methane will increase, making the development of coalbed methane less than the expected output, resulting in huge economic losses. Affected by the coal seam gas desorption hysteresis effect, the desorption isotherm is needed to evaluate the gas production capacity, gas production rate, recoverable reserves, and recovery factor in the development of coal seam gas

## Nomenclature

$V$ :	Gas volume
$V_{ad}$ :	Volume of adsorbed gas
$V_{de}$ :	Volume of desorbed gas
$k$ :	Henry gas dissolution constant
$P$ :	Gas pressure
$C_r$ :	Residual adsorption amounts
$V_0^d$ :	Langmuir volume constants
$P_L^d$ :	Langmuir pressure constants
$R^2$ :	Fitting degree
$S_{ad}$ :	Adsorption concentration of the adsorbent
$K_{ad}$ :	Freundlich adsorption parameters
$C_{e_{ad}}^n$ :	Adsorption equilibrium concentration
$S_{de}$ :	Desorption concentration of the adsorbent
$K_{de}$ :	Freundlich desorption parameters
$C_{e_{de}}^n$ :	Desorption equilibrium concentration
HI:	Hysteresis index
$n_{ad}$ :	Mass of adsorbed gas
$n_{de}$ :	Mass of desorbed gas
$P_L$ :	Langmuir pressure
$A_{ad}$ :	Areas under the adsorption curves
$A_{de}$ :	Areas under the desorption curves
$A_{hy}$ :	Actual measured hysteresis area
$A_{hf}$ :	Area of ideal nonreversible hysteresis
$A_{sf}$ :	Area of ideal nonreversible adsorption area.

## Data Availability

The data that supports the findings of the study are available in the supplementary material of this article.

## Conflicts of Interest

No potential conflict of interest was reported by the authors.

## Acknowledgments

This project is granted by the National Natural Science Foundation of China (41472130).

## References

- [1] S. Li, D. Tang, H. Xu, and T. Shu, "Progress in geological researches on the deep coalbed methane reservoirs," *Earth Science Frontiers*, vol. 23, no. 3, pp. 10–16, 2016.
- [2] M. He, H. Xie, S. Peng, and Y. Jiang, "Study on rock mechanics in deep mining engineering," *Chinese Journal of Rock Mechanics and Engineering*, vol. 24, no. 16, 2005.
- [3] W. Zhang, Y. Yan, X. Kong et al., "Structure and composition characteristics of deformed high-rank coals in the south of Qinshui basin and their influence on CBM adsorption/desorption," *Journal of University of Chinese Academy of Sciences*, vol. 31, no. 1, pp. 98–107, 2014.
- [4] K. Jessen, G. Tang, and A. Kovscek, "Laboratory and simulation investigation of enhanced coalbed methane recovery by gas injection," *Transport in Porous Media*, vol. 73, no. 2, pp. 141–159, 2008.
- [5] S. Harpalani, B. Prusty, and P. Dutta, "Methane/CO<sub>2</sub> sorption modeling for coalbed methane production and CO<sub>2</sub> sequestration," *Energy & Fuels*, vol. 20, no. 4, pp. 1591–1599, 2006.
- [6] Z. Pan, L. Connell, M. Camilleri, and L. Connelly, "Effects of matrix moisture on gas diffusion and flow in coal," *Fuel*, vol. 89, no. 11, pp. 3207–3217, 2010.
- [7] S. Zhang, J. Ye, S. Tang, D. Ma, and Y. Huo, "Theoretical analysis of coal-methane adsorption/desorption mechanism and its reversibility experimental study," *Natural Gas Industry*, vol. 25, no. 1, pp. 44–46, 2005.
- [8] G. Liu, Z. Zhang, X. Zhang, and R. S. Lu, "Pore distribution regularity and adsorption-desorption characteristics of gas coal and coking coal," *Chinese Journal of Rock Mechanics and Engineering*, vol. 28, no. 8, pp. 1587–1590, 2009.
- [9] Z. Song, G. Liu, X. Yang, and Z. X. Zhang, "Adsorption-desorption characteristic on deformed coal under the conditions of high temperature and pressure and equilibrium water," *Journal of Mining and Safety Engineering*, vol. 29, no. 4, pp. 591–595, 2012.
- [10] F. Jian Huo and Z. Y. Xuehai, "Analysis on coalbed methane desorption stage and calculation on max instant desorption value of tectonic coal," *Coal Science and Technology*, vol. 43, no. 4, pp. 57–62, 2015.
- [11] M. Dongmin, L. Laixin, L. Xiaoping et al., "Contrastive experiment of adsorption-desorption between CH<sub>4</sub> and CO<sub>2</sub> in coal seam 4 of Dafosi coal mine," *Journal of Coal*, vol. 39, no. 9, pp. 1938–1944, 2014.
- [12] M. Dongmin, M. Wei, and L. Yabin, "Desorption hysteresis characteristics of CBM," *Journal of China Coal Society*, vol. 37, no. 11, pp. 1885–1889, 2012.
- [13] M. Dongmin, Z. Suian, and L. Yabin, "Isothermal adsorption and desorption experiment of coal and experimental results accuracy fitting," *Journal of China Coal Society*, vol. 36, no. 3, pp. 477–480, 2011.
- [14] S. Xianbo, C. Run, L. Xiaoying, and J. H. Li, "Desorption characteristic curves of carbon dioxide and methane in coal and their application," *Natural Gas Industry*, vol. 28, no. 7, pp. 17–19, 2008.
- [15] S. Xianbo, C. Run, L. Xiaoying, and Y. Song, "Application of adsorption potential theory in the fractionation of coalbed gas during the process of adsorption/desorption," *Acta Geologica Sinica*, vol. 82, no. 10, pp. 1382–1389, 2008.
- [16] Q. Xingdong, Y. Huan, D. Morteza, P. Tan Sugata, and A. Hertanto, "Experiments on the capillary condensation/evaporation hysteresis of pure fluids and binary mixtures in cylindrical nanopores," *The Journal of Physical Chemistry C*, vol. 125, no. 10, pp. 5802–5815, 2021.
- [17] L. He, H. Mei, X. Hu, M. Dejam, Z. Kou, and M. Zhang, "Advanced flowing material balance to determine original gas in place of shale gas considering adsorption hysteresis," *SPE Reservoir Evaluation & Engineering*, vol. 22, no. 4, pp. 1282–1292, 2019.
- [18] W. Gongda, R. Tingxiang, Q. Qingxin, K. Wang, and L. Zhang, "Mechanism of adsorption-desorption hysteresis and its influence on deep CBM recovery," *Journal of China Coal Society*, vol. 41, no. 1, pp. 49–56, 2016.
- [19] L. Xianzhao and K. Shaozhong, "Hysteresis in process of rainfall in filtration-runoff on hill slope in loess area," *Advances in Water Science*, vol. 12, no. 1, pp. 56–60, 2001.

## Research Article

# Shale Heterogeneity in Western Hunan and Hubei: A Case Study from the Lower Silurian Longmaxi Formation in Well Laidi 1 in the Laifeng-Xianfeng Block, Hubei Province

Peng Zhang <sup>1</sup>, Junwei Yang <sup>1</sup>, Yuqi Huang <sup>1</sup>, Jinchuan Zhang <sup>2</sup>, Xuan Tang <sup>2</sup>,  
and Chengwei Liu <sup>1</sup>

<sup>1</sup>School of Mining & Civil Engineering, Liupanshui Normal University, Liupanshui 553004, China

<sup>2</sup>School of Energy, China University of Geosciences (Beijing), Beijing 100083, China

Correspondence should be addressed to Junwei Yang; 86635174@qq.com

Received 9 October 2021; Accepted 1 December 2021; Published 7 January 2022

Academic Editor: Kouqi Liu

Copyright © 2022 Peng Zhang et al. This is an open access article distributed under the Creative Commons Attribution License, which permits unrestricted use, distribution, and reproduction in any medium, provided the original work is properly cited.

Shale heterogeneity directly determines the alteration ability and gas content of shale reservoirs, and its study is a core research topic in shale gas exploitation and development. In this study, the shale from the Longmaxi Formation from well Ld1 located in western Hunan and Hubei is investigated. The shale's heterogeneity is analyzed based on shale mineral rocks, microslices, geochemistry, and low-temperature N<sub>2</sub> adsorption-desorption. It is found that the shales of the Longmaxi Formation from well Ld1 are mainly composed of siliceous shale, mixed shale, and clayey shale. The three types of shale facies exhibit strong heterogeneity in terms of the occurrence state of organic matter, organic content, mineral composition, microstructure and structure, brittleness, and micropore type. Sedimentation, late diagenesis, and terrigenous input are the main factors influencing the shale's heterogeneity. With a total organic carbon (TOC) of 0.41%-4.18% and an organic matter maturity (R<sub>o</sub>) of 3.09%-3.42%, the shales of the Longmaxi Formation from well Ld1 are in an overmature stage, and their mineral composition is mainly quartz (5%-66%) and clay minerals (17.8%-73.8%). The main pore types are intergranular pores, intragranular pores, microfractures, and organic pores. The results of the low-temperature N<sub>2</sub> adsorption-desorption experiment show that the shale pores are mainly composed of micropores and mesopores with narrow throats and complex structures, and their main morphology is of a thin-necked and wide-body ink-bottle pore. Based on the Frenkel-Halsey-Hill (FHH) model, the pore fractal dimension is studied to obtain the fractal dimension D1 (2.73-2.76, mean 2.74) under low relative pressure ( $P/P_0 \leq 0.5$ ) and D2 (2.80-2.89, mean 2.85) under high relative pressure ( $P/P_0 > 0.5$ ). The shales of the Longmaxi Formation in the study area have a strong adsorption and gas storage capacity; however, the pore structure is complex and the connectivity is poor, which, in turn, imposes high requirements on reservoir reformation measures during exploitation. Moreover, the fractal dimension has a positive correlation with organic matter abundance, TOC, clay mineral content, and pyrite content and a negative correlation with quartz content. Since the organic matter contained in the shales of the Longmaxi Formation in the study area is in the overmature stage, the adsorption capacity of the shales is reduced, and the controlling effect of organic matter abundance on the same is not apparent.

## 1. Introduction

The formation of shale reservoirs is influenced by tectonic movements, sedimentation, and late diagenesis. Both macroscopic properties (rock composition, texture/structure, spatial distribution, etc.) and microscopic properties (organic matter occurrence, pore network, mechanical parameters,

etc.) are strongly heterogeneous, and therefore, studies on heterogeneity are important ways to gain insights into reservoir characteristics [1-3]. Many domestic and international studies have shown that microscopic heterogeneity has a great influence on shale gas storage [4-7], enrichment, and migration in the following ways: (1) the mineral composition of shale reservoirs is complex, and their mineral and

organic matter compositions play an important role in the occurrence and enrichment of shale gas; (2) the heterogeneity of nanoscale pore structures and distributions of shales, and the development characteristics of fissures and microfissures result in different shale gas contents, gas release capacity, and gas seepage and affect the production of shale gas; (3) carbon and sediment are buried underground and give rise to different organic matter occurrence states through complex and diverse sedimentation and diagenesis processes [8]. Organic matter not only affects the hydrocarbon generation capacity of shale but also affects the diagenesis process and the development of organic matter pores, thus, affecting the shale reservoir's performance and its gas-bearing characteristics [9]. In addition, the occurrence state of organic matter is affected by inorganic components [10], and the composite compound degree of inorganic and organic matter usually exceeds 85%. Organic matter in shale exists in disseminated organic matter, in the mineral asphalt matrix, in organic clay complexes, organic matter-stucco complexes, etc. Studies on shale heterogeneity usually deal with macroheterogeneity and microheterogeneity up to the micron level. However, shale gas materializes in the pores of nanoscale organic matter and minerals of shale reservoirs in various forms, such as through adsorption, dissociation, and dissolution, and its reservoir space is even smaller than the micro-scale; therefore, a more detailed study on shale heterogeneity is necessary [11, 12]. The heterogeneity of shale itself has a great influence on its quality and alteration ability and plays a critical role in controlling the enrichment and high yield of shale gas in the late period. The region of western Hunan and Hubei is a key shale gas development area adjacent to the Sichuan Basin. Previous studies in this region have mostly focused on the content characteristics and vertical and horizontal changes in organic matter. However, there have been few studies on different shale mineral compositions/lithofacies characteristics, micro-nanoscale organic matter occurrence, micropore and pore structures, rock mechanical properties, etc. [13–15]. In this study, the marine shale of the Longmaxi Formation in Laifeng, Hubei is taken as the research object, and the lithofacies in this Formation are analyzed and categorized. The genesis and morphology of inorganic minerals and their contact relationship with organic matter are analyzed at the micro-nanoscale, and the occurrence modes of inorganic minerals and organic matter in different shale lithofacies are established. A comparative study on the differences in the total organic carbon, pore types, pore characteristics, and pore size distribution in different lithofacies is carried out to reveal the diverse development mechanisms of the shale reservoir. In addition, the heterogeneity characteristics of the pore structure of the marine shale reservoirs are studied to quantify the heterogeneity parameters of the pore structure and discuss their influence on the occurrence and migration of shale gas.

## 2. Geological Background

The study area is located in the central part of the Yangtze paraplatform and southwest wing of the Yidu-Hefeng anticline in the Western Hunan Hubei fold-thrust belt in the

middle of the Yangtze paraplatform, and a small part is located in the Huaguoping anticline. The entire area trends NE-SW, and the Lianghekou syncline is relatively wide and gentle. Under the influence of the early Caledonian movement, the area of the Yangtze plate in the late Ordovician increased and gradually extended to the Yangtze region, making the Yangtze sea occur in a semiclosed state. The crust in the middle and upper Yangtze region sank and the sea level rose, depositing a set of siliceous shale, which is one of the main source rocks in the region. The Indosinian movement ended the marine sedimentary history of the middle upper Yangtze paraplatform and formed the rudiment of the present structure in the study area [16]. The early Yanshanian fold movement had the greatest impact on the study area, resulting in the strong deformation of the entire area's caprock and the formation of NE trending folds and faults, which basically established the current structural pattern. This period was also the main hydrocarbon generation period of the Longmaxi Formation. From the late Yanshanian to the early Himalayan, the middle and upper Yangtze region entered a stage of extensional action of great significance in the Pacific tectonic domain. However, the activities of this stage are different from east to west and from north to south. Western Hunan and Hubei were less affected by the late Yanshanian early Himalayan tectonic movement, and the tectonic features formed in the early Yanshanian are basically unchanged. In the late Himalayan period, the study area suffered strong uplift and denudation, resulting in the upper Paleozoic and Mesozoic strata remaining only in the syncline core, while the lower Paleozoic strata in the anticline core are exposed at the surface (Figure 1).

## 3. Experiment and Methods

*3.1. Samples and Logging Response Characteristics.* The shale samples used in the experiment were taken from the core of the Longmaxi Formation in well Ld1. The well was drilled 20 m into the Upper Ordovician Pagoda Formation, and the target stratum was the lithologic member enriched with organic matter of the Longmaxi Formation in the Silurian system, with a depth of 898.16~949.10 m and a thickness of 50.94 m. Based on the characteristics of the sudden change in the lithology and lithofacies, rapid deepening or shallowing of the water depth and obvious changes in the logging curve shape, the Longmaxi formation is divided into three members from bottom to top, namely, the Long 1 member (929.41~949.10 m), the Long 2 member (910.31~929.41 m), and the Long 3 member (898.16~910.31 m). The two interfaces of the Long 2 member, the Long 1 member, and the Long 3 member show lithologic mutation, and the response characteristics of the logging curves are also similar. Lithologically, the two interfaces change from argillaceous siltstone below to carbonaceous silty shale above. In the logging curves, the GR curve changes suddenly from bottom to top, the GR value above the interface increases obviously, the curve shape changes from straight sawtooth to bell, the AC curve is a sudden interface, the AC value above the bottom interface increases obviously, and the RD

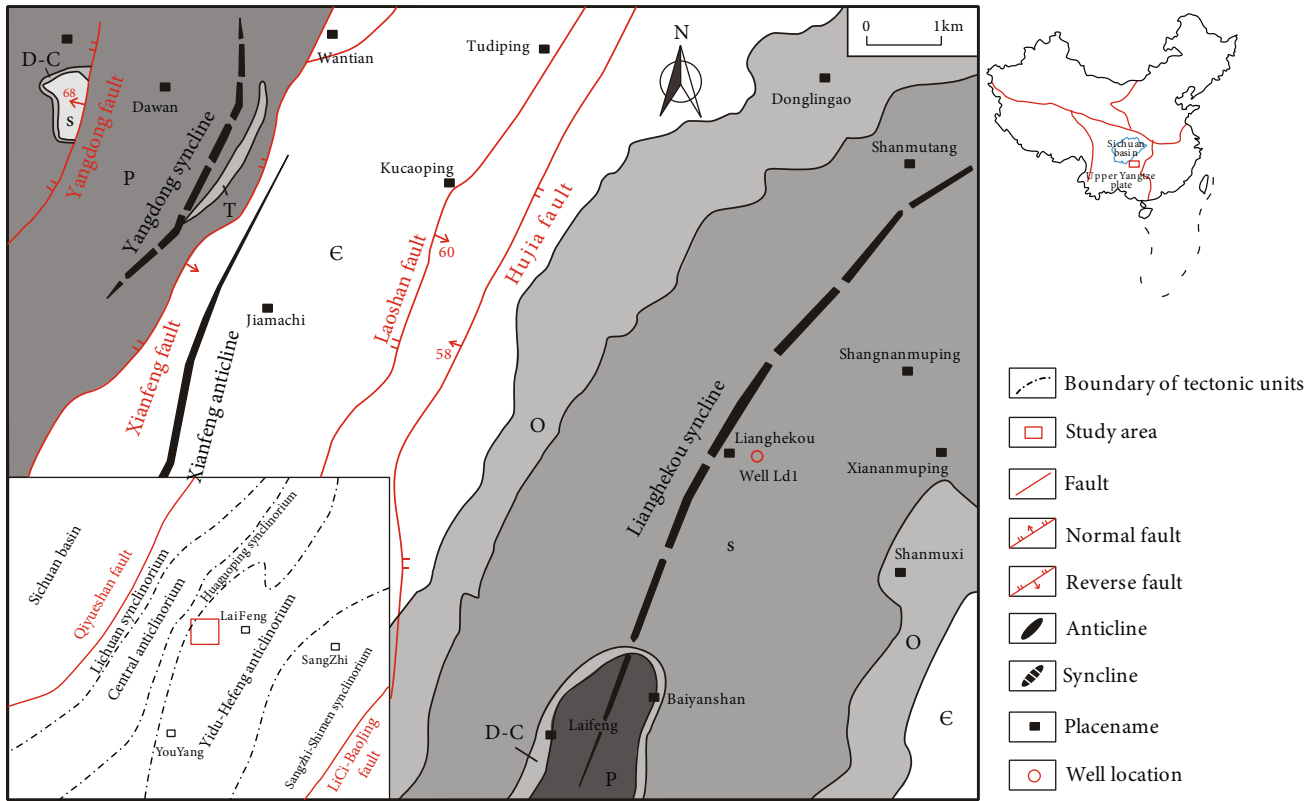


FIGURE 1: Geological background and location of well Ld1 in the study area.

value decreases [17]. The sedimentary environment fluctuates from deep-water shelf facies in the lower part of the Longyi member to shallow water shelf facies and tidal flat facies above (Figure 2).

**3.2. Experiment Instruments and Methods.** The X-ray diffraction (XRD) experiment was conducted with a D8 ADVANCE X-ray diffractometer (Bruker, Germany) under the conditions of Cu target,  $K\alpha$  radiation, X-ray tube, a voltage of 40 kV, and an electric current of 30 mA. A comparative analysis was carried out based on the standard powder diffraction data provided by the International Centre for Diffraction Data (ICDD) and according to its standard analysis methods and diffraction criteria (consistent interplanar spacing and diffraction intensity). About 50-100 g of samples was taken at each sampling site, and they were crushed and divided into samples of about 5 g. The collected samples were ground in a grinding bowl to a particle size of 48  $\mu\text{m}$ .

The TOC experiment was conducted with a C-S580A carbon-sulfur analyzer (Germany). According to the national standard SYT-T5116-1997, the samples were processed with dilute hydrochloric acid to remove the carbonate. According to the repeated analysis of the standard samples, the TOC analysis accuracy was greater than 0.5%. The vitrinite reflectance ( $R_o$ ) was measured with a microphotometer at a temperature of 23°C and a humidity of 30%. The microscope was amplified 125 times, with a resolution of 0.01%.

The microsurface morphology and structural characteristics of the shale samples were observed under a ZEISS

SIGMA field emission scanning electron microscope. When the shale samples were prepared, their surface was etched using Ar-ion milling technology and bombarded by a high-speed ion beam to form an ultrasmooth surface that cannot be obtained through conventional mechanical milling; this was done to avoid damage to the surface of the shale samples caused by mechanical milling and to retain the original pore morphology on the surface. Afterward, gold film with a thickness of 10-20 nm was plated on the milled surface to enhance its conductivity.

A micromeritics ASAP 2020 specific surface area and porosity adsorption instrument (America) was used to carry out the low-temperature nitrogen adsorption experiment on the samples. Its measuring aperture range is 0.35-500 nm, and the lower limit of the specific surface was 0.0005  $\text{m}^2/\text{g}$ . Before the experiment, the samples were first vacuumed at a high temperature of approximately 150°C to remove the remaining bound water and capillary water. Then, nitrogen, with a purity above 99.999%, was taken as the adsorbate to measure the adsorption capacity of the samples under different relative pressures. Next, the nitrogen adsorption-desorption isothermal curve was recorded and plotted with the relative pressure as the abscissa and the adsorption capacity of the unit mass sample as the ordinate. According to the BET equation, the BET linear graph was plotted with a relative pressure range of 0.05-0.35; the specific surface area of the shale sample was obtained, and the desorption branch of the nitrogen adsorption isothermal curve was calculated using the Barret-Joyner-Halenda aperture distribution test

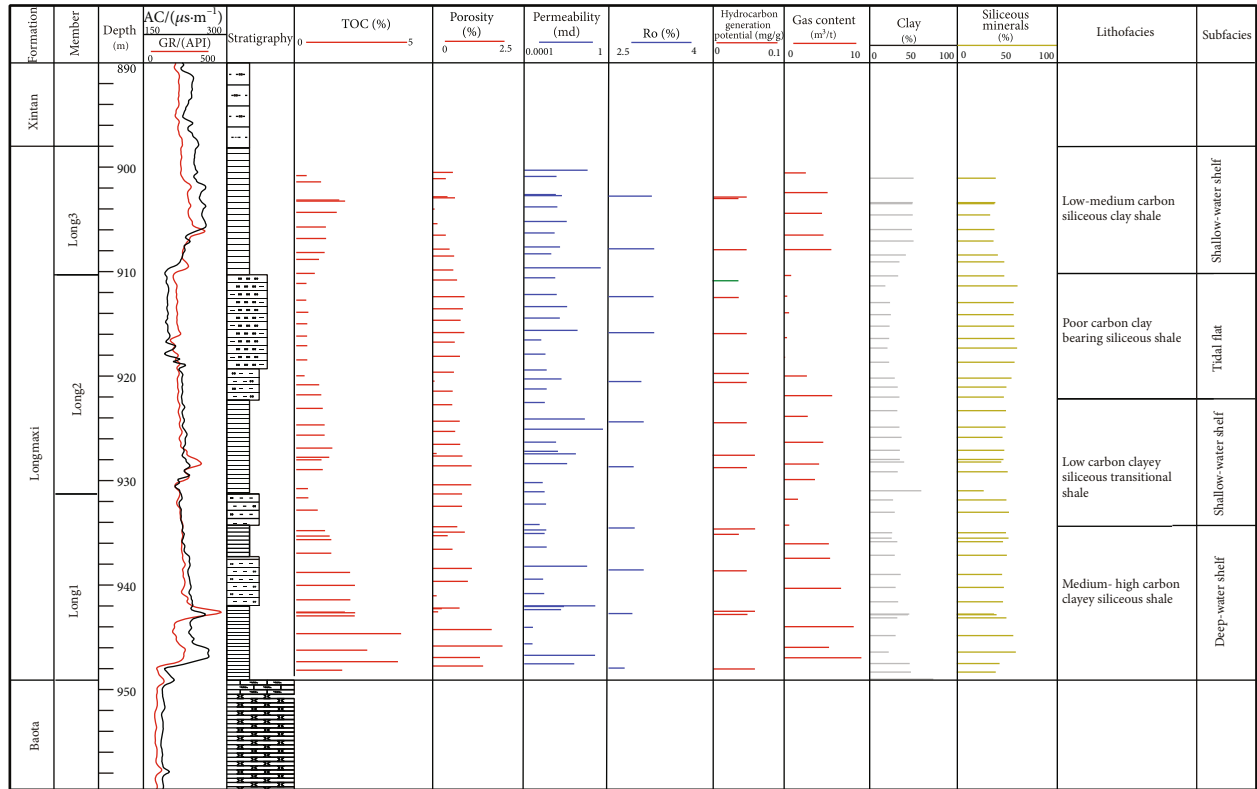


FIGURE 2: Comprehensive column of the Longmaxi Formation in well Laidi 1 in the Laifeng-Xianfeng block, Hubei Province.

(BJH) method to obtain the pore size distribution of the shale sample.

#### 4. Rock Matrix Heterogeneity

Shale is mainly composed of inorganic minerals, organic matter, and pores. Inorganic minerals and organic matter constitute the rock matrix. The properties of the rock matrix have an important impact on the development of the reservoir space and its gas storage performance. Therefore, studying the properties of the rock matrix is of great significance in the study of reservoir properties. Specifically, organic matter and clay minerals are the main factors that determine the adsorption capacity of shale, and a high content of brittle minerals is a key factor affecting the cost and efficiency of shale gas exploitation in the late stage. The nanoscale pores in shale are the main space where free shale gas resides. Therefore, studies on the heterogeneity of shale matrixes and organic matter are of great significance to identify and exploit high-quality gas-bearing intervals. Shale lithofacies is the external representation of various heterogeneity characteristics of shale enriched with organic matter and includes macro information, such as rock type, structure, and construction, and microinformation, such as inorganic minerals and organic composition; it is a direct evaluation indicator of the original shale quality [18–20].

**4.1. Shale Minerals and Organic Geochemical Characteristics.** X-ray diffraction tests on 54 shale samples from well Ld1 show that the shale is mainly composed of quartz (5%–

66%, mean 36.9%) and clay minerals (17.8%–73.8%, mean 39.4%), followed by feldspar (3.2%–25.4%, mean 14.7%), carbonate minerals (0.6%–13.7%, mean 5.5%), and pyrite (0.7%–9.6%, mean 2.8%). Among them, the clay minerals include illite (39%–81%, mean 58%), illite/smectite (4%–58%, mean 29%), and chlorite (4%–21%, mean 12.5%). The main organic matter type is type II<sub>1</sub>, followed by type II<sub>2</sub>; the macerals are mainly represented by saprolite and inertinite and lack vitrinite and exinite; the saprolite is dominated by disseminated mineral asphalt matrixes. According to the analysis of 45 samples, the TOC of the shale is 0.33% ~ 4.18% and is greater than 1% in the main body, with an average of 1.33%. Specifically, the TOC of Member 1, Member 2, and Member 3 is 0.48% ~ 4.18% (mean: 2.05%), 0.33% ~ 1.44% (mean: 0.77%), and 0.42% ~ 1.95% (mean: 1.24%), respectively. The organic matter maturity ( $R_o$ ) of 11 samples ranges from 2.79% to 3.32%, with an average of 3.11%. The samples are in the overmature stage, and their overall maturity increases from bottom to top [21–23]. This can be attributed to the organic matter in the upper part of the Longmaxi Formation being catalyzed by inorganic minerals, such as clay minerals, which promote the evolution of organic matter. Based on the data of the three members, as well as the contents of siliceous minerals (quartz + feldspar), carbonate minerals (dolomite + calcite), and clay minerals, the shale of the Longmaxi Formation can be divided into siliceous shale, clayey shale, and mixed shale, no calcareous shale is present (Figure 3), and it is divided according to the single mineral content is subdivided (10%, 25%, 50%, and 75%). By referring to the practical experience of shale

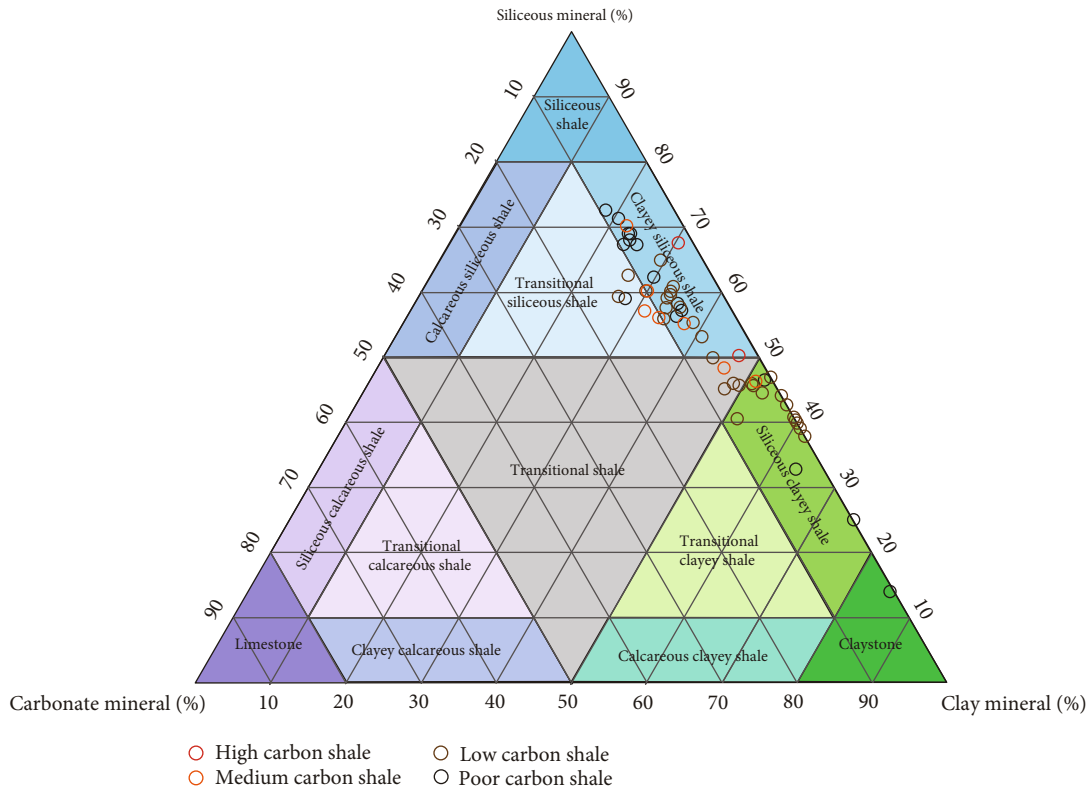


FIGURE 3: Classification of shale facies and comparison of organic carbon contents.

gas exploitation and development in the Sichuan Basin, the shale is divided into five types based on organic content, i.e., carbon-rich (TOC > 4%), high-carbon (3% < TOC < 4%), medium-carbon (2% < TOC < 3%), low-carbon (1% < TOC < 2%), and carbon-poor (TOC < 1%) shale, and the shale of the Longmaxi Formation can be further divided into four subgroups: medium-high carbon clayey siliceous shale, low-carbon clayey siliceous mixed shale, carbon-poor clayey siliceous shale, and low-medium carbon clayey shale.

#### 4.2. Shale Lithofacies Characteristics

##### (1) Medium-high carbon clayey siliceous shale

This type of shale is mainly distributed in the lower part of Member 1, with a TOC greater than 2%. Its sedimentary environment is a deep-water continental shelf, where the rock color is deep dark and the organic content is high. The genesis and morphology of the inorganic components are diverse. Graptolites are developed in great quantity and dominated by orthograptus in hypertrophic shapes, where a large number of radiolarians can be observed. The quartz mainly includes biological quartz, diagenetic authigenic quartz, and a small amount of terrigenous quartz, with a high content of quartz and an average value of greater than 50%; the content of clay minerals is low, ranging from 25% to 36%; the content of carbonates is lower than 10%; pyrite is relatively developed, and includes framboidal pyrite, pyrite aggregate, etc. Microcrystalline quartz, clay minerals, and

pyrite are encapsulated in contiguous solid asphalt, and framboidal pyrite is also rich in organic matter; in the longitudinal direction, the heterogeneity of organic matter occurrence in this lithofacies is weak, and the cyclical change in the sedimentary environment is not obvious (Figure 4(a)).

##### (2) Low-carbon clayey siliceous mixed shale

This type of shale has a TOC lower than the medium-high carbon clayey siliceous shale, and its organic carbon content, which is mainly distributed in Member 2, is 1%–2%. The sedimentary environment is a shallow-water continental shelf, and the inorganic components are also diverse, but their proportion varies with different genesis. The content of quartz is 40%–50%, and the amount of terrigenous quartz is greater than high, with large particle sizes and sub-angular edges; the content of clay minerals is 40%–50%, and a small amount of carbonate and pyrite is present. The content of graptolite is high, and solid asphalt exists between the terrigenous quartz particles and clay minerals. Because the content of terrigenous quartz and clay minerals is high and the organic content is lower, this shale has little difference from clay siliceous shale (Figure 4(b)).

##### (3) Carbon-poor clayey siliceous shale

Compared with the low-carbon clayey siliceous mixed shale, this shale has a lower TOC (less than 1%). It is mainly distributed in the upper part of Member 1 and Member 2. The sedimentary environment is the shallow area of a

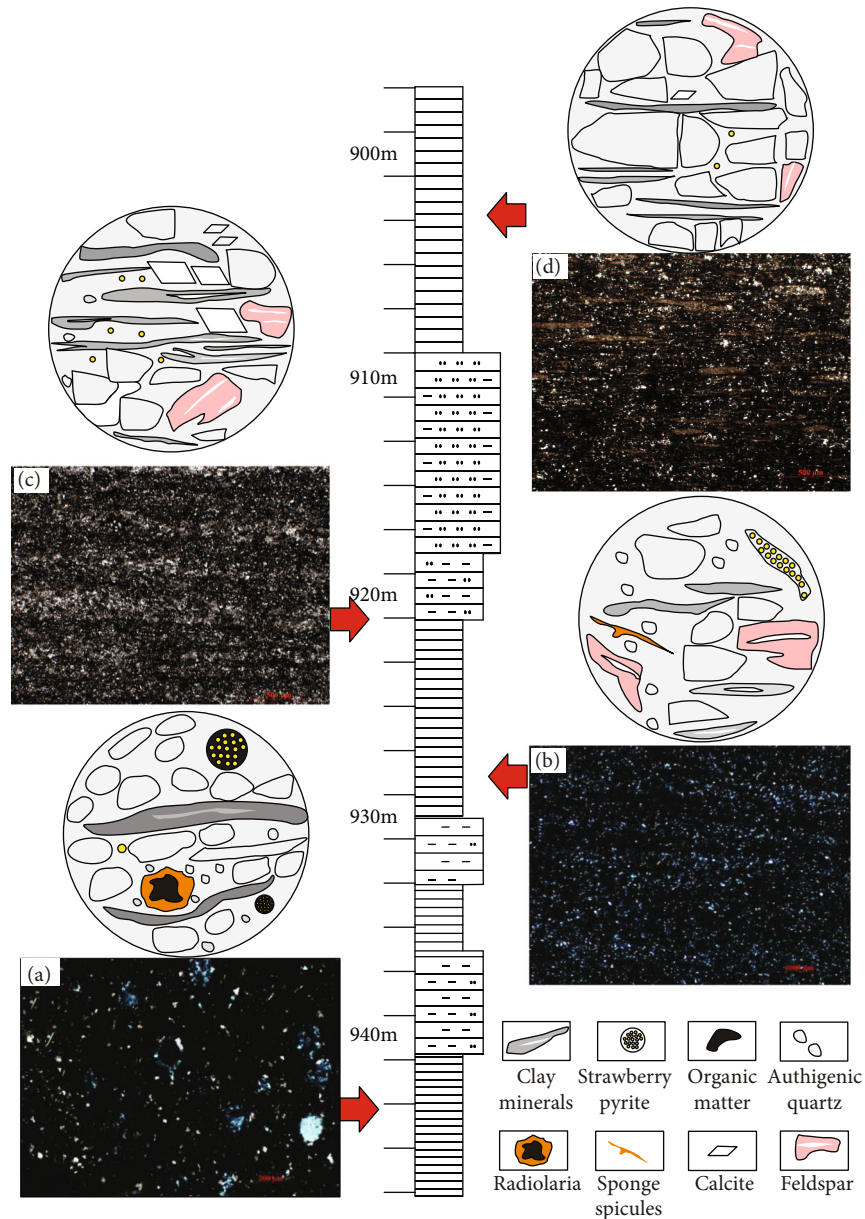


FIGURE 4: Lithofacies characteristics of the Longmaxi Formation in well Ld1.

shallow-water continental shelf or the lower part of the intertidal zone to the subtidal zone, with strong hydrodynamic force. The rocks have a lighter color, lower organic content, and less graptolite. Tidal bedding is developed and the inorganic components are more diverse. The content of quartz and clay minerals is lower, with both ranging from 25% to 50%; the content of carbonate is higher, ranging from 10% to 25%. Solid asphalt is present between the terrigenous quartz particles and the clay minerals, and there are no solid particles between the flaky laminated clay minerals that adsorb amorphous organic matter; with the reduction in the clay minerals, the adsorbed organic matter also decreases. The content of pyrite is lower, so its encapsulated organic matter is also reduced. In this shale, the area of the change in the organic matter enriched with inorganic minerals (e.g., from high to low) is obvious, result-

ing in the frequent alternation of bright and dark laminae and clearer boundaries between laminae. The thickness of a single lamina ranges from 0.5 mm to 2.0 mm.

#### (4) Low-medium carbon clayey shale

This type of shale has a TOC of 1%-2% and is mainly distributed in Member 1. The sedimentary environment is a shallow-water continental shelf, and the genesis and category of inorganic components are relatively simple. Quartz is mainly terrigenous, with a large particle size and angular edges; it is poorly rounded and has a content of 30%-40%. The enrichment of organic matter is inhibited and diluted, the content of terrigenous feldspar is higher, and the content of clay minerals is 50%-70%; the content of carbonate is usually not greater than 10%; pyrite is rare and is

present sporadically. Solid asphalt seldom exists between the mineral particles, and bright and dark lamina composed of framboidal pyrite and organic matter is more obvious, with the thickness of a single lamina being 0.3–3.0 mm. The organic matter is relatively enriched in the clayey lamina at the bottom, and the silty lamina at the upper part is reduced, showing a frequent alternation in the enrichment and reduction of organic matter. This feature reflects the frequent alternation of the sedimentary environment, and the geological cycle of the emergence, death, and burial of hydrocarbon-generating organisms (Figure 4(d)).

The formation of shale is controlled by various factors, such as basin structure, physical and chemical conditions of a water body, climate change, sediment supply, and regional sea-level change. The shale of the Longmaxi Formation in the study area gradually evolved in sequence from siliceous shale to mixed shale and then clayey shale. In addition, terrigenous detrital minerals and clay minerals gradually increase from the bottom to the top, with organic carbon content gradually decreasing from the bottom to the top. The shale structure gradually changes from a uniform block structure to a sandy band structure, presenting a graded bedding development. This indicates that the terrigenous detrital supply was enhanced and that the sedimentary environment transitioned from a reducing environment to an oxidizing one.

Shale brittleness evaluation is the main basis for engineering fracturing modification and interval optimization. At present, the commonly used methods include the mineral composition method, the elastic parameter method, and a combination of both. Limited by experiments and materials, the mineral composition method ( $w$ , mineral mass percent) is selected in this study to analyze shale brittleness [24], i.e.,

$$\text{Brit} = \frac{\omega_{\text{Quartz}} + \omega_{\text{Carbonate}}}{\omega_{\text{Quartz}} + \omega_{\text{Carbonate}} + \omega_{\text{Clay}}}. \quad (1)$$

Through calculation, it is found that the shale brittleness of the Longmaxi Formation is 0.36–0.81, among which the brittleness of the siliceous shale is 0.59–0.81, which is significantly better than that of the clayey shale (0.35–0.48) and the mixed shale (0.49–0.53). The longitudinal changes in the brittle minerals and organic carbon content are the main causes for the heterogeneity of the shale's brittleness.

## 5. Reservoir Space Heterogeneity

From SEM, the development status of different pores and fractures in shale can be obtained and their parameters can be obtained semiquantitatively. According to the classification scheme of pore morphology occurrence, the pores obtained by SEM are divided into four types: organic pore, intragranular pore, intergranular pore, and micro-fissure. The pore structure of shale, i.e., pore size, distribution, throat geometry, and connectivity, controls the dynamic process of adsorption-desorption of gas molecules in shale, which is the key factor for evaluating the gas storage capacity, seepage capacity, and later development value of shale [28–31].

**5.1. Pore Type Heterogeneity.** The shale of the Longmaxi Formation in well Ld1 mainly contains inorganic pores (intergranular pores, flocculent mineral intragranular pores, and microfractures) and organic matter micropores. The morphology of the inorganic pores is mainly affected by the shape, contact relationship, and arrangement of particles. The development of pores in different lithofacies is highly heterogeneous. The siliceous shale was deposited in an anoxic deepwater environment, where the pyrite was relatively developed and the intergranular pores of the framboidal pyrite aggregate were almost filled with migrating organic matter. Due to the high content of authigenic quartz and detrital quartz transformed by microorganisms in the siliceous shale, more intergranular pores and intragranular pores associated with quartz particles are developed (Figure 4(c)). In addition, the shale of the Longmaxi Formation is characterized by great burial depth and a high degree of thermal evolution, and more bubble-shaped and spongy organic pores easily formed after the light hydrocarbon components generated from organic matter were released. Spongy organic pores are more commonly found in the migrating organic matter from the overmature siliceous shale (Figures 5(a)–5(c)). In the mixed shale, the content of calcite and dolomite is generally over 10%. Therefore, compared with clayey and siliceous shale, the marginal dissolution pores and intergranular dissolution pores of calcite and dolomite in the mixed shale are developed with a larger pore size ( $>1 \mu\text{m}$ ), which is greater than the organic pores ( $<150 \text{ nm}$ ) and the clayey intergranular pores ( $<500 \text{ nm}$ ) (Figures 4(d)–4(f)); in addition, most of the dissolution pores are filled with migrating organic matter [25, 26]. In the clayey shale, the content of clay minerals reaches up to 73.8%, while the organic content is low, and the pores are mostly interlayer pores and intergranular pores of stripped clay minerals, as well as migrating organic pores (Figures 5(g)–5(i)).

The nitrogen adsorption-desorption isothermal curve of the shale samples is shaped like a reverse “S.” The adsorption isothermal curve of the shale samples belongs to the typical type IV. The desorption curve is much steeper than the adsorption curve at the medium relative pressure ( $0.4 < P/P_0 < 0.6$ ) and shows a steep drop trend, forming a broad H2-H3 hysteresis loop (Figure 6). The adsorption and desorption curves draw closer at the end. This indicates that most of the pores are micropores and that the pore type is dominated by silty thin-necked and wide-body ink-bottle composite pores. Since the high-pressure mercury intrusion method to measure pore structures can cause shale fractures, it is difficult to distinguish microfractures produced from natural fractures. Therefore, six samples of the Longmaxi Formation in well Ld1 were analyzed using the liquid nitrogen adsorption-desorption method. The experimental results show that: the BET specific surface area of the shale of the Longmaxi Formation ranges from  $5.35 \text{ m}^2/\text{g}$  to  $15.20 \text{ m}^2/\text{g}$ , with an average of  $7.90 \text{ m}^2/\text{g}$ , which is a significant variation; the range of the average pore size is  $3.48 \text{ nm} \sim 5.14 \text{ nm}$ , with an average of  $4.10 \text{ nm}$ . According to the classification standard of the International Union of Pure and Applied Chemistry (IUPAC), pores with a pore size of

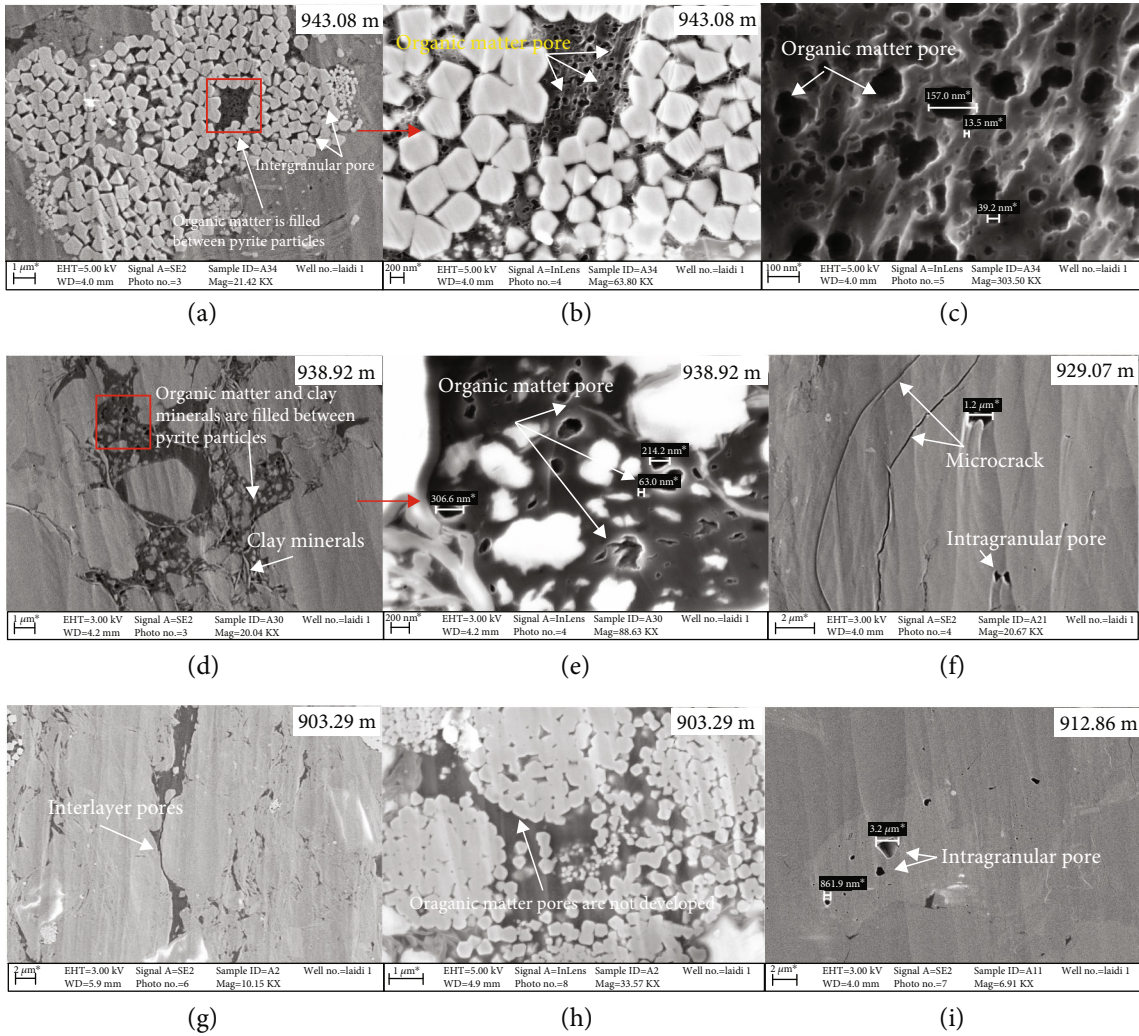


FIGURE 5: Pore distribution and morphological characteristics of shale.

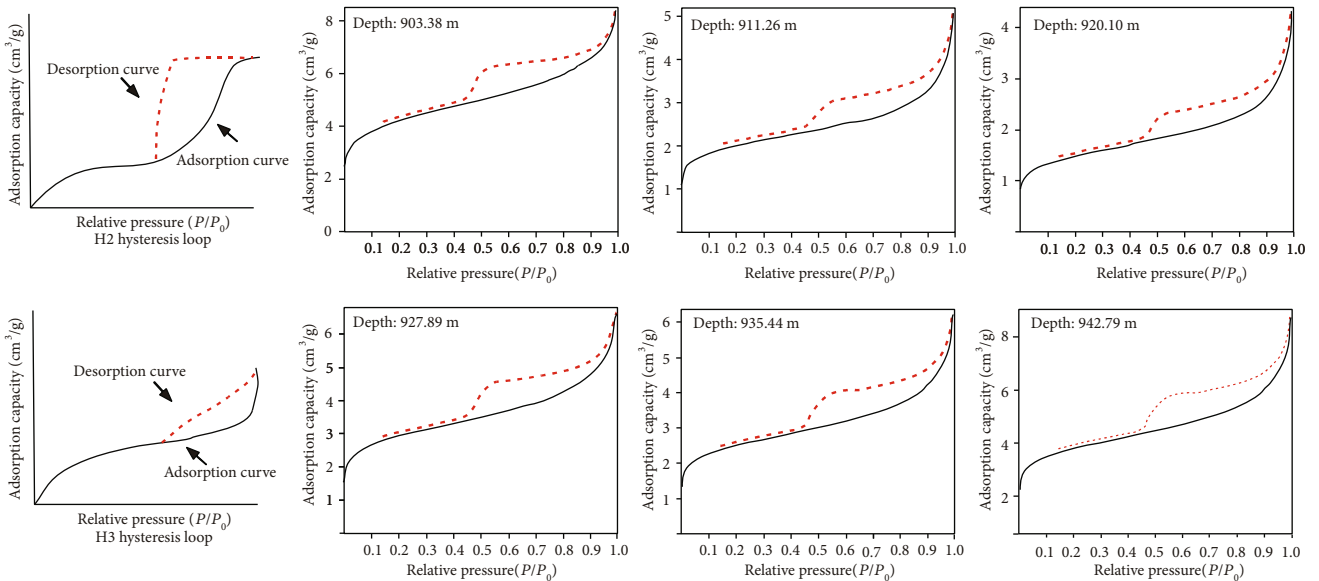


FIGURE 6: Characteristics of the  $N_2$  adsorption and desorption at low temperatures in the Longmaxi Formation.

TABLE 1: Statistical table of the shale pore volume of the Longmaxi Formation of well Ld1.

Serial Number	Depth (m)	Pore volume ( $10^{-3} \text{ cm}^3/\text{g}$ )				Pore volume ratio (%)		
		Micropore	Mesopore	Macropore	Total pore volume	Micropore	Mesopore	Macropore
1	903.38	1.93	2.87	0.14	4.94	39.1	58.1	2.8
2	911.26	0.81	1.37	0.35	2.53	32.0	54.2	13.8
3	920.10	0.57	1.05	0.31	1.93	29.5	54.4	16.1
4	927.89	1.27	2.04	0.18	3.49	36.4	58.5	5.2
5	935.44	0.99	1.38	0.13	2.50	39.6	55.2	5.2
6	942.79	1.73	2.56	0.13	4.42	39.1	57.9	2.9
Average value		1.22	1.88	0.21	3.30	36.0	56.4	7.7

less than 2 nm are micropores, those with a pore size of 2 nm–50 nm are mesopores, and those with a pore size greater than 50 nm are macropores. The samples from well Ld1 contain all these three types of pores, with micropores and mesopores forming the majority; they have the highest proportion in terms of specific surface area and pore volume. Specifically, the pore volume proportion of the micropores is 29.5% ~ 39.6% and 36.0% on average; that of the mesopores is 54.2% ~ 58.5%, and 56.4% on average; and that of the macropores is 2.8% ~ 16.1%, and 7.7% on average. It is speculated that the micropores and mesopores are the main places where shale gas is present in the Longmaxi Formation. Specifically, the intragranular pores among the pyrite and clay minerals, the organic pores, and the nanoscale microfractures are the main spaces where the shale gas is present (Table 1).

**5.2. Pore Structure Heterogeneity.** The fractal theory has been adopted to describe the complexity of pore structures or the surface roughness of porous media. The commonly used parameter is the fractal dimension  $D$ , which is directly proportional to the complexity of the pore structure and the surface roughness of porous media. Generally, its value is 2–3. Based on the data from the low-pressure nitrogen adsorption experiment, the calculation formula for the fractal dimension was obtained according to the Frenkel-Halsey-Hill (FHH) model [17–20]:

$$\ln V = k \ln (\ln P_0/P) + C, \quad (2)$$

$$D = k + 3, \quad (3)$$

where  $V$  is the volume of gas absorbed when the equilibrium pressure is  $P$ , in  $\text{m}^3$ ;  $P_0$  is the saturated vapor pressure, in MPa;  $k$  is a constant related to the adsorption mechanism and the fractal dimension; and  $C$  is a constant. Due to the difference in the adsorption mechanism and the pore size, there are two different pore fractal dimensions,  $D1$  and  $D2$ , on the nitrogen adsorption curve under the relative pressure of 0–0.5 and 0.5–1, which are used to describe the surface roughness and the complexity of the pore structure of the shale pores, respectively. Also, they can be used to describe the characteristics of large and small pores in the shale (the pore size corresponding to the relative pressure of 0.5 on

the nitrogen adsorption curve is the breaking point). According to equation (2), the data of the low-pressure nitrogen adsorption were organized, and  $\ln V$  was plotted for  $\ln (\ln P_0/P)$ . The slope of the different curves obtained by fitting is the value of  $k$ . Then, the fractal dimension,  $D$ , can be obtained according to equation (3).

The emergence and rapid development of fractal theories provide theoretical support for the quantitative analysis of the pore structures of shales. According to the low-temperature nitrogen adsorption experiment, the calculation models of the shale fractal dimension mainly include FHH, BET, and thermodynamic models. The FHH model is widely used in shale reservoirs and has the best fitting performance [27]. With the FHH model as the theoretical basis, mathematical calculation and piecewise fitting were carried out on the data of the low-temperature adsorption-desorption experiment (Figure 7). The fractal dimension is denoted by  $D1$  in the stage with low pressure ( $P/P_0 \leq 0.5$ ) and  $D2$  in the stage with high pressure ( $P/P_0 > 0.5$ ) in the adsorption process. According to the calculation results of the clayey shale samples of the Longmaxi Formation,  $D1$  is 2.7284–2.7562 (mean 2.7432) and  $D2$  is 2.7984–2.8850 (mean 2.8455) (Table 2).

**5.3. Porosity and Permeability Characteristics.** The porosity distribution range of 44 shale samples from the Longmaxi Formation in well Ld1 as measured by the pulse method is 0.06%–2.09%, with an average of 0.73%; among these, the porosity between 0.5% and 1% dominates, indicating that the overall porosity is relatively low. Member 1 has the highest porosity, followed by Member 2. Member 3 has the lowest porosity due to its low brittle mineral content, high clay mineral content, and weak compressive strength, as well as large pores and fissures that are filled by clay minerals. Moreover, the relative content of clay minerals and brittle minerals is an important factor that influences the porosity and permeability of shale. Through the analysis of the relationship between porosity and permeability, it has been demonstrated that the porosity and permeability of siliceous shales are significantly higher than those of other shales. Under stress, highly brittle shales are more likely to produce interconnected pore networks and fracturing-induced cracks later. The permeability range of the shales is  $(0.00025 \sim 0.60) \times 10^{-3} \mu\text{m}^2$ , with an average of  $0.0462 \times 10^{-3} \mu\text{m}^2$ ; the

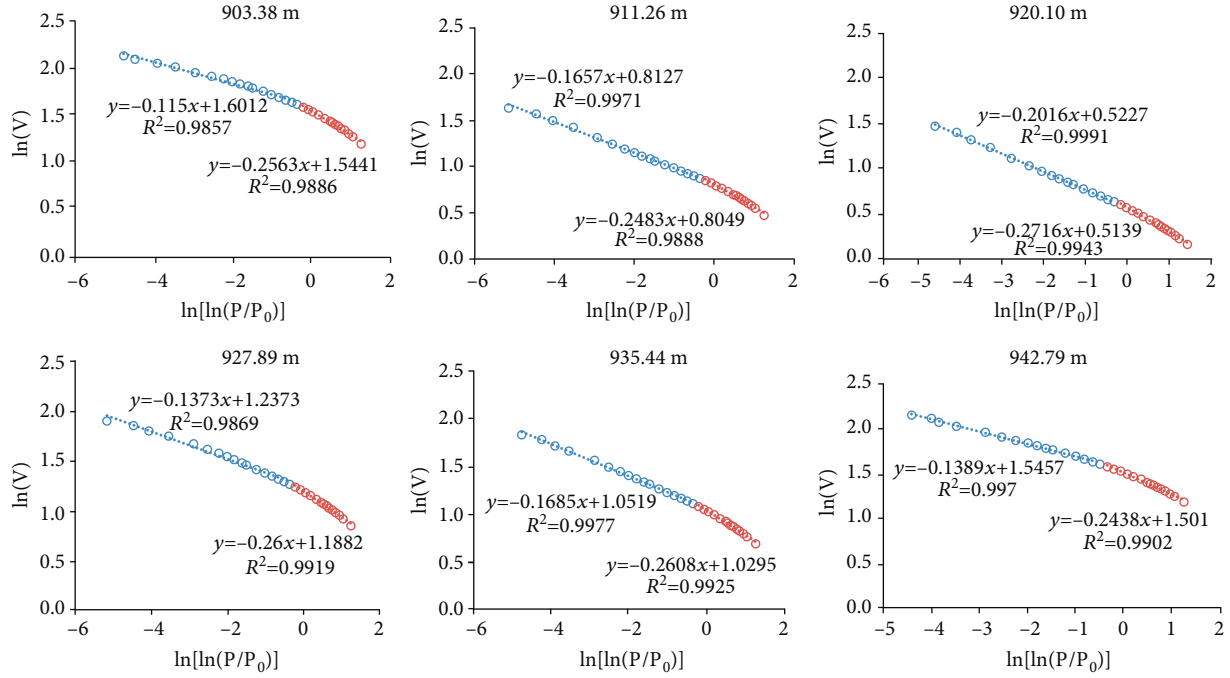


FIGURE 7: Fitting lines of pore fractal dimensions for the Longmaxi Formation shales.

TABLE 2: Fractal dimensions of the Longmaxi Formation shale from nitrogen adsorption and reservoir characteristic parameters.

Serial number	Depth (m)	D1	Fitting equation	$R^2/D1$	D2	Fitting equation	$R^2/D2$
1	903.38	2.74	$y = -0.26x + 1.54$	0.99	2.89	$y = -0.12x + 1.60$	0.99
2	911.26	2.75	$y = -0.25x + 0.8$	0.99	2.83	$y = -0.17x + 0.81$	0.99
3	920.10	2.73	$y = -0.25x + 0.8$	0.99	2.80	$y = -0.27x + 0.51$	0.99
4	927.89	2.74	$y = -0.14x + 1.24$	0.99	2.86	$y = -0.26x + 1.19$	0.99
5	935.44	2.74	$y = -0.17x + 1.05$	0.99	2.83	$y = -0.26x + 1.03$	0.99
6	942.79	2.76	$y = -0.14x + 1.55$	0.99	2.86	$y = -0.24x + 1.50$	0.99

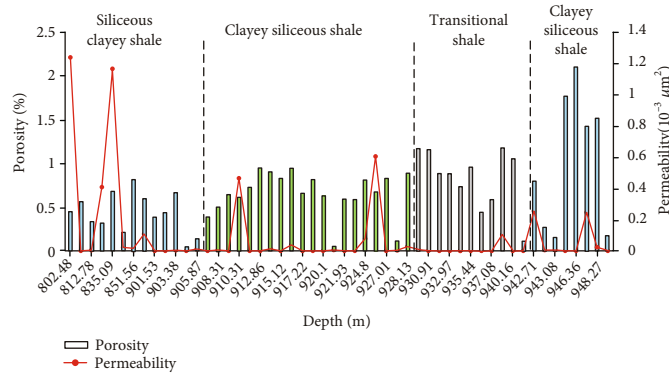


FIGURE 8: Pore and seepage characteristics of the Longmaxi Formation shale.

majority of the permeability lies between  $(0.001 \sim 0.01) \times 10^{-3} \mu\text{m}^2$ , with a wide range of changes. The permeability of the shales is extremely low on the whole, and the correlation between porosity and permeability is poor, which may be caused by unlinked pores (Figure 8).

## 6. Discussion

*6.1. Effective Characterization and Evaluation of the Pore Structure.* In this study, the pore structure of shale samples from the Longmaxi Formation was studied using high-

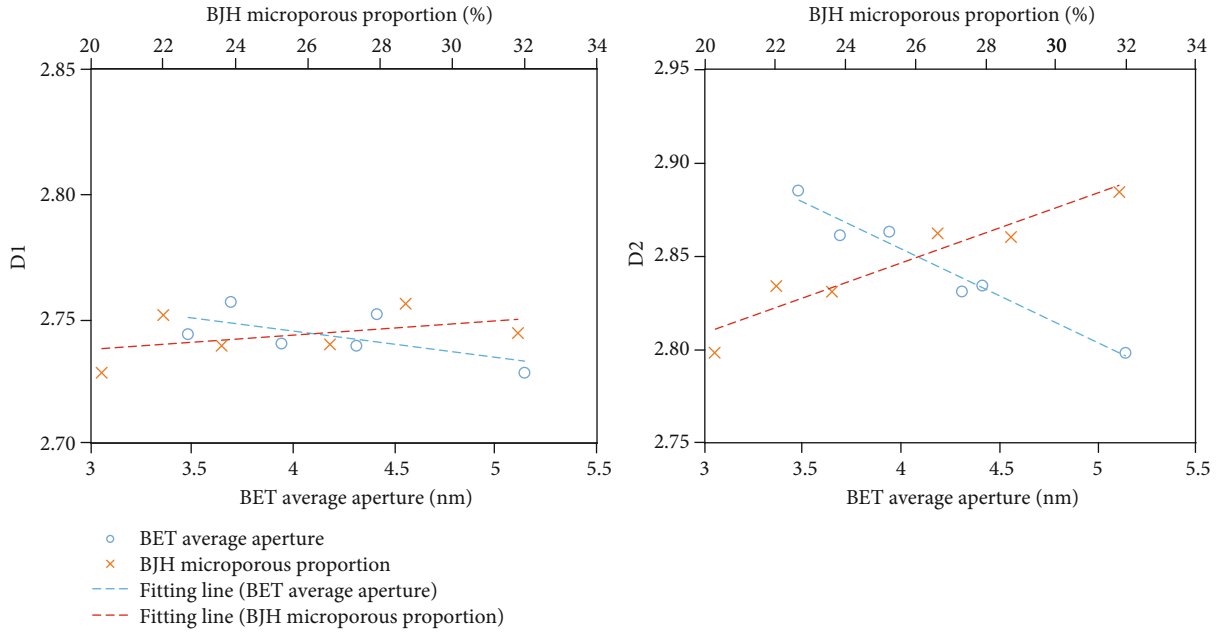


FIGURE 9: Relationship between fractal dimension and pore size.

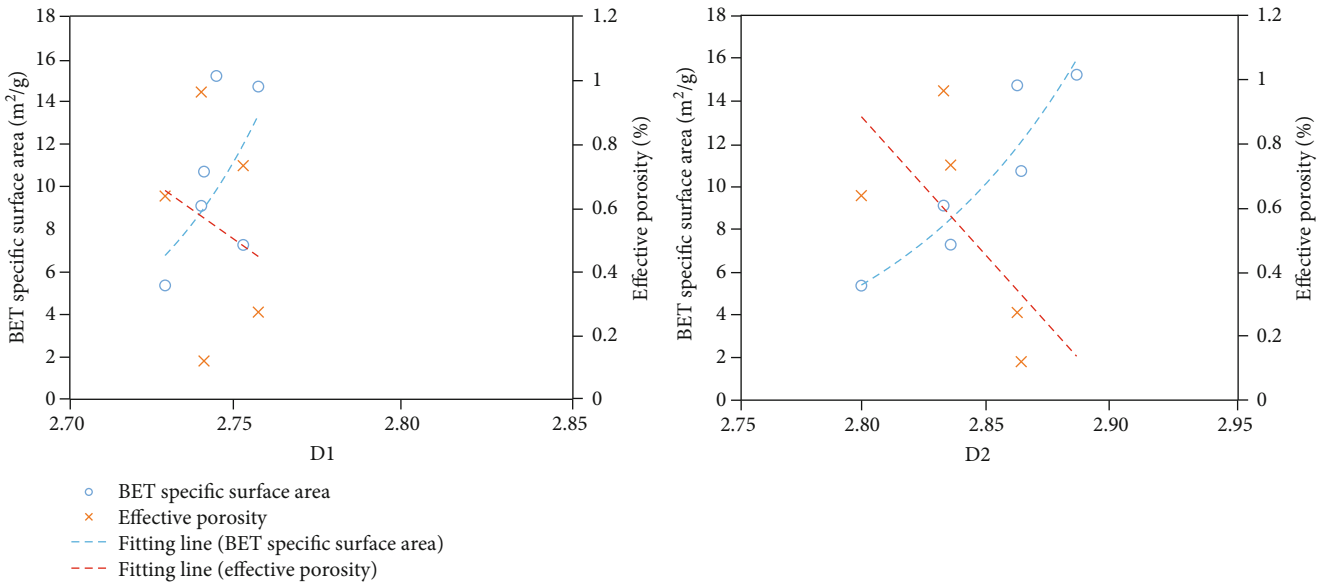


FIGURE 10: Relationship between reservoir property and fractal dimension.

pressure mercury intrusion and low-temperature nitrogen adsorption-desorption experiments to mainly characterize the pore size, pore complexity, etc. Comparing the correlation between the characterization parameters of different pore structures and the fractal dimension shows that the fractal dimension not only characterizes the surface roughness and complexity of the pores but also has a good correlation with the pore size (Figure 9). The smaller the average pore size in the shale, the larger is the proportion of micropores; further, the more complex the pore structure, the larger is the corresponding fractal dimension. *D2* can better characterize the pore complexity and has a better correlation with the pore size. In contrast, although *D1* has a certain

correlation with the pore size, the complete correlation is not obvious. This is because pore size can affect shale reservoir capacity to a certain extent; however, it is not a controlling factor. *D1* mainly reflects the rock reservoir performance, and therefore, the trend of *D1* changing with pore size is not obvious.

Correlation analysis between the physical parameters of the shale reservoir and the fractal dimension was carried out (Figure 10), and the results show that a certain correlation exists between the effective porosity and the specific surface area of rocks and the fractal dimension. Additionally, there is a negative correlation between the effective porosity and the fractal dimension. This is because as the pore

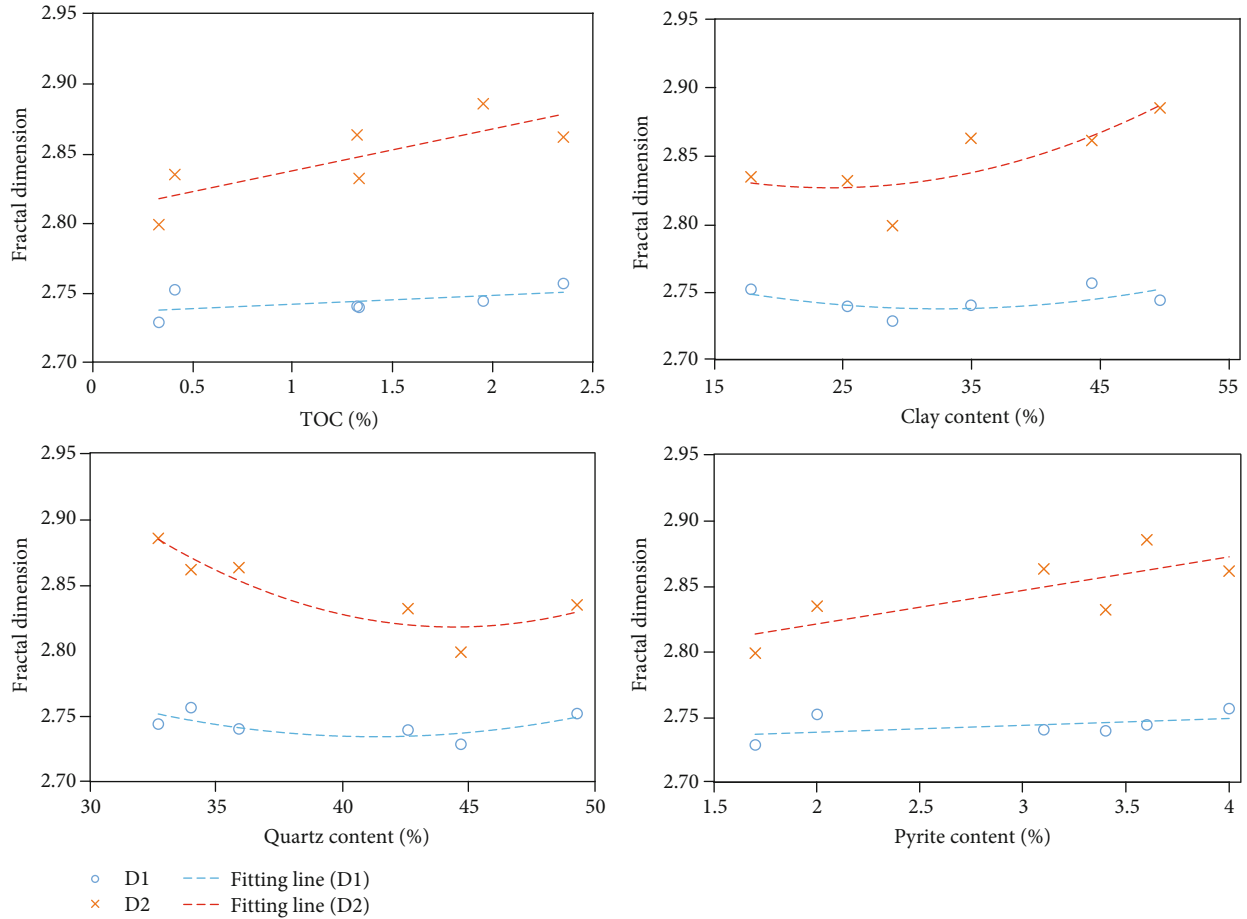


FIGURE 11: Main controlling factors of pore structure.

complexity increases, the connectivity of pores decreases, and a large number of independent pores that are not effective pores are formed, resulting in a decrease in the effective porosity. Although the connectivity of independent pores is poor, reflecting the unsatisfactory physical characteristics of the reservoir, they can still store fluids and are of great significance with respect to the enrichment of shale gas. In the late development stage, artificial methods are adopted to increase the pore connectivity, thereby effectively improving the reservoir's physical properties and making the gas therein recoverable. Moreover, there is a good positive correlation between the specific surface area of the shale and the fractal dimension, and the increasing trend is extremely obvious with the increase in  $D1$ , and the slope of the fitting curve is large. Shale gas mainly exists in shale pores in free and adsorbed states. The gas adsorption capacity of shale is an important parameter of its gas storage capacity. A greater specific surface area means a stronger adsorption capacity of shale, i.e., a larger fractal dimension. In particular, shales with a larger  $D1$  have a stronger adsorption capacity.

The fractal dimension based on the low-temperature  $N_2$  adsorption-desorption experiment is a parameter that can fully characterize the pore structure.  $D1$  can effectively reflect the adsorption and gas storage capacity of shale, and

$D2$  can comprehensively reflect the size and complexity of shale pores. For shale gas reservoirs, a greater  $D1$  value indicates that the rocks have a stronger ability to store free gas and adsorb gas, which is beneficial to shale gas enrichment. However, the  $D2$  value should not be too large or too small. If  $D2$  is too small, it indicates that the rock reservoir space is simple and mainly composed of macropores, and therefore, the adsorption capacity will not be high; if  $D2$  is too large, it indicates that the rock pore structure is too complex and that the pore connectivity is extremely poor, resulting in difficulty in fracturing, exploitation, and mediocre economic efficiency. The shale of the Longmaxi Formation in the study area has large fractal dimensions ( $D1$  and  $D2$ ), indicating that there is a large proportion of micropores and mesopores in the reservoir space, with a small average pore size and a large specific surface area; this is conducive to the occurrence and storage of shale gas, especially adsorbed shale gas. However, due to the complex pore structure, poor connectivity, and small effective porosity, gas circulation is poor, and high requirements were imposed on the reservoir reconstruction measures during exploitation.

**6.2. Influencing Factors of Pore Structure.** It has been demonstrated that the development of shale pores is mainly

influenced by factors such as mineral composition, organic matter abundance, organic matter maturity, and diagenesis. In this study, correlation analysis was performed on the fractal dimension, organic matter abundance, and mineral composition (in this study, the organic matter maturity of shale samples from the Longmaxi Formation differed very little; therefore, the effect of maturity on the fractal dimension was excluded in the correlation analysis). The results show that the fractal dimension has a positive correlation with TOC (Figure 11), but  $D1$  exhibits a weak increasing trend with the increase in TOC; this is because the shale samples in this study have high organic matter maturity and are in the overmature stage. In addition, it has been demonstrated that when the organic matter maturity is too high ( $R_o > 3.0\%$ ) [32–34], organic matter is carbonized, some organic pores may collapse, and the adsorption capacity of organic matter will be greatly reduced so that the increase in the organic matter will not significantly improve the adsorption capacity of the shale. The fractal dimension is positively correlated with the content of clay minerals and pyrite but is negatively correlated with the content of quartz. This is because the clay minerals in the shale of the Longmaxi Formation in Laifeng, Hubei are mainly illite, which has a relatively weak adsorption capacity. As a result, the overall adsorption capacity of the clay minerals is low, and with the increased content, more intergranular pores and intergranular pores are developed, which improves the complexity of the pores. However, the improvement of the shale adsorption capacity is limited. Quartz is the main brittle mineral in rock and mainly develops intergranular pores with large pore sizes and simple structures. With the increasing content of quartz, the proportion of mesopores and macropores increases, the pore structure tends to be simple, and the adsorption and gas storage capacity of the shale decreases slightly. In addition, the presence of pyrite strongly indicates a reducing environment. The development of common organic matter between framboidal pyrite crystals is beneficial to the development and preservation of organic pores. Therefore, the fitting curve of the correlation between the fractal dimension and the pyrite content is consistent with that between the fractal dimension and the TOC.

## 7. Conclusion

(1) In well Ld1, the shale of the Longmaxi Formation is mainly siliceous shale, mixed shale, and clayey shale. Among them, the siliceous shale is mainly developed at the bottom and middle-upper part of the Longmaxi Formation; the mixed shale is mainly developed in the middle part, and; the clayey shale is mainly developed in the upper part. In the longitudinal direction, the mineral composition of the shale of the Longmaxi formation is highly heterogeneous; the amount of clay minerals gradually increases from bottom to top, and terrigenous detrital input also gradually increases from bottom to top. This indicates that the sea level gradually decreased from the early stage of the deposition of the Longmaxi Formation to the late stage and that the sedimentary

environment gradually changed from a reducing environment to an oxidizing one. The siliceous shale (mostly high-carbon shale) at the bottom of the Longmaxi Formation has a high organic carbon content, and its microstructure is mostly blocky. The organic carbon content of the mixed shale and the clayey shale is relatively reduced as compared to the siliceous shale, and most are composed of low-carbon and carbon-poor shale, with obviously laminated microstructures. Furthermore, the occurrence, content, and brittleness of organic matter in the shales of different lithofacies are heterogeneous. Specifically, the siliceous shale at the bottom has the characteristics of high organic carbon content and good brittleness and is the key sweet interval in the study area

- (2) According to the combined characterization and analysis based on mercury intrusion and low-temperature  $N_2$  adsorption-desorption experiments, it is found that the pore structure of the shale in the Longmaxi Formation is complex and highly heterogeneous, with micropores and mesopores being the main pores and ink bottle pore being the main pore morphology. In addition, the fractal dimension of shale samples from the Longmaxi Formation was calculated based on the FHH equation; the results were as follows:  $D1$  is 2.7284–2.7562 (mean: 2.7432) and  $D2$  is 2.7984–2.8850 (mean: 2.8455), both of which are large. It is demonstrated by further analysis that the fractal dimension of pores can accurately represent the pore size, pore complexity, pore adsorption capacity, and gas storage capacity and can be used as a more comprehensive and effective characterization parameter of pore structure. The pore structure characteristics of the shale from the Longmaxi Formation in Laifeng, Hubei, are mainly as follows: a large proportion of micropores and mesopores are present in the reservoir space, the small average pore size is small, and the specific surface area is large, which is conducive to the occurrence and storage of shale gas, especially adsorbed shale gas; however, the complex pore structure, poor connectivity, and small effective porosity are not conducive to gas circulation. Therefore, higher requirements are required for reservoir reconstruction measures during exploitation
- (3) The reservoir space of the shale from the Longmaxi Formation in Laifeng, Hubei, is mainly affected by organic matter abundance and mineral composition, and there is a positive correlation between the fractal dimension and the organic matter abundance. However, since most of the organic matter is in the overmature stage and has a reduced adsorption capacity, its controlling effect on the adsorption capacity of the shale is not obvious; the fractal dimension is positively correlated with the clay mineral and pyrite content but is negatively correlated with the quartz content

## Data Availability

The data used to support the findings of this study are included within the article and are available from the corresponding author upon request.

## Conflicts of Interest

The authors declare that they have no conflicts of interest.

## Acknowledgments

This research was jointly supported by the Technical Fund Project of the Guizhou Science and Technology Department (QKHJC No. [2019]1293), Fund Project of the Department of Education of Guizhou Province (QJH No. KY [2018]029), Fund Program of the Science and Technology Department of Liupanshui City (52020-2018-03-03).

## References

- [1] R. G. Loucks, R. M. Reed, S. C. Ruppel, D. M. Jarvie, and D. M. Jarvie, "Morphology, genesis and distribution of nanometer-scale pores in siliceous mudstones of the Mississippian Barnett shale," *Journal of Sedimentary Research*, vol. 79, no. 12, pp. 848–861, 2009.
- [2] J. Klaver, G. Desbois, G. Littke, and J. L. Urai, "BIB-SEM characterization of pore space morphology and distribution in postmature to overmature samples from the Haynesville and Bossier Shales," *Marine and Petroleum Geology*, vol. 59, pp. 451–466, 2015.
- [3] R. G. Loucks, R. M. Reed, S. C. Ruppel, and U. Hammes, "Spectrum of pore types and networks in mudrocks and a descriptive classification for matrix-related mudrock pores—Spectrum of pore types and networks in mudrocks and a descriptive classification for matrix-related mudrock pores," *AAPG Bulletin*, vol. 96, no. 6, pp. 1071–1098, 2012.
- [4] X. Z. Wang, L. X. Zhang, and C. Gao, "The heterogeneity of shale gas reservoir in the Yanchang formation, Xiasiwang area, Ordos Basin," *Earth Science Frontiers*, vol. 23, pp. 134–145, 2016.
- [5] F. D. Zhao, Y. H. Guo, Y. M. Zhu, G. Wang, X. Chong, and X. M. Hu, "Analysis of microscale heterogeneity characteristics in marine shale gas reservoir: pore heterogeneity and its quantitative characterization," *Journal of China University of Mining and Technology*, vol. 17, pp. 296–307, 2018.
- [6] Z. X. Zuo, X. B. Zhang, S. B. Chen, Q. H. Si, C. Zhang, and Z. Liu, "Heterogeneity of shale gas reservoirs in coal measures: a case study of the Taiyuan and Shanxi formations in the Ningwu Basin," *Acta Geologica Sinica*, vol. 91, pp. 1130–1140, 2017.
- [7] X. B. Zhang, Z. Xi, C. Zuo, Q. H. Zhang, and Y. Z. Si, "Inter-layer heterogeneity in pore structure of shale gas reservoir in the Yima area, Henan Province," *Acta Geoscientifica Sinica*, vol. 37, pp. 340–348, 2016.
- [8] C. Y. Lin, L. J. Tan, and C. L. Yu, "Research on the heterogeneous distribution of petroleum (I): original of the theory of hydrocarbon accumulation," *Lithologic Reservoirs*, vol. 19, pp. 16–21, 2007.
- [9] X. M. Xiao, Z. G. Song, Y. N. Zhu, H. Tian, and H. W. Yin, "Summary of shale gas research in north American and revelations to shale gas exploration of lower Paleozoic strata in China south area," *Journal of China Coal Society*, vol. 38, pp. 721–727, 2013.
- [10] L. F. Lu, J. G. Cai, W. H. Liu, G. E. Teng, and J. Wan, "Occurrence and thermost ability of absorbed organic matter on clay minerals in mudstones and muddy sediments," *Oil & Gas Geology*, vol. 34, pp. 16–26, 2013.
- [11] Y. Cai, D. Liu, Z. Pan, Y. Yao, J. Li, and Y. Qiu, "Pore structure and its impact on CH<sub>4</sub> adsorption capacity and flow capability of bituminous and subbituminous coals from Northeast China," *Fuel*, vol. 103, pp. 258–268, 2013.
- [12] C. Liang, Z. X. Jiang, Y. C. Cao, M. H. Wu, L. Guo, and C. Zhang, "Deep-water depositional mechanisms and significance for unconventional hydrocarbon exploration: a case study from the lower Silurian Longmaxi shale in the southeastern Sichuan Basin," *AAPG Bulletin*, vol. 100, no. 5, pp. 773–794, 2016.
- [13] C. Liang, Z. Jiang, Y. Yang, and X. Wei, "Shale lithofacies and reservoir space of the Wufeng-Longmaxi Formation, Sichuan Basin, China," *Petroleum Exploration and Development*, vol. 39, no. 6, pp. 736–743, 2012.
- [14] F. Y. Wang, Z. Y. He, X. H. Meng, L. Y. Bao, and H. Zhang, "Occurrence of shale gas and prediction of original gas in-place (OGIP)," *Natural Gas Geoscience*, vol. 22, pp. 501–510, 2011.
- [15] F. Yang, B. Y. Hu, S. Xu, Q. B. Meng, and B. M. Krooss, "Thermodynamic characteristic of methane sorption on shales from oil, gas, and condensate windows," *Energy & Fuels*, vol. 32, no. 10, pp. 10443–10456, 2018.
- [16] B. Li, G. Q. Wei, K. Y. Hong, C. S. Peng, X. L. Hu, and L. L. Zhu, "Evaluation and understanding on the shale gas wells in complex tectonic provinces outside Sichuan Basin, South China: a case study from Well Laiye 1 in Laifeng-Xianfeng block, Hubei," *Natural Gas Industry*, vol. 36, pp. 29–35, 2016.
- [17] Y. L. Zheng, C. L. Mu, Z. H. Xiao, X. P. Wang, X. L. Liu, and Y. Chen, "Characteristics and gas-bearing controlling factors of shale gas reservoir in complex tectonic provinces: a case from the lower Silurian Longmaxi formation of Well Laidi 1 in Laifeng-Xianfeng block, Hubei province," *Marine Origin Petroleum Geology*, vol. 25, pp. 108–120, 2020.
- [18] J. Yu, J. Ma, J. G. Lu, Y. Cao, S. B. Feng, and W. C. Li, "Application of mercury injection and rate-controlled mercury penetration in quantitative characterization of microscopic pore structure of tight reservoirs: a case study of the Chang 7 reservoir in Huachi-Heshui area, the Ordos Basin," *Petroleum Geology & Experiment*, vol. 37, pp. 789–795, 2015.
- [19] F. Yang, Z. F. Ning, Q. Wang, D. T. Kong, K. Peng, and L. F. Xiao, "Fractal characteristics of nanopore in shales," *Natural Gas Geoscience*, vol. 25, pp. 618–623, 2014.
- [20] Z. D. Xi, S. H. Tang, J. Li, and L. Li, "Investigation of pore structure and fractal characteristics of marine-continental transitional shale in the east central of Qinshui Basin," *Natural Gas Geoscience*, vol. 28, pp. 366–376, 2017.
- [21] P. Zhang, Y. Q. Huang, J. C. Zhang, H. Y. Liu, and J. W. Yang, "Fractal characteristics of the Longtan formation transitional shale in Northwest Guizhou," *Journal of China Coal Society*, vol. 43, pp. 1580–1588, 2018.
- [22] J. H. Zhao, Z. J. Jin, Z. K. Jin et al., "Lithofacies types and sedimentary environment of shale in Wufeng-Longmaxi formation, Sichuan Basin," *Acta Petrolei Sinica*, vol. 37, pp. 572–586, 2016.

- [23] Y. M. Wang, S. F. Wang, D. Z. Dong et al., "Lithofacies characterization of Longmaxi formation of the lower Silurian, southern Sichuan," *Earth Science Frontiers*, vol. 23, pp. 119–133, 2016.
- [24] J. Z. Yi and C. Wang, "Differential pore development characteristics in various shale lithofacies of Longmaxi formation in Jiaoshiha area, Sichuan Basin," *Petroleum Geology & Experiment*, vol. 40, pp. 13–19, 2018.
- [25] C. Zhong, Q. R. Qin, and J. L. Zhou, "Brittleness evaluation of organic-rich shale in Longmaxi formation in Dingshan area, southeastern Sichuan," *Geological Science and Technology Information*, vol. 379, pp. 167–174, 2018.
- [26] Y. Hou, S. He, J. Yi et al., "Effect of pore structure on methane sorption potential of shales," *Petroleum Exploration and Development*, vol. 41, no. 2, pp. 272–281, 2014.
- [27] H. Tian, S. C. Zhang, and S. B. Liu, "Determination of organic rich shale pore features by mercury injection and gas adsorption methods," *Acta Petrolei Sinica*, vol. 33, pp. 419–427, 2012.
- [28] L. Hu, Y. M. Zhu, S. B. Chen, and Z. L. Du, "Fractal characteristics of shale pore structure of Longmaxi formation in Shuanghe area in southern Sichuan," *Xinjiang Petroleum Geology*, vol. 34, pp. 79–82, 2013.
- [29] B. W. Du, X. H. Peng, S. K. Xie, and B. Zheng, "Exploration potential analysis of shale gas in the lower cretaceous, Gamba-Tingri basin of Tibet," *Petroleum Geology and Recovery Efficiency*, vol. 22, pp. 51–54, 2015.
- [30] T. T. Cao, Z. G. Song, G. X. Liu, Q. Yin, and H. Y. Luo, "Characteristics of shale pores, fractal imension and their controlling factors determined by nitrogen dsorption and mercury injection methods," *Petroleum Geology and Recovery Efficiency*, vol. 23, pp. 1–8, 2016.
- [31] Y. Gao, L. Mao, and R. Ma, "Pore structure characteristics and its fractal dimensions of transitional shales," *Science Technology and Engineering*, vol. 17, pp. 77–85, 2017.
- [32] D. L. Xie, Y. H. Guo, and D. F. Zhao, "Fractal characteristics of adsorption pore of shale based on low temperature nitrogen experiment," *Journal of China Coal Society*, vol. 39, pp. 2466–2472, 2014.
- [33] Y. M. Wang, D. Z. Dong, X. Z. Cheng, J. L. Huang, S. F. Wang, and S. Q. Wang, "Electric property evidences of the carbonification of organic matters in marine shales and its geologic significance: a case of the lower Cambrian Qiongzhusi shale in southern Sichuan Basin," *Natural Gas Industry*, vol. 34, pp. 1–7, 2014.
- [34] F. Yang, Z. F. Ning, Q. Wang, and H. Q. Liu, "Pore structure of Cambrian shales from the Sichuan Basin in China and implications to gas storage," *Marine and Petroleum Geology*, vol. 70, pp. 14–26, 2016.

## Research Article

# Stress Distribution and Mechanical Behaviour of Rock Mass Containing Two Openings Underground: Analytical and Numerical Studies

Lihai Tan <sup>1,2</sup>, Gaofeng Wang <sup>1</sup>, Ting Ren,<sup>2</sup> Linming Dou <sup>1</sup>, Xiaohan Yang,<sup>2</sup> and Shikang Song<sup>3</sup>

<sup>1</sup>School of Mines, China University of Mining and Technology, Xuzhou, Jiangsu 221116, China

<sup>2</sup>School of Civil, Mining and Environmental Engineering, University of Wollongong, NSW, 2522 Wollongong, Australia

<sup>3</sup>Shaanxi Zhengtong Coal Industry Co., Ltd., Xianyang 713600, China

Correspondence should be addressed to Gaofeng Wang; wanggaofengcumt@126.com

Received 12 September 2021; Accepted 7 October 2021; Published 22 November 2021

Academic Editor: Kouqi Liu

Copyright © 2021 Lihai Tan et al. This is an open access article distributed under the Creative Commons Attribution License, which permits unrestricted use, distribution, and reproduction in any medium, provided the original work is properly cited.

In this study, stress solution for rock mass containing two rectangular openings was calculated based on the Schwarz alternating method to investigate the stress distribution in rock mass around openings with different layouts. In addition, large-scale numerical models were further established for the two-opening system by means of the PFC-FLAC coupling method, in which the stress evolution, failure patterns, and acoustic emission (AE) events were presented. With the combination of analytical and numerical solutions, the interaction mechanism between two openings under different layouts was discussed from the perspective of stress and failure. The result shows that the confining stress within a certain range contributes to relieving tensile stress concentration around openings. The stress condition within the connecting area and coalescence pattern between two adjacent openings is dominated by their layout. Compared with small-size rock specimens in laboratory tests, the failure patterns around openings show a better agreement with the stress concentration characteristics determined by analytical stress solutions.

## 1. Introduction

There exist a large number of openings with different shapes and sizes underground in various mines, like roadways and tunnels in service and goafs waiting for filling or which have been abandoned, which may present potential environmental issues and security risks. Under high geostress, rock mass around openings or flaws may be subjected to high stress concentration, which may lead to initial failure triggering the instability of rock structures [1–8].

The analytical solution and failure behaviour for rock mass containing a circular opening have been comprehensively investigated by a wide range of literature. It has been reported that there are three kinds of failure, namely, tensile cracks, spalling cracks, and far-field cracks within the rock mass [9–11]. Under uniaxial compressive conditions without confining

stress, the initial tensile cracks usually appear in the top and bottom of the openings, which are tensile stress concentration areas. Spalling cracks appear around the side walls of the openings because of high compressive stress concentration. Similar failure patterns also happened to rock mass containing a non-circular opening reported by other studies [12].

In addition, the analytical stress solution for plates containing a single opening has been also comprehensively investigated to explain the mechanical behaviour of rock mass around the opening by a lot of studies [13–18]. Based on the complex variable method, stress solution for elastic plates containing an opening with typical shapes, such as circular, elliptical, triangular, and rectangular shapes, has been calculated by Ukadgaonker and Awasare [19–21], Ukadgaonker and Rao [22], and Sharma [23]. Combining analytical solution and laboratory test, Wu and Ma [12]

calculated the stress concentration factor on the periphery of a horseshoe-shaped opening and discussed its effect on the failure patterns of rock specimens. Tan et al. [24] considered six kinds of holes with typical shapes in practical rock engineering and discussed the shape effect on stress distribution and failure patterns around the openings based on the analytical solutions combined with numerical and experimental results.

When there exists more than one opening within an area underground, the adjacent openings may change the stress distribution around an opening significantly and thus lead to complicated failure patterns [25]. The interaction between two openings has also been discussed by many studies from the perspective of analytical stress solution. Zhang et al. [26, 27] proposed a method to calculate stress solution for plates containing two or more openings with arbitrary shapes based on the Schwarz alternating principle. This method was further improved by Tan et al. [28] for a better solution accuracy, based on which the effects of opening layouts and confining stress on the stress distribution and failure patterns for two U-shaped openings and two arched openings were investigated, respectively. Besides analytical solutions, laboratory experiments for rock specimens containing two or more flaws or openings have also been widely carried out to understand the mechanical interaction mechanism between two defects. Zhou et al. [29] conducted uniaxial compression tests combined with acoustic emission (AE) and digital image correlation (DIC) techniques and then analyzed the fracture coalescence behaviour around marble specimens containing two rectangular openings. Zhao et al. [30] conducted a series of uniaxial compressive tests on rock specimens containing several circular openings and found that openings were strongly affected by each other with complicated failure patterns. Similar results were also presented by Lin et al. [31] when studying the crack initiation and coalescence patterns within rock specimens containing multiple openings under uniaxial compression. It can be concluded that the fracturing behaviour and specimen stability are significantly affected by opening layout including their distance and the connecting angle between them. However, in laboratory tests, the size of specimens is usually small relative to openings within them, which may lead to a strong boundary effect interfering with the mechanical behaviour of rock mass around openings. To address this problem, numerical modelling methods have been widely employed, which can avoid the boundary effect on interesting areas by establishing a large-scale numerical model. Among them, the finite element method (FEM) and finite difference method (FDM) are popular in terms of the solution for deformation problems in rock engineering but are not good at describing material fracturing behaviour. The discrete element method (DEM) is another leading numerical method dealing with rock failure problems, but DEM numerical modelling may give rise to huge calculation costs for the problem about a small interesting part in a large model with a great number of particles. In view of this, coupling the DEM method with the FEM method or FDM method is an interesting alternative promising the solution accuracy for mechanical behaviour of rock mass close to the opening within a large

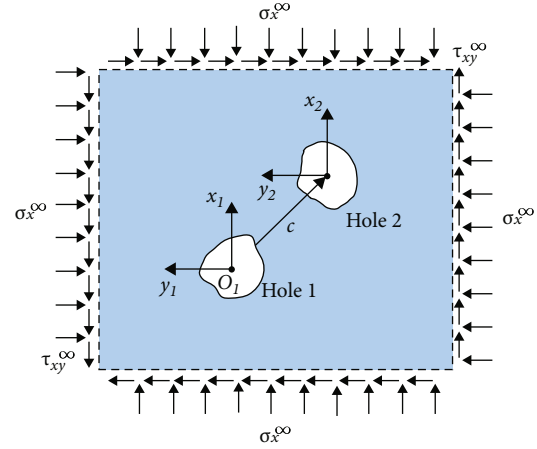


FIGURE 1: Schematic diagram of a plate containing two openings.

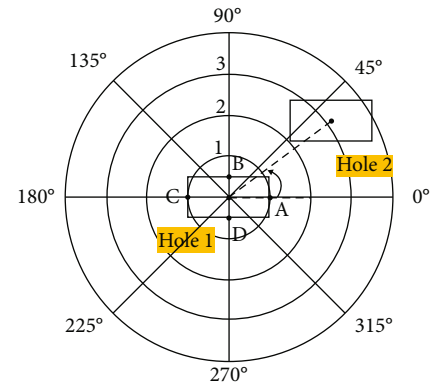


FIGURE 2: Schematic diagram of the configuration of two rectangular holes.

model with little effect from the model boundary. In particular, coupling simulation with particle flow code (PFC) and fast Lagrangian analysis of continua (FLAC) has been widely used in rock engineering [32–34].

In this study, analytical solutions as well as numerical simulations were conducted for a better understanding of the stress distribution and mechanical behaviour of rock mass around openings under a large-scale area. The influence of the connecting angle of two adjacent openings on stress distribution was discussed based on the analytical stress solutions calculated by the Schwarz alternating method. This influence on the failure patterns of surrounding rock mass was further investigated based on PFC-FLAC coupling numerical simulations.

## 2. Analytical Stress Solution of Plates Containing a Single Opening

**2.1. Mapping Function.** Rock mass around openings in deep mines underground can usually be simplified to be an infinite elastic plate [35, 36]. With conformal mapping, the region outside a unit circle in the  $\zeta$ -plane can be mapped

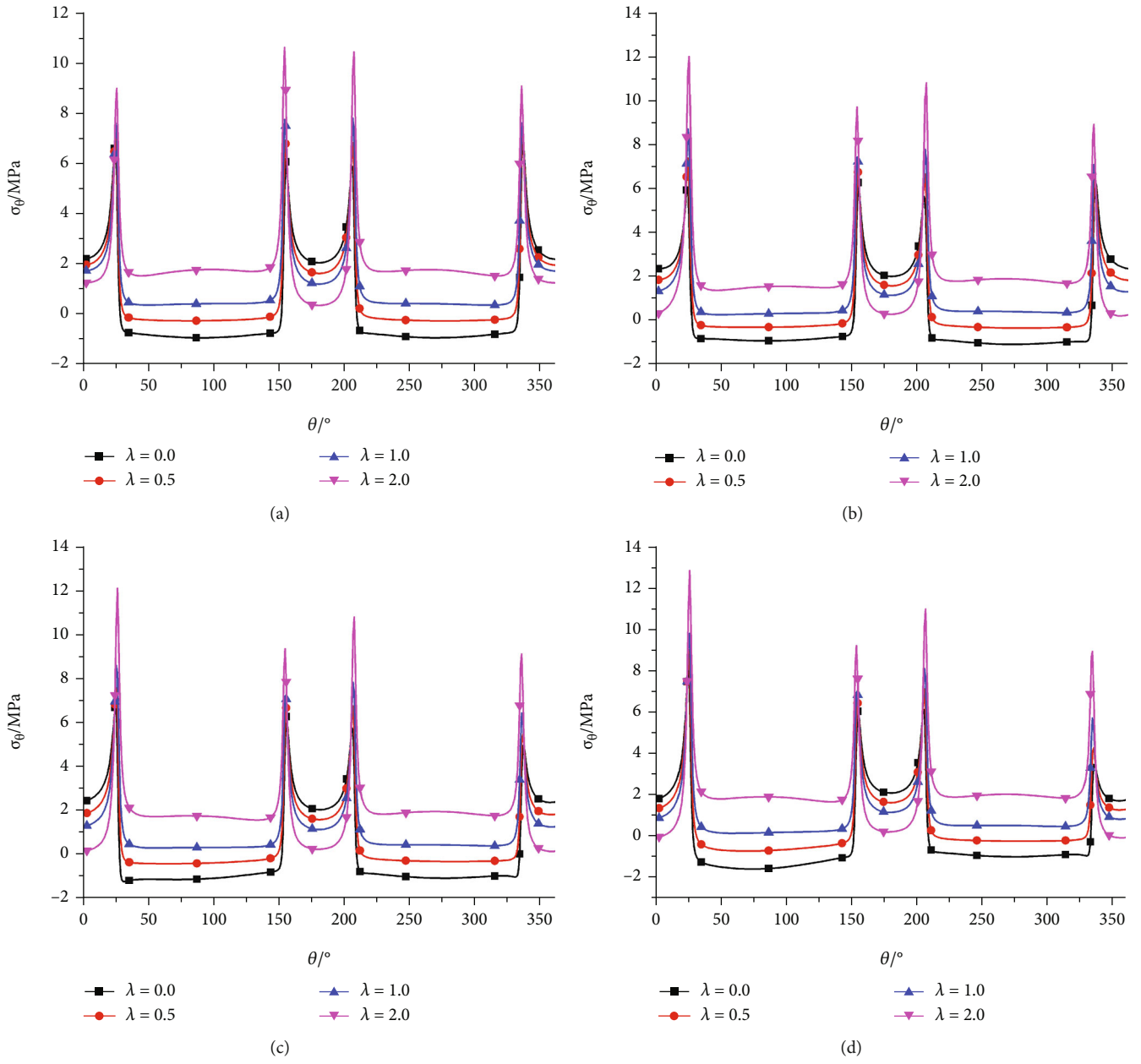


FIGURE 3: Continued.

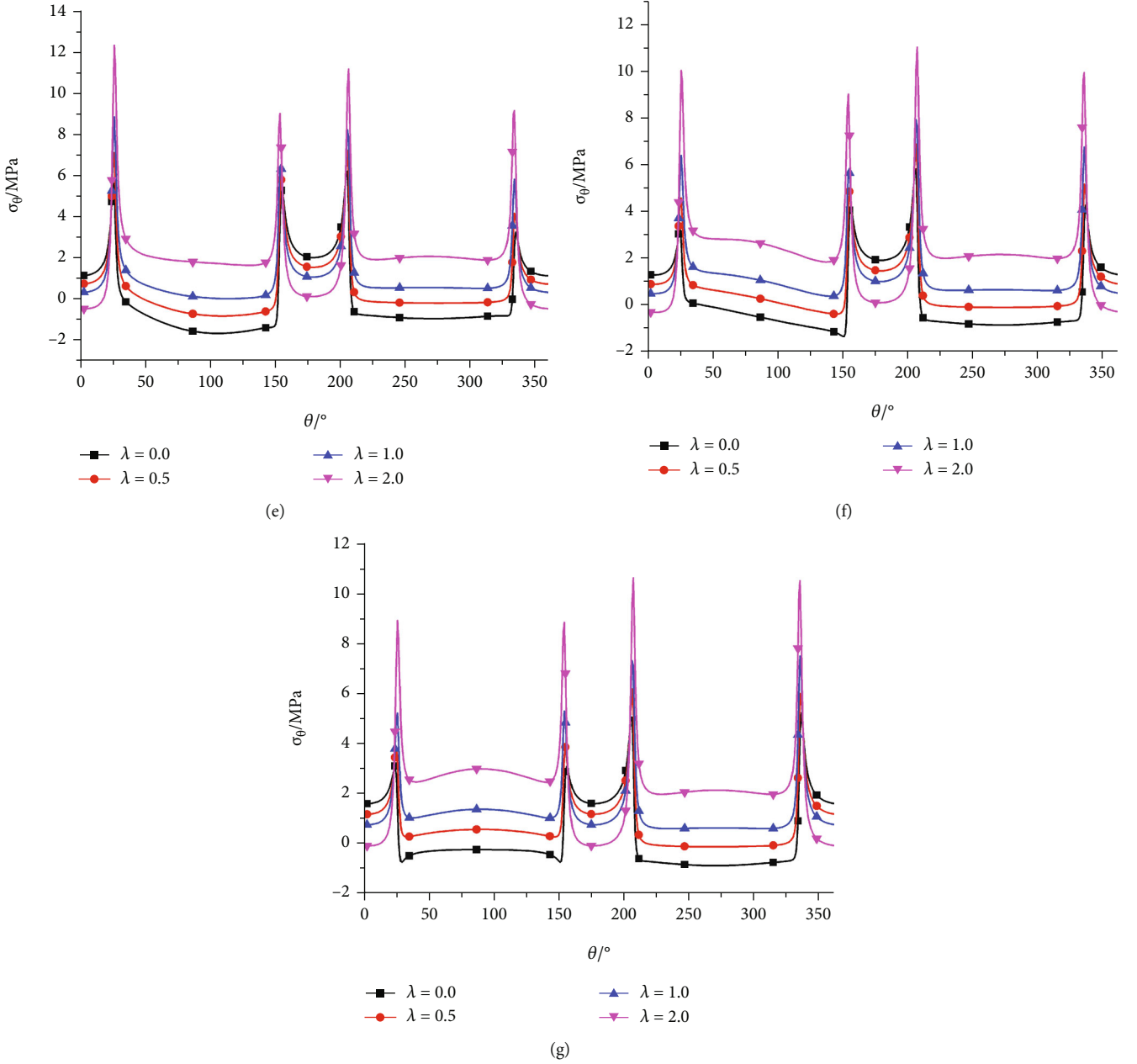


FIGURE 3: Hoop stress around Hole 1 in different cases: (a)  $\alpha = 0^\circ$ ; (b)  $\alpha = 15^\circ$ ; (c)  $\alpha = 30^\circ$ ; (d)  $\alpha = 45^\circ$ ; (e)  $\alpha = 60^\circ$ ; (f)  $\alpha = 75^\circ$ ; (g)  $\alpha = 90^\circ$ .

onto a simply connected region outside an opening in the  $z$ -plane by a mapping function in the following form:

$$Z = \omega(\zeta) = \sum_{k=1}^{\infty} C_k \zeta^{2-k}, \quad (1)$$

where  $C_k = A_k + iB_k$ . Both  $A_k$  and  $B_k$  are real constants.

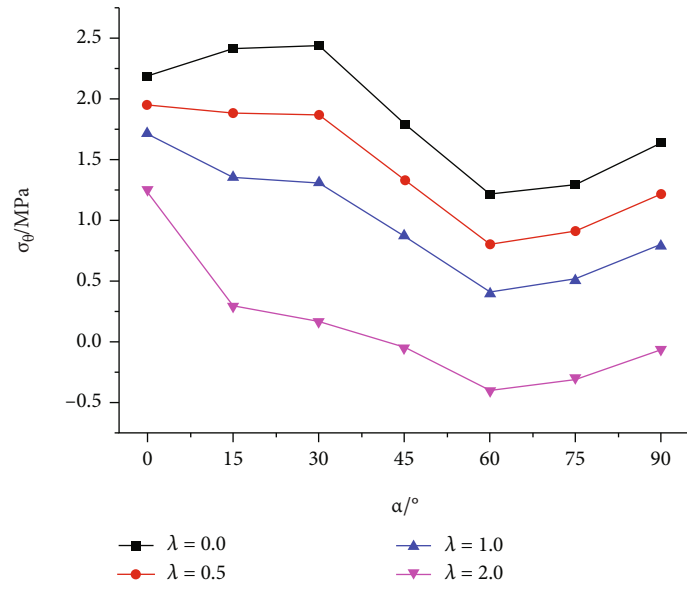
With  $C_k$  truncated to  $m$  terms, the mapping function can be written as

$$Z = \omega(\zeta) = \sum_{k=1}^m C_k \zeta^{2-k}. \quad (2)$$

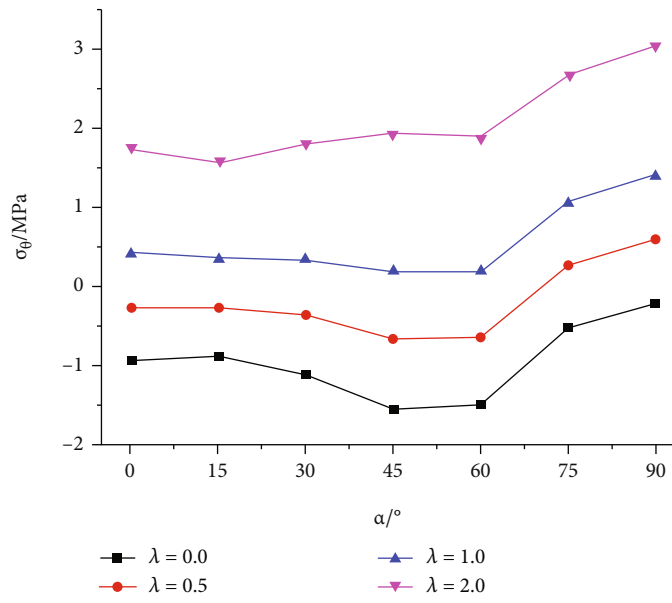
For  $m$  points on the unit circle in the  $\zeta$ -plane with coordinates of  $(1, \theta_j)$ , the coordinates of their mapping points are  $(r_j, \alpha_j)$  in the  $z$ -plane. According to the orthogonality of trigonometric functions,  $A_k$  and  $B_k$  can be calculated by [37, 38]

$$\begin{cases} A_k = \frac{1}{m} \sum_{j=1}^m \{r_j \cos \alpha_j \cos [(k-2)\theta_j] - r_j \sin \alpha_j \sin [(k-2)\theta_j]\}, \\ B_k = \frac{1}{m} \sum_{j=1}^m \{r_j \cos \alpha_j \sin [(k-2)\theta_j] + r_j \sin \alpha_j \cos [(k-2)\theta_j]\}. \end{cases} \quad (3)$$

By sampling  $2n$  points uniformly on the unit circle in the

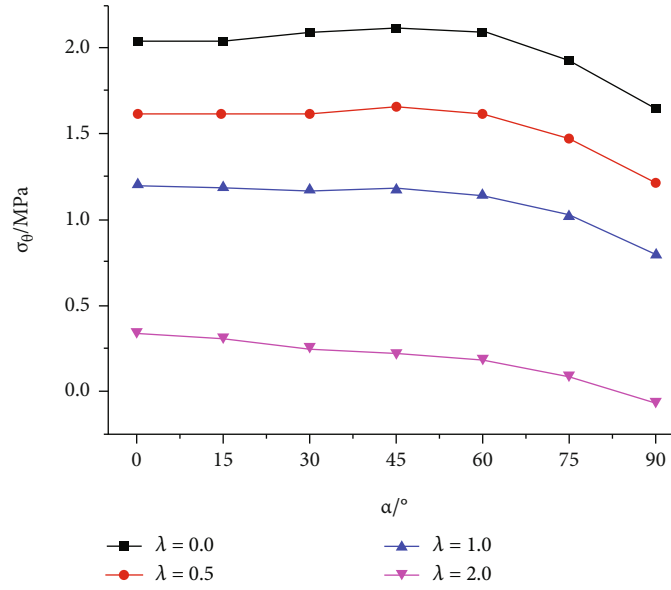


(a)

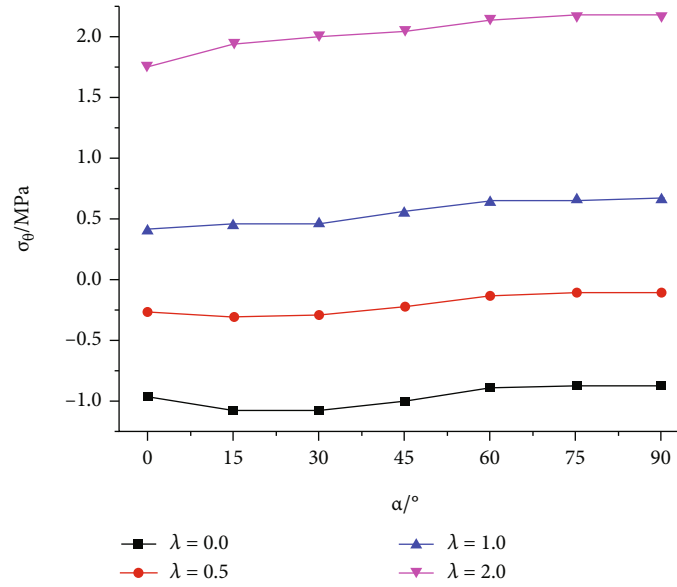


(b)

FIGURE 4: Continued.



(c)



(d)

FIGURE 4: Hoop stress at monitoring points: (a) point A; (b) point B; (c) point C; (d) point D.

$\zeta$ -plane, the sampled points in two groups  $\sigma_{e,j}(1, \theta_{e,j})$  and  $\sigma_{o,j}(1, \theta_{o,j})$  can be expressed as

$$\begin{cases} \theta_{e,j} = \frac{2\pi j}{n}, \\ \theta_{o,j} = \frac{\pi(2j-1)}{n}, \end{cases} \quad j = 1, 2, 3, \dots, n. \quad (4)$$

By keeping submitting  $\sigma_{e,j}$  and  $\sigma_{o,j}$  into Equation (3) alternately and moving the calculated mapping points into the opening boundary during iterations, the optimal values of  $A_k$  and  $B_k$  can be quickly determined once the convergence is reached. For a rectangular opening whose size is

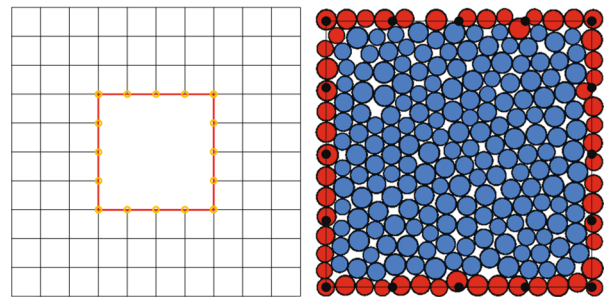


FIGURE 5: Schematic diagram of an approach of FDM-DEM.

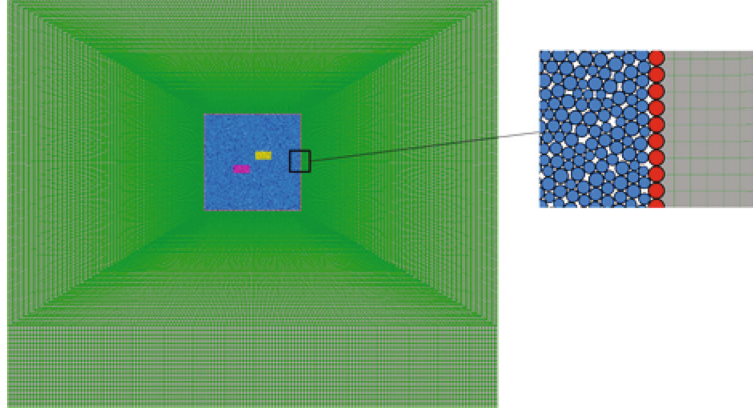


FIGURE 6: Schematic diagram of FDM-DEM numerical modelling.

$40 \times 20$  (width  $\times$  height), the optimal mapping function calculated by this method can be expressed as

$$\omega(\zeta) = \left[ 17.422\zeta + 5.354\zeta^{-1} - 2.531\zeta^{-3} - 0.436\zeta^{-5} + 0.083 \times 10^{-3}\zeta^{-7} \right]. \quad (5)$$

**2.2. Principles of Schwarz Alternating Method.** As shown in Figure 1, there is an infinite plate containing two openings, namely, Hole 1 and Hole 2. Mapping functions for them are  $Z_1 = \omega(\zeta_1)$  and  $Z_2 = \omega(\zeta_2)$ , respectively. Two coordinate systems, namely, the  $x_1O_1y_1$  coordinate system and  $x_2O_2y_2$  coordinate system, are defined in the plate. The origin of the former one is the centroid of Hole 1, and that of the later one is the centroid of Hole 2. For a point whose coordinate is  $z_1$  in the former coordinate system and  $z_2$  in the later one, the relation between them is  $z_1 = z_2 + c$ .

The stress solution for the plate is calculated according to an improved Schwarz alternating method [28]. When there is only a hole (Hole 1) in the plate, the boundary stress condition can be expressed as [22]

$$\varphi_0(\sigma) + \frac{\omega(\sigma)}{\omega'(\sigma)} \overline{\varphi_0'(\sigma)} + \overline{\psi_0(\sigma)} = -2B\omega(\sigma) - (B' - iC') \overline{\omega(\sigma)}. \quad (6)$$

The two complex stress functions  $\varphi_1^{(0)}(\zeta)$  and  $\psi_1^{(0)}(\zeta)$  for the plate containing Hole 1 can be expressed as [39]

$$\begin{cases} \varphi_1^{(0)}(\zeta) = B\omega(\zeta) + \varphi_0(\zeta), \\ \psi_1^{(0)}(\zeta) = (B' + iC')\omega(\zeta) + \psi_0(\zeta). \end{cases} \quad (7)$$

$B$ ,  $B'$ , and  $C'$  are constants relating to the far-field stress condition, which are expressed as

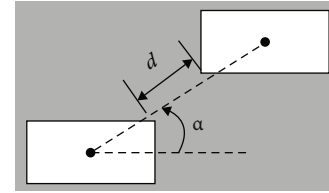


FIGURE 7: Layouts of two openings in different numerical models.

$$\begin{cases} B = \frac{\sigma_x^\infty + \sigma_y^\infty}{4}, \\ B' = \frac{\sigma_y^\infty - \sigma_x^\infty}{2}, \\ C' = \tau_{xy}^\infty, \end{cases} \quad (8)$$

where  $\sigma_x^\infty$ ,  $\sigma_y^\infty$ , and  $\tau_{xy}^\infty$  are far-field vertical stress, horizontal stress, and shear stress, respectively.

The surface force on the suppositional boundary of unexcavated Hole 2 caused by Hole 1 can be calculated by

$$f_2^1(\sigma_2) = \varphi_1^0(\gamma_1) + \frac{\omega_1(\gamma_1)}{\omega_1'(\gamma_1)} \overline{\varphi_1^{0'(\gamma_1)}} + \overline{\psi_1^0(\gamma_1)}, \quad (9)$$

where  $\sigma_2$  is a point on the boundary of the mapping unit circle in  $\zeta_2$  plate for Hole 2 and  $\gamma_1$  is its corresponding point in  $\zeta_1$  plate.

The coordinate transformation from  $\sigma_2$  to  $\gamma_1$  is realized by  $s$  series of steps. Firstly,  $\sigma_2$  is transformed into  $t_2$  in the  $Z_2$  plate by the mapping function  $z_2 = \omega_2(\sigma_2)$ . Next,  $t_2$  in the  $x_2O_2y_2$  coordinate system into  $\eta_1$  in the  $x_1O_1y_1$  coordinate system via  $\eta_1 = t_2 + c$ . The last step is the transformation of  $\eta_1$  into  $\gamma_1$ . Zhang and Lu [27] realized this transformation with the employment of inverse mapping function. Though it is feasible, this method may cause an evitable solution error. Alternatively, the optimization method suggested by Tan et al. [28], which promised little error of the coordinate transformation, is used in this study.

TABLE 1: The mesoparameters of numerical models in PFC.

Particle parameters			Parallel bond parameters		
$E_c$	3.0 GPa	Effective modulus	$\bar{E}$	3.0 GPa	Bond effective modulus
$k_n/k_s$	1.0	Ratio of particle normal to shear stiffness	$\bar{k}_n/\bar{k}_s$	1.0	Ratio of normal to shear stiffness of the parallel bond
$\mu$	0.577	Particle friction coefficient	$\bar{\sigma}$	25.0 MPa	Tensile strength of the parallel bond
$R_{\max}$	0.75 m	The maximum particle radius	$\bar{\tau}$	15.0 MPa	Shear strength of the parallel bond
$R_{\min}$	0.5 m	The minimum particle radius			
$\rho$	2.5 g/cm <sup>3</sup>	Particle density			

In the first iteration, the boundary stress condition can be expressed as

$$\varphi_2^{(1)}(\sigma_2) + \frac{\omega_2(\sigma_2)}{\omega_2'(\sigma_2)} \overline{\varphi_2^{(1)'}}(\sigma_2) + \overline{\psi_2^{(1)}}(\sigma_2) = -f_2^1(\sigma_2). \quad (10)$$

The stress function  $\varphi_2^1(\zeta_2)$  and  $\psi_2^1(\zeta_2)$  at the first iteration are the combination of  $\varphi_2^0(\zeta_2)$  and  $\varphi_2^{(1)}(\zeta_2)$  and that of  $\psi_2^0(\zeta_2)$  and  $\psi_2^{(1)}(\zeta_2)$ , respectively.

In the next iteration, the redundant surface force around the boundary of Hole 1 is calculated by the current stress functions. Then, the iterations will be conducted alternately until the desired solution accuracy is achieved.

**2.3. Calculation Models.** Based on the method introduced above, the stress solutions for plates containing two rectangular holes with different contacting angles are conducted and analysed. The schematic diagram of the two-hole system is shown in Figure 2.  $\sigma_x^\infty$  was set as 1 MPa. The hole shape, size, and configuration are the same as those in the DEM simulations.

As shown in Figure 3, under the influence of the adjacent hole, shear stresses at the periphery of Hole 1 were no longer at symmetrical patterns. Such asymmetry is not obvious with the connecting angle of 0°. However, when the holes' connecting line is oblique, the difference between the stress on the side closer to the adjacent hole and on the other side is notable.

Combining Figure 3 with Figure 4 shows that, for monitoring points *A* and *B* which are closer to the adjacent hole, notable fluctuations of hoop stress are observed with the increase of the connecting angle. In contrast, hoop stress at points *C* and *D* which are further from the adjacent hole is relatively flat, indicating that they are less affected by the connecting angle.

This phenomenon demonstrates that interactive effects between adjacent holes mainly concentrate on the connecting area. With a lateral stress ratio of 0, roof and floor regions of Hole 1 are in intensified tensile stresses; when the lateral stress ratio rises up to the range of 0.5 to 1.0, the intensification level of tensile stress around holes drop dramatically. This illustrates that, under confining conditions, stability of the hole system will be considerably improved with the axial stress ratio being at a reasonable range. Nonetheless, when the axial stress ratio reaches 2.0, tensile stress intensification will reoccur at parts of the

hole system, and continuous increasing of the axial stress ratio will impose negative effects on the stability of the hole system.

When  $\lambda$  is 0, tensile stress around Hole 1 is at its roof or floor, which reaches the maximum when the connecting angle is 45°. Accordingly, the stability of the hole system is minimized, and the initial failure is mainly characterized by tensile cracks at the roof of Hole 1 and the floor of Hole 2. Then, with connecting angle increasing, tensile levels gradually decline. When the connecting angle reaches 75°, stress at the roof of the hole converts to be compressive, while that at the floor remains tensile on relatively stable levels, which indicates that initial tensile failures might occur at the floor of Hole 1 or the roof of Hole 2.

### 3. DEM-FDM Coupling Numerical Modelling

**3.1. Principles of DEM-FDM Coupling Numerical Modelling.** The discrete element method (DEM) has been used widely for studying the mechanism of rock's deformation and failure characteristics microscopically in the field of rock and soil mechanics, for it can reflect physical phenomena such as rock mass failure and fracture propagation [40, 41]. The computing efficiency of DEM, however, compares unfavourably with the finite element method (FEM) or finite difference method (FDM) based on the continuous medium mechanics theory. When the model includes excessive particles, DEM is inappropriate for simulating large-scale rock engineering; the computation may be time-consuming and requires powerful computing capability that PC cannot afford. Whereas its limitation, a discrete-continuum method was adopted [42]. The surrounding rock mass around openings in the desired study area was stimulated by PFC, while other regions by FLAC, which combines virtues such as failure accuracy of DEM and time-saving of FDM.

The basic principle of PFC/FLAC coupling is the exchange of data including forces and velocities between elements from FLAC and particles from PFC along the interfaces. The communication between the codes of PFC and FLAC is achieved by FISH socket connection that resembles TCP/IP transmission over the Internet. It allows the exchange of data in FISH arrays in binary on the same machine or two different machines on the same network without the defect of data loss. A dominant approach of PFC/FLAC coupling described by the Itasca consulting group, shown in Figure 5, has been adopted by the majority [43]. In this approach, the data structure that supports

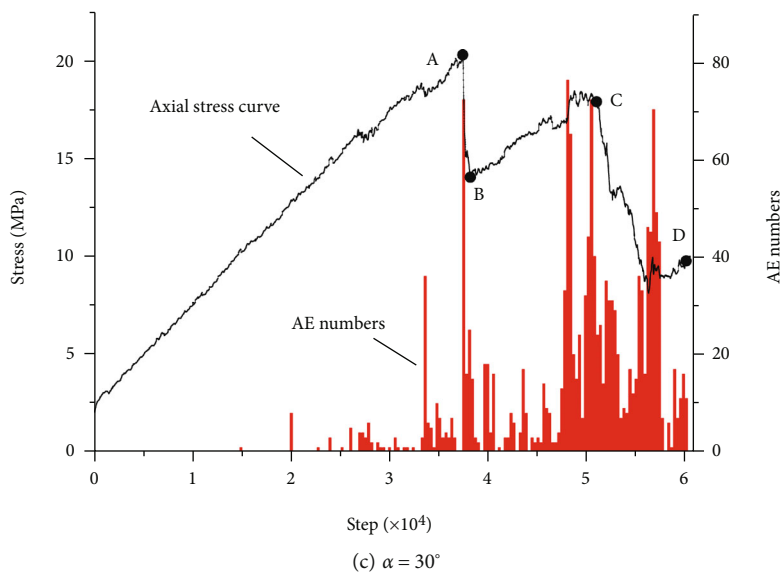
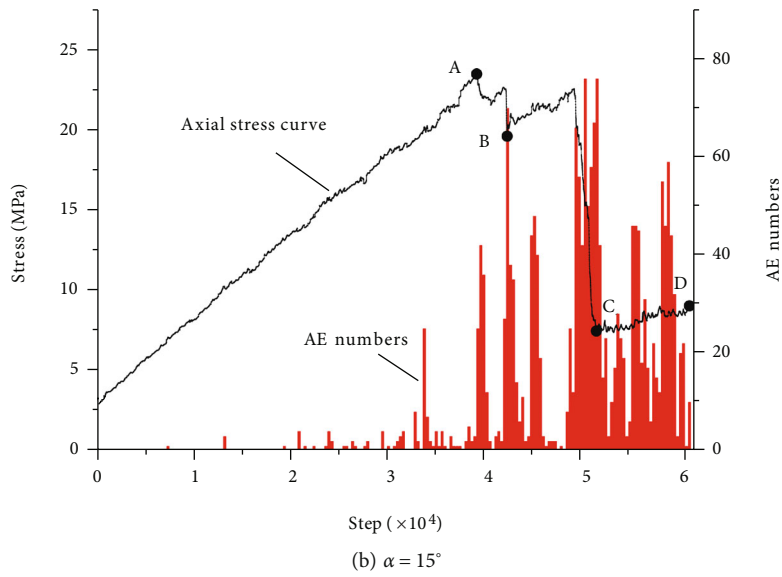
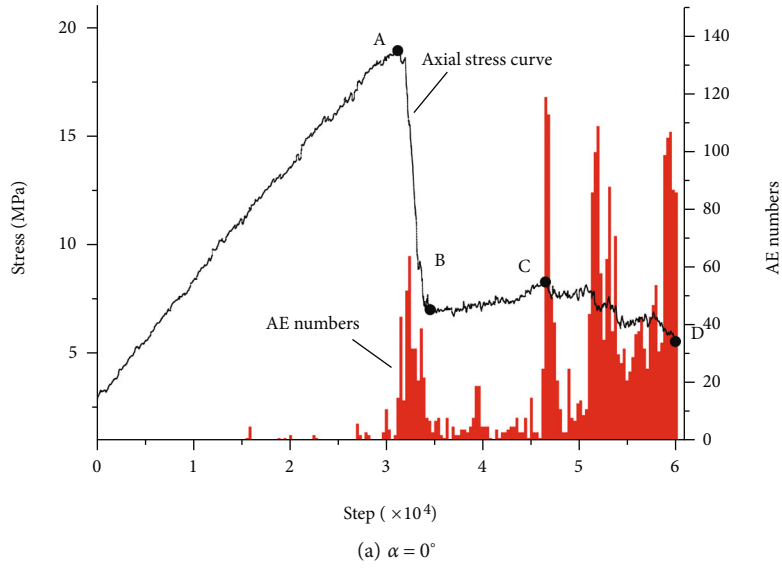
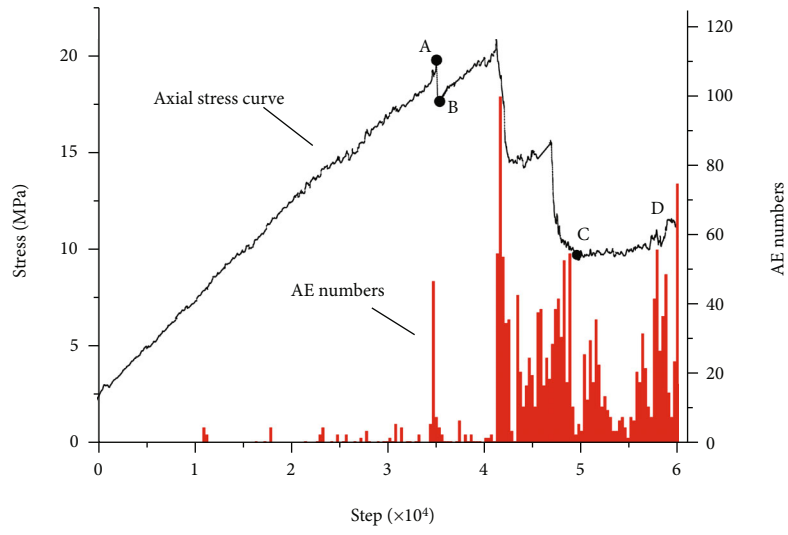
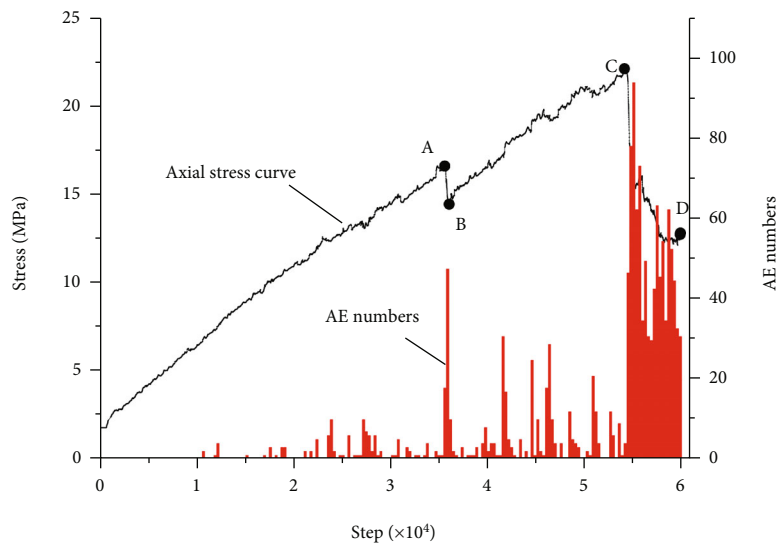


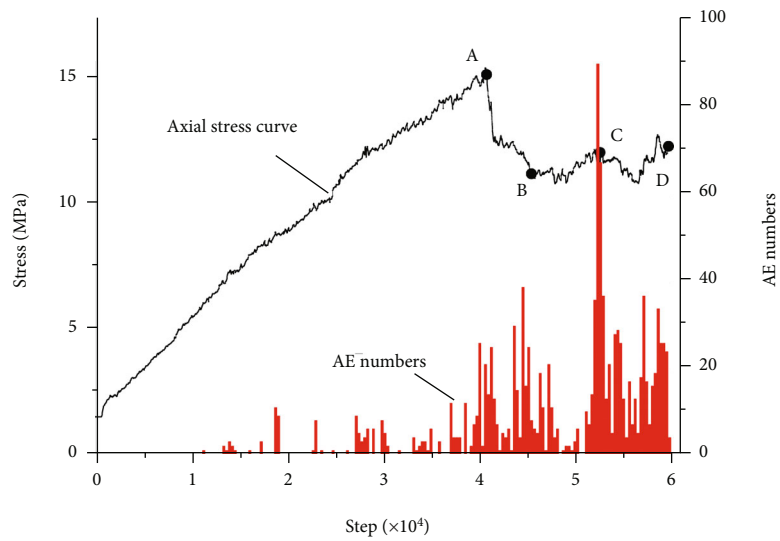
FIGURE 8: Continued.



(d)  $\alpha = 45^\circ$



(e)  $\alpha = 60^\circ$



(f)  $\alpha = 75^\circ$

FIGURE 8: Continued.

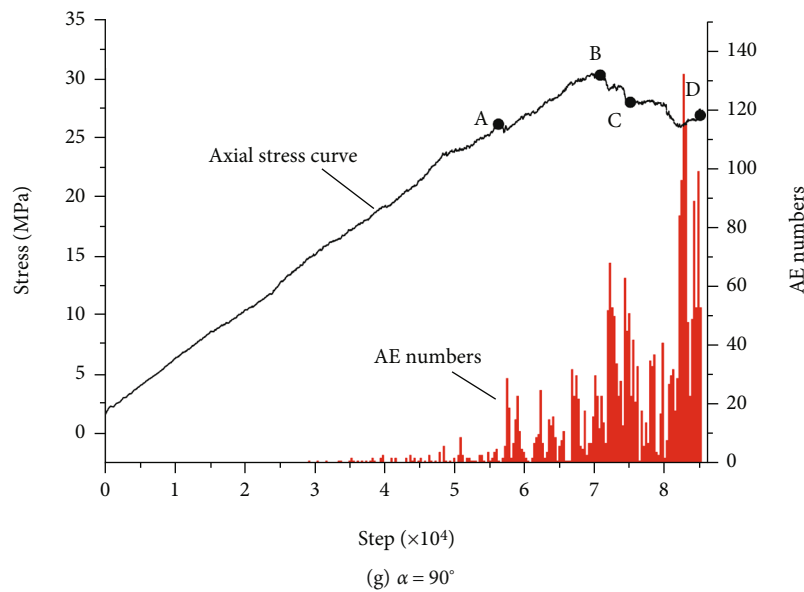


FIGURE 8: Stress curves and AE numbers of numerical specimens.

communication is defined as a segment list. Each segment corresponds to the edge of a FLAC zone along the inclusion boundary. A set of controlled particles is identified in PFC2D by finding the particles that intersect the segments, and each controlled particle is associated with only one segment. The time steps in both codes are identical, which is achieved by running FLAC in static mode and PFC2D with differential density scaling. When a computing cycle completes, the forces at the segment end points are applied directly to the corresponding FLAC grid points and the velocities of the FLAC grid points are passed to PFC2D via the corresponding segment end points; the linear interpolation procedure is used to map these velocities to the PFC2D controlled particles.

The approach above requires neither special modelling skills nor small-sized mesh around the boundary, making PFC/FLAC coupling convenient as well as reducing the number of meshes in the FLAC model. The basic preconditions for this approach, however, are that data along the boundary should be linear distribution rather than erratic fluctuation. It is achievable only if the boundary is far enough from the source of stress disturbance (such as goaf underground), which means that the size of the PFC model should be large enough to realize PFC/FLAC coupling with acceptable coupling precision. In view of this, as shown in Figure 6, a refined approach that transfers the data exchange mode from “segment-particle” to “grid-particle” was proposed. Regular particles were created one by one along the boundary, which accurately matched to certain grids on the other side. Instead of being calculated by the linear interpolation algorithm, the velocities set in each particle were derived from unique corresponding grids during the data exchange process. Though this approach requires higher mesh density in FLAC as well as complex PFC modelling approaches, the increased meshes in FLAC have limited effects on computing speed since FDM, showing an effi-

ciency advantage over DEM, was applied by FLAC. In the actual test, the particle number in PFC is responsible for much of the long computing time of FDM-DEM coupling simulation while the mesh number in FLAC for little. This approach reaches the maximum coupling precision under the condition that the particle number is determined, with computing time considered at the same time.

**3.2. Numerical Models.** The layout of two rectangular openings is illustrated in Figure 7. The distance between two-hole centroids  $d = 20$  m. The connecting angle  $\alpha$  is defined as the angle of the line segment between centroids of two holes with respect to the horizontal direction.

Figure 7 illustrates the layout of two rectangular openings in numerical models. Combined goafs in model 1 were on the same horizontal plane. The connecting angle  $\alpha$  is the angle of the line segment between centroids of two holes with respect to the horizontal direction. In this study, connecting angles from  $0^\circ$  to  $90^\circ$  with an interval of  $15^\circ$  are considered. The size of the rectangular opening and of the DEM models is  $40 \text{ m} \times 20 \text{ m}$  and  $120 \text{ m} \times 120$  (length  $\times$  width), respectively. The shortest distance  $d$  between two openings is 1 m. The mesoparameters of numerical specimens are listed in Table 1.

**3.3. Stress and AE Characteristics.** Acoustic emission (AE) activity is closely related to evolution and propagation of rock defects. Recording AE numbers of goaf models during the failure process under compression can provide significant information about the goaf's instability behaviour, which is conducive to revealing the failure mechanism of rock mass around openings. In numerical simulation, AE events originating from material failure can be accessed by tracking bond breakage between particles. Particles are associated with each other by a defined bond between them. When the bond strength of contact is overcome, strain

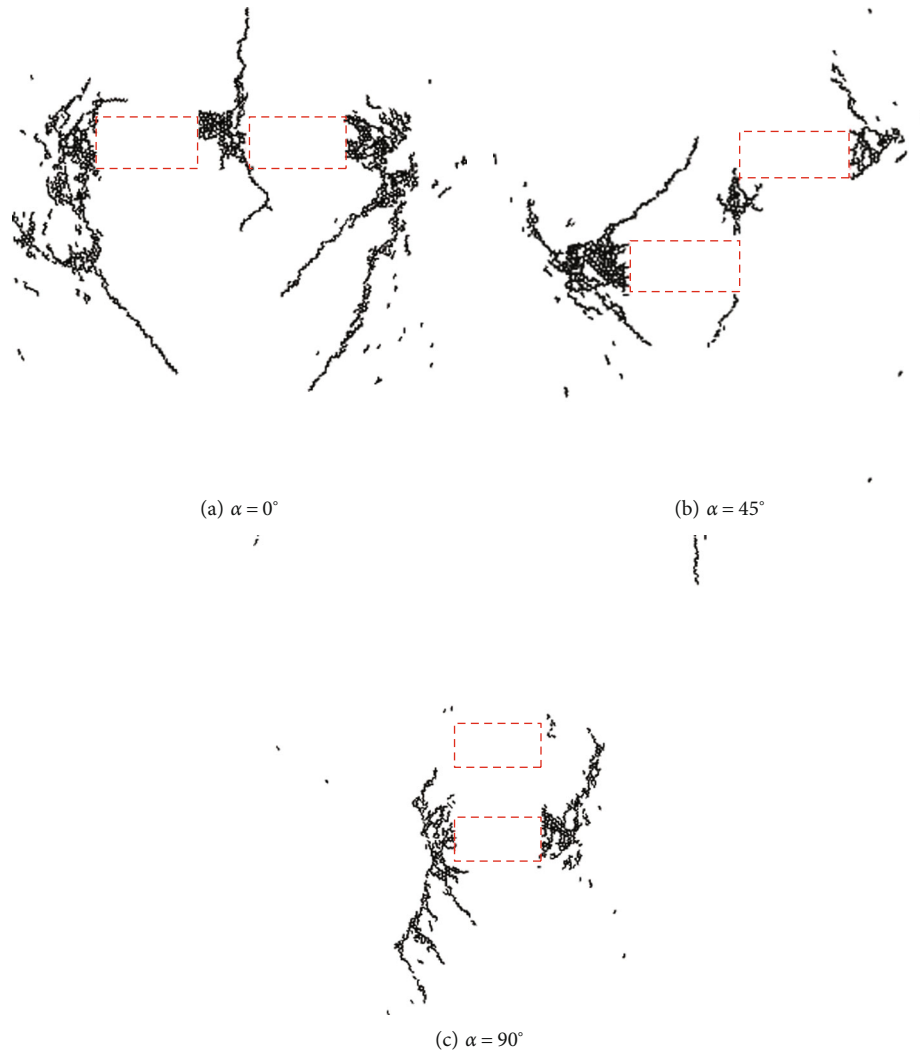


FIGURE 9: Representative failure patterns of numerical models containing two openings.

energy stored in the particle contacts will be released as kinetic energy in the form of a seismic wave that could be an indication of an AE activity, based on which, the simulation of AE can be reached [44]. This method has been widely adopted in the field of rock mass engineering. Although the particle size and number are limited by the computing capability of computers, AE characteristic in rock revealed by PFC numerical simulation is consistent with that revealed by laboratory tests, which is very significant to the study of AE behaviours in rock under different conditions [45].

The stress condition at the DEM model boundaries is relatively stable, which cannot reflect the stress change in the rock mass around the openings. The stress of a monitoring point, which is 60 m right above and away from the middle point of the line segment between the centroids of the two openings, was recorded. The stress curves as well as acoustic emission numbers obtained in the simulations on different models are shown in Figure 8. At the stages of initial loading, each model is mostly in linear elastic deformation, with little AE events observed. Then, AE events become more and more frequent with slight stress curve

fluctuation in the prepeak stage. Some typical points with significant AE burst and stress change are marked in each curve. It can be seen that there is an obvious correlation between AE event and stress evolution. Almost every AE burst happens with corresponding stress fluctuation, which may indicate sudden appearance of failure within rock mass. Large numbers of AE events emerged in the postpeak stage with intensive failure, but because of the confinement of the far-field rock mass, postpeak stress remains stable to the end of calculation.

**3.4. Failure Patterns.** The ultimate failure patterns around openings with three representative connecting angles are plotted in Figure 9. When two openings exist at the same horizontal level ( $\alpha = 0^\circ$ ), cracks initiate at the top of the connecting area between them. Then, intensive failure appears in the connecting area, indicating that the connecting area lost its bearing capacity. Tensile cracks initiate at the top and the bottom of the damaged connecting rock mass, respectively, and propagate along the loading direction. At the same time, failure is observed in the corners of the

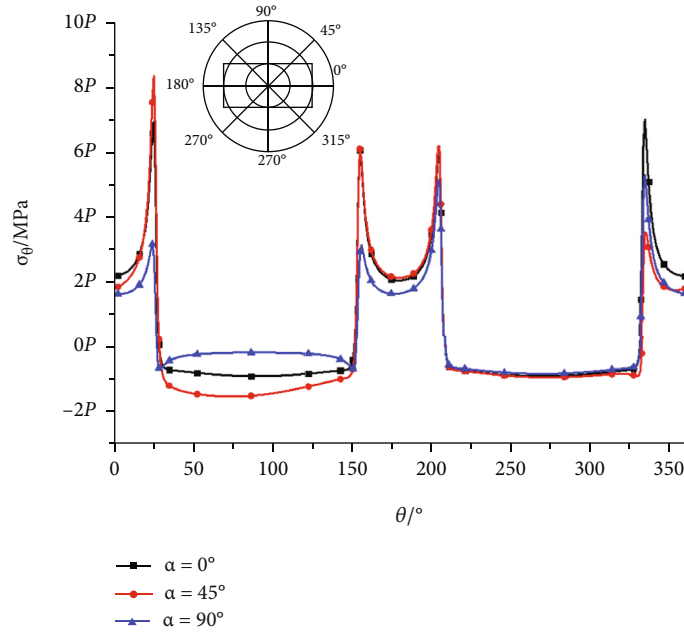


FIGURE 10: The hoop stress distribution curves around Hole 1.

openings. Later, tensile cracks from the damaged pillar continue to develop; both side walls of the goaf are squeezed to deform and spalled subsequently, resulting in sloughing at last. Lots of failure appears around openings and causes the instability of the surrounding rock mass. When  $\alpha = 45^\circ$ , failure only exists in a narrow area between the floor of the upper goaf and the roof of the lower goaf; adjacent side walls between two openings (the left side wall of the upper goaf and the right of the lower) both remain almost intact. When  $\theta = 90^\circ$ , failure forms at the side walls of the lower opening and spreads around them. Inclined cracks from the failure zone are observed. All the failure zones, however, mainly concentrate around the lower opening, contrary to what happened to the upper goaf, the region around which remains almost intact with only little failure near the opening's corners.

The analytical stress solutions around Hole 1 for the three representative kinds of two-opening systems under uniaxial compressive stress conditions, whose failure patterns are given in Figure 9, are plotted in Figure 10. It can be seen that compressive stress concentration appears at opening corners and tensile stress is observed in the roof and floor of the openings in all cases, but stress distribution and concentration level vary from case to case. When the connecting angle is  $0^\circ$  or  $90^\circ$ , two openings are symmetrical to each other about X or Y axis. Accordingly, the stress in the two-opening system also shows symmetrical distribution. When the connecting angle is  $45^\circ$ , the stress concentration at the upper left corner of Hole 1 close to the adjacent hole is much stronger than that in the two-opening system with other connecting angles. Combining Figures 9 and 10 shows that when  $\alpha = 0^\circ$ , the highest compressive stress concentration appears in the connecting area, which leads to the coalescence between two openings. In contrast, when  $\alpha = 90^\circ$ , the stress around the connecting area is relatively lower than

that in other areas and no failure is found in this area in numerical simulation.

#### 4. Discussion

This study emphasizes the stress distribution and failure patterns of rock mass surrounding openings within a large-scale area without model boundary effect. As the numerical model size is much greater than the opening size, the failure patterns of rock mass around openings in numerical models are in line with the stress concentration areas determined by analytical stress solutions. Though rock mass is a kind of elastic-plastic material, for hard rock with strong brittleness, it is mainly subjected to elastic deformation in the pre-peak stage. Therefore, the analytical elastic solutions for plates containing openings can be an important reference of failure predication within the surrounding rock mass.

There have been a great number of studies on the mechanical behaviour of rock mass containing openings or flaws based on laboratory experiments. However, mechanical tests for rock specimens may lead to an evitable boundary effect, which may significantly interfere with the stress distribution and fracturing evolution of rock mass around openings. Many laboratory tests show that the rock specimens are finally broken by tensile or shear cracks connecting opening corners and specimen boundaries. Figure 11 presents the failure patterns of rock specimens containing two rectangular openings under uniaxial compression tests conducted by Zhou et al. [29]. Comparing Figure 11 with Figure 9 shows that the coalescence patterns between openings in rock specimens agree well with the corresponding large-scale numerical models. However, for all rock specimens, the instability is dominated by macro shear or tensile cracks from openings and through the whole specimen, which are suppressed in the large-scale numerical models.

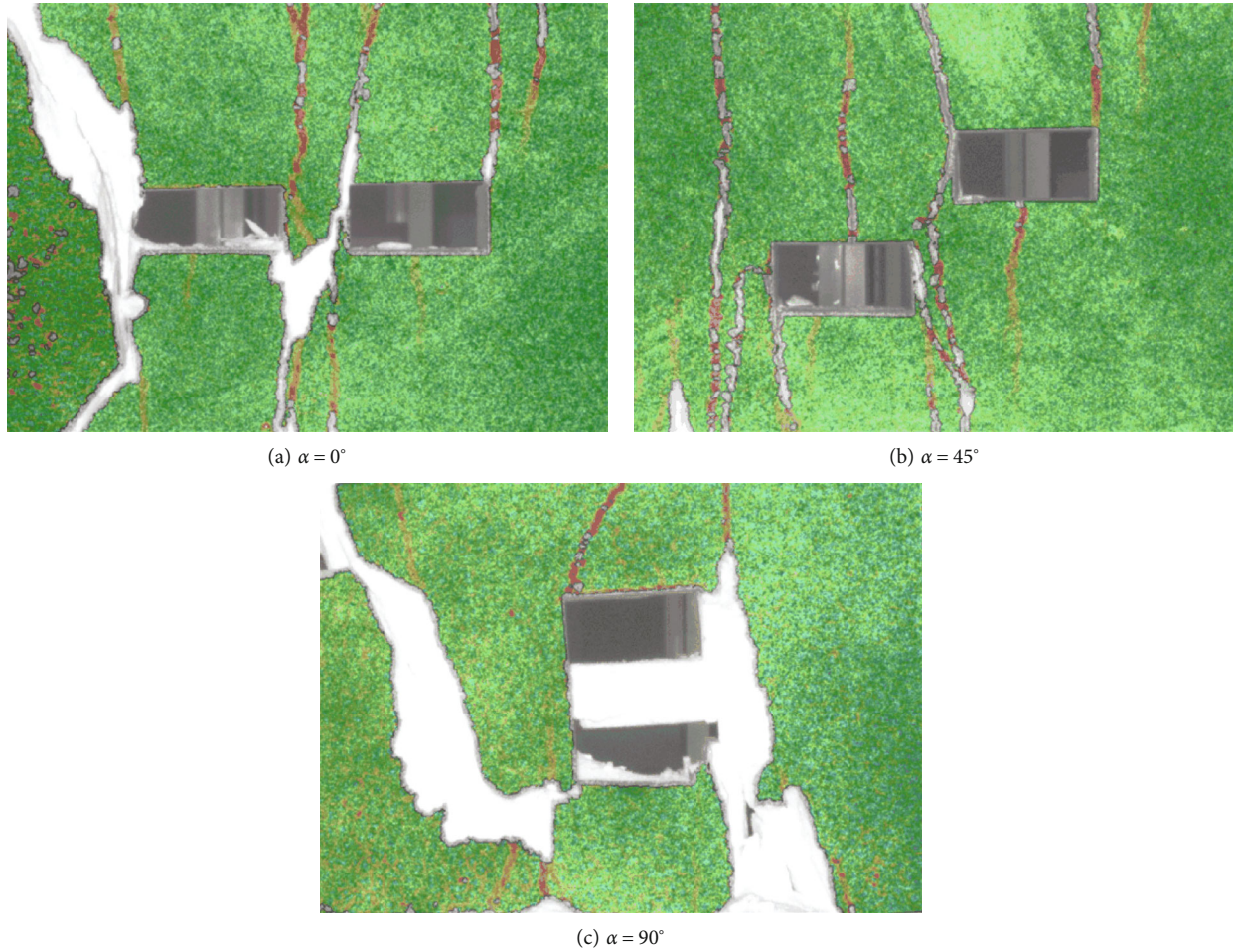


FIGURE 11: Representative failure patterns of rock specimens containing two openings (after Zhou et al. [29]).

For the one hand, strong interaction between the rock specimen boundaries and openings may promote crack propagation from openings to boundaries. For another, rock mass in the large-scale area may also contribute to confining the development of cracks. Therefore, the laboratory tests may exaggerate the influence of deep-buried openings on rock mass stability. The large-scale numerical modelling via the PFC-FLAC coupling method is expected to be an important addition to the study of the mechanical behaviour of deep-buried surrounding rock mass.

## 5. Conclusions

In this study, the Schwarz alternating method based on complex variable theory was used to calculate the stress solution for the two-opening system. In addition, PFC-FLAC coupling numerical modelling was employed to study the mechanical behaviour of rock mass containing two rectangular openings with different connecting angles underground. With the combination of numerical and analytical solutions, the effect of connecting angles on the stress distribution and failure characteristics of rock mass around openings was discussed. The main conclusions of this paper include the following:

- (1) According to the analytical stress solutions for elastic plates containing two rectangular openings, the existence of confining stress within a certain range contributes to relief of the tensile stress concentration around the openings, which is supposed to help improve the stability of rock mass around openings. With the increase of lateral pressure coefficient, the stress field changes gradually and tensile stress concentration may appear again in new areas once it reaches a certain level
- (2) The opening layout mainly affects the stress distribution in the connecting area between two adjacent openings, which further dominates the coalescence pattern and stability of the two-opening system. Under uniaxial compression, the connecting area is a high compressive stress concentration area in which appears coalescence failure during numerical tests when the two openings are arranged horizontally. When the connecting angle is  $90^\circ$ , the connecting area is a low-stress area and remains intact during the numerical test
- (3) The AE characteristics in the numerical models show that massive failure mainly happens in rock mass in the postpeak stage, which follows the coalescence between the two openings. In the prepeak stage, rock

mass around openings is mainly subjected to elastic deformation. The positions of initial failure always agree well with the stress concentration areas determined by analytical solutions

## Data Availability

The figures and tables used to support the findings of this study are included in the article.

## Conflicts of Interest

The authors declare that there is no conflict of interest regarding the publication of this paper.

## Acknowledgments

This research was funded by the Fundamental Research Funds for the Central Universities, grant number 2020QN44.

## References

- [1] R.-H. Cao, R. Yao, T. Hu, C. Wang, K. Li, and J. Meng, "Failure and mechanical behavior of transversely isotropic rock under compression-shear tests: laboratory testing and numerical simulation," *Engineering Fracture Mechanics*, vol. 241, article 107389, 2021.
- [2] Z. Zhou, X. Cai, X. Li, W. Cao, and X. du, "Dynamic response and energy evolution of sandstone under coupled static-dynamic compression: insights from experimental study into deep rock engineering applications," *Rock Mechanics and Rock Engineering*, vol. 53, no. 3, pp. 1305–1331, 2020.
- [3] X. Cai, Z. Zhou, L. Tan, H. Zang, and Z. Song, "Fracture behavior and damage mechanisms of sandstone subjected to wetting-drying cycles107109," *Engineering Fracture Mechanics*, vol. 234, 2020.
- [4] L. Tan, T. Ren, X. Yang, and X. He, "A numerical simulation study on mechanical behaviour of coal with bedding planes under coupled static and dynamic load," *International Journal of Mining Science and Technology*, vol. 28, no. 5, pp. 791–797, 2018.
- [5] K. Zhou, L. Dou, S. Gong, J. Li, J. Zhang, and J. Cao, "Study of rock burst risk evolution in front of deep longwall panel based on passive seismic velocity tomography," *Geofluids*, vol. 2020, Article ID 8888413, 14 pages, 2020.
- [6] Z. Song, H. Konietzky, and X. Cai, "Modulus degradation of concrete exposed to compressive fatigue loading: insights from lab testing," *Structural Engineering and Mechanics*, vol. 78, no. 3, 2021.
- [7] X. Cai, Z. Zhou, L. Tan, H. Zang, and Z. Song, "Water saturation effects on thermal infrared radiation features of rock materials during deformation and fracturing," *Rock Mechanics and Rock Engineering*, vol. 53, no. 11, pp. 4839–4856, 2020.
- [8] L. Zeng, W. Lyu, J. Li et al., "Natural fractures and their influence on shale gas enrichment in Sichuan Basin, China," *Journal of Natural Gas Science and Engineering*, vol. 30, pp. 1–9, 2016.
- [9] B. J. Carter, E. Z. Lajtai, and Y. Yuan, "Tensile fracture from circular cavities loaded in compression," *International Journal of Fracture*, vol. 57, no. 3, pp. 221–236, 1992.
- [10] M. A. Lotidis, P. P. Nomikos, and A. I. Sofianos, "Numerical simulation of granite plates containing a cylindrical opening in compression," *Procedia Engineering*, vol. 191, pp. 242–247, 2017.
- [11] E. Dzik and E. Lajtai, "Primary fracture propagation from circular cavities loaded in compression," *International Journal of Fracture*, vol. 79, no. 1, pp. 49–64, 1996.
- [12] H. Wu and D. Ma, "Fracture response and mechanisms of brittle rock with different numbers of openings under uniaxial loading," *Geomechanics and Engineering*, vol. 25, no. 6, pp. 481–493, 2021.
- [13] H. Wu, P. H. Kulatilake, G. Zhao, W. Liang, and E. Wang, "A comprehensive study of fracture evolution of brittle rock containing an inverted U-shaped cavity under uniaxial compression," *Computers and Geotechnics*, vol. 116, article 103219, 2019.
- [14] P. Dharmin, J. Khushbu, and P. Chetan, "A review on stress analysis of an infinite plate with cut-outs," *International Journal of Scientific and Research Publications*, vol. 2, no. 11, pp. 1–7, 2019.
- [15] X.-L. Gao, "A general solution of an infinite elastic plate with an elliptic hole under biaxial loading," *International Journal of Pressure Vessels and Piping*, vol. 67, no. 1, pp. 95–104, 1996.
- [16] A. Sharma, B. P. Khushbu, and C. P. Nirav, "A general solution for the stresses around internally pressurized circular hole in symmetric laminates," *Stress*, vol. 2, p. 12, 2011.
- [17] D. S. Sharma, N. P. Patel, and K. C. Panchal, "Stress distribution around triangular hole in orthotropic plate," *Nirma University Journal of Engineering and Technology (NUJET)*, vol. 1, no. 2, pp. 61–65, 2000.
- [18] H. Wu, G. Zhao, and W. Liang, "Mechanical properties and fracture characteristics of pre-holed rocks subjected to uniaxial loading: a comparative analysis of five hole shapes," *Theoretical and Applied Fracture Mechanics*, vol. 105, article 102433, 2020.
- [19] V. Ukadgaonker and P. Awastare, "A novel method of stress-analysis of an infinite-plate with rounded corners of a rectangular hole under uniform edge loading," *Indian Journal of Engineering & Materialsences*, vol. 1, no. 1, pp. 17–25, 1994.
- [20] V. Ukadgaonker and P. Awastare, "A novel method of stress analysis of an infinite plate with elliptical hole with uniform loading at infinity," *Journal of The Institution of Engineers (India)*, vol. 73, pp. 309–311, 1993.
- [21] V. Ukadgaonker and P. Awastare, "A novel method of stress-analysis of infinite-plate with circular hole with uniform loading at infinity," *Indian Journal of Technology*, vol. 31, no. 7, pp. 539–541, 1993.
- [22] V. Ukadgaonker and D. Rao, "Stress distribution around triangular holes in anisotropic plates," *Composite Structures*, vol. 45, no. 3, pp. 171–183, 1999.
- [23] D. S. Sharma, "Stress distribution around circular/elliptical/triangular holes in infinite composite plate," *Engineering Letters*, vol. 20, no. 1, p. 1, 2012.
- [24] L. Tan, T. Ren, L. Dou, X. Yang, M. Qiao, and H. Peng, "Analytical stress solution and mechanical properties for rock mass containing a hole with complex shape," *Theoretical and Applied Fracture Mechanics*, vol. 114, article 103002, 2021.
- [25] L. Tan, T. Ren, L. Dou, X. Cai, X. Yang, and Q. Zhou, "Dynamic response and fracture evolution of marble specimens containing rectangular cavities subjected to dynamic loading," *Bulletin of Engineering Geology and the Environment*, vol. 80, no. 10, pp. 7701–7716, 2021.

- [26] L. Q. Zhang, Z. Q. Yue, C. F. Lee, L. G. Tham, and Z. F. Yang, "Stress solution of multiple elliptic hole problem in plane elasticity," *Journal of Engineering Mechanics*, vol. 129, no. 12, pp. 1394–1407, 2003.
- [27] L.-Q. Zhang and A.-Z. Lu, "An analytic algorithm of stresses for any double hole problem in plane elastostatics," *Journal of Applied Mechanics*, vol. 68, no. 2, pp. 350–353, 2000.
- [28] L. Tan, T. Ren, L. Dou, X. Yang, X. Cai, and M. Qiao, "Analytical stress solution for rock mass containing two holes based on an improved Schwarz alternating method," *Theoretical and Applied Fracture Mechanics*, vol. 116, article 103092, 2021.
- [29] Z. Zhou, L. Tan, W. Cao, Z. Zhou, and X. Cai, "Fracture evolution and failure behaviour of marble specimens containing rectangular cavities under uniaxial loading," *Engineering Fracture Mechanics*, vol. 184, pp. 183–201, 2017.
- [30] X.-D. Zhao, H.-X. Zhang, and W.-C. Zhu, "Fracture evolution around pre-existing cylindrical cavities in brittle rocks under uniaxial compression," *Transactions of Nonferrous Metals Society of China*, vol. 24, no. 3, pp. 806–815, 2014.
- [31] P. Lin, R. H. Wong, and C. Tang, "Experimental study of coalescence mechanisms and failure under uniaxial compression of granite containing multiple holes," *International Journal of Rock Mechanics and Mining Sciences*, vol. 77, pp. 313–327, 2015.
- [32] M. Jia, Y. Yang, B. Liu, and S. Wu, "PFC/FLAC coupled simulation of dynamic compaction in granular soils," *Granular Matter*, vol. 20, no. 4, p. 76, 2018.
- [33] C. Shi, W. Li, and Q. Meng, "A dynamic strain-rate-dependent contact model and its application in Hongshiyuan landslide," *Geofluids*, vol. 2021, Article ID 9993693, 23 pages, 2021.
- [34] D. Saiang, "Stability analysis of the blast-induced damage zone by continuum and coupled continuum-discontinuum methods," *Engineering Geology*, vol. 116, no. 1-2, pp. 1–11, 2010.
- [35] B. Brady and E. T. Brown, *Rock mechanics for underground mining*, Allen & Unwin, 2006.
- [36] L. Müller, "Rock mechanics," *Rock Mechanics*, vol. 6, no. 1, pp. 1-2, 1974.
- [37] J. H. Zhu, J. H. Yang, G. P. Shi, J. Wang, and J. P. Cai, "Calculating method for conformal mapping from exterior of unit circle to exterior of cavern with arbitrary excavation cross-section," *Rock and Soil Mechanics*, vol. 1, pp. 175–183, 2014.
- [38] L. Tan, T. Ren, L. Dou, X. Yang, G. Wang, and H. Peng, "Analytical stress solution and numerical mechanical behavior of rock mass containing an opening under different confining stress conditions," *Mathematics*, vol. 9, no. 19, p. 2462, 2021.
- [39] D. S. Sharma, "Stress distribution around polygonal holes," *International Journal of Mechanical Sciences*, vol. 65, no. 1, pp. 115–124, 2012.
- [40] Z. Song, H. Konietzky, and M. Herbst, "Bonded-particle model-based simulation of artificial rock subjected to cyclic loading," *Acta Geotechnica*, vol. 14, no. 4, pp. 955–971, 2019.
- [41] J. Wang, S. Yang, W. Wei, J. Zhang, and Z. Song, "Drawing mechanisms for top coal in longwall top coal caving (LTCC): a review of two decades of literature," *International Journal of Coal Science & Technology*, 2021.
- [42] B. Indraratna, N. T. Ngo, C. Rujikiatkamjorn, and S. W. Sloan, "Coupled discrete element-finite difference method for analysing the load-deformation behaviour of a single stone column in soft soil," *Computers and Geotechnics*, vol. 63, pp. 267–278, 2015.
- [43] W. Song and R. Hong, "PFC/FLAC coupled numerical simulation of excavation damage zone in deep schist tunnel," *Applied Mechanics & Materials*, vol. 236-237, pp. 622–626, 2012.
- [44] J. F. Hazzard and R. P. Young, "Simulating acoustic emissions in bonded-particle models of rock," *International Journal of Rock Mechanics and Mining Sciences*, vol. 37, no. 5, pp. 867–872, 2000.
- [45] M. Cai, P. K. Kaiser, H. Morioka et al., "FLAC/PFC coupled numerical simulation of AE in large-scale underground excavations," *International Journal of Rock Mechanics and Mining Sciences*, vol. 44, no. 4, pp. 550–564, 2007.